# Thèse

pour obtenir le grade de Docteur d'Aix-Marseille Université

en Océanographie

# Dynamique du phytoplancton en mer Méditerranée: Approches par mesures à haute fréquence, modélisation et statistiques bayésiennes

Mathilde E. Dugenne

Soutenue le 06 Juin 2017 devant le jury composé de:

Mme Sophie Rabouille, LOV, Rapporteur
Mr Samuel Soubeyrand, BioSP, Rapporteur
Mme Claude Estournel, LA, Examinatrice
Mme Melika Baklouti, MIO, Examinatrice
Mme Mélilotus Thyssen, MIO, Membre invitée
Mr Francesco D'Ovidio, LOCEAN, Examinateur
Mr Denys Pommeret, I2M, Directeur de thèse
Mr Gérald Grégori, MIO, Co-directeur de thèse

**Résumé**

L'ensemble des écosystèmes marins repose sur le phytoplancton pour convertir le carbone atmosphérique en matière organique par le processus de photosynthèse. Deux approches sont présentées pour mesurer la productivité du phytoplancton en tenant compte de l'évolution temporelle de la taille des cellules. Elles traduisent, par essence, l'assimilation progressive du carbone inorganique au cours du cycle de vie d'une cellule et sa réallocation d'une génération à l'autre au moment de la division cellulaire. Dans le milieu naturel, ce flux de carbone dépend des communautés phytoplanctoniques et de leurs sensibilités. L'observation du phytoplancton dans un milieu perturbé à faible échelle de temps et/ou d'espace est essentielle pour anticiper les effets du changement climatique. La Méditerranée en particulier est amenée à modifier rapidement son climat et les populations qu'elle abrite. En mer Méditerranée comme dans l'océan global, les campagnes de mesures sont à la base des scénarios qui traduisent l'impact de l'environnement sur le fonctionnement et la capacité du phytoplancton à tamponner les émissions de gaz issues de l'activité humaine.

L'ensemble des conditions qui régulent la croissance du phytoplancton est groupé au sein de la niche écologique (Hutchinson, 1957). L'une des causes principales du déclin ou de la prolifération des populations naturelles provient de la régulation rapide de leur capacité de reproduction par la température, la lumière ou les sels nutritifs. La description des niches est un enjeu majeur pour le Panel Intergouvernemental sur le Changement Climatique qui cherche à caractériser les accumulations soudaines de phytoplancton à la surface du globe (e.g. efflorescences). Les *types fonctionnels* regroupent des populations aux traits adaptatifs singuliers qui leur permettent de se distinguer après une perturbation. En écologie, ces traits servent à définir les stratégies de croissance de populations aux niches partitionnées. Typiquement, les cellules de petites tailles montrent des capacités d'assimilation des nutriments accrues alors que les cellules de grandes tailles sont peu contrôlées par les échelons trophiques supérieurs aux taux de croissance plus faible. L'appareil pigmentaire des cellules est aussi un trait distinct qui permet de colonisé des milieux défavorables situés en profondeur.

Les prédictions issues de la modélisation sont marquées par de fortes incertitudes qui peuvent être assimilées par des programmes de suivi à long terme du phytoplancton dans son environnement naturel (Hallegraeff, 2010). Ces suivis devraient permettre d'identifier les acteurs clé de la production primaire en milieu marin en mesurant la réponse à plus ou moins court terme de *types fonctionnels* soumis à des gradients hydrologiques. L'évaluation du taux de croissance du phytoplancton dans son milieu naturel est donc essentielle. Plusieurs modèles de populations, qui tiennent compte de la diversité des cellules au sein d'une population donnée, valident ici l'approche par cytométrie en flux pour mesurer le taux de croissance intrinsèque de groupes ataxonomiques. Même s'ils ne se composent pas de populations au sens génétique du terme, ces groupes sont formés de cellules aux stratégies de croissance adaptées à la température du milieu, à l'optimisation de la collecte d'énergie lumineuse pour la photosynthèse ou encore à la compétition pour une ressource limitante.

Mots-clé : Phytoplancton / Taux de croissance / Production primaire / Niche écologique / mer Méditerranée / Traits adaptatifs

**Abstract**

The photosynthetic conversion of atmospheric carbon into organic matter is important for all marine ecosystems. Two approaches are presented to measure phytoplankton productivity from the temporal evolution of cells' size. They traduce the incremental assimilation of inorganic carbon during cells' lifespan, before its reallocation to the next generation of cells produced by division. In the sea, the carbon flux depends on phytoplankton communities and their inherent sensitivity. The short time/spatial scale monitoring of phytoplankton in disturbed ecosystems is essential to foresee the Global change. Climate and inhabiting populations will especially reacts to Global change in the Mediterranean Sea. In the Mediterranean and in the global Ocean, observations programs are fundamental for climatic scenario used to predict the effect of environmental changes on the buffering capacity of $CO_2$ emissions induced by phytoplankton productivity.

The ecological niche groups the integrated conditions of phytoplankton growth (Hutchinson, 1957). One of the major source of natural populations' decline or bloom is caused by the intrinsic regulation of growth by temperature, light and dissolved nutrients. The main objective of the Intergovernmental Panel on Climate Change is to sufficiently describe phytoplankton' niche to understand the recurrent blooms observed all over the globe. Functional types group populations with distinct traits, adapted to peculiar perturbations. In ecology, functional traits are used to define the growth strategies of populations with separated niches. In general, small cells show a better affinity for limiting nutrients although large cells manage to efficiently escape from the top-down pressure. The pigments apparatus is also distinct in population found in unfavourable places located in depth.

The outcomes of climatic simulations display a large uncertainty that may be reduced by the assimilation of dataset collected during long-term surveys of natural phytoplankton populations (Hallegraeff, 2010). Surveys should be used to identify the main actor of primary productivity in the ocean by measuring their growth capacity under wide hydrological gradients. The evaluation of *in situ* growth rates is essential during this process. Several population models which take into account the diversity of cells stages, yield to valide approximations of growth rates for ataxonomic groups defined by flow cytometry. Although they are not considered as strict populations, groups show distinct growth strategies adapted to *in situ* temperature, light collection or competition for a limited ressource.

Key words: Phytoplankton / Growth rates / Primary production / Growth niche / Mediterranean Sea / Adaptive traits

*Un évènement rare ne signifie pas qu'il a une probabilité nulle d'arriver. Nous sommes actuellement 7,493,817,845 sur Terre*

*1 chance sur 7,493,817,845*

*Merci pour cette chance*

# Contents

# 1.0 Introduction générale

Les objectifs de cette thèse peuvent être résumés en deux points, qui ont tous deux fait l'objet d'une inférence bayésienne:

1. Déterminer les taux de croissance et de production *in situ* du phytoplancton grâce à la mesure à haute fréquence de la dynamique intrinsèque des cellules par cytométrie en flux automatisée.

2. Définir la niche hydrologique de différents groupes de phytoplancton à partir de l'estimation de ces taux en prenant en considération l'adaptation thermique des cellules et leur limitation potentielle par la lumière et les sels nutritifs.

Ces deux points sont détaillés dans ce manuscript. L'introduction générale (chapitre 1) présente l'ensemble des sujets (section 1.1), des mécanismes (sections 1.2 et 1.3) et des contextes (section 1.4) abordés dans les chapitres suivants. Le modèle de taux de croissance du phytoplancton est introduit et validé dans le chapitre 2. La première application de ce modèle est exposée dans le chapitre 3, avec des données acquises dans l'étang de Berre en octobre 2011. En 2013, deux campagnes hauturières ont permis d'estimer les taux de production primaire associés au bassin méditerranéen nord occidental en période de plongée d'eau profonde et d'efflorescence. Ces données, détaillées dans le chapitre 4, ont servi à définir la niche écologique de plusieurs groupes fonctionnels phytoplanctoniques par rapport à la température de l'eau, les teneurs en sels nutritifs et la quantité de lumière perçue disponible pour la photosynthèse (chapitre 5). L'inférence des paramètres qui déterminent l'effet de ces stimuli sur la croissance du phytoplancton est finalement décrite dans les chapitres 6 et 7, dans le cadre des campagnes DeWEX et HotMix.

## 1.1 Le phytoplancton: Définition, rôle et impact

*La photosynthèse du phytoplancton: source d'$O_2$, puits de $CO_2$*

Lorsqu'un micro-organisme marin unicellulaire libre ou membre d'une colonie vit de la photosynthèse tout en étant tributaire des courants, il fait parti du phytoplancton (du grec *plante dérivante*).
A l'instar des plantes terrestres, le phytoplancton nourrit l'ensemble des réseaux trophiques marins à partir de la matière organique produite par l'assimilation du $CO_2$ dissous et la récolte d'énergie lumineuse par les pigments photosynthétiques. Ces pigments sont des molécules photosensibles qui, chez les cellules eucaryotes, sont organisées au sein d'organites spécialisés dérivés de l'endosymbiose de cyanobactéries (Bhattacharya et Medlin, 1998; Falkowski *et al.*, 2004), les chloroplastes (Figure 1).

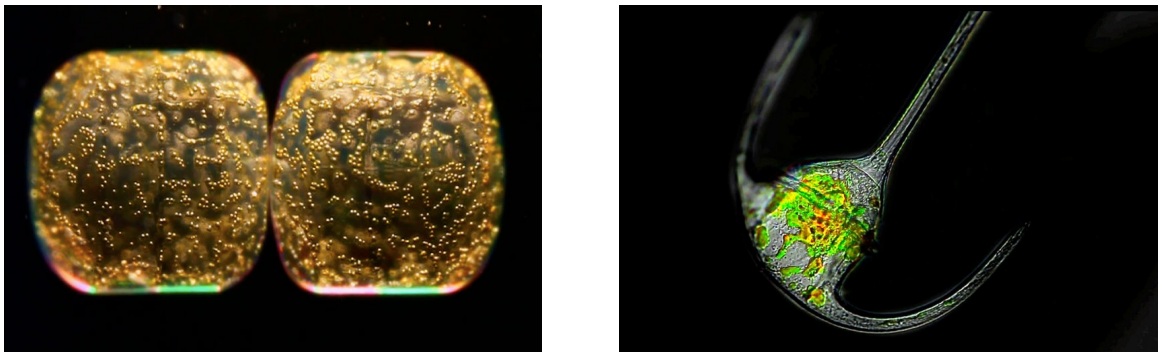

(a) Diatomée centrique aux chloroplastes apparents (C. Sardet, Tara Oceans)

(b) Ceratium contenant des chloroplastes représentés en vert (U. et C. Sardet)

Figure 1.1: Les chloroplastes contiennent les pigments qui récoltent l'énergie lumineuse pour la photosynthèse (photos: planktonchronicles.org)

La synthèse de glucides, régie par la formule (E 1.1):

$$6\,CO_2 + 12\,H_2O + \text{lumière} \rightarrow C_6H_{12}O_6 + 6\,H_2O + 6O_2 \tag{1.1}$$

est due à la récolte de l'énergie lumineuse et au transfert d'électrons (Figure 2a), catalysé par le centre de réaction des photosystèmes I et II, qui fournit à la fois le pouvoir réducteur (NADPH) et l'énergie (ATP) nécessaire aux réactions métaboliques du cycle de Calvin (Figure 2b). La réduction du $CO_2$ dissous en glucides contribue à tamponner les émissions anthropiques du gaz à effet de serre depuis l'essor de l'ère industrielle. C'est par le biais de son assimilation par le phytoplancton et de son transfert vers les sédiments de l'océan profond, processus connu sous le terme de pompe biologique de carbone (Siegenthaler et Sarmiento, 1993; Falskoswki *et al.*, 1998), que ces organismes ont contribué à la sequestration de 30% des émissions de $CO_2$ anthropique (Sabine, 2004; Khatiwala *et al.*, 2013; Le Quéré *et al.*, 2015). Chaque année, entre 5 et 15 Pg de carbone sont transférés vers l'océan profond soit par transfert direct du phytoplancton par agrégation et sédimentation soit après avoir transité par d'autres échelons trophiques (Henson *et al.*, 2011). L'une des voies indirectes alimente la boucle microbienne (Azam, 1983) via la décomposition de la matière organique particulaire (POC) par les bactéries hétérotrophes.

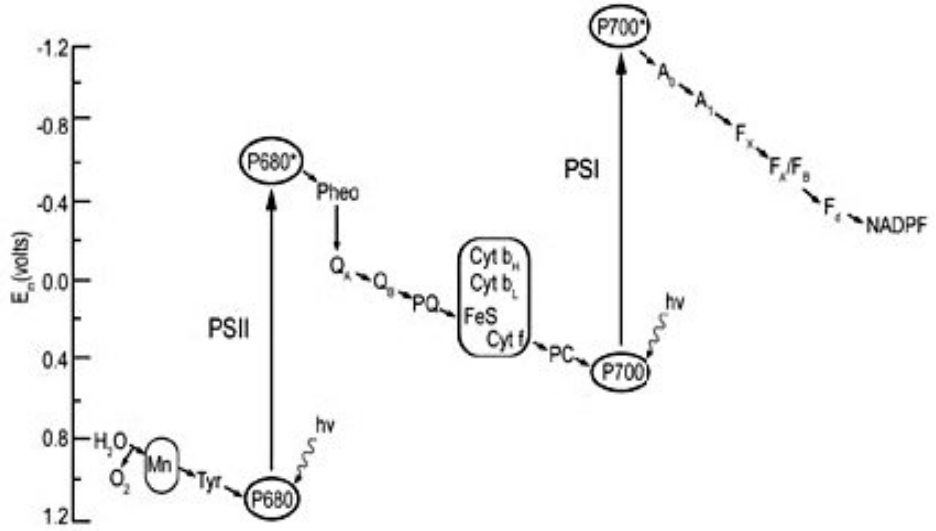


(a) Le schéma en Z des photosystèmes (PS) I et II eucaryotes. La chlorophylle *a* du centre réactionnel du PS II absorbe les photons (h$\nu$) à 680 nm (P680). Cette molécule capte un électron et devient énergiquement instable (P680*). L' électron active la production d'ATP par la pompe à protons ATP synthase. Il est ensuite transféré via une chaîne de cytochromes (Cyt) jusqu'au PS I. Le centre réactionnel du PS I se libère de l'électron énergétique pour servir à la production de NADPH.

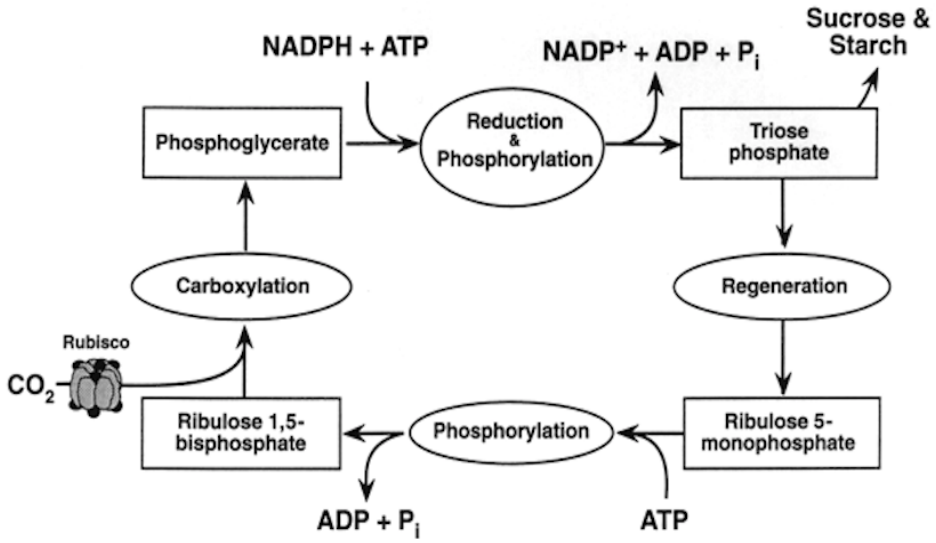


(b) Le cycle de Calvin. L'ATP et le NADPH produits au cours du transfert d'électrons apportent l'énergie et le pouvoir réducteur nécessaires à la synthèse de glucides à partir du $CO_2$ atmosphérique et d'une série de réactions chimiques catalysées par diverses enzymes dont la RUBISCO.

Figure 1.2: La photosynthèse constitue une suite de transferts énergétiques (a) et de réactions chimiques (b) visant à la synthèse de dérivés du glucose à partir du $CO_2$ atmosphérique et de molécules d'$H_2O$

Les bactéries minéralisent la fraction labile du POC laissant de côté la matière réfractaire (demie-vie>50 ans), qui représente un stock global de 624 Pg C dans l'océan profond, soit 95% du réservoir de DOC (carbone organique dissous) océanique (Jiao *et al.*, 2010). L'autre voie consiste en sa consommation par le zooplancton. La photosynthèse s'accompagne aussi de la libération de molécules d'oxygène dans l'océan, qui peuvent diffuser vers l'atmosphère lorsque les pressions partielles d'oxygène dissous dans l'océan et dans l'atmosphère ne sont plus à l'équilibre. L'augmentation de la température à la surface de la terre est responsable de la diminution de la solubilité de l'$O_2$ gazeux dans l'eau, provoquant l'écart à cet équilibre et un flux net d'oxygène en faveur de l'océan

vers l'atmosphère dans les régions où le mélange des eaux est faible (Bopp *et al.*, 2002) (Figure 3).

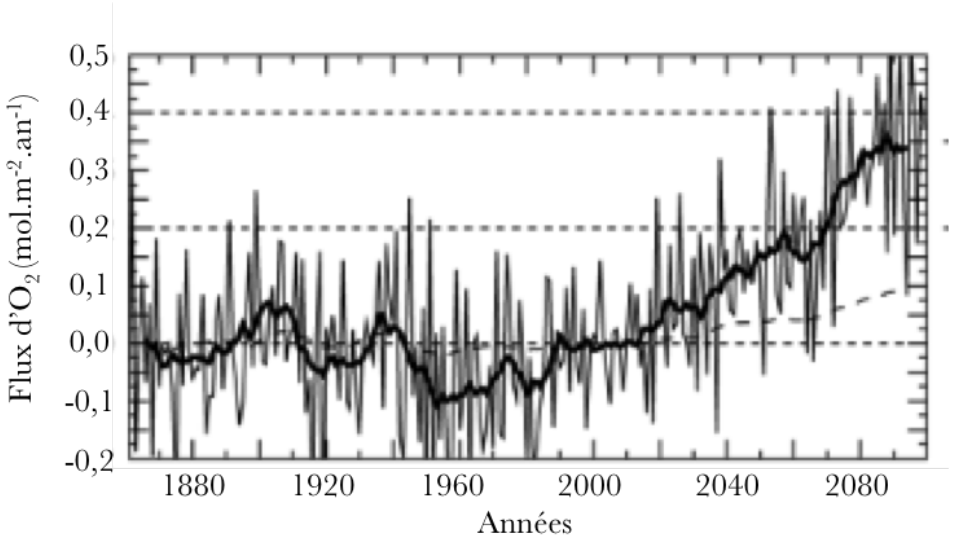


Figure 1.3: Simulation du flux global moyen d'oxygène entre l'océan et l'atmosphère prédit jusqu'à 2100 sur la base du scénario de changement climatique IPCC SRES98-A2. Les valeurs positives représentent une flux net depuis l'océan vers l'atmosphère.

*La diversité du phytoplancton: Traits écologiques liés à la taille, à la fluorescence et aux cycles de la matière*

Les organismes phytoplanctoniques sont infiniment petits et contiennent nettement moins de carbone que les plantes terrestres (Table 1). Ils ont pourtant très peu évolué depuis l'apparition du premier eucaryote unicellulaire autotrophe dont les fossiles datent de 1,5 milliard d'années (Falkowski *et al.*, 2004). Leur succès évolutif est en partie lié à la diversité de leurs traits écologiques, tel que la taille, qui encore aujourd'hui fait figure de 'paradoxe' (Figure 4). Certaines cellules peuvent se regrouper en colonies pouvant atteindre la dizaine de mm (*Trichodesmium*) mais les cellules les plus petites, qui mesurent en moyenne 0,6 $\mu$m de diamètre, et les plus abondantes sont des cyanobactéries du genre *Prochlorococcus* (Chisholm *et al.*, 1992). Comme la taille, la biomasse en carbone varie sur plusieurs ordres de grandeur. Son dosage par espèce demande généralement une quantité de matériel incompatible avec les concentrations observées en milieu naturel, c'est pourquoi elle est le plus souvent estimée grâce à la conversion de mesures de biovolume (Strathmann, 1967 ;Verity *et al.*, 1992; Menden-Deuer *et al.*, 2000). Le biovolume représente l'espace qu'occupe une cellule dans l'espace tridimensionnel. Il peut être évalué par microscopie, mesures optiques (cf. Annexe A) ou par prise d'images *in situ* (cf. Annexe B). Malgré sa faible biomasse, Field *et al.* (1998) ont estimé que le phytoplancton peut contribuer à hauteur de la moitié de la production annuelle d'$O_2$ gazeux présent dans l'atmosphère. C'est d'ailleurs l'apparition des premiers organismes photosynthétiques, les cyanobactéries, qui a majoritairement contribué aux flux d'oxygène vers l'atmosphère au cours du 'Great Oxidation Event' qui débuta il y a 2,8 milliard d'années (Riding, 1992; Lyons *et al.*, 2014).

Table 1.1: Ordres de grandeur du phytoplancton (liste non exhaustive)

| Taxon | Nomenclature en classes de taille de *Sieburth* (1978) | Quota en Carbone (fg C.individus$^{-1}$) | Diamètre $\phi$ ($\mu$m) |
|---|---|---|---|
| **Cyanophyceae** | | | |
| *Prochlorococcus sp.* | Pico | 50[a] | 0,5-0,7[a] |
| *Synechococcus sp.* | Pico | 90-250[b] | 0,8-1,5 [c] |
| Colonie de *Trichodesmium* | Meso | (11-25).10$^6$ [d] | (2-5).10$^3$ [e] |
| **Cryptophyceae** | | | |
| *Cryptomonas sp.* | Nano | 152.10$^3$ [f] | 16,5-17,5 [f] |
| **Haptophyceae** | | | |
| **Prymnesiophyceae** | | | |
| *Emiliana huxleyi* | Nano | 4 570[f] | 5,1 [f] |
| *Phaeocystis sp.* | Nano | 5 520[f] | 5,6 [f] |
| **Alveophyceae** | | | |
| **Dinophyceae** | | | |
| *Dinophysis sp.* | Micro | 1 300.10$^3$ [g] | 30[g] |
| *Ceratium fusus* | Micro | 3 300.10$^3$ [h] | 150-300[h] |
| *Akashiwo sanguinea* | Micro | 2 920.10$^3$ [f] | 56-76 [f] |
| **Heterokontophyceae** | | | |
| **Dictyochophyceae** | | | |
| *Dictyocha fibula* | Nano/Micro | 4 100.10$^3$ [i] | 35-65[j,k] |
| *Distephanus speculum* | Nano/Micro | (250-620).10$^3$ [i,g] | 50-100[l] |
| **Bacillariophyceae** | | | |
| *Minidiscus trioculatus* | Pico/Nano | 4 000[g] | 2-5[g,m] |
| *Ditylum brightwelli* | Micro | (300-25 000).10$^3$ [n] | 30-70[o] |
| *Coscinodiscus sp.* | Micro | (100-530 000).10$^3$ [n] | 20-200[n,p] |
| **Chlorophyceae** | | | |
| **Prasinophyceae** | | | |
| *Micromonas sp.* | Pico | 800[f] | 1,4-2[q] |
| *Chlamydomonas sp.* | Nano | 970.10$^3$ [f] | 18,6 [f] |
| plantes terrestres | Mega | 10$^{10}$-10$^{23}$ [r] | (10-150).10$^4$ [s] |

Signification des classes de taille: Pico- ($\phi$ < 3 $\mu$m) Nano- ( 3 $\mu$m < $\phi$ < 20 $\mu$m) Micro- (20 $\mu$m < $\phi$ < 200 $\mu$m) Meso- (0,2 cm < $\phi$ < 2 cm) Mega- (2 cm < $\phi$ < 200 cm)

Références: [a] Partensky *et al.* (1999) [b] Bertilsson *et al.* (2003) [c] Morel *et al.* (1993) [d] Luo *et al.* (2012) [e] Capone *et al.* (1997) [f] Montagnes *et al.* (1994) [g] Zigone *et al.* (2011) [h] Menden-Deuer et Lessard (2000) [i] Cassis *et al.* (2005) [j] Hernandez-Becerril *et al.* (2001) [k] Rigual-Hernandez *et al.* (2010) [l] Tsutsui *et al.* (2009) [m] Miklasz *et al.* (2010) [n] Leblanc *et al.* (2012) [o] Moller *et al.* (2001) [p] Taniguchi *et al.* (2014) [q] Durand *et al.* (2000) [r] Enquist *et al.* (1998) [s] Li *et al.* (2005)

Cette découverte s'est appuyée sur la transposition des travaux de Yentsch et Menzel (1963), qui ont caractérisé la quantité de biomasse algale grâce à l'extraction de la chlorophylle, aux mesures de couleur de l'eau des satellites en orbite (télédétection). Paradoxalement, malgré leur petite taille, la présence des pigments dans les cellules phytoplanctoniques permet de quantifier et de cartographier son abondance globale depuis l'espace, même à de très faibles teneurs (<1 $\mu$g.dm$^{-3}$) (Antoine *et al.*, 1996). De la même façon qu'ils servent à produire de l'énergie sous forme d'ATP, l'énergie emmagasinée par les photopigments peut être libérée sous forme de lumière pour que les molécules de pigment excitées retournent à leur état fondamental.

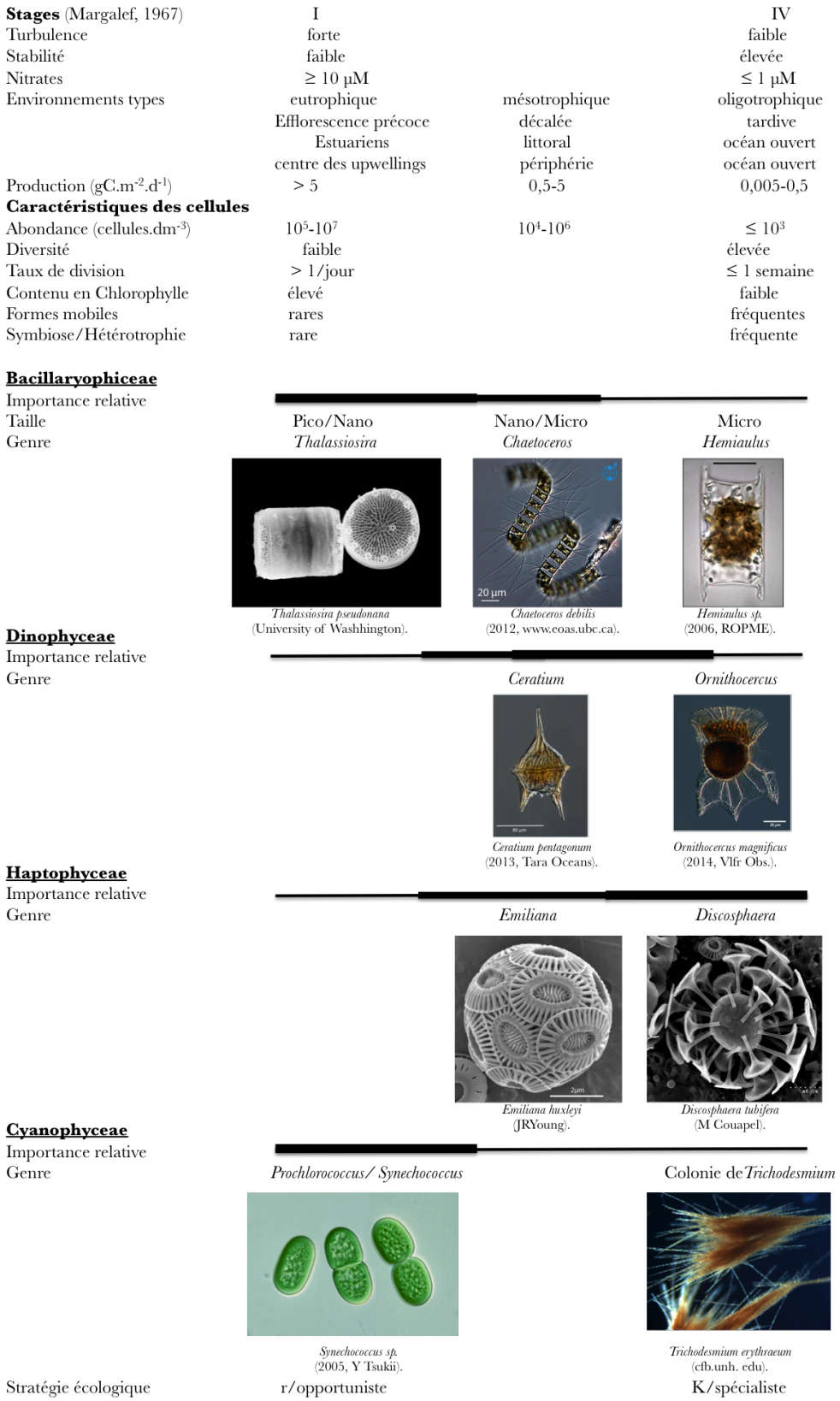


Figure 1.4: Diversité des traits écologiques du phytoplancton (modifié d'après Huneke et Mulder, 2011)

La lumière réémise par les pigments est caractérisée par un spectre de longueurs d'onde, propres à la nature des pigments contenus dans les cellules (spectre de fluorescence). Cette réaction photochimique se nomme l'autofluorescence, elle est supposée

directement proportionnelle à la quantité de pigments (Falkowski and Kiefer, 1985) (E 1.2).

$$F = PAR.[Chl\,a].a_{phytoplancton}.\phi_f \tag{1.2}$$

PAR: photons photosynthétiquement actifs. $[Chl\,a]$: teneur *in vivo* en pigments de $Chl\,a$. $a_{phytoplancton}$: coefficient d'absorption de la $Chl\,a$. Il dépend principalement du diamètre des cellules et est donc spécifique à une espèce donnée. $\phi_f$, le rendement ou efficacité de la fluorescence après absorption lumineuse.

Toutefois, lorsque l'intensité lumineuse perçue par les photopigments est telle qu'ils parviennent à saturation, excédant la capacité de la cellule à utiliser la lumière pour la photosynthèse (phénomène de *quenching* ou de dissipation de la fluorescence), l'énergie absorbée est alors dispersée pour éviter d'endommager les pigments et la fluorescence ne répond plus directement à son quota cellulaire (Behrenfeld *et al.*, 2009).

Trois types de pigment sont utilisés par les cellules pour faire la photosynthèse: les chlorophylles (a,b,c), les caroténoïdes et les phycobilliprotéines (phycoérithrine, phycocyanine). Ces molécules, regroupées au sein de complexes collecteurs, captent l'énergie des photons correspondant aux niveaux d'énergie des électrons disponibles de leurs atomes. Le complexe collecteur d'énergie lumineuse du photosystème II comporte entre 200 et 300 molécules de chlorophylle chez les eucaryotes (Goussias *et al.*, 2002). L'absorption des photons est donc décrite sur l'ensemble du spectre lumineux visible et va dépendre de la nature des pigments présents dans les photosystèmes (Figure 5).

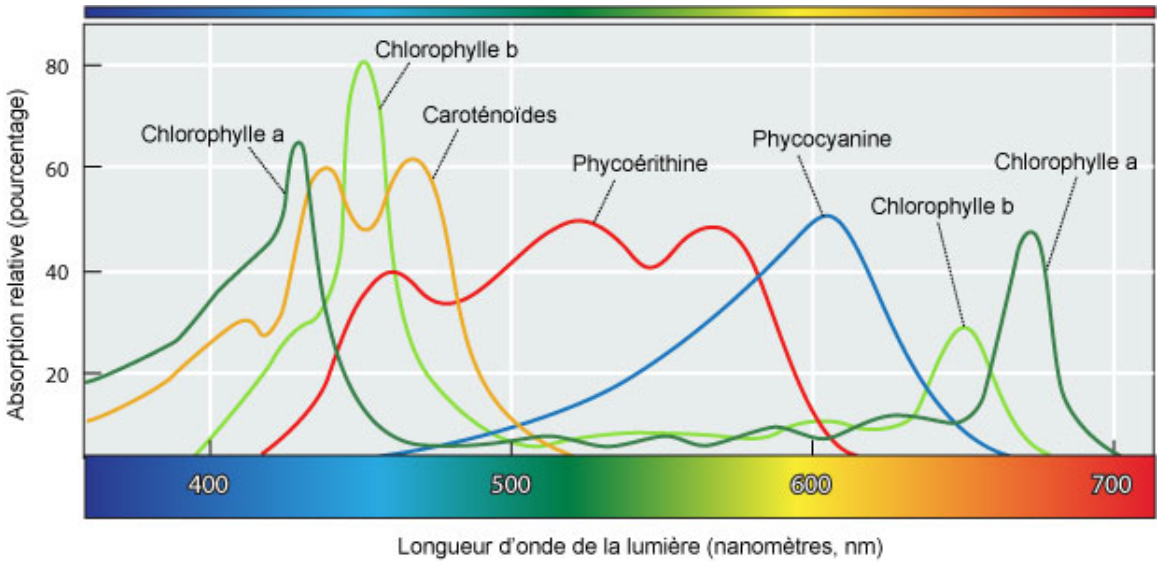


Figure 1.5: Spectre d'absorption de l'énergie lumineuse visible par les pigments photosynthétiques

La chlorophylle *a* est ubiquitaire chez le phytoplancton et le seul pigment directement actif dans la conversion de l'énergie lumineuse en énergie chimique. Elle est par conséquent utilisée comme marqueur de la biomasse phytoplanctonique aussi bien par la télédétection, qui se base sur ses propriétés d'absorbance, que par d'autres mesures optiques comme la cytométrie en flux qui en quantifie la fluorescence (cf. Annexe A). Les autres pigments sont des pigments accessoires, qui constituent l'antenne collectrice du centre réactionnel et permettent de capter les photons qui ne sont pas directement absorbés par la chlorophylle *a*. Certains de ces pigments sont dits diagnostiques puisqu'ils peuvent servir à distinguer différents groupes de phytoplancton toujours sur la base de mesures optiques de fluorescence (cytométrie en flux, fluorimétrie) ou d'absorption (High

Performance Liquid Chromatography, spectrométrie, télédétection) (Table 2) (Jeffrey *et al.*, 1997).

Table 1.2: Principaux pigments marqueurs permettant d'identifier divers taxons de phytoplancton par fluorimétrie ou spectrométrie

| Taxon | Pigment | Bande d'absorption (nm) | Bande de fluorescence (nm) |
|---|---|---|---|
| | Chlorophylles | | |
| aspécifique | *Chl a* | 435-440/670-680 | 680 |
| **Chlorophyceae** | *Chl b** | 470-485/650 | 680 |
| **Prymnesiophyceae** | *Chl c** | 460-470/630-640 | 680 |
| | Caroténoides* | 430-570 | 680 |
| **Bacillariophyceae** | Fucoxanthin* | 460-4530 | 680 |
| aspécifique | $\beta$-carotène* | 485-495 | 680 |
| **Cryptophyceae**/ | Phycoérythrine | 500-570 | 550-580 |
| **Cyanophyceae** | | | |
| **Cyanophyceae** | Phycocyanine | 550-650 | 630-660 |

*: Ces pigments n'émettent pas de fluorescence directe. Ils transmettent l'énergie des électrons à la *Chl a* qui autofluoresce par résonance.

Nair *et al.* (2008) ont synthétisé les caractéristiques du phytoplancton qui permettent de relier certains groupes, identifiés sur le terrain grâce à leurs signatures optiques de fluorescence/absorption/rétrodiffusion, aux réactions biogéochimiques qu'ils catalysent. Ces réactions sont liées au concept de groupe ou *guilde* fonctionnel, souvent polyphylétique, défini par Le Quéré en 2005. Les *Phytoplankton Functional Types* (PFTs) englobent l'ensemble des organismes qui partagent des traits communs, qu'ils soient phénotypiques, comme la taille (Sieburth, 1978) et les pigments (Phinney et Cucci, 1989; Hirata *et al.*, 2011), ou fonctionnels, par rétroactions chimiques (Burton *et al.*, 1983) ou traits écologiques (Simberloff et Dayan, 1961; McGuill *et al.*, 2006):

1. La fraction des plus petites classes de taille définie par Sieburth, **l'ultraphytoplancton** (Li *et al.*, 1993), qui comprend à la fois les compartiments pico- et nanoplanctonique ($\phi$< 10 $\mu$m), domine la biomasse phytoplanctonique dans les milieux stratifiés. Si le picoplancton représente la fraction la plus efficace pour assimiler les nutriments à cause de son faible rapport surface:volume (S:V) (Chisholm, 1992), le nanoplancton présente les capacités d'absorption lumineuse les plus élevées (Uitz *et al.*, 2008). Leur rapport S:V leur confère une faible vitesse de sédimentation et leur permet donc de rester en surface où ils alimentent la boucle microbienne contrairement au microphytoplancton qui est majoritairement exporté vers l'océan profond (Legendre et LeFèvre, 1979). En milieu oligotrophe tel que la mer Méditerranée, ces cellules assimilent entre 30% et 60% du $CO_2$ atmosphérique converti en matière organique (Uitz *et al.*, 2010).

2. Certaines espèces de dinophytes, prasinophytes et d'haptophytes, comme *Phaeocystis*, produisent un agent chimique, le **DiméthylSulfure** (DMS), qui, lorsqu'il

diffuse dans l'atmosphère, contrebalance les effets du changement climatique sur l'augmentation de la température à la surface des océans. Dans l'atmosphère, il réagit avec d'autres espèces chimiques pour former des aérosols qui se condensent et réfléchissent les rayonnements solaires incidents en direction de l'espace. *Phaeocystis* se développe et s'accumule de façon régulière aux pôles et aux latitudes tempérées où il atteint des concentrations de l'ordre de $10^7$ cellules.dm$^{-3}$ (Schoemann *et al.*, 2005). Le mucilage qu'il forme en colonie présente le double avantage de stocker les nutriments lorsqu'ils deviennent limitants et de prévenir la prédation du zooplancton. De ce fait, les efflorescences de *Phaeocystis* sont généralement reminéralisées par le compartiment bactérien. L'induction de blooms de *Phaeocystis* en zones côtières introduit des concentrations de DMS (5-50 nM) jusqu'à 100 fois plus élevées que dans l'océan ouvert et diminue de -0,08 à -0,56 W.m$^{-2}$ le budget radiatif de la Terre (Ayers et Gillett, 2000).

3. Les organismes **calcifiants**, les coccolithophores, arborent des plaques de carbonate de calcium, $CaCO_3$, ou coccolithes à l'extérieur de leur membranes cellulaires. La première fonction de ces agents est en lien avec la protection des cellules contre les chocs osmotiques, la turbulence physique, la prédation et la lyse virale (Young, 1994). Les coccolithes servent également de ballast aux cellules, qui peuvent réguler leur densité par la voie de biosynthèse de la calcite, et à d'autres particules qui s'y agrègent lorsqu'elles relarguent des exopolymères (TEP) et sédimentent au fond des océans: la vitesse de sédimentation des agrégats de cellules calcifiantes peut être jusqu'à 4 fois plus élevée ($v$=1,7 cm.s$^{-1}$) que pour les cellules non calcifiantes (Engel *et al.*, 2009). Ils favorisent l'export de matière particulaire et sa séquestration. Les efflorescences d'*Emiliana huxleyi*, où l'on dénombre entre $10^6$-$10^8$ cellules.dm$^{-3}$, sont visibles par satellite et génèrent un flux de C estimé entre 80 et 300 mgC.m$^{-2}$.d$^{-1}$ (Schmidt *et al.*, 2013). Ce flux n'est toutefois pas optimal à cause du processus de formation des calcites. La formation de $CaCO_3$ intervient lors de la précipitation des ions bicarbonates avec les ions calcium: $Ca^{2+} + 2HCO_3^- \rightarrow CaCO_3 + H_20 + CO_2$. Cette réaction relargue du $CO_2$ sous forme dissoute à l'interface air-océan qui peut ensuite diffuser vers l'atmosphère: c'est ce que l'on appelle la contrebalance du système des carbonates (*Carbonate Counter Pump*), qui peut réduire la quantité de $CO_2$ exportée de 1 à 4% (Salter *et al.*, 2014).

4. Les organismes **silicifiants**, comme les bacillariophyceae et les dichtyochophyceae, arborent aussi des plaques extramembranaires mais composées de silice biogénique $SiO_2$ ($\rho_{SiO_2}$=2,070 kg.m$^{-3}$). Ce sont des acteurs majeurs du cycle du Si. La formation des frustules/squelettes de silice biogénique sert $infine$ de moyen de locomotion entre les différentes masses d'eau par jeu de densité. Raven et Waite (2004) ont émis l'hypothèse que l'augmentation de la biosynthèse de silice en réponse à un stress environnemental permet aux cellules de se déplacer plus rapidement vers des habitats favorables à leur croissance. Dans les habitats stratifiés, la présence d'une nutricline profonde agit généralement comme une barrière physique empêchant la diffusion des nutriments vers la surface. Comme les calcites, la présence de silice offre également une protection contre les prédateurs/parasites et les rayonnements UVs. Les diatomées peuvent être entraînées vers le fond à des vitesses de 30 m.d$^{-1}$, contribuant à l'export du stock de C et de Si. Leur contribution à la production primaire globale a été estimée à 40% par Sarthou *et al.* (2005) et est principalement

due à des épisodes saisonniers de forte multiplication ($\mu$>3 $d^{-1}$) (Martin-Jézéquel *et al.*, 2000). Les diatomées forment des efflorescences régulières aux pôles, lorsque le fer ne limite plus la production, et dans les zones côtières tempérées.

5. Les **fixateurs de diazote** ($N_2$) sont généralement représentés par des cellules de petite taille, entre 3 et 10 $\mu$m, du clade des cyanobactéries (Zehr *et al.*, 2001). En milieu pélagique, la réduction du $N_2$ en $NH_4^+$, catalysée par la nitrogénase, est responsable d'une source de N directement assimilable par le phytoplancton estimée à 110 Tg N.$an^{-1}$ (Gruber et Sarmiento, 1997). Ces organismes peuvent vivre librement ou être confinés au sein d'une colonie, comme *Trichodesmium* qui domine la biomasse des diazotrophes, ou d'une cellule par symbiose, comme *Rhizosolenia*. Ils s'accumulent en zones oligotrophes, dans les eaux tropicales des océans Atlantique, Pacifique et Indien, parce que la nitrogénase leur permet de fixer la forme dissoute du $N_2$ là où les autres sources d'azote inorganiques, comme les apports terrigènes ou éoliens, viennent à manquer. *Trichodesmium* forme des marées rouges saisonnières par l'accumulation de centaines de milliers de colonies.$m^{-2}$ (Tyrrell *et al.*, 2003) sur une couverture spatiale qui peut s'étendre jusqu'à 90 000 $km^2$ (Dupouy *et al.*, 1988). Ces efflorescences supportent un transfert important de matière organique au sein des réseaux trophiques en alimentant à la fois la boucle microbienne et les prédateurs, qui excrètent quotidiennement 50% de leurs apports en N (O'Neil *et al.*, 1996). En symbiose, *Rhizosolenia* contribue à fournir du N réduit à ses hôtes tout en étant protégée des prédateurs et en profitant de leur flottabilité (Foster *et al.*, 2011).

L'observation du phytoplancton de manière globale est aujourd'hui possible grâce aux images satellites. Deux types de variables sont mesurées par les capteurs optiques montés sur les satellites d'observation de la Terre:
–La rétrodiffusion, liée à la taille des particules en suspension dans l'océan, équivalente aux mesures de cytométrie en flux.
– Le spectre d'absorption de l'irradiance incidente par les pigments, qui permet, comme pour la fluorescence en cytométrie en flux, de distinguer certains taxons selon leurs signatures pigmentaires.

La rétrodiffusion de la lumière incidente est une mesure qui varie généralement avec le cycle de vie du phytoplancton, reflétant l'accroissement cellulaire et les divisions successives du cycle cellulaire (Durand, 1995; Dall'Olmo *et al.*, 2011). L'absorption fluorescence mesurée par cytométrie, HPLC ou calculée par les algorithmes multi-spectraux de couleur de l'océan (Alvain *et al.*, 2005), peuvent désormais apporter des réponses sur le lien entre la climatologie des successions écologiques et le fonctionnement/production global de grands biomes.

*La production du phytoplancton: Biomes et niches écologiques*

L'estimation de la contribution relative des différents groupes de phytoplancton à la biomasse et à la production primaire océanique représente l'une des avancées majeures de l'océanographie. Reliées aux différents traits écologiques et aux mécanismes de production et d'exports, ces mesures ont permis de régionaliser le globe en zones fonctionnellement distinctes (Longhurst, 1998). En compilant ces données, Sarmiento et Gruber (2006) rapportent que la couche 'photosynthétique' de l'océan (i.e. euphotique), délimitée par

la profondeur où seulement 1% de l'irradiance incidente persiste après son atténuation verticale progressive, abrite globalement 4 ensembles de provinces distinctes en matière d'éléments nutritifs disponibles et de biomasse algale (Figure 6).

1. **High Nutrients Low Chlorophyll**: Ces zones, comme l'Océan Antarctique, sont riches en nutriments régénérés par la boucle microbienne (i.e. production régénérée) à cause de la remontée (upwelling) des eaux de fond (e.g. $PO_4^{3-}$>1 $\mu$M). Pourtant la biomasse phytoplanctonique, dominée par le picophytoplancton (Morel *et al.*, 1991), y est limitée à 0,2 $\mu$g.dm$^{-3}$ en moyenne à cause de la déficience d'éléments traces (Fe<0,1 nM), d'une faible intensité lumineuse et d'une intense pression de prédation (Minas et Minas, 1992).

2. **High Nutrients High Chlorophyll**: Ces zones, localisées en bordures côtières, bénéficient du lessivage des sols et de l'apport de poussières atmosphériques qui fertilisent la production basée sur l'apport allochtone de nutriments (i.e. production nouvelle). Le phytoplancton, principalement dominé par le microplancton, y produit des efflorescences en suivant le rythme saisonnier de l'irradiance et l'instabilité dynamique des masses d'eau lié aux mouvements turbulents (Margalef, 1978). Ces mouvements alliés à la faible efficacité de prédation favorisent l'export direct du phytoplancton par sédimentation (i.e. production exportée) (Legendre et Le Fèvre, 1989).

3. **Low Nutrients Low Chlorophyll**: Ces zones, qui représentent 75% de l'océan ouvert, s'étendent en majorité au niveau des latitudes subtropicales de part et d'autre de l'équateur. Ce sont des déserts biologiques qui ne comptent qu'en moyenne 0,2 $\mu$g.dm$^{-3}$ de Chlorophylle (Yolder *et al.*, 1993 in Falkowski *et al.*, 1998). Elles sont caractérisées par une circulation rotative des courants (gyres), la stratification quasi-permanente des eaux de surface, le faible apport de nutriments (i.e. oligotrophie) et la co-dominance des cyanobactéries *Prochlorococcus* et *Synechococcus*. La production, qui s'appuie sur la régénération des nutriments, y est assurée à 50% par le picophytoplancton. La mer Méditerranée fait également partie de cette province même si certaines zones abritent des efflorescences régulières.

4. **Low Nutrients High Chlorophyll**: Ces zones sont situées aux latitudes tempérées (Atlantique Nord, Benguela). Le mélange des masses d'eau par la circulation thermohaline y est intense et supporte une biomasse très élevée ($[Chla]$ ~ 20$\mu$g.cm$^{-3}$) mais éphémère (Barlow, 1984). L'assimilation des nutriments par le phytoplancton, jusqu'à plusieurs dizaine de mmol N par heure (Probyn *et al.*, 1996), entraîne un épuisement ($[NO_3^-]$ < 1$\mu$g.cm$^{-3}$) rapide de la couche de surface qui sera de nouveau enrichie par la circulation profonde en hiver. Cette dynamique entraîne la succession d'espèces dominantes limitées par divers nutriments, des diatomées microplanctoniques vers les classes de tailles inférieures dont l'assimilation est généralement plus efficace en conditions limitantes (Probyn *et al.*, 1992; Lochte *et al.*, 1993). Dans le cas extrême du Benguela, la prolifération du phytoplancton, toxique pour certaines espèces, entraîne également l'épuisement d'oxygène dissous par le processus inverse de la photosynthèse, la respiration (Pitcher *et al.*, 2014).

Chaque biome dépeint des conditions particulières qui s'expliquent par la dynamique du phytoplancton. En 1949, Riley a formalisé l'équation, connue sous le nom d'advection-diffusion (E 1.3), qui relie la variation de biomasse phytoplanctonique, en un point et un instant donné, à un ensemble de termes sources/puits tels que les champs de courant (e.g. upwellings et downwellings), le broutage par les prédateurs et généralement la limitation en ressources qui influence directement le taux de croissance intrinsèque (cf Chapitre 1.3).

$$\begin{aligned} \frac{\partial N(t,x)}{\partial t} &= -\mathbf{U}\frac{\partial N(t,x)}{\partial x} + \mathbf{K}\frac{\partial N^2(t,x)}{\partial x^2} + rN(t,x) \\ r &= \mu - l \\ \mu &= f(\text{Température, Irradiance, Sels nutritifs...}) \end{aligned} \tag{1.3}$$

t: temps [T], x: site géographique, N: Abondance [CELLS][L]$^{-3}$, U: champ des vitesses de courant [L][T]$^{-1}$
K: Coefficient de diffusion [L]$^2$[T]$^{-1}$, r: taux de croissance apparent [T]$^{-1}$, $\mu$: taux de croissance [T]$^{-1}$ intrinsèque, l: taux de pertes par lyse virale/prédation/sénescence [T]$^{-1}$

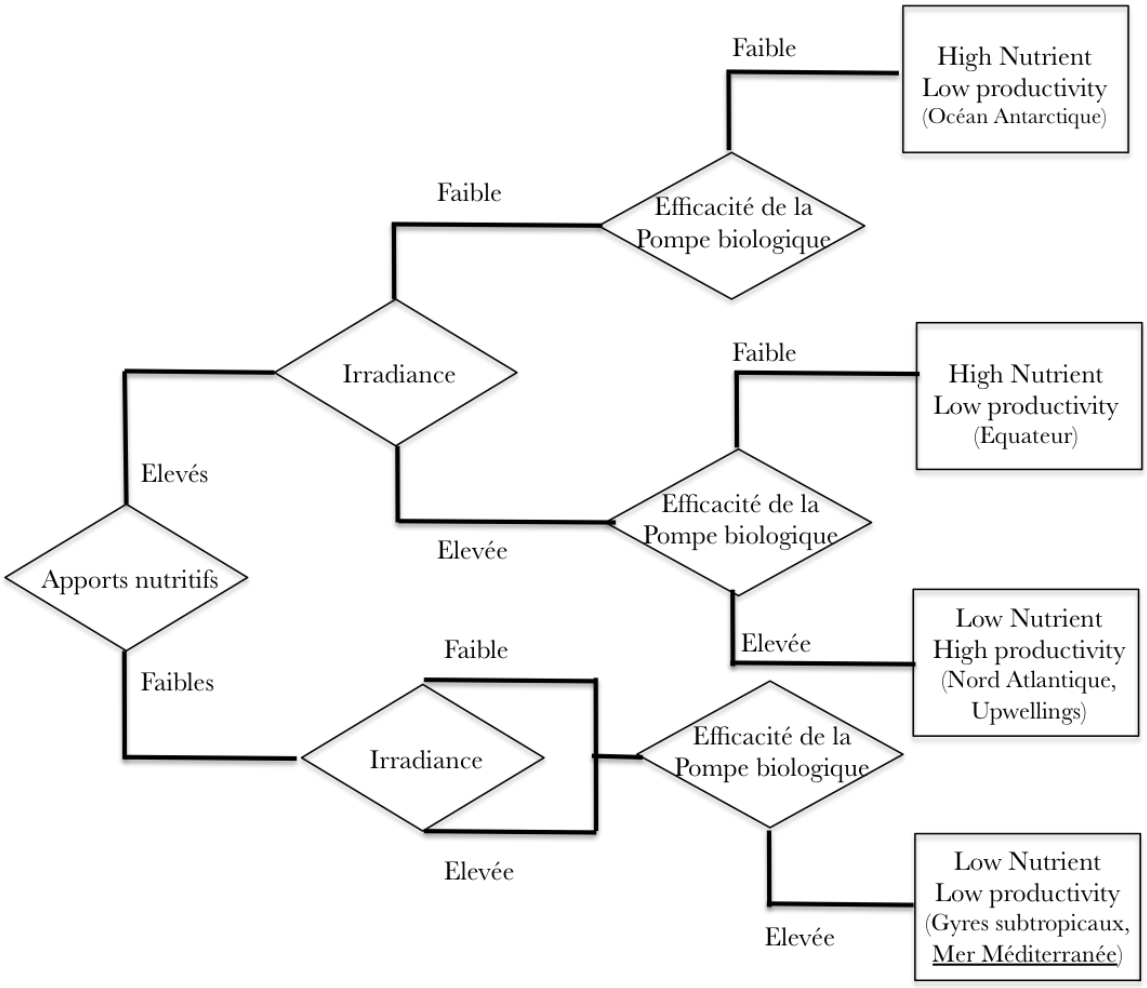


Figure 1.6: Grands biomes de production primaire océanique (modifié d'après Sarmiento et Gruber, 2006)

Comme tout organisme vivant, les espèces du phytoplancton répondent aux variations de leur environment selon le modèle de niche écologique de Gause. D'après Hutchinson, la niche écologique contient l'ensemble des conditions viables pour un organisme et caractérise les resources et interactions depuis un état dit limitant jusqu'à un état optimal.

D'Ovidio *et al.* ont récemment décrit les niches de plusieurs types de phytoplancton (e.g. *Prochlorococcus*, *Synechococcus*, nanoeukaryotes, diatomées, coccolithophores) en rapport avec les conditions hydrologiques *in situ*; mettant en avant la faible échelle de temps et d'espace à laquelle ces organismes sont astreints, comme l'avait noté Hutchinson dans *The paradox of the Plankton*. En établissant des modèles de niche, tels que ceux basés sur les statistiques bayésiennes (cf. Annexe C), les principaux facteurs qui régulent la biomasse/production phytoplanctonique sont progressivement identifiés et servent aux prédictions scénarisées de l'intensification de la dynamique des forçages en lien avec le changement climatique. Le paradoxe du plancton a été clairement énoncé en 1961 par Hutchinson. Une des hypothèses qui explique ce paradigme tient de l'extrême fugacité qui caractérise la durée de vie du phytoplancton ainsi que le dynamisme de son environnement. Autrement dit, des espèces qui partagent la même niche écologique peuvent cohabiter à condition que des perturbations viennent régulièrement renforcer la ségrégation spatiale et/ou temporelle de leur niche (Reynolds *et al.*, 1993; Huisman et Weissing, 1999). C'est en réponse à ces perturbations environnementales que la dynamique interne et *a fortiori* la dynamique externe du phytoplancton observent un changement de régime ou *regime shift* décrit par les successions autogéniques (Roelke et Spatharis, 2015). L'influence que ce dynamisme a sur la croissance du phytoplancton provoque l'évolution permanente d'un consortium de populations dont les espèces vont osciller entre dominance et cohabitation sans jamais atteindre l'état d'équilibre (Naselli-Flores *et al.*, 2003).

## 1.2 Cycle de vie et mesure de dynamique intrinsèque

*Courbes et taux de croissance*

Les cellules de phytoplancton ont un cycle de vie basé sur 4 étapes: la croissance, la reproduction, la quiescence et la sénescence. Les phases de croissance et de reproduction ont la particularité d'être rapide, conférant aux populations une capacité adaptative et évolutive exceptionnelle (Collins *et al.*, 2014). Elles ont pour but d'assurer la transmission du matériel génétique d'une génération à l'autre à travers la réplication de l'ADN d'une cellule et sa répartition équitable chez ses deux cellules filles lors de la reproduction asexuée ou de la fusion de deux gamètes par reproduction sexuée. A chaque génération, le matériel génétique d'une cellule subit des mutations, avec une probabilité comprise entre $10^{-5}$ et $10^{-10}$ (Ness *et al.*, 2012), en raison de son interaction avec un milieu mutagène lié à la présence d'herbicides (Huertas *et al.*, 2010), l'augmentation des UVs (Buma *et al.*, 2001; Hader *et al.*, 2007) et la température (Costas *et al.*, 2014). Les mutations, qui dépassent la simple plasticité phénotypique (i.e. processus d'acclimatation physiologique des cellules), et le mode de vie du phytoplancton ont été progressivement sélectionnés aux échelles de temps géologiques pour façonner les lignées actuelles (Von Dawson *et al.*, 2011). Hormis la phase sexuée, le cycle cellulaire consiste en la répétition séquentielle, généralement entraînée par un rythme circadien (i.e. 24 heures), des phases de croissance et de reproduction asexuée selon une suite d'étapes contrôlées. Néanmoins lorsque les cellules expérimentent des conditions suboptimales, elles sont forcées de quitter ce cycle pour la phase réversible de quiescence, ou dormance, voire la phase irréversible de mort cellulaire programmée (i.e. sénescence). Typiquement, la dynamique d'une population en milieu contrôlé suit une courbe logistique (Figure 7) qui symbolise:

1. La phase initiale de **latence**: C'est lors de cette phase que les organismes, inadaptés à leur nouvel environnement, subsistent d'un métabolisme basal dans les conditions de culture. Cette adaptation passe notamment par la synthèse d'ATP, de ribosomes et du cortège d'enzymes nécessaires au métabolisme actif des cellules et qui requiert un certain temps.

2. La phase de **croissance exponentielle**: C'est l'étape qui suit la phase d'adaptation. La machinerie cellulaire y est engagée pour permettre la division par scissiparité ou fission binaire d'une cellule mère en deux cellules filles (cf. la reproduction cellulaire). La durée de la division peut varier selon les conditions du milieu mais sera toujours optimale après la phase d'adaptation.

3. La phase stationnaire ou **K**: K (capacité limite) est la densité maximale d'une population en milieu contrôlé non conservatif. Dans ces milieux, le stock de sels nutritifs n'est pas constant. C'est généralement le cas des expériences en micro/mésocosmes et en batch. Cette phase intervient après plusieurs générations de cellules et marque le début de carence en sels nutritifs. La dynamique y est stationnaire soit parce que le taux de croissance intrinsèque est égal au taux de mortalité soit parce que les cellules entrent toutes en phase de quiescence.

4. La phase de **sénescence**: Cette phase apparaît lorsque le taux de mortalité surpasse le taux de croissance intrinsèque, qui peut être nul. La densité de population décline alors progressivement des suites de l'épuisement totale en nutriments ou même de la production de toxines. Les dommages cellulaires occasionnés au cours de cette phase sont généralement irréversibles et ne permettent pas aux cellules de reprendre le cours des étapes de croissance même en changeant de milieu.

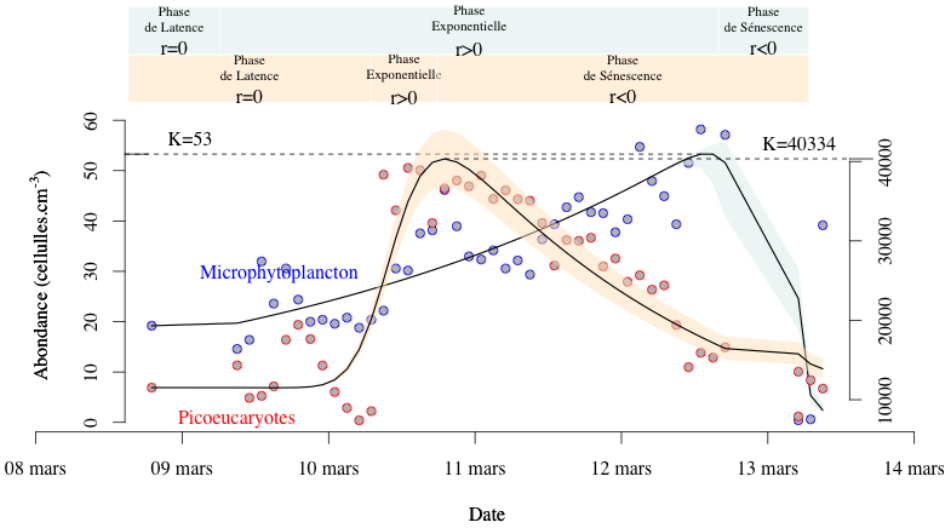


Figure 1.7: Courbes de croissance de groupes phytoplanctoniques suivi par cytométrie en flux à haute fréquence au cours d'une expérience en mésocosme dans l'étang de Thau en mars 2015 (cf. Chapitre 2). Les modèles de courbes ont été prédits selon la méthode de Horowitz *et al.* ( 2010). r, taux de croissance apparent d'une population, est égal à la différence entre son taux de croissance intrinsèque induit par reproduction végétative ($\mu$) et son taux de pertes par mortalité ($l$). La phase stationnaire est quasi-inexistante pour les deux populations.

Au cours de la croissance végétative, les populations se multiplient par puissance de 2. Leur dynamique suit une augmentation exponentielle décrite par la relation de Matlhus (E 1.4):

$$\begin{aligned} \frac{dN(t)}{dt} &= \mu N(t) \\ \mu &= \frac{1}{t - t_0} log_e(\frac{N(t)}{N(t_0)}) \\ N(t) &= N(t_0) exp(\mu t) \end{aligned} \tag{1.4}$$

N(t): Abondance au temps $t$, $\mu$: taux de croissance intrinsèque $[T]^{-1}$, $N(t_0)$: Abondance initiale

Le taux de croissance intrinsèque d'une population correspond donc à la pente observée de la courbe (log transformée) de croissance en phase exponentielle. Le temps de génération, noté $t_g$ correspond au temps au bout duquel la densité de population double d'effectif. Il se déduit du taux de croissance grâce à la relation suivante (E 1.5):

$$\begin{aligned} t_g &= t_{N=2.N(t_0)} - t_0 \\ &= \frac{log_e(2)}{\mu} \\ &= \frac{0,69}{\mu} \end{aligned} \tag{1.5}$$

$t_g$: temps de génération $[T]^{-1}$, N(t): Abondance au temps $t$, $\mu$: taux de croissance intrinsèque $[T]^{-1}$, $N(t_0)$: Abondance initiale

En milieu naturel, le temps de génération du phytoplancton est compris entre 0,1 et 100 jours (Fouilland et Mostajir, 2010 dans Kirchman, 2012). Furnas (1991) a estimé des temps de génération variables de 0,6, 0,5, 0,8, 0,7 et 0,2 jour pour des cellules de *Synechococcus*, picoeucaryotes, nanoeucaryotes, dinoflagellés et diatomées respectivement en milieu oligotrophe. En comparaison de milieux mésotrophe et eutrophe, c'est aussi en milieu oligotrophe que Goldman (1979) a rapporté le taux de croissance mesuré *in situ* le plus élevé (6.6 jour$^{-1}$), correspondant à un temps de génération de 0,1 jour. Sur cette durée, la biomasse d'une cellule de phytoplancton sera allouée à différents composés qui ont pour fonction d'assurer la maintenance cellulaire, la croissance et la reproduction ou la sénescence via un ensemble de réactions métaboliques.

*L'accroissement cellulaire*

L'accroissement cellulaire est déterminé par trois phases distinctes, ou interphase, au cours desquelles une cellule est amenée à dupliquer son ADN et son quota cellulaire en C en vue de la reproduction végétative (Mocquet *et al.*, 2010). Le premier stade de croissance de la cellule, nommée $G1$, pour *Gap* 1, sépare la naissance d'une cellule fille de son entrée en phase de réplication de l'ADN, la phase $S$. C'est généralement la phase la plus longue chez les eucaryotes, sa durée peut représenter 55% du temps de génération pour certaines espèces (Vaulot *et al.*, 1987). La phase de synthèse d'ADN, $S$, correspond à la duplication du génome de chaque cellule pour assurer la transmission héréditaire du matériel génétique à la génération suivante. Chez certaines espèces, les cellules peuvent être réparties au sein d'un cycle complexe où prévalent différents niveaux de ploïdie. Le

phytoplankton est généralement haploïde (1N) ou diploïde (2N) mais certaines espèces alternent les stades à une, deux, trois, quatre, etc. copie(s) (N) du génome condensé dans une ou plusieurs chromatide(s) (Binder et Chisholm, 1995). Pendant la phase $S$, chaque chromatide est reproduite à l'identique par l'ADN polymérase qui se sert de la complémentarité des bases nucléotidiques (A-T et G-C) selon un mécanisme semi-conservatif. Ce status est transitoire puisqu'une fois divisées, les cellules retrouvent la quantité d'ADN présente avant leur entrée en phase de réplication. Comme l'ADN, la biomasse du phytoplancton oscille entre deux extrema au cours d'un cycle cellulaire: le maximum de taille et d'ADN par cellule est atteint avant l'entrée en mitose, peut rester à l'équilibre pendant la mitose (Mocquet *et al.*, 2012), et diminue progressivement d'un facteur deux à la séparation des cellules filles (i.e. cytocinèse) (Figure 8). Ces processus ont été formalisés par des modèles afin d'estimer la quantité de cellules qui se divisent au cours d'un suivi temporel selon les méthodes respectives:

1. du cycle cellulaire par lequel on estime la fraction de cellules associées à chaque phase du cycle par marquage ADN (cf. Annexe D).

2. de population structurée en taille par lequel on estime la probabilité pour chaque cellule d'être en phase active de croissance ou de division via des observations successives de distribution du biovolume (cf. Annexe D).

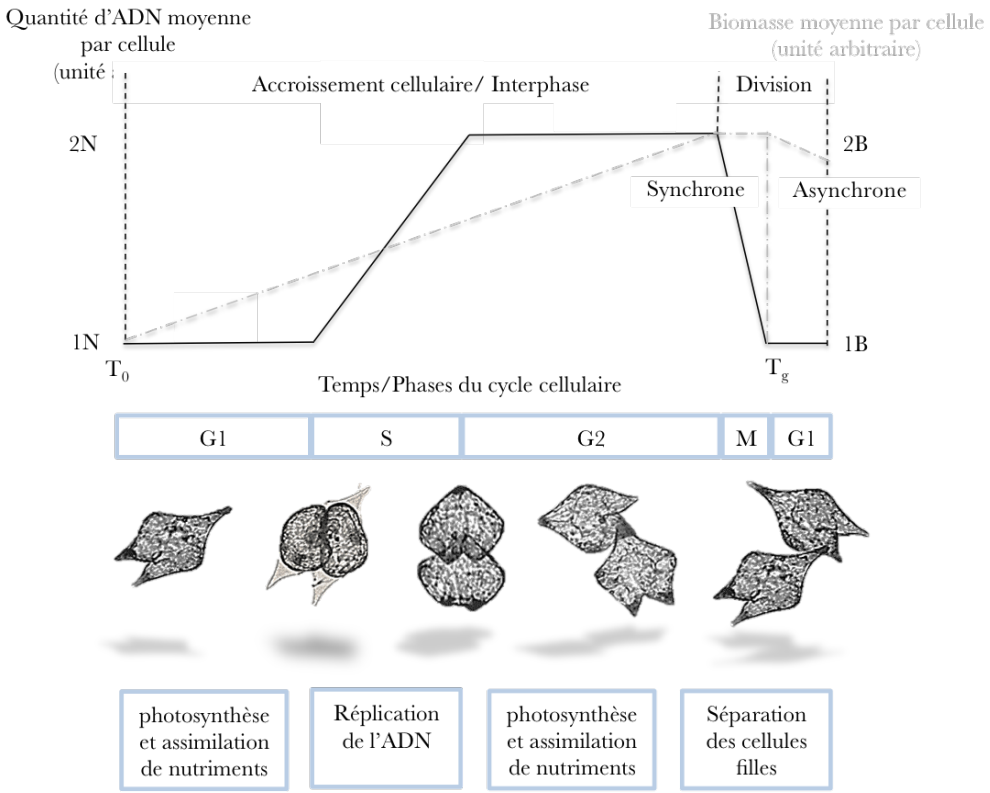


Figure 1.8: Les stades du cycle cellulaire. L'alternance de l'interphase avec la division asexuée de cellules végétatives est le principal mode de reproduction du phytoplancton. L'interphase est marquée par la réplication du noyau des cellules (phase $S$) au cours de laquelle la quantité d'ADN, équivalente à 1N, sera doublée pour former un ensemble de chromatides soeurs. Une fois son ADN entièrement répliqué, la cellule va poursuivre une série d'étapes qui abouti, à la fin de la mitose, à la répartition équitable de l'ensemble des organites et de la biomasse dans chaque cellule fille (i.e. cytocinèse). Lorsque toutes les cellules d'une même population se divisent en même temps, on parle de division synchrone marquée par la chute brutale d'un facteur 2 de la biomasse cellulaire moyenne à la séparation des cellules filles. Les étapes de la cytocinèse (10-30 min) sont illustrées par la série d'observations au microscope d'une cellule de *Protoperidinium* (Gribble *et al.*, 2009)

Les deux chromatides soeurs se condensent au cours du second et dernier stade de croissance de la cellule, $G2$ pour $Gap2$. C'est la phase qui précède directement la mitose. Elle sert principalement à préparer la division, notamment à travers la synthèse des composés du cytosquelette impliqués dans le transport des chromatides vers les pôles cellulaires (e.g. microtubules, centrioles). Pour toutes les cellules, les phases $G1$, $S$ et $G2$ marquent l'accroissement de la biomasse grâce à la mobilisation du $CO_2$ et des nutriments assimilés de façon à être répartis équitablement dans chaque cellule fille. Les mesures temporelles d'assimilation de l'azote (Mocquet, 2010) et du phosphore (Stross, 1974) chez le phytoplancton montrent que l'incorporation des nutriments est un processus cyclique, au rythme circadien, régulièrement répété et fortement influencé par les phases du cycle cellulaire (Hildebrand et Dahlin, 2000). Pour une première approche, Reynolds (2006) s'est basé sur le calcul du flux diffusif de $CO_2$ à travers la membrane pour estimer que pour une cellule supposée sphérique de *Chlorella* de diamètre $\phi$=$2r$ ~ 4 $\mu$m, surface $a$=$\pi.r^2$ ~ 50 $\mu m^2$, volume $v$=$\frac{4.\pi}{3}r^3$ ~ 30 $\mu m^3$, $a:v$ ~ 1,7 $\mu m^{-1}$, le temps de doublement de biomasse requis pour la division asexuée approcherait:

$$\begin{aligned} t_{2B_0} &= \frac{B_0}{a.K_{CO_2}.\frac{d[CO_2]}{r}} \\ t_{2B_0} &= \frac{v.Q_{molaire}(C)}{a.K_{CO_2}.\frac{d[CO_2]}{r}} \\ &= \frac{30.10^{-18}.20.10^3}{50.10^{-12}.10^{-9}.\frac{10.10^{-3}}{2.10^{-6}}} \\ &\sim 40\,min \end{aligned} \tag{1.6}$$

$B_0$: Biomasse initiale en C [MOLE], $Q_{molaire}(C)$: Quota molaire de C par cellule [MOLE].[L]$^{-3}$, $K_{CO_2}$: Coefficient de diffusion à travers la membrane [L]$^2$.[T]$^{-1}$, d[$CO_2$]: Concentration en $CO_2$ à l'équilibre [MOLE].[L]$^{-3}$

lorsque la quantité de C qui doit être assimilée par la cellule pour un doublement en taille correspond à son quota cellulaire initial ($B_0$) et que le gradient de concentration en $CO_2$ est intégré sur une épaisseur égale au rayon $r$ de la cellule. Par comparaison, une cellule végétative de Protoperidinium, qui présente un rapport S:V plus faible, avec $\phi$=103 $\mu$m (Gribble *et al.*, 2009), $a$=8 300 $\mu m^2$, $v$=230 220 $\mu m^3$ (cf. Annexe B), $a:v$ ~ 0,04 $\mu m^{-1}$, $B_0$=$5.10^{-9}$ mol de C, atteindrait le double de sa taille en 33 jours sans mécanisme de concentration du C.

La biomasse du phytoplancton est constituée d'un certain nombre d'atomes élémentaires que l'on distingue selon qu'ils soit majoritaires (macroéléments) ou simplement présents à l'état de trace (nM). Comme tous les organismes vivants, le matériel cellulaire est principalement composé d'atomes de C, H, O, N et P. Les analyses stoechiométriques ont montré que le contenu cellulaire du phytoplancton en macroéléments, et notamment le rapport élémentaire dit rapport de Redfield, est relativement constant en milieu naturel et même proche de celui des composés dissous dans l'eau (Figure 9a). Pour Redfield, les cycles élémentaires des composés dissous sont avant tout liés à l'absorption ATP-dépendante des nitrates $NO_3^-$ (Falkoswki, 1985), du dioxide de carbone $CO_2$ (Falkowski et Raven, 2007) et des orthophosphates $PO_4^{3-}$ (Nalewajko et Lean, 1980; Plaetzer *et al.*, 2005) entre autres,

nécessaire aux réactions impliquées dans les différentes voies métaboliques du phytoplancton (Figure 9b). Ce rapport équivaut à 106C:16N:1P (Redfield, 1934). Ces trois atomes sont les éléments constitutifs de base de l'ensemble des matériaux biosynthétisés, que ce soit pour les acides aminés, les acides nucléiques, les membranes phospholipidiques (e.g. thylakoïdes), l'ATP, les polysaccharides (i.e. produits de la photosynthèse) etc. (Figure 9c). En moyenne, le cytoplasme d'une cellule contient 1300 kg.m$^{-3}$ de protéines, 1500 kg.m$^{-3}$ de carbohydrates et 1700 kg.m$^{-3}$ d'acides aminés (Reynolds, 2006). Pour maintenir l'homéostasie de leur quota intracellulaire, les cellules sont amenées à réguler la synthèse/stockage/dégradation de ces biomatériaux en fonction des ressources extérieures (Geider et La Roche, 2002). Entre autres le C est généralement alloué à divers biocomposés en fonction de la teneur en sels nutritifs du milieu (Palmucci *et al.*, 2011). En condition limitante de N et $pCO_2$ constante, le rapport C:N peut s'équilibrer grâce à l'accumulation de composés à forte teneur en C et faible teneur en N comme les lipides (+50% entre [N]=55 $\mu$M et [N]=275 $\mu$M) ou les carbohydrates (+ 4% entre [N]=55 $\mu$M et [N]=275 $\mu$M), au détriment des protéines (- 30% entre [N]=55 $\mu$M et [N]=275 $\mu$M).

A ces composés s'ajoutent des atomes spécifiquement requis par certains taxons comme le silicium chez les bacillariophyceae ou le calcium pour les haptophytes calcifiants. Le rapport de Redfield devient alors 106C:16N:1P:1,3Si et 106C:16N:1P:23Ca respectivement (Ho *et al.*, 2003). Les éléments traces comme les métaux ou les vitamines, interviennent dans la biosynthèse de composés à faible rapport stoechiométrique. De manière générale, les métaux sont présents sous forme d'ions dans l'eau de mer, porteurs de charges électriques nécessaires à de nombreuses réactions d'oxydoréduction ainsi qu'au transfert d'électrons. Chez le phytoplancton, le fer entre dans la composition des molécules de ferrédoxine, qui interviennent au cours de la photosynthèse. Le manganèse est présent dans la chlorophylle a. Le zinc sert à la biosynthèse d'ADN polymérases. Les vitamines, comme la vitamine B12, sont également essentielles à la croissance du phytoplancton puisqu'elles servent de co-facteurs aux réactions enzymatiques (Swift, 1980). En conditions optimales, le carbone représente entre 20 et 80% du poids sec des cellules, l'azote, 3-15%, le phosphore 1-1,2%, le fer, 0,03-0,1%, la silice, 0,3-30% (Reynolds, 2006). Comme l'accroissement cellulaire est principalement lié à la photosynthèse, son amplitude est naturellement contrebalancée par la réaction métabolique inverse: la respiration cellulaire.

$$C_6H_{12}O_6 \; + \; 6\,H_2O \; + \; 6O_2 \; \rightarrow \; 6\,CO_2 \; + \; 12\,H_2O \tag{1.7}$$

Au cours de cette réaction, le Ribulose Bisphosphate réagit avec des molécules d'oxygène et libère du $CO_2$ et de l'énergie pour le métabolisme cellulaire. Parce qu'elle nécessite des molécules d'$O_2$, on parle de respiration aérobie ou photorespiration. Comme les réactions antagonistes de photosynthèse et de photorespiration sont catalysées par la même enzyme, la RUBISCO, au niveau du même site actif, la fixation du $CO_2$ est continuellement en compétition avec sa libération. La différence de vitesse de réaction favorise cependant la carboxylation à 80%, ce qui signifie qu'à terme, jusqu'à 2% des produits de la photosynthèse sont utilisés pour la respiration à température optimale (Lopez-Sandoval *et al.*, 2014). La balance entre assimilation et libération du $CO_2$ n'est pourtant pas constante puisque contrairement à la respiration, la photosynthèse ne peut avoir lieu qu'en présence de lumière (phase claire de la photosynthèse). Le taux de respiration cellulaire est généralement plus élevé pendant la journée que pendant la nuit à cause du pool de carbohydrates, substrats de la réaction, produits à cette période (Markager *et al.*, 1992). Les concentrations de $CO_2$ et d'$O_2$ dans le milieu peuvent également déséquilibrer cette balance. La RUBISCO présente une constante de demie-saturation pour le $CO_2$ estimée

entre 12 et 60 $\mu$M selon les espèces, largement supérieure à celle de l'$O_2$ comprise entre 200 et 2000 $\mu$M chez les algues photosynthétiques (Badger *et al.*, 1997).

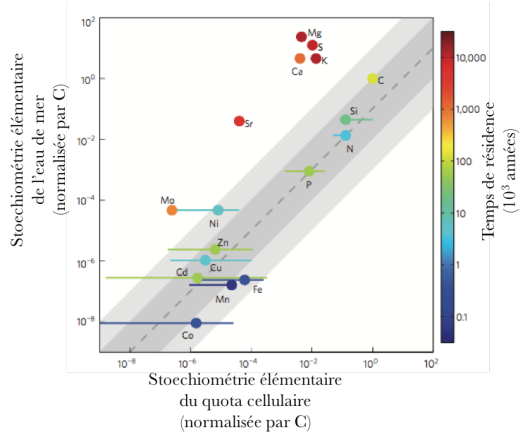


(a) Comparaison entre les stoechiométries de l'eau de mer et du phytoplancton (d'après Moore *et al.*, 2013)

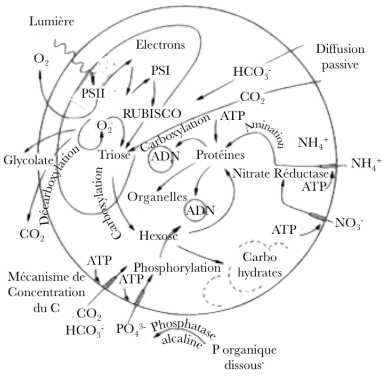


(b) Les principales voies métaboliques du phytoplancton (d'après Reynolds, 2006)

| Biocomposés | Composition atomique | % de la biomasse en poids sec |
|---|---|---|
| Acide aminés | - | 0-12 |
| Protéines | $C_{4,43}H_7O_{1,44}N_{1,16}S_{0,019}$ | 30-65 |
| ADN | $C_{9,75}H_{13,75}O_8N_{3,75}P$ | 0,5-3 |
| ARN | $C_{9,5}H_{14,25}O_8N_{3,75}P$ | 3-15 |
| Lipides | $C_{40}H_{74}O_5$ | 10-50 |
| Chlorophylle a | $C_{55}H_{72}O_5N_4Mg$ | 0,2-5 |
| Pigments accessoires | $C_{39-48}H_{52-68}O_{0-8}$ | 0,2-5 |
| ATP | $C_{10}H_{16}O_{13}N_5P_3$ | <0,1 |
| Carbohydrates | $C_6H_{12}O_6$ | 5-45 |

(c) La stoechiométrie élémentaire des biocomposés (d'après Geider et La Roche, 2002)

Figure 1.9: Composition du phytoplancton.

Toute concentration en $CO_2$ inférieure à la constante de demie-saturation de la RUBISCO va favoriser les étapes d'oxydation des produits photosynthétiques au détriment de la carboxylation. Si dans l'atmosphère, la proportion des gaz $O_2$ et $CO_2$ est de l'ordre de 21% et <1%, dans l'océan les concentrations atteignent des valeurs moyennes de 250 $\mu$M et 10 $\mu$M à 20°C respectivement. Pourtant, grâce à des mécanismes adaptatifs de concentration du $CO_2$ (Falkowski et Raven, 1997), le développement du phytoplancton *in vivo* n'est pas contraint en substance par des teneurs équivalentes (Raven et Johnston, 1991). Ces mécanismes sont utilisés à la fois par les domaines procaryote et eucaryote pour favoriser la carboxylation et palier aux faibles teneurs en $CO_2$. La concentration du $CO_2$ repose généralement sur le couplage des réactions de carboxylation/décarboxylation impliquant d'autres enzymes (e.g. la PEP carboxylase pour les organismes C4) ainsi

qu'un transport actif de carbone inorganique dissous ($CO_2$ ou $HCO_3^-$) vers les thylakoïdes (Raven *et al.*, 2012). Ils permettent aux cellules d'accumuler à proximité des sites actifs de RUBISCO plus de molécules de $CO_2$ qu'il ne serait possible par simple diffusion à travers la membrane.

Les processus d'excrétion contribuent également à diminuer la taille des cellules. Ce phénomène correspond au relarguage passif et/ou actif de photosynthétats en dehors de la cellule lorsque la fixation du $CO_2$ surpasse ses besoins métaboliques (Fogg, 1983). L'exudation de composés dissous à faible poids moléculaire, comme les acides aminés, par les cellules peut être liée à la diffusion et est donc taille-dépendante. Au contraire, l'exudation des molécules à fort poids moléculaire est un phénomène coûteux en énergie puisqu'il requiert la présence de canaux transmembranaires souvent ATP-dépendants pour transporter les biomatériaux vers le milieu extérieur. C'est donc uniquement quand les cellules peuvent pallier à ce coût énergétique que l'exudation peut atteindre un taux journalier de 5% de la biomasse en C (Bjornsen, 1988). Plusieurs hypothèses tendent à expliquer l'exudation. Cette stratégie permettrait de maintenir le rapport de Redfield en conditions limitantes voire de baisser $infine$ la pression de compétition pour les ressources inorganiques vis-à-vis des bactéries hétérotrophes qui assimilent rapidement la matière dissoute organique labile au détriment des composés inorganiques (Grover, 2000; Thornton, 2014). Au contraire, une taille suboptimale est souvent le signe d'un stress environnemental qui peut pousser la cellule à stocker les nutriments dans une vacuole au delà de leur besoin, via une assimilation de *luxe*, ou à s'enkyster (cf. la quiescence cellulaire) pour attendre des conditions de croissance plus favorables.

*La reproduction cellulaire*

Deux modes de reproduction aboutissent à la formation de nouveaux individus pour assurer le développement et maintenir le patrimoine génétique des populations phytoplanctoniques (Figure 10): la division en phase asexuée ou mitose, qui conduit à la naissance de deux individus strictement identiques, et la fusion des gamètes en phase sexuée, qui assure la diversification génétique par recombinaison (Lakeman *et al.*, 2009). Pour compléter leur cycle cellulaire, les cellules du phytoplancton entrent en mitose suite à l'interphase. La mitose est le processus le plus fréquemment utilisé par le phytoplancton pour se multiplier. Sa durée varie selon les espèces mais n'est plus soumise à des régulations internes lorsque la première étape est enclenchée (Olson *et al.*, 1986; Dagenais-Bellefeuille *et al.*, 2008). La fission binaire des cellules se produit à la fin d'une séquence de quatre étapes distinctes (Figure 10a):

1. La **prophase** marque la fragmentation de la membrane nucléaire dans le cytoplasme et la condensation des chromosomes dupliqués. Les molécules d'ADN se lient à des protéines matrices, dites *cohésines*, et s'enroulent progressivement sur elles-même. Chaque paire de centrioles qui se sont dupliqués à l'interphase migre vers un pôle opposé de la cellule, d'où s'étend la fuseau mitotique. L'assemblage des microtubules s'allonge pour déterminer l'orientation du plan de migration des chromatides soeurs, attachées au niveau de leur centromère.

2. La **métaphase** fait intervenir l'alignement des centromères au centre de la cellule selon un axe perpendiculaire à celui du fuseau microtubulaire, la *plaque métaphasique*. Les microtubules se fixent aux kinétochores présents au niveau des centromères de

chaque chromatide soeur. Un deuxième faisceau polaire va permettre l'élongation de la cellule.

3. L'**anaphase** consiste en la migration des chromatides vers les pôles de la cellule. C'est pourtant le stade le plus court de la mitose. Il débute par la division simultanée des centromères pour permettre la séparation des paires de chromatides soeurs. L'intervention de protéases pour cliver les cohésines assure aussi la libération des chromatides. Ce signal est régulé par le facteur déclencheur de l'anaphase (l'*anaphase-promoting-complex*). Les microtubules liés au kinétochores se raccourcissent progressivement, par détachement de sous-unités de tubuline, pour attirer les chromatides aux pôles cellulaires. Les microtules polaires s'allongent pour éloigner les chromatides l'une de l'autre et préparer la cytocinèse.

4. La **télophase** marque l'arrivée des chromosomes aux pôles cellulaires. L'appareil fusorial des kinétochores est alors dégradé avec les kinétochores. Les microtubules polaires continuent l'élongation de la membrane plasmique pour préparer la cytocinèse. Une nouvelle membrane nucléaire se forme autour de chaque groupe de chromosomes. L'ADN est décondensé de façon à induire l'expression des gènes, notamment ceux impliqués dans le formation du nucléole.

A la fin de la mitose, les cellules possèdent deux copies identiques de l'ADN répliqué en phase S réparties dans deux noyaux distincts positionnés aux pôles. A ce stade, les deux cellules filles seront effectivement séparées l'une de l'autre au bout de 10 à 30 minutes par le processus de cytocinèse. La membrane plasmique s'invagine et tous les organites qui ont été dupliqués à l'interphase se séparent pour former deux organismes distincts. Lorsque les espèces arborent des plaques extramembranaires, telles que la thèque chez les dinophyceae ou le frustule des bacillariophyceae, les cellules filles sont contraintes soit de synthétiser à nouveau ces composés lorsque la plaque parentale est détruite (i.e. Eleuthéroschisie) soit de compléter l'une et l'autre des sous-unités parentales qui sont conservées.

La reproduction sexuée correspond à l'alternance de syngamie (i.e. fusion des gamètes) et de la méïose (division sans réplication) dans un ordre qui n'est pas fixé. Dans tous les cas, la méïose permet de réduire la ploïdie, par division réductionnelle, soit des gamètes lorsque le cycle suit l'ordre méïose-syngamie, soit du zygote lorsque l'ordre est inversé. Lorsque la reproduction est dioïque, le zygote présentera un patrimoine génétique issu de gamètes non-identiques génétiquement. Au cours de la méïose, des chromosomes homologues sont répliqués et peuvent se recombiner par crossing-over avant de subir plusieurs cycles de division, où les chromatides soeurs restent premièrement appariées avant de se séparer à la mitose. L'émergence de gamètes et de zygotes issus de la reproduction sexuée est difficile à instaurer en culture. A cause de leurs formes cryptiques, ces stades sont parfois confondus avec d'autres organismes de la phase végétative (Figueroa *et al.*, 2015). Seules 22 espèces de dinophyceae sur 2000 ont été identifiés comme potentiellement capables de reproduction sexuée (Pfiester et Anderson, 1987). En culture, la reproduction sexuée des dinophyceae peut être induite par déplétion graduelle de nutriments, comme les composés azotés, phosphorés ou le fer, ou des températures suboptimales. Lorsque les conditions deviennent défavorables au développement complet du phytoplancton (i.e. depaupasie), les cellules végétatives, généralement trop petites, se différencient en gamètes par gamétogénèse. Les gamètes produites dépendent du type de cycle de vie des espèces reproductrices.

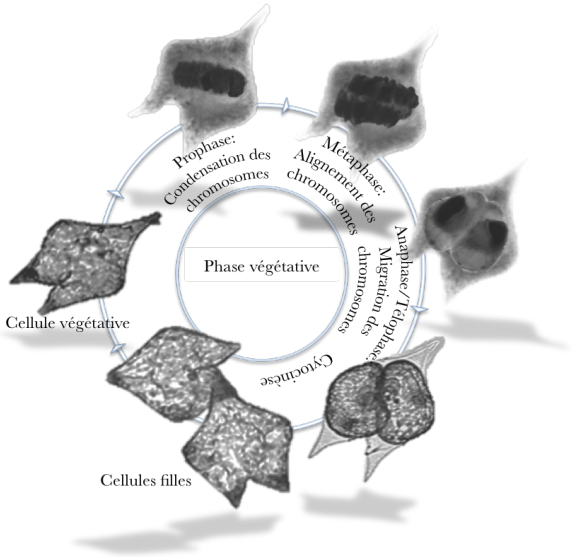


(a) La reproduction asexuée ou mitose.

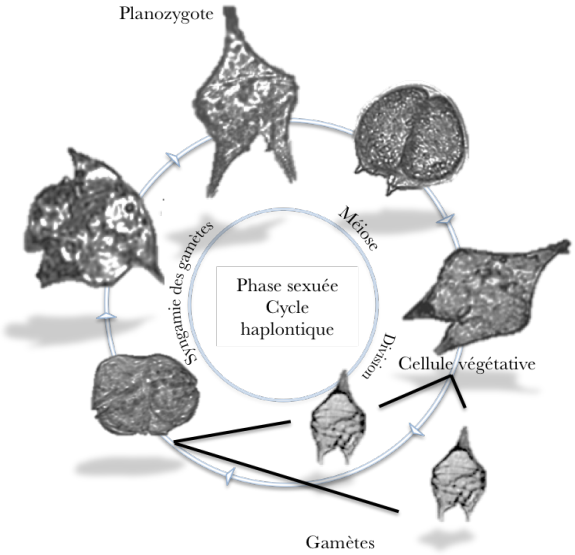


(b) La reproduction sexuée des organismes au cycle de vie haplontique.

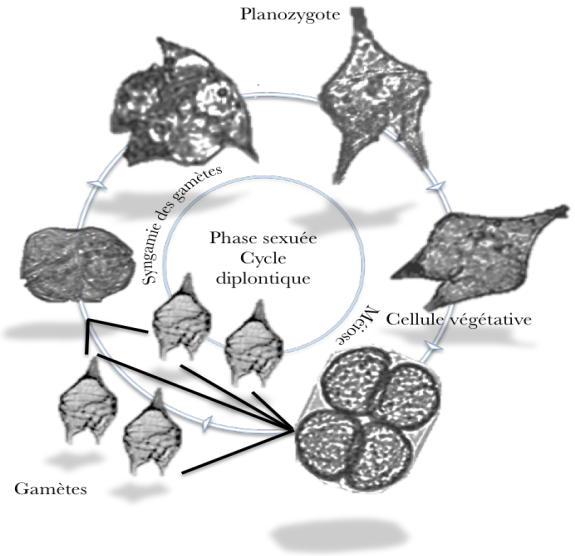


(c) La reproduction sexuée des organismes au cycle de vie diplontique (*Protoperidinium* ne présente pas de cycle diplontique, les cellules ne correspondant pas au bon stade de développement ont été placées de façon à illustrer les étapes d'un tel cycle).

Figure 1.10: La reproduction du phytoplancton illustrée par une série d'observations microscopique de cellules de *Protoperidinium* (Grubble *et al.*, 2009)

Lorsque le cycle est majoritairement haplontique, comme c'est le cas chez les dinophyceae, les gamètes produites sont haploïdes et dites hologames, comme les cellules végétatives et seul le zygote est diploïde (Figure 10b). Lorsqu'il est diplontique, les cellules végétatives et le zygote contiennent 2N chromosomes et la méïose réductionnelle conduit à la formation de gamètes haploïdes, dites hétérogames (Figure 10c). La gamétogénèse conduit à la formation d'une à plusieurs paires de gamètes par méïose(s) successive(s). Elle est engagée par la rencontre, souvent guidée par les phéromones (Frenkel *et al.*, 2014), et la formation d'un tube de conjugaison entre deux gamètes.

Ces gamètes vont fusionner (i.e. syngamie), d'abord par le cytoplasme (i.e. plasmogamie) suivie par la formation d'un seul et même noyau contenant le matériel génétique des deux gamètes (i.e. karyogamie). Ces étapes terminées marquent la naissance d'un planozygote. La plupart du temps le planozygote s'enkyste pour entrer en période de dormance. Quand il ne s'enkyste pas, le planozygote peut reprendre le cours de la phase asexuée et se diviser pour devenir une cellule végétative. S'il ne parvient ni à s'enkyster ni à se diviser directement, le zygote entre en phase de sénescence et enclenche la nécrose.

*La quiescence cellulaire*

La quiescence cellulaire fait référence à un stade de vie par lequel une cellule présente un métabolisme anormalement réduit qui empêche toute division. Le ralentissement métabolique est principalement lié à des changements structuraux des cellules en dormance: accumulation des lipides (jusqu'à 40% du poids sec total) et des pigments accessoires, augmentation du nombre de vacuoles, déformation des thylakoïdes, etc. (Binder et Anderson, 1990; Chapman *et al.*, 1982) (Figure 11).

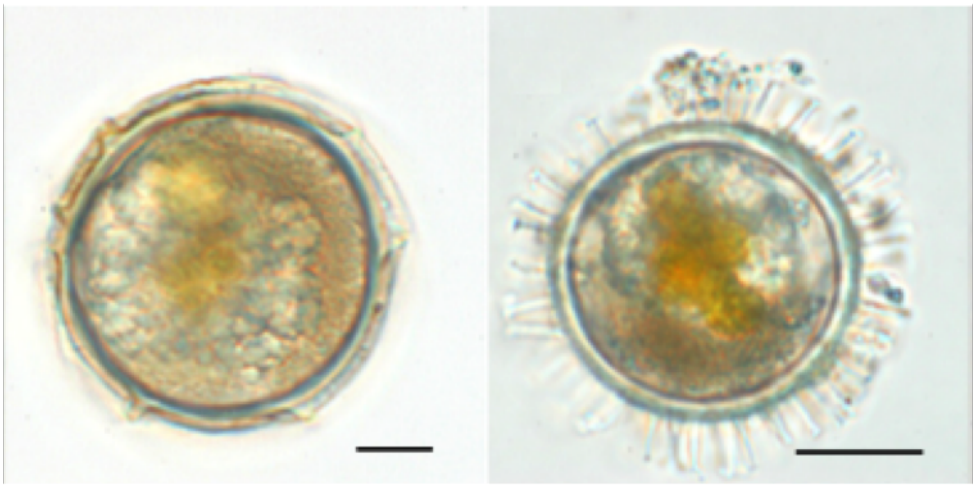

Figure 1.11: Spores d'*Alexandrium pseudogonyaulax* et *Protoceratium reticulatum* (Bravo *et al.*, 2014). Les cellules en dormance ont un métabolisme réduit induit par des changements structuraux tels que l'accumulation de caroténoïdes. Certaines arborent des épines pour se protéger des prédateurs. Barre d'échelle: 10 $\mu$m.

Ce stade, nommé G0, est perçu comme une stratégie de survie du phytoplancton, et placé en marge du cycle cellulaire puisque les cellules quiescentes ne répliquent pas leur ADN et n'entrent pas en mitose. Cette stratégie augmente considérablement la capacité de résilience du phytoplancton face aux environnements défavorables (Ribeiro *et al.*, 2011). Parce qu'ils ne souffrent pas des changements de conditions environnementales et qu'ils présentent une capacité de dispersion accrue, les organismes nés de la germination de cellules en quiescence sont distribués très largement à la surface du globe (Tang

et Gobler, 2015). Par rapport aux changements globaux, elles assurent également le maintien du plus large stock de diversité génétique qui a directement influencé les capacités d'adaptation du phytoplancton sur des périodes de temps géologiques (Falkowski *et al.*, 2004). Contrairement à la sénescence, cette étape est réversible et les cellules, alors appelées kystes ou spores, restent viables. L'entrée en phase de dormance passe par une différentiation visible des cellules lorsqu'elles s'entourent d'une paroi externe organique (sporopollenine) ou calcaire (Bravo *et al.*, 2014). Cette paroi n'empêche pas la diffusion des nutriments vers le cytoplasme pour assurer le métabolisme basal de la cellule. Certaines sont pourvues d'épines afin de limiter la prédation (Rengefors *et al.*, 1998), les dommages mécaniques ou physiques (UVs) (Martinez *et al.*, 2012). La sortie de quiescence est souvent liée à un changement des conditions environnementales qui favorisent de nouveau la reproduction des cellules, soit par multiplication végétative soit par germination d'un planomeïocyte (Figure 12).

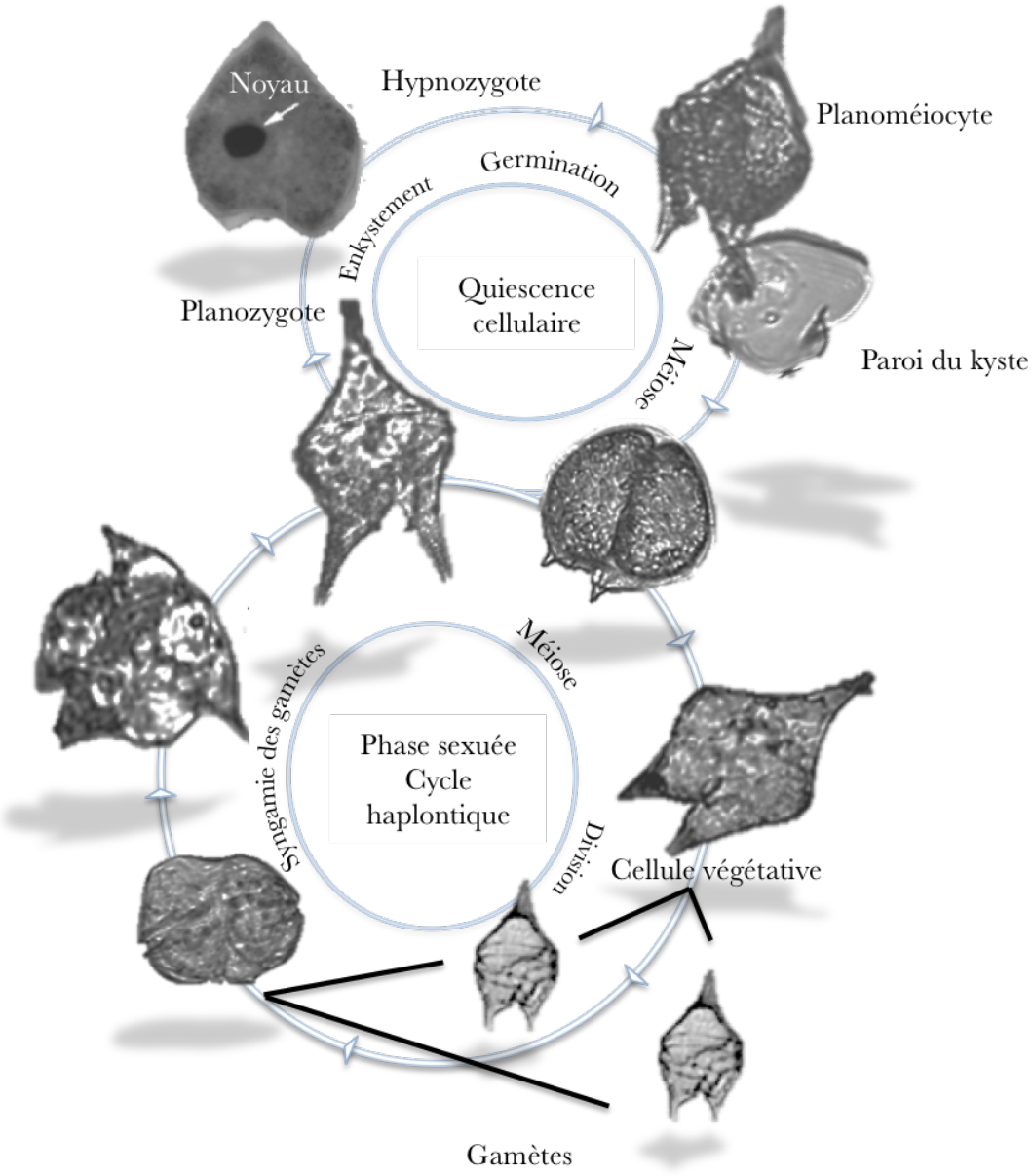


Figure 1.12: La quiescence cellulaire. Les étapes de l'enkystement sont illustrées par la série d'observations au microscope d'une cellule de *Protoperidinium* (Gribble *et al.*, 2009)

Chez certaines espèces de phytoplancton, la reproduction sexuée, qui aboutit à la formation d'un planozygote, est systématiquement suivie de la sporulation pour favoriser la conservation des recombinaisons génétiques induites par la méiose (Dale, 1983). D'autres espèces ne passent pas par le stade de kyste pour former le planozygote. L'enkystement est également fréquent pour la phase asexuée du cycle de vie des organismes en dormance. La dormance est très souvent associée aux espèces de dinophyceae et bacillariophyceae, chez qui on a découvert de nombreux spores fossilisés datant d'épisodes d'extinction marquants (Sims *et al.*, 2006). Le défaut de quiescence des autres clades vient probablement de la perte de cette capacité pour certaines lignées. Les cellules de phytoplancton qui atteignent le plancher océanique et s'enfouissent dans les sédiments forment un pool de C durablement séquestré dans les océans lorsqu'il n'est pas remobilisé par resuspension naturelle ou pour produire des biocombustibles. La présence de plusieurs milliers de kystes par $cm^2$ forme des stocks très localisés de cellules en dormance, appelés 'banques', qui peuvent représenter la deuxième source de matière organique particulaire (POM) reminéralisable (Della Tommasa *et al.*, 2004). De nombreuses banques de kystes qui se sont accumulées à la surface des sédiments et en profondeur peuvent être datées par carottage. Certaines de ces banques, datant de plusieurs jours (sédiments de surface) dans les zones de fort mélange hydrodynamique (Marcus et Boero, 1998) à plusieurs dizaines d'années (sédiments à 30-50 cm de profondeur) (McQuoid *et al.*, 2001), contiennent des organismes encore viables, c'est-à-dire qu'ils ont encore la capacité de germer en conditions adéquates, grâce à la quiescence. L'étude de Kremp et Anderson (2000) a montré que la température, l'irradiance et l'oxygène ne sont pas les seuls facteurs clés du contrôle de la germination de ces spores. La transition par une période de dormance fixe, qui apparaît comme une étape de maturation régulée par l'horloge interne des cellules, est également une condition nécessaire au désenkystement (Anderson et Kiefer, 1987). Cette étape de maturation peut durer entre 12 heures et 1 année selon les espèces. Pour de nombreux écosystèmes, le cycle annuel de germination des spores pérennise l'initiation d'épisodes d'efflorescence puisqu'il aboutit à la libération d'un inoculum important de cellules végétatives capables de se multiplier par la suite via le cycle asexué (Steindinger, 1975; Nehring, 1993). Au contraire, la sporulation est un évènement majeur marquant le déclin des efflorescences une fois les nutriments épuisés dans la couche de surface (Heaney *et al.*, 1983).

*La mort cellulaire*

L'apoptose ou mort cellulaire programmée est un procédé bien connu du développement des êtres vivants, en particulier des métazoaires. En ce qui concerne le phytoplancton, ce mécanisme n'a été inclus dans les termes de pertes, $l$, qui régissent les équations de dynamique des population *in situ* (E 1.3) qu'à compter de l'étude de Reynolds (1980), même s'il était considéré comme négligeable par rapport à la pression de prédation et à la sédimentation. Les études d'Agusti *et al.* (1998) et de Sigee *et al.* (2007) présentent toutefois la mort cellulaire comme un facteur important des successions écologiques du phytoplancton et du déclin des efflorescences observées en milieu naturel. C'est un phénomène contrôlé de façon endogène, puisqu'il est encodé par le génome, qui conduit à la contraction du protoplasme des cellules jusqu'à la perte de la viabilité et de l'intégrité structurale par lyse cellulaire (Franklin *et al.*, 2006). La première étape consiste systématiquement en la dislocation d'un composé présent dans la membrane interne des cellules, la phosphatidylserine (Segovia et Berges, 2009). Ensuite les molécules d'ADN

sont condensées et fragmentées et le protoplasme réduit de taille. Le stade final, ou nécrose, de la cellule marque le relarguage de l'ensemble des composites cellulaires compromis dans l'environnement qui peuvent déclencher l'apoptose des cellules voisines par allélopathie (Vardi *et al.*, 2007). L'encodage du programme de mort cellulaire contient des séquences de gènes spécifiques de protéines soit inhibitrices (IAP), c'est-à-dire qu'elles répriment l'expression de gènes qui conduisent à l'apoptose (Deveraux *et al.*, 1997), soit activatrices de la mort cellulaire (e.g. caspases) (Bialik *et al.*, 2010). Le mode d'action de ces dernières implique souvent la perméabilisation des membranes par fixation aux pores membranaires des cellules et de leurs organites (e.g. mitochondries, appareil de Golgi, chloroplastes) ainsi que la fragmentation des chromosomes. Ce procédé a été mis en évidence chez les espèces de bacillariophyceae, dinophyceae, haptophyceae et certaines cyanobactéries. Deux types de facteurs peuvent provoquer l'activation du programme de mort cellulaire. Les facteurs exogènes sont dus à l'absence de composés requis pour le métabolisme basal des cellules (Berges et Falkoswki, 1998) et/ou à l'adversité des conditions biotiques (e.g. infection virale, allélopathie) et abiotiques (e.g. carence, obscurité, UVs, chocs thermiques et osmotiques) (Jimenez *et al.*,2009) (Figure 13).

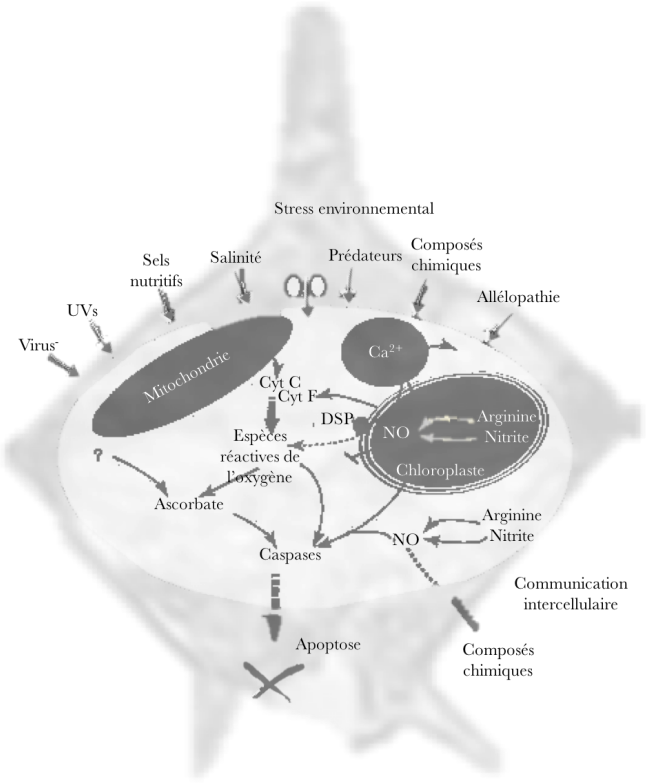


Figure 1.13: Signalisation cellulaire de l'apoptose par stress oxydatif. Lorsqu'un stress environnemental est perçue par la cellule, la production d'oxyde nitrique (NO) et d'espèces réactives de l'oxygène (ROS) altèrent certains composés (Ascorbate) et la balance d'oxydo-réduction des organites et du protoplasme. Ces composés toxiques activent la transcription/traduction de gènes (capsases) et des protéines marqueurs de l'apoptose (Death Specific Protein) (d'après Bidle, 2016).

Vardi *et al.*, 1999 ont montré que le stress oxydatif induit par une limitation de $CO_2$ peut conduire à l'activation soit de l'enkystement soit de l'apoptose par l'intermédiaire d'enzymes de clivage protéique, les protéases cystéine aspartique (capsases). Ces mécanismes sont privilégiés par les cellules en réponse respectivement à l'inhibition et l'activation de la même voie de médiation. Les voies de stress métabolique, de contrôle métabolique,

de signalisation et d'activation du programme de mort cellulaire sont très conservés par les lignées de phytoplancton. Elles ont été sélectionnées à l'échelle de temps adaptative (3 milliards d'années, Bidle *et al.*, 2016) pour conduire au succès écologique de ces producteurs, notamment pour se défendre des virus (Bidle, 2015). Les facteurs endogènes traduisent le plus souvent le fait qu'une cellule ne peut subir qu'un nombre limité de divisions au cours de sa vie (Hellweger, 2008). Ce phénomène est bien connu chez les bacillariophyceae pour qui la division asexuée, contrainte par la présence du frustule, aboutit à la formation de cellules filles asymétriques. Comme pour la réplication de l'ADN, la division des diatomées est semie-conservative puisque chaque cellule fille va se développer au sein de l'espace cloisonné par les deux parois du frustule et produire une paroi emboîtée pour compléter le frustule. Ce cloisonnement entraîne la diminution progressive de la taille des cellules à chaque génération jusqu'à ne plus pouvoir recouvrir un état cellulaire viable autrement que par reproduction sexuée (Chepurnov *et al.*, 2004).

*Le contrôle du cycle cellulaire*

Chez tous les organismes le passage d'une phase du cycle cellulaire à l'autre n'est permis qu'après l'activation de points de contrôle servant à arrêter le déroulement du cycle cellulaire en cas de carence nutritionnelle (point de contrôle G1/S), de défaut de réplication ou de mutations délétères (S), de défaut d'organisation pour préparer la mitose (G2/S) ou en assurer son bon déroulement (M). L'ensemble de ces points de contrôle, appelés *points de restriction*, peut conduire les cellules à entrer en phase de quiescence (G0) jusqu'à leur arrivée dans un environnement plus favorable. Ces mécanismes, qui s'appuient principalement sur l'activité de kinases cyclines dépendantes *Cdk* (i.e. enzymes composées d'une sous-unité enzymatique, la kinase, associée à une protéine de cycline), sont relativement bien conservés chez les eucaryotes et procaryotes. Les cyclines sont transcrites et dégradées de façon cyclique pendant le cycle cellulaire (Bloom et Cross, 2008). Les kinases servent à phosphoryler (ajout d'un groupement $PO_4^{3-}$ sur certains acides aminés protéiques) différentes protéines de façon à les activer ou inactiver selon l'emplacement où le groupement $PO_4^{3-}$ est ajouté. Elles ne sont elles-mêmes activées que lorsqu'elles forment un complexe avec les cyclines.

Les protéines cibles des *Cdk* pendant le cycle cellulaire ne sont pas toutes connues, mais elles ont toutes un lien avec l'avancée du cycle cellulaire en fonction de l'étape où elles sont activées. Par exemple, le point de restriction G1/S est le point le plus sensible à différents facteurs internes et externes. Parmi les facteurs internes, l'état nutritionnel et la taille des cellules semblent des points clés pour permettre l'aboutissement de la synthèse des protéines nécessaires à la phase S. La réplication de l'ADN est un processus bien contrôlé chez les cellules qui demandent notamment l'assimilation de phosphate pour synthétiser les molécules d'ATP, le ribulose-5-P qui entre dans la composition des acides nucléiques ou des phospholipides membranaires et de sources d'azote qui composent les acides aminés de l'ensemble des protéines de la machinerie cellulaire et certains nucléotides. Certaines études portant sur le budget énergétique alloué à l'assimilation des nutriments et la croissance cellulaire ont donné naissance au dogme de taille minimale, au delà de laquelle toute cellule sera amenée à répliquer son ADN et se diviser (Muller *et al.*, 2011). Le point critique, dénommé *Commitment* ou *Restriction Point*, du cycle qui correspond au moment où la cellule atteint ce seuil est situé en phase $G1$.

Dans un effort pour relier le statut nutritif des cellules avec le point de restriction G1, Mocquet *et al.* (2010) ont modélisé la probabilité de transition des phases G1-S

en fonction du quota cellulaire de nutriments essentiels, de façon à ce qu'elle tende vers 0 lorsque les cellules sont soumises à une carence sévère. Chez les procaryotes, pour qui on ne distingue pas de réel phases $G1$, $S$ et $G2$, ce point s'apparente au contrôle du nombre de fourchettes de réplication formées simultanément par rapport à leur taille (Bremer et Churchward, 1994). En milieu naturel, les cellules d'une même population sont généralement asynchrones, c'est-à-dire qu'elles ne sont pas toutes au même point d'avancement du cycle cellulaire. A cause de ce phénomène, les analyses successives à l'échelle de la cellule montrent souvent une distribution continue en classes de taille, que ce soit au cours de l'interphase ou au cours de la division (cf. Annexe D); ce qui laisse à penser que le spectre de taille des cellules qui entrent en division continue de s'élargir une fois passé la taille minimale.

Les dommages occasionnés lors de la réplication de l'ADN ou de sa mutation sont également examinés par la machinerie de réparation cellulaire pour s'assurer de l'intégrité du génome avant qu'il ne soit transmis à la génération de cellules suivantes. De plus certaines espèces comme les diatomées ou les coccolitophores sont dépendantes de l'assimilation de silice (Brzezinski *et al.*, 1990) et d'ions carbonate $CO_3^{2-}$ respectivement pour synthétiser leur paroi externe. Les organismes auxotrophes ne synthétisent pas eux-mêmes certaines vitamines ou facteurs de croissance (e.g. cytokinines); ils peuvent également être limités par les teneurs apportées par le milieu extérieur (Mooney et Von Staden, 1985). Une carence entraîne généralement la cessation de l'avancée du cycle en phase G1 et augmente sensiblement le temps de génération (Vaulot *et al.*, 1987; Muller *et al.*, 2008). Cet arrêt est néanmoins réversible et les cellules entrent en phase S après augmentation de la concentration limitante. Si l'ensemble des points contrôlés par les $Cdk$ à ce niveau du cycle cellulaire (i.e. état nutritionnel supérieur au niveau basal, présence de facteurs de croissance et intégrité du génome) sont favorables au passage de la cellule en phase S, alors son engagement vers la mitose est irréversible pour ne pas garder de copie supplémentaire du matériel génétique.

La photopériode influence la durée de la phase $G2$ (Jacquet *et al.*, 2001). De par son rythme circadien, la lumière est considérée comme le premier facteur qui orchestre le contrôle du cycle cellulaire par une horloge interne, codée par le groupe de gènes *Per* (Takahashi, 1992), poussant les cellules à s'accroître pendant la journée et à se diviser la nuit, à l'abris des UVs. Un facteur, le $Licensing\,Factor$, est requis par toutes les cellules pour qu'elles initient la réplication de l'ADN. Ce facteur est ensuite détruit au cours de la réplication pour prévenir un deuxième cycle de duplication sans entrer en phase $M$. C'est pendant la phase $M$ que ce facteur, qui n'est pas perméable à la membrane du noyau, peut se lier à nouveau à l'ADN des cellules. Seuls les procaryotes présentent un découplage entre la phase de réplication et la phase de mitose. Cette dernière est généralement plus courte que la phase $S$ ce qui peut entraîner un excès variable du nombre de copies d'ADN par cellule. Comme les bactéries ont la faculté d'initier plusieurs cycles de duplication avant la mitose au niveau de l'origine de réplication, certaines espèces comme $Prochlorococcus\,sp$ présentent couramment entre 1 et 5 copies d'ADN par cellule (Vaulot, 1995).

Un autre point de contrôle, en phase G2/M assure le passage des cellules en phase de mitose. Ce point, activé par la $Cdk$ dénommé $M\,Promoting\,Factor$, ou facteur stimulant de la phase $M$ ($mpf$), sert à bloquer le cycle quand l'ADN n'a pas été correctement dupliqué. Le dernier point de contrôle agit juste avant l'anaphase pour s'assurer que les chromosomes (unique chez les procaryotes) sont correctement ancrés au fuseau mitotique au niveau de leur centromère pour permettre la migration de chaque chromatide

soeur d'un bout à l'autre de la cellule. L'*Anaphase Promoting Complex* est un complexe protéique qui enclenche la destruction des cohésines par des protéases au niveau des centromères des chromatides. Lorsque le complexe de cohésines est détruit, chaque chromatide peut migrer vers un pôle de la cellule par contraction du fuseau mitotique. En plus des cohésines, l'APC est responsable de la protéolyse de différentes cyclines responsables de l'activation de la réplication de l'ADN et de la synthèse du fuseau mitotique et de l'inhibition de la cytocynèse (Cross et Umen, 2015).

## 1.3 Sensibilité à l'environnement

La distribution du phytoplancton est contrôlée de façon intrinsèque par le taux de croissance ($\mu$) des populations. A cela s'ajoutent les facteurs extérieurs qui complexifient les moyens de prédire les conséquences d'un changement de milieu sur le développement du phytoplancton. Le taux de perte ($l$) lié à la prédation, à la mort cellulaire, mais aussi leur transport physique au cours du déplacement des masses d'eau (d'ordre 1, U, et d'ordre 2, K) sont autant de variables qui contrôlent la présence du phytoplancton en un point de l'espace à un moment donné (cf E 1.3). Tributaire des courants pour se déplacer, le phytoplancton présente une hétérogénéité spatiale fortement influencée par les échelles de circulation océanique. Même si certaines espèces présentent des adaptations liées à la mobilité active (e.g. flagelle, frustule/vacuoles), leur capacité de déplacement est généralement négligeable par rapport aux vitesses du courant. Deux ordres de grandeur sont modélisés pour prédire le transport du plancton en milieu pélagique. Les mouvements d'ordre 1 traduisent un déplacement vectoriel dirigé par les composantes horizontales ($\vec{u}$: ouest → est, $\vec{v}$: sud → nord) et verticale ($\vec{w}$: niveau 0 → océan profond) du champ de courant (U=$\{\vec{u},\vec{v},\vec{w}\}$). Les mouvements d'ordre 2 sont contrôlés par un coefficient de turbulence méso-échelle, noté K ($km^2.s^{-1}$). Généralement simulés par un processus stochastique gaussien, ils correspondent à une diffusion passive des particules dans toutes les directions de l'espace. Ce mouvement caractérise également les nutriments qui diffusent de façon passive à travers les masses d'eau et les membranes biologiques contre le gradient de concentration en suivant la loi de Fick (E 1.8):

$$F = -K.\frac{\partial C}{\partial x} \tag{1.8}$$

F: flux diffusif de plancton ou de nutriments, K: coefficient de diffusion, C: concentration en plancton ou en sels nutritifs, x: direction du gradient de concentration

Si l'on considère seulement le flux d'individus dans un modèle spatialisé comme celui de l'advection-diffusion-réaction, la variation temporelle de la densité d'individus au site $x$, correspondant à un puits de plancton, sera stimulée par le flux de plancton provenant de sites sources adjacents:

$$\begin{aligned} \frac{\partial C(x,t)}{t} &= -\frac{\partial C(x,t)}{\partial x} \\ \frac{\partial C(x,t)}{t} &= K\frac{\partial^2 C(x,t)}{\partial x^2} \end{aligned} \tag{1.9}$$

Ce système admet la solution analytique suivante: $C(x,t) = \frac{C_0}{2\sqrt{2\pi Kt}} exp^{-\frac{x^2}{4Kt}}$, d'où la ressemblance avec la densité de la distribution normale centrée sur la position initiale

$C_0 = C(x = 0, t = 0)$ avec un écart-type de $\sqrt{2Kt}$:

A partir de la formulation générale $C(x,t) = t^{-\alpha}F(\eta)$ et des valeurs spécifiques

$$\eta = \frac{x^2}{4Kt}, \alpha = \frac{1}{2},$$

$$\frac{\partial C(x,t)}{\partial t} = -\alpha t^{-\alpha-1}F(\eta) + t^{-\alpha}\frac{dF}{d\eta}\frac{\partial \eta}{\partial t} = -\alpha t^{-\alpha-1}F(\eta) + t^{-\alpha}(-\eta t^{-1})\frac{dF}{d\eta} =$$

$$-\alpha t^{-\alpha-1}F(\eta) - \eta t^{-\alpha-1}\frac{dF}{d\eta}$$

$$\frac{\partial C(x,t)}{\partial x} = t^{-\alpha}\frac{dF}{d\eta}\frac{\partial \eta}{\partial x} = t^{-\alpha}\frac{dF}{d\eta}\frac{2}{4Kt}x = \frac{x}{2K}t^{-\alpha-1}\frac{dF}{d\eta}$$

$$\frac{\partial^2 C(x,t)}{\partial x^2} = \frac{t^{-\alpha-1}}{2K}\frac{dF}{d\eta} + \frac{x}{2K}t^{-\alpha-1}\frac{d^2F}{d\eta^2}\frac{\partial \eta}{\partial x} = \frac{t^{-\alpha-1}}{2K}\frac{dF}{d\eta} + \frac{d^2F}{d\eta^2}\frac{t^{-\alpha-1}}{K}\eta$$

$$(1.9) \Leftrightarrow -\alpha t^{-\alpha-1}F(\eta) - \eta t^{-\alpha-1}\frac{dF}{d\eta} = \frac{1}{2}t^{-\alpha-1}\frac{dF}{d\eta} + t^{-\alpha-1}\eta\frac{d^2F}{d\eta^2}$$

$$\Leftrightarrow -\alpha F(\eta) - \eta\frac{dF}{d\eta} = \frac{1}{2}\frac{dF}{d\eta} + \eta\frac{d^2F}{d\eta^2} \Leftrightarrow \eta\frac{d}{d\eta}\left(\frac{dF}{d\eta} + F\right) + \frac{1}{2}\left(\frac{dF}{d\eta} + 2\alpha F\right) = 0$$

$$\Leftrightarrow \eta\frac{d}{d\eta}\left(\frac{dF}{d\eta} + F\right) + \frac{1}{2}\left(\frac{dF}{d\eta} + F\right) = 0 \text{ avec, } \alpha = \frac{1}{2}$$

$$\Leftrightarrow \left(\frac{dF}{d\eta} + F(\eta)\right) = 0 \text{ qui a pour solution } F(\eta) = cexp^{-\eta} = cexp^{-\frac{x^2}{4Kt}}$$

D'où, $C(x,t) = t^{-1/2}F(\eta) = \frac{c}{\sqrt{t}}exp^{-\frac{x^2}{4Kt}} = \frac{C_0}{\sqrt{4\pi Kt}}exp^{-\frac{x^2}{4Kt}}$ avec la condition initiale

$$c = \frac{C_0}{\sqrt{4\pi K}}$$

(1.10)

La représentation des échelles de variabilité spatio-temporelle de la distribution physique du plancton, *patchiness*, est possible par l'analyse diagnostique du déplacement des organismes planctoniques le long de trajectoires dirigées par les courants en fonction de la vitesse, ou inversement du taux, exposant de Lyapunov $\lambda(x,t,\delta_0,\delta)$, auquel se séparent des structures Lagrangiennes proches (D'Ovidio *et al.*, 2004):

$$\begin{aligned} \delta &= \delta_0.exp(\lambda(x,t,\delta_0,\delta)t) \\ \lambda(x,t,\delta_0,\delta) &= \frac{1}{\tau}.log_e(\frac{\delta}{\delta_0}) \end{aligned} \tag{1.11}$$

t: position temporelle [T], x: position spatiale [L], $\tau$: intervalle de temps [T], $\lambda$: taux d'étirement de trajectoires proches $[T]^{-1}$, $\delta_0$: distance initiale entre le point x et le début de la trajectoire [L], $\delta$: distance finale entre les trajectoires de référence et prédite à partir du point x [L]

Le calcul de l'exposant de Lyapunov sur un intervalle de temps fixé comparable aux transitions de successions écologiques (e.g. initiation du bloom), *Finite Time Lyapunov Exponent*, ou par rapport à une distance finie d'interêt (méso-échelle: 10-100 km), *Finite Size Lyapunov Exponent* permet d'identifier la présence de fronts spatio-temporel qui séparent des masses d'eau avec leurs caractéristiques physique, chimique et biologique.

Selon cet historique, les différentes espèces de plancton suivent une dynamique particulière liée aux contrôles des nutriments (bottom-up) et/ou des prédateurs (top-down) sous couverture d'une niche apparente. L'ensemble de ces facteurs influencent de façon hiérarchique le déséquilibre et la forte hétérogénéité spatio-temporelle des populations de phytoplancton. Ce déséquilibre est soutenu par des variations inter et intra-spécifiques des individus qui présentent des capacité d'adaptations physiologiques à l'échelle cellulaire également dynamiques. L'apport des analyses *in situ* à haute fréquence pour modéliser, par réduction d'échelle, la dynamique complexe du plancton est manifestement indissociable d'une meilleure appréhension de toutes les échelles de variation qui la structure, de l'échelle de variation la plus fine à l'échelle globale.

*La température: relations empiriques, implications physiologiques et dynamiques*

Dans le milieu naturel, il existe de nombreux gradients de température liés aux échelles climatiques spatiales et temporelles. Même si Longhurst lui a préféré une explication en lien avec la circulation océanique globale, le premier facteur invoqué pour expliquer l'hétérogénéité spatiale du phytoplancton à l'échelle globale a naturellement été la température, avec son gradient méridional symétrique de l'équateur aux tropiques, où elle atteint 30°C, aux pôles où l'eau gèle par -2°C (White et Cayan, 1998). Avec la salinité, la température de l'eau est le moteur le plus puissant de circulation des masses d'eau par jeu de densité. La circulation thermohaline est à l'origine de la plongée d'eau dense et froide au fond des océans, phénomène de convection présent notamment en Méditerranée Nord Occidentale, et la remontée d'eau plus légère en surface par subduction. Si la température moyenne au fond des océans ne varie que très peu autour de la moyenne de 2°C, la température de surface est largement influencée par les flux radiatifs de chaleur émis par rayonnement solaire, 4 fois plus élevée à l'équateur q'aux pôles.

Typiquement, le rayonnement solaire induit une séquelle thermique résultant de plusieurs échelles spatiales, de l'échelle globale jusqu'à la couverture nuageuse, et temporelles, à l'échelle circadienne (e.g. photopériode), saisonnière (e.g. moussons), annuelle (e.g. saisons), pluri-annuelle (El Nino), géologiques (période glaciaire/inter-glaciaire), qui s'entremêlent. Le gradient vertical peut également être très prononcé lorsque les masses d'eau sont stratifiées, la présence de la thermocline agit alors comme une barrière de densité entre la surface et le fond, ou au contraire à l'équilibre lorsqu'elles sont mélangées par le vent ou la convection. La profondeur de la couche de mélange, définie comme la profondeur à laquelle le gradient de température ne dépasse pas les 0,2°C, est une grandeur variable de quelques mm à des dizaine de mètres d'heure en heure (e.g. micro-instabilités de Langmuir), voire entre 10 et 1000 mètres sur quelques jours (e.g. efflorescence printanière) (Kantha et Clayson, 2003).

De manière générale, la température stimule les vitesses de catalisation jusqu'à atteindre un niveau dit optimal, au delà duquel son effet devient délétère par dénaturation enzymatique. La réponse des organismes aux changements de température est un processus non-sélectif lié à l'influence que cette grandeur a sur les réactions biochimiques catalysées par les enzymes cellulaires (Figure 14a). Comme quasiment toutes les voies métaboliques du phytoplancton dépendent de ces protéines et de leur cinétique, l'ensemble des stades du cycle de vie peut être influencé par l'induction d'un stress thermique. Pour les algues toxiques, la température contrôle principalement la germination des kystes et le déclenchement d'efflorescences par croissance soudaine (Hallegraeff, 2010). D'un point de vue global, 30% de la variabilité métabolique a été attribué à des variations thermiques

(Toseland *et al.*, 2013), notamment par un effet significatif sur:

1. La **(Dé)carboxylation** (1). Les enzymes impliquées dans la chaîne de transfert d'électrons et la formation de carbohydrates pendant la photosynthèse, comme la plastoquinone et la RUBISCO sont sensibles au stress thermique. Le substrat nécessaire à la RUBISCO est lui reformé grâce à des réactions de décarboxylation catalysées par diverses décarboxylases. Des expériences d'incubation montrent que pour les espèces antarctiques comme pour les espèces tropicales, la RUBISCO présente une forte résistance à l'augmentation de la température jusqu'à des valeurs comprises entre 40-50°C avant d'être négativement régulée par l'excès de chaleur (Descolas-Gros et De Billy, 1987) (Figure 14c).

2. La **(Dés)amination** (2). La Nitrate Réductase (NR) est une enzyme qui intervient dès le premier maillon de la chaîne de réactions du métabolisme des molécules organiques azotées comme les acides aminés ou les acides nucléiques (Campbell, 1988). Dans le cytoplasme des cellules, elle catalyse la réduction des ions nitrates ($NO_3^-$) en nitrites ($NO_2^-$) eux-même réduits en ammonium ($NH_4^+$) à différentes vitesses selon la température. A l'inverse, la perte d'un groupement amine ($NH_3$) des acides aminés ou des nucléotides est catalysée par les désaminases. Les travaux de Gao *et al.* (2000) ont montré que la température optimale de la NR, se situe aux alentours de 16°C, au-delà de laquelle, l'enzyme devient instable et son activité est sévèrement compromise (Figure 14d).

3. La **(Dé)phosphorylation** (3). La production de l'unité moléculaire d'énergie, l'ATP, la synthèse des acides nucléiques, le contrôle du cycle cellulaire ont tous lieu par l'intermédiaire de protéines phosphorylantes, les kinases. A l'inverse, les phosphatases, comme la phosphatase alcaline (PAL) restorent le stock de phosphates ($PO_4^{3-}$) à partir de ces macromolécules. La phosphatase alcaline est une enzyme qui peut être relarguée dans le milieu extracellulaire pour absorber du phosphate après clivage de molécules organiques dissoutes. Chez différentes espèces, son activité est positivement corrélée à l'augmentation de température jusqu'à un maximum atteint entre 30 et 45°C à partir duquel elle diminue légèrement (Healey et Hendzel, 1979) (Figure 14e).

Toutes ces mesures d'activités présentent des réponses relativement similaires représentées par la forme unique des courbes de réactions: l'augmentation de la température induit l'activation des cinétiques enzymatiques jusqu'à une température optimale où l'apport de chaleur devient rapidement néfaste pour les enzymes (Figure 14b). De même l'optimum d'activité reste invariant selon les espèces ce qui suggère qu'il constitue une propriété intrinsèque des enzymes en elles-mêmes émergeant d'un mécanisme commun. En fait, ce mécanisme repose sur l'effet de la température sur la collision et donc la séparation des atomes des molécules impliquées dans toutes les réactions chimiques. L'initiation des réactions chimiques requière un apport d'énergie, fourni par la chaleur, pour déstabiliser les liaisons chimiques existantes. L'action de la température sur la vitesse de réaction chimique a été formalisée par la loi exponentielle d'Arrhenuis en 1989 (E 1.12).

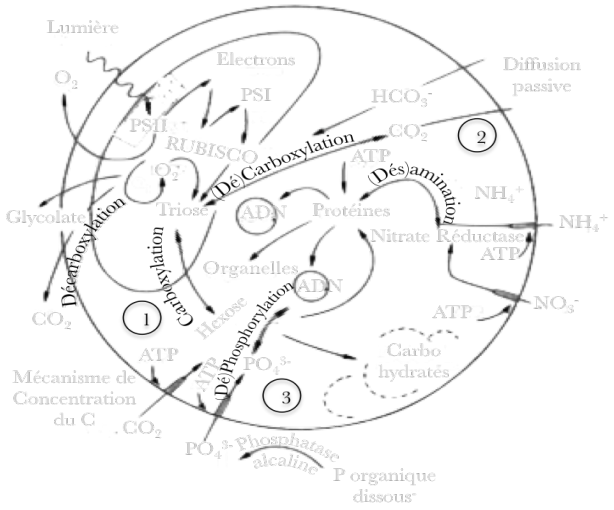


(a) Les principales voies métaboliques influencées par la température (modifié de Reynolds, 2006)

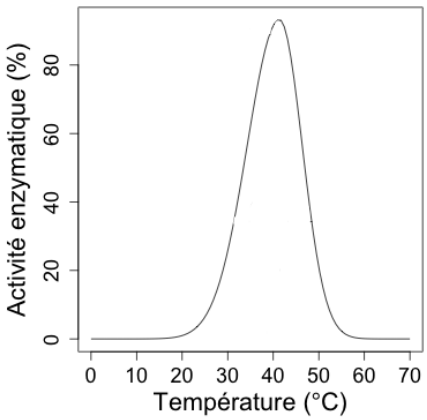


(b) Réponse générale de l'activité enzymatique à la température

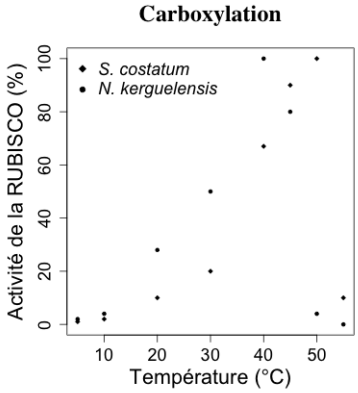


(c) Température vs activité de carboxylation de la RUBISCO (d'après Descolas-Gros et De Billy, 1987)

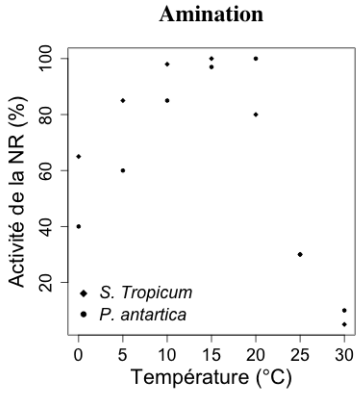


(d) Température vs activité d'amination de la Nitrate réductase (NR) (d'après Gao *et al.*, 2000)

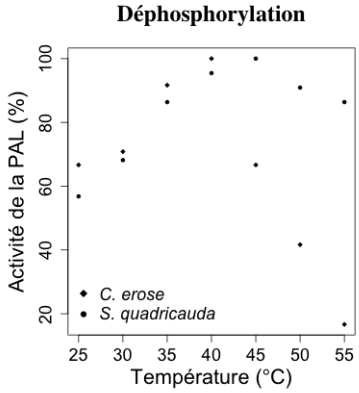


(e) Température vs activité de déphosphorylation de la Phosphatase alcaline (PAL) (d'après Healey et Hendzel, 1979)

Figure 1.14: Influence de la température sur le métabolisme et l'activité enzymatique du phytoplancton.

$$k = Ae^{\frac{E}{R}\cdot\left(\frac{1}{T_{opt}}-\frac{1}{T}\right)} \tag{1.12}$$

E: Energie d'activation enzymatique [kcal][MOLE]$^{-1}$, R=8,3: Constante des gaz parfait [kcal][K]$^{-1}$[MOLE]$^{-1}$, k: vitesse de réaction, T: Température [K], A: Constante de collision moléculaire

Cette loi prédit l'activation des cinétiques enzymatiques avec l'augmentation de la température, autrement considérée comme l'énergie d'activation enzymatique, notée E.

E est une valeur qui peut se calculer à partir de valeurs empiriques de $Q_{10}$, défini comme le changement des taux d'activation mesurés avec un écart de température de 10°C, soit:

$$\left.\begin{array}{l} k(T=t) = Ae^{-\frac{E}{Rt}} \\ k(T=t+10) = Ae^{-\frac{E}{R(t+10)}} \end{array}\right\} Q_{10} = \frac{k(T=t+10)}{k(T=t)} = e^{-\frac{E}{R}.\left(\frac{1}{t+10}-\frac{1}{t}\right)} \tag{1.13}$$

$$\text{d'où } Q_{10} = e^{\frac{10.E}{RT^2}} \text{ et } E = R.T^2.\frac{log_e(Q_{10})}{10}$$

E: Energie d'activation enzymatique [kcal][MOLE]$^{-1}$, R=8,3: Constante des gaz parfait [kcal][K]$^{-1}$[MOLE]$^{-1}$, k: constante de réaction, T: Température [K]

Cette activation n'est plus croissante lorsque la température dépasse une valeur dite optimale et la valeur du $Q_{10}$ devient inférieure à 1. L'énergie apportée par la chaleur devient néfaste aux enzymes qui se déstructurent à son effet, on parle de dénaturation. Ces stades d'activation/dénaturation sont retranscrits par approximation de la loi de Gausse:

$$\left.\begin{array}{l} k(T) = Ae^{\frac{E}{R}.\left(\frac{1}{T_{opt}}-\frac{1}{T}\right)} \\ E = \frac{R(T-T_{opt})^2.log_e(Q_{10})}{10} \end{array}\right\} k = Ae^{\frac{R.(T-T_{opt})^2.log_e(Q_{10})}{10.R}.\left(\frac{T-T_{opt}}{T.T_{opt}}\right)} \tag{1.14}$$

$$k = Ae^{\left(\frac{log_e(Q_{10}).(T-T_{opt})^2}{10.T_{opt}}-\frac{log_e(Q_{10}).(T-T_{opt})^2}{10T}\right)}$$

$$k = Ae^{\left(-\frac{log_e(Q_{10})}{10}.(T-2T_{opt}+T_{opt}^2T^{-1})\right)}.e^{-\left(\frac{-log_e(Q_{10}).(T-T_{opt})^2}{10.T_{opt}}\right)}$$

$$\text{d'où } k \sim k_{max}(T)e^{\left(-\frac{(T-T_{opt})^2}{2.\Delta_{T^{\pm}}^2}\right)}$$

En phase d'activation, T <$T_{opt}$ et $\log_e(Q_{10}^-)$> 0 ($Q_{10}^-$>1), $\mu$ augmente exponentiellement avec la température. Lorsque l'optimum est atteint, la vitesse de réaction devient maximale et supporte le taux de croissance $\mu = \mu_{max}$. Lorsque les températures surpassent T $_{opt}$, T >$T_{opt}$ et $\log_e(Q_{10}^+)$< 0 ($Q_{10}^+$<1), $\mu$ diminue exponentiellement avec la température. La distinction entre les coefficients $Q_{10}^-$ et $Q_{10}^+$, autrement modélisé par $\Delta_{T^{\pm}}$ assure l'asymétrie potentielle des courbes d'activation et de dénaturation enzymatiques (Figure 15). En 1972, Eppley a pour la première fois compilé les mesures d'optimal de croissance ($\mu$) de nombreuses populations en conditions contrôlées non-carencées en réponse au gradient thermique. Comme le décrit la loi d'Arrhenius, Eppley s'attendait à observer l'augmentation exponentielle de la reproduction du phytoplancton avec la température:

$$\mu_{max} = log_e(2).0,851.(1,066^T) \tag{1.15}$$

$\mu_{max}$: Taux de croissance intrinsèque en conditions optimales [T]$^{-1}$, T: Température d'incubation [°C]

Même si le phytoplancton moderne est globalement acclimaté à la température du milieu dans lequel il vit, avec un optimum correspondant à la température moyenne *in*

*situ*, son taux de reproduction peut rapidement diminuer en conditions suboptimales et serait plus sensible au réchauffement climatique qu'au refroidissement (Thomas *et al.*, 2012). En sa qualité d'ectotherme, la capacité de résilience du phytoplancton face à un stress thermique a été soumise à une forte pression d'adaptation évolutive qui a progressivement façonné les lignées actuelles (Figure 15).

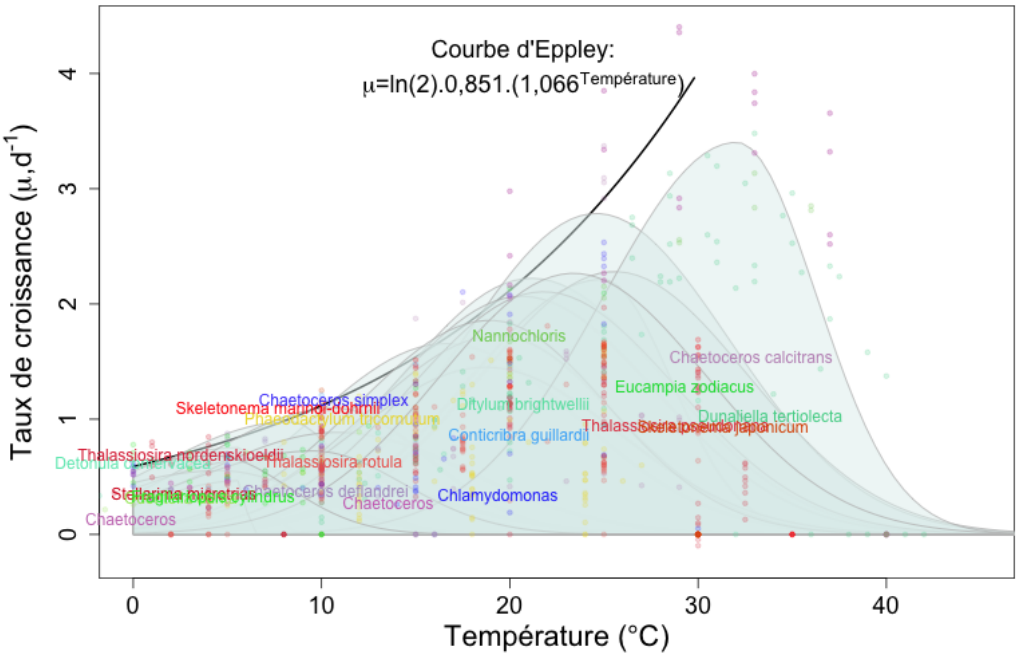


Figure 1.15: L'influence de la température sur le taux de croissance spécifique du phytoplancton en milieu contrôlé (d'après les données compilées par Thomas *et al.*, http://mridulkthomas.weebly.com/data–code.html)

Par analogie avec l'activité enzymatique, la réponse du phytoplancton à la température peut être prédite par la relation suivante:

$$\begin{aligned}\mu &= \mu_{max} e^{\left(-\frac{(T-T_{opt})^2}{2.\Delta^2_{T\pm}}\right)} \\ &= log_e(2).0,851.(1,066^T).e^{\left(-\frac{(T-T_{opt})^2}{2.\Delta^2_{T\pm}}\right)} \text{ si l'on introduit la relation d'Eppley}\end{aligned} \tag{1.16}$$

$\mu$: Taux de croissance intrinsèque $[T]^{-1}$, T: Température d'incubation [°C], $T_{opt}$: Température optimale de croissance [°C]

Vis-à-vis de la température, on distingue chez les cellules du phytoplancton deux types de comportements: les organismes eurythermes s'acclimatent à une large gamme de température tandis que les stenothermes présentent une faible tolérance aux variations thermiques. L'évolution du phytoplancton compte parmi les enjeux majeurs des études sur le futur du changement climatique. Les études intégrées sur le siècle dernier montrent que la biomasse des producteurs primaires a déjà diminuée de 1% tous les ans (Boyce *et al.*, 2010). Ce déclin n'atteint pas les populations avec la même ampleur, les bacillaryophyceae représentent les organismes les plus touchés par l'augmentation globale de la température à la surface des océans (Bopp *et al.*, 2005).

*Les nutriments: relations empiriques, implications physiologiques et dynamiques*

Plusieurs phénomènes saisonniers, tel que les moussons ou les upwellings, ou au contraire transitoires tels que les ruissellements/crues ou le mélange des masses d'eau par un épisode de vent (cf. Chapitre 3) sont à l'origine de 'pulses' nutritifs qui alimentent la production primaire nouvelle ou régénérée (Glibert *et al.*, 2016). La dynamique métabolique ou plasticité nutritionnelle est l'une des hypothèses avancées par Bonin (1982) pour expliquer le paradoxe du plancton. Cette notion est à la base de toute une théorie, appelée la *Dynamic Energy Budget* (DEB) *Theory*, vérifiée par les espèces de phytoplancton en milieu contrôlé et même naturel. Le ratio élémentaire de 106C:16N:1P est une valeur moyenne observée par les populations de phytoplancton, dans lesquelles se mélangent des individus dis 'survivants' qui allouent la plus grande partie de leur resource à la maintenance et à l'optimisation de l'acquisition des ressources et d'autres dis 'bloomer' qui mobilisent rapidement leur réserve pour la croissance et la division (Klausmeier *et al.*, 2004; Arrigo, 2005; Muller *et al.*, 2011). De nombreux travaux ont quantifié la variabilité intracellulaire alliée au quota de N et P, en particulier vis-à-vis des échelles de changement des concentrations en sels dissous (Geider et LaRoche, 2002). La plupart des efforts de modélisation de la réponse du phytoplancton aux concentrations dissoutes de sels nutritifs dans le milieu se basent sur la combinaison du modèle de Monod et de la théorie de Liebig. Le modèle de Monod décrit la cinétique d'absorption des nutriments vers le cytoplasme de la cellule par le biais de transporteurs transmembranaires, de nature enzymatique, grâce à l'équation de Michaëlis-Menten:

Soit la réaction suivante: $$[\mathrm{S}] + [\mathrm{E}]_{\mathrm{libre}} \underset{\mathrm{k_{-1}}}{\overset{\mathrm{k_1}}{\rightleftharpoons}} [\mathrm{ES}] \overset{\mathrm{k_2}}{\rightleftharpoons} [\mathrm{S}]_{\mathrm{intracellulaire}} + [\mathrm{E}]_{\mathrm{libre}}$$

La loi d'action de masse prédit que le taux de réaction chimique est directement proportionnel au produit des concentrations des réactifs, le substrat dissous $[S]$ et la forme libre de l'enzyme $[E]_{libre}$. D'où:

$$\frac{d[ES]}{dt} = k_1.[E]_{libre}.[S] - k_2.[ES]$$
$$V = \frac{d[S]_{intracellulaire}}{dt} = k_2.[ES]$$

Lorsque la formation du complexe enzyme-substrat est constante au cours du temps et que l'on considère la quantité totale de transporteurs $[E] = [E]_{libre} + [ES]$,

$$\frac{d[ES]^*}{dt} = k_1.[E]^*_{libre}.[S] - k_2.[ES]^* = 0$$
$$[ES]^* = \frac{k_1}{k_2}.([E]^* - [ES]^*).[S] = \frac{k_1.[E]^*.[S]}{k_2 + k_1.[S]}$$

D'où:

$$\begin{aligned} V =& k_2.[ES]^* = \frac{k_2.[E].[S]}{\frac{k_2}{k_1} + [S]} \\ V =& \frac{V_{max}.[S]}{K_S + [S]}, \text{avec } V_{max} = k_2.[E] \text{ et } K_S = \frac{k_2}{k_1} \end{aligned} \tag{1.17}$$

V: vitesse de réaction, $V_{max}$: vitesse maximale, [S]: concentration du substrat, $K_S$: constante de demie-saturation

Transposée à la production primaire, le modèle devient:

$$P = \frac{P_{max}.[S]}{K_S + [S]} \tag{1.18}$$

P: production primaire ou taux de croissance intrinsèque, $P_{max}$: production maximale, [S]: concentration en sels nutritif dissous, $K_S$: constante de demie-saturation

Pour ce modèle, ce sont les protéines qui assurent le transport des sels nutritifs vers le cytoplasme (i.e. transporteurs), qui jouent le rôle d'enzymes. Le substrat représente l'ensemble des ressources nécessaires à la croissance du phytoplancton. En milieu oligotrophe, lorsque la teneur en nutriments est faible, la vitesse d'assimilation des nutriments devient directement proportionnelle à la quantité de substrat dissous:

$$\begin{aligned} V &= \frac{V_{max}.[S]}{K_S} \\ V &= \alpha.[S] \text{ avec } \alpha = \frac{V_{max}}{K_S} \end{aligned} \tag{1.19}$$

$\alpha$: Affinité de la cellule pour le substrat S

Naturellement le dioxide de carbone, l'azote et le phosphore sont les éléments les plus utilisés auxquels s'ajoute le silicium pour les diatomées et d'autres éléments nécessaires à la croissance de certaines espèces (Figure 16).

La loi de Liebig (1955) prédit qu'en présence de plusieurs ressources potentiellement limitantes, la dynamique d'une espèce sera toujours déterminée par celle qui a la teneur la plus faible. Par exemple, pour les ressources en azote, noté N, et en phosphore, noté P, la production *in fine* peut être contrôlée par la relation suivante:

$$P = P_{max}.min\left(\frac{[N]}{K_N + [N]}, \frac{[P]}{K_P + [P]}\right) \tag{1.20}$$

P: production primaire ou taux de croissance intrinsèque, $P_{max}$: production maximale, [S]: concentration en sel nutritif dissous, $K_S$: constante de demie-saturation

D'autres auteurs se sont intéressés à la plasticité nutritionnelle du phytoplancton pour comprendre leur potentiel de survie en cas de carence sévère (Bonachela *et al.*, 2011). Généralement, ces avancés prennent en compte l'effet de la rétroaction des teneurs en sels dissous dans l'eau de mer pour modéliser la cinétique d'assimilation des nutriments de façon plus réaliste. Ensembles, le gradient de concentration et la synthèse de canaux transmembranaires représentent des alternatives dynamiques aux constantes définies dans l'équation de Michaëlis-Menten:

1. La constante de demie-saturation , $K_S$, est estimée comme le quotient de $K_2$, taux de dissociation du complexe enzyme-substrat qui conduit au relarguage de nutriments dans le cytoplasme, et de $K_1$, le taux de rencontre entre les sels présents dans l'environnement proche de la cellule avec le transporteur. Cette constante est donc liée à l'afflux d'ions dans l'environnement proche, qui n'est généralement pas à l'équilibre avec le milieu extérieur. Le déséquilibre entre les ions à proximité de la membrane et la charge globale du milieu est à l'origine du flux d'assimilation du substrat par diffusion selon la loi de Fick: $\phi_S = 4.\pi.D.r.([S]_{ext} - [S]_{proche})$.

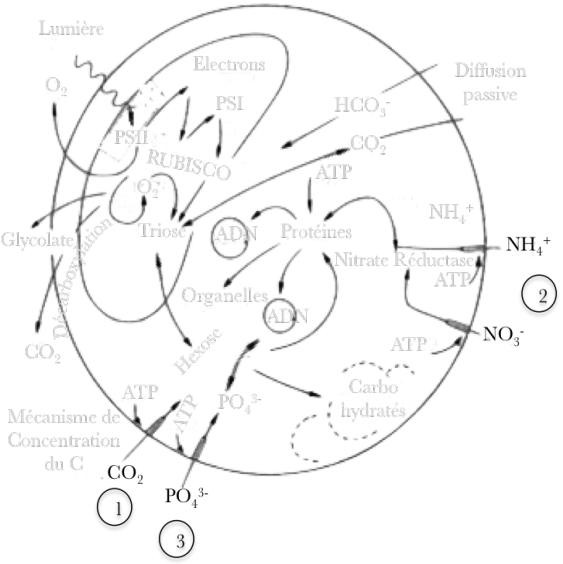


(a) Les principales voies métaboliques qui requièrent l'assimilation de nutriments (modifié de Reynolds, 2006)

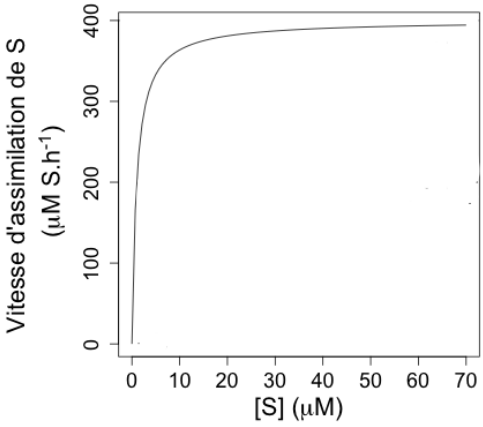


(b) Réponse générale de l'assimilation enzymatique à la concentration en sels dissous

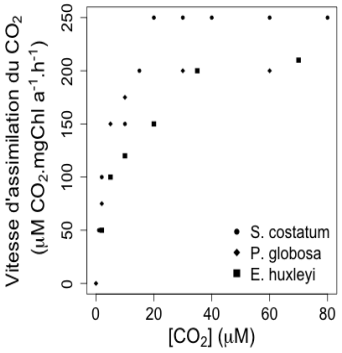


(c) Vitesse d'assimilation du $CO_2$ vs $[CO_2]$ (D'après Rost *et al.*, 2003)

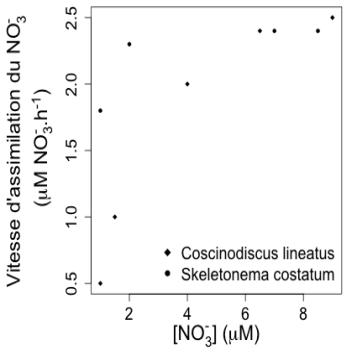


(d) Vitesse d'assimilation du $NO_3^-$ vs $[NO_3^-]$ (D'après Eppley *et al.*, 1969)

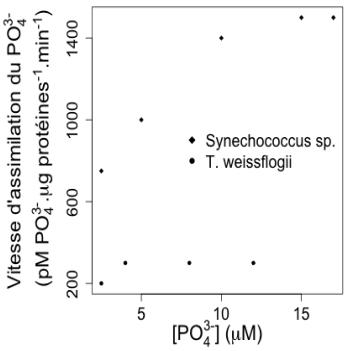


(e) Vitesse d'assimilation du $PO_4^{3-}$ vs $[PO_4^{3-}]$ (D'après Donald *et al.*, 1997)

Figure 1.16: Cinétiques d'assimilation de nutriments par le système de transporteurs enzymatiques du phytoplancton

Cette relation allométrique, puisqu'elle relie la capacité de diffusion des nutriments au rayon de la cellule ($r$) (Figure 17), prédit que le flux d'ions rapporté au volume de la cellule ($\frac{4.\pi.r^3}{3}$) et donc l'affinité apparente des petites cellules pour un substrat limitant sera supérieure au grandes cellules, proportionnellement à $r^{-2}$ (Chisholm, 1992; Maranon, 2008; Lindermann *et al.*, 2016). Bonachela a formulé la rétroaction de la limitation par diffusion sur la constante apparente de demie-saturation, $K'_S$: $K'_S \rightarrow K_S * (1 + \frac{V_{max}}{4.\pi.D.r.K_S})$. Si la vitesse d'assimilation du substrat, $V$, est supérieure au flux de diffusion, $\phi_S$, alors les liens enzymes/substrat peuvent créer un déficit local ($[S]_{ext}$>$[S]_{proche}$).

2. La vitesse d'assimilation maximale, $V_{max}$, est estimée à partir du produit de $K_2$, taux de dissociation du complexe enzyme-substrat qui conduit au relarguage de nutriment dans le cytoplasme, et de [E], le nombre de transporteurs membranaires. Dans l'approche d'assimilation dynamique décrite par Bonachela *et al.* (2011), la quantité [E] est influencée par rétroaction par la teneur en substrat du milieu via un flux de synthèse de nouveaux transporteurs, $\phi_E$. Cette quantité doit être régulée au niveau interne par la voie de transcription/traduction des gènes de transporteurs. Le transport actif du nitrate $NO_3^-$ par le symport couplé à une pompe à protons ATP-dépendante est typiquement rétro-régulé au niveau de la transcription du gène NAT ($Nitrate\ Transporter$) par la quantité et la forme d'azote disponible pour promouvoir la croissance des cellules (Hildebrand et Dahlin, 2000). Si le quota cellulaire est suffisant pour assurer la maintenance et la croissance cellulaire, cette voie doit être inhibée pour ne pas entraîner de coût énergétique non justifié. Au contraire, si la teneur extérieure en sels nutritifs entraîne une carence des cellules, elle doit être activée pour permettre la synthèse de nouveaux canaux et favoriser le taux de rencontre transporteurs/substrat ($K_1$). Cette hypothèse fait donc appel au modèle de quota cellulaire, formalisé par Droop en 1973: $\mu(S) = \mu_{max}.\left(1 - \frac{Q_{[S]_{min}}}{Q_{[S]}}\right)$, avec $Q_{[S]_{min}}$, le quota cellulaire minimum vital en substrat $S$. Par rapport à la plasticité de la surface effective d'absorption, proportionnelle au nombre de canaux présents sur la membrane, le flux de synthèse de nouveaux transporteurs, $\phi_E$, devient: $\phi_E = v.F\left(\frac{Q_{[S]_{max}} - Q_{[S]}}{Q_{[S]_{max}} - Q_{[S]_{min}}} + 1 - [E]_{libre}\right)$, avec $v$, le taux de transcription/traduction des gènes de transporteurs et $F$, une fonction croissante bornée entre $[\![-1,1]\!]$.

Cette approche souligne l'importance des quotas cellulaires dans le contrôle de l'assimilation des nutriments par le phytoplancton. Si l'on se réfère à la loi de Liebig, le rapport nutritif optimal, $R^*$, défini par le quotient des quotas cellulaires minimum vitaux en considérant l'ensemble des ressources potentiellement limitantes peut également servir à prédire la dynamique de coexistence des espèces dans le contexte de compétition de niches d'Hutchinson (Tilman, 1982). Dans le cas d'une ressource limitante R, ce rapport équivaut à la quantité de nutriments à laquelle on observe un taux apparent de production, $r$, nul. Ce qui signifie que si le milieu contient une quantité de nutriments supérieure au $R^*$, une espèce sera en mesure de se développer et qu'elle exclura inévitablement un compétiteur si elle présente une valeur de $R^*$ inférieure à celui-ci (Grover, 1997).

Lorsque $\mu$ et $l$ sont égaux, le modèle de Droop s'écrit:

$$(1) : l = \mu_{max}.(1 - \frac{Q_{min}}{Q^*}) \Leftrightarrow Q^* = \frac{\mu_{max}.Q_{min}}{\mu_{max} - l} \tag{1.21}$$

En utilisant le modèle de Monod pour décrire la cinétique à l'équilibre du quota cellulaire $Q^*$ en fonction de la concentration dissoute en ressource $R^*$, il apparait:

$$(2) : \left.\begin{array}{l} \frac{dQ(Q^*)}{dt} = \frac{V_{max}.R^*}{K_R + R^*} - \mu.Q^* = 0 \\ \mu = l \end{array}\right\} Q^* = \frac{1}{l}.\frac{V_{max}.R^*}{K_R + R^*} \tag{1.22}$$

Par combinaison des équations (1) et (2), on obtient:

$$R^* = \frac{\mu_{max}.Q_{min}.K_R.l}{V_{max}.(\mu_{max} - l) - \mu_{max}.Q_{min}.l} \tag{1.23}$$

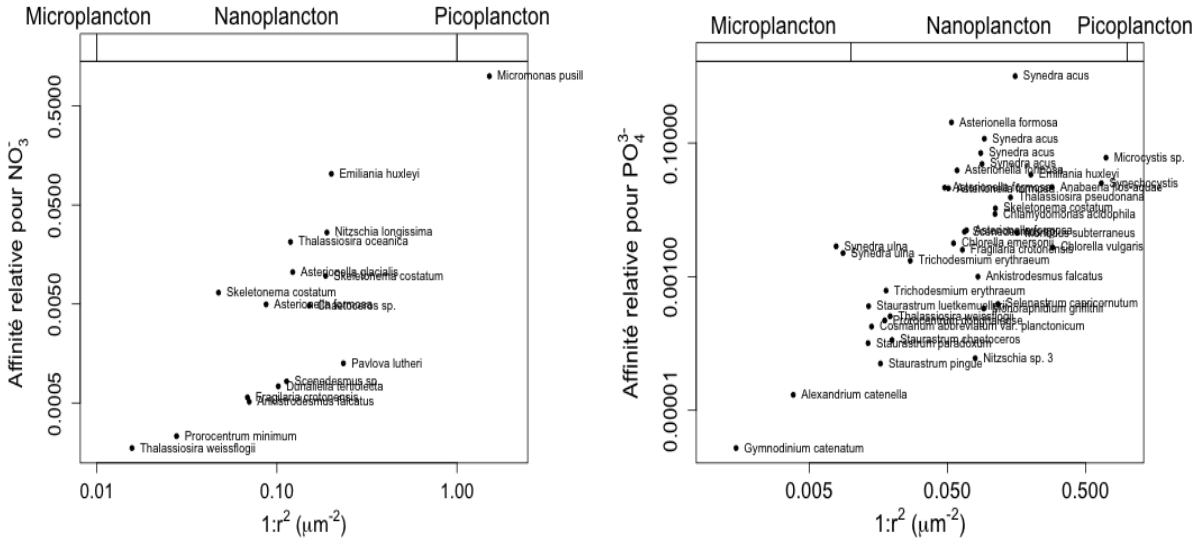


(a) $\alpha_{NO_3^-}$ vs $1:r^2$ (b) $\alpha_{PO_4^{3-}}$ vs $1:r^2$

Figure 1.17: Relation allométrique entre l'affinité du phytoplancton, $\alpha \sim \frac{V_{max}}{K}$, pour les ions nitrates $NO_3^-$ et phosphates $PO_4^{3-}$ et la surface des cellules ($\sim r^2$) d'après les données compilées par Edwards *et al.*, 2015

Dans l'équation (E 1.23), il apparaît clairement que la plasticité des valeurs de $\mu_{max}$, $V_{max}$, $K$ et $Q_{min}$ sont autant de conditions qui, influencées par la taille des organismes, leur capacité de croissance et de reproduction, peuvent équilibrer la dynamique de compétition exclusive ou aboutir à l'équilibre/coexistence entre deux espèces (Grover *et al.*, 2011) (Figure 18).

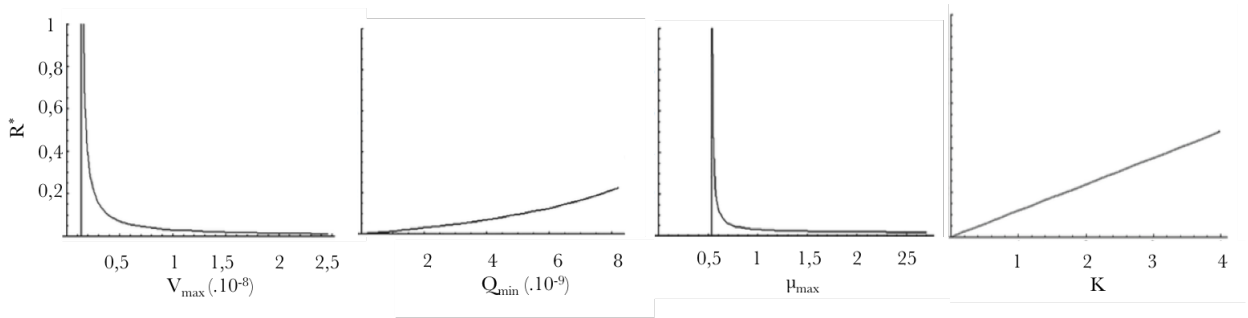


Figure 1.18: Influence des variables liées au quota cellulaire du phytoplancton et à l'assimilation des nutriments sur R* (Litchman, 2007). Les régulations endogènes de ces valeurs (plasticité) conduisent à une dynamique complexe où le déséquilibre favorise la coexistence du phytoplancton en milieu naturel.

Malgré les efforts pour prendre en compte la plasticité nutritionnelle du phytoplancton, ce type d'approche n'appréhende pas encore le temps d'adaptation physiologique (Allen et Polimene, 2011), qui retarde n'importe quel mécanisme d'adaptation au milieu environnemental comme c'est le cas pour la phase de latence observée en milieu contrôlé, ou le couplage avec d'autres compartiments de l'écosystème, bactérien ou zooplancton, qui agissent soit comme compétiteur pour l'acquisition des ressources soit comme source de composés inorganiques dissous après reminéralisation ou excrétion (Kirchman, 1994).

D'après la méta-analyse réalisée par Downing *et al.* (1999), la réponse du taux de croissance du phytoplancton au cours de bio-essais d'enrichissement du milieu devient significative après en moyenne 3 jours pour le nitrate, 4 jours pour le fer et seulement au bout de 10 jours pour la silice. Dans les océans, le taux de renouvellement et de consommation, dit *turnover*, des macronutriments varie entre la journée et l'année, influencé par des processus écologiques où s'entremêlent différentes échelles de temps liées au cycle de vie des organismes et à leur dynamique (Moore *et al.*, 2013).

*L'irradiance: relations empiriques, implications physiologiques et dynamiques*

La production primaire est influencée, de façon intrinsèque, par le flux de photons incidents émanant de l'irradiance solaire puisque la lumière constitue le moteur énergétique de base des organismes photo-autotrophes comme le phytoplancton. La quantité de lumière qui parvient à la surface des océans résulte de l'émission des rayons incidents du soleil moins la quantité rétrodiffusée et absorbée dans l'atmosphère, estimée entre 10 et 40% selon les conditions météorologiques. Cette grandeur est naturellement contrainte par la distance entre le soleil et la Terre, représentée par un gradient latitudinal, la quantité de gaz à effet-de-serre, de vapeur d'eau, d'ozone, la couverture nuageuse, etc. (Kirk, 2011). La lumière blanche, que l'on distingue à l'oeil est constituée du spectre lumineux visible de longueurs d'onde comprises entre 400-700 nm, dont l'énergie peut-être absorbée à des niveaux discrets (i.e. quantas) par les photopigments (*Photosynthetically Available Radiation*). Les UVs sont les rayons les plus énergétiques. Ils sont fortement absorbés par la matière organique dissoute, en revanche ils provoquent des dommages cellulaires irréversibles chez le phytoplancton. A la surface des océans, une partie de ce spectre est réfléchie vers l'atmosphère et l'autre est progressivement absorbée par les particules en suspension, qu'elles soient détritiques (e.g. Colored Dissolved Organic Matter) ou actives comme le phytoplancton (Yentsch, 1962). A cause de l'extinction progressive des rayons incidents en profondeur, des longueurs d'onde élevées (rouge) aux faibles longueurs d'onde (bleu), la photosynthèse est une réaction généralement restreinte au niveau d'une couche où la lumière parvient jusqu'au seuil de 1% de l'irradiance incidente, appelée couche euphotique (Kirk, 1994). La charge particulaire océanique est globalement décrite par la classification optique des masses d'eau de Morel et Prieur (1977):

1. **Type I**: Océan ouvert, pauvre en matière dissoute et en phytoplancton, qui constituent les particules majoritairement responsables des propriétés optiques marines. Le coefficient d'atténuation lumineuse est prédit à partir des variations en concentrations phytoplanctoniques, toute autre source d'absorption lumineuse étant considérée comme négligeable. La profondeur moyenne de la couche euphotique atteint entre 10-120 m (Morel, 1988).

2. **Type II**: Eaux côtières riches en phytoplancton mais aussi en sédiments remis en suspension, en particules détritiques et terrigènes provenant des apports fluviaux ou des aérosols atmosphériques qui contribuent tout autant aux propriétés optiques marines. A cause de la turbidité accrue des eaux de type II, la profondeur moyenne de la couche euphotique est restreinte entre 10 et 20 m (Morel *et al.*, 2006).

Même lorsque la profondeur de la couche euphotique atteint 100m, la photosynthèse est réduite à un espace qui ne dépasse pas plus de 2% du volume total des océans (Falkowski, 1994). A ces variations d'ordre général des propriétés optiques des masses

d'eau s'ajoutent des fluctuations à méso et micro-échelles de la lumière perçue par les organismes (Denman et Gargett, 1983). Même si le phytoplancton peut survivre à des périodes d'extinctions lumineuses prolongées, l'absence de lumière finit par induire soit la versatilité du régime trophique pour les espèces qui en sont capables (e.g. mixotrophie), la mobilisation des réserves, la baisse du métabolisme énergétique (e.g. dormance) ou la mort cellulaire (McMinn et Martin, 2013). Le mélange des masses d'eau, sous l'action du vent hivernal, est un phénomène régulier qui cause l'export du phytoplancton en dehors de la couche euphotique mais néanmoins nécessaire pour préconditionner les efflorescences en milieu tempéré. Sur la colonne d'eau, la profondeur à laquelle le taux de respiration compense la production du phytoplancton est appelée profondeur critique. L'intensité de compensation est généralement réduite à 1-4 $\mu$moles de photons.m$^{-2}$.s$^{-1}$ chez les espèces de phytoplancton (Kirk, 2011). Pour Sverdrup (1953), ce n'est que lorsque la profondeur de la couche de mélange se stabilise au-dessus de la profondeur critique que la croissance du phytoplancton peut supporter une production primaire nette positive ($r$>0). Bien avant le déclenchement de la dormance ou de la mort cellulaire programmée par des niveaux lumineux trop faibles, le phytoplancton doit naturellement s'adapter au rythme circadien de la photopériode qui l'oblige à rester régulièrement dans l'obscurité entre le crépuscule et l'aube. La croissance active du phytoplancton due à l'anabolisme est une phase qui requiert l'énergie des photons (e.g. phase claire de la photosynthèse), restreinte pendant la journée et toujours contrebalancée par les réactions qui libèrent de l'énergie (i.e. cataboliques ), comme la respiration cellulaire. La lumière fournit la ressource en photons, équivalente à 3,62.10$^{-19}$J par photon (Morel et Smith, 1974), nécessaires à l'excitation des photopigments et au transfert d'électrons impliqués dans les réactions photochimiques qui conduisent à la formation d'ATP et de NADPH, jusqu'à la réduction du $CO_2$.

Lorsque les complexes collecteurs d'énergies sont *ouverts*, l'antenne $P_{680}$ est réduite et les plastoquinones oxydées pour être en mesure d'atteindre l'état excité, $P^*_{680}$, et initier le transfert d'électrons jusqu'au PS I. Jusqu'à ce que $P_{680}$ cède son électron et recouvre son état stable (~ 0,6ms) par la réaction couplée d'oxydation de l'eau: $2H_2O \rightarrow 4H^+ + 4e^- + O_2$, le complexe ne peut plus capter de photons, il est dit *fermé*.

Lorsque tous les complexes sont fermés, soit sous l'action d'une lumière saturante soit d'un bloquant du transport d'électrons (e.g. DCMU), la consommation d'$O_2$ permet d'estimer le taux de respiration du phytoplancton. Ce taux est souvent considéré comme constant en fonction de l'intensité lumineuse même si Geider et MacIntyre (1987) ont mesuré des taux de respiration moyens 7 fois plus importants lorsque les complexes sont ouverts et permettent la synthèse des substrats cataboliques. Au contraire, lorsque le PSII est ouvert, la production d'oxygène sert à définir le taux de production brute du phytoplancton après conversion du rapport stoechiométrique $CO_2$:$O_2$ de la photosynthèse (0,8-1) (Figure 19a).

Lorsque la production primaire n'est pas directement estimée à partir de la production d'$O_2$ ou de la fixation d'un isotope radioactif du $CO_2$, la fluorescence émise par les molécules de *Chla* peut être utilisée pour parvenir à estimer le rendement quantique, $\phi$, de la chaîne de transport d'électrons initiée par le PSII (Kolber et Falkowski, 1993).

Le taux de production d'oxygène par molécule de *Chla* (mole $O_2$.mg $Chla^{-1}$.s$^{-1}$) est mesuré une fois l'énergie lumineuse, E ($\mu$moles quanta.m$^{-2}$.s$^{-1}$), absorbée par la cross-section du PSII, $\sigma_{PSII}$ (m$^2$.mole PSII$^{-1}$), rapportée au quota cellulaire par molécule de *Chla*, $n_{PSII}$ (mole PSII.mg Chla$^{-1}$), et réémise sous forme de fluorescence par les molécules de *Chlorophylle a* des centres réactionnels ouverts à l'équilibre (Figure 20b).

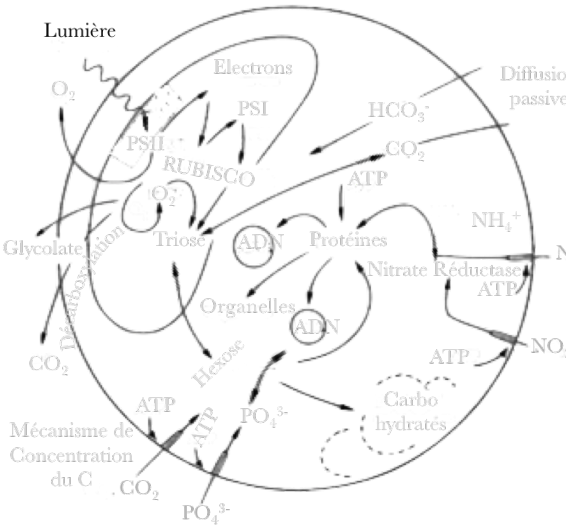


(a) Les principales voies métaboliques qui requièrent la capture de l'énergie lumineuse (modifié de Reynolds, 2006)

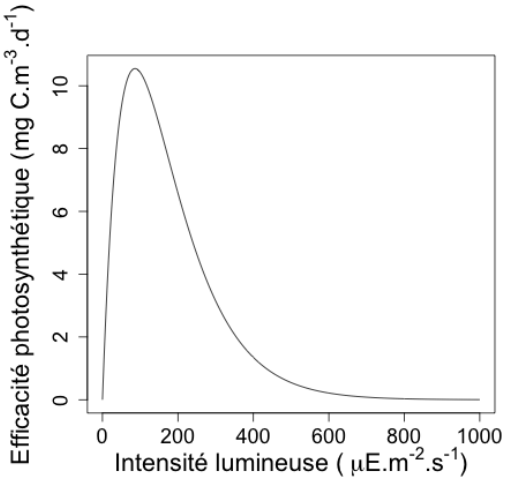


(b) Réponse générale de l'efficacité photosynthétique à l'intensité lumineuse

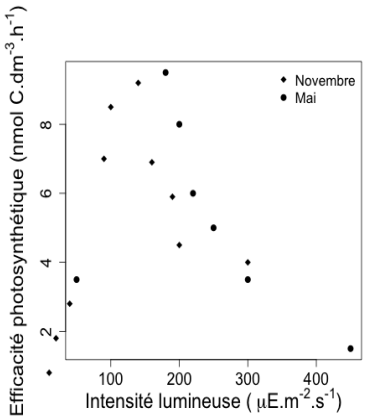


(c) Vitesse d'assimilation du $^{14}C$ vs E à différentes périodes de l'année (D'après Bjorkman et al., 2015)

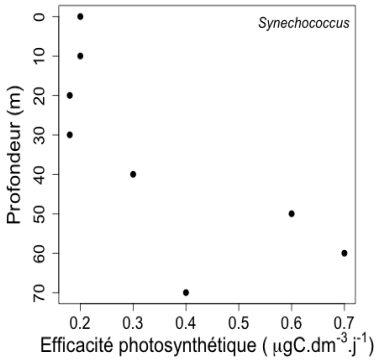


(d) Vitesse d'assimilation du $^{14}C$ vs profondeur pour *Synechococcus* (D'après Neuer et al., 1992)

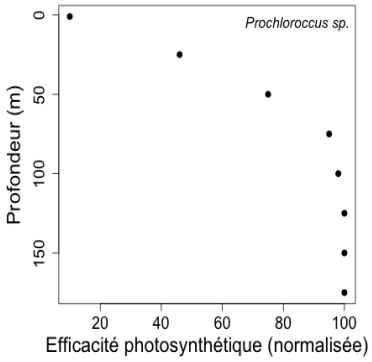


(e) Vitesse d'assimilation du $^{14}C$ vs profondeur pour *Prochlorococcus* (D'après Bjorkman et al., 2015)

Figure 1.19: Efficacité de la photosynthèse par le phytoplancton en fonction de l'intensité lumineuse reçue

La proportion de centres ouverts à l'équilibre, $Q_p$, est estimée par rapport au taux de quenching de l'émission maximale de fluorescence, $F_m$ atteinte lorsque tous les centres sont ouverts sous lumière saturante, et la fluorescence à l'équilibre sous lumière non-saturante, $F_{eq}$: $Q_p = (F_m - F_{eq}) : (F_m - F_0)$. Cette quantité multipliée par le rendement de production d'$O_2$ par électron transféré, $\phi_{e^-}$ ($1O_2$:$4e^-$), conduit aux mesures de production d'$O_2$/consommation de $CO_2$ *in fine*:

$$P^{Chla}(O_2) = E.\sigma_{PSII}.n_{PSII}.Q_p.\phi_{e^-} = ETR.\phi_{e^-} \text{ avec } ETR = E.\sigma_{PSII}.n_{PSII}.Q_p \quad (1.24)$$

$P^{Chla}$: production d'oxygène par photosynthèse rapportée au quota cellulaire en *Chla* $[MOLE][G]^{-1}[T]^{-1}$, E: Intensité lumineuse $[Quanta].[L]^{-2}.[T]^{-1}$, $\sigma_{PSII}$: cross-section absorbante du PSII $[L]^2.[MOLE]^{-1}$, $n_{PSII}$: quota cellulaire en PSII $[MOLE][G]^{-1}$, $Q_p$: Quenching photochimique $[MOLE][MOLE]^{-1}$, $\phi_{e^-}$: rendement du transfert d'électron $[MOLE][MOLE]^{-1}$, ETR: taux de transport des électrons $[MOLE][G]^{-1}[T]^{-1}$

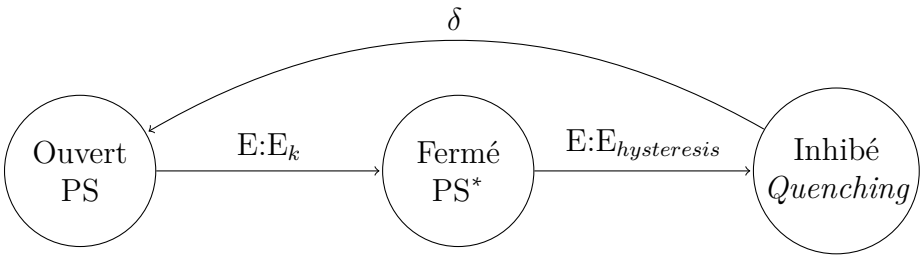


(a) Principaux états des "usines" photosynthétiques contenant les photosystèmes (PS) du phytoplancton (Eilers et Peeters, 1988). A l'obscurité, les centres réactionnels sont à l'état réduit et n'assurent pas de transfert d'électrons nécessaire à la photosynthèse. Les PS sont dits ouverts. Lorsque les photons (E) parviennent a délivrer un électron correspondant à un niveau énergétique supérieur, le PS devient fermé ou instable ($PS^*$) avec une probabilité proportionnelle au ratio de l'émission de photon incidente sur l'émission optimale, $E_k$, à laquelle toutes les unités photosynthétiques sont fermées. Il est alors capable de produire le NADPH nécessaire à la synthèse des carbohydrates. Lorsque les PS reçoivent encore plus d'énergie, $E > E_{hysteresis}$, ils parviennent à un état suboptimal. Ils sont inhibés puisque le taux de renouvellement des PS réduits, $\delta$, devient limitant, ce qui conduit à la baisse de la fluorescence émise par les molécules de *Chlorophylle a*, phénomène dit de *quenching*. Le quenching apparaît sous lumière saturante soit parce que la quantité de PS ouverts augmente par rapport à la quantité de PS fermés (i.e. quenching photochimique), soit parce l'excès énergétique entraîne des dommages radiatifs comme la dénaturation chimique (i.e. quenching non-photochimique).

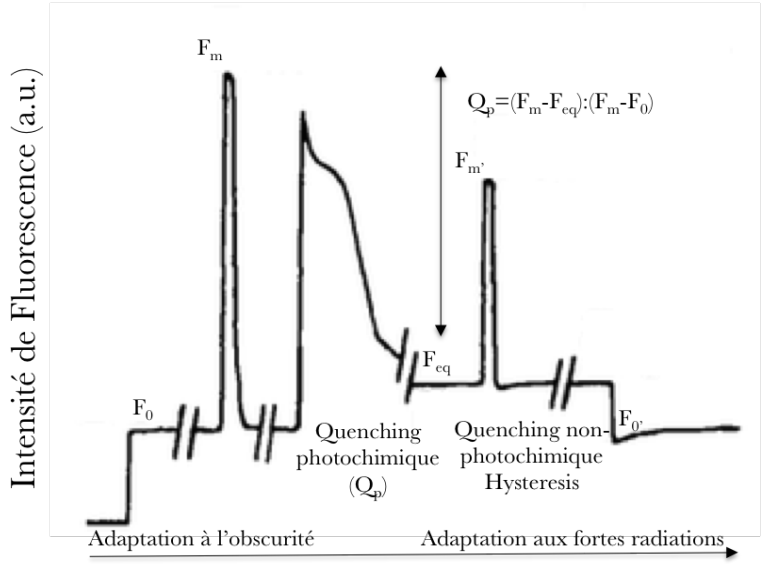


(b) Mesures des composantes variables de fluorescence émise par les molécules de *Chlorophylle a* pour estimer l'efficacité du transport d'électrons photosynthétique, $\phi$, (d'après Genty *et al.*, 1989).

Figure 1.20: Influence de l'intensité lumineuse sur le transfert d'électrons photosynthétique.

Plus l'intensité lumineuse est importante, plus la proportion de centres réactionnels du PSII ouverts est grande, le quenching faible ($F_{eq} \rightarrow F_m$), et la production d'oxygène élevée. Webb et al. (1974) ont proposé une formule pour prédire l'action de la lumière sur la production photosynthétique, correspondant à la courbe P-E. La lumière, comme n'importe quelle resource nutritive est alors limitante pour la fixation du $CO_2$, qui augmente linéairement avec l'intensité lumineuse jusqu'à saturation des PS. Si l'on considère la probabilité P(X$\in \mathscr{L}$), qu'au moins un quanta (X >0) atteigne une 'usine' photosynthétique ouverte (i.e. centres réactionnels des PS I et II combinés) au cours du temps de transfert des électrons avec une fréquence moyenne proportionnelle à la densité du flux de photons, E, $\lambda = E : E_k$, alors la production primaire devient proportionnelle à

la probabilité du succès effectif Prob(x >0), qui suit la loi de Poisson, de l'excitation de l'ensemble des N usines présentes dans la cellule:

$$
\begin{aligned}
&Prob(x = 0) \sim Poisson(\lambda) \\
&Prob(x = 0) = \frac{exp^{-\lambda}.\lambda^{x}}{x!} \\
&Prob(x = 0) = exp^{-\lambda} \\
&Prob(x = 0) = exp^{-\frac{E}{E_k}} \\
&\text{d'où } \; P = P_{max}.Prob(x{>}0) \\
&P = P_{max}.(1 - Prob(x = 0)) \\
&P = P_{max}.\left(1 - exp^{-\frac{E}{E_k}}\right) \\
&P = P_{max}.\left(1 - exp^{-\frac{\alpha.E}{P_{max}}}\right) \text{ avec } E_k = \frac{P_{max}}{\alpha} \\
&P = P_{max}.(1 - exp^{-N.\sigma.t.E})
\end{aligned}
\tag{1.25}
$$

P: production primaire ou taux de croissance intrinsèque, $P_{max}$: production maximale, $\alpha$: pente de la relation initiale linéaire P-E ou efficacité photosynthétique, E: Intensité lumineuse [Quanta].[L]$^{-2}$.[T]$^{-1}$, $E_k$: Intensité lumineuse optimale [Quanta].[L]$^{-2}$.[T]$^{-1}$, $\sigma$ : surface d'absorption de la chlorophylle a [L]$^{-2}$ et t: temps de transfert des électrons [T]$^{-1}$

Le paramètre $\alpha$ (mg C.quanta$^{-1}$.m$^2$.mg Chla$^{-1}$) est une mesure qui peut avoir une dynamique propre lorsque l'on prend en compte la variabilité du rendement photosynthétique, $\phi$, associé l'acclimatation des microalgues aux faibles intensités lumineuses, la photo-acclimatation. $\alpha$ se défini comme le produit de la cross-section totale d'absorption quantique du spectre intégré de flux de photons par molécule de *Chl a*, $a^*_{Chla}$ (m$^2$.mgChla$^{-1}$), et du rendement quantique maximal de la photosynthèse, $\phi_{Chla}$ (mgC.quanta$^{-1}$) (Falkowski, 1994). Comme $a^*$ est égal à la quantité d'unités photosynthétiques (PSU) multiplié par la cross-section unitaire des PS et $\phi_{max}$ est estimé à partir du ratio $\sigma_{PSII} : \sigma_{PSU}$, on obtient:

$$\alpha = N.\sigma_{PSII} \tag{1.26}$$

La surface d'absorption absolue disponible par cellule est fortement liée à la capacité du phytoplancton à ajuster le ratio Chla:C, $\theta$. De façon intuitive, plus le nombre de molécules de Chl a augmente au sein de la cellule, plus efficace sera la production initiale par photosynthèse chez les organismes cultivés ou naturellement placés à de faibles niveaux lumineux, comme c'est la cas en profondeur (Behrenfeld *et al.*, 2006). Par ajustement énergétique dynamique, les cellules *shade-adapted* augmentent le nombre N de sites photosynthétiques fermés, en même temps que $\theta$ (Geider, 1993; Ross et Geider, 2009). En moyenne, le poids en Chl a varie entre 1 et 6% du poids sec du phytoplancton et $\theta$, entre 1:30 et 1:60 (Riemann et al., 1989). La présence d'un maximum de Chlorophylle profond, le *Deep Chlorophyll Maximum*, largement distribué dans tous les océans démontre que, si ce n'est par la combinaison de multiples facteurs comme les nutriments ou la prédation, le phytoplancton a la capacité de maintenir une production photosynthétique élevée même lorsque la lumière est fortement atténuée (Cullen, 1982).

En plus de l'activation par la lumière, divers auteurs comme Platt (1976) ont inclus un coefficient supplémentaire à l'équation P-E pour représenter de façon explicite le processus indépendant de photoinhibition ou *quenching*, modélisé par la loi de Poisson d'espérance E:$E_{hysteresis}$, responsable de la diminution du rendement photosynthétique et de la fluorescence (i.e. Hysteresis) aux fortes intensités lumineuse. La production primaire correspond alors à la probabilité que l'activation de la lumière soit effective, Prob (Activation > 0), tout en n'atteignant pas une émission de photons inhibitrice, Prob(Inhibition = 0), comme c'est la cas lorsque E surpasse l'intensité d'hysteresis, $E_{hysteresis}$:

$$\begin{aligned} P &= P_{max}.Prob(Activation>0).Prob(Inhibition = 0) \\ P &= P_{max}.\left(1 - exp^{-\frac{E}{E_k}}\right).\left(exp^{-\frac{E}{E_{hysteresis}}}\right) \\ P &= P_{max}.\left(1 - exp^{-\frac{\alpha.E}{P_{max}}}\right).exp^{-\frac{\beta.E}{P_{max}}} \text{ avec } E_{hysteresis} = \frac{P_{max}}{\beta} \end{aligned} \tag{1.27}$$

P: production primaire ou taux de croissance intrinsèque, $P_{max}$: production maximale, $\alpha$: pente de la relation initiale linéaire P-E ou efficacité photosynthétique, $\beta$: efficacité de la photoinhibition, E: Intensité lumineuse [Quanta].[L]$^{-2}$.[T]$^{-1}$, $E_k$: Intensité lumineuse optimale [Quanta].[L]$^{-2}$.[T]$^{-1}$, $E_{hysteresis}$: Intensité lumineuse photoinhibitrice [Quanta].[L]$^{-2}$.[T]$^{-1}$

La photoinhibition peut être due à la dégradation de protéines clés de la chaîne de transport des électrons, comme la protéine D1 présente dans le photosystème II pour faire transiter les électrons des molécules d'eau vers le centre réactionnel $P_{680}$ (Marshall *et al.*, 2000), sans que la machinerie de réparation ne puisse remédier aux dommages de fortes irradiations (Prasil *et al.*, 1992). La quantité de PS II fonctionnel, N, diminue alors et peux restreindre la valeur de $P_{max}$. Lorsque les enzymes du cycle de Calvin parviennent à saturation de la cinétique de réduction du $CO_2$, une rétroaction peut également entraîner la diminution du taux de transfert des électrons, $\tau_{PSII}$. En milieu naturel, la photoinhibition restreint souvent la production primaire dans la couche de surface parce que la lumière n'y est pas encore fortement atténuée (Ryther et Menzel, 1959; Harris, 1978). Comme pour $\alpha$, l'efficacité de photoinhibition est modulée en fonction des conditions environnementales. Plusieurs mécanismes ont été décrit pour expliquer comment les cellules irradiées à de fortes intensités lumineuses surpassent la limitation de la croissance induite par le quenching par des adaptations physiologiques. Behrenfeld *et al.* ont démontré que le taux de transfert d'électrons depuis la molécule d'$H_2O$ jusqu'à son incorporation au $CO_2$ pouvait être sensiblement augmenté au cours d'une exposition lumineuse sursaturante à condition qu'il n'excède pas les capacités réactives du cycle de Calvin. Même lorsque les capacités réactives des réactions sombres de la photosynthèse deviennent limitantes pour la production, la température du milieu peut contrebalancer cet effet grâce à l'activation des cinétiques enzymatiques (Eilers et Peeters, 1988).

*La prédation: relations empiriques, implications physiologiques et dynamiques*

Les interactions trophiques sont les moteurs clés du transfert énergétique le long des maillons des chaînes alimentaires. S'ils sont présents sous la contrainte d'un cycle de vie plus long, les prédateurs concentrent la production secondaire du $CO_2$ atmosphérique fixé par la production primaire vers les niveaux trophiques supérieurs. En milieu marin,

les principaux compartiments herbivores, représentés par le microzooplancton, inférieur à 200 $\mu$m comme les dinoflagellés, nanoflagellés, ciliés ou tintinnides, et certaines larves de crustacés, protistes et métazoaires, font le pont vers les maillons supérieurs qui ne peuvent pas se nourrir d'organismes si petits. La complexité de contrôle top-down du phytoplancton est dépendante de multiples facteurs tels que le mode de prédation, l'intensité de la pression de prédation, le niveau trophique ou encore la biodiversité des écosystèmes (Williams et Martinez, 2000). On distingue différentes stratégies de prédation chez le plancton herbivore, certains sont spécialistes d'un type ou d'une classe de proie particulière quand d'autres ont a un mode d'ingestion plus opportuniste ou généraliste sans distinguer la nature des proies. La réponse des prédateurs suite à une augmentation de la densité des proies peut-être interprétée soit par le biais de la dynamique effective (e.g. nouveaux individus) (Lotka, 1924; Volterra, 1926) pour laquelle le nombre de phytoplanctons ingérés par prédateur, qui reflète la probabilité de rencontre entre prédateur et proie tous deux tributaires des courants, est directement proportionnel à son effectif soit par la dynamique fonctionnelle (e.g. taux d'ingestion) (Murdoch, 1969). Dans le premier cas, la dynamique du phytoplancton s'écrit grâce au système différentiel en considérant que le taux de mortalité intrinsèque du phytoplancton est négligeable devant la prédation:

$$\text{Système proie-prédateur de Lotka-Volterra} \begin{cases} \dfrac{dP}{dt} = \mu P - \gamma PZ \\ \dfrac{dZ}{dt} = \alpha\gamma ZP - dZ \end{cases} \tag{1.28}$$

P: Effectif du phytoplancton, $\mu$: Taux de croissance intrinsèque $[T]^{-1}$, $\gamma$: Taux de prédation par le zooplancton $[T]^{-1}$, Z: Effectif du zooplancton, $\alpha$: Efficacité de conversion de l'effectif du phytoplancton en effectif de zooplancton, d: Taux de mortalité du zooplancton

En 1994, Landry *et al.* ont proposé une méthode pour déterminer les paramètres $\mu$ et g, souvent difficiles à estimer dans le milieu naturel à partir d'observations *in situ* simultanées de phytoplancton et de zooplancton. La méthode de la dilution consiste à diluer plusieurs fois un même échantillon avec des concentrations croissantes d'eau de mer filtrée pour diminuer linéairement la probabilité de rencontre entre prédateur et proie. La dilution est d'ailleurs l'une des hypothèses (*Disturbance-Recovery Hypothesis*) pour expliquer comment, après une période de mélange intense qui entraîne l'approfondissement de la couche dans laquelle se développe le phytoplancton, et restreint la pression de prédation durant une fenêtre de temps suffisamment grande pour permettre le découplage de la dynamique proie-prédateur, le taux de croissance apparent du phytoplancton augmente pour soutenir une efflorescence (Landry et Hassett, 1982; Lindemann et St John, 2014). Au contraire, la stabilisation de la colonne d'eau en période de restratification augmente la probabilité de rencontre entre le phytoplancton, devenu très abondant, et les prédateurs qui, lorsqu'ils profitent de l'opulence des proies pour maximiser le taux d'ingestion, entraînent le déclin progressif des blooms. Dans l'hypothèse que le taux de croissance intrinsèque du phytoplancton n'est pas affecté par la dilution, l'incubation des échantillons sur une période de 24 heures va suivre la dynamique suivante:

$\dfrac{dp}{dt} = \mu p - gDp$, avec $g = \gamma Z$ et Z considéré constant pendant la période d'incubation

$$p_0 = p_{t=0} = DP_0$$

Par intégration, on obtient:

$$\begin{aligned}
&\int_{p_0}^{p(t)} \frac{dp}{p} = \int_0^t dt(\mu - gD) \\
&log_e\left(\frac{p(t)}{p_0}\right) = (\mu - gD)t \\
&y = \beta_0 + \beta_1 D \text{ , avec } y = \frac{1}{t} log_e\left(\frac{p(t)}{p_0}\right) \text{ , } \beta_0 = \mu \text{ et } \beta_1 = -g \\
&p(t) = p_0 exp^{(\mu - gD)t}
\end{aligned} \tag{1.29}$$

La régression linéaire des mesures du taux de croissance apparent de chaque échantillon dilué $\frac{1}{t} log_e\left(\frac{p(t)}{p_0}\right)$ par rapport aux facteurs de dilution, D, permet d'estimer simultanément les taux $\mu$, ordonnée à l'origine, et g, pente de la droite, de la population dans l'échantillon initial. L'une des hypothèses majeur de ce modèle repose sur la diminution linéaire du taux de prédation en réponse à un facteur de dilution croissant. Cependant, il arrive que dans un milieu riche en phytoplancton, comme c'est typiquement le cas dans les écosystèmes eutrophes, la quantité de phytoplancton n'est plus limitante pour la croissance du zooplancton qui parvient à saturation du taux de prédation. Pour représenter ce mécanisme de saturation, il est possible de formuler le comportement asymptotique de la prédation simplement en considérant un système bilinéaire régi par un système de deux dynamiques lorsque p dépasse une certaine valeur pour laquelle le nombre de proies consommées par prédateur n'augmente plus, $P_s$:

$$\frac{dp}{dt} = \begin{cases} \mu p - gDp \text{ si } p<P_s \\ \\ \mu p - gDP_s \text{ si } p \geqslant P_s \end{cases} \tag{1.30}$$

La solution du système lorsque $p \geqslant P_s$ est donnée par:

$$\begin{aligned}
&\frac{dp}{p} = dt\left(\mu - gDP_s\frac{1}{p}\right) \\
&\frac{dp}{p} = dt\left(\mu - gDP_s\frac{1}{p_0 exp(\mu t)}\right) \\
&\frac{dp}{p} = \mu dt - gP_s dt\frac{1}{P_0 exp(\mu t)} \text{ avec } p_0 = DP_0 \\
&\text{Par intégration, } log\left(\frac{p(t)}{p_0}\right) = \int_{t=0}^t \mu dt - g\frac{P_s}{P_0}\int_{t=0}^t exp(-\mu t)dt \\
&log\left(\frac{p(t)}{p_0}\right) = \mu t + \frac{gP_s}{\mu P_0}(exp(-\mu t) - 1) \\
&p(t) = p_0 exp(\mu t) exp\left(\frac{gP_s}{\mu P_0}(exp(-\mu t) - 1)\right)
\end{aligned} \tag{1.31}$$

A l'approche de l'asymptote, le comportement du taux de prédation n'est plus constant et requiert un modèle ou une fonction, $G(P)$, pour représenter l'adoucissement de la pente entre taux de croissance et facteur de dilution, selon le deuxième cas de figure: la réponse fonctionnelle. Parmi les plus utilisées, les formules d'Holling et d'Ivlev s'écrivent respectivement:

$$\begin{aligned}
&\text{Holling: } G(P) = g_{max}\frac{P}{k_P + P} \\
&\text{Ivlev: } G(P) = g_{max}(1 - exp(-k_P P))
\end{aligned} \tag{1.32}$$

En réalité, ce type de dynamique décrit par seulement deux variables d'état n'est plus réaliste dès que l'on considère la préférence des prédateurs pour certaines proies. De nouvelles applications de la méthode de dilution, qui impliquent un tri sélectif du phytoplancton avant incubation (Caceres *et al.*, 2013; Taniguchi *et al.*, 2014), ainsi que le développement de nouvelles techniques, comme les isotopes stables $\delta^{13}C$ et $\delta^{15}N$, ont mis en avant la nécessité de distinguer différents compartiments au sein même des variables d'état $P$ et $Z$. Les ratios d'isotopes stables $^{12}$C:$^{13}$C ($\delta^{13}C$) et $^{14}$N:$^{15}$N ($\delta^{15}N$) permettent de déterminer respectivement la source de carbone organique à la base de l'alimentation du zooplancton et leur position au sein des réseaux trophiques. En 1966, Jorgensen a caractérisé les facteurs clés de l'herbivorie sélective en milieu marin, en présentant particulièrement la taille du phytoplancton comme principale cible des prédateurs. Au sein d'une classe de taille comme le nanophytoplancton, l'action de la prédation n'entraîne pas de modifications du mode de distribution en taille mais diminue toutes proportions gardées la quantité absolue d'individus présents qui peuvent actuellement être observés (Parsons *et al.*, 1967). Le trait conservatif de la proportion de prédation de certaines classes de proies est désormais un facteur important de la formulation de la prédation des systèmes P-Z . Dans un modèle de sélection dynamique, Fasham (1990) a d'abord considéré la proportion de différents types de proies pour représenter le changement de comportement du zooplancton si jamais la pression de prédation était tellement ciblée qu'elle entraînerait l'extinction complète d'un trait biologique parmi la communauté de proies, au lieu de quoi, passée une certaine limite, *feeding threshold*, liée à la probabilité de rencontre, le prédateur est amené à ingérer un autre type de proies selon un mode dit d'*active switching* (Gentleman *et al.*, 2003). La rétroaction de l'effectif de proies sur le compartiment de prédateur dans un tel système promeut de façon effective la coexistence du phytoplanctons et la stabilité de la circulation de flux de carbone au sein des réseaux trophiques (Hutson, 1984).

## 1.4 La mer Méditerranée et ses étangs

*Les grands bassins méditerranéens*

La mer Méditerranée est une mer semi-fermée à la circulation générale cyclonique: les eaux d'origine atlantique (AW) entrent par le détroit de Gibraltar, circulent le long des bassins Alboran et Algérien, passent le canal de Sicile, longent le littoral sud-est méditerranéen, puis remontent au nord avant de passer par les bassins Thyrrhénien, Liguro-Provençal et Alboran (Figure 21). Le temps moyen de résidence des eaux atlantiques en mer Méditerranée est proche de 70 ans (Roether et al. 2013). La différence de salinité entre les eaux atlantiques et méditerranéennes (MW) entraîne la circulation thermohaline des masses d'eau. Les eaux de surface forment une masse d'eau moins dense que les eaux sous-jacentes d'une profondeur d'environ 100-200 m sur 10 km de large. Dans le bassin Liguro-Provençal, le courant Nord peut longer le littoral français à une vitesse de 10 cm.s$^{-1}$. Due à la consommation progressive des sels nutritifs au long de leurs trajets, les eaux de surface méditerranéennes forment un gradient longitudinal de teneurs en phosphates, nitrates et silicates (Béthoux et al., 2002), qui limite fortement la croissance du phytoplancton (Sournia, 1973). On parle d'oligotrophie en mer Occidentale et d'ultraoligotrophie en mer Orientale (Pujo-Pay et al., 2011). La circulation thermohaline a aussi lieu de façon récurrente dans certains sous-bassins: au niveau du bassin Levantin, les eaux de surface plongent pour former les eaux intermédiaires (LIW),

en mer Adriatique et au niveau du bassin Nord Occidental, les regimes de vent entraînent la convection en hiver. Les eaux méditerranéennes sont plus salées puisque l'évaporation surpasse la désalinisation induite par la pluie et l'apport des rivières (AW:3 6-37; MW: 38-39) (Millot et Taupier-Letage, 2005).

Située en milieu tempéré, la Méditerranée est fortement influencée par le cycle saisonnier. Certains bassins en particulier montrent des variations importantes de production primaire au cours de l'année. D'après les mesures satellites de chlorophylle a, les bassins Alboran, Liguro-Provençal et Adriatique abritent des communautés avec un fort potentiel de reproduction qui tendent à s'accumuler en surface au printemps (D'Ortenzio et Ribera D'alcala, 2009). On parle d'efflorescence printanière. Cette efflorescence s'étend sur une fenêtre de temps relativement longue, de début mars à début juin (Mayot et al., 2016). Les principales raisons de l'efflorescence en mer Méditerranée se résument à l'apport prolongé de sels nutritifs par la convection hivernale suivi de la restratificiation thermique de la couche surface qui permet au phytoplancton de prolonger le temps passé dans la zone éclairée (Sverdrup, 1953; Longhturst, 1998). Certains phénomènes attenants tels que les pulses de sels nutritifs (Thyssen et al., 2015) ou les fronts physiques (Olita et al., 2014) contribuent à la variabilité de la fenêtre spatio-temporelle des efflorescences. A l'inverse de ces zones fortement productives, l'ensemble du bassin oriental est caractérisé par une très faible biomasse en chlorophylle a, $< 0.1$ mg.m$^{-3}$, qui reste stable au cours de l'année. Les phosphates et les nitrates sont présents essentiellement à l'état de traces ($\sim$ 1-100 nM) (Krom et al., 1991). A cause de phénomènes tels que la convection d'eau profonde ou les efflorescences algales, aussi observées dans l'océan global mais à échelle réduite (d'où l'emploi du terme *mini ocean*), la mer Méditerranée est particulièrement adaptée pour étudier les effets du changement climatique sur les processus physiques qui affectent aussi bien la circulation générale mais aussi la production primaire (Robinson and Golnaraghi, 1994).

La convection d'eau profonde en particulier, est un phénomène sensible aux variations de la circulation océanique et des forçages atmosphériques (Lavigne, 2013). La profondeur du mélange induit par la plongée des eaux de surface est un paramètre clé du préconditionnement des efflorescences observées en Méditerranée Nord Occidentale (Séverin et al., 2014). La production totale de la mer Méditerranée a été estimée à hauteur de 0.5 Pg C.an$^{-1}$, soit 1% de la production océanique globale (45 Pg C.an$^{-1}$) (Uitz et al., 2010). Malgré sa faible superficie comparée à la surface globale des océans (1%), la mer Méditerranée contribue à hauteur de 1,02% à la séquestration des émissions anthropiques de $CO_2$, soit 1,6-2,5 Pg C contre 150 $\pm$ 26 Pg C dans l'océan global (Schneider et al., 2010; Khatiwala et al., 2013). L'une des composantes attenantes aux mesures de production en mer Méditerranée et à l'utilisation de ses ressources concerne les étendues d'eau qui lui sont associées. A ce jour, plus d'une centaine d'étangs communiquent directement avec la mer Méditerranée (Perez-Ruzafa *et al.*, 2010). Le mélange entre les eaux d'origines marines et terrestres et la proximité des milieux exploités influencent considérablement les communautés phytoplanctoniques qu'elles abritent. De manière générale, les étangs comptent parmi les écosystèmes les plus productifs de la planète. Les lagunes méditerranéennes Nord Occidentale peuvent produire près de 100-200 g C.m$^2$.an$^{-1}$ (Vaulot et Frisoni, 1986). Par comparaison, la production totale de la mer Méditerranée rapportée à sa surface équivaut à 70 g C.m$^{-2}$.an$^{-1}$ (Uitz et al., 2012).

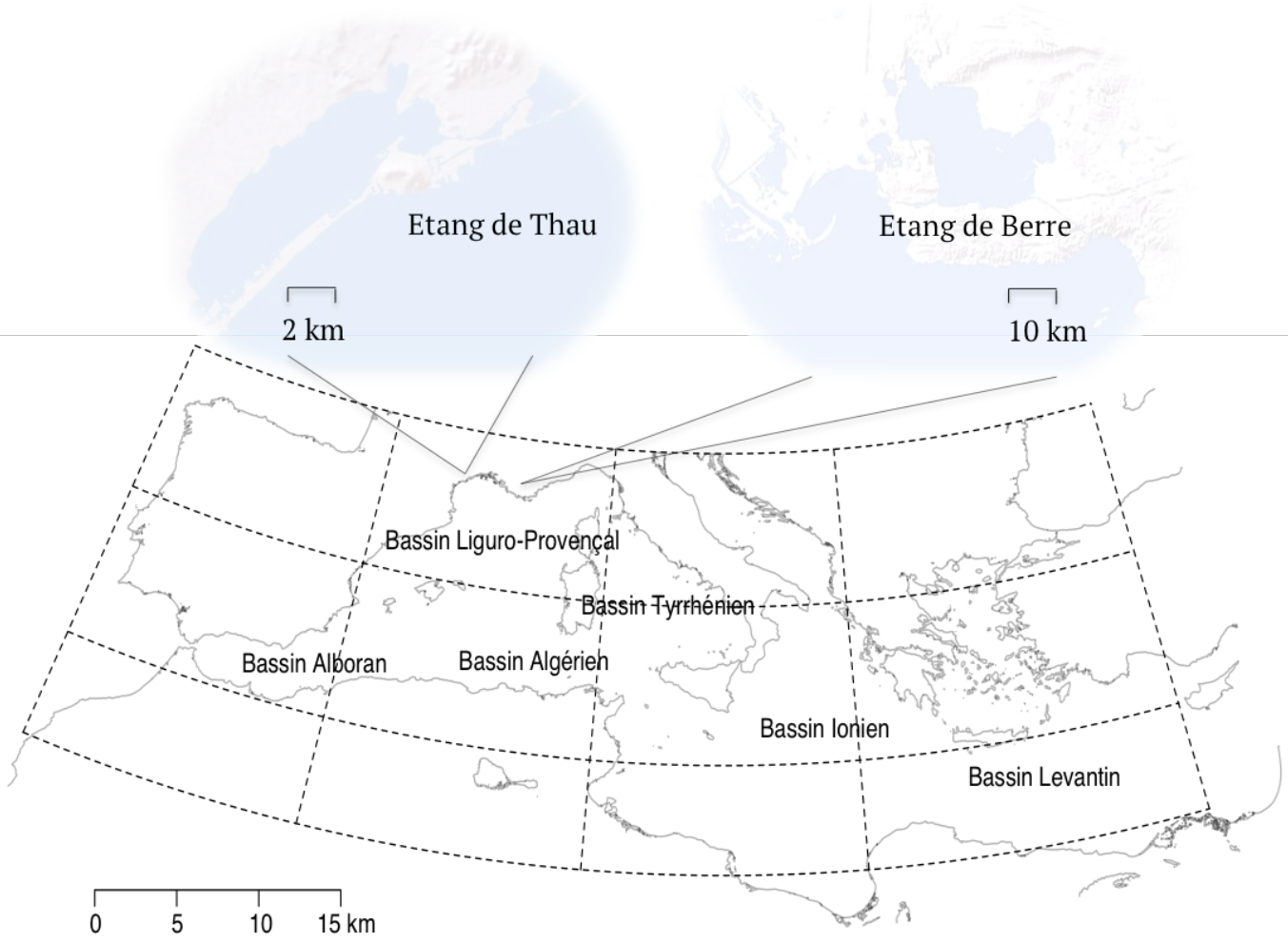


Figure 1.21: Bassins et lagunes méditerranéens

*L'étang de Berre*

L'étang de Berre compte parmi les plus importantes lagunes méditerranéennes en terme de superficie, 155 km$^2$, située au nord de la métropole de Marseille. Les échanges avec la mer Méditerranée ont lieu à travers le canal de Caronte. D'une profondeur moyenne de 6 m, pour un maximum à 9 m, l'étang fait l'objet d'un suivi écologique mensuel depuis 1994. Le suivi s'appuie sur la caractérisation hydrologiques des masses d'eau par des mesures de température, salinité, concentration en oxygène et en chlorophylle a (Nérini et al., 2000), en plus de l'inventaire d'espèces clé de voûte de la dynamique de l'écosystème. Parmi ces espèces, les herbiers de *Zostera* (Bernard et al., 2007; Manté et al., 2013), certains mollusques (Bonhomme, 2006), et polychètes benthiques (Stora et Arnoux, 1983), l'ichtyofaune (Le Diréach et al., 2013), le zooplancton (Delpy et al., 2013) et le phytoplancton (Malkassian, 2012). Le suivi a été instauré suite à l'industrialisation de la lagune et à l'implantation de la centrale hydroélectrique de St Chamas en 1966.

La centrale soumet l'étang de Berre à de fortes contraintes hydrologiques de déversement d'eau douce lié à son activité (Minas, 1974). Le contraste entre l'eau douce apportée par les rivières et la centrale (salinité de 10-20) et les eaux méditerranéennes (salinité de 37.5-38) qui remontent le long du canal de Caronte stratifie les masses d'eau de surface

et de fond par gradient de densité (Nérini et al., 2001). Ce gradient limite la diffusion de l'oxygène sur la colonne d'eau et ne peut être réduit que sous l'effet du vent (Minas, 1976). Les apports de la rivière Durance chargés en sels nutritifs ont particulièrement enrichi la lagune en nitrogen (N) et phosphore (P), en plus d'une activité de reminéralisation intense (Gouze et al. 2008). En 2011, entre 50% de N et 15% de P provenaient des eaux usagées de la centrale. Entre 1994 et 2012, la concentration en nitrates a atteint 35 $\mu$M en hiver des suites de l'intensification des activités de la centrale, pour une teneur historique qui se situait entre 1-3 $\mu$M avant son installation (Gauze, 2008; Raimbault et al., 2013).

La persistence de fortes concentrations de nutriments au printemps a contribué à fortement alimenter les communautés phytoplanctoniques. A quatre reprises, la biomasse totale en chlorophylle a dépassé le seuil de 100 $\mu$g.dm$^{-3}$ (Malkassian, 2012). Si elle a d'abord été attribuée à la dominance de quelques genres tels que *Prorocentrum*, *Cyclotella* ou *Chaetoceros*, la composition des communautés de phytoplancton se diversifie. Le suivi mensuel qui a été réalisé depuis 1995 par le biais d'identification au microscope et qui est désormais soutenu par les analyses en cytométrie en flux, montre que les espèces présentes dans l'étang sont en constante évolution. *Prorocentrum minimum*, une espèce d'algue toxique, a pratiquement disparu depuis 2000 alors qu'*Akashiwo sanguinea* apparaît dorénavant fréquemment de façon sporadique dans l'étang de Vaïne (Figure 22). La biomasse présente soutient deux pics de production primaire supérieurs à 1000 mg C.m$^{-3}$.j$^{-1}$ au printemps et en automne. Les études comparatives désignent l'étang de Berre comme la lagune méditerranéenne la plus productive (Kim, 1983).

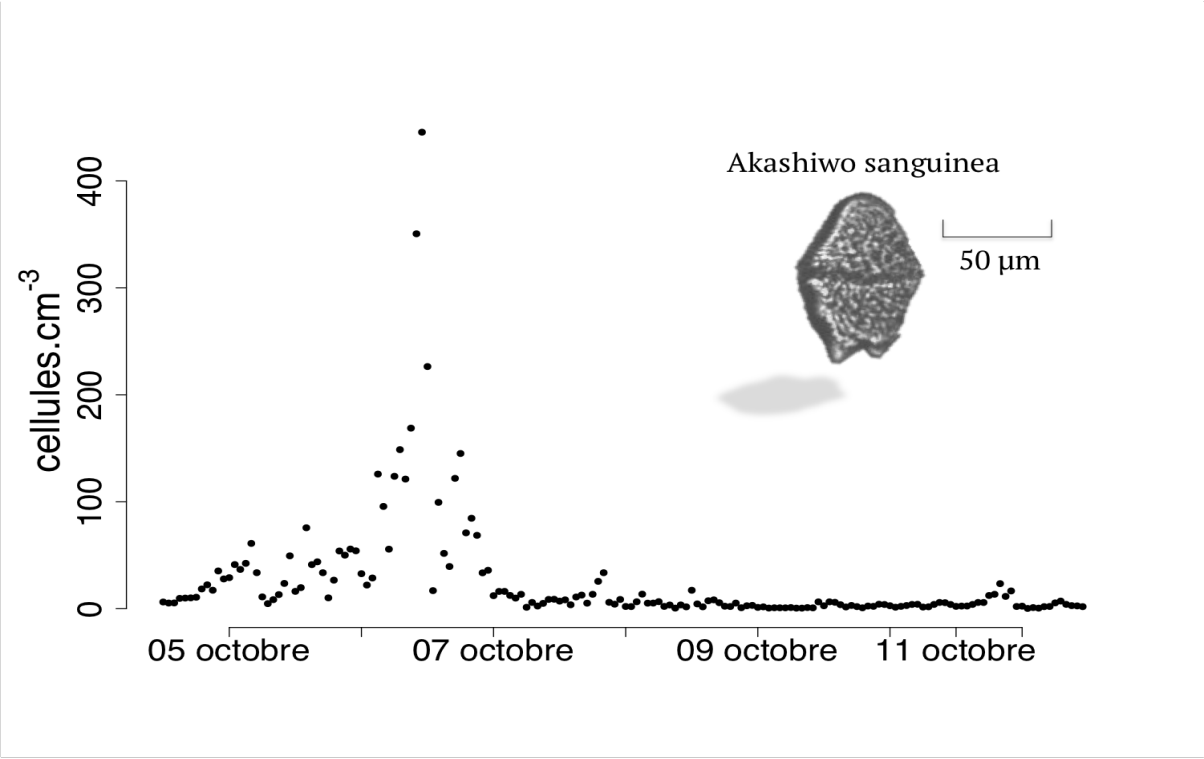


Figure 1.22: Abondance d'*Akashiwo sanguinea* mesurée à haute fréquence par cytométrie en flux dans l'étang de Vaïne en octobre 2011

*L'étang de Thau*

L'étang de Thau est situé sur le littoral sud français, près de la ville de Sète (43°24'N-3°36'E). Sa superficie couvre 75 km$^2$, pour une profondeur moyenne de 4m et une profondeur maximale de 10m. L'étang est connecté à la mer Méditerranée par trois canaux. L'hydrologie de l'étang est continuellement caractérisée depuis 1971 par le bias de mesures de température, salinité et de teneurs en sels nutritifs. Contrairement à l'étang de Berre, la salinité de Thau est proche de la salinité observée en mer Méditerranée (32.6-38.0). Le phytoplankton fait l'object d'une série d'observation qui a démarré en 1987, notamment à partir de la cytométrie en flux, sous l'égide du Réseau d'observation et de surveillance du phytoplancton et des phycotoxines (REPHY). La plus petite algue unicellulaire eukaryote, *Ostreococcus tauri*, y a été découverte en 1994 (Courties et al., 1994). Plus récemment, des algues du genre *Synechococcus* ont fait leur apparition dans l'étang sous l'impulsion du réchauffement de la température (+ 0.045°.an$^{-1}$) et de l'appauvrissement en nutriments (Bec et al., 2005; Collos et al., 2009). Les teneurs en phosphore (P) sont désormais sous le seuil de détection des instruments de mesure (< 0.1 $\mu$M) alors qu'elle ont atteints 10 $\mu$M à proximité de zones industrielles (Casellas et al., 1990). En raison des actions menées pour lutter contre l'eutrophisation de l'étang, les nitrates (N) sont également présents à l'état de trace (< 0.05 $\mu$M). N et P ne permettent pas de supporter une production basée sur des apports allochtones, dite production *nouvelle*.

La production, essentiellement basée sur l'activité de reminéralisation (production *régénérée*), est relativement faible. Les faibles teneurs en sels nutritifs ainsi que la présence d'organismes filtreurs sont tous deux responsables des faibles valeurs de biomasse phytoplanctonique observées dans l'étang de Thau (Souchu et al., 2001). La concentration en chlorophylle est comprise entre 0.1 et 2 $\mu$g.dm$^{-3}$ même si des pulses nutritifs liés aux précipitations permettent de soutenir de façon sporadiques des efflorescences de diatomées du genre *Thalassiosira* (Collos et al., 1997). Depuis 1998, l'espèce *Alexandrium catenella* prolifère de manière récurrente et menace la conchyliculture de l'étang (Lilly et al., 2002). En dehors de cette période, la production primaire peut aussi être soutenue par les cellules de picophytoplancton (< 2 $\mu$m), dont le taux de division peut atteindre plus de deux divisions.d$^{-1}$ (Bec et al., 2005). La production journalière de carbone organique par le picophytoplancton peut atteindre 42%. L'enrichissement de la lagune en sels nutritifs a mis en avant la saisonnalité des régimes de limitations sur cette fraction de taille. La production primaire totale de l'étang de Thau est généralement inférieure à celle de l'étang de Berre, avec 400 mg C.m$^{-3}$.d$^{-1}$ (Vaulot et Frisoni, 1986).

# 2.0 Phytoplankton population models: Introducing multiple stages to study the cell cycle

**Abstract**

In this paper, we provide several validations of two referred populations models to predict phytoplankton *in situ* growth rates. Both approaches integrate multiple stages to model asynchronous populations, whose cells are dispersed in the cell cycle. The *cell cycle method* is used to represent cells distributed in the classical cell cycle stages: the $1^{st}$ and $2^{nd}$ *Gap* ($G1$, $G2$) which separate the *Synthesis* ($S$) and *Mitosis* ($M$) stages, where cells present distinct amount of DNA (McDuff and Chisholm, 1962; Carpenter and Chang, 1998). The *size-structured population* model justifies the transitions between interphase and mitosis with diel observations of cells proportions in individual size classes (Sosik et al., 2003). DNA and size are individually measured by flow cytometry through the emission of a DNA-binding fluorochrome fluorescence and cells' scattering. We used an autonomous flow cytometer to evaluate each model performances with comparison of cells counts. Two datasets were collected under controlled conditions to study the validity of the *cell cycle* and *size-structured population* approaches. Two monocultures of a diatom (*Thalassiosira pseudonana*) and a chlorophyte (*Chlamydomonas concordia*), grown in a microcosm under a 12:12h LD cycle and constant temperature of 17°C during 20 days, were monitored every hour by a Cytosense. A natural assemblage of populations was studied in a mesocosm deployed during 5 days with the same instrument (Thau lagoon, NW Mediterranean). Comparisons show that the *cell cycle method* is indicated to study monogenic populations and may also be extended to particular groups defined by flow cytometry. The *size-structured population* method shows a good agreement with *in situ* growth rates determined by cells counts and mitotic index.

M. Dugenne, M. Thyssen, B. Mostajir, L. Duforêt, W. Moutier, N. Guiselin, L. Courcot, A. Barani, G. Grégori

## 2.1 Introduction

***Phytoplankton populations:***

Phytoplankton populations group drifting unicellular or colonial algae reproducing mostly by binary fission. These microscopic organisms measure less than 300 $\mu$m but buffered half of the anthropic $CO_2$ emissions by injecting the product of photosynthesis towards the deep ocean (Sabine et al., 2004). In terms of diversity, phytoplankton is also a large contributor of global biodiversity. In the Sea, phytoplankton diversity is shaping productivity (Vallina et al., 2014). The study of phytoplankton turnover is crucial for the management of natural resources simulated under climatic scenario (Cheung et al, 2011). Phytoplankton has a short life time compared to any other primary producers (Steele et al., 1989). Their life span is determined by the moment cells enter mitosis to produce two

daughter cells by binary fission. Before they divide, cells grow during the *Gaps* in order to allocate their biomass with no or limited net decrease of carbon in each daughter cell. Diatoms are an exception since they undergo a gradual size reduction over generations (Armbrust and Chisholm, 1992). The binary fission has been constrained by evolution to ensure that the hereditary information of a mother cell is also passed to separate daughter cells. To assure the passage of DNA copies, the separation of daughter cells (i.e. cytokinesis) during the *mitosis* is systematically preceded by the replication of the DNA copie(s) during the $S$ stage. Based on this mechanism, the generation time of natural phytoplankton populations may last less than 8 hours or up to 100 days (Kirchman, 2002). The average generation time of oceanic populations is 20 days. Due to multifactorial controls, the variability of phytoplankton productivity is high both on spatial and temporal scales (Steele, 1972). The perception of this variability in natural populations may not even be realistic since observations are biased by the frequency at which they have been measured (Levin, 1992). This paper focus on two approaches to model population dynamics that can be easily applied with flow cytometry. Flow cytometry is fast and adapted to unravel the dynamics of populations counting thousands individuals per $cm^3$.

***The cell cycle method:***

The cell cycle approach is based on the distinction of DNA copies through cell cycle stages by a fluorochrome. The fluorescent reagent is stoichiometric in order to perceive the changes of discrete DNA quantity induced by the replication of DNA in the $S$ stage. Cells that replicated their DNA to prepare the mitosis are identified by their 2-fold fluorescence compared to cells in $G1$. Since DNA-replicated cells are bound to divide, the frequency of paired-nuclei cells are indicative of the amount of newly formed cells (McDuff and Chisholm, 1982). The time course of stage-specific fractions is used to determine the duration of the terminal event, marking the effective separation of the two daughter cells, and the fractions of cells that entered mitosis ($f$). Growth rates are derived from the average rates of $\log 1+f$. The method is sensitive to the sampling frequency, as the intervals of observation convey the information to determine the duration of the terminal event.

***The size population method:***

The size-structured population method is based on the distinction of size classes distributions through cell cycle stages. The cells' induced scattering is converted into biovolume in order to observe the entire distribution of cell size. Doublets are identified by their size, corresponding to the 2-fold biomass of single cells produced after their mitotic separation. The time course of size classes proportions is used to determine the number of cells that contributed to the doubling of population density ($N$) through binary fission. Growth rates are derived from the discrete sum of $\log N(t+dt) : N(t)$. The method is sensitive to loss processes that affect unevenly the size distribution. For instance a size-selective grazing may reduce the growth rates predicted by 40 % (Chang, 1993).

***Extension of the methods***

The short life cycle of phytoplankton are determinant for their evolutionary capacities (Collins et al., 2014). In the past, they lived through perturbations by rapid adaptation which shaped phytoplankton diversification (Jackson and Cheetham, 1999). Yet, the study of rigorous population diversity may not be directly linked to marine productivity (Cermeno et al., 2013). From a statistical point a view, the aggregation of upright diversity is more discriminative than taxonomic species presence in order to predict the variation of primary productivity (Kruk et al., 2002). Recent statistical and mechanistic models include

the effects of fluctuations of light, temperature and nutritive ressource. For Ramon Margalef, the fitness of distincts life forms has been optimised to adapt to these fluctuations induced by local turbulence (Margalef, 1978). The growth strategies that favour some association of species under environmental conditions are cross-taxonomic and overlap. The categorisation of $r$ and $K$ strategists gives an example for ecological succession. Terms $r$ and $K$ referred to the intrinsic growth rates and the carrying capacity of the environment for a logistic growth. 'Survivalist', 'bloomer' and 'generalist' are other growth strategies that reflect the change of phytoplankton fitness through resource acquisition adaptation. A third classification introduced several *Functional Types* to predict the role of association of species as active actors of the major elements cycles (Reynolds, 1997). The determination of growth rates upon coherent morphological and ecological traits is essential to discriminate the potential sensitivity of phytoplankton to increasing perturbations. The objective of the paper is to validate the population approaches under controlled conditions to predict productivity of functional traits and ecological functions across environmental gradients.

## 2.2 Material and Methods

The collection of high frequency analyses of phytoplankton optical properties was carried out by a Cytosense (Cytobuoy, b.v.). The Cytosense is design to study individual or colonial phytoplankton cells in the size range 0.8-800 $\mu$m. Phytoplankton is detected by the red autofluorescence emitted after the excitation of chlorophyll a molecules with a 488 nm coherent laser. At the passage of single particles in the laser beam, the red, orange, yellow fluorescences (FLR, FLO, FLY) and the sideward scatter (SWS) are collected by photomultiplier tubes. The forward light scatter (FWS) is turned into electrons by photodiodes. Samples were pumped with a peristaltic pump towards the laser beam at a speed of 5 $\mu$l.s$^{-1}$ to analyse 5 cm$^{-3}$. Cells are driven though the fluidic path by a particle-free sheath fluid composed of 0.2 $\mu$m filtered samples medium. The post-processing analyses were realised in batch with the CytoClus software (Cytobuoy, b.v.). Groups were defined manually using the projection of light scatter and autofluorescence signals. Two monospecific cultures and a natural assemblage were monitored to validate populations-based growth rates. Since populations were maintained under controlled conditions, the estimations of *in situ* growth rates based on the cell cycle and the size-structured population methods were compared to the uncorrected rates of density doublings ($\mu_{Ab}$) following:

$$\mu_{Ab} = \frac{1}{dt} log_e \left( \frac{N(t+dt)}{N(t)} \right) \qquad (2.1)$$

Datasets

### Monocultures

Two monospecific cultures of *Thalassiosira pseudonana* (Bacillariophyta) and *Chlamydomonas concordia* (Chlorophyta) were grown in f/2 medium under a constant photons flux of 200 $\mu$mol photons.m$^{-2}$.s$^{-1}$ during a 12:12 h light dark cycle. Cultures of the Roscoff Culture Collection (RCC, http://roscoff-culture-collection.org) were maintained at 17°C during 20 days in 60 dm$^3$ minicosms. The cells were placed under a continuous agitation to homogenise the minicosms. The Cytosense acquired measurements of cells optical properties every 2 hours in batch via a dedicated piloting software.

### Natural assemblage

The natural assemblage of the Thau lagoon (43°24'N-3°36'E, SW France) was studied in an enclosed environment through the deployment of an *in situ* mesocosm from

March 8 2015 to March 13 2015. The 2m-deep mesocosm contained 2 $m^3$ of prefiltered Thau water (100 $\mu$m). The community was placed under a continuous agitation to homogenise the mesocosm. The Cytosense acquired measurements of cells optical properties in 3h intervals. In addition to *in situ* analyses, 5 $cm^3$ samples were preserved in 0.25% glutaraldehyde and frozen in liquid nitrogen to conduct posterior DNA staining analyses.

Microbial growth

The time series of populations' abundance under controlled conditions were modelled by a microbial growth probabilistic model (Horowitz et al., 2010). Besides the population doublings measured during the exponential phase, the model accounts for the time lag of cells adjustment following their introduction in new habitats and the stationary/decline phase due to mortality. Mortality may result from the depletion of ressources or predation. The model assumes that the discrete observations of populations abundance at time $t$ follow a multinomial distribution with transition probability:

1. $P_d(t)\Delta t$ : probability of cell division at time t
2. $P_m(t)\Delta t$ : probability of cell loss at time t
3. $1-[P_m(t)+P_d(t)]\Delta t$ : probability of cell alive in interphase at time t

At each time step, the number of cells $N(t)$ is projected in time to predict the next observation following: $N(t+1) = N(t)[1 + P_d(t)\Delta t - P_m(t)\Delta t]$.

The instantaneous transition rates of cell division ($P_d(t)$) and cell loss ($P_m(t)$) are both logistic expressions dependent of the time (E 2). Parameters were inferred by maximum likelihood estimation.

$$P_d(t) = \frac{P_{d_{max}}}{1 + exp[k_d(t_d - t)]} \qquad P_m(t) = \frac{P_{m_{max}}}{1 + exp[k_m(t_m - t)]} \tag{2.2}$$

$P_d(t)$: instantaneous transition rates of cell division at time $t$, $P_m(t)$: instantaneous transition rates of cell loss at time $t$, $P_{d_{max}}$: maximum transition rates of cell division, $P_{m_{max}}$: maximum transition rates of cell loss, $t_d$: half division rate saturation, $t_m$: half loss rate saturation, $k_d$: steepness of the division rates, $k_m$: steepness of the loss rates

The cell cycle model

***Samples analyses*** Discrete samples from the Thau lagoon were kept frozen up to laboratory analyses to determine the time course of cell cycle fractions over 3 h intervals. Prior analyses, 5 $cm^3$ samples were unfrozen and incubated in the dark during 15 min with a working solution of Picogreen® following the staining protocol of Veldhius et al. (1997). The stock solution was diluted 10 times to prepare 100 $\mu$l aliquots preserved at -20 °C. 100 $\mu$l of the working solution were added per ml of sample to stain the cells. We did not use a pre-treatment with RNAse to increase the penetration of the dye, as advised by Veldhius et al. (1997). The stoichiometric emission of green fluorescence emission of the DNA-fluorochrome complex (525 ± 15 nm) was used to quantify the relative DNA distribution of cells populations during 24 hours.

To compare the preserved populations with *in situ* populations, the stained samples were analysed with the Cytosense. An example of 2D projections of the same sample is shown in figure 1.

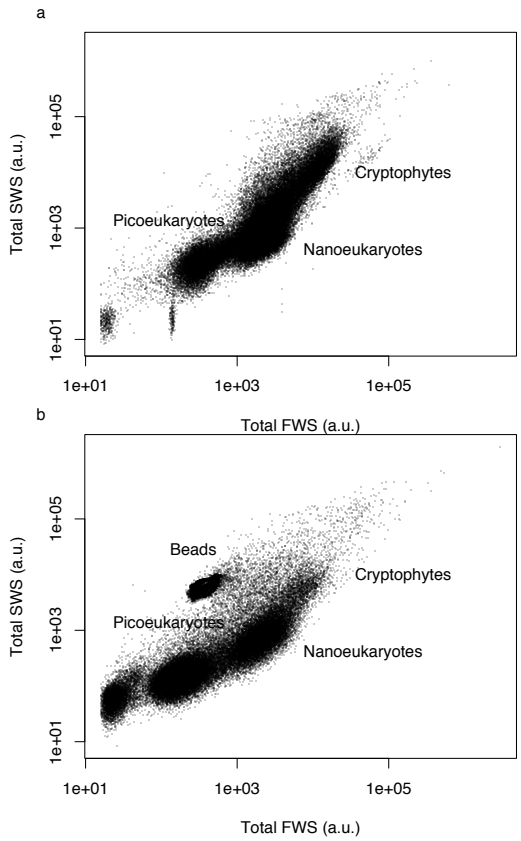


Figure 2.1: 2D projections of the Thau lagoon mesocosm populations optical properties (FWS: Forward Scatter, SWS: Sideward Scatter) measured (a) *in situ* (b) after DNA straining with the Cytosense

We modified its fluidic path to carry over staining samples without affecting the sheath recycling circuit. The bypass of Cytosense sheath circulation was connected to external tanks of artificial sheath fluid and waste. The external sheath was pumped at 80 ml.min$^{-1}$ with the instrument sheath pump. The stained sample was pumped with the peristaltic pump and directed to the waste after the passage in the flow cell. Regular measurements of the sheath pump speed were tested to ensure the regularity of the time required for cells passage in the laser beam. The optical noise of green fluorescence was determined with the free-particle sheath fluid to trigger the emission of Picogreen® by the stained cells. We prevented intercontamination of the stained samples by running a diluted bleach solution (0.1 %) in the fluidic tubing. Short analyses of unstained samples (1 min) were carried out to reveal tubing contamination between each analysis.

***Growth rates estimations*** The integrated signals of green fluorescence per cell were used to analyse the time course of the distribution of the DNA-fluorochrome complex emission. Paired-nuclei were identified by the relative 2-fold increase of green fluorescence, compared to single nucleus. Cells in replication were counted between the 2 modes. The fractions of cells in $G1$ ($f(G1)$), $S$ ($f(S)$) and $G2{+}M$ ($f(G2{+}M)$) were determined every 3 hours to measure populations daily *in situ* growth rates ($\mu_{DNA}$) according to Carpenter and Chang (1988) formulation:

$$
\begin{aligned}
f_i(G2+M) &= \frac{N(t_i+td)-N(t_i)}{N(t_i)} \\
\mu_{DNA} &= \frac{1}{n.t_d}\sum_{i=1}^{n} log_e\left(\frac{N(t_i+td)}{N(t_i)}\right) \\
\mu_{DNA} &= \frac{1}{n.t_d}\sum_{i=1}^{n} log_e(1+f_i(G2+M))
\end{aligned}
\tag{2.3}
$$

$N$: population abundance (cells.cm$^{-3}$), $n$: number of daily samples, $t_d$: duration of the terminal event (d), $f(G2+M)$: fraction of cells in the terminal event (G2+M), $\mu$: daily growth rates (d$^{-1}$)

The duration of the terminal event, making the effective separation of daughter cells (Mitchinson, 1971), is determined by:

$$
\begin{aligned}
t_d &= 2.(t_2-t_1).\frac{\sum_i log_e(1+f_i(G2+M))}{\sum_i log_e(1+f_i(G2+M)+f_i(S))} \\
&\left[\frac{df(S)}{dt}\right]_{t_1} = 0 \\
&\left[\frac{df(G2+M)}{dt}\right]_{t_2} = 0
\end{aligned}
\tag{2.4}
$$

$t_d$: duration of the terminal event (d), $f(G2+M)$: fraction of cells in the terminal event (G2+M), $f(S)$: fraction of cells in the $S$ stage, $t_1$: observation time of the maximum number of cells in stage $S$, $t_2$: observation time of the maximum number of cells in stage $G2+M$.

Equation (4) is derived from multiple stage models applied to a single cohort. An illustration of the time course of the cohort in cell cycle compartments is given in figure 2.

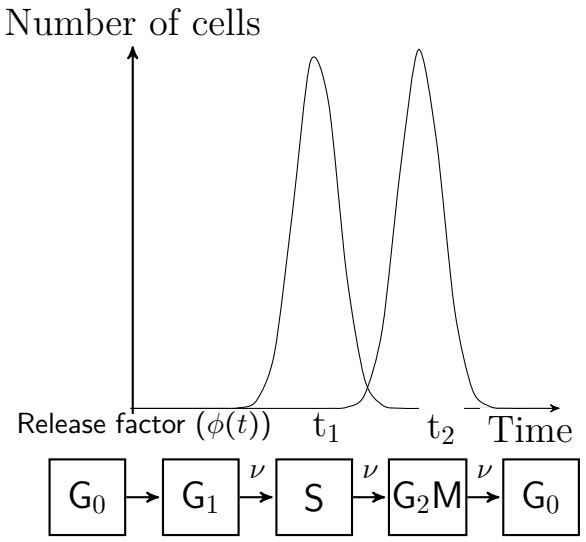


Figure 2.2: Multiple stages compartments in the cell cycle model. At $G_0$, a cohort of cells is released with a factor $\phi(t)$ to the stages $G_1$, $G_2$ and $G_{2+M}$ of the cell cycle. Cells pass the different stages at the same rate ($\nu$). The mode of the cells cohort in stage $S$ is observed at $t_1$. The model of the cells cohort in stage $G2+M$ is observed at $t_2$

***Algorithm*** The mathematical analysis of Watson et al. (1987) was used to attribute cells to the $G1$, $S$ and $G2$ stages of the cell cycle from the histograms of DNA relative fluorescence (Watson et al., 1987). For each histogram, two modes are expected. The first mode correspond to cells in G1 stage, with a single DNA copie. Paired-nuclei, in $G2$ and $M$ stages, forms the $2^{nd}$ mode of distribution. The continuum of cells between modes are in $S$ stage. An example of DNA distribution is shown in figure 3. Cells fluorescences follow a mixture of two Normal distributions, with respectives mean $\mu_1, \mu_2$ and standard deviations $\sigma_1, \sigma_2$. The $S$ stage follows a distribution determined by the difference of Gauss error function. The complete model for the histogram observed at time $t$ is formulated by:

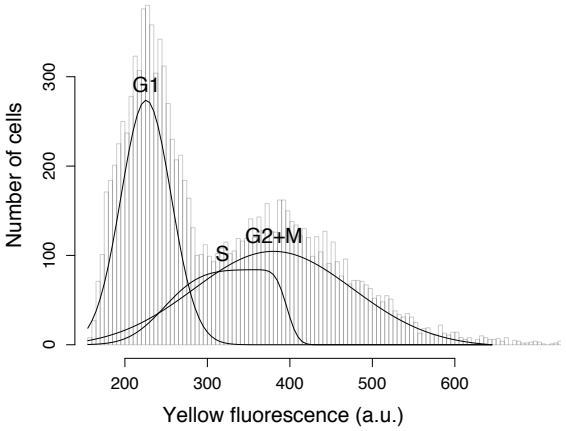


Figure 2.3: Histogram of yellow fluorescence induced by a stoichiometric DNA staining on picoeukaryotes population in the Thau mesocosm

$$
\begin{aligned}
n(x,t) &= n_{G1}(x,t) + n_S(x,t) + n_{G2M}(x,t) \\
n_{G1}(x,t) &= \frac{A_1}{\sigma_1(t)\sqrt{2\pi}} exp\left(-\frac{(x-\mu_1(t))^2}{2\sigma_1(t)^2}\right) \\
n_{G2}(x,t) &= \frac{A_2}{\sigma_2(t)\sqrt{2\pi}} exp\left(-\frac{(x-\mu_2(t))^2}{2\sigma_2(t)^2}\right) \\
n_S(x,t) &= x.P_s(x,t) \\
P_s(x,t) &= erf\left[\left(\frac{x-\mu_2(t)}{\sigma_2(t)}\right) + k_{G2}(t)\right] - \\
& erf\left[\left(\frac{x-\mu_1(t)}{\sigma_1(t)}\right) - k_{G1}(t)\right]
\end{aligned}
\tag{2.5}
$$

$x$: fluorescence (a.u.), $n(x,t)$: number of cells at time $t$ with fluorescence $x$, $n_{G1}(x,t)$: number of cells in $G1$ at time $t$ $n_S(x,t)$: number of cells in $S$ at time $t$, $n_{G2M}(x,t)$: number of cells in $G2M$ at time $t$, $\mu_1$: mean of the Normal distribution for cells in $G1$, $\sigma_1$: standard deviation of the Normal distribution for cells in $G1$, $\mu_2$: mean of the Normal distribution for cells in $G2M$, $\sigma_2$: standard deviation of the Normal distribution for cells in $G2M$, $erf$: Gauss error function

***Uncertainty of estimations*** The uncertainty of the estimation of $\mu_{DNA}$ were es-

timated by MCMC using the posterior distribution of Watson et al. (1987) model's parameters.

On the opposite of size-selective grazing, a stage-selective predation is unlikely to happen in natural populations of phytoplankton. If, during the time course of stage-specific fractions, a specific loss rates, $g(t)$ is evenly distributed among the stages, model outputs are unchanged. In this case, the temporal variations of cells in $S$ and $G_2M$ compartment may be written as :

$$\begin{aligned}\frac{dn_s}{dt} &= \sum_{i=g_1+1}^{g_1+s} \frac{dn_i}{dt} \\ &= \sum_{i=g_1+1}^{g_1+s} \nu(n_{i-1} - n_i) - g n_i \\ \frac{dn_{g_2+M}}{dt} &= \sum_{i=g_1+s+1}^{g_1+s+g_2+m} \frac{dn_i}{dt} \\ &= \sum_{i=g_1+s+1}^{g_1+s+g_2+m} \nu(n_{i-1} - n_i) - g n_i\end{aligned} \tag{2.6}$$

If the mode of cells in $S$ and the mode of cells in $G_2 + M$ are observed respectively at $t_1$ and $t_2$, then:

$$\begin{aligned}&\left[\frac{df_s}{dt}\right]_{t_1} = 0 \\ &<=> \frac{1}{N(t)}\left[\nu(n_{g_1} - n_{g_1+s}) - g(t)N_s(t)\right] \\ &- r(t)f_s(t) = 0 \\ &<=> \frac{1}{N(t)}\nu(n_{g_1} - n_{g_1+s}) \\ &- f_s(t)(\mu(t) - g(t) + g(t)) = 0 \\ &<=> n_{g_1} = n_{g_1+s} \\ &\left[\frac{dg_{g_2+M}}{dt}\right]_{t_2} = 0 \\ &<=> \frac{1}{N(t)}[\nu(n_{g_1+s+1} - n_{g_1+s+g_2+m}) \\ &- g(t)N_{g_2+m}(t)] - r(t)f_{g_2+m}(t) = 0 \\ &<=> \frac{1}{N(t)}\nu(n_{g_1+s+1} - n_{g_1+s+g_2+m}) \\ &- f_{g_2+m}(t)(\mu(t) - g(t) + g(t)) = 0 \\ &<=> n_{g_1+s+1} = n_{g_1+s+g_2+m}\end{aligned} \tag{2.7}$$

The approach consequently yields to the same estimation of growth rates with grazing distributed evenly among the cell cycle stages.

The size-structured population model

***Samples analyses*** The distribution of group-specific size distribution were retrieved from *in situ* analyses of the monocultures and the natural assemblage presents in Thau. Cells light scattering (FWS) intensities were converted into biovolume to measure the number of cells associated to each size class. For the two experiments, we performed a log-log regression between light scatter and real size of calibration beads. A set of silica beads were measured with the Cytosense following the same settings used for phytoplankton analyses. Beads were chosen for their structural similarities with phytoplankton refractive index (Foladori et al., 2008). In additions to 3.0, 5.0 and 7.0 $\mu$m micro spherical beads, we estimated the dimensions of pictures taken by the image-in-flow camera (> 10 $\mu$m) from reconstruction of 3D cell volume (Moberg and Sosik, 2012).

***Growth rates estimations*** The entire distributions of cells' biovolume converted from light scatter were used to analyse the time course of cellular growth and effective cytokinesis during 24 h periods. Cells doublets were identified by the relative 2-fold increase of cells size, compared to single cells. For each day, we used the projection of the initial distribution of cells in size classes to predict the temporal variation of the size distribution due to cellular growth and binary fission. The effective doubling of cells that underwent mitosis determined the size-based growth rates ($\mu_{size}$). The formulation of $\mu_{size}$ follows the approach of Sosik et al. (2003):

$$\mu_{size} = \frac{1}{t+dt} log_e \left( \frac{\hat{N}(t+dt)}{N(t)} \right)$$
$$\mu_{size} = \frac{1}{t+dt} log_e \left( \frac{\sum_{i=1}^{m} \hat{N}_i(t+dt)}{\sum_{i=1}^{m} N_i(t)} \right) \quad (2.8)$$

N: initial population abundance (cells.cm$^{-3}$), i: $i^{th}$ size class , $\hat{N}$: predicted abundance (cells.cm$^{-3}$), $m$: number of size classes, td: temporal integration of the distribution projection (d), $\mu$: daily growth rates (d$^{-1}$)

The prediction of the total cells abundance, summed upon all size classes, is derived from the progressive temporal projection of the initial size distribution, $N(t=0)$, by matrix multiplication. The transition matrix, $A(t)$, contains the probability of transitions across the entire size distribution. These probabilities depend on the progression of cells through the cell cycle. The size-structured population model functions as an non homogeneous Markov chain since the projected distribution is expressed as a function of the antecedent distribution and the dynamic components of $A(t)$.

Lets consider the vector of size classes, $\vec{v}$ and its corresponding absolute and normalised distributions at time t, $\vec{N}(t)$ and $\vec{w}(t)$ respectively. Following a Markov process:

$$\vec{N}(t+dt) = A(t)\vec{N}(t) \text{ and}$$
$$\vec{w}(t+dt) = \frac{A(t)\vec{N}(t)}{\sum A(t)\vec{N}(t)}$$

The multiple stages observed in the population contain observations of cells in each size class (Fig. 4).

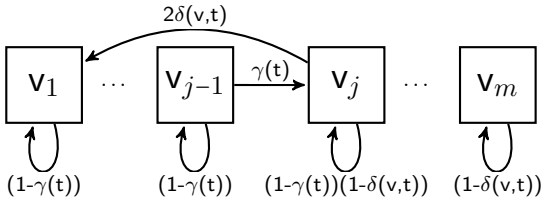


Figure 2.4: Multiple stages compartments in the size-structure population model. Small cells ($v_1$:$v_j$) may grow to the next size class ($\gamma$) or be at equilibrium (1-$\gamma$). Above a particular size ($v_j$=2$v_1$), cells are large enough to divide in two daughter cells with probability $\delta$. If cells reach the last size class ($v_m$), they are no longer able to grow.

***Algorithm*** Probabilities of transitions are described in Dugenne et al. (2014). Two processes are modelled to reproduce the diel variations of the vector of cells proportions in each size class, $\vec{w}(t)$: cellular growth and mitotic division. Both are expressed in terms of function bounded between 0 and 1, since they are probabilities, which vary according to the time and the size classes.

The probability of cells entering mitosis, $\delta$, is based on the equation :

$$\delta(t,v) = \delta_{max} \mathcal{N}(\mu_v, \sigma_v) \mathcal{N}(\mu_t, \sigma_t) \quad (2.9)$$

$\delta$: proportions of cells entering cytokinesis, $\delta_{max}$: maximum proportion of cells entering cytokinesis, $\mu_v$: mean of the size Normal distribution, $\sigma_v$: standard deviation of the size Normal distribution, $\mu_t$: mean of the time Normal distribution, $\sigma_t$: standard deviation of the time Normal distribution

Following Dugenne et al. (submitted), $\delta$ expresses a proportion modelled by the combination of two Normal distributions. One is linked to the size, the other is linked to the timeframe of cell division. Both imply an optimum, reached at $\mu_v$ and $\mu_t$ respectively, for cell division above which the cell size and the timing of division is suboptimal.

The probability of cellular growth, $\gamma$, is based on the equation :

$$\gamma(t) = \gamma_{max}\left[1 - exp\left(-\frac{E(t)}{E^*}\right)\right] \quad (2.10)$$

$\gamma$: proportions of cells growing, $\gamma_{max}$: maximum proportion of cells, E: irradiance, E*: normalising constant

Following Sosik et al. (2003), $\gamma$ expresses a proportion increasing with the light intensity perceived by phytoplankton. Since phytoplankton cells require light to produce organic matter by photosynthesis, $\gamma$ will assume that individual growth, occurring during the interphase, is light-dependent.

A third functional proportion is include in the transition matrix, $A$, to represent cells *stasis*. This proportion defines the probability for cells to maintain their state (i.e size) in equilibrium during the temporal projection (Fig. 4). Since this function illustrates a non-transition, it is modelled by the proportion of cells that neither divided nor grew between $t$ and $t + dt$.

$$[1 - \gamma(t)][1 - \delta(t, v)] \quad (2.11)$$

Lets define $\vec{v}$ as :

$v_i = v_1.2^{(i-1):\Delta v}$ for i 1, 2, ..., m

and the transition matrix $A(t)$:

$$\begin{array}{c} \\ v_1(t+dt) \\ \vdots \\ v_j(t+dt) \\ \vdots \\ v_m(t+dt) \end{array} \begin{array}{c} \begin{array}{ccccc} v_1(t) & \dots & v_j(t) & \dots & v_m(t) \end{array} \\ \begin{pmatrix} 1-\gamma(t) & \dots & 2.\delta(v_j,t) & \dots & 0 \\ & & & & \\ 0 & \ddots & (1-\gamma(t)).(1-\delta(v_j,t)) & \ddots & 0 \\ & & & & \\ 0 & \ddots & 0 & \ddots & 1-\delta(v_m,t) \end{pmatrix} \end{array}$$

Figure 2.5: Matrix transition, A(t). $\delta(v,t)$ denote the proportions of dividing cells, dependent of time and cell size. $\gamma(t)$ denote the proportions of growing cells, dependent of diel irradiance. j=1+1:$\Delta$v

The temporal projection integrates:

$$N_{|v=v_1}(t+dt) = (1-\gamma(t)).N_{|v=v_1}(t) + 2\delta(v_j,t).N_{|v=v_j}(t)$$

$$N_{|v=v_j}(t+dt) = (1-\gamma(t))(1-\delta(v_j,t)).N_{|v=v_j}(t) + \gamma(t).N_{|v=v_{j-1}}(t) + 2\delta(v_{j+1:\Delta v},t).N_{|v=v_{j+1:\Delta v}}(t)$$

$$N_{|v=v_m}(t+dt) = (1-\delta(t)).N_{|v=v_m}(t) + \gamma(t).N_{|v=v_{m-1}}(t)$$

The set of parameters, $\vec{\theta} = [\gamma_{max}, E^*, \delta_{max}, \mu_v, \sigma_v, \mu_t, \sigma_t]$, is estimated by maximum likelihood, assuming errors between observed ($\vec{w}$) and predicted ($\hat{w}$) normalized size distributions are normally distributed. Their standard deviation are estimated by a Markov Chain Monte Carlo (MCMC).

***Simulations of selective losses*** A selective grazing was simulated to scale the predictions of the size-structured population when losses rates are negligible, like it is assumes in the model, or important. At each time-step projection, the model includes a specific loss rates, $l(t)$, and net growth rates (E 12) are compared to the division rates $\Delta(t)$ (E 13).

$$r(t) = \frac{1}{t+dt} log_e\left(\frac{\sum_{i=1}^{m}\hat{N}_i(t+dt)}{\sum_{i=1}^{m}N_i(t)}\right) - l(t) \quad (2.12)$$

$$\Delta(t) = dt.\sum_{i=1}^{m}\delta(v_i,t) \quad (2.13)$$

Grazing rates were used to model losses rates. Two functions of grazing pressure, measured by the ingestion rates, $g$, are taken into account.

The functional-dependent grazing assumes that $g$ is a function of prey's abundance only.

$$g(t) = g_{max}.\mathcal{N}(\mu_t, \sigma_t) \quad (2.14)$$

The size-dependent grazing assumes that $g$ is a function of prey's abundance and size.

$$g(t) = g_{max}.\mathcal{N}(\mu_v, \sigma_v)\mathcal{N}(\mu_t, \sigma_t) \quad (2.15)$$

The parameter $g_{max}$ was fixed by increasing values bounded between 0 and 1 to reflect the intensity of the grazing pressure.

## 2.3 Results

Dynamics

***Monocultures*** The time series of *Thalassiosira pseudonana* and *Chlamydomonas concordia* dynamics during the 20 days experiments in minicosms are shown in figure 6.

The initial concentration of *Thalassiosira pseudonana* started at 1 $10^3$ cells.cm$^{-3}$ and reached a peak at 7 $10^5$ cells.cm$^{-3}$. The exponential phase, marked by positive division transitions rates, did not saturate up to the end of the experiment (April 30). The decay phase with a lag time of 3 days from April 7 with saturating losses transitions rates. On April 30, abundance was 7 $10^4$ cells.cm$^{-3}$.

The initial concentration of *Chlamydomonas concordia* started at 4 $10^4$ cells.cm$^{-3}$ and continuously increased up to 7 $10^5$ cells.cm$^{-3}$. The exponential phase, marked by high division transitions rates, lasted all the experiment. Although the maximum transition rates did not reached *Thalassiosira pseudonana* intensity, with 0.18 compared to 1, the losses rates were kept low enough to prevent the decay phase. With a probability of 0.06, the lag time of the abundance decline started 1 day after the initial transfer of cells in the medium.

***Mesocosm*** The time series of picoeukaryotes, nanoeukaryotes and cryptophytes dynamics in the mesocosm deployed in the Thau lagoon are shown in figure 7.

The initial concentration of picoeukaryotes started at 1.5 $10^4$ cells.cm$^{-3}$. Within 1.5 days, it reached a peak at 4 $10^4$ cells.cm$^{-3}$. The exponential phase, marked by the division transitions rates, started at $t_0$ up to a saturation threshold predicted within the first day of the experiment, on March 9. The threshold of loss transitions rates exceeded division rates with 1 and 0.7 respectively. Saturation at half loss rates was reached on March 11 11:00 LT. After March 11, the abundance dropped to 7 $10^3$ cells.cm$^{-3}$.

The initial concentration of nanoeukaryotes started at 1.1 $10^4$ cells.cm$^{-3}$. The exponential phase started at $t_0$ but both the division rates at saturation and the half-saturation constant delayed its phasing compared to picoeukaryotes. Since the threshold of loss transitions rates did not exceed division rates, with 0.4 and 0.6 respectively, the exponential phase lasted up to the end of the experiment. On March 13. the abundance of nanoeukaryotes increased to 2.7 $10^4$ cells.cm$^{-3}$.

The initial concentration of cryptophytes started at 6.8 $10^2$ cells.cm$^{-3}$. Cells did not divide up to March 11. After this lag phase, the exponential phase started but with relatively low division rates ($P_{d_{max}}$=0.3), compared to the losses rates ($P_{m_{max}}$=1). The decay phase showed a regular decrease of cells abundance up to 3 $10^2$ cells.cm$^{-3}$.

Cell cycle model

***Time series*** Samples of the Thau lagoon were analysed with the Cytosense to estimate DNA-based growth rates ($\mu_{DNA}$) from the time course of stage-specific fractions. The distributions of yellow fluorescence induced by the complex DNA-Picogreen in picoeukaryotes, nanoeukaryotes and cryptophytes cells on March 10 are shown in figure 8.

The distributions of yellow fluorescence emitted by picoeukaryotes cells showed 2 modes located at 210 ± 20 a.u. and 400 ± 30 a.u.. The distinctions between the $G_1$, $S$ and $G_2 + M$ stages were clear in all samples.

The distributions of yellow fluorescence

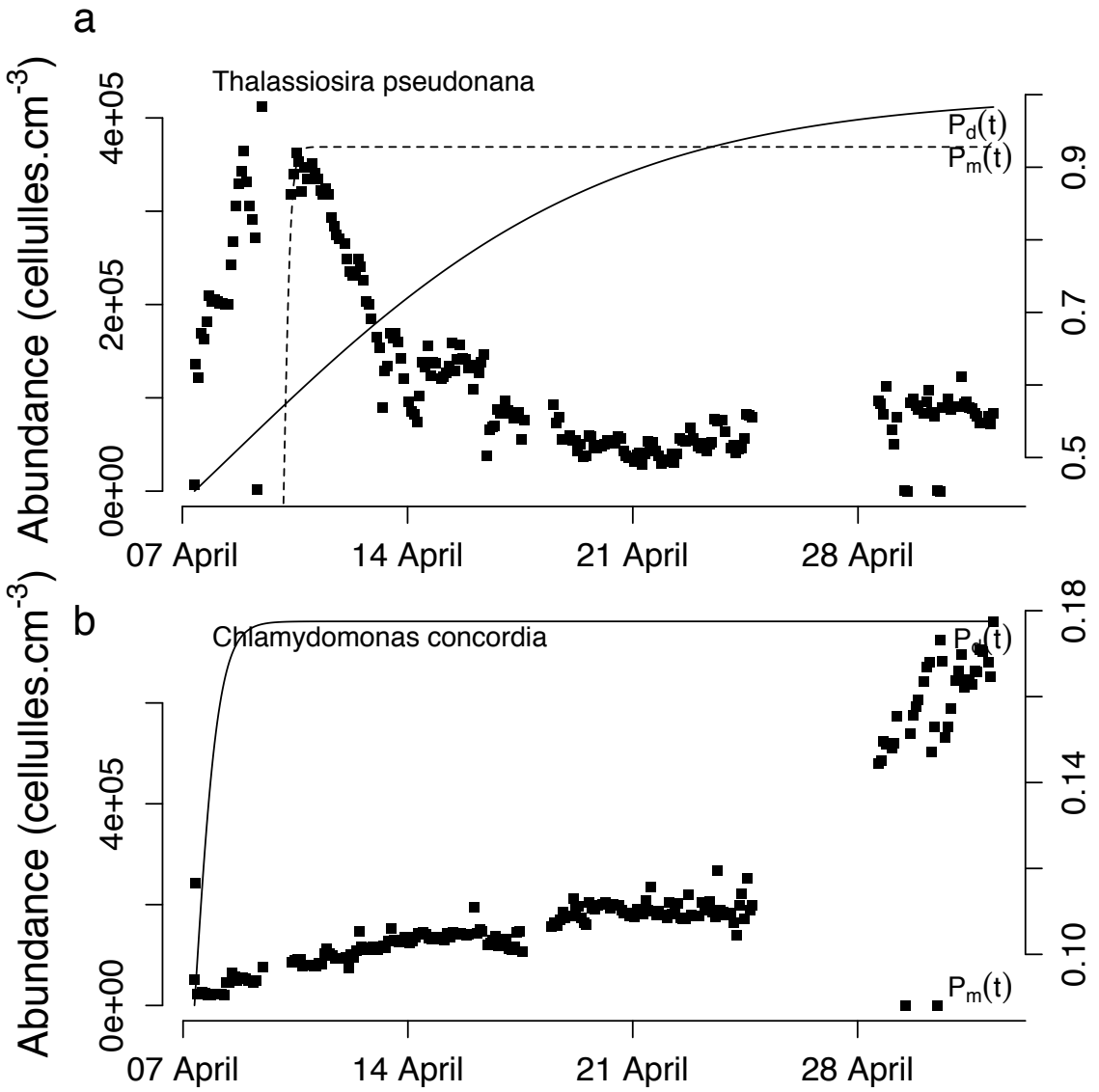


Figure 2.6: Dynamics of (a) *Thalassiosira pseudonana* and (b) *Chlamydomonas concordia* in the microcosms. The smooth line corresponds to the fit of microbial growth curve. The probability of division ($P_d(t)$) is represented with the continuous line and the probability of losses ($P_d(t)$) is represented with the dotted line

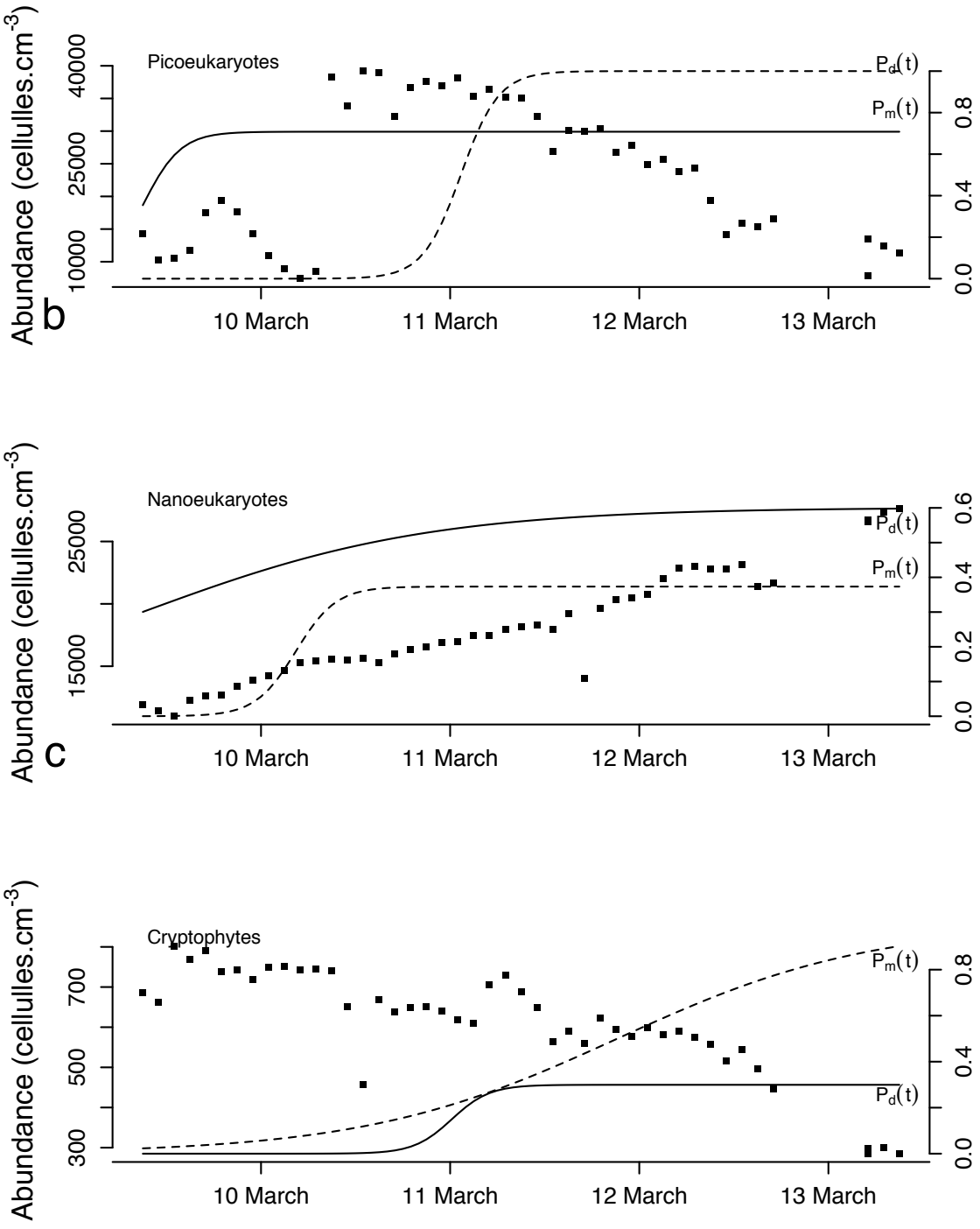


Figure 2.7: Dynamics of (a) picoeukaryotes, (b) nanoeukaryotes and (c) cryptophytes in the mesocosm. The smooth line corresponds to the fit of microbial growth curve. The probability of division ($P_d(t)$) is represented with the continuous line and the probability of losses ($P_d(t)$) is represented with the dotted line

emitted by nanoeukaryotes cells showed 2 modes located at 1800 ± 180 a.u. and 2900 ± 330 a.u.. The $G_1$ and $G_2 + M$ stages were well separated in all samples but due to proximity of the two main modes, the $S$ stage could be unclear.

Although the cryptophyte' population counted between 3 $10^2$ and 7 $10^2$ cells.cm$^{-3}$, the distributions of yellow fluorescence emitted by cells showed 2 separate modes located at 3500 ± 500 a.u. and 7000 ± 1000 a.u.. The $G_1$ stage was always persistent but the $S$ and $G_2 + M$ stages could be unclear due to the small number of individuals.

The time course of stages-specific fractions in all samples is shown in figure 9. In general, cells in the 3 populations moved across the cell cycle regularly. In absolute, the fractions in $S$ ranged between 0.05 and 0.3, in $G_1$ between 0.2 and 0.6 and in $G_2 + M$ between 0.2 and 0.5. For picoeukaryotes, the $G_1$ and $G_2 + M$ stages followed an opposite dynamics. Cells in $G_1$ were more abundant between 09:00 and 19:00 LT whereas peaks of $G_2 + M$ were observed at 03:00 and 21:00 LT. Cells in the $S$ stage followed the pattern of $G_1$ cells with a positive shift of approximately 7 hours. For nanoeukaryotes, the maximum fraction of cells in $G_2 + M$ could be observed in the afternoon while its depression around 20:00 LT corresponded to the peak of $G_1$ cells. The maximum of $G_2 + M$ cells fraction was measured later for cryptophytes between 17:00 and 19:00 LT. The fraction of $G_1$ cells reached 0.8 at 09:00 LT.

***Comparison of growth rates estimations*** The comparison of DNA-based ($\mu_{DNA}$) and abundance-based ($\mu_{Ab}$) growth rates is presented in figure 10.

Picoeukaroytes cells displayed the highest growth rates in the Thau lagoon during the 4-days experiment. The abundance increased by 1.7 and 2.8 folds for respective growth rates of 0.56 d$^{-1}$ and 1.03 d$^{-1}$. For these extrema, the cell cycle approach predicted 0.36 d$^{-1}$ and 1.16 d$^{-1}$. The $\mu_{DNA}$=$a\mu_{Ab}$ regression slope (a=0.98) suggests that DNA-based estimations are close to true growth rates.

Nanoeukaroytes cells showed the second highest growth rates in the Thau lagoon during the 4-days experiment, with extrema of 0.17 d$^{-1}$ and 0.38 d$^{-1}$. The $\mu_{DNA}$=$a\mu_{Ab}$ regression slope (a=1.12) suggests that DNA-based estimations are superior to true growth rates. For the extrema values, the cell cycle method predicted 0.24 d$^{-1}$ and 0.34 d$^{-1}$respectively.

Cryptophytes cells showed the lowest growth rates in the Thau lagoon during the 4-days experiment, which is in agreement with the prediction of division transition rates by the microbial growth model (Figure 7). Growth rates ranged between 0.05 and 0.09 d$^{-1}$. The $\mu_{DNA}$=$a\mu_{Ab}$ regression slope (a=0.6) suggests that DNA-based estimations underestimated true growth rates. This discrepancy was expected since the low absolute abundance constrained the cell cycle estimations.

***Uncertainty of growth rates estimations*** The maximum likelihood estimations (MLE) of DNA-based growth rates and their uncertainties are summarised in Table 1.

| Taxa | March 9 | March 10 | March 11 | March 12 |
|---|---|---|---|---|
| Picoeukaryotes | 0.58 ± 0.03 | 0.36 ± 0.04 | 0.38 ± 0.04 | 1.16 ± 0.03 |
| Nanoeukaryotes | 0.35 ± 0.02 | 0.24 ± 0.02 | 0.29 ± 0.02 | 0.29 ± 0.05 |
| Cryptophytes | 0.09 ± 0.05 | 0.07 ± 0.02 | 0.05 ± 0.04 | 0.08 ± 0.04 |

Table 2.1: Estimations ± Standard deviations (d$^{-1}$) of growth rates estimated by the cell cycle method in the Thau lagoon

Compared to MLEs, the standard deviations were high for cryptophytes which displayed low growth rates. The population was mainly in decline during the experiment and histograms were not sufficiently informative to discriminate the fractions of cells in each stage of the cell cycle.

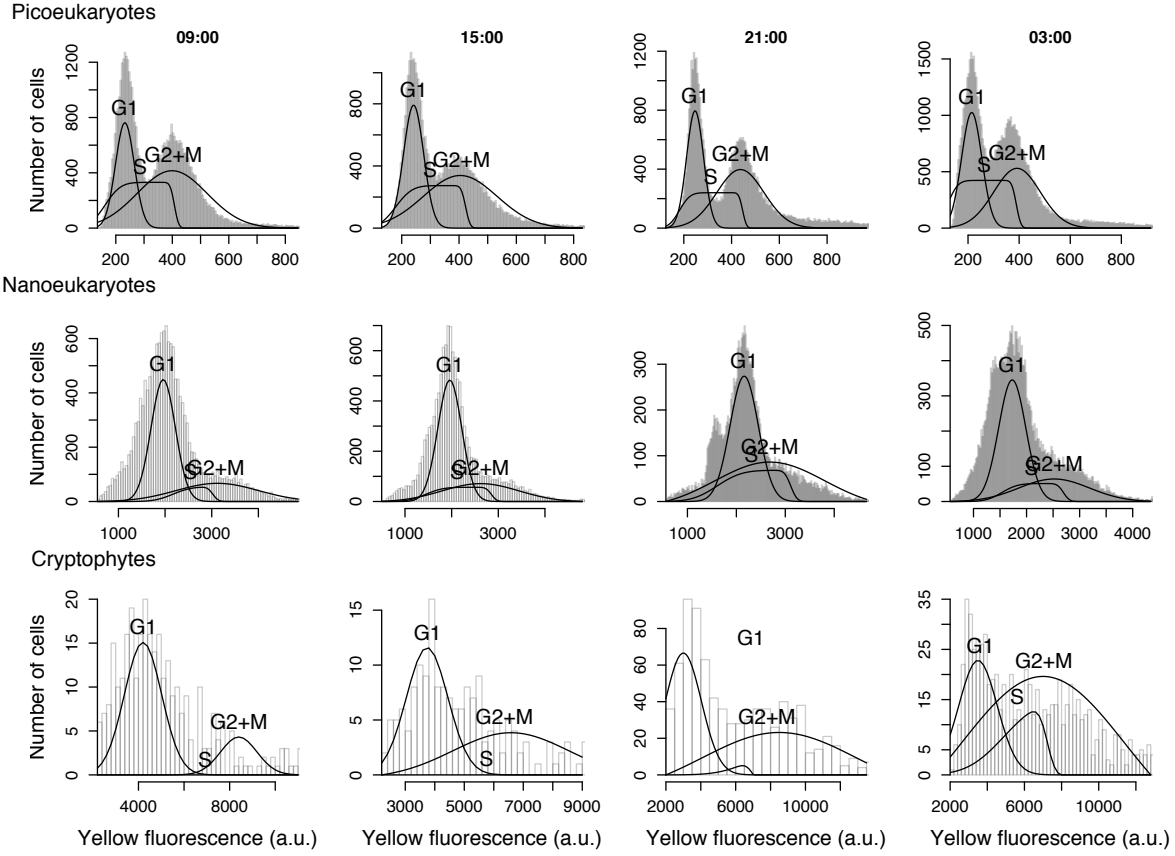


Figure 2.8: Absolute distribution of yellow fluorescence (a.u.) of picoeukaryoes (top panel), nanoeukaryotes (middle panel) and cryptophytes (bottom panel) on March 10 at 09:00 LT (far left), 15:00 LT (left), 21:00 LT (right) and 03:00 LT (far right)

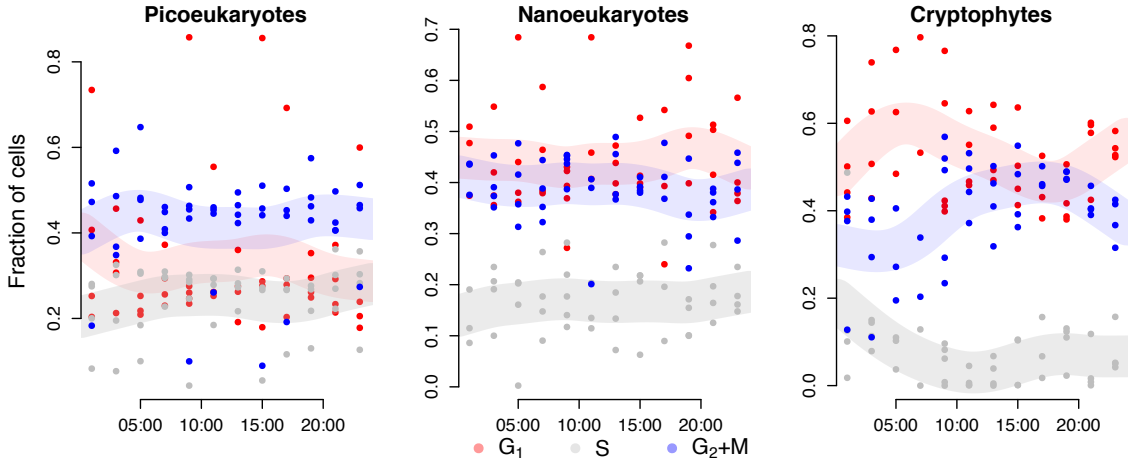


Figure 2.9: Fractions of picoeukaryotes (left panel), nanoeukaryotes (middle panel) and cryptophytes (right panel) cells in $G_1$ (red dots), $S$ (gray dots) and $G_2 + M$ (blue dots) stages. The continuous lines represent cubic smoothing splines.

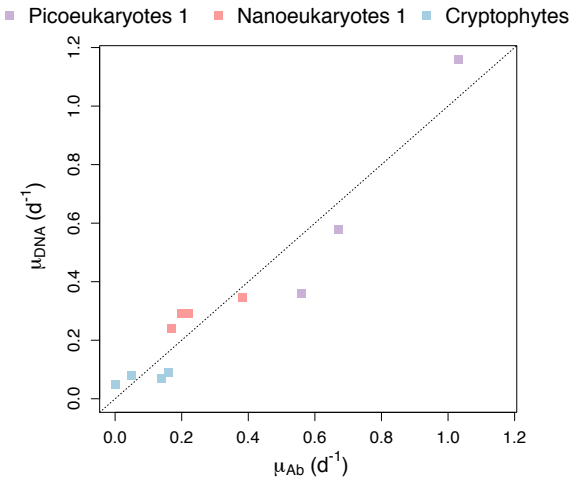


Figure 2.10: Comparisons of DNA-based and abundance-based growth rates of picoeukaryotes (purple squares), nanoeukaryotes (red squares) and cryptophytes (blue squares) populations in the Thau lagoon. The continuous line represent the 1:1 model.

Size-structured population model

***Time series*** The cultures of *Thalassiosira pseudonana* and *Chlamydomonas concordia* were analysed with the Cytosense to record the time course of size distributions required for the estimations of size-based growth rates ($\mu_{size}$).

Individual size were predicted by regression, using the forward scatter signal measured by the Cytosense. The size-structured population model was used to fit the normalized size distribution, containing the proportions of cells in each size class, over 24 hours.

Some observations and predictions of *Thalassiosira pseudonana* size distribution are shown in figure 11. They are presented in figure 12 for cells of *Chlamydomonas concordia*.

The mean equivalent spherical diameter (ESD) of both monocultures measured 7.1 ± 3.4 $\mu$m and 5.2 ± 1.2 $\mu$m respectively. As revealed by the distributions, *Thalassiosira pseudonana* and *Chlamydomonas concordia* cells were not always synchronized to the light:dark cycle (06:30-18:30). The later showed a clear synchronization on D1 in the space of 2 hours (Figure 12). During several days, the decline of size which marks cells' division in the model was not observed, suggesting growth rates inferior to 0.69 $d^{-1}$.

The natural populations of picoeukaryotes, nanoeukaryotes and cryptophytes present in the Thau lagoon were also analysed with the Cytosense to estimate $\mu_{size}$.

The observations and predictions of picoeukaryotes, nanoeukaryotes and cryptophytes size distributions are shown in figure 13, 14 and 15 respectively.

The average ESD of picoeukaryotes cells measured 1.7 ± 0.2 $\mu$m. The diel variations of cells size followed the regular light:dark cycle. Individual cells size started to increase at 07:00 LT up to 19:00 LT.

The average ESD of nanoeukaryotes cells measured 3.4 ± 0.2 $\mu$m. The diel variations of cells size followed the regular light:dark cycle 2 hours sooner than picoeukaryotes cells. Individual cells size started to increase between 05:00 and 07:00 LT up to 17:00 LT.

The average ESD of cryptophytes cells measured 5.4 ± 0.2 $\mu$m. Due to their low abundance, the diel variations of cells size were uncleared compared to picoeukaryotes and nanoeukaryotes. On D1 (March 09), the maximum size was reached at 13:00 LT while on D4 (March 12), size increased until 21:00 LT.

***Comparison of growth rates estimations*** The comparison of size-based ($\mu_{Size}$) and abundance-based ($\mu_{Ab}$) growth rates of *Thalassiosira pseudonana* and *Chlamydomonas concordia* monocultures is presented in figure 16.

Their growth rates ranged between 0.04 and 0.68 $d^{-1}$. $\mu_{Ab}$ varied greatly across the exponential and decay phases. The root mean squared errors for *Thalassiosira pseudonana* were distributed around the average 0.05 ± 0.03 $d^{-1}$. For *Chlamydomonas concordia*, RMSE averaged 0.01 ± 0.01 $d^{-1}$.

The comparison of size-based ($\mu_{Size}$) and abundance-based ($\mu_{Ab}$) growth rates of

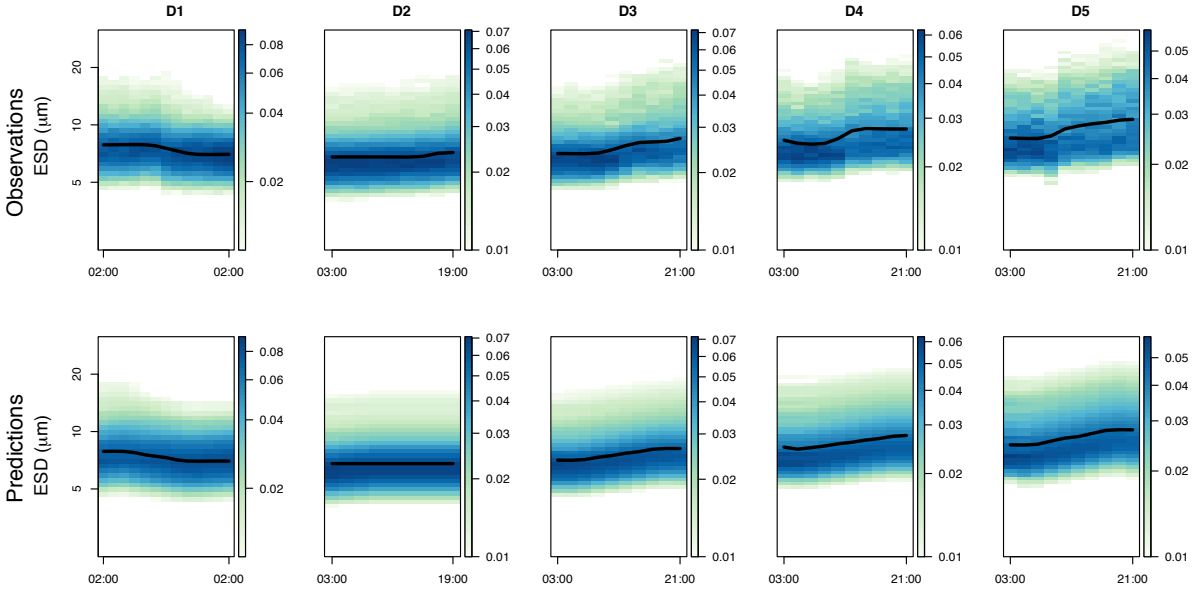


Figure 2.11: Diel variations of the proportions of *Thalassiosira pseudonana* cells in each size class. The continuous lines represent cubic smoothing splines of the median size.

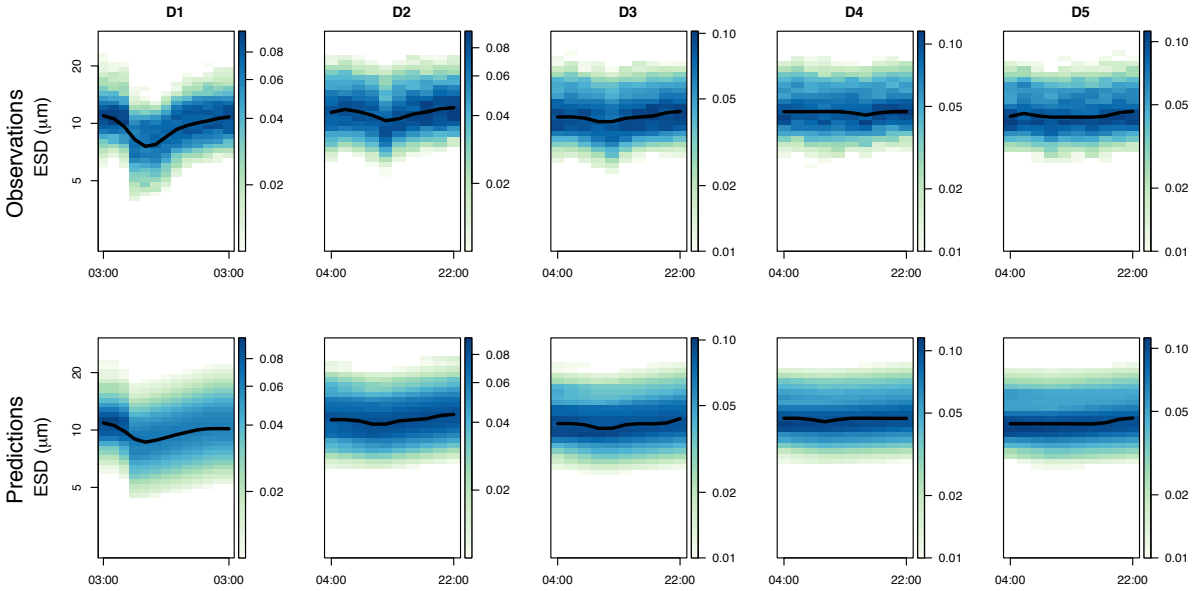


Figure 2.12: Diel variations of the proportions of *Chlamydomonas concordia* cells in each size class. The continuous lines represent cubic smoothing splines of the median size.

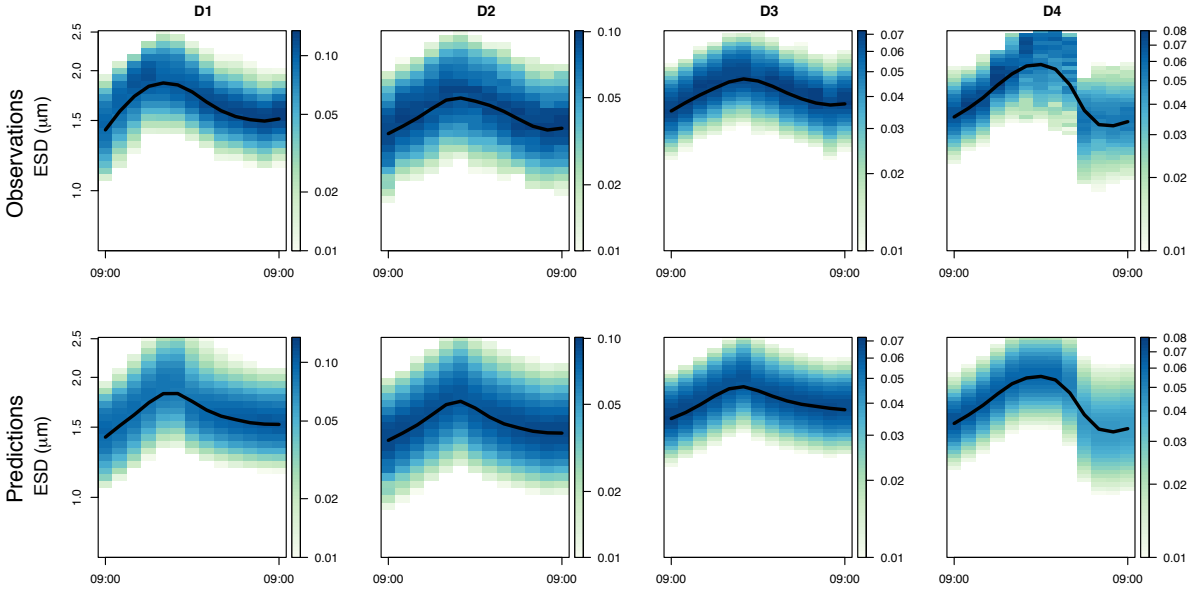


Figure 2.13: Diel variations of the proportions of picoeukaryotes cells in each size class in the Thau lagoon. The continuous lines represent cubic smoothing splines of the median size. D1: March 09, D2: March 10, D3: March 11, D4: March 12

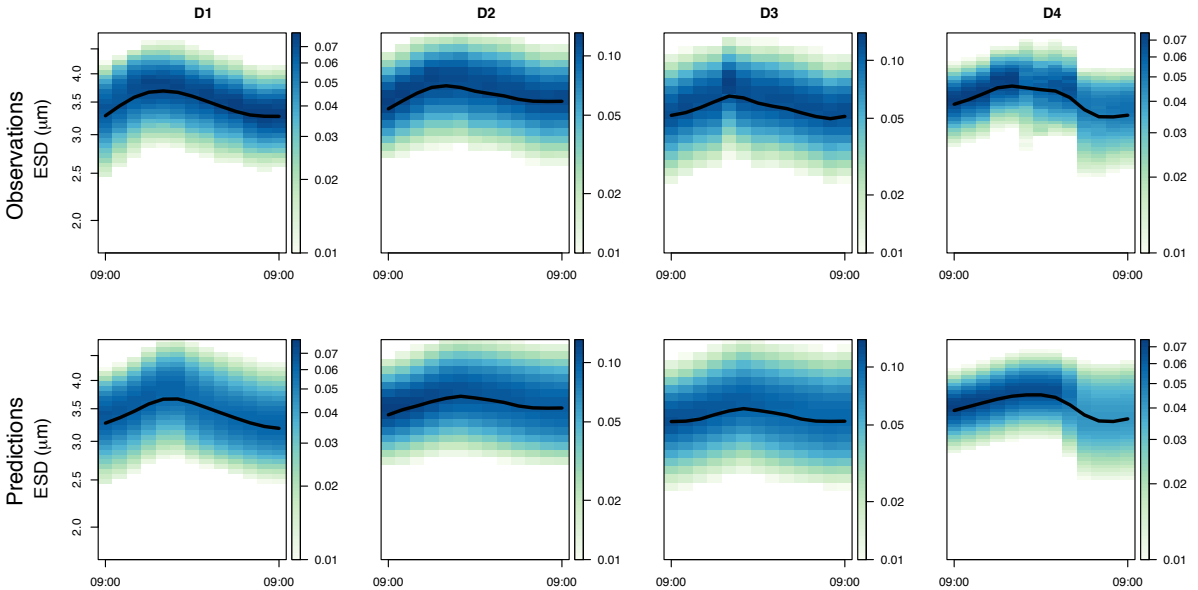


Figure 2.14: Diel variations of the proportions of cryptophytes cells in each size class in the Thau lagoon. The continuous lines represent cubic smoothing splines of the median size. D1: March 09, D2: March 10, D3: March 11, D4: March 12

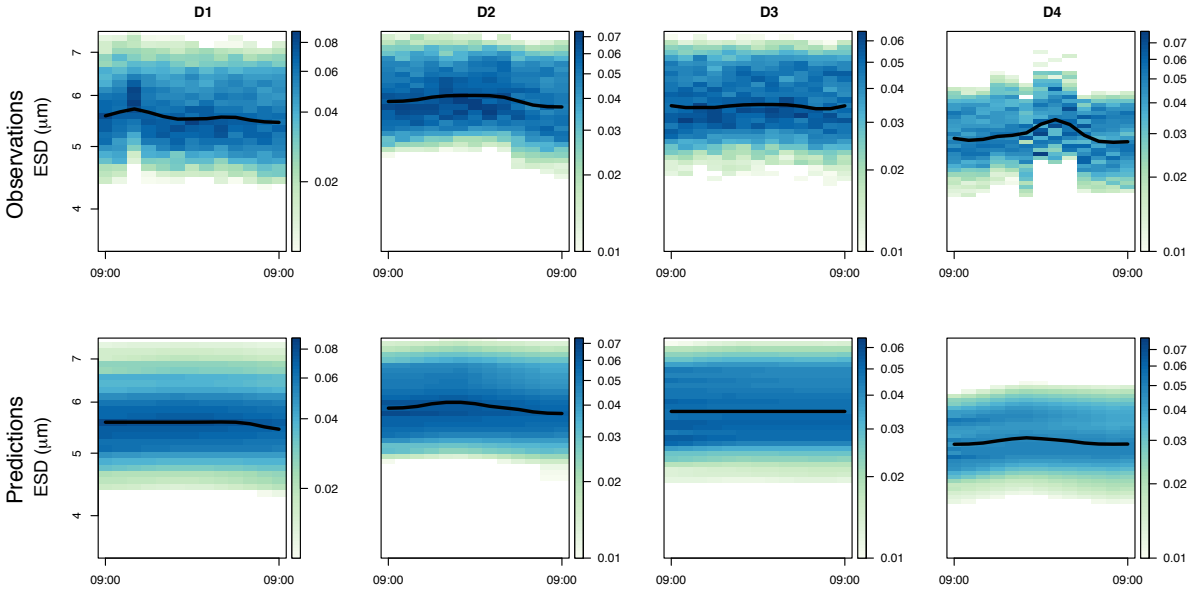


Figure 2.15: Diel variations of the proportions of cryptophytes cells in each size class in the Thau lagoon. The continuous lines represent cubic smoothing splines of the median size. D1: March 09, D2: March 10, D3: March 11, D4: March 12

picoeukaryotes, nanoeukaryotes and cryptophytes populations is presented in figure 17.

The RMSE of the estimations of growth rates of picoeukaryotes, nanoeukaryotes and cryptophytes cells averaged 0.07 ± 0.07 $d^{-1}$, 0.03 ± 0.02 $d^{-1}$ and 0.03 ± 0.02 $d^{-1}$ respectively. The highest difference was observed for the highest growth rates (1.16 $d^{-1}$).

***Uncertainty of growth rates estimations*** The maximum likelihood estimations (MLE) of size-based growth rates and their uncertainties are summarised in Table 2.

| Taxa | D1 | D2 | D3 | D4 | D5 |
|---|---|---|---|---|---|
| *Thalassiosira* | 0.53 ± 0.008 | 2 $10^{-13}$ ± 7 $10^{-14}$ | 0.08 ± 0.01 | 0.12 ± 0.01 | 0.31 ± 0.04 |
| *Chlamydomonas* | 0.59 ± 0.11 | 0.36 ± 0.12 | 0.62 ± 0.04 | 0.27 ± 0.03 | 0.13 ± 0.01 |

Table 2.2: Estimations ± Standard deviations ($d^{-1}$) of growth rates estimated by the size-structured population method in monocultures of *Thalassiosira pseudonana* and *Chlamydomonas concordia*

We measured the effect of selective grazing by simulations. Two types of grazing pressure were applied to the predicted size distribution of cryptophytes in the Thau lagoon at D4. Fit of the altered size distribution were used to quantify the error of estimations under grazing pressure ranging from 0 % to 100 % of a range of fixed growth rates.

A typical functional response was simulated to support the effect of a density-dependent grazing (E 14). An illustration of the absolute dynamics of the cryptophytes population and their corresponding normalized size distribution after grazing is given in figure 18. Since the grazing rates are modulated by the effective of phytoplankton cells only, the decline of absolute abundance is restrained during the division time frame (21:00 and 07:00 LT).

A size-selective grazing was simulated to quantify the effect of size distributions alterations (E 15). The model assumes that doublet cells entering mitosis are preferentially consumed by zooplankton. An illustration of the absolute dynamics of the cryptophytes population and their corresponding normalized size distribution after grazing is given in figure 19. Since the grazing rates are modulated by the effec-

tive and the size of phytoplankton cells, the decline of absolute abundance is restrained during the division time frame (21:00 and 07:00 LT) and the size distribution starts to shift toward small size classes, which are less likely to divide.

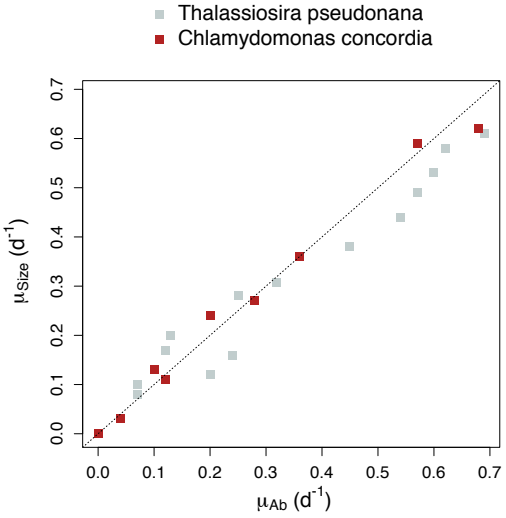


Figure 2.16: Comparisons of Size-based and abundance-based growth rates of *Thalassiosira pseudonana* (purple squares) and *Chlamydomonas concordia* (red squares) monocultures. The continuous line represent the 1:1 model.

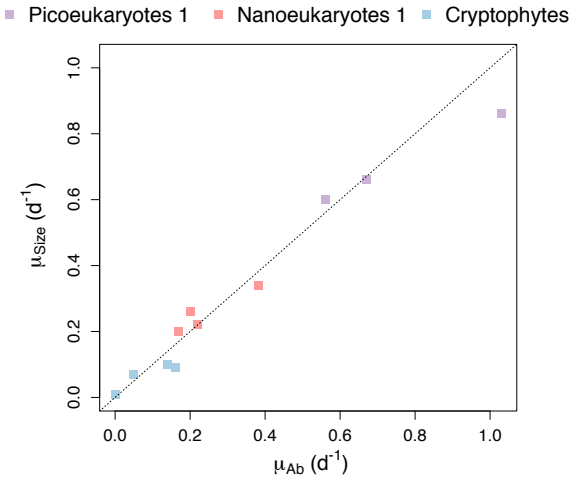


Figure 2.17: Comparisons of Size-based and abundance-based growth rates of picoeukaryotes (purple squares), nanoeukaryotes (red squares) and cryptophytes (blue squares) populations in the Thau lagoon. The continuous line represent the 1:1 model.

Results of the simulations are summarised in Table 3.

As expected, a density-dependent grazing does not alter the predictions of the size-structured population model since the pressure is evenly distributed among the size classes. The temporal variation of normalized proportions, used to predict growth rates in the model, are consequently conserved. However, when the grazing pressure is preferentially directed towards large size classes, this distribution show a slow shift towards low size classes, escaping predation. The altered normalized size distribution yield to consequent overestimations of *in situ* growth rates.

## 2.4 Discussion

Importance of *in situ* growth rates estimations

In the field, phytoplankton growth rates are directly linked to their capacity of $CO_2$ assimilation. They roughly range between 0.06 $d^{-1}$ and 6 $d^{-1}$ with a peak located at 0.6-0.8 $d^{-1}$ which underpin the synchronization of cells to the circardian clock ($log_e(2)$ $\approx$ 0.69 $d^{-1}$) (Goldman, 1979; Eppley, 1981). Using remote sensing, growth rates were mapped across the global ocean, revealing productive or desertic' provinces (Westberry et al., 2008). In the oligotrophic Pacific gyre, the main contributors of primary production are picoplankton cells. Despite their modest individual productivity, picoplankton are essential for nutrient cycling and are actively grazed by protists over short-time scales (Landry et al., 2011). In absolute, there growth rates may reach 0.4 $d^{-1}$ (Barber and Hiscock, 2006). Due to the strong coupling of picoplankton growth and grazing rates, small cells are not blooming (Franks, 2001). On the opposite, microphytoplankton cells have an efficient strategy to escape from grazers and are often found dominent during blooms' onsets. The scaling factor between maximum ingestion rates and predators biovolume is -0.25 (Hansen et al., 1997). Since small predators are limited

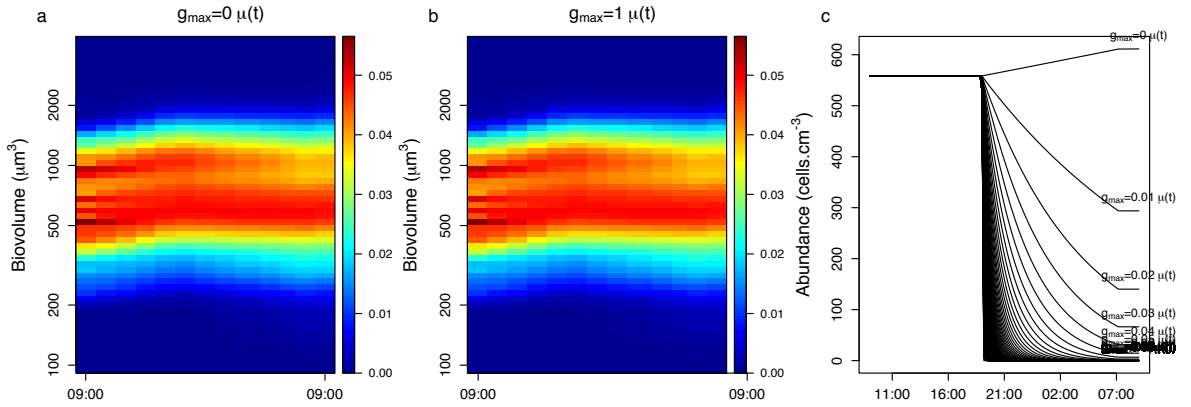


Figure 2.18: The functional-selective grazing simulations. (a) Diel variation of cryptophytes' normalized size distribution under a null grazing pressure. (b) Diel variation of cryptophytes' normalized size distribution under an intense grazing pressure ($g(t) = \mu(t)$). (c) Dynamics of the absolute abundance of cryptophytes under increasing grazing pressures.

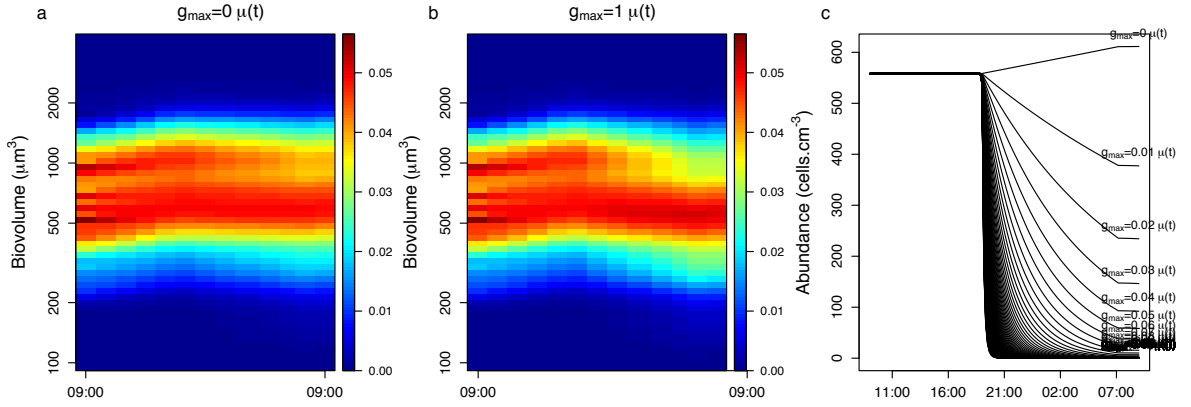


Figure 2.19: The size-selective grazing simulations. (a) Diel variation of cryptophytes' normalized size distribution under a null grazing pressure. (b) Diel variation of cryptophytes' normalized size distribution under an intense grazing pressure ($g(t) = \mu(t)$). (c) Dynamics of the absolute abundance of cryptophytes under increasing grazing pressures.

by the size of their digestive apparatus, the maximum grazing rates has been observed for small preys, preyed by small predators (Hansen et al., 1994). The $r$ and $K$ strategies, derived from the logistic mathematical model, translate the growth rates of phytoplankton populations in such provinces (Margalef, 1978). The life-forms explain the ecological succession of phytoplankton across fertile waters and depleted stratified environments. $r$ strategists systematically display growth rates above 0.8 $d^{-1}$ while $K$ strategists are in steady-state and rely on the organic matter recycling (Calbet and Landry, 2004).

### Current evaluations of *in situ* growth rates

In a global review, Laws listed the drawbacks and methodological artefacts of the current approaches that evaluate phytoplankton *in situ* growth rates (Laws, 2013). Each method is sensitive to the assumptions made to predict the model output. While they show encouraging results under controlled conditions, the extrapolation to natural population is always questionable when it comes to interpret the data correctly.

The cell cycle method is based on the pioneer work of Swift and Durban (1972), later detailed by McDuff and Chisholm (1982). Carpenter and Chang (1988) pointed out the major drawback of the ap-

| Grazing type | $g_{max} : \delta_{max}$ | $\mu$(t)=0.075 | $\mu$(t)=0.12 | $\mu$(t)=0.2 | $\mu$(t)=0.4 | $\mu$(t)=0.6 | $\mu$(t)=1 |
|---|---|---|---|---|---|---|---|
| Density-dependent | | | | | | | |
| | 0.0 | 0.079 | 0.128 | 0.21 | 0.399 | 0.58 | 0.97 |
| | 0.1 | 0.079 | 0.128 | 0.21 | 0.399 | 0.58 | 0.97 |
| | 0.2 | 0.079 | 0.128 | 0.21 | 0.399 | 0.58 | 0.97 |
| | 0.3 | 0.079 | 0.128 | 0.21 | 0.399 | 0.58 | 0.97 |
| | 0.4 | 0.079 | 0.128 | 0.21 | 0.399 | 0.58 | 0.97 |
| | 0.5 | 0.079 | 0.128 | 0.21 | 0.399 | 0.58 | 0.97 |
| Size-dependent | | | | | | | |
| | 0.0 | 0.079 | 0.128 | 0.21 | 0.399 | 0.58 | 0.97 |
| | 0.2 | 0.1 | 0.16 | 0.25 | 0.45 | 0.62 | 0.89 |
| | 0.4 | 0.12 | 0.17 | 0.25 | 0.46 | 0.65 | 0.92 |
| | 0.6 | 0.14 | 0.19 | 0.28 | 0.48 | 0.66 | 0.92 |
| | 0.8 | 0.16 | 0.22 | 0.31 | 0.51 | 0.69 | 0.93 |
| | 1.0 | 0.18 | 0.24 | 0.32 | 0.52 | 0.7 | 0.96 |

Table 2.3: Effects of density-dependent and size-dependent grazing on the prediction of *in situ* growth rates

plication of the method on fixed samples: the estimation of the duration of the terminal event, $t_d$. With live samples, a time-lapse is necessary to evaluate $t_d$ with a series of images although it requires to follow actively a single cell. Since paired-nuclei cells are often mixed with cells in the $S$ stage in preserved samples, Carpenter and Chang proposed to integrate the stages $S$, $G_2$ and $M$ together to estimate *in situ* growth rates. The cell cycle method was used to measure species-specific reproduction rates in natural samples. The accuracy of the evaluation of the terminal event may limit the *in situ* application for scarce populations (Gisselson et al., 1999). The method is also restricted to evenly distributed grazing, which does not affect the time course of fractions of cells in $G_1$, $S$ and $G_2 + M$ (Chang and Carpenter, 1993). Otherwise, the estimation of growth rates may be altered by up to 44 %. They used simulations to prove that the cell cycle method is reliable to measure the intrinsic growth rates, even when loss rates are high. Our estimations of DNA-based growth rates seem to also indicate that the approach is accurate independently of the phase of microbial growth (e.g. exponential, stationary or decay).

The size distribution model is based on the adaptation of Sosik et al. (2003) of Caswell's general structured population models (Caswell, 2001). Since it assumes that the size distribution is only driven by cellular growth and division, the output is sensitive to size-dependent processes such as selective grazing. The active removal of size-specific cells is an issue for the model since it does not account for any cell loss process. Outputs are especially sensitive to division odds. Since they are expressed as a function of cell size, the probability of division may be biased if proportions in some of the size classes are altered. In natural samples, the uncertainty of growth rates evaluation may be estimated by dilution. Hunter-Cervera et al. (2014) showed that the method is robust for *Synechococcus* cells being placed under a wide range of grazing pressure. Our simulations of size-selective grazing indicates that the alteration of the size-based estimations increases proportionally with the grazing pressure, particularly at low growth rates. For a grazing pressure

of the order of 67 % of $\mu_{size}$, representing the maximum value of global $m : \mu$ ratio across various ecosystems, and growth rates above 0.4 $d^{-1}$, the difference of predictions of *in situ* growth rates range between 8 and 20 % of true values (Calbet and Landry, 2004).

Besides the cell cycle method and the size-structure model, the dilution technique was developed to measure the rate of cells increase in serial dilutions with a maximal rate induce by the annulment of encounters with grazers under a large dilution (Landry and Hassett, 1982).The main uncertainties of this method are derived from false assumptions. One assumption is that the clearance rate of predators is constant so that it varies proportionally with the concentration of phytoplankton reduced by dilution (Landry et al., 1995). Some experiments are clearly demonstrating the opposite. Zooplankton ingests phytoplankton up to a threshold concentration above which the response saturates. Since the grazing rates, $g$, is no more constant at saturation, Gallegos (1989) proposed to replace it by a function, the functional response.

The natural case study

In the Thau lagoon, primary production is high compared to the open Mediterranean Sea, with a daily rates of 500 mg $C.m^{-3}.d^{-1}$ (Vaulot and Frisoni, 1986). The lagoon has been fuelled by nutrients drove by human activities. According to Vaquer et al. (1996), phytoplankton species are numerous in the Thau lagoon. They comprise various diatoms (*Chaetoceros, Skeletonema, Ditylum, Thalassiosira*), cryptophyceae (*Cryptomonas*), dinophyceae (*Peridinium, Gymnodinium, Prorocentrum*) and nanoflagellates. Phytoplankton dynamics is regulated by several controls. The bottom-up control caused by nutrients availability in the lagoon was discovered by Collos et al. (1997) who conducted enrichment experiments. The top-down control of protist is also determinant for picoplankton abundance. Even though they account for up to 57 % of the biomass specific productivity, their growth rates is balanced by grazing rates of the order of 0.09-1.66 $d^{-1}$. During the experiment, we observed the simultaneous decline of picoeukaryotes with the increase of several microplankton groups. The dilution approach yielded high estimations of growth rates in summer ($\mu(t)$>$2d^{-1}$). In March, the average growth rates measured by Bec et al. dropped to 0.84 ± 0.03 $d^{-1}$ for the fraction of cells < 2 $\mu$m and 0.47 ± 0.01 $d^{-1}$ for the fraction of cells > 2 $\mu$m. Our applications of the cell cycle method and the size-structure population model to the natural populations of picoeukaryotes, nanoeukaryotes and cryptophytes in the lagoon yielded to similar averaged growth rates of 0.76 ± 0.2 $d^{-1}$, 0.24 ± 0.08 $d^{-1}$ and 0.08 ± 0.06 $d^{-1}$.

## 2.5 Conclusion

Phytoplankton populations group cells in various physiological states. Some are actively multiplying by binary fission while others may be stressed in alternative stage $G_0$. We explored the ability of multiple stage models to account for these variations and correctly predict phytoplankton growth rates under controlled conditions. Since taxonomic methods may be limiting in natural environments, we tested the cell cycle method and the size distribution model on a natural assemblage of the Thau lagoon to determine if they both could be extended to a large community of phytoplankton populations. Among this assemblage, the ataxonomic populations of picoeukaryotes, nanoeukaryotes and cryptophytes were kept in an enclosed mesocosm to follow their dynamics at high frequency. After the confinement, the time course of fractions in the $G_1$, $S$ and $G_2 + M$ stages, identified by fluorescence and the size distributions were both consistent with the variation of cells abundance. Comparisons are encouraging for the two approaches. They sup-

port their potential ability to estimate *in situ* growth rates under uncontrolled conditions. With the size-based approach, introduced by Sosik et al. (2003), the transitions of interphase and mitotic divisions are accurately reproduced for both synchronous and asynchronous populations. This particularity yielded to estimations closed to true growth rates even when division occurred within a 2 hours timeframe. With the DNA-based approach, the yellow fluorescence distributions were marked by two modes corresponding to the 2-fold replication of DNA copies. The pattern of cell cycle transitions of cells in $G_1$, $S$ and $G_2 + M$ were consistent over several days and were used to predict accurate growth rates in the range 0.05-1.2 $d^{-1}$.

## References


Armbrust, E. V. and Chisholm, S. W. (1992), Patterns of cell size change in a marine centric diatoms: variability evolving from clonal isolates, *J. Phycol*, *28*, 146–156.

Barber, R. T. and Hiscock, M. R. (2006), A rising tide lifts all phytoplankton: Growth response of other phytoplankton taxa in diatom-dominated blooms, *Global Biogeochemical Cycles*, *20*, 1–12.

Bec, B., Husseni-Ratrema, J., Collos, Y., Souchu, P. and Vaquer, A. (2005), Phytoplankton seasonal dynamics in a Mediterranean coastal lagoon: emphasis on the picoeukaryote community, *J. Plankt. Res.*, *27*(9), 881–894.

Calbet, A. and Landry, M. R. (2004), Phytoplankton growth, microzooplankton grazing, and carbon cycling in marine systems, *Limnol. Oceanogr.*, *49*(1), 51–57.

Carpenter, E. J. and Chang, J. (1988), Species-specific phytoplankton growth rates via diel DNA synthesis cycles. I. Concept of the method, *Mar. Ecol. Prog. Ser.*, *43*, 105–111.

Caswell, H. (2001), Matrix population models, *2nd ed. Sinaeur.*

Cermeno, P., Rodriguez-Ramos T., Dornelas, M., Figueiras, F. G., Maranon, E., Teixeira, I. and Vallina, S. M. (2013), Species richness in marine phytoplankton communities is not correlated to ecosystem productivity, *Mar. Ecol. Prog. Ser.*, *488*, 1–9.

Chang, J. (1993), The influence of grazing on the estimation of phytoplankton growth rate via cell cycle analysis: Modeling and experimental evidence, *Limnol. Oceanogr.*, *38*(1), 202–212.

Cheung, W. W. L., Dunne, J., Sarmiento, J. L. and Pauly, D. (2011), Integrating ecophysiology and plankton dynamics into projected maximum fisheries catch potential under climate change in the Northeast Atlantic, *J. Mar. Science*, *68*(6), 1008–1018.

Collins, S., Rost, B. and Rynearson, T. A (2014), Evolutionary potential of marine phytoplankton under ocean acidification, *In Evolutionary Applications, J. Wiley and Sons 7*, 140–155.

Collos, Y., Vaquer, A., Bibent, B., Slawyk, G., Garcia, N. and Souchu, P. (1997), Variability in nitrate uptake kinetics of phytoplankton communities in a Mediterranean coastal lagoon, *Estuar. Coastal Shelf Sci.*, *44*, 369–375.

Dugenne, M., Thyssen, M., Nérini, D., Manté, C., Poggiale, J.-C., Garcia, N., Garcia, F. and Grégori, G. J. (2014), Consequence of a sudden wind event on

the dynamics of a coastal phytoplankton community: an insight into specific population growth rates using a single cell high frequency approach, *Frontiers*, *5*(485), 1–14.

Eppley, R. W. (1981), Relations between nutrient assimilation and growth in phytoplankton with a brief review of estimates of growth rate in the ocean, *In Platt, T. ed., Physiological bases of phytoplankton ecology, Can. Bull. Fish. Aquat. Sci.*, *201*, 251–263.

Foladori, P., Quaranta, A. and Ziglio, G. (2008), Use of silica microspheres having refractive index similar to bacteria for conversion of flow cytometric forward light scatter into biovolume, *Water Res.*, *42*, 3757–3766.

Franks, P. J. S. (2001), Phytoplankton blooms in a fluctuating envrionment: the roles of plankton response time scales and grazing, *J. Plankt. Res.*, *23*(12), 1433–1441.

Gisselson, L.-A., Graneli, E. and Carlsson, P. (1999), Using the cell cycle analysis to estimate *in situ* growth rate of the dinoflagellate *Dinophysis acuminata*: drawbacks of the DNA quantification method, *Mar. Ecol. Prog. Ser.*, *184*, 55–82.

Goldman, J. C., McCarthy, J. J. and Peavey, D. G. (1979), Growth rate influence on the chemical composition of phytoplankton in oceanic waters, *Nature*, *279*, 210–215.

Hansen, P. J., Bjornsen, P. K. and Hansen, B. W. (1997), Zooplankton grazing and growth: Scaling within the 2-2000 $\mu$m body size range, *Limnol. Oceanogr.*, *42*(4), 687–704.

Horowitz, J., Normand, M. D., Corradini, M. G. and Peleg, M. (2010), Probabilisitic model of microbial cell growth, division and mortality, *App. Env. Mirc.*, *76*(1), 230–242.

Hunter-Cervera, K., Neubert, M. G., Solow, A. R., Olson, R. J., Shalapyonok, A. and Sosik, H. M. (2014), Diel size distributions reveal seasonal growth dynamics of a coastal phytoplankter, *PNAS*, 1–6.

Gallegos, C. L. (1989), Microzooplankton grazing on phytoplankton in the Rhode River, Maryland: nonlinear feeding kinetics, *Mar. Ecol. Prog. Ser.*, *57*, 23–33.

Jackson, J. B. C. and Cheetham, A. H. (1999), Tempo and mode of speciation in the Sea, *TREE*, *14*, 72–77.

Kirchman, D. L (2002), Calculating microbial growth rates from data on production and standing stocks, *Mar. Ecol. Prog. Ser.*, *233*, 303–306.

Kruk, C., Mazzeo, N., Lacerot, G. and Reynolds, C. S. (2002), Classification schemes fro phytoplankton: a local validation of a functional approach to the analysis of species temporal replacement, *J. Plankton Res.*, *24*(9), 901–912.

Landry, M. R. and Hassett, R. P. (1982), Estimating the grazing impact of marine micro-zooplankton, *Marine Biology*, *67*, 283–288.

Landry, M. R.,Kirshtein, J. and Constantinou, J. (1995), A refined dilution technique for measuring the community grazing impact of microzooplankton, with experimental tests in the central Pacific, *Mar. Ecol. Prog. Ser.*, *120*, 53–63.

Landry, M. R., Selph, K. E. and Yang, E. J. (2011), Decoupled phytoplankton growth and microzooplankton grazing in the deep euphotic zone of the eastern equatorial Pacific, *Mar. Ecol. Prog. Ser.*, *421*, 13–24.

Laws, E. A. (2013), Evaluation of in situ phytoplankton growth rates: A synthesis of data from varied apporaches, *Annu. Rev. Mar. Si.*, *5*, 247–268.

Levin, S. A (1992), The problem of pattern and scale in Ecology: The Robert H. MacArhtur Award lecture, *Ecology*, *73*(6), 1943–1967.

Margalef, R. (1978), Life-forms of phytoplankton as survival alternatives in an unstable environment, *Oceanologica Acta*, *134*, 493–509.

McDuff, R. E. and Chisholm, S. W. (1982), The calculation of in situ growth rates of phytoplankton populations from fractions of cells undergoing mitosis: A clarification, *Limnol. Oceanogr.*, *27*(4), 783–788.

Moberg, E. A. and Sosik, H. M. (2012), Distance maps to estimate cell volume from the two-dimensional plankton images, *Limnol. Oceanogr. Methods*, *10*, 278–288.

Reynolds, C. S. (1997), Vegetation processes in the pelagic- A model for ecosystem theory, *Ecology Institue Oldendrof*.

Sabine, C. L. et al. (2004), The oceanic sink for anthropogenic $CO_2$, *Science*, *305*, 367–371.

Sosik, H. M., Olson, R. J., Neubert, M. G. and Shalapyonok, A. (2003), Growth rates of coastal phytoplankton from time-series measurements with a submersible flow cytometer, *Limnol. Oceanogr.*, *48*(5), 1756–1765.

Steele, J., Carpenter, S., Cohen, J., Dayton, P. and Ricklefs, R. (1989), Comparison of terrestrial and marine ecological systems, *Workshop report Santa Fe, Mexico*, 1–14.

Steele, J. (1972), Factors controlling marine ecosystems, *In D. Dryssen and D. Tagner eds. The changing chemistry of the oceans, Nobel Symp Wiley*, 209–221.

Swift, E. and Durbin, E. G. (1972), The phased division and cytological characterisics of *Pyrocystis spp.* can be used to estimate doubling times of their populations in the sea, *Deep Sea Res.*, *19*, 189–198.

Vallina,S. M., Follows, M. J., Dutkiewicz, S., Montoya, J. M., Cermeno, P. and Loreau, M. (2014), Global relationship between phytoplankton diversity and productivity in the ocean, *Nature comm.*, *5*, 1–10.

Vaquer, A., Troussellier, M., Courties, C. and Bibent, C. (1896), Standing stocks and dynamics of picophytoplankton in the Thau lagoon (northwest Mediterranean coast), *Limnol. Oceanogr.*, *41*(8), 1821–1828.

Vaulot, D. and Frisoni, G.-F. (1886), Phytoplanktonic productivity and nutrients in five Mediterranean lagoons, *Oceanoligica Acta*, *9*(1), 57–64.

Veldhius, M. , Cucci, T. L. and Sieracki, M. E. (1997), Cellular DNA content of marine phytoplankton using two new fluorochromes: taxonomic and ecological implications, *J. Phycol.*, *33*, 527–541.

Watson, J. V., Chambers, S. H. and Smith, P. J. (1987), A pragmatic approach to the analysis of DNA histograms with a definable G1 peak, *Cytometry*, *8*, 1–8.

Westberry, T., Behrenfeld, M. J., Siegel, D. A. and Boss, E. (2008), Carbon-based primary production modeling with vertically resolved photoacclimation, *Global Biogeochemical Cycles*, *22*, 1–18.

# 3.0 Consequence of a sudden wind event on the dynamics of a coastal phytoplankton community: an insight into specific population growth rates using a single cell high frequency approach

**Abstract**

Phytoplankton is a key component in marine ecosystems. It is responsible for most of the marine primary production, particularly in eutrophic lagoons, where it frequently blooms. Because they are very sensitive to their environment, the dynamics of these microbial communities has to be observed over different time scales, however, assessment of short term variability is often out of reach of traditional monitoring methods. To overcome these limitations, we set up a Cytosense automated flow cytometer (Cytobuoy b.v.), designed for high frequency monitoring of phytoplankton composition, abundance, cell size, and pigment content, in one of the largest Mediterranean lagoons, the Berre lagoon (South-Eastern France). During October 2011, it recorded the cell optical properties of 12 groups of pico-, nano-, and microphytoplankton. Daily variations in the cluster optical properties were consistent with individual changes observed using microscopic imaging, during the cell cycle. We therefore used an adaptation of the size-structured matrix population model, developed by Sosik et al. (2003) to process the single cell analysis of the clusters and estimate the division rates of 2 dinoflagellate populations before, during, and after a strong wind event. The increase in the estimated in situ daily cluster growth rates suggest that physiological changes in the cells can prevail over the response of abundance.

M. Dugenne, M. Thyssen, D. Nérini, C. Manté, J-C Poggiale, N. Garcia, F. Garcia, M. Fallet, N. Mayot, G. Bernard, R. Grisel, G. Grégori

## 3.1 Introduction

Phytoplankton is responsible for about 50% of the annual global net primary production, yet its biomass represents only about 0.2% of the entire chlorophyllous biomass (Field et al., 1998). This compartment is made up of mostly drifting autotrophic microorganisms, whose dynamics are important for carbon and nutrient fluxes in the ecosystem. With a high turnover compared to terrestrial plants (Margalef, 1978), phytoplankton plays an essential role in driving the biogeochemical cycles and the Redfield ratio in the ocean (Goldman et al., 1979). However, obtaining an accurate description of the dynamic distribution of phytoplankton can be limited by the methods available for measuring, on a short temporal scale, the processes which may influence it. Various methods have now been developed to investigate phytoplankton, from the single cell level (by microscopy and flow cytometry after in situ sampling), the global scale using bulk methods (in situ fluorimetry and metagenomics)

up to the ocean scale using remote sensing. The ocean color obtained by satellite observations indicates bulk chlorophyll concentrations, used as a proxy for phytoplanktonic biomass, can be highly variable in coastal waters (Antoine et al., 1996). This variability is due to forcings, that control net population growth, grazing, and physical transport (Cloern, 1996), acting over hourly or daily scales. Since conventional sampling strategies hardly reach these scales, a legitimate concern has been raised over the underestimation of the natural short-term dynamics of phytoplankton during oceanographic campaigns and routine surveys (Rantajärvi et al., 1998). Or it is well known that the short generation time of phytoplankton can explain their ability to coexist on the same limited resources (Hutchinson, 1961).

The most efficient method for quantifying phytoplankton productivity is the estimation of the dividing rate of a population (in relation to the cell cycle) indicative of NPP. This combined with the variation in abundance is the only method for quantifying loss rates which is a good indicator of the sensitivity of the phytoplankton to trophic interactions or abiotic forcings. Estimations of dividing rates, expressed as population growth rate, are generally based on DNA measurements with lags from an hour to a day (Binder et al., 1996; Vaulot and Marie, 1999). Unfortunately, this requires important manual handling (i.e., sampling, fixing, storing, staining, and analysis) of the samples. To address these limitations, priority has been given to autonomous flow cytometry (Peeters et al., 1989; Olson et al., 2003), like the Cytosense flow cytometer (Cytobuoy b.v., Netherlands) in order to observe fine-scale temporal dynamics of phytoplankton (Dubelaar and Gerritzen, 2000; Dubelaar and Jonker, 2000; Dubelaar et al., 2004; Thyssen et al., 2008, 2014). Single cell analysis using several optical properties gives a good alternative for estimating growth rates, as they are linked to cell size. As previously reported in Durand (1995) and Binder et al. (1996), periodic increase and decrease in light scatter intensity can be interpreted as a response of cellular growth and division occurring during the cell cycle. Diel variations in the phytoplankton cell dimensions based on flow cytometry proxy therefore represent a necessary compromise for automated measurement requirements in order to calculate growth rates of natural phytoplanktonic groups during high frequency surveys (Sosik et al., 2003). Moreover, image processing allow to further improve the estimations of cell dimensions using mounted imaging systems implemented in the last generation of instruments (Sieracki et al., 1998).

In this study, we report on a high frequency in situ monitoring of phytoplankton in the Berre lagoon during October 2011. The Berre lagoon, located in South Eastern France is one of the largest brackish lagoons off the Mediterranean shore. Since 1995, the site has benefited from a special attention relying on a local ecological survey conducted by the GIPREB Joint Union (Groupement d'Interet Public pour la Rehabilitation de l'Etang de Berre) to observe and report on the eutrophication of the lagoon. However, in this ecosystem, the influence of important seasonal events like natural floods or strong wind events, which may have an influence on light and nutrient availability, are poorly documented and may limit the full understanding of the mechanisms driving the phytoplanktonic variability (Gouze et al., 2008). If previous studies have reported a high eutrophic state characterized by the dominance of only a few species, more recent data highlights a high biodiversity, superior to that found in the nearby Bay of Marseille (Thyssen et al., 2011; Malkassian, 2012). Using a Cytosense automated flow cytometer, equipped with the 'image-in-flow' device, abundances and optical properties were measured every hour for species ranging from pico- to small mi-

crophytoplankton. Pictures of microphytoplanktonic cells were used to estimate cell size from the sideward scatter signal and apply the full size distribution model developed by Sosik et al. (2003). In situ population growth rates were eventually determined and investigated with regards to the environmental variables monitored at the same frequency.

## 3.2 Materials and methods

Study area

The Berre lagoon is located on the SE French coast, close to the city of Marseille (800,000 inhabitants) and the Frioul archipelago where meteorological data (wind speed and direction) is permanently recorded by the meteorological station of the Mediterranean Institute of Oceanography (MIO). It is one of the largest brackish water pools off the Mediterranean shore (with a surface of 155 $km^2$), receiving both seawater via the Caronte channel and freshwater inputs from natural and drifted tributaries (Arc, Touloubre and Durance rivers). It is divided into two shallow sub-basins: the 'Grand Etang' (max. depth 9m) and the 'Etang de Vaine' (max. depth 4m) where the experiment took place. Every month, the GIPREB assesses the vertical structure of the water column at 10 hydrological stations, with one located in the 'Etang de Vaine'. Profiles of temperature, salinity, dissolved oxygen, pH, chlorophyll, turbidity and nutrients ($NO_2^-$, $NO_3^-$, $NH_4^+$, $PO_4^{3-}$) are measured at several depths to provide information on the stratification of the lagoon.

Sampling system

A multi-instrumental platform composed of a Cytosense automated flow cytometer and hydrological sensors was set up in the GIPREB laboratory located on the harbor of Berre l'Etang (Fig. 1). Water was pumped directly from the Vaine lagoon (43°47 N, 5°17 E, 2.5m depth) to the laboratory using a 250m pipe (inner diameter 50 mm). Samples for flow cytometric analyses were taken every hour from a 1 $dm^3$ sampling reservoir and hydrological sensors were placed in an 80 $dm^3$ tank supplied after the subvolume. Every hour, water was pumped (JABASCO pump) at a flow rate of 30 $dm^3.min^{-1}$ for 17min so that the pipe, the sampling reservoir and the tank were flushed and renewed several times prior to measurements. Samples were analyzed using the Cytosense 2 min after the pump stopped, when all air bubbles had disappeared. An evacuation pipe led the water back to the lagoon (by gravity). The JABASCO pump uses flexible impeller technology so that it does not squeeze the water passing through, therefore avoiding the damage to the cells (Thyssen et al., 2009). Between October $1^{st}$ and $14^{th}$ 2011, nitrate ($NO_3^-$) concentration was measured using a Satlantics ISUS V3 nitrate sensor set up in the 80 $dm^3$ tank with a CTD (Hydrolab) which recorded temperature, chlorophyll concentration, turbidity, and salinity (conductivity) of the water. Throughout the month, the phytoplanktonic assemblage was characterized using the Cytosense of the PRECYM flow cytometry platform of the MIO (http://precym.mio.univ-amu.fr). Additional discrete samples were manually collected to determine nutrient ($NO_2^-$, $NO_3^-$, $NH_4^+$, $PO_4^{3-}$) concentration and calibrate the ISUS sensor using a Technicon Autoanalyser (dectection limits: 50nM for nitrate and 20nM for nitrite and phosphate). Ammonium ions ($NH_4^+$) were measured by spectrophotometry. An *in situ* HOBO sensor, fixed near to the pipe inlet, measured incident light intensity and temperature.

Flow cytometry

The Cytosense is a flow cytometer optimized to analyse phytoplankton in the field. It has been specifically designed to anal-

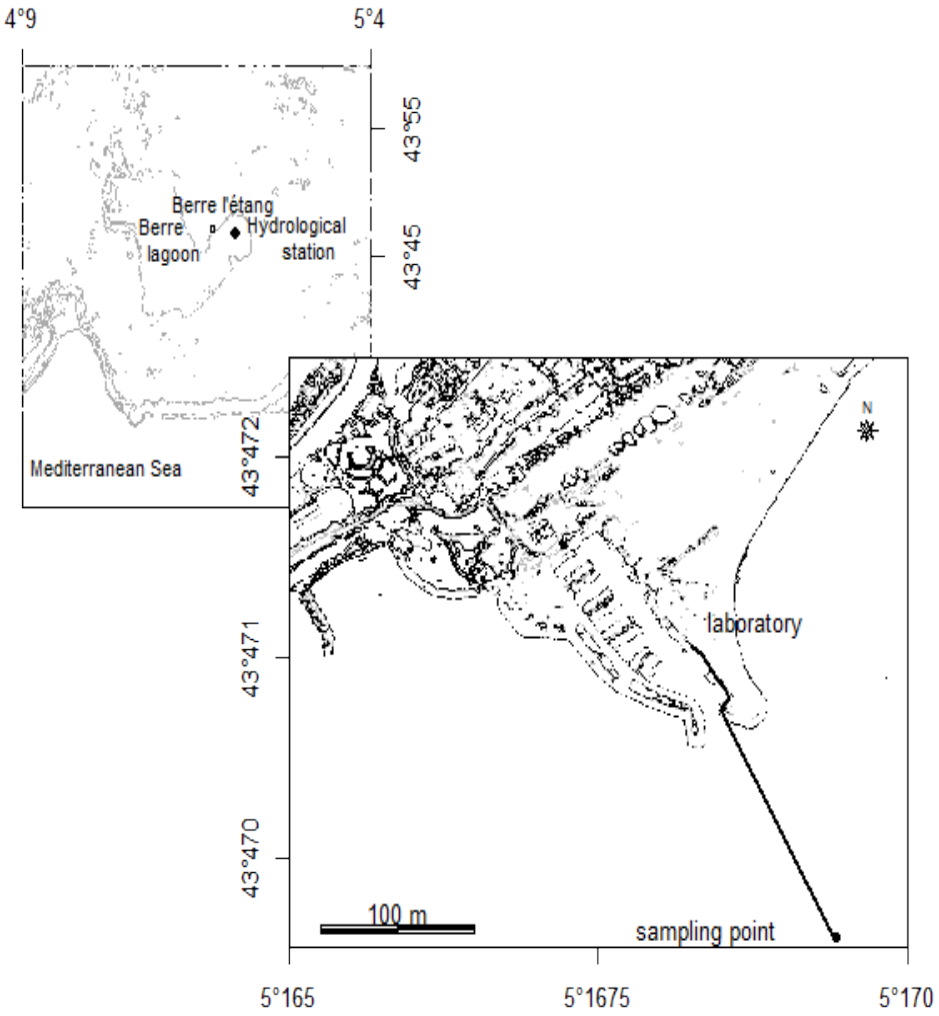


Figure 3.1: Location of the sampling point (black circle) and the 250m pipe (black line) to pump the water to the laboratory, settled on the harbor of Berre l'Etang

yse particles (cells, chains, colonies) of 1-800 $\mu$m diameter and up to several mm in length (chain forming cells). The sample flows in a sheath fluid to an exciting light source (a 488 nm laser beam) at a rate of 9 $mm^3.s^{-1}$ in order to optimize the processing of cells, separation, and alignment. The inherent optical properties of the cells were recorded in full pulse shape as they crossed the laser beam: sideward light scatter (SWS) and red (FLR, 668-734 nm), orange (FLO, 601-668 nm) and yellow (FLY, 536-601 nm) fluorescences were collected on photomultiplier tubes. Forward light scatter (FWS) was collected by a PIN photodiode. Data was acquired in Log scale. The cytoUSB software (Cytobuoy b.v.) was used to control the flow cytometer and acquire the data stored on a computer. Data acquisition was triggered on the chlorophyll-induced red fluorescence (FLR) of the phytoplankton cells. The threshold of the FLR signal was set at 9 mV in order to compute optical pulse shapes of the photosynthetic cells and get rid of the background noise (heterotrophs and detritic particles). Samples were hy-

drodynamically focused in the flow cytometer by the sheath fluid: just prior to the experiment, the cytometer was filled with 1 $\mu$m filtered seawater preserved with a 1% formaldehyde solution. After each analysis, the sheath fluid and the samples were mixed together and the sheath fluid was recycled by filtering through 0.45 and 0.1 $\mu$m integrated Nucleopore filters. A mix of fluorescent beads (Polysciences microspheres of 1.00 ± 0.03 $\mu$m, 1.6 ± 0.1 $\mu$m, 2.9 ± 0.1 $\mu$m, and 10.3 ± 0.4 $\mu$m) was regularly analyzed to ensure quality control, reliable analyses and calibrate cell sizes. Cells sharing similar optical fingerprints were manually grouped in clusters on a set of 2D projections (cytograms) in the Cytoclus software (Cytobuoy b.v.).

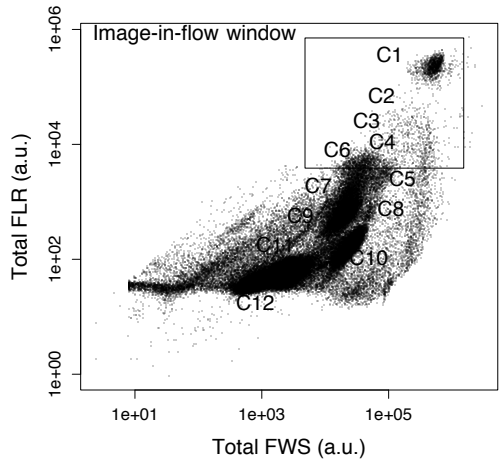


Figure 3.2: Cytogram total red fluorescence (FLR) versus total forward scatter (FWS)

Estimation of cell biovolume

The Cytosense used in this study is equipped with an 'image- in-flow' device controlled by the CytoUSB software (Cytobuoy b.v.). During this survey, cells displaying the highest red fluorescence and scatter intensities (a.u.) were manually gated within a targeted window where a maximum of 60 pictures per analysis (current limitation of the software) were taken (Fig. 2). These pictures were used to identify and estimate the dimensions of the cells in the different clusters. Area, length, and width were automatically calculated after image processing of given files containing the original pictures (Fig. 3A) using the Fiji software, an open source version of the ImageJ software (Schindelin et al., 2012). The first step of the image processing was to automatically segment the picture into foreground (cells) with pixels values of 255 (black) and background with pixels of 0 (white) (Fig. 3B). Noise was filtered (Fig. 3C) and edges between pixels' value were selected as illustrated by figure 3D. Finally we used the external edge as the contour of the cell (Fig. 3E) to compute the measurements. Biovolume of all the pictured cells was estimated considering either spherical or ellipsoidal model according to cell shapes. An exponential function explained 84% of the variance between cell volume and SWS (Fig. 4).

Estimation of *in situ* growth rates

To estimate phytoplankton in situ growth rates, we used the size-structured population model described in Sosik et al. (2003) by applying the regression between cells' volume and sideward scatter intensities to all the cells within a specific cluster. In this model, cells are classified into several size classes according to their dimensions at time $t$. The number of classes, $m$, was chosen in order to cover the entire observed biovolume spectrum from $v_{min}$ to $v_{max}$. Classes were logarithmically spaced as follows:

For i in 1, 2, ..., m $\qquad v_i = v_1 2^{(i-1)\Delta v}$

At any time $t$, the number of cells in size classes, noted $\vec{N}(t)$, was projected to $t + dt$ via matrix multiplication so that:

$$\vec{N}(t + dt) = A(t)\vec{N}(t) \qquad (3.1)$$

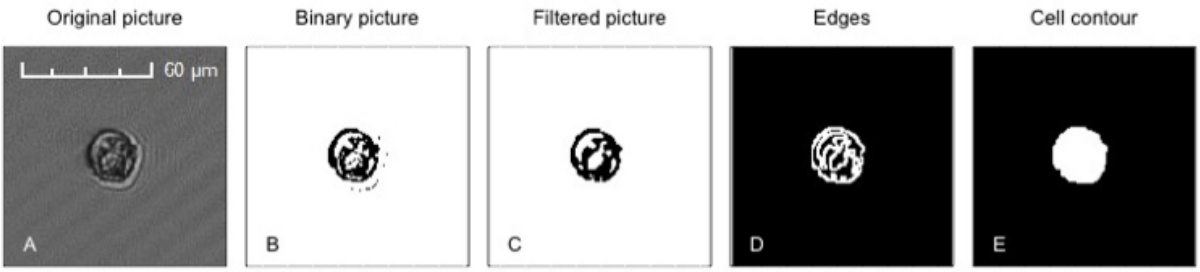


Figure 3.3: Image processing of a *Gymnodinium* picture by the Fiji software in order to extract the cell dimensions. (A) Original picture (B) Binary transformed picture (C) Filtered binary picture (D) edges detection (E) Contour selection

The elements $a_{ij}(t)$ of the matrix A correspond to the fraction of cells of class $j$ at time $t$that becomes cells of the class $i$at time $t+dt$. Changes in cell size are linked to two phases of the cell cycle: the size growth during the interphase and the size decrease after the mitosis. In $dt$, one cell can either go to the direct next size class, that is to say from $v_i$ to $v_{i+1}$ through cellular growth, or can become a cell of half its original size after division. If in $dt$ one cell neither grows nor divides, it remains in the same size class (i.e., *stasis*).

Adjustments have been made in order to apply the model described in Sosik et al. (2003) for growth rate estimations from the dynamics of the clusters in this study. Basic hypothesis were adapted to find the best fit with natural data. Elements corresponding to the fraction of cells that grew between $t$ and $t + dt$ and reached the next size class were directly calculated from:

$$a_{i+1,i}(t) = \gamma(t) \tag{3.2}$$

However, elements corresponding to the fraction of cells that divided between $t$ and $t+dt$ were counted from the fraction of cells that were not currently growing:

$$a_{i,i+1:\Delta v}(t) = 2\delta_{i+1:\Delta v}(1 - \gamma(t)) \tag{3.3}$$

The fractions of cells that has neither grown nor divided between $t$ and $t + dt$ remain:

$$a_{i,i}(t) = (1 - \delta_i)(1 - \gamma(t)) \tag{3.4}$$

The probability of cells growing to the next size class was given by an asymptotic function, assuming that it only depends on the light intensity necessary to photosynthesis:

$$\gamma(t) = \gamma_{max}\left[1 - exp\left(-\frac{E}{E^*}\right)\right] \tag{3.5}$$

E: light intensity, $\gamma_{max}$: maximum proportion of growing cells, E*: diel constant

The probability of cells dividing was given by a normal density function, assuming that it depends on the logarithm of the size spectrum of the vegetative cells only:

$$\delta_i = \delta_{max}\mathcal{N}(\mu_{log_e(v)}, \sigma_{log_e(v)}) \tag{3.6}$$

$\delta_{max}$: maximum proportion of dividing cells, $\mathcal{N}$: Normal distribution

This model was chosen to ensure that only the size distribution of vegetative cells will account for the estimation of the population growth rates. Even if dinoflagellates species are haplontic, the coexistence of asexual and sexual forms is well documented and expected after sediment resuspension induced by turbulent mixing (Kremp and Heiskanen, 1999). Since growth rates are manifestations of the asexual life cycle, the incorrect use of sexual stages could inaccurately estimate division rates. However, dinoflagellate stages are

generally heteromorphic (Pfiester and Anderson, 1987). Vegetative and planozygote/cyst cells can display distinct size (Von Stosch, 1973; Walker, 1982; Anderson et al., 1983; Blackburn et al., 1989; Figueroa et al., 2008) so the Normal distribution should enable either to restrain the size spectrum if sexual or alternative ($G_0$) forms are present or to take into account the entire spectrum if not.

*In fine*, growth rates are predicted according to the following formula:

$$\mu = log_e\left(\frac{\sum_{i=1}^{m}\hat{N}_i(t=24h)}{\sum_{i=1}^{m}N_i(t=0)}\right) \quad (3.7)$$

$N(t=0)$: initial size distribution at t=00:00, $\hat{N}(t=24h)$: fitted size distribution at t = 24 : 00.

The parameters of the projection matrix A were inferred by minimizing the sum of squared differences between observed and projected proportion distributions, $\vec{w}$ , over 24 h.

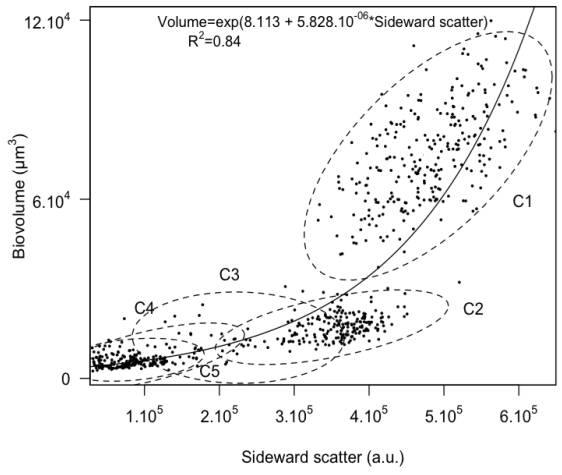


Figure 3.4: Exponential relationship between total sideward scatter and biovolume of pictures ($n$=693)

Statistical analysis

Statistical analysis and model code were run in the R freeware (http://www.r-project.org). The time series of mean wind speed have been fitted using a linear regression in order to select the window within which the temporal trend explained most of the variation of wind speed. Significance of trends of hydrological variables in this window have been estimated by likelihood ratio test adapted to pseudoreplication of observations in time series (Pinheiro and Bates, 2000). To account for the strong serial correlation between measurements, random effects have been modeled as deviations of intercepts between factors grouping measurements equivalent to one period in each time series. Periodicity has been studied using discrete Fourier transforms on detrended time series. The maximum amplitude associated with the harmonic frequency equivalent to one period determined by Fourier analysis have been applied to differences between observed variables and non-linear trends fitted by local polynomial regressions. The mixed-effect linear models with and without a linear trend were:

$$\begin{aligned} Y(t) &= \beta_0 + \beta_1 index(t) + \beta_2 sin(2t\pi) + \beta_2 cos(2t\pi) + \epsilon(t) \\ Y(t) &= \beta_0 + \beta_1 sin(2t\pi) + \beta_1 cos(2t\pi) + \epsilon(t) \end{aligned} \quad (3.8)$$

$t$: time scaled to one period, $\epsilon$(t): iid residuals

For these models, residuals did not reveal any deviations from homoscedasticity and normality. The temporal dependency has been tested by the autocorrelation. Correlation coefficients between environmental variables and cluster abundances were represented with a Principal Component Analysis. Cross-correlation between wind speed time series and all the clusters abundance time series were performed to estimate the lag time between respective maxima. Negative lag time correspond to cluster abundance maximum prior to the wind event and inversely for positive lag time.

## 3.3 Results

Optical resolution of the flow cytometry clusters

Up to 12 flow cytometry clusters of phytoplanktonic cells (arbitrary labeled C1-C12) have been resolved over the sampling period. Each cell contributed to a particular cluster on the basis of the distinct optical properties recorded. Clusters showed a proportional relationship between SWS (correlated to cell biovolume, 0.82, p-value < 0.001) and red fluorescence emitted by chlorophyll pigments. Almost all the clusters were well discriminated on red fluorescence vs. sideward scatter cytogram (Fig. 2). With the same level of red fluorescence, clusters C5 and C8 emitted more orange fluorescence than clusters C6 and C9, respectively. The size spectrum of the cells ranged within the pico-, nano-, and microphytoplankton size classes. Smallest cells were observed in the cluster C12 (mean 0.9 ± 0.1 $\mu$m) and the biggest cells belonged to cluster C1 (mean 56.4 ± 12.2 $\mu$m). Clusters C1-C4 were composed of different dinoflagellates species identified as *Akashiwo sanguinea* (Hirasaka), *Prorocentrum micans* (Erhenberg), *Scrippsiella sp.* (Balech) and *Gymnodinium sp.* (Stein), respectively over the all sampling period. Clusters C5-C10 were assigned to nanophytoplankton with no visual identification possible by the 'image-in-flow' pictures due to the lack of resolution of the pictures. Picophytoplankton was represented by clusters C11 and C12 with mean length estimated by the calibrated beads at 1.1 ± 0.1 $\mu$m and 0.9 ± 0.1 $\mu$m.

Phytoplanktonic community dynamics

**Environmental variables** During October 2011, the wind was the main forcing on the hydrological state of the Berre lagoon and more particularly the intense Mistral blowing from the North (330-360°), with mean speeds exceeding 20 m.s$^{-1}$ (Fig. 5). Turbulent mixing of the water column increased as gusts reached 18.7 ± 3.2 m.s$^{-1}$ between October $7^{th}$ and $9^{th}$ (Fig. 6A). During these 2 days, all the hydrological variables showed significant trends with the exception of *in situ* light intensity ($\chi^2(1)$, n = 79, p-value < 0.05). Mean water temperature measured at the sampling point cooled by 5.2°C between October $05^{th}$ and $11^{th}$ (Fig. 6B). Salinity distribution showed a wider range of variation during the Mistral event, suggesting a gradient between surface and bottom layers prior to the wind. Difference between 0.05 and 0.95 percentiles was 0.19 on October $6^{th}$ and 0.59 on October $8^{th}$. On September $16^{th}$ and October $18^{th}$, the nutrient vertical profiles measured by the GIPREB at surface and bottom depths displayed higher concentrations of recycled nutrients ($NH_4^+$, $PO_4^{3-}$) at the bottom of the lagoon, suggesting the stratification of the water column prior to and after the first Mistral event (Fig. 7). Variation in nitrate concentrations was similar to temperature (Fig. 6C) with a negative trend of -0.04 $\mu$M per hour ($\chi^2(1) = 17.2$, n = 79, p-value < 0.001) which led to a minimum of 0.29 $\mu$M on October $9^{th}$ at 19:00. Chlorophyll concentration reached 20.96 $\mu$g.cm$^{-3}$ on October $6^{th}$ 13:00 (Fig. 6D). After the maximal gust of 25 m.s$^{-1}$, the mean value dropped to 3.97 $\mu$g.dm$^{-3}$. Despite the decrease in chlorophyll concentration, the *in situ* light intensity was not significantly different before or during the Mistral event ($\chi^2(1) = 0.07$, n = 79, p-value = 0.8). The photoperiod was between 08:00 and 19:00 and the light intensity was always maximal at 12:00 (Fig. 6E).

**Community response to the wind event** A Principal Component Analysis was performed to analyze the multivariate time series of hydrological variables and cluster abundances. The main relationships between phytoplankton concentrations and the environment were well represented on the two first components, which explained

Table 3.1: Maximum cross correlation coefficient and associated lag time of wind speed and cluster abundance time series between October $5^{th}$ 00:00 and October $11^{th}$

| Clusters | C1 | C2 | C3 | C4 | C5 | C6 | C7 | C8 | C9 | C10 | C11 | C12 |
|---|---|---|---|---|---|---|---|---|---|---|---|---|
| Coefficient | 0.57 | 0.62 | 0.62 | 0.48 | 0.62 | 0.60 | 0.63 | 0.73 | 0.57 | 0.46 | 0.96 | 0.92 |
| Lag (h) | -32 | -30 | -28 | 132 | -30 | -39 | -14 | -26 | -48 | 49 | 0 | 0 |

59.1% of the total variance.

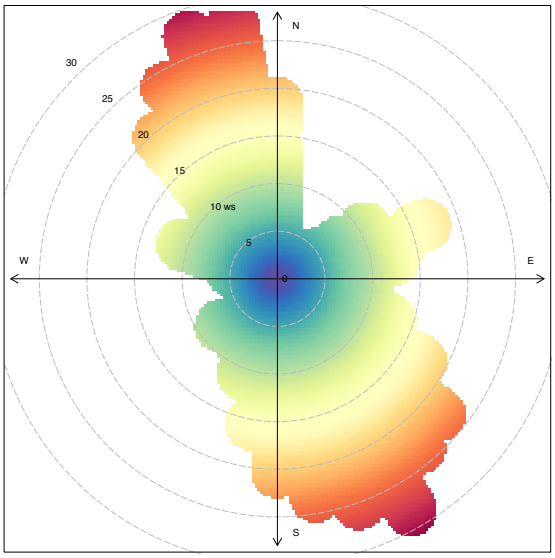


Figure 3.5: Distribution of wind direction during October 2011

High chlorophyll concentration was observed simultaneously with the occurrence of higher abundances of clusters C1-C9 (Fig. 8). The increase of chlorophyll concentration and turbidity in the Berre lagoon was phased with the sudden proliferation of clusters C1-C3, C5, and C8 (correlation coefficient 0.36, 0.46, 0.31, 0.50, and 0.51, respectively, p-value < 0.001), as well as the presence of C9 cells. C9 was the most abundant cluster with mean concentration 17,024 ± 10,880 cells.cm$^{-3}$ between October $05^{th}$ and $06^{th}$ and a maximum of 51,142 cells.cm$^{-3}$ on October $05^{th}$ 20:00. All of these clusters were more abundant before the intensification of the Mistral wind speed (Table 1). The lag time between maximum wind speed and abundances mainly ranged between 24 and 48 h. Turbidity was correlated to high temperature (0.63, p-value < 0.001) and high nitrate concentration (0.26, p-value < 0.001). Conversely, picophytoplankton cluster (C11 and C12) concentrations increased less than 1 h after the wind speed rose (correlation coefficient 0.72 and 0.60, p-value < 0.001). Coefficients of cross correlation were thus maximal for the 0 h lag time between wind speed and abundance time series. Mean abundance was 1,482 ± 1,009 cells.cm$^{-3}$ for C11 and 923 ± 317 cells.cm$^{-3}$ for C12 between October $05^{th}$ and $06^{th}$ and reached 3,787 ± 1,557 cells.cm$^{-3}$ and 1,690 ± 411 cells.cm$^{-3}$ during October $07^{th}$ and $08^{th}$. The increase in these cluster concentrations was reproduced during a second strong Mistral event (Fig. 9), with an incremented amplitude. The abundance of the *Gymnodinium* cluster did not significantly change between October $05^{th}$ and $11^{th}$. The $3^{rd}$ and $4^{th}$ principal component that explained 8.7% and 6.7% of the total variance respectively (data not shown) showed the negative correlation between light intensity and turbidity (-0.14, p-value < 0.1) and the positive influence of light on chlorophyll concentration mostly before the Mistral intensification (0.36, p-value < 0.1).

Dynamics of the phytoplanktonic populations

***Gymnodinium* dynamics** From the pictures taken by the 'image-in-flow' device, cluster C4 has been identified as *Gymnodinium sp.*. Its dynamics was quasi-periodic during the Mistral event (Fig. 10A). The concentration was marked by several peaks of abundance with a mean of 49.9 ±

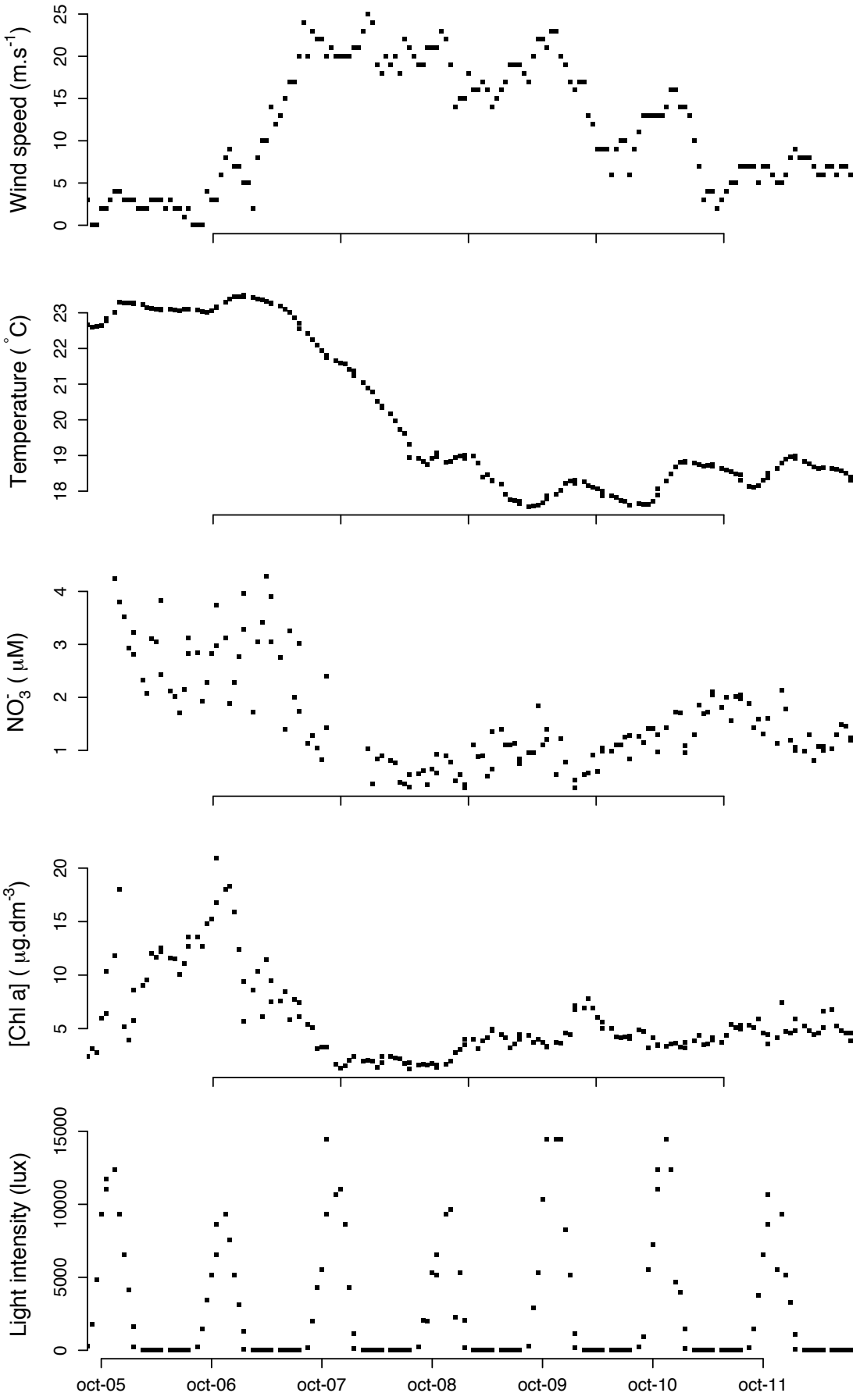


Figure 3.6: Dynamics of the hydrological variables before, during and after the strong wind event. (A) Wind speed (B) Temperature (C) $NO_3^-$ concentration (E) Light intensity

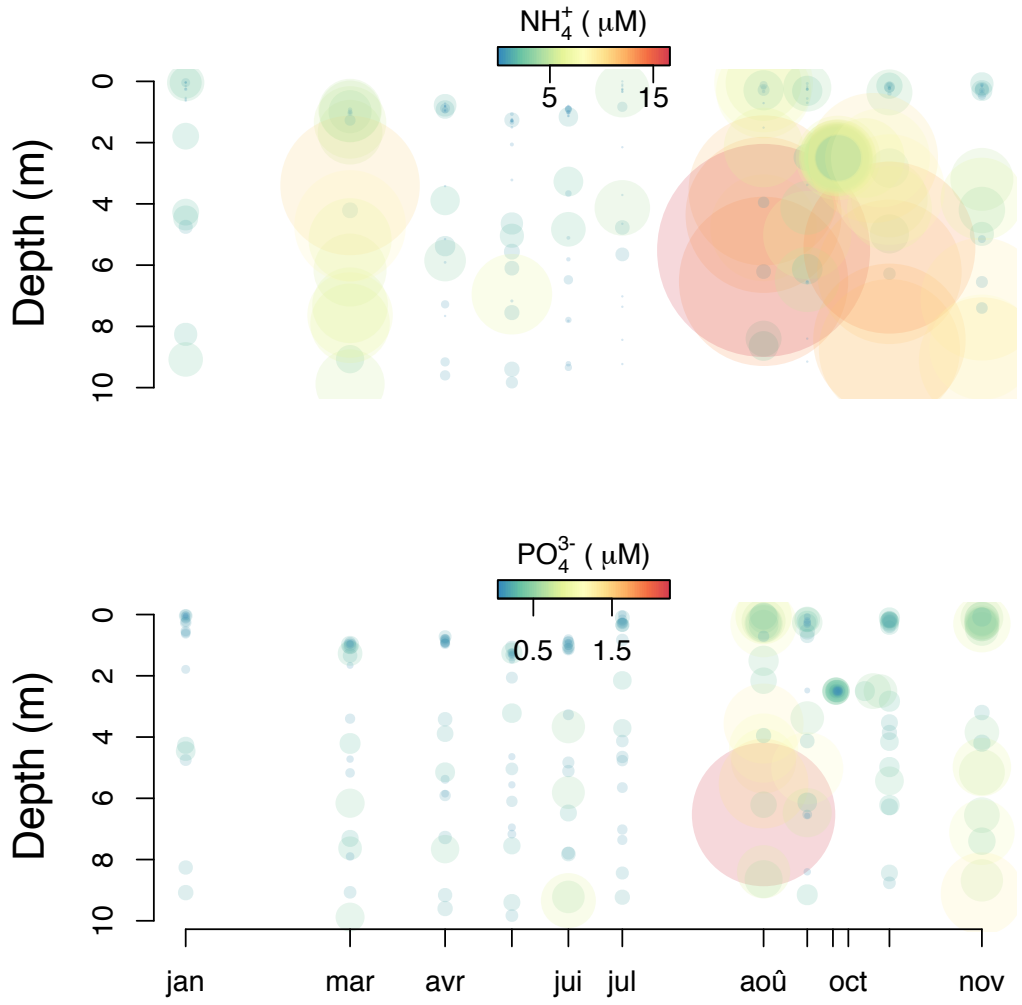


Figure 3.7: 2011 vertical distributions of (A) ammonium and (B) phosphates concentrations measured by the GIPREB at surface and bottom layers at the hydrological station located in the Vaine lagoon

28.8 cells.cm$^{-3}$. The highest concentration reached 142.4 cells.cm$^{-3}$ on October 6$^{th}$ at 19:00 and the abundance regularly dropped down below 50 cells.cm$^{-3}$. Between October 05$^{th}$ and 09$^{th}$, a high abundance was generally observed at the end of the day, but after the lull in the wind two distinct peaks were observed each day. On October 10$^{th}$, maximal concentrations (of 122.8 and 79.2 cells.cm$^{-3}$) were measured at 05:00 and 13:00, respectively. On the 11$^{th}$, they were measured at 03:00 and 13:00, with 82.8 and 71.6 cells.cm$^{-3}$, respectively. The same day, the maximum mean biovolume of the cells was 3 times greater than the minimum, passing from 4,852-16,294 $\mu$m$^3$ (Fig. 10B). During this period, cells were highly phased within cluster C4, making the estimation of growth rates based on the biovolume distribution more reliable (Fig. 11). To apply the model and compare the observed (Fig. 11A) and theoretical (Fig. 11B) distribution of the biovolume, $v_{min}$ and $v_{max}$ were set to 3,785 $\mu$m$^3$ and 59,874 $\mu$m$^3$, $dt$ to 10 min, $\Delta v$ to 1/4 and $m$ to 17. The mean cell biovolume increased 1 h after dawn until ap-

proximately 20:00 (Fig.11D) before it progressively decreased due to mitotic divisions (Fig. 11C). The amplitude of these two processes varied before, during and after the wind event so that growth rates ranged between 0.22 $d^{-1}$ (<1 division per day) and 0.85 $d^{-1}$ (> 1 division per day) (Fig. 10C).

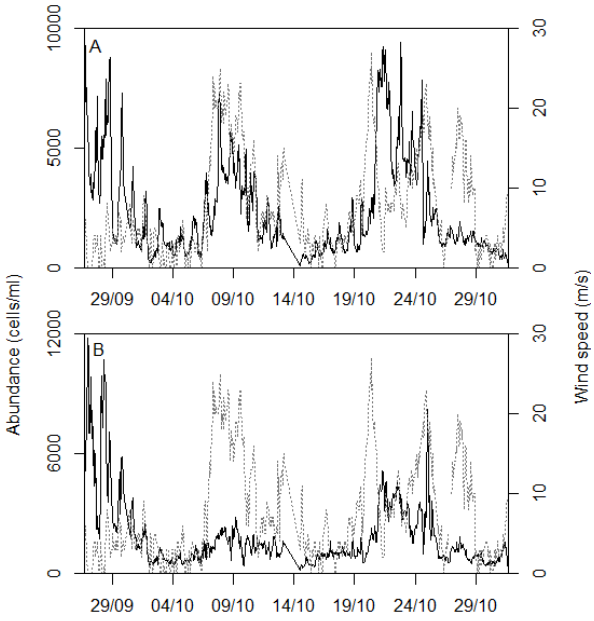


Figure 3.8: Time series of the (A) C11 cluster and (B) C12 cluster abundances (black line) during the sampling period, characterized by two strong Mistral event (gray dotted line)

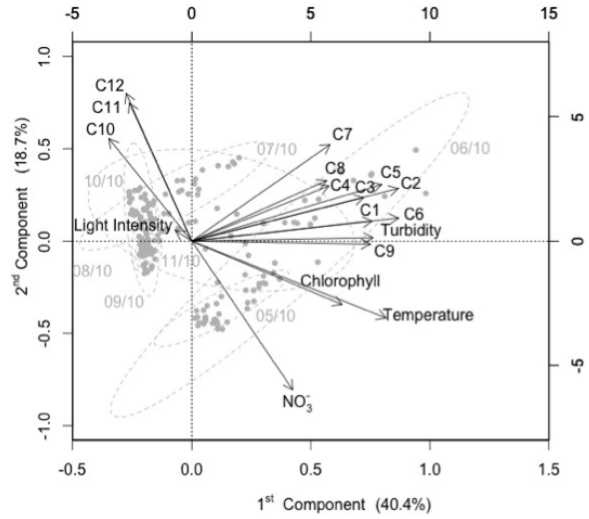


Figure 3.9: Principal component analysis performed on the dataset. Projection of the observations (gray points, i.e. dates from 10/05 to 10/11) and the variables (arrows, i.e. hydrological variables and clusters abundance) on the $1^{st}$ and $2^{nd}$ principal components (59.1 % of the total variance)

**Dynamics of cluster C5** Cells forming the cluster C5 could not be identified on the pictures. It was one of the clusters that showed a sudden peak of abundance on October $6^{th}$, reaching up to 838 cells.$cm^{-3}$ at 15:00 (Fig. 12A). Two hours later, the concentration was 101 cells.$cm^{-3}$ and remained at a mean value of 85.9 ± 57.7 cells.$cm^{-3}$. The cells were well phased with the light/dark period between October $5^{th}$ and $11^{th}$ as indicated by the mean cell biovolume that exhibited a clear diel variation in relation to the cell cycle (Fig. 12B). Cell size began to increase 1h after dawn (09:00), until a few hours after dusk (20:00-23:00). The ratio of max:min mean biovolume ranged from 1.26 on October $7^{th}$ to 1.55 on October $11^{th}$. Between these dates, growth rates progressively increased with regard to the variation of mean biovolume amplitude and reached 0.46 $d^{-1}$ on October $11^{th}$ (Fig. 12C). To apply the model to cluster C5 and compare the observed and theoretical distribution of the biovolume, $v_{min}$ and $v_{max}$ were set to 3,707.6 $\mu m^3$ and 16,017.6 $\mu m^3$, $dt$ to 10 min, $\Delta v$ to 1/9 and $m$ to 20.

## 3.4 Discussion

### Phytoplankton in the Berre lagoon

Because of high nutrients inputs and regeneration (Gouze et al., 2008), the primary production in the Berre lagoon has always been high compared to others Mediterranean lagoons (Minas, 1976; Kim, 1983). High production rates leading to blooms combined with great diversity have made this site a unique area for phytoplankton study.

In October, these blooms have been observed due to persistent summer-like temperatures, causing a thermal stratification of the water column, and the resurgence of nutrients supply by the power plant activities. Before the freshwater discharges were regulated by the power plant, algal proliferation was almost mono-specifically

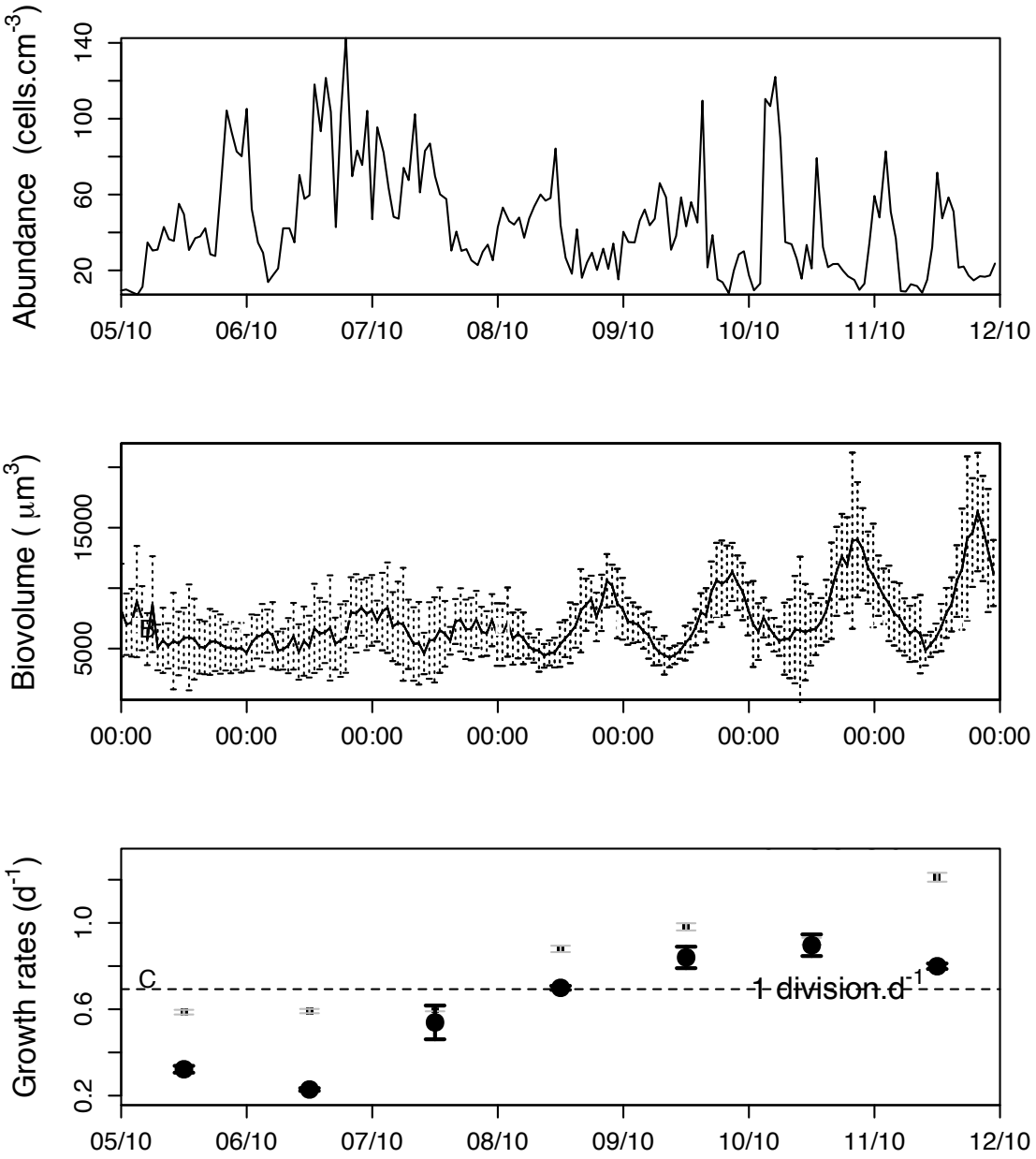


Figure 3.10: Time series of *Gymnodinium* cluster during the strong Mistral event. (A) Population dynamics (B) Variation of the mean cells' biovolume (C) Estimations of the *in situ* growth rates provided by the the ratio between and minimal mean diel biovolume (black squares) and the model (black points). Error intervals correspond to growth rate estimates after applying the biovolume regression model with standard errors

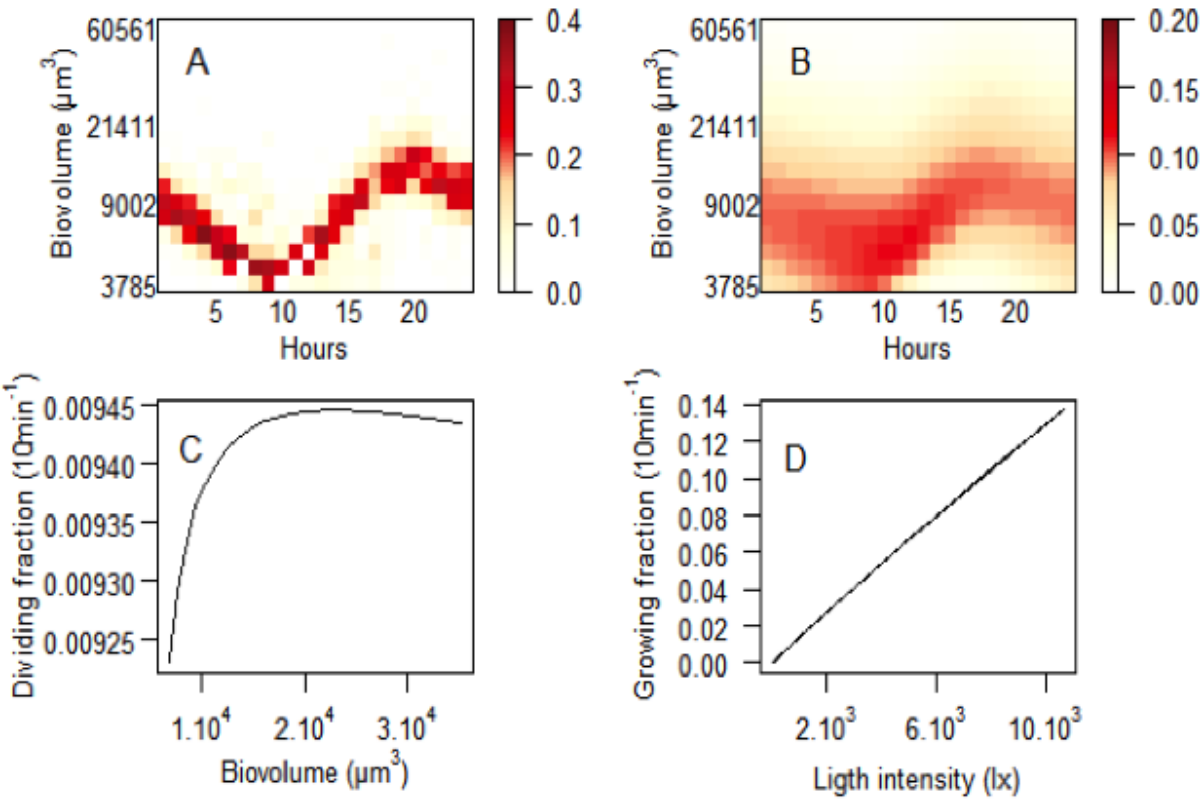


Figure 3.11: Output of the size structured population model applied to cluster C4 on October $11^{th}$ 2011: Diel variations of the (A) observed and (B) theoretical distributions of cell proportions in each size class. The theoretical distribution was estimated only on the basis of two cell cycle processes, division and size growth with probability depending on (C) the biovolume of the cells and on (D) the incident light intensity respectively

dominated by red tide dinoflagellates such as *Prorocentrum minimum*. However, the wind regimes occurring in this region play a major role in mixing and oxygenating the water column. This limits the negative impact of hypoxia that could be induced by the heterotrophic activity. The Mistral is a strong Northerly wind that generally drives the superficial layers of the Berre lagoon toward the Caronte channel to join the Mediterranean Sea (Ulses et al., 2005). It causes the homogenization of the water mass, mixing warm surface layer and colder bottom layer (Nerini et al., 2001). All these forcings drove the phytoplanktonic community to evolve in order to develop within the range of temperature and salinity gradients induced by wind, rivers and freshwater discharges. However, since the regulation of discharge imposed on the hydroelectric plant, species richness has increased (Raimbault et al., 2013). Diatoms (*Chaetoceros sp.*, *Pseudo-Nitzschia sp.*, and *Thalassionema sp.*), dino- and nanoflagellates have been sampled at 10 hydrological stations and identified by microscopy and flow cytometry (data not shown), technique recently implemented in the monitoring strategy of the GIPREB. Flow cytometric analyses by an autonomous flow cytometer have revealed more phytoplankton clusters in the lagoon than in the Bay of Marseille, in the NW Mediterranean Sea (Thyssen et al., 2011). In 2005-2006, 7 clusters were resolved in the Bay of Marseille assigned to pico (2 clusters) and nanophytoplankton (5 clusters) compared to 12 clusters identified in 2011 in the Berre lagoon at the sampling point. Two clusters were assigned to picophytoplankton, 6 clusters of nanophytoplankton and 4 of microphytoplankton. In the microphytoplanktonic clusters, cells were identified as red tide dinoflagellates species such as *Akashiwo sanguinea*, *Pro-*

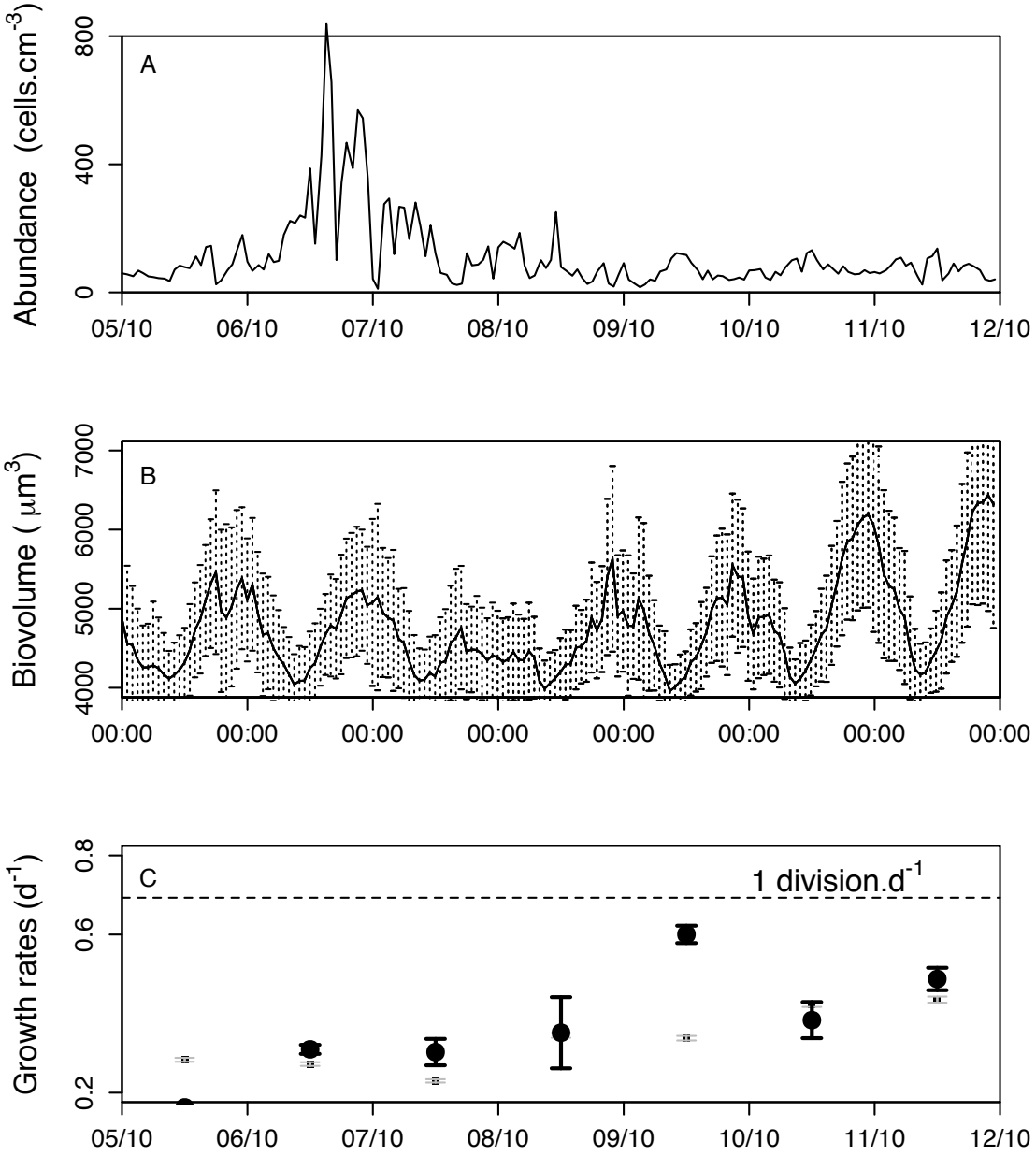


Figure 3.12: Time series of cluster C5 during the strong Mistral event. (A) Population dynamics (B) Variation of the mean cells' biovolume (C) Estimations of the *in situ* growth rates provided by the the ratio between and minimal mean diel biovolume (black squares) and the model (black points). Error intervals correspond to growth rate estimates after applying the biovolume regression model with standard errors

*rocentrum micans*, *Gymnodinium sp.*, and *Scrippsiella sp.*. The first species are eurythermale and euryhaline species, able to grow within temperature (10-30°C) and salinity (10-40) gradients (Matsubara et al., 2007; Dhib et al., 2013).

**Community and production changes to a strong Mistral event in the Berre lagoon**

Offsets of phytoplanktonic production are calculated from the loss and growth rates of natural populations. Loss in net productivity at a fixed point can result from trophic interactions such as grazing and viral lysis as well as physical transport (Riley et al., 1949). For our experiment, the sampling strategy for high frequency characterization of the phytoplankton community has been limited to one depth at a fixed station, and thus represents only a partial view of the response of phytoplankton clusters in the lagoon. However, several 3D hydrodynamical models simulate the circulation in the station location as confined within the Vaine lagoon in case of a strong Mistral event (Leredde et al., 2002; Alekseenko et al., 2013). Moderate turbulent mixing is usually beneficial for large non-motile cells of phytoplankton because it counterbalances their sedimentation and prevents their exportation toward the aphotic layer (Margalef, 1978). The classical succession scheme induced by temporal or spatial ergoclines (Legendre and Demers, 1985) predicts the outbreak of diatoms followed by dinoflagellates when nutrients are depleted in the surface layers. Because of both inputs of freshwater and seawater, maintaining the haline gradient between surface and bottom layers, the deepest part of the Berre lagoon is almost permanently stratified (Nerini et al., 2001). Only strong gusts of wind (>10m.s$^{-1}$) allow the homonogeneization of the water column. In October 2011, automated flow cytometry analyses prior the strong Mistral event revealed the sudden proliferation of red tide dinoflagellates as well as nanophytoplankton clusters. Dinoflagellate species regroup complex microorganisms. Their life cycle implying sexual, asexual, and resting stages as well as their trophic strategy can both justify the potential of dinoflagellates to outcompete other phytoplanktonic species (Schnepf and Elbrachter, 1992; Kremp, 2013). When inorganic compounds are not sufficient in their environment, dinoflagellates can swim in order to have access to the deeper nutrient pool or ingest small prey in food vacuoles if they are mixotrophs (Stoecker, 1999). The proliferation of dinoflagellates during our experiment thus supports the idea that they are K strategists relying on the microbial loop for the uptake of regenerated nutrients (Smayda, 1997; Pitcher et al., 1998; Kudela et al., 2008). On the contrary, high frequency sampling revealed that picophytoplankton clusters might show a reactive capacity superior to other groups such as diatoms, and so be defined as pioneer species. Autonomous sampling has already indicated that picophytoplankton could be the first to develop following a strong wind event (Thyssen et al., 2008). Higher assimilation rates give these small cells an advantage compared to larger species accounting for new production as well (Eppley et al., 1969; Aknes and Egge, 1991). In theory, the concentration of such $r$ strategists should increase within a short lag time after the perturbation. In this study, clusters C11 and C12 started to multiply less than 1 h after the wind speed increase. This behavior was reproduced during a second strong Mistral event, which also favored their proliferation soon after the weather lull, but likely prevented the reappearance of the following successors, accounting for regenerated production fuelled by the organic matter recycling (Legendre and LeFevre, 1989).

**Growth rates estimations**

As sideward scatter is strongly correlated to cell size (Ackleson and Spinrad,

1988; Simon et al., 1994), determination of cell optical properties can provide information about the life cycle of micro-organisms (Kiefer et al., 1979). The model developed by Sosik et al. (2003) is based on the full size distribution that varies during the sequential phases of the cell cycle. Therefore, cells will grow with the support of photosynthesis and divide according to their size. In an attempt to accommodate these simple assumptions to clusters observed in this study, we tested an alternative model for division, relaxing the hypothesis of the strict increase of division rates with biovolume. However, caution should be obviously taken with *in situ* growth rates estimations of dinoflagellate populations, particularly with regard to life stages differentiations (Cetta and Anderson, 1990; Gisselson et al., 1999). No inhibitory effect of high light intensity or UV exposure was expressed in the growth model since the daily red fluorescence variation did not exhibit any depression during the day (data not shown), as can be observed when quenching occurs (Jacquet et al., 1998). This model fitted C4 and C5 clusters size distribution patterns that were, as for dinoflagellates (Sweeney, 1959), phased to the light/dark cycle. Cellular growth began ~ 1 h after dawn and continued briefly after dawn, whereas division mainly occurred during the night, in agreement with the literature (Weiler and Chisholm, 1976). As a greater proportion of cells was in the G1 phase, we changed the dependence relation between division and growth to reflect that division mainly occurred when cellular growth was no more dominant. After the Mistral event, cells reached higher dimensions during the photoperiod, suggesting a possible light limitation. Since duration of the interphase and mitotic divisions was unchanged, growth rates naturally increased. Cells in the *Gymnodinium* cluster underwent from less than one division to more than one division per day after October $9^{th}$. The maximal growth rate was at 0.85 $d^{-1}$ on October $10^{th}$. Growth rates of the C5 cluster were always inferior to 0.69 $d^{-2}$ but they progressively rose to 0.57 $d^{-1}$.

Clusters C1-C3 were not abundant enough relatively to the volume analyzed to ensure a reliable application of the model. The size variation did not show any clear pattern phased to the photoperiod. The shape of size histograms was constant during the day, giving evidence of asynchronous populations (Campbell and Yentsch, 1989). Asynchrony of dinoflagellates appears when spatial migration is triggered by physiological needs, local current, cyst bed or wind rather than by the light/dark cycle (Ralston et al., 2007). Nutritional migration strategy over photo/geotaxis in natural populations leads to deep chlorophyll maximums which coincide with the primary production, near the nutricline (Cullen, 1982). However, synergy between nutrient availability and irradiance needs depends not only on hydrodynamics but also on internal cells' nutritional status, reinforcing the variability within populations (Ji and Franks, 2007). In some particular ecosystems, the vertical distribution of dinoflagellates is typically bimodal, with a second abundance peak at the surface (Townsend et al., 2001). Even if diel size variation can be persistent along the water column, growth rates of population necessarily vary within layers. For populations synchronized to the photoperiod, difference in incident irradiance with depth can induce the retardation of the cell cycle whereas nutrient stratification and pigment quenching due to high UV can also completely invert its timing between deep and surface layers (Vaulot and Marie, 1999). Water mixing could thus influence the growth rate of a patchy population, as it should homogenize the nutrient pool and light availability. The vertical gradient of cell size can lead to growth rate differences between model and mean biovolume estimates. Presence of non-vegetative larger cells (Blackburn et al., 1989), displaying smaller division probability, could explain

the biovolume ratio being superior to the model ratio when mean size is used. Stratification of the water column, as demonstrated by the time series of hydrological variables recorded, should increase the differences between these two estimations. Although there is strong evidence of the inhibitory effects of turbulence on dinoflagellate cell division and growth (Berdalet, 1992), the rise of C4-C5 cluster growth rates at the sampling point with the wind was likely due to higher growth rates at the bottom, suggesting the presence of a nutricline before the mixing, and a decrease in the light limitation due to turbidity dispersal. The influence of drop of temperature on growth rates is improper with no or positive correlation in the range 15-20 °C for phytoplankton (Eppley, 1972) and particularly for species of the genus Gymnodinium (Thomas, 1975; Nielsen, 1996; Yamamoto et al., 2002).

## 3.5 Conclusion

In this study, abundances and optical properties of phytoplankton community were monitored in autumn in one of the biggest European brackish lagoons using an autonomous flow cytometer especially designed for photosynthetic microorganisms. This *in situ* monitoring carried out in the Berre lagoon and remotely operated (thanks to internet connection) enabled to follow at the single cell level the dynamics of a large diversity of phytoplanktonic functional groups, as defined by flow cytometry, in response to brief and sudden environmental forcings. In October, the concentrations of 2 groups of picophytoplankton, 6 groups of nanophytoplankton, and 4 groups of microphytoplankton were measured at high frequency before, during, and after a strong wind event, providing in near real time the *in situ* structure of the phytoplankton community. Data analyses revealed a high variability of the autotrophic community in response to this natural forcing, that has been undetected by the routine survey conducted monthly by a conventional manual sampling. Phytoplankton responses to wind have also been reproduced during a second event and have been previously described in the literature, leading to the definition of the concept of response functional groups (Thyssen et al., 2014).

Besides, a potential application to harmful algal bloom monitoring is conceivable with this technology combining flow cytometry and image analysis (Campbell et al., 2010). In this study, we managed to identify red tide species and their dynamics at population and intrinsic levels. A stable hydrological environment triggered their proliferation before the wind event, resulting in a chlorophyll biomass peak, with the exception of the *Gymnodinium* cluster. The turbulent mixing generally affects the spatial distribution of phytoplankton by physical transport and may hide influence on the net abundance of populations by physiological changes that need to be measured at the individual level. To address this issue, estimates of *in situ* population growth rates have been calculated using the light scatter signal intensity recorded during the passage of each cells through the 488 nm laser beam. This signal was strongly correlated to the biovolume of the cells pictured by the 'image-in-flow' device. Growth rates were calculated from the diel changes of size distribution monitored by the instrument thanks to the high frequency measurements that are difficult to obtain using more conventional methods. The increase of asexual reproductive rates was predicted by the model of Sosik et al. (2003) for the two phased clusters, probably as a result of the attenuation of light/nutrient limitation at the sampling point in response to the homogenization of the water column.

Although chlorophyll biomass dropped during the wind-induced mixing, the evolution of population growth rates suggests that in some cases, the calculation of Net

Primary Production based on ocean color might not match the estimation of photosynthetic carbon fixation. Observing marine microorganisms at the single cell level with an automated flow cytometer operating at high frequency (up to several sampling and analyses per hour) takes into account the short-term variability of phytoplankton. Coupled to other hydrological sensors also operating at high frequency it should bring a new insight into the phytoplankton structure and functioning. It should also fill the gap in the primary production budget estimations based mostly on low frequency sampling (typically every month or twice a month) that cannot take into consideration pulsed events. Not taking into account the fast biomass pulses of phytoplankton could significantly impact the estimations of biogeochemical fluxes and budgets on an annual scale (Lomas et al., 2009).

### 3.6 Acknoledgments

The instatement of the automated platform near the Berre lagoon was supported by the project EC2CO-DRIL (CNRS) of 'In situ Monitoring of phytoplanktonic assemblages dynamics' and the PRECYM flow cytometry platform of the MIO for providing the Cytosense flow cytometer. We thank the GIPREB for logistic support and Beatriz Beker for the identification of phytoplankton species. We are grateful to Mathieu Fallet for his contribution to the images treatment. M. Dugenne benefits from a fellowship of the French Minister of High Education and Research for a phD thesis supervised by Gerald Grégori and Denys Pommeret.

## References

Ackleson, S. G., and Spinrad, R. W. (1988). Size and refractive index of individual marine particulates: a flow cytometric approach. Appl. Opt. 27, 1270-1277.

Aknes, D. L., and Egge, J. K. (1991). A theoretical model for nutrient uptake in phytoplankton. Mar. Ecol. Prog. Ser. 70, 65-72.

Alekseenko, E., Roux, B., Sukhinov, A., Kotarba, R., and Fougere, D. (2013). Coastal hydrodynamics in a windy lagoon. Comput. Fluids 77, 24-35.

Anderson, D. M., Chisholm, S. W., and Watras, C. J. (1983). Importance of life cycle events in the population dynamics of Gonyaulax tamarensis. Mar. Biol. 76, 179-189.

Antoine, D., Andre, J. M., and Morel, L. (1996). Oceanic primary production. Estimation at global scale from satellite (coastal zone color scanner) chlorophyll. Global Biogeochem. Cycles 10, 57-69.

Berdalet, E. (1992). Effects of turbulence on the marine dinoflagellates Gymnodinium nelsonii. J. Phycol. 28, 267-272.

Binder, B. J., Chisholm, S. W., Olson, R. J., Frankel, S. L., and Worden, A. Z. (1996). Dynamics of picophytoplankton, ultraphytoplankton and bacteria in the central equatorial Pacific. Deep-sea Res. II, Top. Stud. Oceanogr. 43, 907-931.

Blackburn, S. I., Hallegraeff, G. M., and Bolch, C. J. (1989). Vegetative reproduction and sexual life cycle of the toxic dinoflagellate Gymnodinium catenatum from Tasmania, Australia. J. Phycol. 25, 577-590.

Campbell, J. W., and Yentsch, C. M. (1989). Variance within homogeneous phytoplankton populations, II: analysis of clonal cultures. Cytometry 10, 596-604.

Campbell, L., Olson, R. J., Sosik, H. M., Araham, A., Henrichs, D. W., Hyatt, C. J., et al. (2010). First harmful Dinophysis (Dinophyceae, Dinophysiales) bloom in the U.S is revealed by automated imaging flow cytometry. J. Phycol. 46, 66-75.

Cetta, C. M., and Anderson, D. M. (1990). Cell cycle studies of the dinoflagellates Gonyaulax polyedra Stein and Gyrodiniumun catenum Hulburt during sexual and asexual reproduction. J. Exp. Mar. Biol. Ecol. 135, 69-84.

Cloern, J. E. (1996). Phytoplankton bloom dynamics in coastal ecosystems: a review with some general lessons from sustained investigation of San Francisco Bay, California. Rev. Geophys. 34, 127-168.

Cullen, J. J. (1982). The deep Chlorophyll maximum: comparing vertical profiles of Chlorophyll a. Can. J. Fish. Aquat. Sci. 39, 791-803.

Dhib, A., Frossard, V., Turki, S., and Aleya, L. (2013). Dynamics of harmful dinoflagellates driven by temperature and salinity in a northeastern Mediterranean lagoon. Environ. Monit. Assess. 185, 3369-3382.

Dubelaar, G. B. J., Geerders, P. J. F., and Jonker, R. R. (2004). High frequency monitoring reveals phytoplankton dynamics. J. Environ. Monit. 6, 946-952.

Dubelaar, G. B. J., and Gerritzen, P. L. (2000). CytoBuoy: a step forward towards using flow cytometry in operational oceanography. Sci. Mar. 64, 255-265.

Dubelaar, G. B. J., and Jonker, R. R. (2000). Flow cytometry as a tool for the study of phytoplankton. Sci. Mar. 64, 135-156.

Durand, M. D. (1995). Phytoplankton Growth and Diel Variations in Beam Attenuation Through Individual Cell Analysis. Thèse de doctorat, MIT/WHOI.

Eppley, R. W. (1972). Temperature and phytoplankton growth in the sea. Fish. Bull. 70, 1063-1085.

Eppley, R. W., Rogers, J. N., and McCarthy, J. J. (1969). Half-saturation constants for uptake of nitrate and ammonium by marine phytoplankton. Limnol. Oceanogr. 14, 912-920.

Field, C. B., Behrenfield, M. J., Randerson, J. T., and Falkowski, P. G. (1998). Primary production of the biosphere: integrating terrestrial and oceanic components. Science 281, 237?240.

Figueroa, R. I., Bravo, I., Ramilo, I., Pazos, Y., and Morono, A. (2008). New life-cycle stages of Gymnodinium catenatum (Dinophyceae): laboratory and field observations. Aquat. Microb. Ecol. 52, 13-23.

Gisselson, L. A., Graneli, E., and Carlsson, P. (1999). Using cell cycle analysis to estimate in situ growth rates of the dinoflagellates Dinophysis acuminate: draw-backs of the DNA quantification method. Mar. Ecol. Prog. Ser. 184, 55-62.

Goldman, J. C., McCarthy, J. J., and Peavey, D. G. (1979). Growth rate influence on the chemical composition of phytoplankton in oceanic waters. Nature 279, 210-215.

Gouze, E., Raimbault, P., Garcia, N., Bernard, G., and Picon, P. (2008). Nutrient and suspended matter discharge by tributaries into the Berre Lagoon (France): the contribution of flood events to the matter budget. C. R. Geosci. 340, 233-244.

Hutchinson, G. P. (1961). The paradox of the plankton. Am. Nat. 95, 137-145.

Jacquet, S., Lennon, J. F., Marie, D., and Vaulot, D. (1998). Picoplankton population dynamics in coastal waters of the Northwestern Mediterranean Sea. Limnol. Oceanogr. 43, 1916-1931.

Ji, R., and Franks, P. J. S. (2007). Vertical migration of dinoflagellates: model analysis of strategies, growth and vertical distribution patterns. Mar. Ecol. Prog. Ser. 344, 49-61.

Kiefer, D. A., Olson, R. J., and Wilson, W. H. (1979). Reflectance spectroscopy of marine phytoplankton. Optical properties as related to age and growth rates. Limnol. Oceanogr. 24, 664-672.

Kim, K. T. (1983). Production primaire pélagique de l'Etang de Berre en 1977 et 1978. Comparaison avec le milieu marin (Méditerranée nord-occidentale). Mar. Biol. 73, 325-341.

Kremp, A. (2013). Diversity of dinoflagellates life cycles: facets and implications of complex strategies, in Biological and Geological Perspectives of Dinoflagellates, eds J. Lewis, F. Marret, and L. Bradley (London: The Micropalaeontological Society; Special Publications; Geological Society), 197-205.

Kremp, A., and Heiskanen, A. S. (1999). Sexuality and cyst formation of the spring-bloom dinoflagellate Scrippsiella hangoei in the coastal northern Baltic Sea. Mar. Biol. 134, 771-777.

Kudela, R. M., Lane, J. Q., and Cochlan, W. P. (2008). The potential role of anthropogenically derived nitrogen in the growth of harmful algae in California, USA. Harmful Algae 8, 103-110.

Legendre, L., and Demers, S. (1985). Auxiliary energy, ergoclines and aquatic biological production. Nat. Can. 112, 5-14.

Legendre, L., and LeFèvre, L. (1989). Hydrodynamical singularities as controls of recycled versus export production in oceans, in Productivity of the Ocean: Present and Past, ed W. H. Berger (Chichester: John Wiley Sons), 44-63.

Leredde, Y., Dekeyser, Y., and Devenon, J. L. (2002). T-S data assimilation to optimize turbulent viscosity: an application to the Berre lagoon hydrodynamics. J. Coast. Res. 18, 555-567.

Lomas, M. W., Roberts, N., Lipschultz, F., Krause, J. W., Nelson, D. M., and Bates, N. R. (2009). Biogeochemical responses to late-winter storms in the Sargasso Sea IV. Rapid succession of major phytoplankton groups. Deep Sea Res. Part I Oceanogr. Res. Pap. 56, 892-909.

Malkassian, A. (2012). Methodes d'analyse Fonctionnelle et Multivariee Appliquees à l'etude du Fonctionnement Ecologique des Assemblages Phytoplanctoniques de l'etang de Berre. These de doctorat, Universite d'Aix-Marseille, France.

Margalef, R. (1978). Life-forms of phytoplankton as survival alternatives in an unstable environment. Oceanol. Acta 1, 493-509.

Matsubara, T., Nagasoe, S., Yamasaki, Y., Shikata, T., Shimasaki, Y., Oshima, Y., et al. (2007). Effects of temperature, salinity, and irradiance on the growth of the dinoflagellate Akashiwo sanguinea. J. Exp. Mar. Biol. Ecol. 342, 226-230.

Minas, M. (1976). Production organique primaire dans un milieu saumâtre eutrophe (Etang de Berre). Effets d'une forte dilution (dérivation des eaux de la Durance). Mar. Biol. 35, 13-29.

Nerini, D., Mante, C., Durbec, J.-P., and Garcia, F. (2001). Une méthode statistique de détermination de séquences caractéristiques dans une série temporelle de plusieurs variables. Application à la physico-chimie des eaux de l'étang de Berre. C.R.Acad.Sci.II.332,457-464.

Nielsen, M. V. (1996). Growth and chemical composition of the toxic dinoflagellate Gymnodinium galatheanum in relation to irradiance, temperature and salinity. Mar. Ecol. Prog. Ser. 136, 205-211.

Olson, R. J., Shalapyonok, A., and Sosik, H. M. (2003). An automated submersible flow cytometer for analyzing pico- and nanophytoplankton: FlowCytobot. Deep Sea Res. Part I Oceanogr. Res. Pap. 50, 301-315.

Peeters, J. C. H., Dubelaar, G. B. J., Ringelberg, J., and Visser, J. W. M. (1989). Optical plankton analyser: a flow cytometer for plankton analysis, 1: design considerations. Cytometry 10, 522-528.

Pfiester, L. A., and Anderson, D. M. (1987). Dinoflagellates reproduction, in Botanical Monographs, Chapter 14, Vol. 21, ed F. J. R. Taylor (Oxford: Blackwell Scientific Publications), 611-648.

Pinheiro, J. C., and Bates, D. M. (2000). Mixed-Effects Models in S and S-Plus. New York, NY: Springer-Verlag.

Pitcher, G. C., Boyd, A. J., Horstman, D. A., and Mitchell-Innes, B. A. (1998). Subsurface dinoflagellate populations, frontal blooms and the formation of red tide in the southern Benguela upwelling system. Mar. Ecol. Prog. Ser. 172, 253-264.

Raimbault, P., Beker, B., Garcia, N., Fornier, M., and Gouze, E. (2013). L'étang de Berre, cycle de la matière, production primaire et communautés phytoplanctoniques, in LAGUN?R, ed GIPREB (Étang de Berre).

Ralston, D. K., McGillicuddy, D. J., and Townsend, D. W. (2007). Asynchronous vertical migration and bimodal distribution of motile phytoplankton. J. Plankton Res. 29, 803-821.

Rantajärvi, E., Olsonen, R., Hällfors, S., Leppänen, J. M., and Raateoja, M. (1998). Effect of sampling frequency on detection of natural variability of phytoplankton: unattended high-frequency measurements on board ferries in the Baltic Sea. J. Mar. Sci. 55, 697-704.

Riley, G. A., Stommel, H., and Bumpus, D. F. (1949). Quantitative ecology of the plankton of the Western-North Atlantic. Bull. Bingham Oceanogr. Collect. 12, 1-169.

Schindelin, J., Arganda-Carreras, I., Frise, E., Kaynig, V., Longair, M.,

Pietzsch, T., et al. (2012). Fiji: an open-source platform for biological-image analysis. Nat. Methods 9, 676-682.

Schnepf, E., and Elbrachter, M. (1992). Nutritional strategies in dinoflagellates. Eur. J. Protistol. 28, 3-24.

Sieracki, C. K., Sieracki, M. E., and Yentsch, C. S. (1998). An imaginig-in-flow system for automated analysis of marine microplankton. Mar. Ecol. Prog. Ser. 168, 285-296.

Simon, N., Barlow, R. G., Marie, D., Partensky, F., and Vaulot, D. (1994). Flow cytometry analysis of oceanic photosynthetic picoeukaryotes. J. Phycol. 30, 922-935

Smayda, T. J. (1997). Harmful algal blooms: their ecophysiology and general relevance to phytoplankton blooms in the sea. Limnol. Oceanogr. 42, 1137-1153

Sosik, H. M., Olson, R. J., Neubert, M. G., and Shalapyonok, A. (2003). Growth rates of coastal phytoplankton from time-series measurements with a submersible flow cytometer. Limnol. Oceanogr. 48, 1756-1765.

Stoecker, D. K. (1999). Mixotrophy among dinoflagellates. J. Eukaryot. Microbiol. 46, 397-401.

Sweeney, B. M. (1959). Endogenous diurnal rhythms in marine dinoflagellates, in International Oceanography Congress Preprints, ed M. Sears (Washington, DC: America Association for the Advancement of science), 204-207.

Thomas, W. H. (1975). Effects of temperature and illuminance on cell division rates of three species of tropical oceanic phytoplankton. J. Phycol. 11, 17-22.

Thyssen, M., Mathieu, D., Garcia, N., and Denis, M. (2008). Short-term variation of phytoplankton assemblages in Mediterranean coastal waters recorded with an automated submerged flow cytometer. J. Plankton Res. 30, 1027-1040.

Thyssen, M., Garcia, N., and Denis, M. (2009). Sub mesoscale phytoplankton distribution in the North East Atlantic surface waters determined with an automated flow cytometer. Biogeosciences 6, 569-583.

Thyssen, M., Beker, B., Ediger, D., Yilmaz, D., Garcia, N., and Denis, M. (2011). Phytoplankton distribution during two contrasted summers in a Mediterranean harbour: combining automated submersible flow cytometry with conventional techniques. Environ. Monit. Assess. 173, 1-16.

Thyssen, M., Grégori, G. J., Grisoni, J., Pedrotti, M., Mousseau, L., Artigas, L. F., et al. (2014). Onset of the spring bloom in the northwestern Mediterranean Sea: influence of environmental pulse events on the in situ hourly-scale dynamics of the phytoplankton community structure. Front. Microbiol. 5:387.

Townsend, D. W., Pettygrew, N. R., and Thomas, A. C. (2001). Offshore of the red tide dinoflagellates Alexandrium sp. in the gulf of maine. Cont. Shelf Res. 21, 347-369.

Ulses, C., Grenz, C., Marsaleix, P., Schaaff, E., Estournel, C., Meulé, S., et al. (2005). Circulation in a semi-enclosed bay under influence of strong freshwater input. J. Mar. Syst. 56, 113-132.

Vaulot, D., and Marie, D. (1999). Diel variability of photosynthetic picoplankton in the equatorial Pacific. J. Geophys. Res. 104, 3297-3310.

Von Stosch, H. A. (1973). Observations on vegetative reproduction and sexual life cycles of two freshwater dinoflagellates, Gymnodinium pseudopalustre Schiller Woloszynskia apiculata sp. Nov. Br. Phycol. J. 8, 105-134

Walker, L. M. (1982). Evidence for a sexual cycle in the Florida red tide dinoflagellate Ptychodiscus brevis (=Gymnodinium breve). Bioscience 32, 809-810.

Weiler, C. S., and Chisholm, S. W. (1976). Phased cell division in natural populations of marine dinoflagellates from shipboard cultures. J. Exp. Mar. Biol. Ecol. 25, 239-247.

Yamamoto, T., OH, S. J., and Kataoka, Y. (2002). Effects of temperature, salinity and irradiance on the growth of the toxic dinoflagellates Gymnodinium catenatum (Dynophyceae) isolated from Hiroshima Bay, Japan. Fish. Sci. 68, 356-363.

# 4.0 Phytoplankton production in surface open waters: Integration of *in situ* flow cytometry and modeling for the DEWEX cruises

**Abstract**

We present the estimations of *in situ* growth rates of populations of Synechococcus, pico- and nano-eukaryotes and cryptophytes, using automated flow cytometry in surface open waters. Automated analyses were scheduled with a Cytosense every hour along the R/V Suroit trajectory during the DeWEX cruises (NW Mediterranean Sea). Cruises were held in wintertime, when phytoplankton is limited by light but nutrients are bought to the surface by a strong mixing, and during the consecutive spring bloom. Growth rates were formally turned into apparent primary productivity (NPP$^*$) after conversion of cell size into C quota. We constrained our estimations within the distinct water masses by integrating a regional circulation scheme along with the continuous measurements of hydrological characteristics. The high standing stock drove high NPP$^*$ during the bloom. Maximal production rates were achieved by nanoeukaryotes (800 mg C.m$^{-3}$.d$^{-1}$). After subsequent high division rates (> 1 division.d$^{-1}$), the initial stock of nanoplankton attained 3.10$^4$ cells.cm$^{-3}$ in spring. Picoeukaryotes maximal production rates was lower (50 mg C.m$^{-3}$.d$^{-1}$) due to their difference in C quota. The population noteworthy displayed the highest division rates (> 2 divisions.d$^{-1}$) during the cruise. Cryptophytes showed similar production rates with a peak of abundance at 5.10$^3$ cells.cm$^{-3}$ in spring while Synechococcus could be density-dominant (10$^5$ cells.cm$^{-3}$) but with the lowest values of NPP$^*$ (< 1 mg C.m$^{-3}$.d$^{-1}$). The examination of PAR, temperature and nutrients controls further highlights the importance of losses rates to differentiate the winter convection and the bloom in the NW Mediterranean Sea.

M. Dugenne, M. Thyssen, D. Lefèvre, P. Conan, C. Estournel, X. Durrieu de Madron, V. Taillandier, C. Bachet, O. Grosso, M. Goutx, T. Séverin, F. Touratier, I. Taupier-Letage, M. Pujo-Pay, D. Pommeret, G. Grégori

## 4.1 Introduction

Phytoplankton groups a coherent unit of unicellular and colonial microorganisms sharing universal structural and functional characteristics. It embodies a fundamental compartment for Earth climate. Cells, distributed on the 70% of the biosphere coverage and along a 200 m deep vertical gradient (i.e. euphotic zone), are actively involved in anthropic gas emissions sequestration by photosynthetic assimilation of the dissolved atmospheric $CO_2$ [Longhurst, 1991]. To understand its role in the carbon pump [Siegenthaler and Sarmiento, 1993], estimation of phytoplankton production is primordial. Primary based on the $^{14}C$ uptake bulk approach [Steeman-Nielsen, 1952], present evaluations are mainly derived from remote sensing ocean colour, converted to biomass production onto synoptic maps [Field et al., 1998]. The oceanic annual production

reaches 45 Pg C.year$^{-1}$, representing 50% of the global $CO_2$ uptake [Berhenfeld et al., 2001]. This flux reflects the high turnover of the autotrophic biomass. Present in transient states that last from days to months [Cloern, 1996], rapid cell divisions are determinant to renew the stock of organic matter that transits along the trophic networks and is exported towards the deep ocean. The fate of the particulate organic carbon is influenced by many factors, including the community of phytoplankton [Legendre, 1990]. While bulk methods (fluorometry, $^{14}C$ uptake) suffer from the integration of any coarse diversity, also involved in ocean stoichiometry [Redfield, 1934; Bonachela et al., 2015], biogeochemical models presently differentiate several Phytoplankton Functional Types (PFTs) compartments [Le Quéré et al, 2005]. They are considered as important if not the main drivers of large scale biogeochemical cycles in the ocean. Among these biogeochemical cycles prevail the functioning of nitrogen fixer [Sohm *et al.*, 2011], dimethylsulfide (DMS) producers [Yoch, 2002], calcifiers [Omta *et al.*, 2013] and silicifiers [Krause, 2008]. The efficiency of carbon uptake and subsequent sequestration varies among groups [Lochte et al., 1993; Le Moigne *et al.*, 2015]. Since it is genuinely shaping the marine biological pump in the ocean [Legendre and Le Fèvre, 1989], size fractions are also considered as PFTs. At present, few methods are able to assess a singular estimation of phytoplankton entire biomass distributions. The fractional contribution of phytoplankton populations to bulk biomass can be measured from remote sensing, fixing the signature of diagnostic pigments to a given size spectra [Uitz *et al.*, 2006; Ciotti and Bricaud, 2006; Brewin *et al.*, 2010; Hirata *et al.*, 2011]. In 2008, Nair *et al.* highlighted the potential of flow cytometry to monitor the trends of PFTs spatial distribution. Flow cytometry has long been involved in discovery and quantification of the presence of the small fraction of phytoplankton cells in the ocean [Chisholm et al., 1988; Chretiennot-Dinet et al., 1995]. The larger size classes remained unresolved until the development of a new generation of flow cytometers specifically designed to aquatic studies. Upgraded instruments determine the occurrence of the broad range of PFTs size grouped by cellular optical properties (light scatter and fluorescence intensities) and images recognition [Rutten et al., 2005; Zhou et al., 2012; Dugenne et al., 2015]. The study of Thyssen *et al.* [2015] was pioneer to initiate the coupling of remote sensing algorithm with advanced flow cytometry to extrapolate the spatial coverage of PFTs community in the North Sea.

Since Ocean Biogeochemical Models (OBM) cope with a manageable complexity [Dickey, 2002], there is a need of sufficiently detailed datasets [Anderson, 2005] to closely adjust *in situ* observations [Friedriches et al., 2007; Friedriches et al., 2009; Doney et al., 2009]. Models are currently parameterise by data assimilation and statistical inference on the current knowledge on phytoplankton physiology and biological rates (e.g. Nutrient assimilation, intrinsic growth, selective grazing, sinking). One group of the Intergovernmental Panel on Climate Change (IPCC) consolidates the work made on Impacts, Adaptation and Vulnerability of organisms confronted to Global Change. It will require simulating the dynamic estimation of these rates in the scope of environmental scenario to anticipate the potential resilience or evolution of PFTs [Collins et al., 2013]. OBM extrapolations are strongly dependent on high frequency inventories of biological data. Biogeochemical fluxes are modulated by the coupled dynamics of physical and ecological processes; thus, underestimation of pulse events and mesoscale structures influence, determinant for primary production, is an issue [Field et al., 1993; Robinson and Lermusiaux, 2002]. Phytoplankton cells tend to divide asexually, entertained by a circadian clock. Their in-

herent plasticity is endowed by the overlap of this daily lifetime with the evolutionary scale. If it endorses various levels of sensitivity in non-equilibrium environments, only single-cell analyses can reveal phytoplankton physiological dynamics. Because it is independent of external factors over short time scales, flow cytometry-derived cell size measurements represents one approach that yield to population *in situ* growth rates predictions [Sosik et al., 2003]. Operated at high frequency (hourly timescale), flow cytometry analyses unravel the shift of cells size observed sequentially as a close indication of cells entering interphase then mitosis stages of the cell cycle [Durand, 1995; Binder et al., 1996]. Formally converted to cell cycle proxy, the diel variations of populations optical properties and image-based stages classification bring strong clues to investigate the variability of primary production from bloom areas [Campbell et al., 2010; Dugenne et al., 2014; Brosnahan et al., 2015] to oligotrophic ecosystems [Hunter-Cervera et al., 2014; Ribalet et al., 2015].

The Mediterranean Sea hosts both bloom and perennial oligotrophic biomasses in less than 1% of the worlds ocean surface [D'Ortenzio and D'Alcala, 2009; Mayot et al., 2016]. It counts 1740 species out of the $\backsim$ 4000 phytoplankton global species diversity [Sournia et al., 1991; Coll et al., 2010]. This biodiversity 'hot spot' is particularly threatened by the evolution of the climate [Mermex group, 2011]. Scientists expect a great repercussion on its biogeochemistry, mediated by phytoplankton resilience or reorganisation. Analogies with global thermohaline circulation [Robinson and Golnaraghi, 1994] combined with a high anthropic pressure indicate the Mediterranean Sea as a reference to foresee the Global Change on a mesoscopic frame [Béthoux et al., 1999]. The Deep Water EXperiment (DeWEX) cruises, in the framework of the French scientific program Mermex, were held in 2013 in order to provide an insight into the current biogeochemical functioning of the provençal basin. Contrasting with the oriental basin, this site regularly accumulates high chlorophyll concentration over the spring period, when fertilized by nutrients upwelling in wintertime. In general, oligotrophy limits the biological pump resulting in small annual carbon sequestration budget ($8.64\ \ 10^{-3}$ Pg C.year$^{-1}$) compared to the global ocean (0.33 Pg C.year$^{-1}$) [Guidi et al., 2015]. Two Legs were scheduled in February and April to provide an insight into the biogeochemical functioning of recent contrasted periods, the wintertime formation of Western Mediterranean Deep Water, analogue to upwellings of the global *conveyor belt* [Borile, 2016], and the consecutive spring bloom, by means of high frequency biogeochemical analyses. With a core focused on the evaluation of primary production during two contrasted periods, the DeWEX cruises covered the high spatio-temporal resolution of PFTs assemblages to unlace their inherent dynamics. The objectives of this study are (i) to propose a methodological workflow to analyse the high frequency flow cytometry datasets collected from spatio-temporal continuum with the aim of (ii) estimating group-specific growth rates/production rates without extensive manipulations and provide (iii) valuable informations on the functional mechanisms driven by winter deep water convection and spring blooms.

## 4.2 Material and Methods

DeWEX: Study area and Sampling strategy

The Deep Water formation EXperiment (DeWEX) cruises were held in February (from Feb-02 to Feb-21, doi:10.17600/13020010) and April (from Apr-02 to Apr-25, doi:10.17600/13020030) 2013 on board of the R/V Suroit. Its trajectory covered the extended Gulf of Lions shelf limited at the East by the Corsican shelf and at the South by the Balearic salinity front (Fig.1).

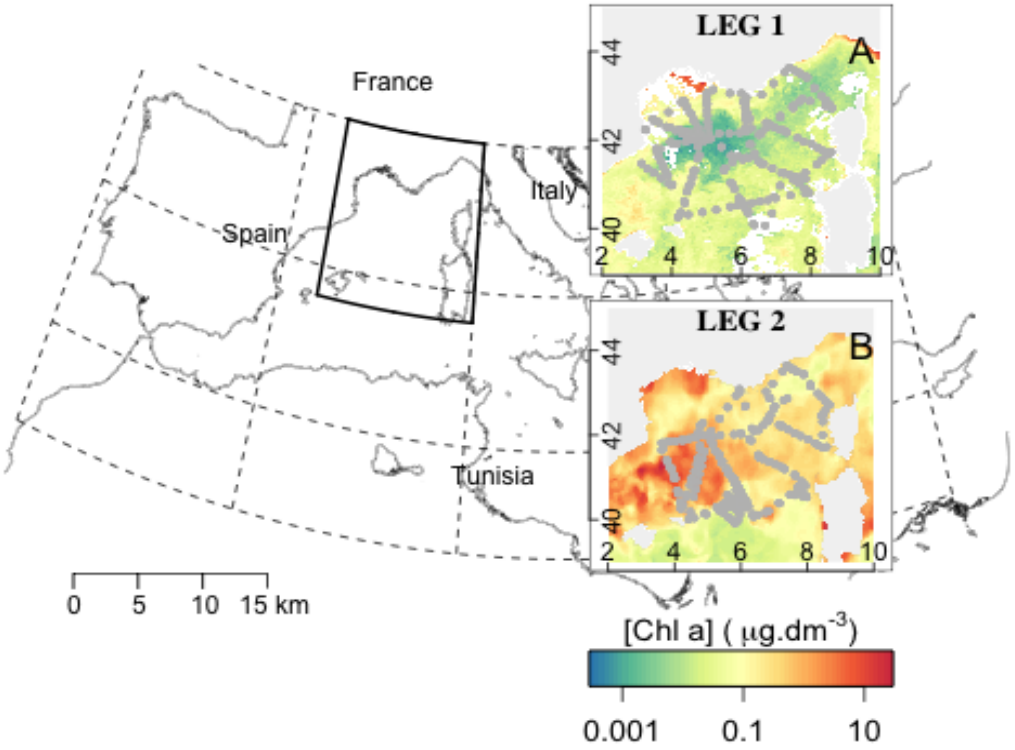


Figure 4.1: North Western Mediterranean Sea: DeWEX spatiotemporal stations (grey dots) superimposed on MODIS (ocean colour) daily interpolated chlorophyll a (http://marine.copernicus.eu/, dataset-oc-med-chl-modis-a-l4-interp-4km-daily-rt-v02) snapshots representative of the Leg 1 (2013-02-01) (A) and the Leg 2 (2013-04-01) (B)

A total of 75 and 100 stations were scheduled during Leg 1 and Leg 2 respectively for the deployment of vertical casts. Casts were monitored in real time by a rosette-mounted equipment including a temperature, conductivity CTD SBE911, a dissolved oxygen sensor SBE43, a Chl a fluorescence fluorometer and a large band radiometer for PAR quantification. Nutrients ($NO_2^-$, $NO_3^-$, $PO_4^{3-}$,$Si(OH)_4$) were collected at 12 discrete depth for analyses by a Seal AA3 auto-analyzer (detection limits: 0.02 $\mu$M, 0.01 $\mu$M, 0.01 $\mu$M, 0.05 $\mu$M) and $NH_4^+$ by a JASCO FP 2020 spectrofluorometer (detection limit: 0.002$\mu$M), in addition to confocal microscopy identification and enumeration of micro and nanophytoplankton (Uthermol). In parallel, a variety of automated sensors, forming the *Surface water continuous acquisition system* (SACES), performed high frequency analyses on a dedicated inflow of surface water pumped continuously at 3 m depth. Biogeochemical sensors were sequentially plugged to the continuous subsurface water inflow to characterise subsurface structures. During the two legs, the R/V was sailing at a mean speed of 5 kn. Analyses of the sensors were scheduled at high frequency in order to map the mesoscale changes of temperature and salinity (thermosalinograph, CTD), Chl a fluorimetry (Fluorometer Westab), turbidity (Turbidity meter OBS Seapoint), $O_2$ concentration (optode), $pCO_2$ (SAMI-$CO_2$) and of phytoplankton abundance with their optical properties (Cytosense, Cytobuoy b.v.). Water was pumped with a STOMOPOM pump to avoid biological contamination with a continuous flow rate of 5 $dm^3.min^{-1}$. Sensors analyses were coupled to the free surface, generalised sigma vertical coordinate, 3D model SYMPHONIE

described by Marsaleix et al. [2009, 2012]. This model has previously been used in the Mediterranean to simulate convection in the open sea [Estournel et al., 2016], ocean circulation on the slope [Rubio et al., 2009] and on the continental shelf [Petrenko et al., 2008]. The configuration used is described in [Estournel et al., 2016] with a horizontal resolution of 1 km. Symphonie provided predictions of the mixed layer depth, defined at the max depth where the temperature gradient does not exceed 0.2°C after 10m. The incident irradiance and the wind speed are given by the ECMWF operational forecasts at 1/8° horizontal resolution and 3 hours temporal resolution. These forecasts were derived from the daily analysis at 00.00 UTC. The mixed layer depth, the irradiance and the wind speed are extracted following the SACES sampling strategy in space and time.

The Cytobuoy manufactured Cytosense is an automated flow cytometer developed to account for the naturally wide range of phytoplankton size and abundance in *in situ* samples. Samples are driven towards the flow cell by a calibrated peristaltic pump running between $<1$ $\mu$l.s$^{-1}$ and 20 $\mu$l.s$^{-1}$. Volume estimations allow phytoplankton abundance to be directly estimated from the counts of phytoplankton cells triggered by the emission of chlorophyll a (*Chl a*) induced Red fluorescence by a 488 nm exciting laser beam (Coherent, 20 mW). During the cruises, the sample flow rate was set at 10 $\mu$l.s$^{-1}$ for two distinct protocols. A 3 min acquisition, resulting in $\backsim$1.5 cm$^3$ analysed per sample, with a threshold of 8 mV was used for the quantification of abundant small size phytoplankton. An extended volume of 5 cm$^3$ was analysed for larger cells with a threshold at 10 mV. The laminar flow of single cells was driven by a particles-free sheath fluid composed of 0.2 $\mu$m filtered seawater. Laser scattering at small angles (FWS) was collected by two distinct photodiodes to check for the sample core alignment. The sideward angle laser scatter (SWS) and Yellow (FLY), Orange (FLO) and Red (FLR) fluorescences were amplified by non-modular PMT tubes. The integrated signal of each channel was recorded along the laser beam width (5 $\mu$m) with a frequency of 4 MHz as a diagnostic tool to discriminate phytoplankton groups based on optical fingerprints. Different sets of 2D projections were plotted in Cytoclus® software to manually gate phytoplankton groups. Groups concentration (cells.cm$^{-3}$), mean (a.u.cell$^{-1}$), sum (product of mean properties per groups concentration, a.u.cm$^{-3}$) and entire distribution of optical properties, light scatter and fluorescence intensities, were processed from the software to assess their inherent dynamics. Up to 150 pictures of microphytoplankton were automatically taken during each acquisition by an *image-in-flow* camera mounted upward the flow cell. The combination of standards beads (PolyScience® Yellow Green Polystyrene $2.0\,\mu m, 3.0\,\mu m, 6.0\,\mu m, 10.0\,\mu m, 20.0\,\mu m$ diameter) and pictures FWS signal were used to convert light scatter to size. A power law relationship explained 91% of the volume variance ($n$ = 20, $R^2$ = 0.95). Volume was calculated from the equivalent spherical diameter (ESD) for standards beads and extrapolation of the pixels distance map for pictures [Moberg and Sosik, 2012].

Growth and primary production rates: Workflow for DeWEX surface continuum

We provide a workflow to analyse the continuous collection of phytoplankton optical properties by automated flow cytometry, with stages detailed in this section. To integrate the spatio-temporal resolution of DeWEX surface continuum, we recommend to (i) identify the distinct water types that hosted different stages of populations through hydrological characteristics, (ii) improve the separation of water masses by resolving the Eulerian trajectories by means of a regional circulation grid,

in order to discriminate the 24 h coherent time series of plankton dynamics. Passed the clustering of the SACES stations, the time series of group-specific size distribution are used to (iii) estimate *in situ* growth rates by a size-structured population model with (iv) productivity using a size to carbon conversion.

**Surface waters Typology**

The application of the size-structured population model to indicate the amount of dividing cells over 24 hours is strongly dependent on the coherence of the diel variation of size distribution. The coherence of plankton dynamics is especially dependent of the successive cell cycle stages populations are experimenting. During DeWEX cruises, all populations defined by flow cytometry were consistent in terms of fluorescences and size estimates for the duration of the two legs. However, in 24 hours, the R/V has crossed different water masses, and hydrologic gradients influenced the continuity of populations dynamics. In general, the dynamics of phytoplankton is non-linearly limited [Geider, 1984] by temperature [Eppley, 1972], light for photosynthetic utilisation [Ryther and Menzel, 1959; Steele, 1962], both in term of quantity (integrated irradiance) and quality (photoperiod), and nutrients concentrations [Droop, 1973]. All variables are influenced by the mixed layer depth causing cells to experiment a longer period out of the euphotic layer, live in cool and enriched mixed water masses when deepened [Marra, 1980]. To account for these gradients, we propose to define the typology of the surface waters present during each Leg and restrict the prediction of populations' growth rates within homogeneous types only. The surface waters typology was based on a statistic partition of the horizontal stations according to the following algorithm:

1. Measures of temperature, salinity, mixed layer depth (MLD) and incident irradiance (PAR) coinciding with flow cytometry analyses were grouped in a distinct table of dimensions $n$ *observations* x 4 *variables*. Temperature and salinity were measured by the thermosalinograph during the $1^{st}$ Leg and the CTD during the $2^{nd}$ Leg, whereas MLD and PAR were predicted from the model Symphonie. Nutrients were quantified in discrete bottles only, thus no directly implicated in the algorithm. However, surface collected samples for $NO_3^-$, $NH_4^+$, and $PO_4^{3-}$ quantification, were used to validate the classification of waters typology a posteriori.

2. Each variable, $x^{Temperature/Salinity/MLD/PAR}$, distribution was fitted to a finite mixture of univariate Gaussian distributions, $\prod_{i=1}^{n}\sum_{k=1}^{G} p_k N_k(x_i \mid \mu_k, \sigma_k)$, whose parameters, $\theta_k = \{p_k, \mu_k, \sigma_k\}$, were optimally inferred by an iterative EM algorithm. The number of mixture components, G, was selected in the space of positive integer $\mathcal{Z}^+$ in order to minimise the Bayesian Information Criterion (BIC) defined as $-2\log likelihood(x, \theta_k) + 3G.log(n) - 1$. Proof of the heterogeneity of the observed distributions has been demonstrated using the parametric bootstrap of the likelihood ratio statistics ($LR = 2.(\log likelihood_{|H_1} - \log likelihood_{|H_0})$) to test for $(H_0) : G = 1$ and $(H_1) : G>1$ [McLachlan, 1897]. Differences of mixture locations ($\mu_{k=1,...,G}$) has been tested through the asymptotic $\mathcal{X}^2$ assumption. Station corresponding to observation $x_i$ was assigned to one component according to its posterior probability, $\tau_k = \frac{p_k f_k(x,\theta_k)}{\sum_l^G p_l f_l(x,\theta_l)}$, with $p_k$ the mixture proportions. The vector of resulting $\tau_k$ was ultimately used to classify stations according to temperature, salinity, MLD and PAR fitted

densities.

3. Each station was combined with observations of the same cluster according to the 4 classifications. Combinations were reduced to exclusive association by binary intersection until the minimal partition was reached.

Weights were applied to the hydrologic dataset to constrained similar environmental conditions by the matrix of oceanographic distances (See following section). The idea was to take into account the surface water circulation to predict the path of the different water masses the R/V crossed on its trajectory. Since, given the trajectories of the 2 Legs, we appeared to analyse stations close in space but with a lag time of several days, the connection of such stations required to correct their apparent proximities, in terms of hydrologic variables, by oceanographic distances. Thus, unless the circulation was rotating, stations that were close in space but separated by days will display an increased distance after correction.

**Plankton Eulerian trajectories**

Aviso Mediterranean products consist in daily grid (1/8° cartesian resolution) of geostrophic velocities determined from the Absolute Dynamic Topography (ADT) and Sea-Level Anomalies (SLA) altimetry datasets (Topex/Poseidon, Jason). Altimeter products are produced by Salto/Duacs and distributed by Aviso, with support from Cnes (http://www.aviso.altimetry.fr/duacs/).
This product shows good agreement with regional *in situ* observations [Jebri *et al.*, 2016]. The daily currents components were compared to the shipboard mounted ADCP(150 kHz BB-RDI) measurements, corresponding to the daily grid and rescaled to Aviso mesh, acquired along the R/V track (data not shown). The Root Mean Squared Error gave the optimal correspondence between Aviso circulation and *in situ* measurements for the 2 legs of DeWEX with $R^2$=0.63. ADCP horizontal/vertical components were filtered under the threshold of 5 $m.s^{-1}$ and saved in a netcdf format after processing by the IFREMER CASCADE matlab program. The magnitude of vertical velocities had a mean of -10 $cm.s^{-1}$ for Leg 1, including the strong mixing patch, and -15 $cm.s^{-1}$ for Leg 2, which yields to negligible vertical advection considering our sampling strategy, O(37-52 $m.h^{-1}$) respectively. Plankton displacement was consequently calculated on a horizontal plan only.

This synoptic flow field was used to integrate plankton trajectories by propagation of the spatial location of each station under daily currents velocities, for a duration equivalent to their lag time with the last station of the Leg. Trajectories were computed using a first order Eulerian (i.e. observing the flow from a fixed point in space) numerical integration of the currents horizontal components, $U(x,y,t) = \{u(x,y,t), v(x,y,t)\}$, in the Cartesian plan with a time step of 5 min (E 1).

$$Stream^{x_0}(t) = x_0 + \int_0^t U(x,y,t).dt \quad (4.1)$$

For each station, 100 streamlines were integrated from positions uniformly distributed within the corresponding grid point (1/8° x 1/8°) to account for the model spatial resolution (Fig. 2).

An oceanographic distances matrix was constructed using the average distance between the sequence of consecutive stations locations and the streamlines locations after the corresponding transport time (E 2) (Fig. 3).

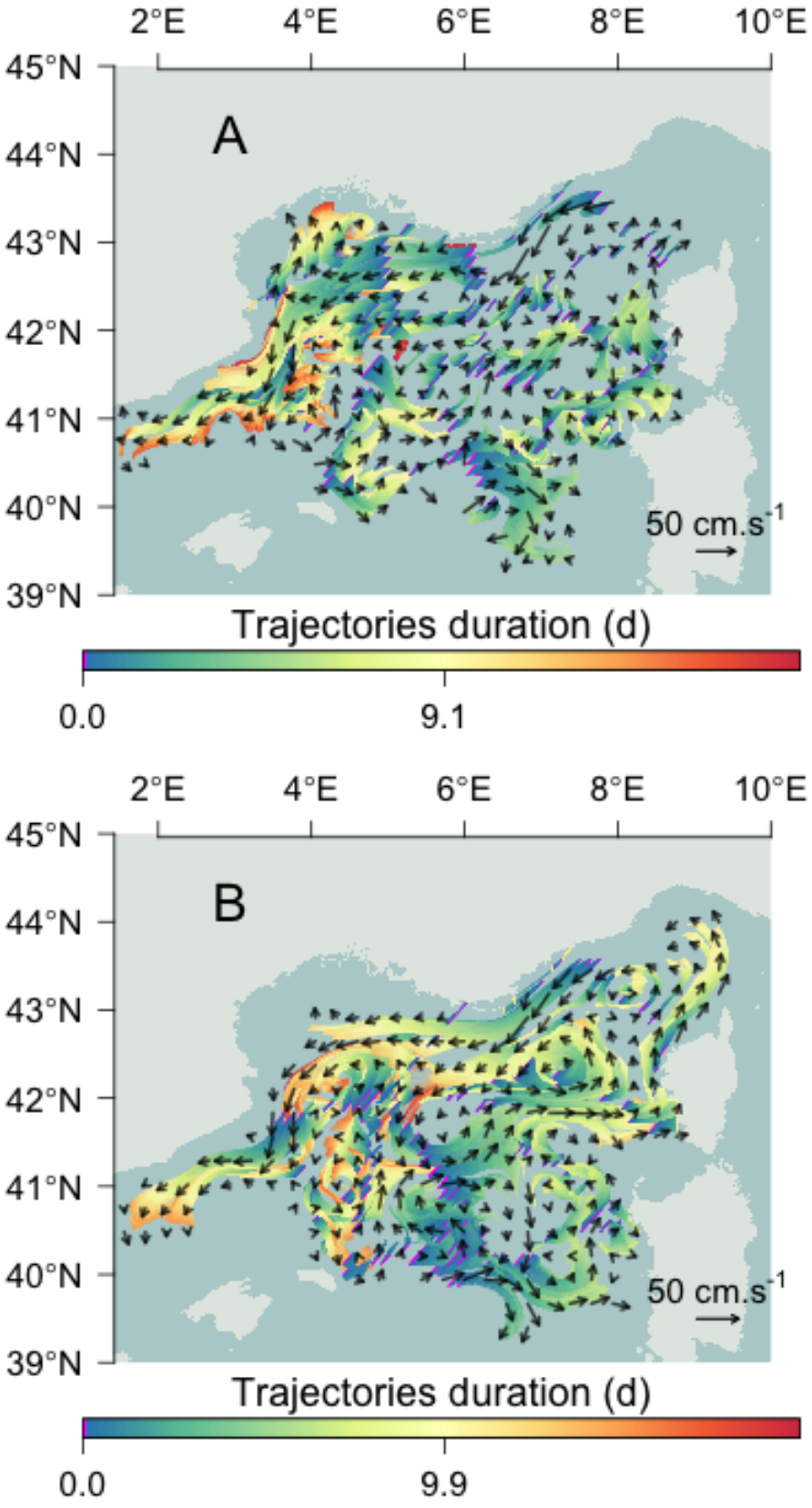


Figure 4.2: Leg 1 (A) and Leg 2 (B) maps of particles trajectories (colored dots) integrated by means of daily altimetry-derived surface currents grid (black arrows) from each station (magenta dots) for a duration equivalent to the entire Leg (20 days).

$$distance(station_{|x_0=(x,y,t)}, station_{|x_n=(x',y',t+n.sampling\ frequency)}) =$$

$$\overline{distance(station_{|x_n=(x',y',t+n.sampling\ frequency)}, Stream^{x_0}(t+n.sampling\ frequency))} \quad (4.2)$$

The forward advection of the flow stream was used to locate consecutive stations positioned along these streamlines and estimate growth rates, $\mu_{Ab}$, from their net abundance changes within a pseudo-Lagrangian (i.e. following the flow of particles) frame [De Verneil and Franks, 2015]. The approach is not truly Lagrangian, as the second order particles diffusion, characterised by *in situ* eddy diffusivity coefficients, was not included to calculate the streamlines from partial differential equations.

**Growth rates modeling**

Plankton organisms drift with currents in natural environments. Their apparent dynamics are partially determined by physical transport, which can be formalised by the advection-diffusion equation (E 3). As a consequence, population apparent growth rates ($r = \mu - l$, with $\mu$ the intrinsic growth rates and $l$ the loss rates) cannot be derived from the diel variation of absolute abundance unless advection/diffusion are resolved, by means of a known currents field U, and second order horizontal diffusion characterised by the coefficient of eddy diffusivity K.

$$\frac{\partial N(x,t)}{\partial t} = rN(x,t) - U\frac{\partial N(x,t)}{\partial x} + K\frac{\partial^2 N(x,t)}{\partial x^2} \quad (4.3)$$

with N: plankton concentration, x: sampling site, t: sampling date U: flow field, K: eddy diffusivity coefficient

To estimate phytoplankton growth rates independently of their net abundance, we used the approach described in Dugenne et al. [2014] adapted from Sosik et al. [2003]. This inverse modeling approach yields to identification of the set of parameters that optimally reproduce the observations of the diel variation of populations size distribution using only cell cycle transitions. In the model, temporal transitions between size classes, $\vec{v}$, are assumed to result from either cellular growth, supported by photosynthetic carbon assimilation, or asexual division. The increase of cell size occurring during the interphase is dependent of the proportions of cells that will grow between $t$ and $t + dt$, noted $\gamma(t)$. This probability is expressed as an asymptotic function of incident irradiance (E 4).

$$\gamma(t) = \gamma_{max}\left[1 - exp\left(-\frac{Irradiance}{Irradiance^{\star}}\right)\right] \quad (4.4)$$

Irradiance: instantaneous PAR, $\gamma_{max}$: maximal proportion of cells growing

On the contrary, the decrease of cell size occurring after the mitosis marks the doubling of cells whose size have been divided by a factor 2. Thus the decrease of cell size is dependent of the proportions of cells that will enter mitosis between $t$ and $t+dt$, noted $\delta(t)$, which ultimately control the population net growth rates (E 5).

$$\mu(t) = \frac{1}{dt}.log_e(1 + \delta(t)) \quad (4.5)$$

Because such proportions show a clear temporal variation, the probability of cells entering mitosis is expressed as a function of both time [Vaulot and Chisholm, 1987;

$$
\begin{array}{c}
 \\
S^{\circ 1}_{t=T_0} \\
S^{\circ 2}_{t=T_0+1\,hour} \\
\vdots \\
S^{\circ 200}_{t=T_0+20\,days}
\end{array}
\begin{array}{c}
\begin{array}{cccc}
S^{\circ 1}_{t=T_0} & S^{\circ 2}_{t=T_0+1\,hour} & \cdots & S^{\circ 200}_{t=T_0+20\,days}
\end{array} \\
\begin{pmatrix}
0 & d(S^{\circ 2}_{t=T_0+1h}, Stream^{T_0->T_0+20d}_{t=T_0+1h}) & \ddots & d(S^{\circ 200}_{t=T_0+20d}, Stream^{T_0->T_0+20d}_{t=T_0+20d}) \\
\ddots & 0 & \ddots & d(S^{\circ 200}_{t=T_0+20d}, Stream^{T_0+1h->T_0+20d}_{t=T_0+20d}) \\
\ddots & \ddots & 0 & d(S^{\circ 200}_{t=T_0+20d}, Stream^{T_0+...->T_0+20d}_{t=T_0+20d}) \\
\ddots & \ddots & \ddots & 0
\end{pmatrix}
\end{array}
$$

Figure 4.3: Oceanographic distance matrix. $S^{\circ\cdots}$ denotes discrete stations sampled by *in situ* flow cytometry and $Stream$, the streamlines integrated with Aviso derived circulation.

André *et al.*, 1999; Jacquet et al., 2001] and cell size [Maranon, 2015] (E 6).

$$\delta(t) = \delta_{max}.f(\mu_v, \sigma_v^2).f(\mu_t, \sigma_t^2) \tag{4.6}$$

f the Normal probability density, v: cell size, $\delta_{max}$: maximal proportion of cells entering mitosis

By analogy with a Markov process, the initial distribution of the cell size, $\vec{N}(0)$, is projected step by step, with a time step of $dt = \frac{10}{60}$ hour, to construct the normalised size distribution, $\vec{w}(t)$, over a 24h period (E 7).

$$\begin{aligned} \hat{\vec{N}}(t+dt) &= A(t).\hat{\vec{N}}(t) \\ \hat{\vec{w}}(t+dt) &= \frac{A(t).\hat{\vec{N}}(t)}{\sum A(t).\hat{\vec{N}}(t)} \end{aligned} \tag{4.7}$$

The tridiagonal transition matrix, $A(t)$ contains:

1. the stasis probability, expressed as the proportions of cells that neither grew nor divide between $t$ and $t + dt$
2. the growth probability ($\gamma$), expressed as the proportions of cells that grew between $t$ and $t + dt$
3. the division probability ($\delta$), expressed as the proportions of cells that entered division between $t$ and $t + dt$

The set of parameters, $\vec{\theta}$, is optimally identified (E 8) assuming that errors follow the Normal distribution, $\Sigma(\vec{\theta})$ (E 9).

$$\begin{aligned} \vec{\theta} &= \{\delta_{max}, Irradiance^{\star}, \delta_{max}, \mu_v, \sigma_v, \mu_t, \sigma_t\} \\ &= argmin(\Sigma(\vec{\theta})) \end{aligned} \tag{4.8}$$

$$\Sigma(\vec{\theta}) = \sum_{t=T_0}^{T_{1\,day}} \sum_{i=1}^{m} (\vec{w} - \hat{\vec{w}}(\vec{\theta}))^2 \tag{4.9}$$

Ultimately, the equivalent of the temporal projection of proportions is conducted on the absolute diel size distribution with the optimal set of parameters to estimate population intrinsic growth rates ($\mu$) on a 24 h period, from which the logarithmic difference of observed abundances is subtracted to obtain population losses rates ($l$) (E 10).

$$\begin{aligned}\mu &= \frac{1}{24.\frac{1}{dt}+1}.log_e\left(\frac{\hat{\vec{N}}(T_{1\,day})}{\vec{N}(T_0)}\right)\\ l &= \mu - \frac{1}{24.\frac{1}{dt}+1}.log_e\left(\frac{\vec{N}(T_{1\,day})}{\vec{N}(T_0)}\right)\end{aligned} \tag{4.10}$$

Since the model allows for any cell to grow, divide or be at equilibrium over the entire integration period, asynchronous population, with growth rates superior to the mean size ratio $\mu_{ratio} = log_e(\overline{v}_{max} : \overline{v}_{min})$ indicative of a synchronous population, are assumed to be well represented. When the horizontal circulation of the plankton along streamlines was consistent with the spatiotemporal positions of the stations, the net growth rates obtained by the size structured population model, denoted $\mu_{size}$, are compared to the net variation of abundance ($\mu_{Ab}$).

**Primary production**

The apparent increase of carbon biomass, defined as the Net Primary Production NPP* (mg C.m$^{-3}$.d$^{-1}$), has been calculated from the predicted absolute size distribution following the biomass conversion formula:

$$\begin{aligned}NPP_{cell} &= \vec{N}_0.\delta(t).C_{cell}\\ &= \vec{N}_0.[exp(\mu(t)) - 1].C_{cell}\end{aligned} \tag{4.11}$$

$C_{cell}$ stands for cell-based carbon conversion factors, measured by allometry $C_{cell}$ (pg C.cell$^{-1}$)=a.Biovolume$^b$ ($\mu$m$^3$). Allometric coefficients (a,b) are summarised in Table 1. Carbon cell quotas were derived from the minimal size class cells reached after presumed mitotic division. This conversion allows to approximate the daily NPP using the approximation of the carbon content of the cells newly-formed after mitotic division over 24 hours (E 11). The estimations result from the apparent mitotic index optimally deduced from the diel dynamics of the normalised size distribution. They do not accommodate any cells removal processes within the period of integration that could be caused by grazing or physical transport.

We examined the role of extrinsic factor on populations distribution by scaling the values of NPP$_{cell}$ to a model of production strictly determined by changes in temperature, PAR, and nutrients [Cullen *et al.*, 1993]. The model assumes that the maximal production rates will be balanced by the combined effect of these limiting variables (E 12):

$$\begin{aligned}&NPP^*(x,t)(mgC.m^{-3}.d^{-1}) = NPP^*_{max}.f(T(x,t)).g(E(x,t)).h(N(x,t))\\ &f(T) = exp\left(-\frac{|T-T_{opt}|^2}{\Delta T_{\pm}^2}\right)\begin{cases} T<T_{opt} : \Delta T_- \\ T>T_{opt} : \Delta T_+ \end{cases}\\ &g(E) = \frac{E}{E_k}.exp\left(1-\frac{E}{E_k}\right)\\ &h(N) = \frac{[NH_4^+]}{k_N + [NH_4^+]}\end{aligned} \tag{4.12}$$

T: temperature (°C), E: incident PAR (E.m$^{-2}$.d$^{-1}$), N: ammonium concentrations ($\mu$M).

Optimal parameters, $\theta$=$\{T_{opt}, \Delta T_{\pm}, E_k, k_N\}$, summarised in Table 2, were identified by Bayesian inference [Dugenne *et al.*, unpublished data].

Table 4.1: Carbon biomass conversion factors. The allometric conversion of cells′ biovolume into carbon biomass is given by: pg C=a.Biovolume$^b$

| Taxon | Mean Biovolume ($\mu$m$^3$.cell$^{-1}$) | Cellular quota (fg C.cell$^{-1}$) | conversion coefficients: (a,b) | Ref |
|---|---|---|---|---|
| Synechococcus | 0.24 ± 0.1 | 76 ± 30 | (0.26, 0.86) | 1 |
| Picoeukaryotes | 3.3 ± 1.4 | 710 ± 250 | (0.26, 0.86) | 1 |
| Nanoeukaryotes | 100 ± 25 | 22,000 ± 5,000 | (0.433, 0.863) | 2 |
| Cryptophytes | 500 ± 130 | 90,000 ± 20,000 | (0.433, 0.863) | 2 |

(1) *Menden-Deuer* and *Lessard* 2000 (2) *Verity et al.* 1992

Table 4.2: MLE parameters of the growth niche model. $\Delta T_-$ and $\Delta T_+$ are half Normal standard deviations under and above the temperature optimum, $T_{opt}$. $E_k$ is the optimal light intensity. $K_N$ is the half-saturation constant of dissolved ammonium uptake

| Taxa | $NPP^{\star}_{max}{}^{(a)}$ | $T_{opt}{}^{(b)}$ | $\Delta T_-{}^{(b)}$ | $\Delta T_+{}^{(b)}$ | $E_k^{(c)}$ | $K_N{}^{(d)}$ |
|---|---|---|---|---|---|---|
| Synechococcus | 1.09 | 13.57 | 0.19 | 0.81 | 216 | 33.4 |
| Picoeukaryotes | 80.9 | 13.71 | 0.21 | 0.92 | 237 | 56.7 |
| Nanoeukaryotes | 908.5 | 14.23 | 0.40 | 1.03 | 282 | 83.1 |
| Cryptophytes | 50.8 | 14.21 | 0.65 | 1.90 | 298 | 94.1 |

$^{(a)}$: mgC.m$^{-3}$.d$^{-1}$ $^{(b)}$: °C $^{(c)}$ $\mu$E.m$^{-2}$.s$^{-1}$ $^{(d)}$ nM

## 4.3 Results

Surfaces waters Typology

The total inertia of station observations was mainly explained by temperature and salinity (Table 3). According to the Bayesian Information Criterion (BIC), the optimal number of mixture components during Leg 1 (Fig 4 left panels) and Leg 2 (Fig 4 right panels) respectively corresponds to 3/2 for temperature ($LR$=112.6/81.4, $p$-value=0/0) (Fig 4a), 3/2 for salinity ($LR$=164.6/136.4, $p$-value=0/0) (Fig 4b), 3/3 for MLD ($LR$=503.2/137.3, $p$-value=0/0) (Fig 4c) and 5/2 for PAR ($LR$=13.99/273.8, $p$-value=0.03/0) (Fig 4d). The intersection of temperature-, salinity-, mixed layer depth- and integrated PAR-based Bayesian clustering supported the distinction of 6 hydrologically-coherent diel time series, denoted $A, B, ..., F$, of consecutive stations analysed within homogeneous water masses in wintertime and 5 time series in springtime, denoted $E, G, ..., K$, (Fig 4 centred panels).

During Leg 1, the variance of temperature and salinity was driven by the WMDW formation, resulting in a vertical mixing reaching 2026 ± 379 m ($p_k$=0.14, $n$=237, $\mathcal{X}^2$=341.9, $p$-value=0) (Fig 5c). The wintertime wind caused the sinking of surface cooler ($\theta_k$=$\{0.64, 13.05, 0.09\}$, $n$=237, $\mathcal{X}^2$=21.1, $p$-value=2.5 $10^{-5}$) (Fig 5a) and saltier ($\theta_k$=$\{0.40, 38.49, 0.04\}$, $n$=237) (Fig 5b) waters within the convective chimney

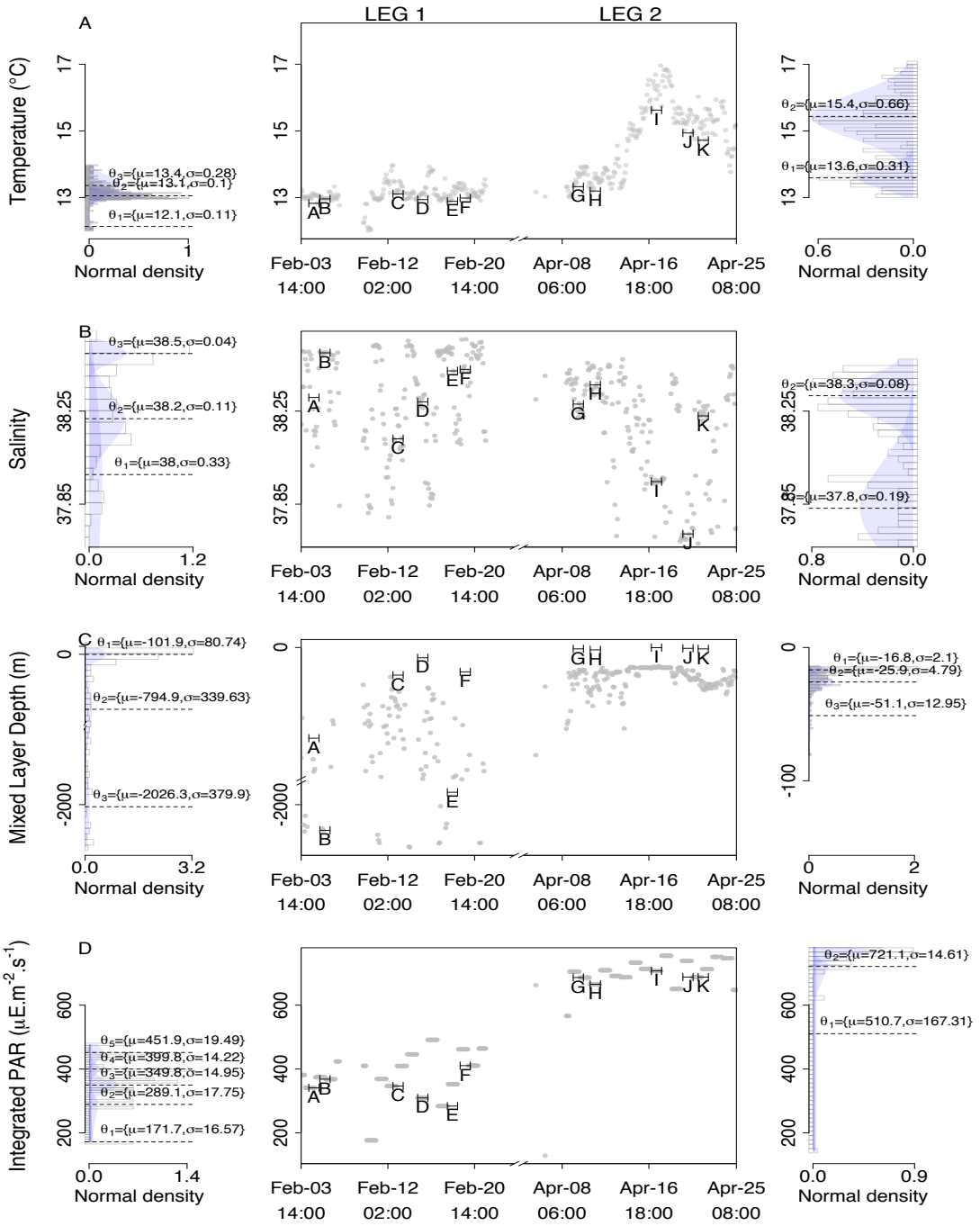


Figure 4.4: Bayesian clustering of surface water types based on temperature (panel a), salinity (panel b), mixed layer depth (panel c) and integrated PAR (panel d) Gaussian finite mixture models with parameters mean ($\mu$) and standard deviation ($\sigma$). Left and right panels represent the distributions of temperature (a), salinity (b), MLD (c) and PAR (d) observations (histograms) and fitted Normal density distribution (blue polygons) during Leg 1 and Leg 2 respectively. Centred panels are the temporal dynamics of water masses characteristics on monthly scales along the R/V track. The 11 diel time series, coherent in terms of temperature, salinity, MLD and PAR, are denoted A,B,... ,K.

(Fig 5). Intensive surface currents, including the Northern current at the north west DeWEX area, delimited boundaries of this diluted patch. At the periphery, waters located in the Gulf of Lions were cooler (T<12.5°C) and fresher (S~38). At south east, the R/V crossed an anticyclonic gyre composed of warm (T>13.5°C) and fresh waters (S<38).

Table 4.3: Cumulative percentage of variance in Principal Component (PC) Analysis

| | | $1^{st}$ PC | $2^{nd}$ PC | $3^{rd}$ PC | $4^{th}$ PC |
|---|---|---|---|---|---|
| LEG 1 | Total Inertia | 40.7% | 70.8% | 86.6% | 100% |
| | Temperature | 33.93 | 12.6 | 9.87 | 43.59 |
| | Salinity | 22.71 | 27.59 | 32.84 | 16.87 |
| | Mixed Layer Depth | 26.12 | 18.89 | 53.29 | 1.7 |
| | Integrated PAR | 17.24 | 40.92 | 4 | 37.84 |
| LEG 2 | Total Inertia | 54.6% | 74.9% | 91.9% | 100% |
| | Temperature | 35.2 | 0.92 | 4.49 | 59.39 |
| | Salinity | 29.4 | 0.06 | 36.23 | 34.32 |
| | Mixed Layer Depth | 19.76 | 32.41 | 42.35 | 5.48 |
| | Integrated PAR | 15.64 | 66.62 | 16.94 | 0.81 |

During Leg 2, the surface water circulation marked a cyclonic gyre located in the southern stations (Fig 2b). This submesoscale structure was characterized by intermediary SST ($\theta_k$=$\{0.47, 15.29, 0.37\}$, $n$=253, $\mathcal{X}^2$=31.4, $p$-value=2.02 $10^{-8}$) (Fig 6a), low peripheral SSS waters ($\theta_k$=$\{0.42, 37.83, 0.19\}$, $n$=253, $\mathcal{X}^2$=136.4, $p$-value=0) (Fig 6b) surrounding high SSS waters ($\theta_k$=$\{0.57, 38.17, 0.15\}$, $n$=253) and the doming of the 29.1 kg.m$^{-3}$ isopycnal at 500 m (Bosse *et al.*, this issue) (Appendix a). Both vertical mixing enriched the epipelagic layer with deep mineralised nutrients like $NO_3^-$ + $NO_2^-$ of mean concentration 7 ± 2.11 $\mu$M at the surface within zone B (Leg 1) and 7.1 $\mu$M at 250m within zone K (Leg 2, Station 83/84) (Appendix b). Within the core of the eddy, high value of $PO_4^{3-}$ (0.30 $\mu$M) and a maximum of oxygen at 210 $\mu$mol.kg$^{-1}$ were also observed at 250m. At the eastern edge, the North Balearic streamline went northward along the Corsican shelf (Fig 2b). Its position marked the difference between stations close to the Sardinian shelf, with temperature closed to 16°C and salinity below 38, and the Corsican shelf, where surface waters approached 15°C and 38.2 (Fig 6).

Mixing zones strongly influenced phytoplankton biomass as they marked the position of the relatively low central abundance patch in wintertime and high abundance in springtime (Appendix b).

### Phytoplankton groups definition

Up to 9 groups of phytoplankton were identified on the basis of their optical properties, including the integral signal of light scatter (FWS and SWS), red and orange fluorescences (FLR and FLO respectively) recorded by automated flow cytometry for the two consecutive Legs (Appendix c). Averages of optical properties overlapped on projections and showed no significant difference from Leg 1 to Leg 2 ($t$-test, $p$-value<0.01). All groups were assigned to a particular PFT composite according to the expertise and standards used during the cruise. Although flow cytometry presents some bias for cells counting, as it underestimates both cells with dim fluorescence and sparse populations, and do not specifically resolve cells phylogeny, we will further refer to flow cytometry clusters by its composite assignation for reading convenience.

Calibration beads of 2 $\mu$m were used to demarcate picophytoplankton (⌀<2 $\mu$m) from the nano- (⌀=3-20 $\mu$m) and microphytoplankton (⌀> 20 $\mu$m) size fractions. Among picophytoplankton, cells assigned to *Synechococcus* group showed a higher FLO intensity compared to the FLR intensity due to the presence of phycoerythrin, while picoeukaryotes exhibited a slightly superior red fluorescence and inferior orange fluorescence intensities. According to the power law function relying FWS to the equivalent spherical diameter (ESD), *Synechococcus* cells exhibited an equivalent median ESD of 0.65 ± 0.08 $\mu m$ (0.3 ± 0.1 $\mu m^3$) in February and in April (Fig 7a). For picoeukary-

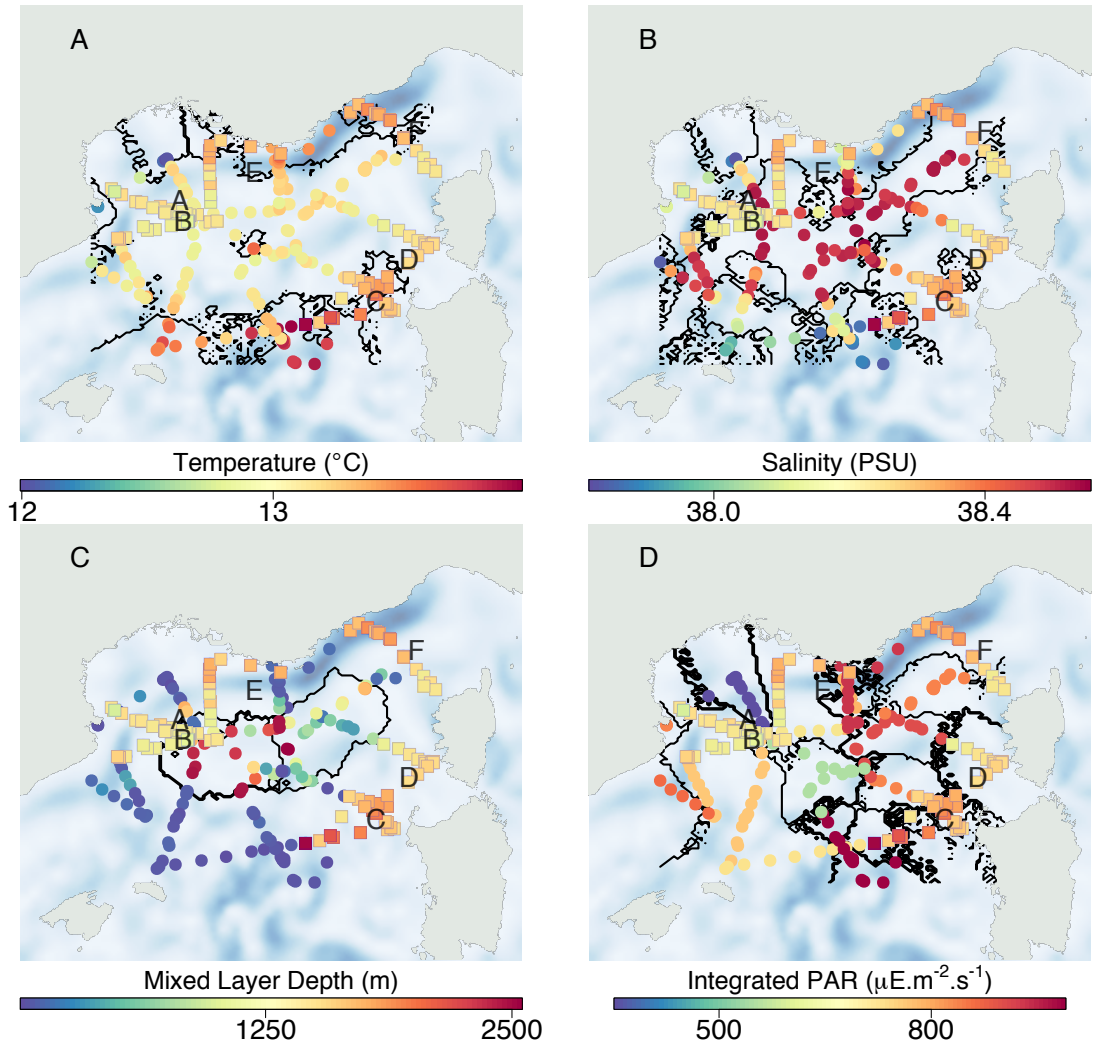


Figure 4.5: Map of surface water types delineation (black lines) of Leg 1 stations (colored dots) superimposed on Aviso $1^{st}$ of February daily currents speed (dark blue: high speed, light blue: slow speed). Water types are clustered using a Bayesian mixture of Gaussian models fitted to temperature (A), salinity (B), mixed layer depth (C) and integrated PAR (D). The 11 diel time series (colored squares), coherent in terms of temperature, salinity, MLD and PAR, are denoted A,B,..., K.

otes cells, the median ESD was 1.5 ± 0.3 $\mu m$ (3.7 ± 2 $\mu m^3$) in Leg 1 and 1.8 ± 0.4 $\mu m$ (5 ± 4 $\mu m^3$) in Leg 2 (Fig 7b). Like *Synechococcus*, cells that emitted orange fluorescence with an intensity superior to the red fluorescence were assigned to a total of 2 distincts cryptophytes groups. Their scattering signal was equivalent or superior to the one of the nanoeukaryotes group. The distinction between nano- and microphytoplankton was based on the pictures taken by the image in flow camera mounted in the Cytosense. Pictures revealed a high diversity of microplankton, spanning several taxa of diatoms, silicoflagellates, ciliates and dinoflagellates. Even though *Prochlorococcus* is present in the Med Sea, it was skipped in this study due to the low sensitivity of the flow cytometer. These small and dim fluorescent cells are out of reach of the flow cytometer used during both legs.

Nanoeukaryotes ESD was on average 6.1 ± 0.7 $\mu m$ (120 ± 40 $\mu m^3$) and 6.5 ± 1.3 $\mu m$ (150 ± 240 $\mu m^3$) for the two respective Legs (Fig 7c). The $2^{nd}$ cluster of cryptophytes was composed of cells larger than nanoeukaryotes, with ESD on average at 10.5

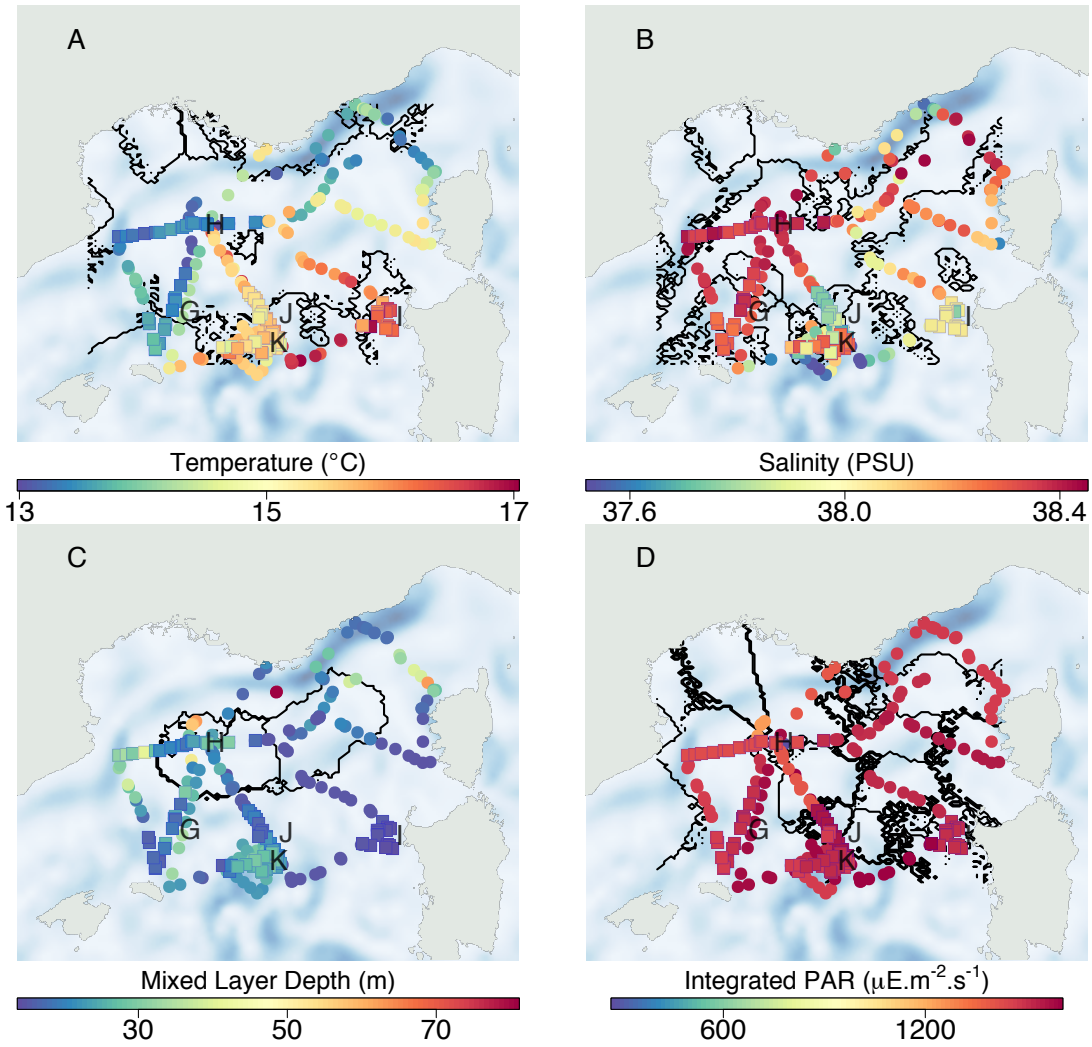


Figure 4.6: Map of surface water types delineation (black lines) of Leg 2 stations (colored dots) superimposed on Aviso $22^{nd}$ of April daily currents speed (dark blue: high speed, light blue: slow speed). Water types are clustered using a Bayesian mixture of Gaussian models fitted to temperature (A), salinity (B), mixed layer depth (C) and integrated PAR (D). The 11 diel time series (colored squares), coherent in terms of temperature, salinity, MLD and PAR, are denoted A,B,..., K.

± 1.0 $\mu m$ (610 ± 160 $\mu m^3$) in February and 10.3 ± 1.1 $\mu m$ (570 ± 150 $\mu m^3$) in April (Fig 7d). Given the temporal variability of cells biovolume, the individual cellular quota of C has been derived from the minimal average cell size according to the allometric regression formula pg C=a.Biovolume$^b$ ($\mu m^3$). This yielded to average C biomass of 76 ± 30 fg C.cell$^{-1}$ for *Synechococcus* cells, 710 ± 50 fg C.cell$^{-1}$ for picoeukaryotes cells, 22,000 ± 5,000 fg C.cell$^{-1}$ for nanoeukaryotes cells and 90,000 ± 20,000 fg C.cell$^{-1}$ for cryptophytes cells (Table 1).

These 4 groups displayed a clear periodic patterns of cellular growth during the light period followed by shifts of cells towards low size classes mainly constrained to the dark period in wintertime. During the following spring, patterns disobeyed from the light-driven signal entertainment and division took place at any time of the day (Fig 7). The sparsity of cells in several areas crossed by the R/V contributed to the large discontinuities observed in Leg 2. In general, patterns within homogenous water types were coherent with the cell cycle-based model suggesting that cells actively moved along the stages of the cell

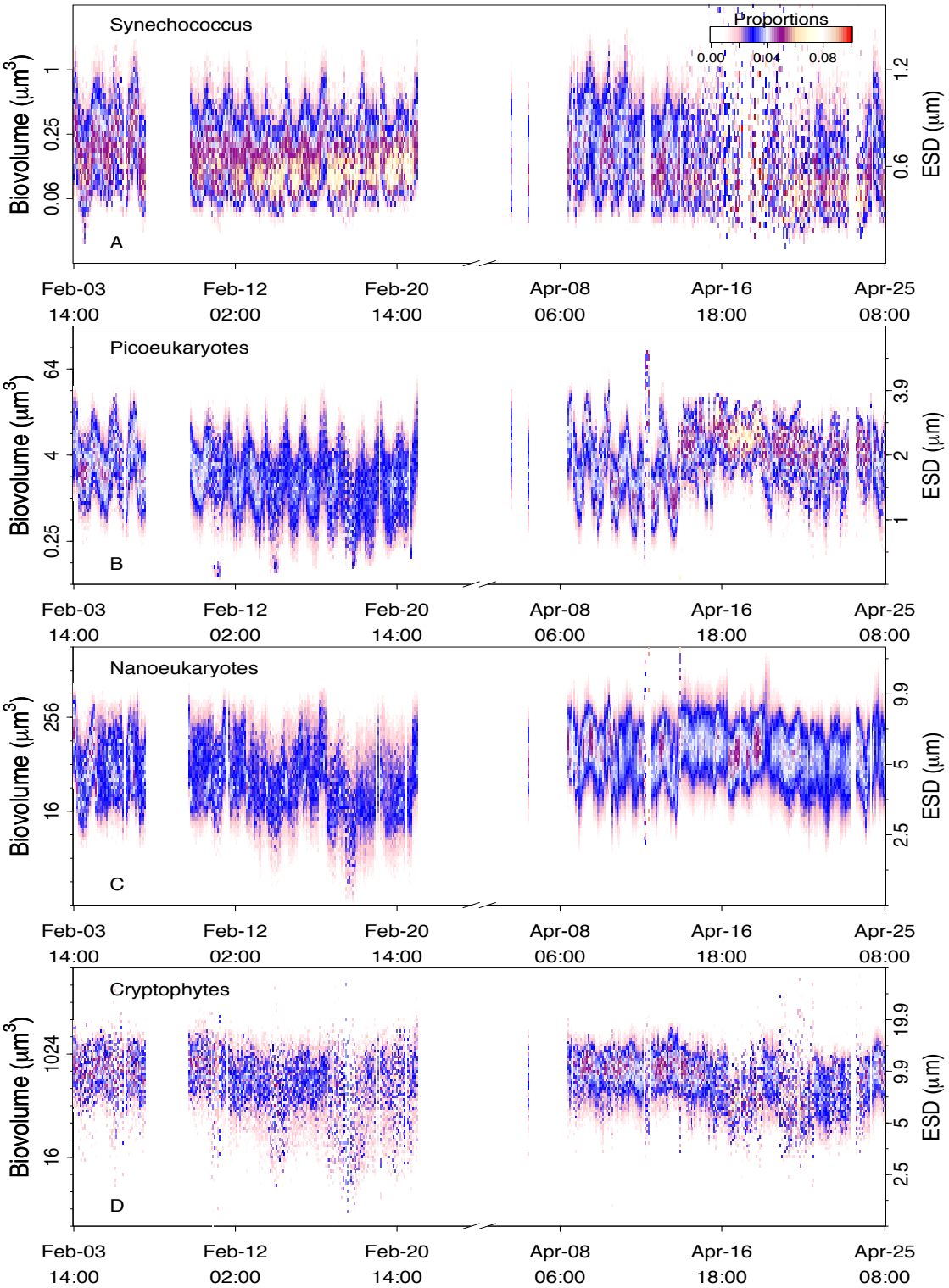


Figure 4.7: Group-specific size proportions distribution (color scale) in biovolume ($\mu m^3$) and equivalent spherical diameter (ESD $\mu$m), derived from flow cytometry forward scatter regression, for Synechococcus (A), picoeukaryotes (B), nanoeukaryotes (C) and cryptophytes (D) cells.

cycle marked by the biomass increase in the interphase and binary fissions in the M-stage. The ratio between extremum size varied between 1.6-2.9, 1.6-4.7, 1.5-2.9 and 1.6-5.0 for *Synechococcus*, picoeukaryotes, nanoeukaryotes and cryptophytes cells respectively (Table 4).

Phytoplankton spatio-temporal distribution

In wintertime, an ubiquitous central patch of relative low abundance arose from wind mixing within the convective chimney (Fig 8, left panel). This contrast with peripheral layers was indicative of the strong dilution of planktonic cells along the water column characterised by the homogeneity of phytoplankton vertical profiles [Silovic *et al.*, this issue] and a low surface bulk chlorophyll a concentration (0.13 $\mu$g.dm$^{-3}$ within the convective chimney and 0.39 $\mu$g.dm$^{-3}$ outside).

Cryptophytes population counted between 5 and 570 cells.cm$^{-3}$ with on average 30 ± 15 cells.cm$^{-3}$ within the patch and 170 ± 100 cells.cm$^{-3}$ outside ($t$-test, $p$-value$<2.10^{-16}$) (Fig 8d). The nanoplanktonic size fraction varied on average from 850 ± 400 cells.cm$^{-3}$ within the patch and 1,710 ± 600 cells.cm$^{-3}$ in periphery ($t$-test, $p$-value$<2.10^{-16}$) (Fig 8c). Picoeukaryotes population grouped around 500 and 15,500 cells.cm$^{-3}$ (Fig 8b) similarly to *Synechococcus*, with 150-15,000 cells.cm$^{-3}$ (Fig 8a). Concentrations varied by several order of magnitude between populations and legs.

An opposite gradient applied in springtime, populations were more abundant in the northern patch of DeWEX spatial coverage (Fig 8, right panel). Measurements of bulk chlorophyll concentration were limited to 0.2 ± 0.1 $\mu$g.dm$^{-3}$ during Leg 1 on average and exceeded 1 $\mu$g.dm$^{-3}$ during Leg 2 (Appendix b). Small size fractions, including nanoeukaryotes, counted at most $10^3$ times more cells than larger cells of cryptophytes and microphytoplankton. For all groups, maximal concentrations were reached in springtime. Nanoplanktonic cells presented a mean concentration of 1.3 $10^3$ ± 6.8 $10^2$ cells.cm$^{-3}$ and 7.9 $10^3$ ± 6.8 $10^3$ cells.cm$^{-3}$ (Fig 8c) during Leg 1 and Leg 2 respectively ($t-test$, $p-value<2.10^{-16}$) (Appendix b).

This size fraction outbursted in spring along with the picoeukaryotes. They presented concentrations up to 9 $10^4$ cells.cm$^{-3}$ and down to 20 cells.cm$^{-3}$ (Fig 8b). *Synechococcus* cells abundance was equally contrasted at that period. Concentrations varied between 10 and $10^4$ cells.cm$^{-3}$ with means of 9,000 ± 13,000 cells.cm$^{-3}$ and 140 ± 140 cells.cm$^{-3}$ in the northern and southern patches respectively ($t$-test, $p$-value$<1.10^{-3}$) (Fig 8a). However, within the southern part of DeWEX coverage, a spot of relatively high abundance was found in the particular physical structure corresponding to the cyclonic gyre (Fig 2). The 29.1 kg.m$^{-3}$ isopycnal doming hosted populations of *Synechococcus*, picoeukaryotes, nanoeukaryotes and cryptophytes counting 2 $10^4$, 4 $10^3$, 15 $10^3$ and 1 $10^3$ cells.cm$^{-3}$ respectively.

Abundance time series appeared more driven by the spatial hydrological gradients and did not show a clear periodic pattern as one could arise from regular division and grazing processes (data not shown). By consequence, resolving intrinsic dynamics required to use a division proxy that is assumed to be invariant of extrinsic forcings (e.g. grazing, sinking) over short timescales and constrained in areas of homogenous water types (Fig 9).

Phytoplankton intrinsic growth and losses rates

The identification of homogeneous water types, by means of hydrological clustering, was used to filter native time series of 24h consecutive measurements of populations size distribution by flow cytometry (Fig 9). *In situ* growth rates were esti-

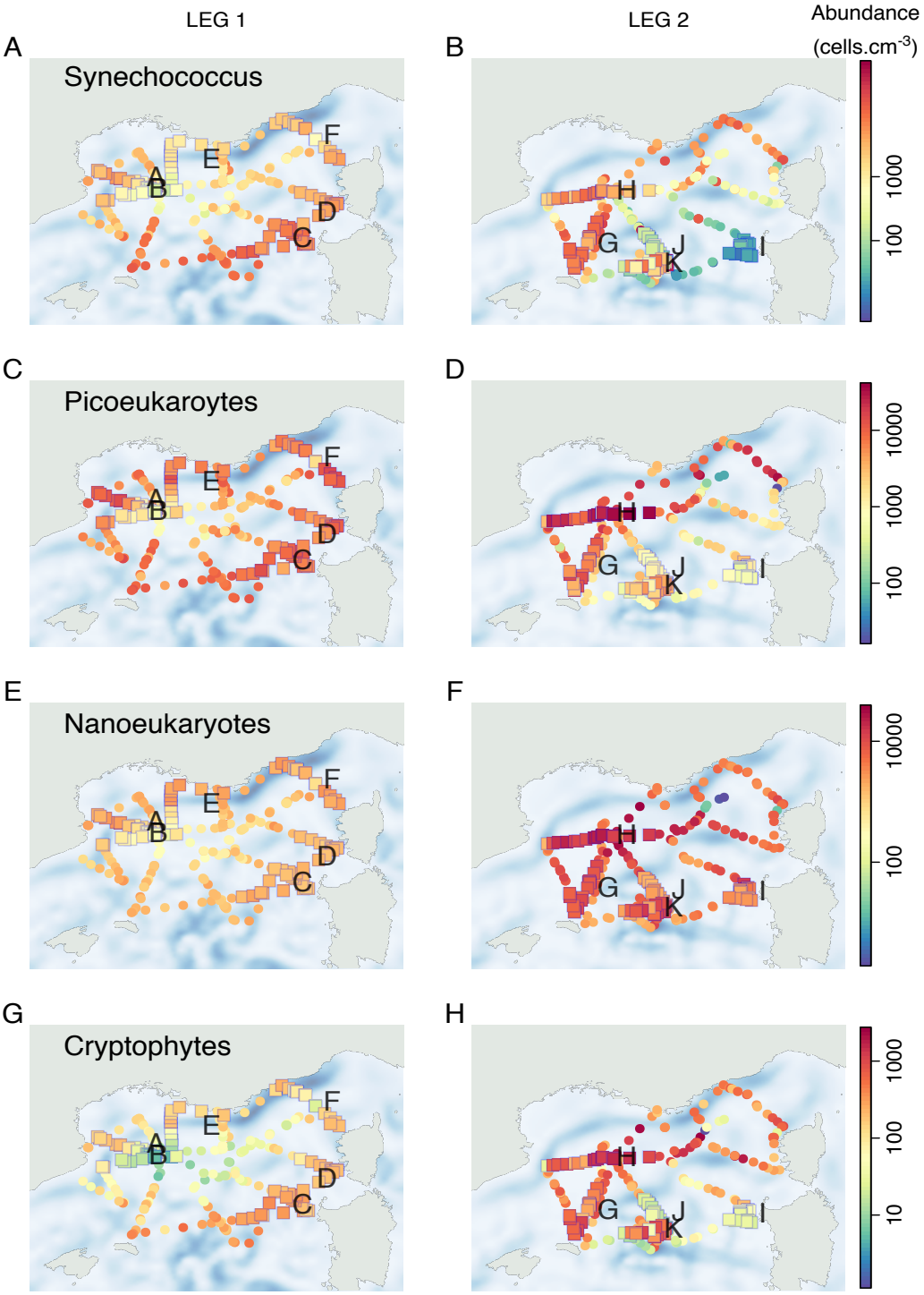


Figure 4.8: Synechococcus (A-B), picoeukaryotes (C-D), nanoeukaryotes (E-F) and cryptophytes (G-H) absolute abundance (colored dots) superimposed on Aviso daily currents speed (dark blue: high speed, light blue: slow speed) during Leg 1 (left panels) and Leg 2 (right panels). The 11 diel time series (colored squares), coherent in terms of temperature, salinity, MLD and PAR, are denoted A,B,..., K.

Table 4.4: Predictions of growth rates during DeWEX. $\mu_{size}$ ($d^{-1}$) is predicted from the size-structured model (see 1.4). $\mu_{Ab}$ ($d^{-1}$) is predicted from plankton Eulerian trajectories (see 1.6). $\mu_{ratio}$ ($d^{-1}$) is predicted from the logarithm of the ratio of max:min average biovolume ($log_e(\frac{\overline{v}_{max}}{\overline{v}_{min}})$). Losses rate $l$ ($d^{-1}$) is predicted from the difference between $\mu_{size}$ and the observed concentration dynamics (see 1.5).

| Zone | *Synechococcus* | | | | Picoeukaryotes | | | | Nanoeukaryotes | | | | Cryptophytes | | | |
|---|---|---|---|---|---|---|---|---|---|---|---|---|---|---|---|---|
| | $\mu_{ratio}$ | $\mu_{Ab}$ | $\mu_{size}$ | $l$ | $\mu_{ratio}$ | $\mu_{Ab}$ | $\mu_{size}$ | $l$ | $\mu_{ratio}$ | $\mu_{Ab}$ | $\mu_{size}$ | $l$ | $\mu_{ratio}$ | $\mu_{Ab}$ | $\mu_{size}$ | $l$ |
| A | 0.68 | 0.86 | 0.71 | 0.17 | 0.99 | 0.98 | 0.86 | 0.37 | 0.59 | 0.46 | 0.71 | 0.18 | 0.48 | 0.3 | 0.21 | -0.09 |
| B | 0.68 | - | 0.76 | 0.12 | 1.17 | - | 1.07 | -0.08 | 0.43 | - | 0.36 | 0.09 | 0.45 | - | 0.35 | -0.06 |
| C | 0.77 | 0.61 | 0.95 | 0.7 | 1.12 | 0.93 | 1.3 | 0.94 | 0.48 | 0.26 | 0.41 | 0.3 | 0.52 | 0.81 | 0.34 | 0.1 |
| D | 0.47 | 1.03 | 0.57 | 0.35 | 1.18 | 1.25 | 0.47 | 0.2 | 0.59 | 0.53 | 0.23 | 0.07 | 0.69 | 0.76 | 0.65 | 0.37 |
| E | 1.09 | - | 0.3 | -0.11 | 1.25 | - | 0.5 | -0.05 | 0.69 | - | 0.65 | 0.08 | 1.6 | - | 1.19 | 0.52 |
| F | 0.57 | 2.25 | 0.72 | 0.36 | 1.15 | 2.37 | 0.94 | 0.06 | 0.64 | 1.35 | 0.72 | 0.22 | 0.6 | 2.31 | 0.35 | -0.11 |
| G | 0.76 | 0.55 | 0.66 | 0.25 | 1.55 | 1.33 | 1.64 | 1.16 | 1.05 | 0.7 | 0.73 | 0.42 | 0.47 | 1.83 | 0.37 | -0.31 |
| H | 0.91 | - | 0.18 | -0.31 | 1.45 | - | 0.49 | -0.32 | 0.95 | - | 0.8 | 0.38 | 0.5 | - | 0.42 | -0.37 |
| I | - | - | - | - | 0.5 | 1.07 | 0.55 | 0.26 | 1.1 | 0.49 | 1.19 | 1 | 0.92 | 0.6 | 0.9 | 0.62 |
| J | 0.77 | 1.44 | 1.27 | -0.12 | 0.68 | 1.01 | 0.69 | 0.43 | 0.42 | 0.5 | 0.44 | 0.31 | 1.3 | 1.31 | 1.45 | 1.22 |
| K | 0.83 | 2.64 | 1.19 | 0.03 | 1.15 | 0.6 | 1.01 | 0.5 | 0.54 | 0.5 | 0.68 | 0.14 | 0.58 | 1.25 | 0.66 | -0.16 |

mated from the predicted absolute distribution of cells in size classes, derived from the temporal projection of the initial distribution transiting with probabilities explicitly parameterise in $\vec{\theta}$. $\vec{\theta}$ has been determined to optimally reproduce the observations of the normalised size distribution accounting for cellular growth and division of *Synechococcus* (Appendix d), picoeukaryotes (Appendix e), nanoeukaryotes (Appendix f) and cryptophytes (Appendix g) cells. Predictions are summarised in Table 4.

Daily growth rates closely followed the logarithm of the ratio between size range ($\mu_{ratio}$), indicative of the dividing fraction of synchronous populations (Table 4). The estimations for the 4 populations showed a high inter-water types variability but not a clear distinction between groups.

For *Synechococcus*, $\mu_{size}$ was maximal in Leg 2 within water types located in the southern cyclonic gyre (zones J-K), where abundance was also maximal (2 $10^4$ cells.cm$^{-3}$) with mean of 2.9 $10^3$ ± 2.7 $10^3$ cells.cm$^{-3}$ (Appendix b) and the delta of concentrations along streamlines high ($\mu_{Ab}$: 1.44-2.64 d$^{-1}$). It reached 1.27 d$^{-1}$ and 1.19 d$^{-1}$ respectively, with losses rates restricted to 2% of the growth rates, while in zone I, concentrations were too low to estimate growth rates from the size-structured population model with enough reliability. One of the lowest estimations, 0.3 $d^{-1}$, was derived from time series in Leg 1, in the northern patch of the convective chimney (zone E), suggesting that division mainly took place on a period greater than 1 day in bottom-reaching convection (Fig 4). However, in wintertime, growth rates reached 0.95 d$^{-1}$ in zone C, located at the western edge of Sardinia, with intermediary salinity (38.14 ± 0.1) and temperature (13.3 ± 02°C) (Appendix b). In this zone, the losses rate was similarly high, representing 73 % of the *in situ* growth rate.

For picoeukaryotes, the amplitudes of the average size distribution rarely fell below 2. Predictions from $\mu_{ratio}$ and $\mu_{Size}$ were not significantly different with the exception of zones D, E and H where cells were smaller (Appendix e). The maximal estimations of *in situ* growth rates were located in the convective zone B and zone C, reaching 1.07 and 1.3 d$^{-1}$ during Leg 1, and at the Southern zones G and K during Leg

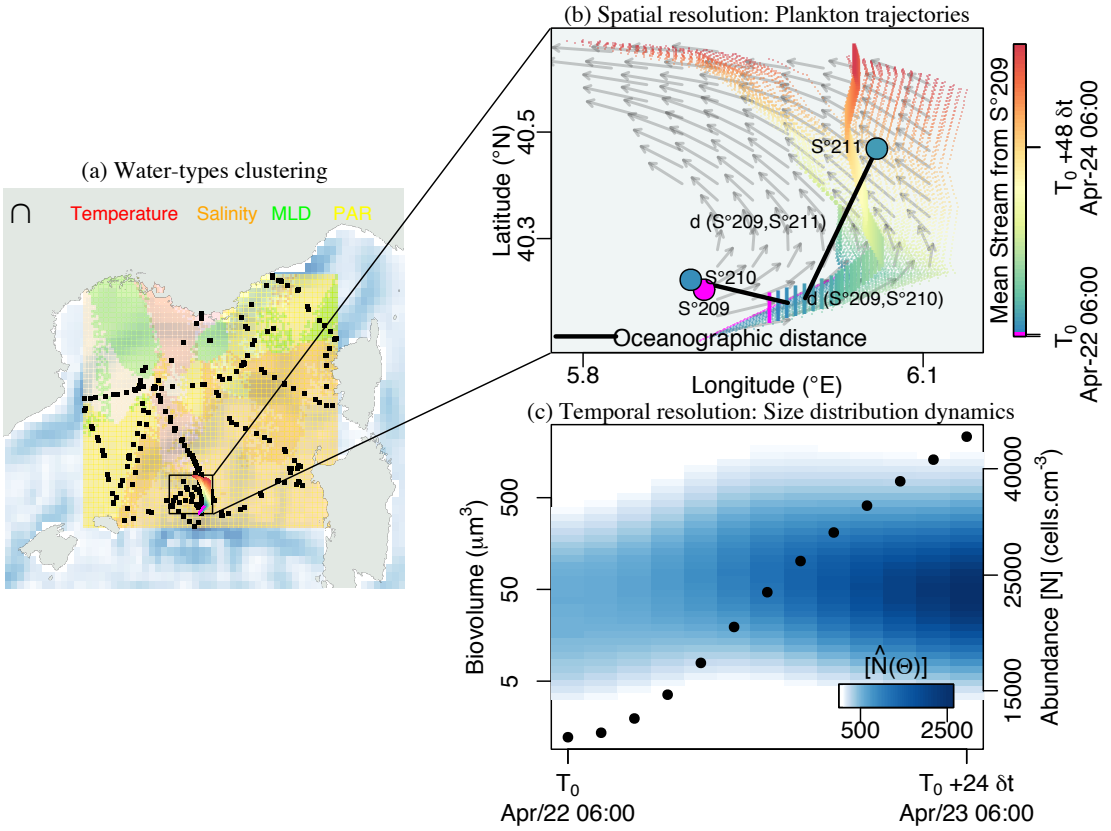


Figure 4.9: Workflow of the methodological approach used to apprehend the DeWEX spatio-temporal resolution of stations with a time lag $\delta t$ of one hour (S°). First a spatial analysis, combining the Bayesian clustering of surface water types (a) weighted by an oceanographic distance matrix calculated by means of plankton trajectories (b), has been performed to cluster native time series along the coherent R/V track (black dots). Once stations are identified as components of an homogeneous historical hydrological context, the dynamics of populations size distributions (blue size classes) is modeled (c), using a set of optimal parameters ($\Theta$), to reproduce observations based on cellular growth and division. This model is based on the assumption that populations' shift towards low size classes are indicative of binary fission, resulting in effective doublings (light blue to dark blue). The integrated changes of population absolute effective, $\hat{N}(\Theta)$ (black dots), are in term predicted to estimate *in situ* growth rates ($\mu_{Size}$) according to formula 4.10. When possible, populations net dynamics (black dots) along current streams were used to estimate Lagrangian growth rates ($\mu_{Ab}$), with $\mu_{Ab}$=$(1:\delta t).log_e([N]_{S°x}:[N]_{S°x+\delta t})$.

2, where $\mu_{Size}$ equaled 1.64 and 1.01 $d^{-1}$. Where cells were the most abundant, in periphery of the convective chimney for wintertime (zones D, E) and in zone H (2.3 $10^4$ ± 9.9 $10^3$ cells.cm$^{-3}$) for springtime (Table 4), division rates were inferior to 1 division per day. Losses rate was minimal in zone F, with $\mu_{Ab}$=2.37 $d^{-1}$, within the stream that flew along the Corsican shelf toward the Northern current. Apart from this area, losses rates varied between 40 and 70 % of $\mu_{Size}$.

Nanoeukaryotes growth rates displayed a wide range of variation during the cruises. In zone I, sampled at the western edge of Sardinia in springtime, it scored 1.19 $d^{-1}$. The equivalent area (zone C), of Leg 1 presented a growth rate below 0.69 $d^{-1}$. The lowest $\mu_{Size}$ appeared in zone D, with 0.23 $d^{-1}$, analysed on a day of relatively low irradiance (Fig 4), during which the size distribution showed an increase in daylight and stasis in the dark (Appendix f). In the convective zone E (Leg 1), the difference of the logarithmic concentration ($\mu_{Ab}$) peaked to 2.89 $d^{-1}$ as it accounted for the gradient of relatively low abundance with the convective chimney to peripheral richer area (Fig 8). Following *Synechococcus* and picoeukaryotes, nanoeukaryotes losses rates

were high in zone C, representing 70 % of the *in situ* growth rates.

For cryptophytes, the highest growth rates were predicted in the stratified zones D, E in wintertime ($\mu_{Size}$: 0.65/1.19 $d^{-1}$ respectively) and in the southern zones I, J, K in springtime ($\mu_{Size}$: 0.9/1.45/0.66 $d^{-1}$ respectively). The coupling between growth and losses rates was also the highest as $l$ ranged between 50 and 80 % of $\mu_{Size}$. In zones A, B, C, G and H, growth rates ranged between 0.20-0.40 $d^{-1}$, in relation to the limited amplitude of the size distributions (Appendix g).

Phytoplankton apparent production

Populations intrinsic growth rates ($\mu_{Size}$) were used to approximate the apparent net production of phytoplankton, in the absence of particles grazing and sinking, according to the amount of newly formed cells by binary fission ($NPP^*_{Cell}$). Estimations were log-transformed to compare values that varied of 6 orders of magnitude, all populations included (shapiro-test, $p$-value <0.1). The range of $NPP^*_{Cell}$ varied from 0.9 $10^{-3}$ mg $C.m^{-3}.d^{-1}$ for *Synechococcus* cells ($\overline{NPP}^*_{Cell}$= 0.6 ± 1.2 mg $C.m^{-3}.d^{-1}$) to 800 mg $C.m^{-3}.d^{-1}$ for nanoeukaryotes cells ($\overline{NPP}^*_{Cell}$= 180 ± 360 mg $C.m^{-3}.d^{-1}$) (Fig 10a). Picoeukaryotes and cryptophytes displayed intermediary productive rates with means of 20 ± 50 mg $C.m^{-3}.d^{-1}$ and 12 ± 14 mg $C.m^{-3}.d^{-1}$ (Fig 10a). The overall contribution ranged from 1.5 % to 0.3 % for *Synechococcus*, 23 % to 6 % for picoeukaryotes, 56 % to 88 % for nanoeukaryotes and 19 % to 5 % for cryptophytes in respective Legs. Considering the difference between populations C quota and the similar values of *in situ* growth rates predictions, $NPP^*_{Cell}$ were mainly driven by approximations of cells biomass and initial standing crop.

Although *Synechococcus* production was limited by cellular quota of 76 ± 30 fg $C.cell^{-1}$ (Table 1), cells were abundant in the periphery of the convective chimney during Leg 1 and in the western area delimited between the northern current and the northward streamlines that circulate from the cyclonic gyre in Leg 2. The highest rates were sustained in zone C during Leg 1 and zone G of Leg 2, $NPP^*_{Cell}$= 1.3/5.6 mg $C.m^{-3}.d^{-1}$ with initial concentrations of 11,050/11,150 $cells.cm^{-3}$ (Fig 8). Means between Leg 1 and Leg 2 were not significantly different ($t$-test, $p$-value= 0.32) (Fig 10b-c). This situation was analogous for picoeukaryotes cells ($t$-test, $p$-value= 0.92), that managed to fix C at rates of 12/100 mg $C.m^{-3}.d^{-1}$ in zones C and G from initial stock of 7,200/11,500 $cells.cm^{-3}$ (Fig 10d-e). Despite having the highest cellular quotas, with mean of 90,000 ± 20,000 fg $C.cell^{-1}$ (Table 1), cryptophytes were penalised by their relatively low concentrations in both legs ($t$-test, $p$-value= 0.19). Following *Synechococcus* and picoeukaryotes, maximal rates were observed in zones C, G and K with values of 10/25/45 mg $C.m^{-3}.d^{-1}$ and abundance of 290/560/12 $cells.cm^{-3}$ (Fig 10f-g). The population of nanoeukaryotes was composed of both abundant, with a maximum of 15,000 $cells.cm^{-3}$ with the cyclonic gyre in Leg 2, and large cells, 22,000 ± 5,000 fg $C.cell^{-1}$ (Table 1). The minimal production rates was measured in Leg 1, with 5 mg $C.m^{-3}.d^{-1}$ in zone D where the *in situ* growth rates was 0.23 $d^{-1}$ and the initial concentration was only 1,400 $cells.cm^{-3}$. Overall means significantly differ between Legs ($t$-test, $p$-value <0.05). In springtime, $NPP^*_{Cell}$ remarkably exceeded 800 mg $C.m^{-3}.d^{-1}$ in zone I and 400 mg $C.m^{-3}.d^{-1}$ in zones K and G (Fig 10h-i). The bulk net production, measured by $^{14}C$ incubations in subsurface samples, yielded to the significant distinction of average values, 7 ± 5 mg $C.m^{-3}.d^{-1}$ in wintertime and 72 ± 75 mg $C.m^{-3}.d^{-1}$ in springtime, with a peak of production at 250 mg $C.m^{-3}.d^{-1}$ located at the far northwestern corner of DeWEX coverage area (Fig 10a).

A parameterisation of potential group-specific productivity is introduced in equa-

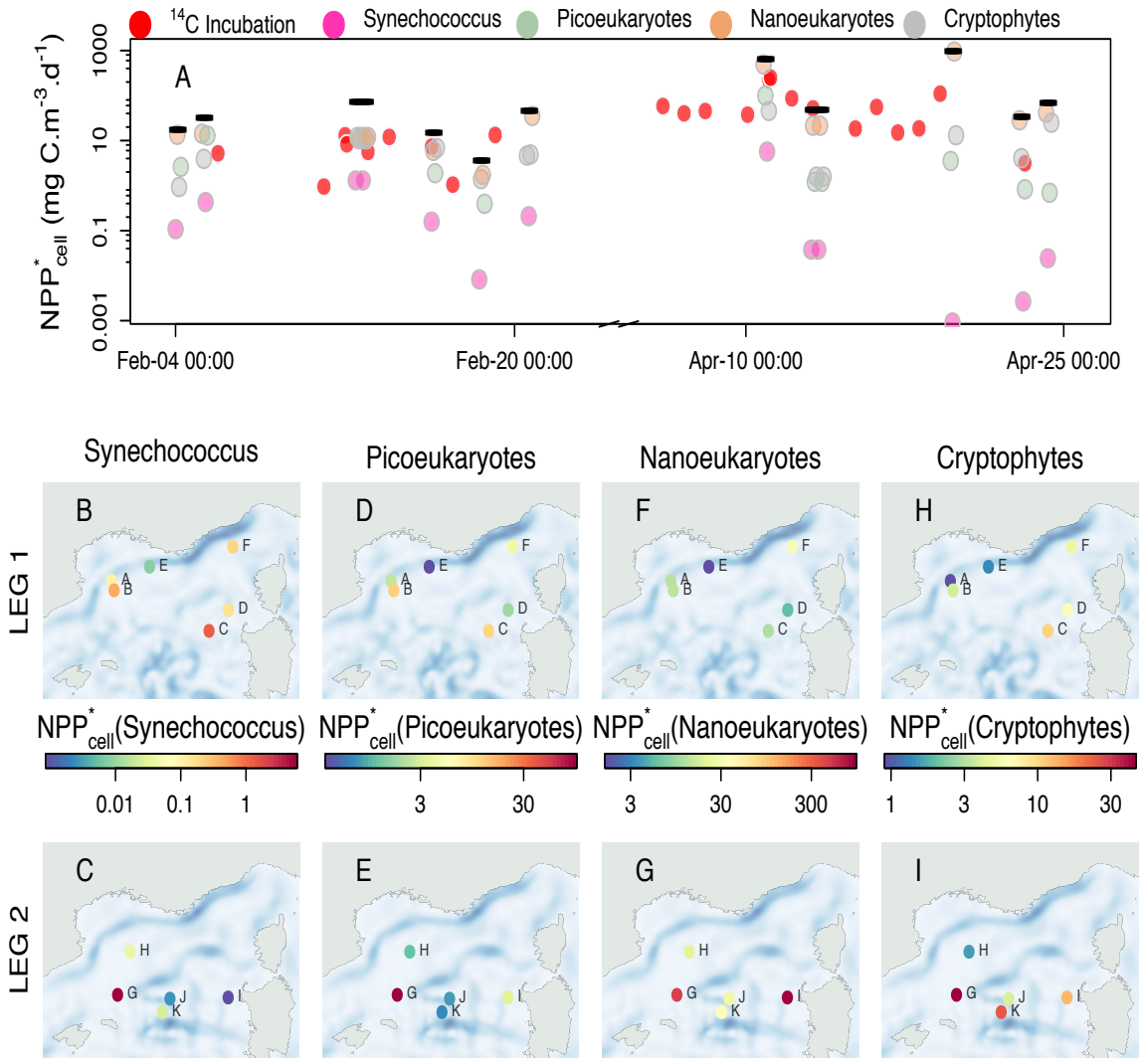


Figure 4.10: Estimations of net primary production during DeWEX (A) based on $^{14}$C bulk incubation (red dots) and flow cytometry derivation of apparent biomass of newly-formed cells ($NPP^*_{cell}$) in Synechococcus (magenta dots), picoeukaryotes (green dots), nanoeukaryotes (orange dots) and cryptophytes (grey dots) populations. Leg 1 and Leg 2 maps of Synechococcus (B-C), picoeukaryotes (D-E), nanoeukaryotes (F-G) and cryptophytes (H-I) $NPP^*_{cell}$ (colored dots) superimposed on Aviso daily currents speed (dark blue: high speed, light blue: slow speed). The 11 diel time series, coherent in terms of temperature, salinity, MLD and PAR, are denoted A,B,..., K.

tion E12 to model the co-occurrent effects of growth limiting factors on net community primary production, independently of the stock (Table 2). Mean temperature, light and ammonium concentration represent the state variables of the model. The comparison between observed $NPP^*_{Cell}$ and model predictions is shown in Appendix h ($R^2$=0.2). Objective analyses of surface temperature and $NH_4^+$ concentration were performed to extrapolate the punctual predictions of $NPP^*_{Cell}$ to the entire provencal basin in wintertime (Fig 11) and springtime (Fig 12). Incident PAR was fixed to the optimal irradiance of each population to avoid any temporal artefact. In wintertime, the convective patch brought at the surface 13.05°C waters, above any optimal temperature, but did not change significantly the concentration of ammonium (Fig 11). The gradient of temperature from the Gulf of Lions to the Balearic front, as indicated by Finite Size Lyapunov Exponent values, globally drove the variations of the sum of individual production rates, Net Primary Community Production ($NPCP^*$). Rates peaked to 800 mg $C.m^{-3}.d^{-1}$ in the small patch of ~ 14°C southern waters that corresponded to nanoeukaryotes $T_{opt}$. In springtime, this patch was even warmer (T> 16°C) and exceeded the optimum of all populations growth curves (Fig 12). High predictions of $NPCP^*$ are consequently restricted to the north, close to the french coasts and around the western spot of nutritive waters.

## 4.4 Discussion

We used a dedicated system of autonomous sensors to qualify, in term of hydrological and biological dynamics, the early 2013 mesoscale structures of subsurface water masses in the entire Liguro-provencal basin (NW Mediterranean Sea). We introduce its past and recent biogeochemical functioning (4.1) before discussing about the ability of automated flow cytometry, used in a resolved circulation context, to exploit populations enumeration and physiological dynamics. This will be further argued in the paragraph regarding the characterisation of a peculiar bloom community (4.2) and its dynamics (4.3) without extensive manipulations and incubations.

### Historic and recent functioning of the Mediterranean Sea

The NW Mediterranean Sea has long proved to host blooming plankton communities [Sournia, 1973; Béthoux, 1981] despite its general oligotrophic status [Moutin and Prieur, 2012]. The provencal basin is enclosed, at North by a speed westward outflow of the Ligurian basin, the Northern current, at South by an eastward current that flows along the balearic salinity front. They cause a reduced cyclonic horizontal circulation (Fig 2) and a weak stratification in its core [Millot, 1987; Bosse *et al.*, this issue; Houpert *et al.*, this issue]. The combination of intense Mistral regime and reduced advection favours the fertilisation of the surface due to a strong wind mixing, reaching the remineralised layers of the deep water column in wintertime [Conan *et al.*, 1999; Séverin *et al.*, 2014]. The destratification-restratification phases occupy a sporadic window, from late November to March [MEDOC group, 1970; Mertens and Scott, 1997; Houpert *et al.*, this issue]. It reverberates on spring, sometimes as soon as February-March [Olita *et al.*, 2014], with blooms that exert an influence on the entire annual productive budget [Gacic *et al.*, 2002; Bosc *et al.*, 2004; Mayot *et al.*, this issue]. Peaks of production increase the global budget of C assimilation by up to 44 % in the western basin compared to the ultraoligotrophic eastern basin [Estrada, 1996 and ref within]. By forcing the buoyancy loss of surface waters, the atmospheric heat flux triggers the Ekman upwelling and acts as a pre-conditioning requirement for bloom onset [MEDOC group,

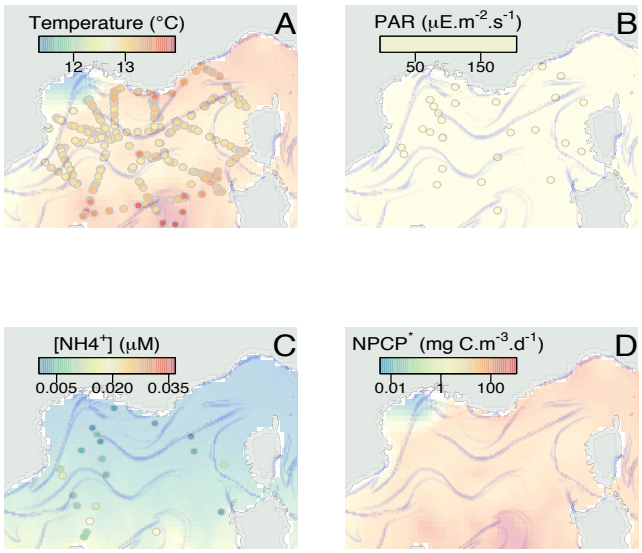


Figure 4.11: Synoptical objective analysis of Temperature (A), PAR (B), $NH_4^+$ concentration (C), and predicted apparent net primary community production (NPCP) (D) during Leg 1, with surface casts punctual analyses superimposed (colored dots). High Finite Size Lyapunov Exponent (blue lines), derived from Aviso 2013-02-05 surface currents grid, is superimposed to underline hydrological fronts for the period.

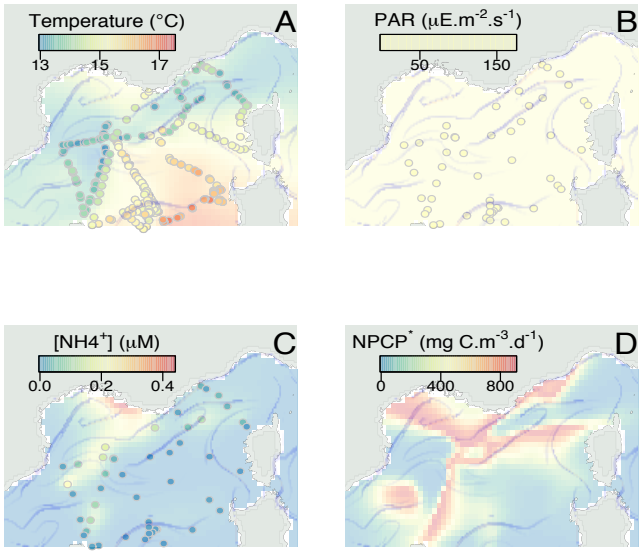


Figure 4.12: Synoptical objective analysis of Temperature (A), PAR (B), $NH_4^+$ concentration (C), and predicted apparent net primary community production (NPCP) (D) during Leg 2, with surface casts punctual analyses superimposed (colored dots). High Finite Size Lyapunov Exponent (blue lines), derived from Aviso 2013-04-22 surface currents grid, is superimposed to underline hydrological fronts for the period.

1970; Marty *et al.*, 2002]. In February 2013, convection reached the bottom layers, at 2000 m depth (Fig 4), and brought up to 7 $\mu$M of $NO_3^-$ + $NO_2^-$ and 0.30 $\mu$M of $PO_4^{3-}$. Concentrations were uniformly distributed in the core of the convective chimney and cyclonic eddies (Fig 8). The Chlorophyll a concentration averaged 0.2 ± 0.1 $\mu$g Chl a.dm$^{-3}$ (Appendix b). A value similar to the entire western basin and other oligotrophic regions of the global ocean [D'Ortenzio and Ribera D'Alcala, 2009].

This process eventually determines the amount of atmospheric $CO_2$ assimilated by phytoplankton available for high trophic compartments and sequestrated in the sediment though the *biological pump* [Longhurst and Harrison, 1989]. In the frame of the MEDIPROD survey, Jacques [1988] estimated that a quarter of the spring 1969 primary production was used to produce the net accumulation of phytoplankton biomass in surface waters, another quarter fuelled the regeneration loop and the remainder was exported toward the deep ocean. In the NW Med Sea, the spring sequel of winter convection generally portrays an intense primary production (50 mg C.m$^{-3}$.d$^{-1}$ with $[\overline{Chla}]$=1 $\mu$g.dm$^{-3}$ *in* Jacques *et al.*, 1973; 5-10 g C.m$^{-3}$.d$^{-1}$ with $[\overline{Chla}]$=0.2 $\mu$g.dm$^{-3}$ *in* Vidussi *et al.*, 2000; 180 mg C.m$^{-3}$.d$^{-1}$ with $[\overline{Chla}]$=0.15 $\mu$g.dm$^{-3}$ *in* Marty and Chiavérini, 2002; 430 mgC.m$^{-3}$.d$^{-1}$ on average with $[\overline{Chla}]$=0.6 $\mu$g.dm$^{-3}$ *in* this study), with accumulation of bulk chlorophyll a concentrations superior to 1 $\mu$g Chl a.dm$^{-3}$ in restratified layers (Fig 1). Outside this period, continuous autonomous measurements revealed that chlorophyll concentration falls below 0.5 $\mu$g Chl a.dm$^{-3}$ [D'Ortenzio and D'Alcala, 2009; Mayot *et al.*, this issue]. When not in a advantageous period, phytoplankton standing crop is drastically reduced to a basal regenerated production in wintertime (40 mg C.m$^{-3}$.d$^{-1}$ with $[\overline{Chla}]$=0.5 $\mu$g.dm$^{-3}$ *in* Jacques *et al.*, 1973; 2,5 mg C.m$^{-3}$.d$^{-1}$ *in* Moutin *et al.*, 1999; <10 mg C.m$^{-3}$.d$^{-1}$ *in* Garcia *et al.*, 2006; 50 mg C.m$^{-3}$.d$^{-1}$ on average with $[\overline{Chla}]$=0.2 $\mu$g.dm$^{-3}$ *in* this study) and summertime (5 mg C.m$^{-3}$.d$^{-1}$ *in* Calbet *et al.*, 1996; 36 mg C.m$^{-3}$.d$^{-1}$ *in* Marty and Chiavérini, 2002; 3 mg C.m$^{-3}$.d$^{-1}$ *in* Moutin and Raimbault, 2002) or eventually reaches a secondary peak in fall (72 mg C.m$^{-3}$.d$^{-1}$ *in* Marty and Chiavérini, 2002), as would do typical temperate ecosystems [Winder and Cloern, 2010].

Nature of the early 2013 phytoplankton community: Investigation by automated flow cytometry

Margalef's Mandala predicts the ordination of species succession when the environment transits from fertile turbulent systems to depleted stratified layers. Such a process is univocal with the winter-spring transition in the NW Mediterranean Sea. To support his theory, Margalef recalled the mathematical formulation of Riley [1949] on the punctual dynamics of a phytoplankton population under the control of sink and source incomes. A population accumulates when its intrinsic growth rate, $\mu$, exceeds the simultaneous losses rate, $l$, and inversely. If the term of losses rate endorses multiples sources of cells instantaneous removal, water instability can paradoxically counterbalances the natural segregation of superficial light and the gravitational sinking of nutrients and cells out of the euphotic layer [Huisman *et al.*, 2002].

## Phytoplankton size and biomass fractions

The 2013 wintertime concentration of Chlorophyll a averaged 0.2 ± 0.1 $\mu$g Chl a.dm$^{-3}$ and peaked to 3 $\mu$g Chl a.dm$^{-3}$ in springtime. The difference of standing crop was significant compared to the annual mean [Mayot *et al.*, this issue] but the relative composition of phytoplankton groups, revealed by flow cytometry, remained stable.

Picoplankters are defined by the fraction being lost under 2 $\mu$m porous filters [Sieburth *et al.*, 1978]. They are ubiquitous [Partensky *et al.*, 1999] but globally dominate oligotrophic regions where they manage to develop solely on the regeneration of nutrients [Platt *et al.*, 1983]. The small size-fraction contributes to marine production by 10 % to 80 %, as a power law function of the total production [Agawin *et al.*, 2000]. In the NW Mediterranean Sea, picoplankton may account for the main source of organic matter for secondary producers [Hagstrom *et al.*, 1988; Magazzu and Decembrini, 1995; Agawin *et al.*, 1998; Jacquet *et al.*, 1998]. Mediterranean picoplankters are numerically dominated by two genera, *Synechococcus* [Waterbury *et al.*, 1979] and *Prochlorococcus* [Chisholm *et al.*, 1988] [Mella-Flores *et al.*, 2011]. *Synechococcus* cells were first distinguished by the emission of intense orange fluorescence derived from phycoerythrin excitation under blue light [Olson *et al.*, 1988]. In cultures, there C quota vary between 92 ± 13 and 213 ± 7 fg C.cell$^{-1}$ [Bertilsson *et al.*, 2003] and decrease to < 140 fg C.cell$^{-1}$ in natural environments [Agawin *et al.*, 1998], 76 ± 30 fg C.cell$^{-1}$ (Table 1, this study). The mean cell biovolume departs from a mean of 0.3 ± 0.1 $\mu$m$^3$, and an equivalent spherical diameter of 0.65 ± 0.08 $\mu$m, in this study (Fig 7) or between 0.2-1.15 $\mu$m$^3$ in the course of 1997-1998, $\overline{\text{ESD}}$=0.9 ± 0.14 $\mu$m [Agawin *et al.*, 1998]. With these low cellular quotas, *Synechococcus* cells represented from less than 1 % of the total biomass in C to 5 % of the total biomass in C (data not shown). Using the sum of *Synechococcus* and picoeukaryotes biomasses, picoplankton stocks fall in the global stock average [Buithenius *et al.*, 2012] with 4.9 ± 4.8 $\mu$g C.dm$^{-3}$ on average.

Picoeukaryotes include cells of many taxa in the eukaryote domain [Simon *et al.*, 1994], including the smallest eukaryote cell to date *Ostreococcus* discovered in a Mediterranean lagoon [Courties *et al.*, 1994]. With picoprokaryotes, they work as an apparent ecological unit of marine ecosystems, made of numerous organisms with high metabolic and dispersal rates [Raven, 1998; Raven et al., 2005; Massana and Logares, 2013] whose diversity is often critically overviewed [Vaulot *et al.*, 2002; Worden and Not, 2008; De Vargas *et al.*, 2015]. A mean C quota of 710 ± 250 fg C.cell$^{-1}$ (Table 4) and abundances of 5,800 ± 3,600 cells.cm$^{-3}$ during Leg 1 and 6,900 ± 8,500 cells.cm$^{-3}$ during Leg 2 (Appendix b) drive picoeukaryotes cells to account for 2-44 % and 0.2-8 % of respective phytoplankton standing crop in this study. Average biomass, 4.7 ± 4 $\mu$g.dm$^{-3}$, was close to the value found in springtime 1998, 5 $\mu$g.dm$^{-3}$ [Arin *et al.*, 2002]. Globally, Mediterranean sea's picoeukaryotes span in importance radiolarians, alveolates, dinoflagelates and stramenopiles [Not *et al.*, 2009], in the size spectrum 0.9-3.5 $\mu$m (for *Ostreococcus taurii* and *Phaeocystis cordata* respectively). The daily range of size (ESD) amplitudes measured during DeWEX encompassed a 0.2-2.5 $\mu$m order of magnitude, with a mean of 1.75 ± 0.3 $\mu$m. A global compilation from Vaulot *et al.* [2008] reports picoeukaryotes description in an extended size range 0.8-3 $\mu$m. This restriction suggests that population dynamics parameters and particularly *in situ* growth rates, can be infer from size variation of a confined cytometric cluster even though it contains many taxa [Binder and Chisholm, 1995; Blanchot *et al.*, 1997; André *et al.*, 1999]. Further studies showed the consistence between picoeukaryotes cluster-specific growth rates and size-specific $^{14}$C incubations productions rates [André *et al.*, 1999].

Flow cytometry measures of *in situ* growth rates based on the size-structured model and the net variation of abundance within a mesocosm deployed in a coastal Mediterranean lagoon also support this usage for both picoeukaryotes and nanoeukaryotes clusters (*unpublished data*). With picoeukaryotes, Durand [1995] re-

ported the size variation of the entire nanoplanktonic size-fraction in the field to estimate a cluster-specific division rates based on the dawn to dusk mean size ratio. This follows the conservative allometric law of the size-dependence of individual metabolic rates [Peters, 1983; Ward *et al.*, 2012]. Nanoplankters compose the fraction being lost under 20 $\mu$m porous filters but adhering to 2 $\mu$m porous filters [Sieburth *et al.*, 1978]. They often include several family such as cryptophyceae, diagnose by the presence of orange fluorescing $\alpha$-Carotene [Jeffrey, 1980]. 2 genera of cryptophyceae are present during the spring bloom in the NW Mediterranean Sea, *Plagioselmis prolonga*, in the size range 6.0-13.0 $\mu$m, and *Cryptomonas acuta*, of 8.1 $\mu$m [Percopo *et al.*, 2011]. Nanoplanktonic cryptophytes's size varied between 3-17 $\mu$m during DeWEX (Fig 7), with an average cellular quota of 90 ± 20 pg C.cell$^{-1}$ (Table 1). Cells that did not emit a high orange fluorescence were classified within the nanoeukaryotes PFTs composite. Nanoeukaryotes displayed a lower size and biomass, with 5 ± 0.8 $\mu$m and 22 ± 5 pg C.cell$^{-1}$ on average respectively. Cells C quota are derived from the allometric (log-log) regression coefficients of microalgae reported in Menden-Deuer and Lessard [2000], built from cryptophytes biomass and further nanoplanktonic prymnesiophytes, chrysophytes, prasinophytes, diatoms and dinoflagellates ($10^{0.5}$-$10^{2.5}$ pg C.cell$^{-1}$). In the Gulf of Lions, the 2-10 $\mu$m size fraction belong, in importance, to diverse genera of *Coscinodiscophyceae* (*Arcocellulus*: 3.5-8.7 $\mu$m, *Minidiscus*: 2.7-4.3 $\mu$m, *Thalassiosira*: 2.7-16.3 $\mu$m), *Dinophyceae* (*Heterocaspa*: 7.0-10.6 $\mu$m), *Coccolithophyceae* (*Anthosphaera*: 2.9 $\mu$m, *Gephytocapsa*: 4.7-8.3 $\mu$m), *Prymnsiophyceae* (*Chrysochromulina*: 3.2-4.0 $\mu$m) [Procopo *et al.*, 2011].

Microplankters are retained on 20 $\mu$m porous filters [Sieburth *et al.*, 1978]. This size fraction can be underestimated in 5 cm$^3$ subsampled used for flow cytometry [Thyssen *et al.*, 2008]. Concomitant microscopic counts showed a ratio cytometry:microscopy of 4 ± 5 in wintertime and 3.6 ± 7 in springtime. The inverse trend supposes that microplankters were not dominant, even during the spring bloom. In costal stations of the NW Mediterranean Sea, the concentration of microplankton rarely exceeds 4 individuals per cm$^{-3}$, and the peak of concentration is not necessarily during the spring bloom as it can vary from one year to another [Gomez and Gorski, 2003]. By integration of the concentration (Leg 1: 7,500 ± 6,900 cells.dm$^{-3}$, 12,000 ± 16,000 cells.dm$^{-3}$) and biomass (120-18,000 pg C.cell$^{-1}$), it contributed on average to 9 ± 8 % of the C stock, with a maximum at 90 % in in a single northern station during Leg 2, in 2013 (Table 1). Most of the image-in-flow pictures (available on http://www.mio.univ-amu.fr/cytobase/) count in springtime, silicoflagellates in the size range 30-40 $\mu$m, diatoms chains of length 40-120 $\mu$m, single diatoms of 25-80 $\mu$m, dinoflagellates of 30-200 $\mu$m. On average, the mixture of microplanktonic cells clustered by flow cytometry measured 24 ± 6 $\mu$m. In the Gulf of Lions, the microplanktonic size fraction belongs, in importance, to diverse genera of *Dinophyceae* (*Protoperidinium*: 35 $\mu$m, *Ceratium*: > 53 $\mu$m *in* Tunin-Ley *et al.*, 2009), *Prymnsiophyceae* (*Hyalolithus*: 30 $\mu$m), *Dictyochophyceae* (*Dictyocha fibula*: 10-45 $\mu$m) [Procopo *et al.*, 2011]. A group of naked ciliates was distinguished from image-in-flow pictures and a clear pigmentary signature, orange fluorescence, that might be caused by the ingestion of cyanobacteria [Mostajir *et al.*, 1998]. The group containing *Strombidium* cells at concentration of 91 ± 173 cells.dm$^{-3}$ of size 25-35 $\mu$m, contributed to less than 2 % total C stock, probably due to long generation times [Pérez *et al.*, 1997].

**Hydrological structuration of PFTs distribution**

Mesoscale structures shape the spatio-temporal distribution of phytoplankton by contextualising the growth niche in which plankton inhabits and is bound to evolve [D'Ovidio *et al.*, 2010; Lévy *et al.*, 2015]. Several studies have described the hydrological structures in the liguro-provencal basin and their link with phytoplankton community, starting with Margalef [1985]. The permanent streams that flows westward along the southern french coasts, the Northern current, and eastward along the northern Balearic coasts, the Balearic density front, delimit the cyclonic circulation in the basin (Fig 2). Continuous records of temperature and salinity sensors point out the presence of distinct water masses reported in Bosse *et al.* [this issue] and Houpert *et al.* [this issue]. The presence of hydrological fronts, such as the boundaries of the Northern current and the North Balearic front, marks the potential stretching of water masses on a temporal (Finite Temporal Lyapunov Exponent) or spatial (Finite Size Lyapunov Exponent) window by the integration of Lyapunov Exponent (Fig 11-12).

Enclosed by these fronts, the wintertime convection entertains phototroph cells down to 2500 m (Fig 4). Initiated in the Gulf of Lion (42 °N, 5 °E) [Bosse *et al.*, this issue], the convective chimney spreads over a 50-100 km patch located between 4-8°E and 40.5-42.5°N. This patch contains mixed vertical profiles of cool ($\overline{T}$=13.05 ± 0.09°C) and salty ($\overline{S}$=38.49 ± 0.04) water that ultimately form the Western Mediterranean Deep Water (Fig 4-5). Due to the bottom-reaching convection, the dense surface layers, caused by consequent heat losses and evaporation, mixed with the warm/salty Levantine Intermediate Water (300-500 m) and Western Deep waters. Since it did not reach the LIW, the NW edge surface layers formed an intermediate mixed patch of Winter Intermediate Water (T < 12.8°C, S < 38.3). The year to year variability of WMDW formation is high but an intensification of means of observations in the field pictures a clear trend of temperature increase (+0.0032 ± 0.0005°C.yr$^{-1}$) and salt concentration (+0.0033 ± 0.0002 yr$^{-1}$) that started at the Western Mediterranean Transient event in 2005 [CIESM, 2009; Houpert *et al.*, this issue]. If this trend is crucial to the deep storage of the excess of anthropogenic $CO_2$ [Touratier *et al.*, 2016], heat and salt caused by surface evaporation [Ribera D'Alcala *et al.*, 2003], it seems that the maximal depth reached by winter mixing is also a good indicator of the spring bloom integrated stock that follows [Marty and Chiavérini, 2010; Lavigne *et al.*, 2013]. During deep convection, not only surface temperature and salinity are progressively mixed together with dense water masses but phytoplankton stock is also diluted along the water column. A process called 'phyto-convection' by Backhaus *et al.* [1999] which is recurrent in any part of the global ocean where the 'conveyor-belt' happens. The surface concentration of *Synechococcus*, picoeukaryotes, nanoeukaryotes and cryptophytes decreased by 80 %, 75 %, 58 % and 84 % on average within the patch compared to the periphery. The percentage of decrease correspond to the magnitude of dilution of the mixed depth in this study (83 % with $(\mu_{MLD}[m], \sigma_{MLD}[m])$ = $\{\theta(MLD)_1 = (114; 130), \theta(MLD)_2 = (690; 780)\}$). With a concentration of 0.13 $\mu$g.dm$^{-3}$ in the center of the basin and 0.39 $\mu$g.dm$^{-3}$ outside, the bulk Chl a biomass decreased by 70 %. The variation of abundance further highlights the priority of physical control among PFTs distribution during deep convection. The dilution didn't affect the relative dominance of picoeukaryotes at 55 % ([cells.cm$^{-3}$]=$\{\theta(MLD)_1 = (8,000; 3,000), \theta(MLD)_2 = (5,000; 3,500)\}$), *Synechococcus* at 30 % ([cells.cm$^{-3}$]= $\{\theta(MLD)_1 = (6,200; 3,600), \theta(MLD)_2 = (2,400; 2,200)\}$), Nanoeukaryotes at

14 % ([cells.cm$^{-3}$]=$\{\theta(MLD)_1$ = $(1,500;440), \theta(MLD)_2$ = $(1,200;3,750)\}$) and cryptophytes at 1% ([cells.cm$^{-3}$]= $\{\theta(MLD)_1$ = $(220;100), \theta(MLD)_2$ = $(85;70)\}$) (Fig 8), despite the difference of their specific growth rates (Table 5). Groups concentration reached the same order of magnitude of previous enumerations reported in Denis *et al.* [2010], although flow cytometry instrumentations suffer distinct counting limitations [Thyssen *et al.*, 2014]. At South, a central anticyclonic eddy captured a core of warm (T > 13.1°C) and fresh (S < 38.1) Winter Deep Water surmounted by Atlantic Water (Fig. 4-5). In the Atlantic jet meander, *Synechococcus* and cryptophytes concentrations are among the highest recorded at that period ([Synechococcus]=5,600 ± 3,800 cells.cm$^{-3}$, [cryptophytes]=200 ± 115 cells.cm$^{-3}$) (Fig 8), a situation previously reported in Tolosa *et al.* [2004] and Jacquet *et al.* [2010]. From February to March, the cool/salty patch spread out of the convective chimney through submesocale eddies [Testor and Gascard, 2006, Bosse *et al.*, this issue] and the decrease of heat losses trigger the restratification of the surface layers with WMDP restrained below 400 m [Béthoux *et al.*, 1990]. The Winter Intermediate Waters with $\theta$=12.97 ± 0.07°C and S=38.42 ± 0.02 circulates between 150-400 m and Modified Atlantic Waters between 0-100 m [Send *et al.*, 1999].

In springtime, the restratification of the upper layer accentuates the dynamics of horizontal currents, through plumes and meso-/submesoscale eddies (Fig 2) that drive the spatial distribution of chlorophyll a concentration [Olita *et al.*, 2014; Casella *et al.*, 2014] and primary production [Olita *et al.*, 2011]. The core of Modified Atlantic Water, continuously affected by local climate conditions along its transit [Millot, 1999], located at N, showed a clear distinction with recent Atlantic Water flowing from the Alboran and Algerian basins [Schroeder *et al.*, 2006; Marty and Chiavérini, 2010]. With a temperature of 13.5 ± 0.3°C and salinity of 38.31 ± 0.08 ($\theta(S)_2$) on average, the former contrasted with warm ($\overline{T}$=15.5 ± 0.6°C) and fresh ($\theta(S)_1$=37.8 ± 0.17) AW (Fig 4-6). The interface between the northern dense surface layer and southern light water masse, referred as the North Balearic Front [Garcia *et al.*, 1994], marks the separation between high ([$\overline{Chla}$]=1.6 ± 2.1 $\mu$g.dm$^{-3}$) and low ([$\overline{Chla}$]=0.35 ± 0.3 $\mu$g.dm$^{-3}$) chlorophyll a concentrations respectively. The main Chl a patch hosted high concentrations of Nanoeukaryotes ([cells.cm$^{-3}$]=$\{\theta(S)_1$ = $(3,800;3,400), \theta(S)_2$ = $(11,000;7,050)\}$), picoeukaryotes ([cells.cm$^{-3}$]=$\{\theta(S)_1$ = $(2,100;3,600), \theta(S)_2$ = $(10,500;9,700)\}$), *Synechococcus* ([cells.cm$^{-3}$]=$\{\theta(S)_1$ = $(1,300;2,700), \theta(S)_2$ = $(5,000;5,000)\}$) and cryptophytes ([cells.cm$^{-3}$]=$\{\theta(S)_1$ = $(160;300), \theta(S)_2$ = $(700;575)\}$). The same type of instrument measured respective concentrations of 2,200 ± 1,600 cells.cm$^{-3}$ (nanoeukaryotes), 8,000 ± 6,000 cells.cm$^{-3}$ (picoeukaryotes), 9,000 ± 7,000 cells.cm$^{-3}$ (*Synechococcus*) and 220 ± 275 cells.cm$^{-3}$ (cryptophytes) in 2012 spring in the Bay of Villefranche [Thyssen *et al.*, 2014]. The relative contribution of each PFTs composite varied compared to wintertime, with the co-dominance of nanoeukaryotes (45%) also reported in Navarro *et al.* [2014], picoeukaryotes (35%), *Synechococcus* (18%) and cryptophytes (2%), but remained fairly similar between spring water masses. The coexistence of plankton species in nature was introduced early by Hutchinson [1961] in *The paradox of the plankton.* The theory relies on several mechanisms proper to phytoplankton lifetime and the integrated action of bottom/top controls. For instance, the differential phasing of populations intrinsic dynamics, illustrated in Appendix d-g, would counterbalance the evolution of a consortium towards the equilibrium where one species outcompetes the others. By opposition to wintertime, group dynamics was largely uncorrelated to the daily photope-

riod in spring. Some groups experimented a relatively short window of division (Table 4). Usually determined by chemotaxonomy, the liguro-provencal spring bloom has been mainly attributed to diatoms pigments in its early stage [Vidussi *et al.*, 2000; Marty *et al.*, 2002; Sammartino *et al.*, 2015]. In light of the recent collection of bloom species by Procopo *et al.* [2011] and complementary microscopic counts (K. Leblanc, *pers. comm.*), it seems that recent spring blooms are mainly dominated by small diatoms of the nanoplanktonic size range (e.g. *Minidiscus*). Compared to microplankton, pico- and nanoeukaryotes do not rely on high turbulence to remain in the euphotic layer and fuel the recycling loop [Fasham, 1985; Michaels and Silver, 1988; Caron *et al.*, 1999; Turley *et al.*, 2000; Lefort and Gasol, 2014]. Only in a particular southern mesoscale structure, PFTs relative abundance was enriched with a high contribution of *Synechococcus* (45 %) and nanoeukaryotes (37 %) following the same wintertime mesoscale structure. In the patch of relative low Chl a concentration, the cyclonic eddy emerged from a chiseling front, at the interface of an anticyclonic gyre that spread from the Algerian jet [Millot, 1985] and the cyclonic meander of the eastward North Balearic front (similar to the wintertime eddy) [Ayoub *et al.*, 1998]. In its core, the mixing of AW and LIW resulted in the doming of warm ($\overline{T}$=15.1°C) and salty surface waters ($\overline{S}$=38.2) depleted in $NO_3$ linked to the topography of the basin [Millot, 1985; Herbaut, 1994; Millot and Taupier-Letage, 2005].

Dynamics of the early 2013 phytoplankton community: Investigation by automated flow cytometry

Townsend *et al.* [1992], Behrenfeld [2010] and Mayot *et al.* [this issue] report that phytoplankton may grow at rates that support its local accumulation long before the timeframe generally occupied by blooms. Lindemann and St John [2014] summed up the existing explanations of phytoplankton blooms in temperate ecosystems. Blooms outbreak in the sequel of new inputs of nutrients within the euphotic layer and dilution of grazers stocks [Auger *et al.*, 2014] caused by the deepening of the density barrier that hold recycled nutrients in depth. They stop when the interactions of nutrients depletion and grazing recoupling dynamics [Franks, 2001], as respective bottom-up and top-down forcings, exert a subsequent control on plankton production. This hypothesis was termed *Dilution-Recoupling Hypothesis* by Behrenfeld [2010] and takes into account the restratification of the density barrier above the depth where integrated production equals respiration, Sverdrup's *Critical depth* [1953]. If the onset of the bloom was generally attributed to large cells rather than small cells, because of their ability to escape a slow-inertial grazing pressure under enriched conditions [Kiørboe 1993, 2008; Irigoien et al. 2005; Barton et al. 2013], the recent review of Maranon *et al.* [2013] portrayes a peak of division capacity at intermediate cells size as an outcome of nutrients trade-offs. In nature, bottom-up and top-down controls act in synergy as intrinsic and extrinsic factors that constrain both standing crop and biological rates of plankton communities.

**Fractional growth and production rates**

According to Furnas [1990], *in situ* growth rates of marine populations range between 0.1-3.6 doublings per day as a function of taxonomic membership and biomass. During DeWEX, *in situ* growth and losses rates were highly variable from one water-type to the other. The influence of Mediterranean circulation in shaping the biological rates of phytoplankton growth and grazing is known since the study of Casotti *et al.* [2003]. The surface average growth rates ($0.71 \pm 0.35$ $d^{-1}$), that might decline with

depth, were consistent with the bulk measures (0.2-0.8 $d^{-1}$) reported in the Alboran basin by Arin *et al.* [2002]. Considering the overall estimations of $\mu$ in this study, it is not clear wether PFTs affiliation and periods have a real influence on phytoplankton growth capacity. *Synechococcus* growth rates ranged from 0.18 to 1.27 $d^{-1}$ (Table 4), values close the summertime values, 0.23-1.07 $d^{-1}$, reported in Agawin and Austi [1997], and 0.95 $d^{-1}$ in Jacquet *et al.* [1998]. Both extrema were measured in springtime, in concordance to absolute concentrations. The study of Agawin *et al.* [1998] yielded to *Synechococcus* apparent net production rates between 0.01-1 mg $C.m^{-3}.d^{-1}$ by means of a biovolume to C conversion over the course of 1997-1998 (February to May). In the present study, the net C uptake rose to 0.87 mg $C.m^{-3}.d^{-1}$ with 7,500 $cells.cm^{-3}$ and fell to 3 $10^{-3}$ mg $C.m^{-3}.d^{-1}$ at 50 $cells.cm^{-3}$. Partensky *et al.* [1999] already noted that the high productivity of *Synechococcus* is a common feature of all oligotrophic areas. The average production rates of picoeukaryotes cells attained 12 ± 30 mg $C.m^{-3}.d^{-1}$ in this study. Extrema were found in springtime, with a net apparent production between 1 mg $C.m^{-3}.d^{-1}$ ([picoeukaryotes]< 1,000 $cells.cm^{-3}$) and 60 mg $C.m^{-3}.d^{-1}$ ([picoeukaryotes]~ 6,000 $cells.cm^{-3}$). In the compilation of Magazzu and Decembrini [1995], the average picoplankton production rates varied between 0.18 mg $C.m^{-3}.h^{-1}$ (~ 2.2 mg $C.m^{-3}.d^{-1}$) and 1.64 mg $C.m^{-3}.h^{-1}$ (~ 19.6 mg $C.m^{-3}.d^{-1}$). *Synechococcus*, picoeukaryotes and Nanophytoplankton growth rates were seasonally described in the Bay of Villefranche (NW Mediterranean Sea) in 1990. Ferrier-Pages and Rassoulzadegan [1994] measured rates of 0.20-1.44, 0.2-2.4, 0.6-2.4 $d^{-1}$ respectively in wintertime and 0.20-1.92, 2.0-4.0, 0.48-2.4 $d^{-1}$ in springtime. In this study, the nanoplanktonic size fraction (nanoeukaryotes and cryptophytes) showed close growth rates, with 0.62 ± 0.26 $d^{-1}$ and 0.62 ± 0.39 $d^{-1}$ on average. If they divide at the same rates, the relative dominance of nanoeukaryotes in term of concentration is responsible for the peak of production observed in springtime (800 mg $C.m^{-3}.d^{-2}$). Its contribution to primary production largely exceeded any other PFTs composites capacities during both Legs (50 % and 80 % respectively), in accordance with Uitz *et al.* [2012]. Despite their high C quota and growth rates (> 1 $d^{-1}$), cryptophytes productivity ranged between 1-45 mg $C.m^{-3}.d^{-1}$. *Cryptophyceae* specific growth rates were determined in spring 2004 in the center of the liguro-provencal basin, above 0.75 $d^{-1}$ [Gutierrez-Rodriguez *et al.*, 2010]. Individual photosynthetic rates ($NPP^{*}_{Cell}$ [pg $C.cm^{-3}.d^{-1}$]:Abundance[$cells.cm^{-3}$]) were coherent with cellular C quota as they ranged between 0.02-0.5 pg $C.cell^{-1}.d^{-1}$ for *Synechococcus*, 0.3-8.6 pg $C.cell^{-1}.d^{-1}$ for picoeukaryotes, 4-64 pg $C.cell^{-1}.d^{-1}$ for nanoeukaryotes and 27-1983 pg $C.cell^{-1}.d^{-1}$ for cryptophytes. Beyond the Mediterranean Sea, the allometric response of individual productivity is largely encountered in all marine ecosystems [Maranon *et al.*, 2007]. During the 2002 spring bloom, Cermeno *et al.* [2006] established a first size fractioned evaluation of NPP (100 mg $C.m^{-3}.h^{-1}$ ~ 1000 mg $C.m^{-3}.d^{-1}$ 80 % micro- 20 % nano-) by measuring the $^{14}C$ particulate organic carbon production rates in a NW coastal Spanish station. The vicinity of the coasts in Cermeno's study and the occurrence of deep convection during DeWEX are primordial to fuel peaks of production in the Mediterranean Sea around April. By comparison, Raveh *et al.* [2015] conducted $^{14}C$ incubations at the same period of DEWEX (April 2013) in the ultraoligotrophic eastern basin and measured production rates of 48 mg $C.m^{-3}.12h^{-1}$ only, with Chl a concentration of 0.2 $\mu g.dm^{-3}$.

A combination of processes, such as mortality, sinking and motility, forge the observations from which we derive growth rates in natural populations. Mortality and

sinking losses rates can range from 0.04-0.3 $d^{-1}$ and 0.01-1 $d^{-1}$ depending on the populations/size fractions [Kirchman, 1999; Ptackinc *et al.*, 2003; Brussaard, 2004]. With their external plate, coccolitophores and diatoms display sinking speed of up to 35 $m.d^{-1}$ and would therefore leave the 200 m euphotic layer in 5 days without a turbulent retention [Eppley *et al.*, 1967; Smayda; 1970; Bach *et al.*, 2012]. In the Mediterranean, mortality rates reach 1.9 $d^{-1}$ at surface and rapidly drop to 0.03 $d^{-1}$ with depth [Agusti *et al.*, 1998]. As a pelagic drifter, phytoplankton is continuously entertained by the currents flow. Its passive motility may be genuinely resolved in the frame of Lagrangian studies to account for direct temporal dynamics along the streams [Li, 1993]. This type of analyses either require a post-processing of the data acquired independently of the flow, consequently termed *Pseudo-Lagragian* [DeVerneil and Franks, 2015] or a dedicated sampling strategy to track water masses with drifters [Hillmer and Imberger, 2007; Landry *et al.*, 2009] and/or satellite diagnostic [Dogliolo *et al.*, 2013; D'Ovidio *et al.*, 2015]. We used the first approach to propagate plankton trajectories on the timescale of each Leg during DeWEX with a regional surface circulation model available at http://www.aviso.altimetry.fr/duacs/. The later will be possible considering the development of automated flow cytometer designed to work into drifting buoy [Dubelaar and Gerritzen, 2000]. The Lagrangian net population growth rates along streamlines corresponding to the differential dynamics of concentrations, $\mu_{Ab}$ (Table 4), account on average for 1.21 ± 0.15 times the predictions of the size-structured population model and a significant $R^2$ (0.68, n=30). Altimeter geostrophic velocities are also useful to calculate Finite Size Lyapunov Exponent on map reporting the main position of water masses stirring [Ottino, 1989; Aurell *et al.*, 1997; D'Ovidio *et al.*, 2004]. The mapping of FSLE is generally presented to match the absolute planktonic distribution with spatial constraints [Abraham, 1998; Martin, 2003; Lehahn *et al.*, 2007]. Due to instrumental limitations, the specific production rates field is not taken into account despite the observation of similar patchiness [Falkoswki *et al.*, 1991; Mc Guilicuddy *et al.*, 1998; Martin and Richards, 2002]. In consequent studies, the logarithm of the ratio of maximum average size over minimum average size has been used to appraise the basal value of population division rates [Binder *et al.*, 1996]. In this study, the overall ratio of dawn-to-dusk average size is not statistically different from the estimation allowing the asynchrony of populations individuals (Table 4), with the exception of cryptophytes for which the number of cells analysed was sometimes critically low (Fig 8). That means that globally *Synechococcus*, picoeukaryotes and nanoeukaryotes cells were bound to divide in a tight timeframe and any cells that did not were negligible (Appendix d-g).

We used the populations-specific apparent production to predict the control of resource availability and used the sum to yield a part of the net primary community production, NPCP (excluding sparse microphytoplankton). For phytoplankton, potential limiting resource includes the temperature, light intensities and nutrients concentration. Their effects are formalised by different pair of equation-parameters relying on empirical or mechanic functions, see review of Tian [2006]. The formulas-parameters (Table 2) employed in this study were identified using complementary but concordant values of group-specific primary production rates acquired during DeWEX cruises [Dugenne *et al.*, unpublished data]. In the BIOMELL biogeochemical box model designed to study the global fluxes dynamics that transit between bacteria, phytoplankton and zooplankton at the DYFAMED observatory station (43.4°N, 7.8°E) [Lévy *et al.*, 1998], ammonium half assimilation constant range between 4-24

nM. Our scaling of primary production to ammonium concentration rather suggests 30-90 nM. The optimal temperature ranged between 13.5-14.2 °C instead of 15 °C in BIOMELL. The optimal Photosynthetic Available Radiation is close to 220 $\mu$E.m$^{-2}$.s$^{-1}$ although Morel [1991] suggested 20-40 $\mu$E.m$^{-2}$.s$^{-1}$. This model used partially the parameterisation of Andersen and Nival [1988], which report a complete limitation of growth under 11 °C. Without an explicit parameterisation of removal processes, apparent NPCP should have been homogeneous in wintertime over the entire basin (Fig 11). On the contrary, the restratification of the basin in springtime caused the accumulation of plankton within stable water masses constrained by divergent fronts (Fig 12).The initial flux of surface phytoplankton production was continuously diluted over the entire water column along with the stock. Independently of the stock, *Synechococcus* production accounted for 0.34 ± 0.3 %, 29 ± 21 % for picoeukaryotes, 44 ± 39 % for nanoeukaryotes and 27 ± 17 % for cryptophytes in wintertime. In springtime, the progressive accumulation of fast growing populations redistributed the group-specific contribution to primary productivity, with 0.13 ± 0.2 % for *Synechococcus*, 7 ± 10 % for picoeukaryotes, 77 ± 18 % for nanoeukaryotes and 16 ± 12 % for cryptophytes (Fig 10).

**Losses rates and potential export**

Top-down controls operate in cascade from the top predators that coerce an intense force on intermediary trophic levels and release the trophic pressure of basal compartments. For phytoplankton, trophic pressure is exerted from various types of grazers, including microzooplankton, ciliates, tintinnides, nanoflagellates, and viral infectious agents [Calbet and Landry, 2004; Calbet, 2008]. In the case of selective grazing, the systematic removal of large individuals in phytoplankton communities is intertwined with the estimation of phytoplankton growth rates based on the size [Kiørboe, 1993]. For an intraspecific grazing, the estimation of specific growth rates via cell-cycle proxies remains unchanged if the pressure is evenly distributed over the different stages since we are using the normalised not the absolute distributions [Carpenter and Chang, 1988]. By introducing G2M-specific grazing rates in their cell-cycle model, Chang and Dam [1993] found that simulations could be 18-44 % biased compared to the true growth rates. There is no proof of selective grazing on Mediterranean picoplankton [Perez *et al.*, 1996; Christaki *et al.*, 2001] or prymnesiophytes/diatoms/green algae/cyanobacteria/pelagophytes/dinophytes [Latasa *et al.*, 2005]. Considering these studies, it is reasonable to overlook grazing on confined populations as predators will unlikely discriminated cells entering the mitosis stage against newly formed cells or cells in interphase among PFTs composites. An hypothesis further supported by *Synechococcus* constant grazing rates measured in daily incubations [Christaki *et al.*, 1999]. The bulk response of secondary producers was investigated during DeWEX by enumeration and classification of zooplankton species. The low planktonic biomass patch in the winter convection zone indicate dilution process coherent with the low ratio $l$:$\mu_{size}$ estimated by flow cytometry (Table 4). Increased grazing pressure during spring restratification, up to 6000 individuals.m$^{-3}$ in the convective patch correlated to high food availability [Donoso *et al.*, this issue]. According to the zooplankton carbon demand, the grazing pressure averaged 60 % of the daily standing crop and was dependent on phytoplankton compartments (B. Hunt *pers. comm.*). These production flux are close to the presently reported loss rates measured by flow cytometry and the global grazer demand reviewed in Calbet and Landry [2004]. Losses rates showed a net increase

in springtime ($\bar{l}_{Leg1}$=0.3 d$^{-1}$, $\bar{l}_{Leg2}$=0.52 d$^{-1}$) and a dissociation between size classes ($\bar{l}_{picoeukaryotes}$=0.32 d$^{-1}$, $\bar{l}_{nanoeukaryotes}$=0.3 d$^{-1}$, $\bar{l}_{cryptophytes}$=0.16 d$^{-1}$, $\bar{l}_{Synechococcus}$=0.11 d$^{-1}$). During Leg 2, removal of picoeukaryotes and nanoeukaryotes approached 70 and 60 % respectively in a zone of reduced advection (Table 4). For Agawin and Agusti [1997], high losses rates on *Synechococcus* explain the observed discrepancies between the high growth rates but low stock at surface compared to the DCM in period of stratification. The variation of losses rates during DeWEX reproduced the results reported in Gutierrez *et al.* [2010], as they mainly mirrored the observed difference in growth rates ($R^2$=0.53, slope=0.4$^{***}$). The coupling of prey/predators dynamics during DeWEX bloom promises a good efficiency of C transfer/recycling within food webs, to the detriment of direct C export [Clegg and Whitfield, 1990; Wassmann, 1998]; this is in agreement with high bacterial carbon demand [Turley *et al.*, 2000] or even entire heterotrophic carbon demand [Duarte *et al.*, 2013] measured in the Mediterranean Sea ($R^2$=0.35 in this study).

In the generic model of Legendre and Le Fèvre [1989], ultraplankton (< 5$\mu$m, Murphy and Haugen, 1985) contributes to export production by a progressive aggregation of sinking particles to larger cells cluster, the marine snow, by contrast with microplankton that sinks quickly out of the euphotic zone without a proper turbulent retention force. Aggregation of small cells account for 43 % in the Atlantic oligotrophic gyre [Lomas and Moran, 2011], 87 % in the Pacific ocean [Richardson and Jackson, 2007], 47 % in the Mediterranean Sea [Guidi *et al.*, 2009, with the inferior limit of aggregate: 250 $\mu$m]. The downward flux of C depends on the particle size distribution (PSD) of the community present in the euphotic layer [Guidi *et al.*, 2016]. Free-living picoplankters and nanoplankters are consequently favoured by their small size to withstand gravity [Raven, 1986] and to fuel the recycling loop [Fogg, 1986; Landry and Hassett, 1982]. Considering that settling rates of particles are determined by the Stokes law [1851] and using the cells density excess of 50 kg.m$^{-3}$ reported in Raven [1998], the radii of *Synechococcus*, picoeukaryotes, nanoeukaryotes and cryptophytes yields to surface sinking fluxes of 0.05-0.14 cm.d$^{-1}$, 0.17-1.3 cm.d$^{-1}$, 1.5-8 cm.d$^{-1}$ and 4-20 cm.d$^{-1}$. In the absence of large sinking particles and strong vertical velocities, phytoplankton POC can drive an export flux of 4% of the production [Moutin and Raimbault, 2002]. In the Western Mediterranean Sea, the ratio of exported POC on net primary production, denoted *e-ratio* [Buesseler, 1998], can vary between 0.53 % in fall and 1.69 % in winter, depending on the seasonal net primary production [Ramondenc *et al.*, 2016] and the presence of fast-sinking particles [Rigual-Hernandez *et al.*, 2013]. With a correlation of $\rho$(current speed,Abundance)=-0.3, the role of enhanced vertical circulation is clear in that it is shaping the apparent deprivation of surface water during a deep convection event and the possible accumulation in reduced water motions (Fig 1). In Huisman *et al.* theory [1999], Sverdrup's critical depth is replaced by the critical vertical turbulence to explain that a bloom may happen in absence of stratification if phytoplankton growth rates exceed the mixing rates. Vertical circulation was intense during February 2013 consecutive to wind mixing. Out of the convective chimney, the absolute vertical speed did not exceed 0.08 m.s$^{-1}$ but bottom-reaching convection caused surface populations to sink at 2026 ± 379 m depth, with absolute speed of 0.7-46 cm.s$^{-1}$, while the plankton-depleted layer was brought to the surface with absolute speed of 5-53 cm.s$^{-1}$. In this context, phytoplankton cells would make a complete convective loop in the mixed layer in approximately 4 hours (median), representing a delay on their daily internal clock that would cause a maximal de-

crease of the growth rates by only 15 %. In terms of photosynthetic rates, a 4h mixing scale may show little impact given the temporal capacity of phytoplankton (< 1 h during daylight, 0 during the night) to adjust the content of light harvesting pigments (Chl a:C) under the decrease of light [Marra, 1978; Falkowski, 1980; Falkowski and Wirick, 1981]. Given the solution of Sverdrup's dynamics equation, the ratio of the critical depth (1:Kd)($\mu$:l) ant the MLD was always inferior to 1 with the exception of coastal zones (D,F) in wintertime and superior to 1 in springtime. In springtime, the absolute vertical speed within the core of the convection equaled the entire Leg coverage with 0.08 $m.s^{-1}$.

### 4.5 Conclusion

As part of the Mermex program, DeWEX was aiming at drawing a global overview of the two main biogeochemical forcings happening in the liguro-provencal Mediterranean basin: the winter deep convection and the sequel spring bloom. The first event brings remineralised nutrients within the euphotic layers where they instantaneously sustain phytoplankton growth, indicated by high division rates for various populations of *Synechococcus*, picoeukaryotes, nanoeukaryotes and cryptophytes (> 1 division per day). The second event is characterised by the accumulation of several 'bloomer' taxa that will succeed to each other, controlled by physical and biological factors. By means of *in situ* flow cytometry, we were able to provide observations of phytoplankton size fractions, ranging from picoplankton to microplankton, in terms of both stock and/or productivity. The 2013 Legs were critical to describe the peculiar bloom, since mainly attributed to small size-fractions, that ensued the bottom-reaching winter deep convection initiated in the Gulf of Lions. The net group-specific primary production reached values superior to 800 mg $C.m^{-3}.d^{-1}$ that were never previously described in this area. The apparent net primary productivity relied in importance on *Synechococcus* (< 1%), picoeukaryotes (7%), cryptophytes (15%) and nanoeukaryotes (77%). The presence of nanoeukaryotes, that combined both high contribution to total phytoplanktonic biomass, as a result of their relative C quotas, and high growth rates as soon as the deep convection occurred, was determinant for photosynthetic $CO_2$ uptake. The fast turnover, favorised by surface temperature and the progressive increase of nutrients and light, ultimately led to the net proliferation of this planktonic population. Cells removal, driven by the combination of grazing, mortality and motility, represented a percentage of up to 70 % of specific growth rates. In particular, the convective chimney brought productive populations down to 2000 m. The development of automated flow cytometry in link with phytoplankton monitoring is now expending and we expect this type of survey to start if not continue to characterise the main biological drivers of atmospheric $CO_2$ uptake in a continuously threatened environment.

## References


Abraham, E. R. (1998), The generation of plankton patchiness by turbulent stirring, *Nature*, *391*(5), 577–580.

Agawin, N. S. R. and S. Agusti (1997), Abundance, frequency of dividing cells and growth rates of *Synechococcus* sp. (cyanobateria) in the stratified Northwest Mediterranean Sea, *J. of Plankton Res.*, *19* (11), 1599–1615.

Agawin, N. S. R., C. M. Duarte and S. Agusti (1998), Growth and abundance of *Synechococcus* sp. in a Mediter-

ranean Bay: seasonality and relationship with temperature, *Mar. Ecol. Prog. Ser.*, *170*, 45–53.

Agawin, N. S. R., C. M. Duarte and S. Agusti (2000), Nutrient and temperature control of the contribution of picoplankton to phytoplankton biomass and production, *Limnol. Oceanogr.*, *45* (3), 591–600.

Agusti, S., M. P. Mura and E. Benavent (1998), Dissolved esterase activity as a tracer of phytoplankton lysis: Evidence of high phytoplankton lysis rates in the northwestern Mediterranean, *Limnol. Oceanogr.*, *43* (8), 1836–1849.

Andersen, V. and P. Nival (1988), Modèle d'écosystème pélagique des eaux côtières de la Mer Ligure, *Oceanologica acta*, 211–217.

Anderson, T. R. (2000), Plankton functional type modelling: running before we can walk?, *Journal of Plankton Research*, *27* (11), 1073–1081.

André, J-M, C. Navarette, J. Blanchot and M-H Radenac (1999), Picophytoplankton dynamics in the equatorial Pacific: Growth and grazing rates from cytometric counts, *J. of Geophys. Res.*, *104*, 3369–3380.

Arin, L., X. Anxelu, G. Moran and M. Estrada (2002), Phytoplankton size distribution and growth rates in the Alboran Sea (SW Mediterranean): short term variability related to mesoscale hydrodynamics, *J. of Plankton Research*, *24*(10), 1019–1033.

Auger, P. A., C. Ulses, C. Estournel, L. Stemmann, S. Somot and F. Diaz (2014), Interannual control of plankton communities by deep winter mixing and prey/predator interactions in the NW Mediterranean: results from a 30-year 3D modeling study, *Prog. in Oceanogr.*, *124*, 12–27.

Aurell, E., G. Boffetta, A. Crisanti, G. Paladin and A. Vulpiani (1997), Predictability in the large: an extension of the concept of Lyapunov exponent, *J. Phys. (A)*, *30*, 1–26.

Ayoub, N., P-Y Le Traon and P. De Mey (1998), A description of the Mediterranean surface variable circulation from combined ERS-1 and TOPEX/POSEIDON altimetric data, *J. of Marine Systems*, *18*, 3–40.

Bach, L. T., U. Riebesell, S. Sett, S. Febiri, P. Rzepka and K. G. Schultz (2012), An approach for particle sinking velocity measurements in the 3-400 $\mu$m size range and considerations on the effect of temperature on sinking rates, *Mar. Biol.*, *159*, 1853–1864.

Backhaus, J. O., H. Wehde, E. Nost Hegseth and J. Kampf (1999), 'Phytoconvection': the role of oceanic convection in primary production, *Mar. Ecol. Prog. Ser.*, *189*, 77–92.

Barton, A. D., A. J. Pershing, E. Litchman, N. R. Record, K. F. Edwards, Z. V. Finkel, T. Kioreboe and B. A. Ward (2013), The biogeography of marine plankton traits, *Ecology Letters*, *16*, 522–534.

Behrenfeld, M., J. Randerson, C. McClain, G. Feldman, S. Los, C. Tucker, P. Falkowski, C. Field, R. Frouin, W. Esaias, D. Kolber and N. Pollack (2000), Temporal variations in the photosynthetic biosphere, *Science*, *291*, 2594–2597.

Behrenfeld, M. (2010), Abandoning Sverdrup's Critical Depth Hypothesis on phytoplankton blooms, *Ecology*, *91*(4), 977–989.

Bertilsson, S., O. Berglund, D. M. Karl and S. W. Chisholm (2003), Elemental composition of marine *Prochlorococcus* and *Synechococcus*: Implications for the

ecological stoichiometry of the sea, *Limnol. Oceanogr.*, *48*(5), 1721–1731.

Béthoux, J-P (1981), Le phosphore et l'azote en mer Méditerranée, bilans et fertilité potentielle, *Marine Chemistry*, *10*, 141–158.

Béthoux, J-P, B. Gentil, J. Raunet and D. Taillez (1990), Warming trend in the western Mediterranean deep water, *Nature*, *347*, 660–662.

Béthoux, J-P, B. Gentili, P. Morin, E. Nicolas, C. Pierre and D. Ruiz-Pino (1999), The Mediterranean Sea: a miniature ocean for climatic and environmental studies and a key for the climatic functioning of the North Atlantic, *Progr. in Oceanogr.*, *44*, 131–146.

Binder, B. J. and S. W. Chisholm (1995), Cell cycle regulation in marine *Synechococcus* sp. Strains, *Applied and environmental microbiology*, *61*(2), 708–717.

Binder, B. J., S. W. Chisholm, R. J. Olson, S. L. Frankel and A. Z. Worden (1996), Dynamics of picophytoplankton, ultraplankton and bacteria in the central equatorial Pacific, *Deep-Sea Research II*, *43*(4-6), 907–931.

Blanchot J., J-M André, C. Navarette and J. Neveux (1997), Picophytoplankton dynamics in the equatorial Pacific: diel cycling from flow-cytometer observations, *Life Sciences*, *320*, 925–931.

Bonachella, J. A., C. A. Klausmeir, K. Edwards, E. Litchman and S. A. Levin (2015), The role of phytoplankton diversity in the emergent oceanic stoichiometry, *J. Plankton Res.*, *0*(0), 1–15.

Borile, F. (2016), On the Mediterranean conveyor belt system, *phD Thesis*, 1–93.

Bosc, E., A. Bricaud and D. Antoine (2004), Seasonal and interannual variability in algal biomass and primary production in the Mediterranean Sea, as derived from 4 years of SeaWIFS observations, *Global Biogeochemical cycles*, *18*, 1–17.

Bosse, A., P. Testor, L. Houpert, P. Damien, L. Prieur, D. Hayes, V. Taillandier, X. Durrieu de Madron, F. d'Ortenzio, L. Coppola, J. Karstensen and L. Mortier (2016), Scales and dynamics of submesoscale coherent vortices formed by deep convection in the northwestern Mediterranean Sea, *J. Geophys. Res.*, *This issue*.

Brewin, R. J. W., S. Sathyendranath, T. Hirata, S. J. Lavender, R. M. Barciela and N. J. Hardman-Mountford (2010), A three-component model of phytoplankton size class for the Atlantic Ocean, *Ecological Modelling*, *221*, 1472–1483.

Brussaard, C. P. D. (2004), Viral control of phytoplankton populations- a review, *The Journal of Eukaryotic Microbiology*, *51*(2), 125–138.

Brosnahan, M. L., L. Velo-suarez, D. K. Ralston, S. E. Fox, T. R. Sehein, A. Shalapyonok, H. M. Sosik, R. J. Olson and D. M. Anderson (2015), Rapid growth and concerted sexual transitions by a bloom of the harmful dinoflagellate *Alexandrium fundyense* (Dinophyceae), *Limnol. Oceanogr.*, *60*, 2059–2078.

Buesseler, K. O. (1998), The decoupling of production and particulate export in the surface ocean, *Global biogeochemical cycles*, *12*(2), 297–310.

Buithenius, E. T. (2012), Picophytoplankton biomass distribution in the global ocean, *Earth Syst. Sci. Data*, *4*, 37–46.

Calbet, A., M. Alcaraz, E. Saiz, M. Estrada and I. Trepat (1996), Planktonic herbivorous food webs in the catalan Sea (NW Mediterranean): tempo-

ral variability and comparison of indices of phyto-zooplankton coupling based on state variables and rate processes, *J. of Plankton Research*, *18*(12), 2329–2347.

Calbet, A., and M. R. Landry (2004), Phytoplankton growth, microzooplankton grazing, and carbon cycling in marine systems, *Limnol. Oceanogr.*, *49*(1), 51–57.

Calbet, A. (2008), The trophic roles of microzooplankton in marine systems, *J. of Marine Science*, *65*, 325–331.

Campbell, L., R. J. Olson, H. M. Sosik, A. Abraham, D. W. Henrichs, C. J. Hyatt and E. J. Buskey (2010), First harmful dinophysis (Dinophyceae, Dinophysiales) bloom in the U.S. is revealed by automated imaging flow cytometry, *J. Phycol.*, *46*, 66–75.

Caron, D. A., E. R. Peele, E. Lin Lim and M. R. Dennett (1999), Picophytoplankton and nanoplankton and their trophic coupling in surface waters of the Sargasso Sea south of Bermuda, *Limnol. Oceangr.*, *44*(2), 259–272.

Carpenter, E. J. and J. Chang (1988), Species-specific phytoplankton growth rates via diel DNA synthesis cycles. I. Concept of the method, *Mar. Ecol. Prog. Ser.*, *43*, 105–111.

Casella, E., P. Tepisch, X. Couvelard, R. M. A. Caldera and K. Schroeder (2014), Ecosystem dynamics in the Liguro-Provençal Basin: the role of eddies in the biological production, *Mediterranean Marine Science*, *15*(2), 274–286.

Casotti, R., A. Landolfi, C. Brunet, F. D'Ortenzio, O. Mangoni and M. Ribera D'Alcala (2003), Composition and dynamics of the phytoplankton of the Ionian Sea (eastern Mediterranean), *J. Geophys. Res.*, *108*(9), 1–19.

Cermeno, P., E. Maranon, V. Perez, P. Serret, E. Fernandez and C. G. Castro (2006), Phytoplankton size structure and primary production in a highly dynamic coastal ecosystem (Ria de Vigo, NW-Spain): Seasonal and short-time scale variability, *Estuarine, Coastal and Shelf Science*, *67*, 251–266.

Chang, J. and H. G. Dam (1993), The influence of grazing on the estimation of phytoplankton growth rate via cell cycle anlaysis: Modeling and experimental evidence, *Limnol. Oceanogr.*, *38*(1), 202–212.

Chisholm, S. W. (1988), A novel free-living prochlorophyte abundant in the euphotic oceanic zone, *Nature*, 334–340.

Chretiennot-Dinet, M-J, C. Courties, A. Vaquer, J. Neveux, H. Claustre, J. Lautier and M. C. Machado (1995), A new marine picoeucaryote: *Ostreococcus tauri* gen. et sp. nov. (Chlorophyta, Prasinophyceae), *Phycologia*,*34*(4), 285–292.

Christacki, U., S. Jacquet, J. R. Dolan, D. Vaulot and F. Rassoulzadegan (1999), Growth and grazing on *Prochlorococcus* and *Synechococcus* by two marine ciliates, *Limnol. Oceanogr.*,*44*(1), 52–61.

Christacki, U., A. Giannakourou, F. Van Wambeke and G. J. Grégori (2001), Nanoflagellate predation on auto- and heterotrophic picoplankton in the oligotrophic Mediterranean Sea, *J. of Plankton Res.*,*23*(11), 1297–1310.

CIESM (2009),Dynamics of Mediterranean deep waters, *F. Briand (eds), CIESM Workshop Monographs, Monaco*, *38*, 132.

Ciotti, A. M. and A. Bricaud (2006), Retrievals of a size parameter for phytoplankton and spectral light absorption

by colored detrital matter from water-leaving radiances at SeaWIFS channels in a continental shelf region off Brazil, *Limnol. Oceanogr. Methods*, *4*, 237–253.

Clegg, S. L. and M. Whitfield (1990), A generalized model for the scavenging of trace metals in the open ocean-I . Particle cycling, *Deep-Sea Research*, *37*(5), 809–832.

Cloern, J. E. (1996), Phytoplankton bloom dynamics in coastal ecosystems: A review with some general lessons from sustained investigation of San Francisco Bay, California, *Review of Geophysics*, *34*, 127–168.

Coll, M. et al. (2010), The biodiversity of the Mediterranean Sea: Estimates, patterns and threats, *Plos ONE*, *5*(8), 1–36.

Collins, S., B. Rost and T. A. Rynearson (2013), Evolutionary potential of marine phytoplankton under ocean acidification, *Evolutionary Applications*, *7*, 140–155.

Conan, P., C. Turley, E. Stutt, M. Pujo-Pay and F. Van Wambeke (1999), Relationship between phytoplankton efficiency and the proportion of bacterial production to primary production in the Mediterranean Sea, *Aquat. Microb. Ecol.*, *17*, 131–144.

Courties, C., A. Vaquer, M. Troussellier, J. Lautier, M. J. Chrétiennot-Dinet, J. Neveux, C. Machado and H. Claustre (1994),Smallest eukaryotic organism, *Nature*, *370*, 255.

Cullen, J. J., R. J. Geider, J. Ishizaka, D. A. Kiefer, J. Marra, E. Sakshaug and J. A. Raven (1993), Toward a general description of phytoplankton growth for biogeochemical models, *G. T. Evans and M. J. R. Fasham (eds) NATO ASI Series, Springer*, *10*, 153–176.

Denis, M., M. Thyssen, V. Martin, B. Manca and F. Vidussi (2010), Ultraphytoplankton basin-scale distribution in the eastern Mediterranean Sea in winter: link to hydrodynamism and nutrients, *Biogeosciences*, *7*, 2227–2244.

De Vargas et al. (2015), Eukaryotic plankton diversity in the sunlit ocean, *Science*, *348*(6237), 1–12.

De Verneil, A. and P. J. S. Franks (2015), A pseudo-Lagrangian method for remapping ocean biogeochemical tracer data: Calculation of net Chl-a growth rates, *J. of Geophys. Res. Oceans*, *120*, 1–18.

Dickey, T. D. (2002), Emerging ocean observations for interdisciplinary data assimilation systems, *J. of Marine systems*, *40*, 5–48.

Doglioli, A. M., F. Nencioli, A. A. Petrenko and G. Rougier (2013), A software package and hardware tools for in situ Experiments in a Lagrangian Reference Frame, *J. of Atmospheric and oceanic technology*, *30*, 1940–1950.

Doney, S. C., I. Lima, J. K. Moore, K. Lindsay, M. Behrenfeld, T. K. Westberry, N. Mahowald, D. M. Glover and T. Takahashi (2009), Skill metrics for confronting global upper ocean ecosystem-biogeochemistry models against field and remote sensing data, *J. of Marine systems*, *76*, 95–112.

Donoso, K., M. Pagano, L. Berline, B. P. V. Hunt and F. Carlotti (2016), Zooplankton community response to the winter-spring transition in the NW Mediterranean Sea, *J. Geophys. Res. Oceans*, *This issue.*

D'Ortenzio, F. and M. Ribera D'Alcala (2009), On the trophic regimes of the Mediterranean Sea: a satellite analysis, *Biogeosciences*, *6*, 139–148.

D'Ovidio F., S. De Monte, S. Alvain, Y. Dandonneau and M. Lévy (2010), Fluid dynamical niches of phytoplankton types, *PNAS Early Edition*, 1–5.

D'Ovidio F., V. Fernandez, E. Hernandez-Garcia and C. Lopez (2004), Mixing structures in the Mediterranean Sea from Finite-Size Lyapunov Exponents, *Geophys. Res. Let.*, *31*(17), 1–8.

D'Ovidio F., A. Della Penna, T. W. Trull, F. Nencioli, M-I Pujol, M-H Rio, Y-H Park, C. Cotté, M. Zhou and S. Blain (2015), The biogeochemical structuring role of horizontal stirring: Lagrangian perspectives on iron delivery downstream of the Kerguelen Plateau, *Biogeosciences*, *12*, 5567–5581.

Droop, M. R. (1973), Some thoughts on nutrient limitation in algae, *J. Phycol.*, *9*, 261–271.

Duarte, C. M., A. Regaudie-de-Gioux, J. M. Arrieta, A. Delgado-Huertas and S. Agusti (2013), The oligotrophic ocean is heterotrophic, *Annu. Rev. Mar. Sci.*, *5*, 551–569.

Dubelaar, G. B. J. and P. L. Gerritzen (2000), CytoBuoy: a step forward towards using flow cytometry in operational oceanography, *Sci. Mar.*, *64*(2), 255–265.

Dugenne, M., M. Thyssen, D. Nérini, C. Mante, J-C Poggiale, N. Garcia, F. Garcia and G. J. Grégori (2014), Consequence of a sudden wind event on the dynamics of a costal phytoplankton community: an insight into specific population growth rates using a single cell high frequency approach, *Frontiers in Microbiology*, *5*(485), 1–14.

Dugenne, M., M. Thyssen, N. Garcia, N. Mayot, G. Bernard and G. J. Grégori (2015), Monitoring of a potential harmful algal species in the Berre lagoon by automated *in situ* flow cytometry, *H-J Ceccaldi et al. (eds), Marine Productivity: Perturbations and Resilience of Socio-ecosystems, Springer 2015*, 117–126.

Durand, M. D. (1995), Phytoplankton growth and diel variations in beam attenuation through individual cell analysis, *phD Thesis*, 1–16.

Eppley, R. W., R. W. Holmes and J. D. H. Strickland (1967), Sinking rates of marine phytoplankton measured with a fluorometer, *J. exp. mar. Biol. Ecol.*, *1*, 191–208.

Eppley, R. W. (1972), Temperature and phytoplankton growth in the sea, *Fishery bulletin*, *70*(4), 1063–1085.

Estournel, C., P. Testor, P. Damien, F. D'Ortenzio, P. Marsaleix, P. Conan, F. Kessouri, X. Durrieu de Madron, L. Coppola, J. M. Lellouche, S. Belamari, L. Mortier, C. Ulses, M. N. Bouin and L. Prieur (2016), High resolution modeling of dense water formation in the north-western Mediterranean during winter 2012-2013: Processes and budget, *J. Geophys. Res. Oceans*, *121*, 5367–5392.

Estrada, M. (1996), Primary production in the northwestern Mediterranean, *Scientia Marina*, *60*(2), 55–64.

Falkowski, P. G. (1980), Light-Shade adaptation, *Plant Physiol.*, *66*, 592–595.

Falkowski, P. G. and C. D. Wirick (1981), A simulation model of he effects of vertical mixing on primary productivity, *Marine Biology*, *65*, 69–75.

Falkowski, P. G., D. Ziemann, Z. Kolber and P. K. Bienfang (1991), Role of eddy pumping in enhancing primary production in the ocean, *Nature*, *352*, 55–58.

Fasham, M. J. R. (1985), Flow analysis of Materials in the Marine Euphotic Zone, *Ecosystem Theory for biological oceanography, R. E. Ulanowicz and T. Platt (eds), Canadian bulletin of fisheries and aquatic Sciences*, *213*, 139–162.

Ferrier-Pages, C. and F. Rassoulzadegan (1994), Seasonal impact of the microzooplankton on pico- and nanoplankton growth rates in the northwest Mediterranean Sea, *Mar. Ecol. Prog. Ser.*, *108*, 283–294.

Field, J., B. Kagan, C. Lin, V. Ryabchenko, J. Sarmiento and J. Steele (1993), Global Extrapolation, *G. T. Evans and M. J. R. Fashman (eds) Towards a model of Ocean biogeochemical processes. NATO ASI I 10, Springer-Verlag, Berlin*, 21–46.

Field, C. B., M. J. Behrenfeld, J. T. Randerson and P. Falkoswki (1998), Primary Production of the Biosphere: Integrating Terrestrial and Oceanic Components, *Science*, *281*, 237–240.

Fogg, G. E. (1986), Picoplankton, *F. Megusar and M. Gantar (eds), Perspectives in microbial ecology, Slovene Society for Microbiology, Ljubljana*, 96–100.

Franks, P. J. S. (2001), Phytoplankton blooms in a fluctuating environment: the roles of plankton response time scales and grazing, *J.of Plankton Res.*, *23*(12), 1433–1441.

Friedriches et al (2007), Assessment of skill and portability in regional marine biogeochemical models: Role of multiple planktonic groups, *J. Geophys. Res.*, *112*, 1–22.

Friedriches et al (2009), Assessing the uncertainties of model estimates of primary productivity in the tropical Pacific Ocean, *J. of Marine Systems*, *76*, 113–133.

Furnas, M. J. (1990), *In situ* growth rates of marine phytoplankton: approaches to measurement, community and species growth rates, *J. of Plankton Res.*, *12*(6), 1117–1151.

Gacic M., G. Civitarese, S. Miserocchi, V. Cardin , A. Crise and E. Mauri (2002), The open-ocean convection in the Southern Adriatic: a controlling mechanism of the spring phytoplankton bloom, *Continental Shelf Res.*, *22*, 1897–1908.

Garcia, M. J. L., C. Millot, J. Font, E. Garcia-Ladona (1994), Surface circulation variability in the Balearic Basin, *J. Geophys. Res.*, *99*(2), 3285–3296.

Garcia, N., P. Raimbault, E. Gouze and V. Sandroni (2002), Fixation de diazote et production primaire en Méditerranée occidentale, *C.R. Biologies*, *329*, 742–750.

Geider, R. J. (1984), Light and nutrient effects on microbial physiology, *phD Thesis*, *29*, 1–184.

Gomez F. and G. Gorsky (2003), Annual microplankton cycles in Villefranche Bay, Ligurian Sea, NW Mediterranean, *J. of Plankton Res.*, *25*(4), 323–339.

Guidi, L., L. Stemmann, G. A. Jackson, F. Ibanez, H. Claustre, L. Legendre, M. Picheral and G. Gorsky (2009), Effects of phytoplankton community on production, size and export of large aggregates: A world-ocean analysis, *Limnol. Oceanogr.*, *54*(6), 1951–1963.

Guidi, L., L. Legendre, G. Reygondeau, J. Uitz, L. Stermmann and S. A. Henson (2015), A new look at ocean carbon remineralization for estimating deepwater sequestration, *Global Biogeochemical Cycles*, *29*, 1–267.

Guidi, L. et al. (2016), Plankton networks driving carbon export in the oligotrophic ocean, *Nature*, *532*, 465–470.

Gutierrez-Rodriguez, A., M. Latasa, M. Estrada, M. Vidal and C. Marrase (2010), Carbon fluxes through major phytoplankton groups during the spring bloom and post-bloom in the Northwestern Mediterranean Sea, *Deep-Sea Research I*, *57*, 486–509.

Hagstrom, A., F. Azam, A. Andersson, J. Wikner and F. Rassoulzadegan (1988), Microbial loop in an oligotrophic pelagic marine ecosystem: possible roles of cyanobacteria and nanoflagellates in the organic fluxes, *Mar. Ecol. Prog. Ser.*, *49*, 171–178.

Herbaut, C. (1994), Etude de la circulation océanique en méditerranée occidentale, *PhD Thesis*, 1–187.

Hillmer, I. and J. Imberger (2007), Estimating in situ phytoplankton growth rates with a Lagrangian sampling strategy, *Limnol. Oceanogr. Methods*, *5*, 495–509.

Hirata, T., N. J. Hardman-Mountford, R. J. W. Brewin, J. Alken, R. Barlow, K. Suzuki, T. Isada, E. Howell, T. Hashioka, M. Noguchi-Aita and Y. Yamanaka (2011), Synoptic relationships between surface chlorophyll-a and diagnostic pigments specific to phytoplankton functional types, *Biogeosciences*, *8*, 311–327.

Houpert L., X. Durrieu de Madron, P. Testor, A. Bosse, F. D'Ortenzio, M. N. Bouin, D. Dausse, H. Le Goff, S. Kunesch, M. Lebaste, L. Coppola, L. Mortier and P. Raimbault (2016), Observations of open-ocean deep convection in the northwestern Mediterranean Sea: Seasonal and interannual variability of mixing and deep water masses for the 2007-2013 period, *J. of Geophys. Res. Oceans*, *This issue*.

Huisman, J., P. Van Oostveen and F. J. Weissing (1999), Species dynamics in phytoplankton blooms: Incomplete mixing and competition for light, *The American naturalist*, *154*(1), 46–68.

Huisman, J., M. Arrayas, U. Ebert and B. Sommeijer (2002), How do sinking phytoplankton species manage to persist?, *The American naturalist*, *159*(3), 245–254.

Hunter-Cervera, K. R., M. G. Neubert, A. R. Solow, R. J. Olson, A. Shalapyonok and H. M. Sosik (2014), Diel size distributions reveal seasonal growth dynamics of a coastal phytoplankter, *PNAS*, 1–6.

Hutchinson,G. E. (1961), The paradox of the Plankton, *The American naturalist*, *95*(82), 137–145.

Irigoien, X., K. J. Flynn and R. P. Harris (2005), Phytoplankton blooms: a 'loophole' in microzooplankton grazing impact?, *J. of Plankton Res.*, *27*(4), 313–321.

Jacques, G. (1988), Flux de carbone en milieu pélagique de Méditerranée occidentale lors de la floraison printanière, *Oceanologica acta*, *23*, 251–265.

Jacquet, S., J-F Lennon, D. Marie and D. Vaulot (1998), Picoplankton population dynamics in coastal waters of the northwestern Mediterranean Sea, *Limnol. Oceanogr.*, *43*(8), 1916–1931.

Jacquet, S., F. Partensky, D. Marie, R. Casotti and D. Vaulot (2001), Cell cycle regulation by light in *Prochlorococcus* Strains, *Applied and Environmental microbiology*, *67*(2), 782–790.

Jacquet, S., L. Prieur, P. Nival and D. Vaulot (2010), Structure and variability of the microbial community associated to the Alboran Sea frontal system (Western Mediterranean) in winter, *J.*

*of Oceanography, Research and Data*, *3*, 47–75.

Jebri, F., F. Birol, B. Zakardjian, J. Bouffard, C. Sammari (2016), Exploiting coastal altimetry to improve the surface circulation scheme over the central Mediterranean Sea, *J. of Geophys. Res. Oceans*, *121*, 4888–4909.

Jeffrey, S. W. (1980), Algal pigment systems, *P. G. Falkowski (eds), Primary Productivity in the Sea, Plenum Press New York*, 33–58.

Kiørboe,T. (1993), Turbulence, Phytoplankton cell size, and the structure of pelagic food webs, *Advances in Marine Biology 29*, 1–61.

Kiørboe,T. (2008), A mechanistic approach to plankton ecology, *Princeton University Press*.

Kirchman, D. L. (1999), Phytoplankton death in the Sea, *Nature*, *398*, 293–294.

Krause, J. W. (2008), Silicon biogeochemistry in the open-ocean surface waters: Insights from the Sargasso Sea and Equatorial Pacific, *phD Thesis*.

Landry, M. R.and R. P. Hassett (1982), Estimating he grazing impact of marine micro-zooplankton, *Marine Biology,67*, 283–288.

Landry, M. R., M. D. Ohman, R. Goericke, M. R. Stuckel and K. Tsyrklevich (2009), Lagrangian studies of phytoplankton growth and grazing relationships in a coastal upwelling ecosystem off Southern California, *Progress in Oceanography,83*, 208–216.

Latasa, M., X. Anxelu, G. Moran, R. Scharek and M. Estrada (2005), Estimating the carbon flux through main phytoplankton groups in the northwestern Mediterranean, *Limnol. Oceanogr.,50*(5), 1447–1458.

Lavigne, H. (2013), Impact de la variabilité saisonnière de la profondeur de la couche de mélange sur le cycle saisonnier du phytoplancton en Méditerranée, *PhD Thesis*, 1–145.

Lefort, T., and J. M. Gasol (2014), Short-time scale coupling of picoplankton community structure and single-cell heterotrophic activity in winter in coastal NW Mediterranean Sea waters, *J. of Plankton Res.*, *36*(1), 243–258.

Legendre, L. and J. Le Fèvre (1989), Hydrodynamical singularities as controls of recycled versus export production in oceans, *W. H. Berger et al. (eds) Productivity of the ocean: Present and past. Wiley*, 49–63.

Legendre, L. (1990), The significance of microalgal blooms for fisheries and for the export of particulate organic carbon in oceans, *J. of Plankton Res.*, *12*(4), 681–699.

Lehahn, Y., F. D'Ovidio, M. Lévy and E. Heifetz (2007), Stirring of the northeast Atlantic spring bloom: A Lagrangian analysis based on multisatellite data, *J. Geophys. Res.*, *112*(C08005), 1–15.

Le Moigne, F. A. C. et al. (2015), Carbon export efficiency and phytoplankton community composition in the Atlantic sector of the Arctic Ocean, *J. Geophys. Res. Oceans*, *120*, 3896–3912.

Le Quéré, C., et al. (2005), Ecosystem dynamics based on plankton functional types for global ocean biogeochemistry models, *Global Change Biology*, *11*, 2016–2040.

Lévy M., L. Mémery and J-M André (1998), Simulation of primary production and export fluxes in the Northwestern Mediterranean Sea, *J. of Marine Research*, *56*, 197–238.

Lévy M., O. Jahn, S. Dutkiewicz, M. J. Follows and F. d'Ovidio (2015), The dynamical landscape of marine phytoplankton diversity, *J. R. Soc. Interface*, *12*, 1–11.

Li, W. K. W. (1993), Estimation of primary production by flow cytometry, *mar. Sci. Symp.*, *197*, 79–91.

Lidemann, C. and M. A. St John (2014), A seasonal diary of phytoplankton in the North Atlantic, *Frontiers in Marine Science*, *1*(37), 1–6.

Lochte, K., H. W. Ducklow, M. J. R. Fasham and C. Stienen (1993), Plankton succession and carbon cycling at 47°N 20°W during the JGOFS North Atlantic Bloom experiment, *Deep-Sea Research II*, *40*(1/2), 91–114.

Lomas, M. W. and S. B. Moran (2011), Evidence fro aggregation and export of cyanobacteria and nano-eukaryotes from the Sargasso Sea euphotic zone, *Biogeosciences*, *8*, 203–216.

Longhurst, A. R. and W. G.Harrison (1989), The biological pump: Profiles of plankton production and consumption in the upper ocean, *Prog. Oceanog.*, *22*, 47–123.

Longhurst, A. R. (1991), Role of the marine biosphere in the global carbon cycle, *Limnol. Oceanogr.*, *36*(8), 1507–1526.

Magazzu, G. and F. Decembrini (1995), Primary production, biomass and abundance of phototrophic picoplankton in the Mediterranean Sea: a review, *Aquat. microb. Ecol.*, *9*, 97–104.

Maranon, E., P. Cermeno, J. Rodriguez, M. V. Zubkov, R. P. Harris (2007), Scaling of phytoplankton photosynthesis and cell size in the ocean, *Limnol. Oceanogr.*, *52*(5), 2190–2198.

Maranon, E., P. Cermeno, D. C. Lopez-Sandoval, T. Rodriguez-Ramos, C. Sobrino, M. Huertas-Ortega, J. M. Blanco and J. Rodriguez (2013), Unimodal size scaling of phytoplankton growth and he size dependence of nutrient uptake and use, *Ecology Letters*, *16*, 371–379.

Maranon, E. (2015), Cell size as a key determinant of phytoplankton metabolism and community structure, *Annu. Rev. Mar. Sci.*, *7*, 241–264.

Margalef R. (1985), Mediterranean Marine ecosystems, *M. Moraitou-Apostolopoulou and V. Kiotsis (eds) NATO Conference series Series I: Ecology, Springer Science Business Media*, 1–401.

Marra, J. (1978), Phytoplankton photosynthetic response to vertical movement in a mixed layer, *Marine Biology*, *46*, 203–208.

Marra, J. (1980), Vertical mixing and primary production, *Falkowski, P. G. (eds) Primary productivity in the Sea, Plenum Press*, 121–137.

Marsaleix, P., F. Auclair, C. Estournel (2009), Low-order pressure gradient schemes in sigma coordinate models: The Seamount test revisited, *Ocean Modelling*, *30*,169–177.

Marsaleix, P., F. Auclair, T. Duhaut, C. Estournel, C. Nguyen and C. Ulses (2012), Alternatives to the Robert-Asselin filter, *Ocean Modelling*, *41*,53–66.

Martin, A. P. and K. J. Richards (2002), Patchy productivity in the open ocean, *Global biogeochemical cycles*, *16*(2), 1–9.

Martin, A. P. (2003), Phytoplankton patchiness: the role of lateral stirring and mixing, *Prog. in Oceanogr.*, *57*, 125–174.

Marty, J-C and J. Chiavérini (2002), Seasonal and interannual variations in phytoplankton production at DYFAMED time-series station, northwestern Mediterranean Sea, *Deep-Sea Research II*, *49*, 2017–2030.

Marty, J-C and J. Chiavérini (2010), Hydrological changes in the Ligurian Sea (NW Mediterranean, DYFAMED site) during 1995-2007 and biogeochemical consequences, *Biogeosciences*, *7*, 2117–2128.

Marty, J-C, J. Chiavérini, M-D Pizay and B. Avril (2002), Seasonal and interannual dynamics of nutrients and phytoplankton pigments in the western Mediterranean Sea at the DYFAMED time-series station (1991-1999), *Deep-Sea Research II*, *49*, 1965–1985.

Massana, R., and R. Logares (2013), Eukaryotic versus prokaryotic marine picoplankton ecology, *Environmental Microbiology*, *15*(5), 1254–1261.

Mayot, N., F. D'Ortenzio, M. R. D'Alacala, H. Lavigne and H. Claustre (2016), Interannual variability of the Mediterranean trophic regimes from ocean color satellites, *Biogeosciences*, *13*,1901–1917.

Mayot, N., F. D'Ortenzio, V. Taillandier, L. Prieur, O. Pasqueron de Fommervault, H. Claustre, A. Bosse, P. Bosse, P. Testor and P. Conan (2016), Impacts of the deep convection on the phytoplankton blooms in temperate seas: a multiplatform approach over a complete annual cycle (2012-2013 DEWEX experiment), *J. Geophys. Res.*, *This issue*.

McGuilicuddy, D. J., A. R. Robindon, D. A. Siegel, H. W. Jannasch, R. Johnson, T. D. Dickey, J. McNeils, A. F. Michaels and A. H. Knap (1998), Influence of mesoscale eddies on new production in the Sargasso Sea, *Nature*, *394*, 263–266.

McLachlan, G. J. (1987), On bootstrapping the likelihood ratio test statistics for the number of components in a Normal mixture, *Journal of the Royal Statistical Society, ser. C*, *36*(3), 318–324.

MEDOC (1970), Observation of formation of deep water in the Mediterranean Sea, 1969, *Nature*, *227*, 1937–1970.

Mella-Flores, D. et al. (2011), Is the distribution of *Prochlorococcus* and *Synechococcus* ecotypes in the Mediterranean Sea affected by global warming?, *Biogeosciences*, *8*,2785–2804.

Menden-Deuer S. and E. J. Lessard (2000), Carbon to volume relationships for dinoflagellates, diatoms and other protist plankton, *Limnol. Oceanogr.*, *45*(3),569–579.

Mermex group (2011), Marine ecosystems' responses to climatic and anthropogenic forcings in the Mediterranean, *Prog. in Oceanogr.*, *91*,97–166.

Mertens, C. and F. Schott (1997), Interannual variability of deep-water formation in the Northwestern Mediterranean, *J. of Physical Oceanography*, *28*, 1410–1424.

Michaels, A. F. and M. W. Silver (1988), Primary production, sinking fluxes and the microbial food web, *Deep-Sea Research*, *35*(4), 473–490.

Millot, C. (1985), Some features of the Algerian current, *J. Geophys. Res.*, *90*(4), 7169–7176.

Millot, C. (1999), Circulation in the Western Mediterranean Sea, *J. of Marine Systems*, *20*, 423–442.

Millot, C. and I. Taupier-Letage (2005), Circulation in the Mediterranean Sea, *Hbd Env. Chem.*, *5*(K), 29–66.

Moberg, E. A. and H. M. Sosik (2012), Distance maps to estimate cell volume from two-dimensional plankton images, *Limnol. Oceanogr.*, *10*,278–288.

Morel, A. (1991), Light and marine photosynthesis: a spectral model with geochemical and climatological implications, *Prog. Oceanogr.*, *26*,263–306.

Mostajir B., J. Bustillos-Guzman, H. Claustre and F. Rassoulzadegan (1998), Pigment dynamics associated with the grazing of a ciliate and a flagellate feeding on a cyanobacterium, *Oceanologica acta*, *21*(4), 581–588.

Moutin, T., P. Raimbault and J-C Poggiale (1999), Production primaire dans les eaux de surface de la Méditerranée occidentale. Calcul de la production journalière, *Life Sciences*, *322*, 651–659.

Moutin, T. and P. Raimbault (2002), Primary production, carbon export and nutrients availability in western and eastern Mediterranean Sea in early summer 1996 (MINOS cruise), *J. of Marine Systems*, *33-34*, 273–288.

Moutin, T. and L. Prieur (2012), Influence of anticyclonic eddies on the Biogeochemistry from the oligotrophic to the ultraoligotrophic Mediterranean (BOUM cruise), *Biogeosciences*, *9*, 3827–3855.

Murphy, L. S. and E. M. Haugen (1985), The distribution and abundance of phototrophic ultraplankton in the North Atlantic, *Limnol. Oceanogr.*, *30*(1), 47–58.

Navarro, G., S. Alvain, V. Vantrepotte and L. E. Huertas (2014), Identification of dominant phytoplankton functional types in the Mediterranean Sea based on a regionalized remote sensing approach, *Remote Sensing of Env.*, *152*, 557–575.

Not F., J. Del Campo, V. Balagué, C. De Vargas and R. Massana (2009), New insights into the diversity of marine picoeukaryotes, *Plos ONE*, *4*(9), 1–7.

Olita, A., R. Sorgente, A. Ribotti, L. Fazioli, A. Perilli (2011), Pelagic primary production in the Algero-Provençal Basin by means of multisensor satellite data: focus on interannual variability and its drivers, *Ocean Dynamics*, *61*, 1005–1016.

Olita, A., S. Sparnocchia, S. Cusi, L. Faziolo, R. Sorgente, J. Tinore and A. Ribotti (2014), Observations of a phytoplankton spring bloom onset triggered by a density front in NW Mediterranean, *Ocean Sci.*, *10*, 657–666.

Olson, R. J., S. W. Chisholm, E. R. Zettler and E. V. Armbrust (1988), Analysis of *Synechococcus* pigment types in the sea using single and dual beam flow cytometry, *Deep-Sea Research*, *35*(3), 425–440.

Omta, A. W., G. A. K. Van Voom, R. E. M. Rickaby and M. J. Follows (2013), On the potential role of marine calcifiers in galcial-interglacial dynamics, *Global Biogeochemical cycles*, *27*, 692–704.

Ottino, J. M. (1989), The kinematics of mixing stretching, chaos and transport, *Cambridge Univ. Press, Cambridge (UK), 1989.*

Partensky, F., J. Blanchot and D. Vaulot (1999), Differential distribution and ecology of *Prochlorococcus* and *Synechococcus* in oceanic waters: a review, *Bulletin de l'Institut océanographique de Monaco*, *19*, 457–475.

Percopo, I., R. Siano, F. Cerino, D. Sarno and A. Zingone (2011), Phytoplankton diversity during the spring

bloom in the northwestern Mediterranean Sea, *Botanica Marina*, *54*, 243–267.

Perez, M. T., J. R. Dolan, F. Rassoulzadegan and B. Mostajir (1996), Predation on marine picoplankton populations examined with an 'add-in' approach, *J. of Plankton Res.*, *18*(4), 635–641.

Perez, M. T., J. R. Dolan and E. Fukai (1997), Planktonic oligotrich ciliates in the NW Mediterranean: growth rates and consumption by copepods, *Mar. Ecol. Prog. Ser.*, *155*, 89–101.

Peters, R.H. (1983), The ecological implications of body size, *Cambridge studies in ecology*, *2*, 1–325.

Petrenko, A., C. Dufau and C. Estournel (2008), Barotropic eastward currents in the western Gulf of Lion, north-western Mediterranean Sea, during stratified conditions, *J. of Marine Systems*, *74*, 406–428.

Platt, T., D. V. Subba Rao and B. Irwin (1983), Photosynthesis of picoplankton in the oligotrophic ocean, *Nature*, *301*(24), 702–704.

Ptacnik, R., S. Diehl and S. Berger (2003), Performance of sinking and nonsinking phytoplankton taxa in a gradient of mixing depths, *Limnol. Oceanogr.*, *48*(5), 1903–1912.

Ramondenc, S., M. Goutx, F. Lombard, C. Santinelli, L. Stemmann, G. Gorsky and L. Guidi (2016), An initial carbon export assessment in the Mediterranean Sea based on drifting sediment traps and the Underwater Vision Profiler data sets, *Deep-Sea Research I*, *117*, 107–119.

Raveh, O., N. David, G. Rilov and E. Rahav (2015), The temporal dynamics of coastal phytoplankton and bacterioplankton in the Eastern Mediterranean Sea, *PLOS ONE*, 1–23.

Raven, J. A. (1986), Physiological consequences of extremely small size for autotrophic organisms in the sea, *T. Platt and W. K. W. Li (eds), Photosynthetic Picoplankton, Canadian Bulletin of Fisheries and Aquatic Science*, *214*, 1–70.

Raven, J. A. (1998), Small is beautiful: the picophytoplankton, *Functional Ecology*, *12*, 503–513.

Raven, J. A., Z. V. Finkel and A. J. Irwin (2005), Picophytoplankton: bottom-up and top-down controls on ecology and evolution, *Vie et milieu*, *55*, 209–215.

Redfield A. C. (1934), On the proportions of organic derivatives in sea water and their relation to the composition of plankton, *James Johnstone Memorial volume, University of Liverpool*, 176–192.

Ribalet, F., J. Swalwell, S. Clayton, V. Jimenez, S. Sudek, Y. Lin, Z. I. Johnson, A. Z. Worden and E. A. Armbrust (2015), Light-driven synchrony of *Prochlorococcus* growth and mortality in the subtropical Pacific gyre, *PNAS*, *112*(26), 8008–8012.

Ribera D'Alcala M., G. Civitarese, F. Conversano and R. Lavezza (2003), Nutrient ratios and fluxes hint at overlooked processes in the Mediterranean Sea, *J. of Geophys. Res.*, *108*(9), 1–16.

Richardson, T. L. and G. A. Jackson (2007), Small phytoplankton and carbon export from the surface ocean, *Science*, *315*, 838–840.

Rigual-Hernandez, A. S., M. A. Barcena, R. W. Jordan, F. J. Sierro, J. A. Flores, K. J. S Meier, L. Beaufort and S. Heussner (2013), Diatom fluxes in the NW Mediterranea: evidence from a 12-year sediment trap record and

superficial sediments, *J. of Plankton Res.*, *0*(0), 1–17.

Riley, G. A., H. Stommel and D. F. Bumpus (1949), Quantitative ecology of the plankton of the Western-North Atlantic, *Bull. Bingham Oceanogr. Coll.*, *12*, 1–169.

Robinson, A. R. and M. Golnaraghi (1994), The physical and dynamical oceanography of the Mediterranean Sea, *P. Malanotte-Rizzoli and A.R. Robinson (eds) Ocean Processes in Climate Dynamics: Global and Mediterranean Examples, NATO ASI Ser. C: Math and Phys. Sci. Springer*, 255-301.

Robinson, A. R. and P. F. J. Lermusiaux (2002), Data assimilation for modeling and predicting coupled physical-biological interactions in the Sea, *A.R Robinson, J.J. McCarthy and B.J. Rothschhild (eds) The Sea Volume 12 John Wiley and Sons, New York*, 475–536.

Rubio, A., B. Barnier, G. Jorda M. Espino and P. Marsaleix (2009), Origin and dynamics of mesoscale eddies in the Catalan Sea (NW Mediterranean): Insight from a numerical model study, *J. Geophys. Res.*, *114*(C06009),1–17.

Rutten, T. P. A., B. Sandee and A. R. T. Hofman (2005), Phytoplankton monitoring by high performance flow cytometry: A successful approach, *Cytometry part A*, *64A*,16–26.

Ryther, J. H., D. W. Menzel (1959), Light adaptation by marine phytoplankton, *Limnol. Oceanogr.*, *4*, 492–549.

Sammartino, M., A. Di Cicco, S. Marullo and R. Santoleri (2015), Spatio-temporal variability of micro-, nano- and pico- phytoplankton in the Mediterranean Sea from satellite ocean colour data of SeaWiFS, *Ocean Sci.*, *11*, 759–778.

Schroder, K., G. P. Gasparini, M. Tangherlini and M. Astraldi (2006), Deep and intermediate water in the western Mediterranean under the influence of the Eastern Mediterranean Transient, *Geophys. Res. Let.*, *33*, 1–6.

Send, U., J. Font, G. Krahmann, C. Millot, M. Rhein and J. Tintoré (1999), Recent advances in observing the physical oceanography of the western Mediterranean Sea, *Prog. in Oceanogr.*, *44*, 37–64.

Séverin, T., P. Conan, X. Durrieu de Madron, L. Houpert, M-J Oliver, L. Oriol, J. Caparros, J. F. Ghiglione and M. Pujo-Pay (2014), Impact of open-ocean convection on nutrients, phytoplankton biomass and activity, *Deep-Sea Research I*, *94*, 62–71.

Sieburth, J., V. Smetacek and J. Lenz (1978), Pelagic ecosystem structure: Heterotrophic compartments of the plankton and their relationship to plankton size fractions, *Limnol. Oceanogr.*, *23*(6), 1256–1263.

Siegenthaler, U., and J. L. Sarmiento (1993), Atmospheric carbon dioxide and the ocean, *Nature*, *365*, 119–125.

Silovic, T., N. Barrier, M. Dugenne, D. Lefèbre, M. Thyssen, R. Leroux, P. Fey, M. Denis and G. J. Grégori (2016), Microbial response to winter deep sea convection and spring bloom conditions in the Gulf of Lion (NW Mediterranean), *J. Geophys. Res. Oceans*, *This issue.*

Simon, N., R. G. Barlow, D. Marie, F. Partensky and D. Vaulot (1994), Characterization of oceanic photosynthetic picoeukaryotes by flow cytometry, *J. Phycol.*, *30*, 922–935.

Smayda, T.J. (1970), Normal and accelerated sinking of phytoplankton in the sea, *Marine Geology*, *11*, 105–122.

Sohm, J. A., E. A. Webb and D. G. Capone (2011), Emerging patterns of marine nitrogen fixation, *Nature reviews*, *9*, 499–508.

Sosik, H. M., R. J. Olson, M. G. Neubert and A. Shalapyonok (2003), Growth rates of coastal phytoplankton from time-series measurements with a submersible flow cytometer, *Limnol. Oceanogr.*, *48*(5), 1756–1765.

Sournia, A. (1973), La production primaire planctonique en Méditerranée: Essai de mise à jour *Bull. Etude Commun. Mediter*, *5*, 1–128.

Sournia, A., M-J Chrétiennot-Dinet and M. Ricard (1991), Marine phytoplankton: how many species in the world ocean *J. of Plank. Res.*, *13*(5), 1093–1099.

Steele, J. H. (1962), Environmental control of photosynthesis in the Sea, *Limnol. Oceanogr.*, *7*, 137–150.

Steeman-Nielsen, E. (1952), The use of radioactive carbon ($C^{14}$) for measuring organic production in the sea, *J. Cons. Int. Explor. Mer.*, *18*, 117–140.

Stokes, G. G. (1951), On the effect of the internal friction of fluids on the motion of pendulums, *Trans. Cambridge Phil. Soc. IX, Mathematical and Physical Papers*, *3*, 1–141.

Sverdrup, H. U. (1953), On conditions for the vernal blooming of phytoplankton, *J. Cons. Int. Explor. Mer.*, *18*(3), 287–295.

Testor, P. and J-C Gascard (2006), Post-convection spreading phase in the Northwestern Mediterranean Sea, *Deep-Sea Research I*, *53*, 869–893.

Thyssen, M., G. A. Tarran, M. V. Zubkov, R. J. Holland, G. Grégori, P. H. Burkill and M. Denis (2008), The emergence of automated high-frequency flow cytometry: revealing temporal and spatial phytoplankton variability, *J. of Plankton Res.*, *30*(3), 333–343.

Thyssen, M., G. J. Grégori, J-M Grisoni, M. L. Pedrotti, L. Mousseau, L. F. Artigas, S. Marro, N. Garcia, O. Passafiume and M. J. Denis (2014), Onset of the spring bloom in the northwestern Mediterranean Sea: influence of environmental pulse events on the *in situ* hourly-scale dynamics of the phytoplankton community structure, *Frontiers in Microbiology*, *5*(387), 1–16.

Thyssen, M., S. Alvain, A. Lefèbvre, D. Dessailly, M. Rijkeboer, N. Guiselin, V. Creach and L. F. Artigas (2015), High-resolution analysis of a North sea phytoplankton community structure based on in situ flow cytometry observations and potential implications for remote sensing, *Biogeosciences*, *12*, 4051–4066.

Tian, R. C. (2006), Towards standard parametrizations in marine biological modeling, *Ecological Modelling*, *193*, 363–386.

Tolosa, I., I. Vescovali, N. LeBlond, J-C Marty, S. De Mora and L. Prieur (2004), Distribution of pigments and fatty acid biomarkers in particulate matter from the frontal structure of the Alboran Sea (SW Mediterranean Sea), *Marine Chemistry*, *88*, 103–125.

Touratier F., C. Gouet, L. Houpert, X. Durrieu de Madron, D. Lefèvre, M. Stabholz and V. Guglielmi (2016), Role of deep convection on anthropogenic $CO_2$ sequestration in the Gulf of Lions (northwestern Mediterranean Sea), *Deep-Sea Research I*, *133*, 33–48.

Townsend, D. W., M. D. Keller, M. E. Sieracki and S. G. Ackelson (1992),

Spring phytoplankton blooms in the absence of vertical water column stratification, *Nature*, *360*(5), 59–62.

Tunin-Ley A., F. Ibanez, J-P Labat, A. Zigone and R. Lemée (2009), Phytoplankton biodiversity and NW Mediterranean Sea warming: changes in the dinoflagellate genus *Ceratium* in the $20^{th}$ century, *Mar. Ecol. Prog. Ser.*, *375*, 85–99.

Turley, C. M., M. Bianchi, U. Christaki, P. Conan, J. R. W. Harris, S. Psarra, G. Ruddy, E. D. Stutt, A. Tselepides and F. Van Wambeke (2000), Relationship between primary producers and bacteria in an oligotrophic sea- the Mediterranean and biogeochemical implications, *Mar. Ecol. Prog. Ser.*, *193*, 11–18.

Uitz, J., H. Claustre, A. Morel and S. B. Hooker (2006), Vertical distribution of phytoplankton communities in open ocean: An assessment based on surface chlorophyll, *J. Geophys. Res.*, *111*, 1–23.

Uitz, J., D. Stramski, B. Gentili, F. D'Ortenzio and H. Claustre (2012), Estimates of phytoplankton class-specific and total primary production in the Mediterranean Sea from satellite ocean color observation, *Global biogeochemical cycles*, *26*, 1–10.

Vaulot, D. and S. W. Chisholm (1987), A simple model of the growth of phytoplankton populations in light/dark cycles, *J. of Plankton Res.*, *9*(2), 345–366.

Vaulot, D., K. Romari and F. Not (2002), Are autotrophs less diverse than heterotrophs in marine picoplankton, *TRENDS in Microbiology*, *10*(6), 266–267.

Vaulot, D., W. Eikrem, M. Viprey and H. Moreau (2008), The diversity of small eukaryotic phytoplankton (<3$\mu$m) in marine ecosystems, *FEMS Microbial review*, *32*, 795–820.

Verity, P. G., C. Y. Robertson, C. R. Tronzo, M. G. Andrews, J. R. Nelson and M. E. Sieracki (1992), Relationships between cell volume and the carbon and nitrogen content of marine photosynthetic nanoplankton, *Limnol. Oceanogr.*, *37*(7), 1434–1446.

Vidussi, F., J-C Marty and J. Chiavérini (2000), Phytoplankton pigment variations during the transition from spring bloom to oligotrophy in the northwestern Mediterranean sea, *Deep-Sea Research I*, *47*, 423–445.

Ward, B. A., S. Dutkiewicz, O. Jahn and M. J. Follows (2012), A size-structured food-web model for the global ocean, *Limnol. Oceanogr.*, *57*(6), 1877–1891.

Wassmann, P. (1998), Retention versus export food chains: processes controlling sinking loss from marine pelagic systems, *Hydrobiologica*, *363*, 29–57.

Waterbury, J. B., S. W. Watson, R. R. L. Guillard and L. E. Brand (1979),Widespread occurrence of a unicellular marine planktonic cyanobacterium, *Nature*, *277*, 293–294.

Winder, M. and J. E. Cloern (2010),The annual cycles of phytoplankton biomass, *Phil. Trans. R. Soc.*, *365*, 3215–3326.

Worden, A. Z. and F. Not (2010),Ecology and diversity of picoeukaryotes, *D. L. Kirchman (eds) Microbial Ecology of the Oceans, John Wilez and Sons*, 159–205.

Yoch, D. C. (2002), Dimethylsulfoniopropionate: Its sources, role in the marine food web and biological degradation to Dimethylsulfide, *App. and Env. Mic.*, *68*(12), 5804–5815.

Zhou, Q., W. Chen, H. Zhang, L. Peng, L. Liu, Z. Han, N. Wan, L. Li and L. Song (2012), A flow cytometer based protocol for quantitative analysis of bloom-forming cyanobacteria (*Microcystis*) in lake sediments, *J. of Env. Sciences*, *24*(9), 1709–1716.

## 4.6 Appendix

# Appendix

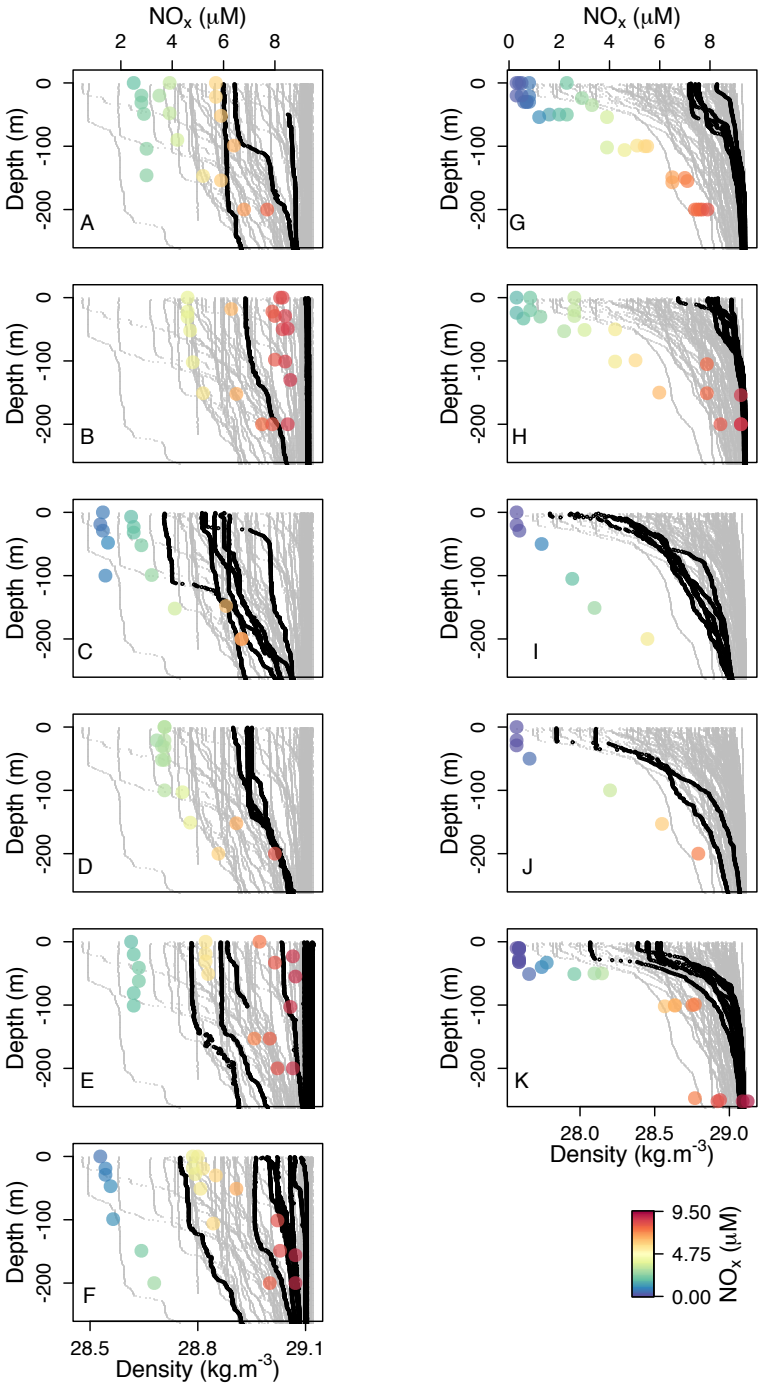


Appendix a: Vertical profiles of water density (black dots: for the zone, grey dots: for the entire Leg) and nutrients concentration (colored dots) within each water type (A,B,...,K)

Appendix b: Hydrologic variables mean ± standard deviation within homogeneous water types (A,B,...,K)

| Hydrologic Variables | LEG 1 | A | B | C |
|---|---|---|---|---|
| | mean ± sd | mean ± sd | mean ± sd | mean ± sd |
| **Casts** | | | | |
| Stations | 1 – 74 | 3 5 6 | 7 9 11 | 31 33 |
| Dates | $Feb/03 - Feb/21$ | $Feb/04 - Feb/05 - Feb/05$ | $Feb/05 - Feb/05 - Feb/06$ | $Feb/12 - Feb/13$ |
| Time | 00 : 12 – 23 : 10 | 18 : 05 – 02 : 59 – 07 : 18 | 10 : 21 – 15 : 47 – 08 : 25 | 23 : 10 – 06 : 37 |
| $NO_x$ ($\mu M$) | 4.8 ± 2.74 | 4 ± 1.6 | 7 ± 2.11 | 1.8 ± 0.78 |
| $NH_4^+$ ($\mu M$) | 0.004 ± 0.005 | 0.001 ± 0.002 | 0.004 ± 0.005 | 0.002 ± 0.002 |
| $PO_4^{3-}$ ($\mu M$) | 0.2 ± 0.14 | 0.16 ± 0.07 | 0.31 ± 0.13 | 0.08 ± 0.01 |
| **SACES** | | | | |
| Dates | $Feb/02 - Feb/21$ | $Feb/04 - Feb/05$ | $Feb/05 - Feb/06$ | $Feb/12 - Feb/13$ |
| Time | 14 : 25 – 17 : 35 | 07 : 00 – 09 : 00 | 09 : 00 – 11 : 00 | 13 : 00 – 15 : 00 |
| Temperature (°C) | 13 ± 0.35 | 13 ± 0.09 | 13 ± 0.07 | 13.3 ± 0.2 |
| Salinity (PSU) | 38.29 ± 0.24 | 38.27 ± 0.24 | 38.45 ± 0.14 | 38.14 ± 0.1 |
| NCP (mmol $O_2.m^{-2}.d^{-1}$) | 21 ± 1.62 | – ± – | – ± – | 22.4 ± 0.05 |
| Chl $a$ ($\mu g.dm^{-3}$) | 0.2 ± 0.11 | 0.2 ± 0.07 | 0.1 ± 0.05 | 0.2 ± 0.02 |
| *Synechococcus* ($cells.cm^{-3}$) | $3.5\,10^{+03} \pm 3.2\,10^{+03}$ | $2.8\,10^{+03} \pm 1.4\,10^{+03}$ | $1\,10^{+03} \pm 7.8\,10^{+02}$ | $7.7\,10^{+03} \pm 2.5\,10^{+03}$ |
| Picoeukaryotes ($cells.cm^{-3}$) | $5.8\,10^{+03} \pm 3.6\,10^{+03}$ | $6.3\,10^{+03} \pm 3.9\,10^{+03}$ | $2.1\,10^{+03} \pm 1.6\,10^{+03}$ | $7.3\,10^{+03} \pm 2.3\,10^{+03}$ |
| Nanoeukaryotes ($cells.cm^{-3}$) | $1.3\,10^{+03} \pm 6.8\,10^{+02}$ | $1.5\,10^{+03} \pm 8.8\,10^{+02}$ | $5.8\,10^{+02} \pm 2.9\,10^{+02}$ | $1.5\,10^{+03} \pm 3.2\,10^{+02}$ |
| Cryptophytes ($cells.cm^{-3}$) | $3.7\,10^{+01} \pm 5.6\,10^{+01}$ | $2.2\,10^{+01} \pm 1.4\,10^{+01}$ | $1.2\,10^{+01} \pm 1.9\,10^{+01}$ | $9\,10^{+01} \pm 7.2\,10^{+01}$ |
| Microphytoplankton Abundance ($cells.cm^{-3}$) | 7.5 ± 6.9 | $1.4\,10^{+01} \pm 8.8$ | 3.5 ± 2.8 | 9.9 ± 2.5 |

| Hydrologic Variables | D | E | F | LEG 2 |
|---|---|---|---|---|
| | mean ± sd | mean ± sd | mean ± sd | mean ± sd |
| **Casts** | | | | |
| Stations | 41 43 | 52 56 59 | 60 63 66 | 1 – 99 |
| Dates | $Feb/15 - Feb/15$ | $Feb/17 - Feb/18 - Feb/18$ | $Feb/19 - Feb/19 - Feb/19$ | $Apr/05 - Apr/24$ |
| Time | 01 : 09 – 09 : 18 | 22 : 18 – 12 : 03 – 16 : 46 | 06 : 04 – 13 : 13 – 22 : 53 | 00 : 11 – 23 : 56 |
| $NO_x$ ($\mu$M) | 3.7 ± 0 | 5 ± 2.51 | 3.7 ± 2.14 | 1.3 ± 1.54 |
| $NH_4^+$ ($\mu M$) | 0.005 ± 0.007 | 0.001 ± 0.001 | 0 ± 0 | 0.038 ± 0.053 |
| $PO_4^{3-}$ ($\mu M$) | 0.12 ± – | 0.01 ± 0.15 | 0.13 ± 0.07 | 0.07 ± 0.06 |
| **SACES** | | | | |
| Dates | $Feb/14 - Feb/16$ | $Feb/17 - Feb/18$ | $Feb/19 - Feb/20$ | $Apr/02 - Apr/25$ |
| Time | 23 : 00 – 01 : 00 | 21 : 00 – 23 : 00 | 03 : 00 – 05 : 00 | 16 : 59 – 17 : 01 |
| Temperature (°C) | 13.1 ± 0.13 | 13.1 ± 0.18 | 13.2 ± 0.14 | 14.5 ± 1.16 |
| Salinity (PSU) | 38.24 ± 0.11 | 38.38 ± 0.16 | 38.4 ± 0.14 | 38.15 ± 0.27 |
| NCP (mmol $O_2.m^{-2}.d^{-1}$) | 21.1 ± 0.16 | 21.3 ± 0.84 | 19.9 ± 1.06 | 22.6 ± 0.36 |
| Chl *a* ($\mu g.dm^{-3}$) | 0.2 ± 0.04 | 0.2 ± 0.13 | 0.2 ± 0.12 | 0.6 ± 0.58 |
| *Synechococcus* (cells.cm$^{-3}$) | $4.4\,10^{+03} \pm 1.2\,10^{+03}$ | $8.4\,10^{+02} \pm 4.9\,10^{+02}$ | $2.5\,10^{+03} \pm 1\,10^{+03}$ | $3.5\,10^{+03} \pm 4.7\,10^{+03}$ |
| Picoeukaryotes (cells.cm$^{-3}$) | $7.1\,10^{+03} \pm 2.5\,10^{+03}$ | $4.7\,10^{+03} \pm 3.6\,10^{+03}$ | $7.9\,10^{+03} \pm 4\,10^{+03}$ | $6.9\,10^{+03} \pm 8.5\,10^{+03}$ |
| Nanoeukaryotes (cells.cm$^{-3}$) | $1.3\,10^{+03} \pm 2.2\,10^{+02}$ | $1.4\,10^{+03} \pm 10\,10^{+02}$ | $1.9\,10^{+03} \pm 6.6\,10^{+02}$ | $7.9\,10^{+03} \pm 6.8\,10^{+03}$ |
| Cryptophytes (cells.cm$^{-3}$) | $3.7\,10^{+01} \pm 2.6\,10^{+01}$ | $1.5\,10^{+01} \pm 1.8\,10^{+01}$ | $2.3\,10^{+01} \pm 1.6\,10^{+01}$ | $2.6\,10^{+02} \pm 3.5\,10^{+02}$ |
| Microphytoplankton (cells.cm$^{-3}$) | $1.1\,10^{+01} \pm 4.1$ | 2.7 ± 2.1 | 7 ± 4 | $1.2\,10^{+01} \pm 1.6\,10^{+01}$ |

| Hydrologic Variables | G | H | I | J | K |
|---|---|---|---|---|---|
| | mean ± sd | mean ± sd | mean ± sd | mean ± sd | mean ± sd |
| **Casts** | | | | | |
| Stations | 22 23 24 25 26 | 31 33 37 | 66 67 | 79 | 81 83 84 85 87 |
| Dates | *Apr*/09 – *Apr*/09 – *Apr*/09 – *Apr*/10 – *Apr*/10 | *Apr*/11 – *Apr*/11 – *Apr*/11 | *Apr*/16 – *Apr*/17 | *Apr*/20 | *Apr*/21 – *Apr*/22 – *Apr*/22 – *Apr*/22 – *Apr*/22 |
| Time | 12 : 59 – 17 : 27 – 21 : 27 – 00 : 24 – 05 : 33 | 00 : 11 – 05 : 05 – 17 : 03 | 23 : 18 – 03 : 16 | 16 : 51 | 21 : 44 – 00 : 39 – 02 : 48 – 04 : 15 – 06 : 41 |
| $NO_x$ ($\mu$M) | 0.9 ± 0.83 | 2.6 ± 0.86 | 0.1 ± – | 0.1 ± – | 0.1 ± 0.05 |
| $NH_4^+$ ($\mu M$) | 0.05 ± 0.044 | 0.045 ± 0.037 | 0.007 ± – | 0.01 ± – | 0.003 ± 0.002 |
| $PO_4^{3-}$ ($\mu M$) | 0.05 ± 0.02 | 0.11 ± 0.04 | 0.02 ± – | 0.04 ± – | 0.03 ± 0.02 |
| **SACES** | | | | | |
| Dates | *Apr*/09 – *Apr*/10 | *Apr*/10 – *Apr*/12 | *Apr*/16 – *Apr*/18 | *Apr*/20 – *Apr*/21 | *Apr*/21 – *Apr*/22 |
| Time | 07 : 00 – 09 : 00 | 23 : 00 – 01 : 00 | 23 : 00 – 01 : 00 | 01 : 00 – 03 : 00 | 13 : 00 – 15 : 00 |
| Temperature (°C) | 13.6 ± 0.18 | 13.5 ± 0.14 | 16.3 ± 0.37 | 15.3 ± 0.21 | 15.1 ± 0.31 |
| Salinity (PSU) | 38.29 ± 0.06 | 38.37 ± 0.07 | 37.95 ± 0.05 | 37.72 ± 0.09 | 38.17 ± 0.15 |
| NCP (mmol $O_2$.m$^{-2}$.d$^{-1}$) | 22.5 ± 0.11 | 22.6 ± 0.23 | 22.4 ± 0.07 | 22.5 ± 0.03 | 22.7 ± 0.1 |
| Chl *a* ($\mu$g.dm$^{-3}$) | 0.9 ± 0.28 | 1.4 ± 0.76 | 0.1 ± 0.05 | 0.1 ± 0.02 | 0.5 ± 0.26 |
| *Synechococcus* (cells.cm$^{-3}$) | $9.4\,10^{+03} \pm 4.8\,10^{+03}$ | $5.2\,10^{+03} \pm 2.6\,10^{+03}$ | $3.2\,10^{+01} \pm 1.4\,10^{+01}$ | $3.3\,10^{+02} \pm 5.6\,10^{+02}$ | $2.9\,10^{+03} \pm 2.7\,10^{+03}$ |
| Picoeukaryotes (cells.cm$^{-3}$) | $8\,10^{+03} \pm 3.5\,10^{+03}$ | $2.3\,10^{+04} \pm 9.9\,10^{+03}$ | $8.1\,10^{+02} \pm 5\,10^{+02}$ | $9.2\,10^{+02} \pm 2.4\,10^{+02}$ | $3.3\,10^{+03} \pm 1.6\,10^{+03}$ |
| Nanoeukaryotes (cells.cm$^{-3}$) | $8.4\,10^{+03} \pm 1.8\,10^{+03}$ | $1.6\,10^{+04} \pm 6.2\,10^{+03}$ | $3.4\,10^{+03} \pm 2.6\,10^{+03}$ | $2\,10^{+03} \pm 2.9\,10^{+02}$ | $8.8\,10^{+03} \pm 4.1\,10^{+03}$ |
| Cryptophytes (cells.cm$^{-3}$) | $3.7\,10^{+02} \pm 1.6\,10^{+02}$ | $7.7\,10^{+02} \pm 2.7\,10^{+02}$ | $1.3\,10^{+01} \pm 4.8$ | $1.7\,10^{+01} \pm 7.1$ | $2\,10^{+02} \pm 1.7\,10^{+02}$ |
| Microphytoplankton (cells.cm$^{-3}$) | 9.1 ± 3.8 | $2\,10^{+01} \pm 1.3\,10^{+01}$ | 1.6 ± 1.2 | 2.8 ± 1.1 | 2.4 ± 1.2 |

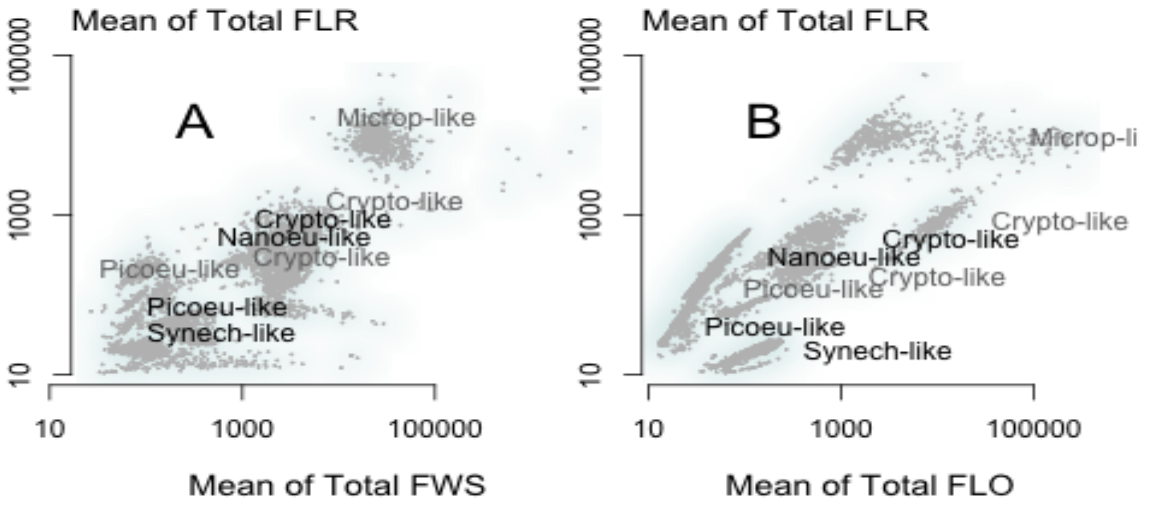


Appendix c: Projection of phytoplankton mean optical properties measured by automated flow cytometry during the 2 Legs of DeWEX: (A) FWS (Forward Scatter) vs FLR (Red Fluorescence), (B) FLO (Orange Fluorescence) vs FLR (Red Fluorescence). Growth rates have been estimated for the groups 'Synech-like' (*Synechococcus*), 'Picoeu-like' (Picoeukaryotes), 'Nanoeu-like' (Nanoeukaryotes) and 'Crypto-like' (Crytpophytes).

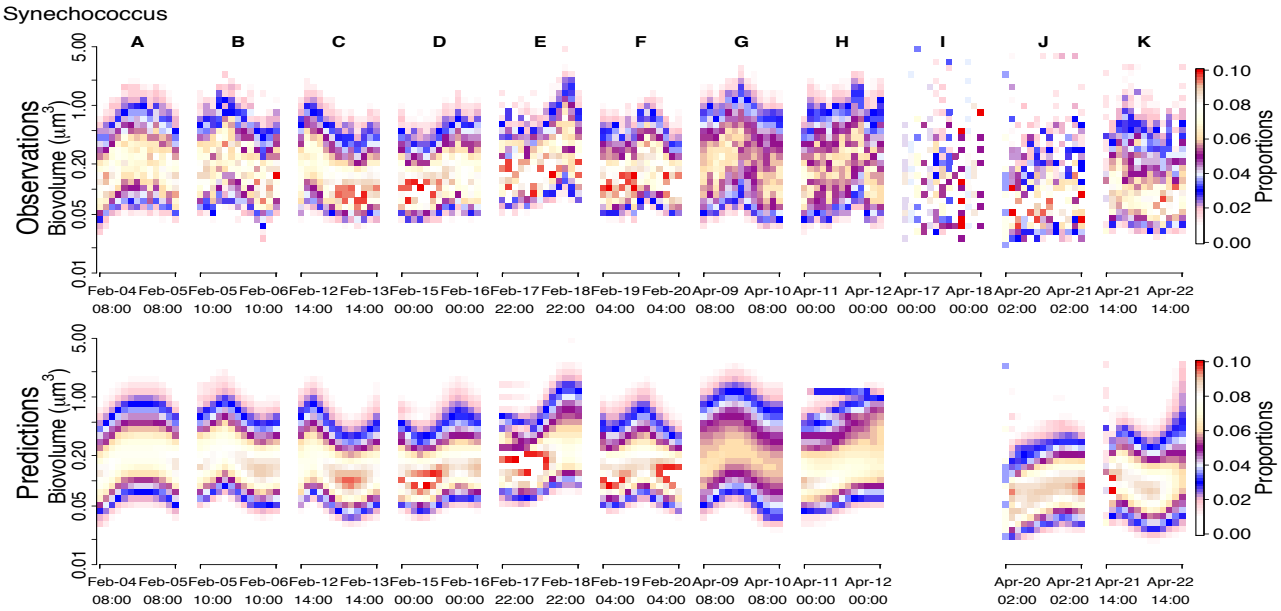


Appendix d: Time series of Synechococcus size distribution within each water types used to estimate *in situ* growth rates. Diel observations of biovolume (top panel) are reproduced via the optimal set of parameters that minimize the difference between observations and predictions (bottom panel)

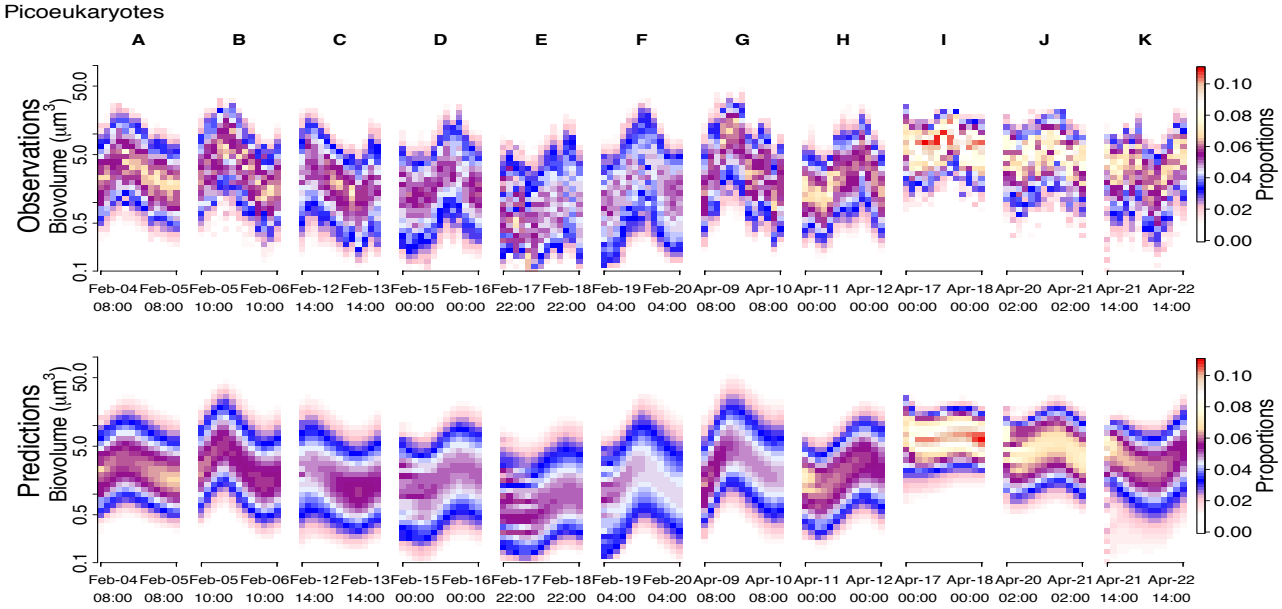


Appendix e: Time series of Picoeukaryotes size distribution within each water types used to estimate *in situ* growth rates. Diel observations of biovolume (top panel) are reproduced via the optimal set of parameters that minimize the difference between observations and predictions (bottom panel)

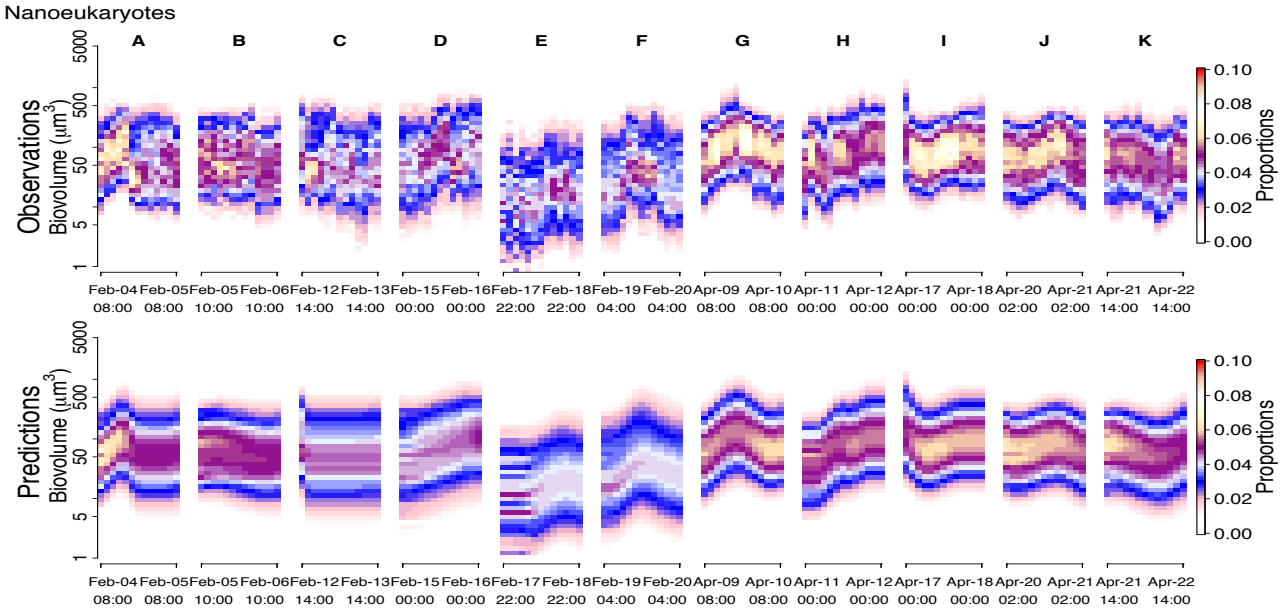


Appendix f: Time series of Nanoeukaryotes size distribution within each water types used to estimate *in situ* growth rates. Diel observations of biovolume (top panel) are reproduced via the optimal set of parameters that minimize the difference between observations and predictions (bottom panel)

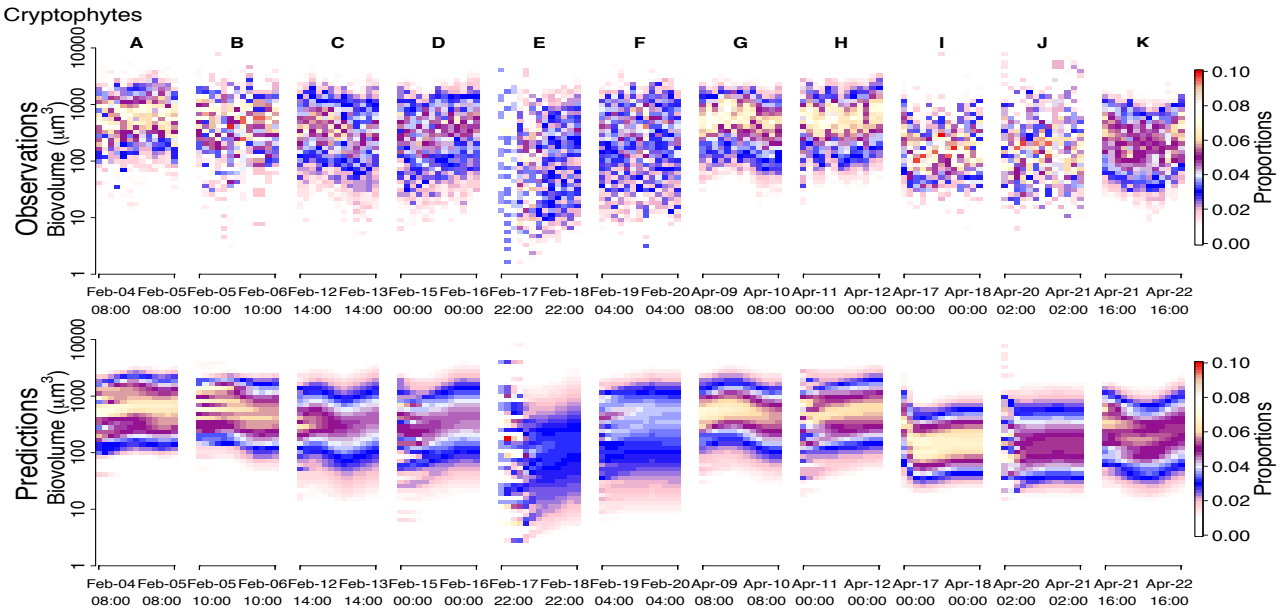


Appendix g: Time series of Cryptophytes size distribution within each water types used to estimate *in situ* growth rates. Diel observations of biovolume (top panel) are reproduced via the optimal set of parameters that minimize the difference between observations and predictions (bottom panel)

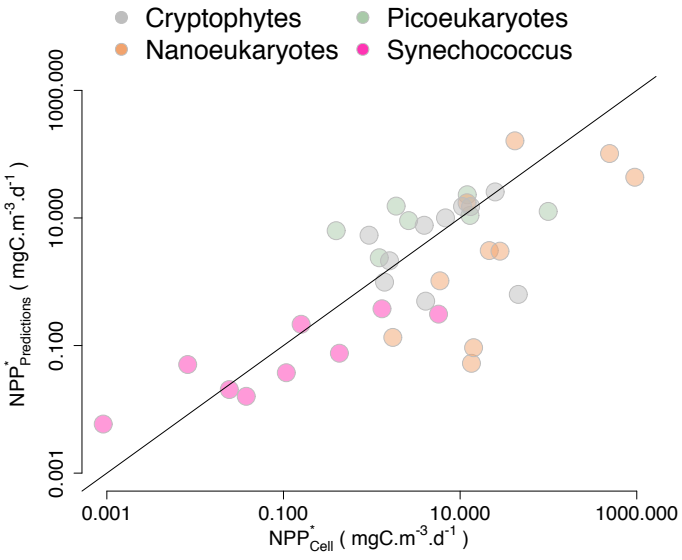


Appendix h: Comparison of estimations of net primary production during DEWEX observed from newly-formed cells biomass ($NPP^*_{cell}$) in Synechococcus (magenta dots), picoeukaryotes (green dots), nanoeukaryotes (orange dots) and cryptophytes (grey dots) populations and predicted by the growth limitations model described in equation 2.12 ($NPP^*_{Predictions}$).

# 5.0 Scaling group-specific primary productivity in Mediterranean surface open waters


**Abstract**

In the present study, we provide an up-to-date parameterisation of a daily productivity model applied in Mediterranean surface open waters for groups of phytoplankton: Synechococcus, picoeukaryotes, nanoeukaryotes and cryptophytes. This model is based on the mechanistic response of primary production to required stimuli of temperature, light and nutrients. Two approaches are described to estimate group-specific production rates by means of continuous *in situ* flow cytometry analyses. The first approach relies on the estimation of growth rates, as a quantitative indicator of the amount of newly-formed cells. The amount is predicted from the diel variation of populations size distribution. The second approach is supported in parallel by the modelling of size distributions. The consecutive incrementation of cells size are converted to carbon biomass during the photoperiod to approximate the photosynthetic assimilation of dissolved $CO_2$. If the fist approach requires the temporal projection of cell cycle transitions (i.e. cellular growth and mitotic division) over the diel period, the later only necessitates to observe the upward shift of a size distribution during 12 hours. Despite a strong shift of productivity, the characterisation of the 2013 transition between winter deep convection and bloom community dynamics yielded to non significant differences between estimations. The application of these approaches to the continuous analyses of phytoplankton during the Deep Water EXperiment (DeWEX) is presented to (i) illustrate the ability of a size-structured population model to establish the group-specific approximations of primary productivity without intrusive manipulations, (ii) identify the co-limitation of the primary production regime in the NW Mediterranean Sea, and (iii) parameterise the functioning of $CO_2$ uptake early in the year (February to May). We show that, in this time frame, all groups reached a maximal productivity constrained by the average surface waters temperature observed at this period (13.5-14.5 °C), the optimal utilisation of light by various pigment organisations (presence/absence of accessory pigments), and the asymptotic kinetics of ammonium ($NH_4^+$) assimilation. In relation to each population stock and C quota, this maximum ranged from 900 mg $C.m^{-3}.d^{-1}$ for nanoeukaryotes, to 80 mg $C.m^{-3}.d^{-1}$ for cryptophytes, 60 mg $C.m^{-3}.d^{-1}$ for picoeukaryotes and < 1 mg $C.m^{-3}.d^{-1}$ for Synechococcus. Following allometry, the individuals production rates, describing the mean capacity of C assimilation per cell, are linked to cell size (BV) by the relationship $Rate = aBV^b$ with a slope b=1.05 and an intercept a=log(0.25). The scope also explained the relative nutrients affinity between phytoplankton size fractions.



M. Dugenne, M. Thyssen, D. Lefèvre, P. Conan, C. Estournel, X. Durrieu de Madron, V. Taillandier, C. Bachet, O. Grosso, M. Goutx, T. Séverin, F. Touratier, I. Taupier-Letage, M. Pujo-Pay, D. Pommeret, G. Grégori

## 5.1 Introduction

Marine primary productivity is measured by the rate of change of autotrophs cells' carbon standing crop over time, whether resulting from the gross photosynthetic anabolism (GPP) or the net by-product of anabolism and catabolism (NPP) (Williams, 1993). One approach to measure PP consists in estimating the product of phytoplankton individuals photosynthetic rates and cells concentrations. The latter range between $10^{-3}$-$10^{5}$ cells.cm$^{-3}$ in natural populations (Cermeno et al., 2008), while assimilation rates vary between $10^{-3}$ and $10^{6}$ pg C.cell$^{-1}$.d$^{-1}$ (Maranon et al., 2007, Maranon, 2008; Lopez-Sandoval et al., 2014; Maranon, 2015). The product yields to production rates between $10^{-9}$-$10^{8}$ $\mu$g C.dm$^{-3}$.d$^{-1}$. Theoretical approximations encompass the global range of observations of marine productivity measured by $^{14}$C incubations, 0-1000 $\mu$g C.dm$^{-3}$.d$^{-1}$ (Buitenhuis et al., 2013). For Lindeman (1942), net primary production corresponds to the amount of particulate organic carbon (POC) available for heterotrophic secondary energy transfer. The resulting flux would thereby be uncorrected for *prior* grazing consumption, export, catabolic respiration, decomposition and/or exudation. After absorption, dissolved inorganic carbon (DIC) remains in the cell in the form of POC if not ulteriorly exuded. Exudation may represent 5 % of the daily NPP (Nagata, 2000). Conserved from exudation, the net uptake of DIC result in the direct allocation of new POC in the stock of present cells. In 24h, this stock is not constant. Cells reproduce either by fusion of gametes (i.e. syngamy) or by binary fission (i.e. cytokinesis) (Sandgren, 1988). By consequence, dynamic measures of phytoplankton stocks, via direct or indirect sampling, is an approach commonly adopted to estimate productivity in the Sea (Falkowski, 1980). The synoptic estimation of marine primary production at the global scale varies around 50 Pg C.yr$^{-1}$ (Behrenfeld et al., 2005; Westberry et al., 2008) with an uncertainty of 10% (Behrenfeld and Falkowski, 1997). In marine ecosystems, the coefficient of variation of phytoplankton biomass ranges between 66% and 450% (Malone and Ducklow, 1990). In natural populations, phytoplankton generation time last from few hours (~5 h) to several days (~10 d) (Furnas, 1990). Quiescence, encystment and sexual phase further increase the generation time under suboptimal growth. Phytoplankton groups ten thousands of species (Jeffrey and Vesk, 1997) whose diversity tends to fluctuate due to permanent disequilibrium disturbances (Connel, 1978). The growth of planktonic drifters is continuously dependent on the external fluctuations of the parcel of water they inhabit. Temperature, light and nutrients availability are almost continuously unstable. They represent the main growth descriptors of phytoplankton niches, directly influencing the life history of phytoplankton cells, their intrinsic dynamics and ultimately the amount of atmospheric $CO_2$ being fixed (Berhenfeld et al., 2008).

Phytoplankton asexual reproduction occurs during the cell cycle, following the succession of stages that continuously resume cellular growth, the *interphase*, to the final event representing binary fission, *Mitosis stage* (Elledge, 1996). If prokaryotes may start several rounds of DNA replication before mitosis (Binder and Chisholm, 1990), stages are generally well separated and distinct from cell size or the amount of DNA (Berdalet *et al.*, 1992). The effective separation of daughter cells during cytokinesis is an ubiquitous, conservative process that insure the generational transmission of the genetic information and of the minimal viable biomass among individuals of a population (Chisholm, 1981; Vaulot, 1995; Dapena *et al.*, 2015). Cells undergoing mitosis are assumed to allocate exactly the same biomass to the new generation of daughter cells. Diatoms, which decrease in size after each mitosis, are an

exception (Armburst and Chisholm, 1992). For other taxa, the standing crop of newly formed cells is equal to the net quantity of atmospheric $CO_2$ fixed by photosynthesis during the interphase (Vaulot *et al.*, 1995; Kirchman, 2002). The global NPP carbon-based model, *CbPM*, described in Berhenfeld *et al.* (2005) is currently based on this principle. Estimations depend on the formulation: $NPP(z) = C(z)\mu(z)$, where $C(z)$ and $\mu(z)$ are depth-dependent standing crop and growth rates. Carbon-based models rely on the monitoring of the differential incrementation of the bulk (Ryther and Menzel, 1965; Siegel *et al.*, 1989; Marra, 2002; Claustre *et al.*, 2008), eventually size-fractioned (Cermeno *et al.*, 2006) standing stock of C. Both approximations can be fairly similar in cultures and natural environment (Li and Goldman, 1981). However, Goldman (1980) found that discrepancies may appear over consequent generations as a function of cells physiological adaptations. Specific metabolic analyses are required to explain why they discord under limiting conditions (Smith and Geider, 1985). Several observations support this hypothesis (Malone, 1980): reduction of growth rates co-occurs with increase of cells size in cultures (Gieder *et al.*, 1986 and ref. within; Chisholm, 1992; Tang, 1995; Maranon *et al.*, 2013) and natural populations (Le Bouteiller *et al.*, 2003; Chang *et al.*, 2013). In quasi-absence of C uptake under null irradiance, the entire diel production is restricted to the photoperiod $\tau$ (Legendre *et al.*, 1983; Marra *et al.*, 1988). In this case, the net carbon increase results from the photosynthetic assimilation of $CO_2$ by oxygenic photosynthesis. Eppley and Sharp (1975), Williams *et al.* (1979) and Moutin *et al.* (1999) conducted experiments that support this assumption. In these studies, the net absorption of $^{14}C$ did not increase after 12h bottles incubation. For Bender *et al.*, (1999), the period of incubation determines if the productivity measured is close to net (24 hours incubations) or gross (short term incubations) C uptake rates. Morris (1980) and Hasley *et al.* (2010) advised to further include the major effects of differential C assimilation pathways. Metabolism pathways will partly explain the high variability of PP estimations observed with different approaches.

Independent measurements of PP are rarely conducted on the same sample. Some experiments designed to compared two methods led to rather puzzling conclusions. The sum of cluster-specific net production rates exceeding the bulk $^{14}C$ incubation rates, as described in André *et al.* (1999) or conversely underestimating it (Li, 1994). Is marine productivity following Aristote's quote 'The whole is greater than the sum of its parts'? Historically, global estimations of net primary production depended on holistic models/observations. Reductionist approaches have been recently favoured to take into account the fundamental constituents of the biological pump in order to provide a coherent framework to predict systems' evolution. This will be done by addressing phytoplankton diversity in contrasted ecosystems and measuring their primary production/growth rates. The differential contribution of phytoplankton size fractions (Legendre and LeFèvre, 1991) or functional types (PFTs) (Brewin et al., 2010; Uitz et al., 2010) shaped the primary productivity estimations and the large provinces of marine productive regimes (Longhurst and Harrison, 1989) observed by so far. The mechanism of atmospheric $CO_2$ uptake is a functionally redundant trait, which has been conserved over evolutionary scales to ensure the atmospheric oxygenation. Despite that, the integration of coarse diversity in oceanic biogeochemical models (OBMs) is necessary to foresee the alteration or stability of populations faced to Global change (Falkoswki et al., 1998; Pedros-Allio, 2006; Follows et al., 2007; Follows and Dutkiewicz, 2011). While the broad structure of phytoplankton sentinels is firmly informative, the distinction

of high level of genetic diversity is generally unfruitful (Kruk et al., 2011; Edwards et al., 2013; Bode et al., 2015). Instead of monophyletic taxa, *Functional Plankton Models* include distinct compartments, such as size fractions which play a crucial role for C transfer and export (Legendre and Le Févre, 1995). These models use emergent properties of ecosystems structures which influence phytoplankton fitness and biogeochemical cycles (Litchman and Klausmeier, 2008). Cermeno et al. (2016) thought that primary productivity is locally driven by populations favoured by natural selection. Margalef (1978) distinguished r and K strategists populations. However, the high growth rates displayed by r populations represents only the average of various individual rates (Chisholm et al., 1980; Campbell and Yentsch, 1989). The intraspecific variability is rarely explicited in productivity models. With these rare exceptions, the net primary production is mainly predicted in the frame of probabilistic (Platt and Gallegos, 1980; Woods and Onken, 1982) and mechanistic models (Malone, 1977, Platt, 1975). They are both important to represent the stochastic and determinist regulation of physical dispersion, biological interactions (e.g. predation, competition), and resource requirements (Nogueira et al., 2006; Bolnick et al., 2011).

The lack of representative datasets to validate biogeochemical models in the Mediterranean Sea motivated the present study. Among current models, Lazzari et al. (2012) predicted the variability of the primary production of 9 *Functional Types* by temperature, light, N and P gradients. They used the set of parameters determined for global ocean ecosystem models (Vichi et al., 2007). To support regional simulations of Mediterranean primary production, we must consider its recent evolution (Mermex group, 2011). Surface waters temperature is increasing (Shaltout and Omstedt, 2014) when discharges of allochthonous nutrients are decreasing (Ludwig et al., 2009). The alteration of solar radiation caused by the release of air pollutants and UVs penetration will probably affect primary production by noxious radiation and the attenuation of photosynthetically usable radiation (Nolle et al., 2005). The positive anomalies of Mediterranean sea surface temperature affect the stratification of the water column and the availability of remineralised nutrients in deep layers that support phytoplankton growth after mixing events. These factors are controlling C assimilation rates (doublings of cell carbon per day) in natural populations. The ratio of NPP, expressed in mg $C.m^{-3}.d^{-1}$ to stock biomass expressed in mg $C.m^{-3}$, or assimilation number (Eppley, 1972), may vary by 80 % in coastal ecosystems where productivity is highly dynamic due to the multiplicative effects of temperature, nutrients and light changes (Keller, 1989). Empiric PP variability has not been addressed in the Mediterranean Sea yet. In 2013, phytoplankton group-specific dynamics was unraveled by autonomous single-cell analyses in the North Western Mediterranean Sea, during contrasted productive period (February and April). The objectives of this study are (i) to present a complementary method of NPP rates based on theses analyses, in order to (ii) to provide a reevaluation of the standards parameters predicting daily primary productivity models in the Mediterranean Sea. Scaling marine primary productivity with temperature, light and nutrients will allow to integrate PP on the water column or extrapolate a set of discrete observations on resolutive vertical/horizontal spatial scales and/or temporal scales (e.g. daily to monthly to yearly) (Behrenfeld and Falskowski, 1997).

## 5.2 Material and methods

Size distribution modelling

During the Deep Water EXperiment cruises, an autonomous flow cytometer (Cy-

tosense, Cytobuoy, b.v.) has been deployed to analyse single-cells optical profiles of 4 phytoplankton groups every hour (Fig 1a). Analyses were carried out on surface samples collected along the R/V trajectory. The inverse model described in Sosik et al. (2003) was applied to group-specific diel observations of size distribution. This approach was used to infer populations *in situ* growth rates by reproducing the temporal variability of size distributions with cell cycle transitions. In the model (referred in Dugenne et al., 2014), temporal transitions between size classes, $\vec{v}$, are assumed to result from either cellular growth, supported by photosynthetic carbon assimilation, or asexual division. An inhomogeneous Markov Chain is used to project the initial distribution in time by matrix multiplications. The transitions matrix is a tridiagonal matrix, of dimensions mxm, which contains the dynamics probabilities, $p_{i,j}(t)$, of cells being conveyed in the $m$ size classes between $t$ and $t + dt$:

1. For elements of the main diagonal $p_{i,i}(t)$: the proportions of cells that neither grew nor divide between $t$ and $t + dt$ (*cellular stasis: [1-$\gamma$][1-$\delta$]*)

2. For elements of the diagonal $p_{i+1,i}(t)$: the proportions of cells that grew between $t$ and $t + dt$ (*cellular growth: $\gamma$)*

$$\gamma(t) = \gamma_{max}(1 - exp(-E : E^*)) \quad (5.1)$$

3. For elements of the main diagonal $p_{i,i+1:\Delta v}(t)$: the proportions of cells that entered division between $t$ and $t + dt$ (*mitosis: $\delta$*)

$$\delta(v,t) = \delta_{max}\mathcal{N}(\mu_v,\sigma_v)\mathcal{N}(\mu_t,\sigma_t) \quad (5.2)$$

Probabilities are functions of both time and size (*mitosis*) (E 2), and temporal changes of irradiance (*cellular growth*) (E 1). The set of parameters, $\vec{\theta}$, is estimated by maximum likelihood, assuming that errors between observed ($\vec{w}$) and predicted ($\hat{w}$) normalised size distributions follow a Normal distribution. Their standard deviation are estimated by Markov Chain Monte Carlo (MCMC).

Maximum likelihood parameters ($\hat{\theta}$) were used to fit *Synechococcus* (Fig 1b), picoeukaryotes, nanoeukaryotes and cryptophytes size distributions.

Primary production

The apparent increase of carbon biomass, defined as the Net Primary Production NPP* (mg C.m$^{-3}$.d$^{-1}$), has been calculated from the predicted absolute size distribution following two distinct formula (E 3, E 5):

$$\begin{aligned} NPP_{cell} &= \vec{N}_0.\delta(t).C_{cell} \\ &= \vec{N}_0.(exp(\mu(t)) - 1).C_{cell} \end{aligned} \quad (5.3)$$

Populations specific growth rates ($\mu$) were measured according to equation (E 4).

$$\mu(\hat{\theta}) = \frac{1}{24.\frac{1}{dt} + 1}.log_e\left(\frac{\widehat{\vec{N}}(T_{1\,day},\hat{\theta})}{\vec{N}(T_0)}\right) \quad (5.4)$$

$\mu$: population intrinsic growth rates (d$^{-1}$), $dt$: time step (10 min), $\vec{N}$: absolute size distribution (cells.cm$^{-3}$)

The mean size ratio $\mu_{ratio} = log_e(\overline{v}_{max} : \overline{v}_{min})$ was calculated to provide an indication about the model performance and the synchronicity of populations. Growth rates uncertainties were derived from MCMC run on size distribution.

$$\begin{aligned} &NPP_{size} = \\ &\int_{t\epsilon\tau}\int_{C=0}^{C=+\infty} C_{size}.(N(t+dt) - N(t))dt.dC = \\ &\int_{t\epsilon\tau}\int_{v=0}^{v=+\infty} a.v^b.(N(t+dt) - N(t))dt.dv \end{aligned} \quad (5.5)$$

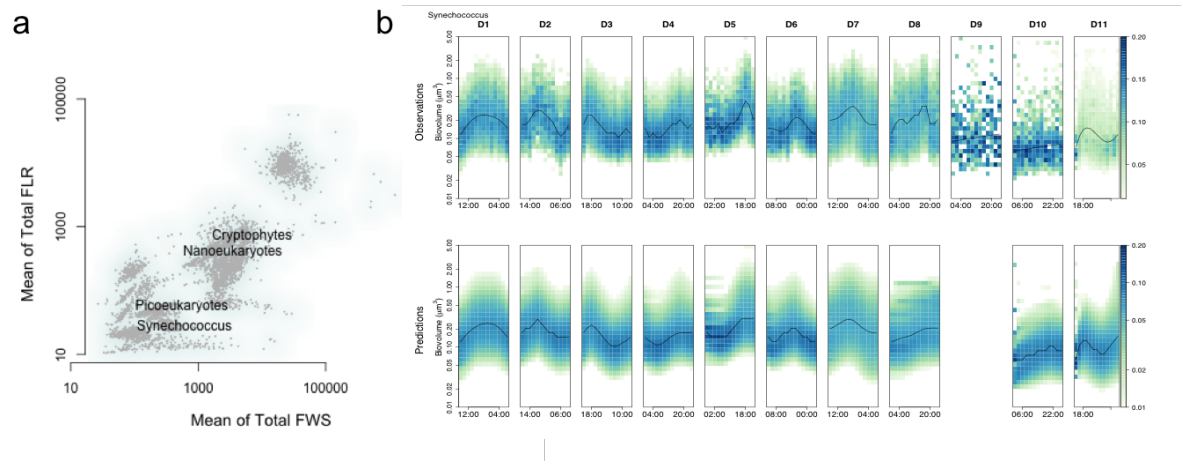


Figure 5.1: 2D projections of clusters' optical properties (FWS: forward scatter, FLR: red fluorescence) resolved during the DEep Water EXperiment (a). Time series of Synechococcus size distribution within each water types used to estimate *in situ* growth rates. Diel observations of biovolume (top panel) are reproduced via the optimal set of parameters that minimise the difference between observations and predictions (bottom panel)

During DeWEX $dt$ was fixed to 2 hours and the photoperiod, $\tau$ (Irradiance $\in \mathscr{R}^{\star}$) limited to 06:00 UT-18:00 UT. The discretised form of equation (E 5) was used to estimate $\mathrm{NPP}_{size}$ :

$$NPP_{size} = \sum_{t=06:00}^{18:00} \sum_{i=1}^{m} a.(\vec{v}_i)^b.(\vec{N}_i(t+dt) - \vec{N}_i(t)) \tag{5.6}$$

The mean carbon differential $\delta\overline{C} = \overline{C}_{max} - \overline{C}_{min}$ was calculated to provide an indication about the model performance and the synchronicity of populations. Uncertainties were accounted by changing the amount of size classes, $m$, defined by $v_i = v_{min} 2^{\frac{i-1}{dv}}$ with i $\in$ (1,2,...,m).

$C_{cell}$ (E 3) and $C_{size}(\vec{v})$ (E 5) stand for cell-based and size-based carbon conversion factors respectively. Size to carbon factors (a,b) used for the different size fractions are summarised in Table 1. Carbon cell quotas were derived from the minimale size class cells reached after presumed mitotic division. These factors allow us to approximate the daily NPP using either the approximation of the carbon content of the cells newly-formed after mitotic division over 24 hours or the photosynthetic carbon assimilation derived from the increase of cellular volume, $\vec{v}$, during the interphase. Compared to $\mathrm{NPP}_{cell}$, $\mathrm{NPP}_{size}$ only requires a 12h integration of the size-structured population model. Both estimations result from the apparent variation of populations size distribution and therefore do not accommodate any cells removal processes within the period of integration that could be caused by grazing or physical transport.

Table 5.1: Carbon biomass conversion factors. The allometric conversion of cells' biovolume into carbon biomass is given by: pg C=a.Biovolume$^b$

| Taxon | Mean Biovolume ($\mu$m$^3$.cell$^{-1}$) | Cellular quota (fg C.cell$^{-1}$) | conversion coefficients: (a,b) | Ref |
|---|---|---|---|---|
| Synechococcus | 0.24 ± 0.1 | 76 ± 30 | (0.26, 0.86) | 1 |
| Picoeukaryotes | 3.3 ± 1.4 | 710 ± 250 | (0.26, 0.86) | 1 |
| Nanoeukaryotes | 100 ± 25 | 22,000 ± 5,000 | (0.433, 0.863) | 2 |
| Cryptophytes | 500 ± 130 | 90,000 ± 20,000 | (0.433, 0.863) | 2 |

(1) *Menden-Deuer* and *Lessard* 2000 (2) *Verity et al.* 1992

### Production environmental scaling: Growth niche model

Investigation of the environmental control on phytoplankton was conducted by fitting $\mathrm{NPP}^{\star}_{size}$ to growth functions reviewed in Tian (2006). Behrenfeld's concept of *integrated growth environment* is modelled by accounting for the effects of temperature, nutrients and light on phytoplankton production (Behrenfeld *et al.*, 2006). The model assumes that the maximal production rates is balanced by the combined effect of these environmental stimuli scaled between optimal and limiting conditions (E 7).

$$\widehat{NPP^*}(x,t)(mgC.m^{-3}.d^{-1}) = NPP^*_{max}.f(T(x,t)).g(E(x,t)).h(N(x,t)) \quad (5.7)$$

T: temperature (°C), E: incident PAR (E.m$^{-2}$.d$^{-1}$), N: ammonium concentrations ($\mu$M), $x$: geographic site, $t$: time

Average values of temperature, PAR and ammonium concentration were measured between (t-1 day) and (t+1 day) at site $x$ to account for upstream adaptations (Hellweger *et al.*, 2016).

Temperature forcing on maximal production rates is modelled by an asymmetric gaussian curve with distinct standard deviation, $\Delta T_{\pm}$ for temperature lower and greater than the optimum, $T_{opt}$ (Moisan *et al.*, 2002).

$$f(T) = exp\left(-\frac{|T - T_{opt}|^2}{\Delta T^2_{\pm}}\right) \begin{cases} T<T_{opt} : \Delta T_- \\ T>T_{opt} : \Delta T_+ \end{cases} \quad (5.8)$$

The standard response of production to incident photosynthetically available radiation (E), the P-E curve, predicts the increase of the production rates up to the optimal light intensity ($E_k$). Under very high radiation, productivity is photo-inhibited (Steele, 1992).

$$g(E) = \frac{E}{E_k}.exp\left(1 - \frac{E}{E_k}\right) \quad (5.9)$$

We assumed that dissolved ammonium were absorbed from the surface layer as a result of active enzymatic transporter whose kinetics is determined by the Michaelis-Menten uptake equation with half-saturation constant, $k_N$ (E 10).

$$h(N) = \frac{[NH_4^+]}{k_N + [NH_4^+]} \quad (5.10)$$

To fit the growth niche model (E 7), the size-based primary production rates were predicted by changes of temperature, light and nutrients using a maximum likelihood approach based on the Poisson regression. The MLE parameters, $\theta = \{T_{opt}, \sigma^-, \sigma^+, E_k, k_N\}$ were identified assuming the observations of $\widehat{NPP^*}$ follow a Poisson distribution. Standard deviations were derived from MCMC runs and a LRT was performed to test the significance of niche components.

## 5.3 Results

Apparent net primary production estimations (NPP$^*$): Evaluation of models performance, uncertainties and sensitivity

### Models performances

***Size distributions model*** A size-structured population model was used to reproduce the diel variations of size distribution by accounting for cell cycle transitions. For each population defined by flow cytometry (Fig 1a), the Maximum Likelihood Estimation parameters were identified to predict the absolute and normalised (see Fig 1b for *Synechococcus*) number of cells in each size class. A Taylor diagram is presented in Fig 2 to illustrate the quality of model predictions against the direct observations of normalised size distributions for each population (Taylor, 2001). Overall, predictions show a good correlation with observations (0.88-0.98) and a reduced standard deviation (2-10 %). The normalised Root Mean Square Error (RMSE) is larger for cryptophytes predictions due to the relatively low number of cells counted in each size class.

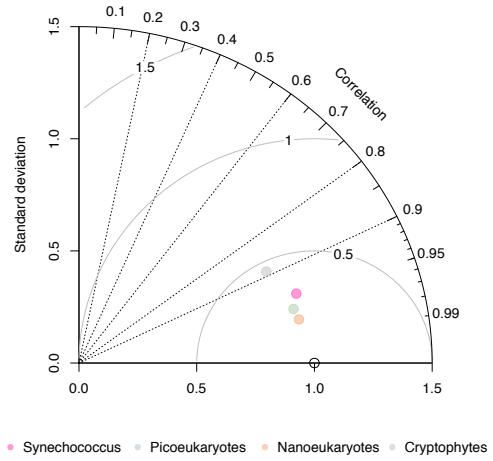


Figure 5.2: Taylor diagram of the size-structured population mode predictions (*Synechococcus*: magenta, picoeukaryotes: green, nanoeukaryotes: orange, cryptophytes: gray). Pearson correlations are plotted along azimuthal angles (dot lines). The normalized standard deviations are plotted on the $y-axis$. RMS errors are plotted along the arcs (continuous lines).

The comparisons between MLE growth rates and the log-ratio of the average size are summarised in Table 2. Picoeukaryotes displayed the highest growth rates on average ($\overline{\hat{\mu}}$=0.87 ± 0.38 $d^{-1}$), followed by *Synechococcus* ($\overline{\hat{\mu}}$=0.73 ± 0.34 $d^{-1}$), and the populations of nanoeukaryotes and cryptophytes ($\overline{\hat{\mu}}$=0.63 ± 0.26 $d^{-1}$, $\overline{\hat{\mu}}$=0.63 ± 0.40 $d^{-1}$ respectively). The log-ratio overestimated their *in situ* growth rates by 6-30 % for much of the populations, with the exception of *Synechococcus*.

Table 5.2: Estimations of populations growth rates by the size distribution model, $\hat{\mu}$ ($d^{-1}$). The log-ratio $\mu_{ratio}$ ($d^{-1}$) is indicative of synchronous populations.

| Taxon | $\hat{\mu}$ | | $\mu_{ratio}$ | | $(\mu_{ratio}$-$\hat{\mu}):\hat{\mu}$ | |
|---|---|---|---|---|---|---|
| | Average | Std | Average | Std | Average | Std |
| Synechococcus | 0.73 | 0.34 | 0.75 | 0.17 | -0.14 | 1.52 |
| Picoeukaryotes | 0.87 | 0.38 | 1.11 | 0.30 | 0.14 | 0.77 |
| Nanoeukaryotes | 0.63 | 0.26 | 0.68 | 0.24 | 0.06 | 0.50 |
| Cryptophytes | 0.63 | 0.40 | 0.74 | 0.38 | 0.27 | 0.41 |

Compared to the average ratio, the median ratio were closer to $\hat{\mu}$, suggesting that some size distributions counted outliers or simply did not include enough observations for cryptophytes (data not shown).

***NPP estimations*** The conform size distributions were used to estimate group-specific net primary productivity from the predicted growth rates, denoted $NPP_{cell}$ (E 3). Since growth rates were not significantly different on average ($t$-test, $n$=11, $p$-value >0.05), the variance of $NPP_{cell}$ was explained by the standing crop of the population. Estimations are presented in Fig 3 and plotted against the independent estimations of $NPP_{size}$ (E 5).

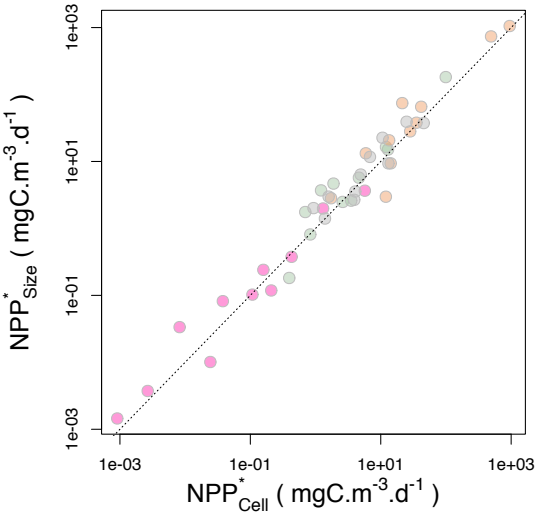


Figure 5.3: Comparison of cell-based ($NPP_{cell}$) and size-based ($NPP_{size}$) production estimations for *Synechococcus* (magenta dots), picoeukaryotes (green dots), nanoeukaryotes (orange dots) and cryptophytes (grey dots). (Dotted line 1:1)

Both NPP estimations are proportional, with a slope of 0.98 ($R^2$=0.99). Differences between estimations were due to the discrepancy between the relative biomass of dividing cells and the amplitude of C assimilation during the photoperiod. *Synechococcus* cells were the less productive with a maximum C fixation of 0.9 mg $C.m^{-3}.d^{-1}$. Picoeukaryotes and cryptophytes accounted for 10 ± 11 % and 25 ± 25 % of the sum of group-specific productivity respectively. With a lower standing crop, cryptophytes population assimilated 25 ± 21 mg $C.m^{-3}.d^{-1}$. Picoeukaryotes productivity av-

eraged 15 ± 16 mg C.m$^{-3}$.d$^{-1}$. Nanoeukaryotes production reached 212 ± 280 mg C.m$^{-3}$.d$^{-1}$ with a peak at 900 mg C.m$^{-3}$.d$^{-1}$. For each population, we evaluated the differential of the mean C uptake to measure their minimal productive capacities. Results are presented in Fig 4. By taking into account the entire size distribution, $\text{NPP}^*_{Size}$ surpassed the amplitude of the average C biomass, $\delta\overline{C}^*_{Size}$. A statistical test, performed on the log transformed estimations yielded to non-significant differences ($t$-test, $n$=30, $p$-value= 0.73). Estimations were log-transformed to compare values that varied of 6 orders of magnitude, all populations included (shapiro test, $p$-value <0.1).

***Growth niche model*** Since group-specific $NPP_{size}$ were predicted by integrating diel size distribution during only 12 hours, they were privileged to fit the growth integrated niche model (E 7-10). The MLE parameters are presented in Table 3.

Table 5.3: MLE parameters of the growth niche model. $\Delta T_-$ and $\Delta T_+$ are half Normal standard deviations under and above the temperature optimum, $T_{opt}$. $E_k$ is the optimal light intensity. $K_N$ is the half-saturation constant of dissolved ammonium uptake

| Taxa | $\text{NPP}^*_{max}{}^{(a)}$ | $\text{T}_{opt}{}^{(b)}$ | $\Delta T_-{}^{(b)}$ | $\Delta T_+{}^{(b)}$ | $E_k^{(c)}$ | $\text{K}_N{}^{(d)}$ |
|---|---|---|---|---|---|---|
| Synechococcus | 1.09 | 13.57 | 0.19 | 0.81 | 216 | 33.4 |
| Picoeukaryotes | 80.9 | 13.71 | 0.21 | 0.92 | 237 | 56.7 |
| Nanoeukaryotes | 908.5 | 14.23 | 0.40 | 1.03 | 282 | 83.1 |
| Cryptophytes | 50.8 | 14.21 | 0.65 | 1.90 | 298 | 94.1 |

$^{(a)}$: mgC.m$^{-3}$.d$^{-1}$ $^{(b)}$: °C $^{(c)}$ $\mu$E.m$^{-2}$.s$^{-1}$ $^{(d)}$ nM

A Taylor diagram is presented in Fig 5 to illustrate the quality of the growth niche model predictions against the estimations of $NPP^*_{size}$ for each population. Overall, predictions correlations ranged between 0.37 and 0.64. Standard deviation were reduced by (5-15%), except for cryptophytes (+ 20%). Altogether, cryptophytes statistics demonstrate a lower quality of the fit, including the normalised Root Mean Square Error (RMSE). The respective RMSE for populations are 0.16 mg C.m$^{-3}$.d$^{-1}$ for *Synechococcus* (observations in the range: 0.005-0.87 mg C.m$^{-3}$.d$^{-1}$), 13 mg C.m$^{-3}$.d$^{-1}$ for picoeukaryotes (observations in the range: 0.93-56.6 mg C.m$^{-3}$.d$^{-1}$), 150 mg C.m$^{-3}$.d$^{-1}$ for nanoeukaryotes (observations in the range: 3-880 mg C.m$^{-3}$.d$^{-1}$) and 24 mg C.m$^{-3}$.d$^{-1}$ for cryptophytes (observations in the range: 1-69 mg C.m$^{-3}$.d$^{-1}$). Observed $NPP^*_{size}$ and predicted $\widehat{NPP}$ are shown in Fig 6.

## Models uncertainties

***Size distributions model*** The transitions probabilities of each size class in time were expressed by time- and size-dependent functions of $\theta = [\gamma_{max}, E^*, \delta_{max}, \mu_v, \sigma_v, \mu_t, \sigma_t]$. The posterior distributions of MLE parameters, $\hat{\theta}$, were approximated by MCMC (E 1-2). 5000 iterations were run to estimate the standard deviation of group-specific growth rates during DeWEX. The time series of growth rates, with their standard deviations, is presented in Fig 7a.

***NPP estimations*** Standard deviations of the cell-based apparent primary productivity, $NPP_{cell}$, was derived from the posterior distributions of size distribution model parameters. We tested the effect of size classes discretisation to measure the standard deviations of the size-based apparent primary productivity, $NPP_{size}$. The time series of NPPs, with their standard deviations, are presented in Fig 7b-c.

***Growth niche model*** The posterior distribution distributions of MLE parameters, $\hat{\theta}$, were approximated by MCMC (E 8-10). The confidence interval of $T_{opt}$, $\Delta T_\pm$, $E_k$ and $k_N$ are defined for each group in Table 4.

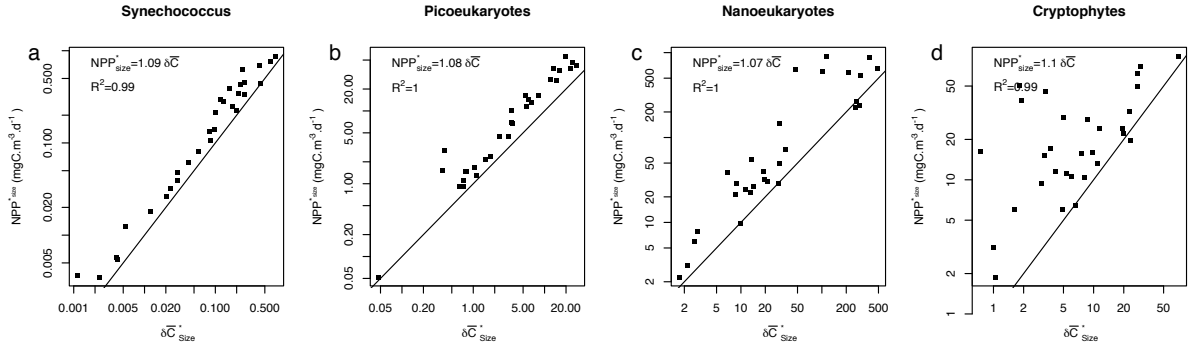


Figure 5.4: Comparison of size-based ($NPP_{size}$) production estimations and differential average C uptake ($\delta\overline{C}$) for *Synechococcus* (a), picoeukaryotes (b), nanoeukaryotes (c) and cryptophytes (d). (Continuous line 1:1)

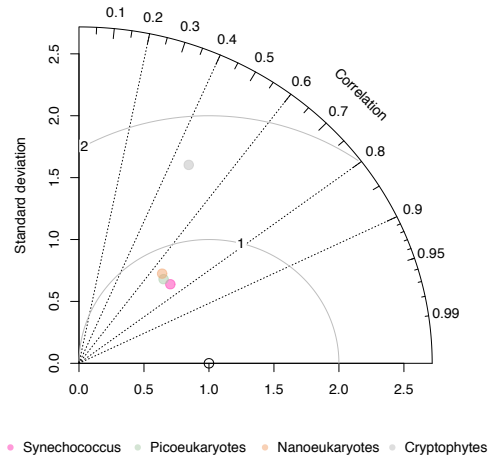


Figure 5.5: Taylor diagram of the growth niche model.

Table 5.4: 95 % confidence interval of the MLE parameters of the growth niche model. $\Delta T_-$ and $\Delta T_+$ are half Normal standard deviations under and above the temperature optimum, $T_{opt}$. $E_k$ is the optimal light intensity. $K_N$ is the half-saturation constant of dissolved ammonium uptake

| Taxa | $NPP^*_{max}{}^{(a)}$ | $T_{opt}{}^{(b)}$ | $\Delta T_-{}^{(b)}$ | $\Delta T_+{}^{(b)}$ | $E_k^{(c)}$ | $K_N{}^{(d)}$ |
|---|---|---|---|---|---|---|
| Synechococcus | 1.07-1.08 | 13.5-13.6 | 0.19-0.20 | 0.78-0.85 | 211-221 | 21-48 |
| Picoeukaryotes | 78-84 | 13.713-13.718 | 0.213-0.217 | 0.90-0.93 | 235-239 | 51-62 |
| Nanoeukaryotes | 900-950 | 14.22-14.23 | 0.39-0.40 | 0.99-1.07 | 275-290 | 80-93 |
| Cryptophytes | 37-69 | 14.18-14.21 | 0.6-0.7 | 1.68-2.18 | 276-323 | 91-120 |

$^{(a)}$: $mgC.m^{-3}.d^{-1}$ $^{(b)}$: °C $^{(c)}$ $\mu E.m^{-2}.s^{-1}$ $^{(d)}$ nM

## Models sensitivity

***Size distribution model*** The sensitivity of growth rates estimations to MLE parameters was measured by the scaled ($w(\theta)$) partial derivative of the model output to each parameter following Soetaert and Herman (2009). The output tested is the estimation of *in situ* growth rates ($\mu(\theta)$) for all populations. The sensitivity is defined by $w(\theta)[\partial\mu(\theta) : \partial\theta]$ with $\vec{\theta} = [\gamma_{max}, E^*, \delta_{max}, \mu_v, \sigma_v, \mu_t, \sigma_t]$ (E 1-2). Results from the sensitivity analyses are summarised in Table 5.

Table 5.5: Average statistics of the sensitivity analyses performed on *Synechococcus*, picoeukaryotes, nanoeukaryotes and cryptophytes growth rates estimations.

| Taxa | $\gamma_{max}$ | $E^*$ | $\delta_{max}$ | $\mu_v$ | $\sigma_v$ | $\mu_t$ | $\sigma_t$ |
|---|---|---|---|---|---|---|---|
| Synechococcus | 0.050 | -0.023 | 0.297 | -0.119 | 0.248 | 0.000 | 0.000 |
| Picoeukaryotes | 0.025 | -0.022 | 0.341 | -0.082 | 0.119 | 0.000 | 0.000 |
| Nanoeukaryotes | 0.022 | -0.012 | 0.309 | -0.053 | 0.061 | 0.000 | 0.000 |
| Cryptophytes | 0.027 | -0.008 | 0.356 | -0.064 | 0.067 | 0.000 | 0.000 |

In absolute, the growth rates estimations by the size distribution model are sensitive to the maximum proportions of dividing cells $\delta_{max}$, and the size-dependent Normal distribution, of parameters $[\mu_v, \sigma_v]$. The parameterisation of cellular growth has little effect on the estimation of growth rates which suggests that cell-based and size-based approximations of primary production should be independent.

***NPP estimations*** The cell-based estimations of apparent primary production ($NPP_{cell}$) measure the biomass of the cells formed by binary fission. This biomass

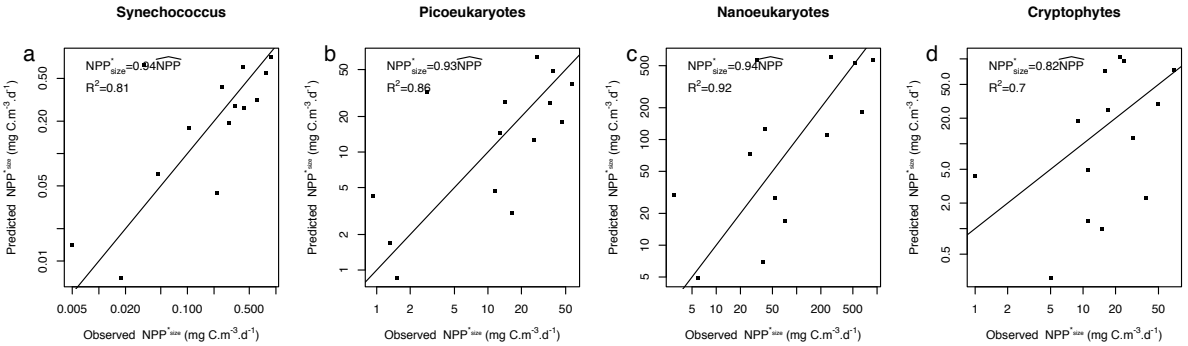


Figure 5.6: Comparison of size-based ($NPP_{size}$) production estimations and growth niche model predictions ($\widehat{NPP}$) for *Synechococcus* (a), picoeukaryotes (b), nanoeukaryotes (c) and cryptophytes (d). (Continuous line 1:1)

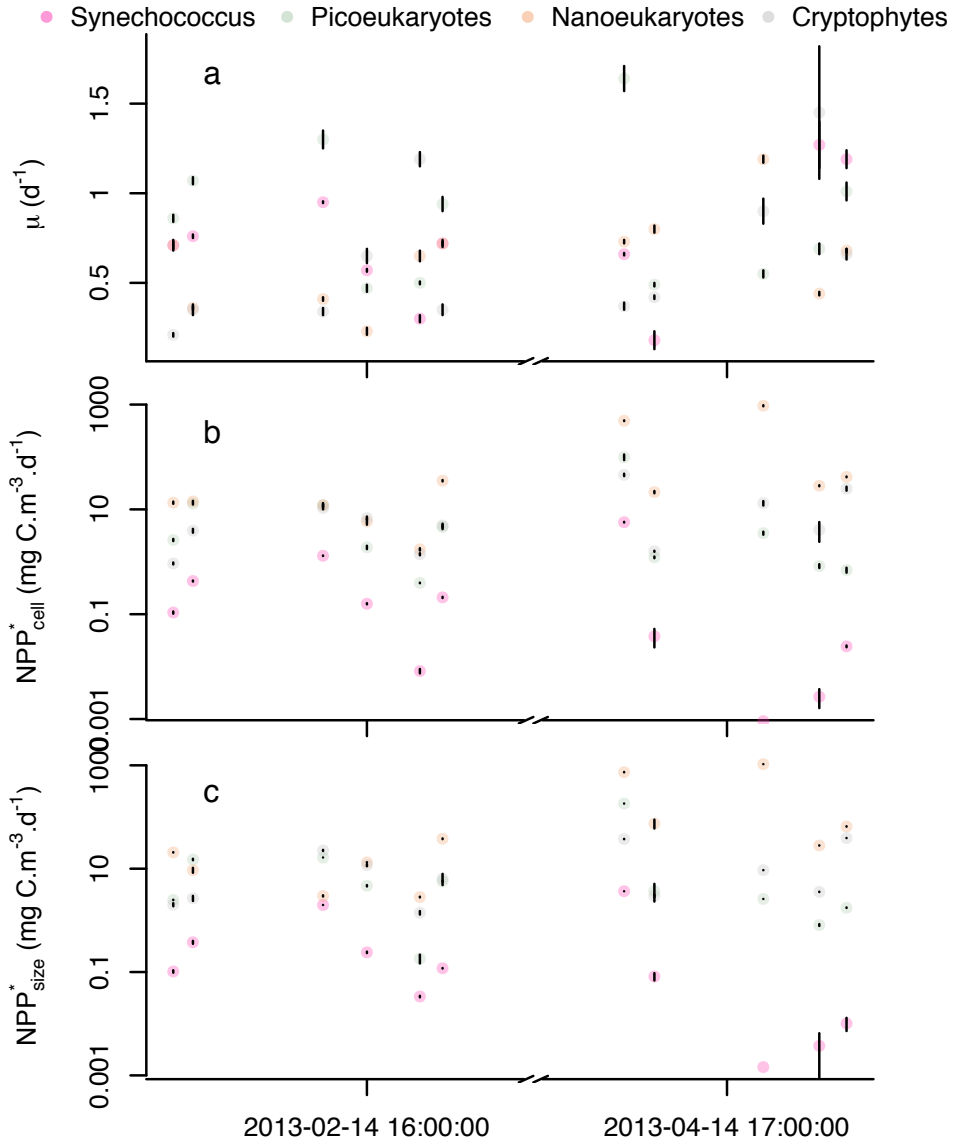


Figure 5.7: (a): Time series of group-specific growth rates, (b): Time series of group-specific cell-based productivity, (c): Time series of group-specific size-based productivity for *Synechocccus* (magenta dots), picoeukaryotes (green dots), nanoeukaryotes (orange dots) and cryptophytes (gray dots).

is derived from the mitotic index ($\delta$), knowing that the number of new cells is equaled to $N(t) - N(0) = N(0).\delta(t) = N(0)[exp(\mu(t)) - 1]$. To test the sensitivity of initial conditions ($N(0)$), we compared our estimations to the average hourly $NPP_{cell}$, obtained from the integration of hourly-averaged cell abundance and hourly growth rates, over a 24 hours period. Comparisons are shown in Fig 8.

***Growth niche model*** The relative importance of the growth niche model components were tested by a Likelihood Ratio Test (LRT).

To measure the significance of the changes in temperature on the estimations of $NPP_{size}$, the log-likelihood of the full model (E 7) was compared to the log-likelihood of the reduced model, not dependent on temperature: $\widehat{NPP^*}(x,t) = NPP^*_{max}.g(E(x,t)).h(N(x,t))$. Result of the test shows a significant influence of temperature on the predictions of the growth niche model for *Synechococcus* (statistics=489, df=3, $p$-value $<2.10^{-16}$), picoeukaryotes (statistics=22056, df=3, $p$-value $<2.10^{-16}$), nanoeukaryotes (statistics=5435, df=3, $p$-value $<2.10^{-16}$) and cryptophytes (statistics=1662, df=3, $p$-value $<2.10^{-16}$).

The effect of light limitation on the estimations of $NPP_{size}$ was tested by comparing the log-likelihood of the full model (E 7) to the log-likelihood of the reduced model, not dependent on light: $\widehat{NPP^*}(x,t) = NPP^*_{max}.f(T(x,t)).h(N(x,t))$. Result of the test shows a significant influence of light utilization on the predictions of the growth niche model for *Synechococcus* (statistics=2753, df=1, $p$-value $<2.10^{-16}$), picoeukaryotes (statistics=16105, df=1, $p$-value $<2.10^{-16}$), nanoeukaryotes (statistics=118, df=1, $p$-value $<2.10^{-16}$) and cryptophytes (statistics=591, df=1, $p$-value $<2.10^{-16}$).

The strength of ammonium limitation on the estimations of $NPP_{size}$ was tested by comparing the log-likelihood of the full model (E 7) to the log-likelihood of the reduced model, not dependent on nutrient concentration: $\widehat{NPP^*}(x,t) = NPP^*_{max}.f(T(x,t)).g(E(x,t))$. Result of the test shows a significant influence of differential nutrient uptake on the predictions of the growth niche model for *Synechococcus* (statistics=1543, df=1, $p$-value $<2.10^{-16}$), picoeukaryotes (statistics=9398, df=1, $p$-value $<2.10^{-16}$), nanoeukaryotes (statistics=23639, df=1, $p$-value $<2.10^{-16}$) and cryptophytes (statistics=1224, df=1, $p$-value $<2.10^{-16}$).

Scaling daily primary productivity to standing crop

### NPP* vs Chl a

The DeWEX cruises were held during two contrasted periods. In wintertime (February), the maximum Chl a concentration did not exceed 0.58 mg.m$^{-3}$. The average Chl a concentration, 1.5 ± 1.2 mg.m$^{-3}$, measured during the spring bloom was significantly higher ($n$=15, $p$-value=0.02) (Fig. 9). The sum of group-specific productivity was explained at 74% by the gradient of Chl a concentration.

### NPP* vs standing crop

Using the conversion coefficients reported in Table 1, populations' abundances were turned into biomass to show the relation between the productivity and their standing crop. The scatter plot is reported in figure 10. The abundance of *Synechococcus* cells varied the most during the cruise (data not shown). In February and April, the average concentrations reached 3.2 10 $^3$ ± 3.5 10$^3$ cells.cm$^{-3}$ and 3.5 10$^3$ ± 4.7 10$^3$ cells.cm$^{-3}$ respectively. Driven by these changes, the productivity of *Synechococcus* varied by 3 orders of magnitude.

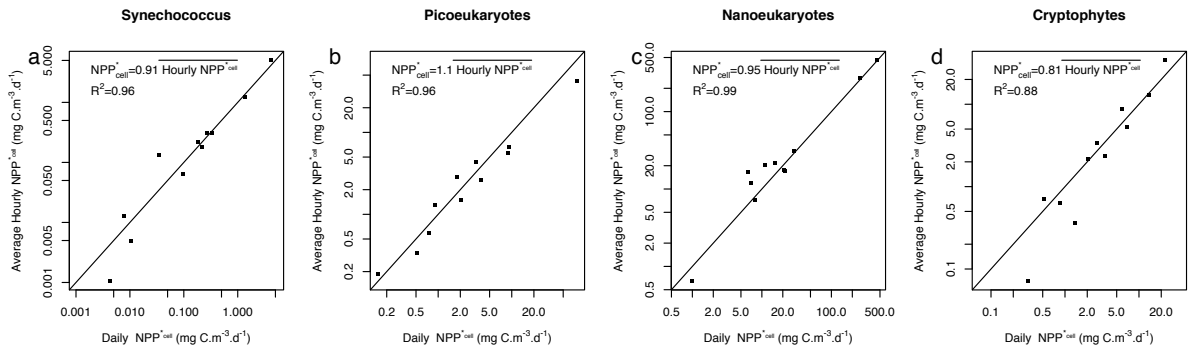


Figure 5.8: Comparison of daily cell-based ($NPP_{cell}$) production estimations and average hourly $NPP_{cell}$ for *Synechococcus* (a), picoeukaryotes (b), nanoeukaryotes (c) and cryptophytes (d). (Continuous line 1:1)

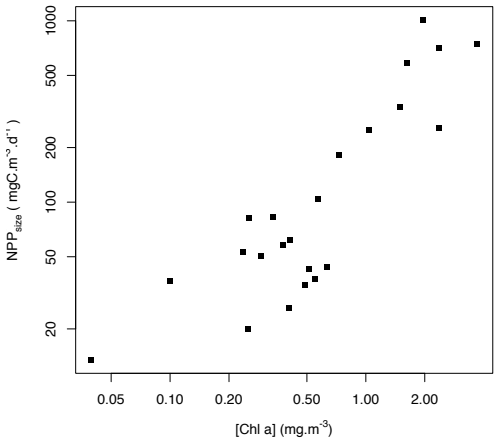


Figure 5.9: Variation of the sum of group-specific apparent productivity in response to bulk Chl a concentrations

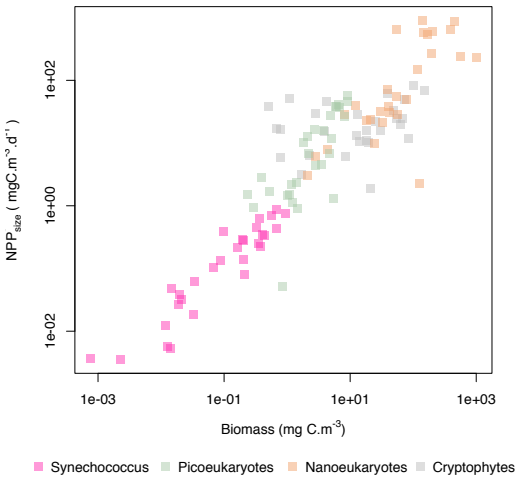


Figure 5.10: Variation of the sum of group-specific apparent productivity in response to standing crop concentrations

Although picoeukaryotes cells were abundant, their low cellular quota (710 ± 250 fg C.cell$^{-1}$) put on a similar order their productivity with cryptophytes' production. Only presents at concentrations of 37 ± 56 cells.cm$^{-3}$ and 260 ± 350 cells.cm$^{-3}$, cryptophytes cells represented between 2 and 42 % of the total production. Nanoeukaryotes cells were abundant with a relatively high cellular quota (22,000 ± 5,000 fg C.cell$^{-1}$). They contributed to PP for up to 96 %. The important changes of population concentrations observed in the North Western Mediterranean Waters accounted for 82 % of the variance of primary production.

## Individuals NPP$^{\star}$ vs cell size

Since 82 % of the variance of productive rates ($NPP^{*}_{size}$) was explained by the difference in standing crop alone, we normalised $NPP^{*}_{size}$ estimations by group's concentrations. The ratio of $NPP^{*}_{size}$:cells.cm$^{-3}$ indicates the potential of cells to produce biomass by photosynthetic $CO_2$ assimilation during the photoperiod. Individual $NPP^{*}_{size}$ estimations are shown in figure 11a. Cryptophytes cells had the highest potential for C assimilation, with on average 220 ± 470 pg C.cell$^{-1}$.d$^{-1}$. Nanoeukaryotes did not reached this capacity. A cell fixed between 0.05 and 210 pg C per day.

Picoeukaryotes' and *Synechococcus*'s average uptake represented only 1.8 ± 1.51 pg C.cell$^{-1}$.d$^{-1}$ and 0.06 ± 0.07 pg C.cell$^{-1}$.d$^{-1}$ respectively. Overall, the cellular productivity covaried with the average size of the cells, as shown in figure 11b. The general coefficients of allometry were derived from the log-log regression of individual productivity against size. Coefficients turned to be close to 1.05 ± 0.04 (95 % interval : 0.99-1.13) for for the slope and -1.3 ± 0.15 (95 % interval : -1.67– -1.07) for the intercept. Both coefficients were significant ($n$=120, $p$-value <0.001). We performed the same analysis on individual groups. Results are shown in Table 6.

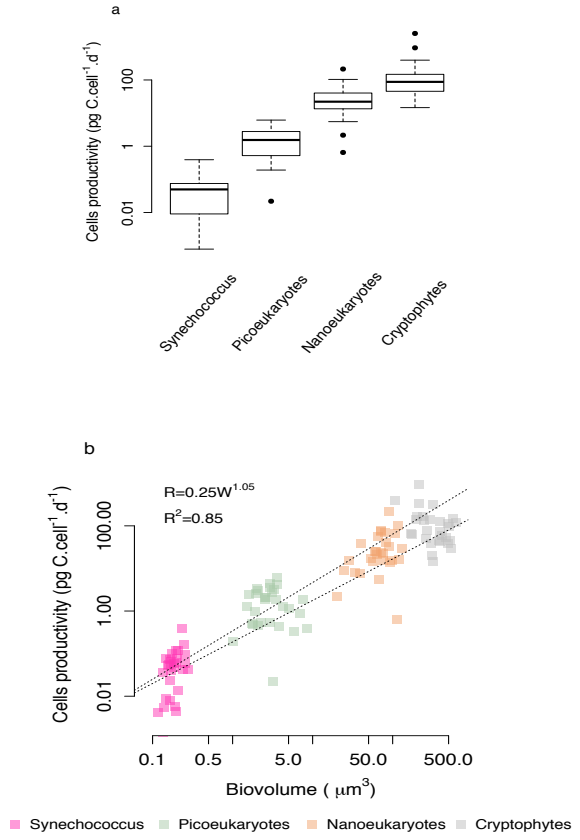


Figure 5.11: (a) Boxplots of group-specific individual production rates. (b) Allometry of group-specific individual production rates. Regression: $log_e(PP) = \beta_0 + \beta_1 log_e(BV)$ (dotted lines IC 95 %)

The population of picoeukaryotes did not follow allometry. The regression slopes are significantly different from zero for *Synechococcus* ($p$-value <0.001), nanoeukaryotes ($p$-value <0.05) and cryptophytes ($p$-value <0.01). For cryptophytes, the slope is negative, which suggests that small cells are more productive. The opposite is observed for *Synechococcus* and nanoeukaryotes cells.

Table 5.6: Allometry coefficients between apparent primary productivity (PP, pg C.cell$^{-1}$.d$^{-1}$) and cell size (BV, $\mu$m$^3$) for *Synechococcus* ($n$=30), picoeukaryotes ($n$=30), nanoeukaryotes ($n$=30) and cryptophytes ($n$=30). Regression : $log_e(PP) = \beta_0 + \beta_1 log_e(BV)$

| Taxon | $\hat{\beta}_0$ | | | $\hat{\beta}_1$ | | |
|---|---|---|---|---|---|---|
| | MLE | Std | IC 95 % | MLE | Std | IC 95 % |
| Synechococcus | 2.91· | 1.48 | -0.11-5.95 | 3.72 *** | 0.84 | 1.98-5.46 |
| Picoeukaryotes | 0.14 | 0.52 | -0.93-1.21 | 0.005 | 0.44 | -0.91-0.92 |
| Nanoeukaryotes | -0.58 | 1.85 | -4.3-3.2 | 0 .87· | 0.44 | -0.03-1.77 |
| Cryptophytes | 11.07*** | 2.44 | 6.05-16.08 | -1.12* | 0.42 | -1.99- -0.26 |

*** : 0.000,** : 0.001,* : 0.01,· : 0.05

Scaling daily primary productivity to environmental variables

### NPP* vs Temperature

The 30 approximations of group-specific daily productivity have been scaled to the gradient of *in situ* temperature by maximum likelihood estimation (Table 4). Fits based on the 95 % confidence interval are shown in figure 12 for *Synechococcus*, picoeukaryotes, nanoeukaryotes and cryptophytes. Their thermal niches overlapped over the range of temperature observed during the DeWEX cruises (11-16°C). The populations of *Synechococcus* and picoeukaryotes were more productive under 13.5-13.7°C (Fig. 12a-12b respectively). For nanoeukaryotes and cryptophytes cells, the optimum went to 14.2°C (Fig. 12c-12d respectively).

### NPP* vs PAR

The 30 approximations of group-specific daily productivity have been scaled to the gradient of daily average Photosynthetic Available Radiation by maximum likelihood estimation (Table 4). Fits based on the

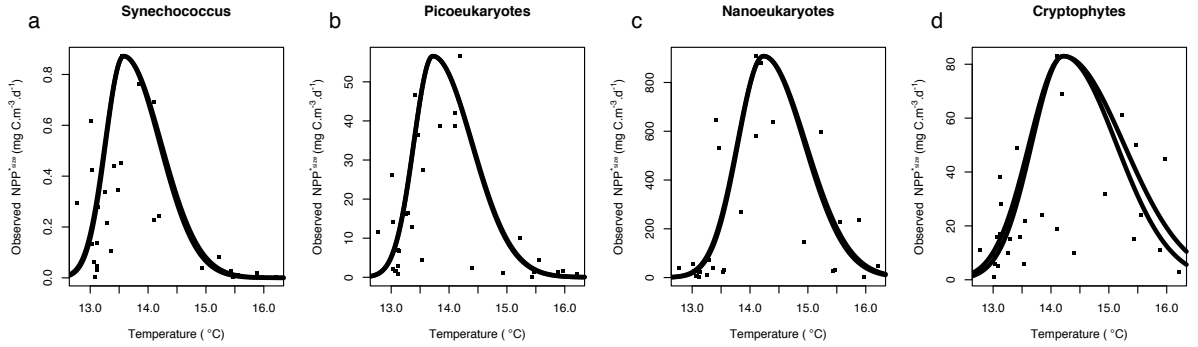


Figure 5.12: Thermal niche of *Synechococcus* (a), picoeukaryotes (b), nanoeukaryotes (c) and cryptophytes (d) productivity. (Continuous line: 95 % confidence interval fit

95 % confidence interval are shown in figure 13. The incident solar radiation efficiently promoted phytoplankton production up to 216 $\mu$E.m$^{-2}$.s$^{-1}$ for Synechococcus (Fig. 13a), 237 $\mu$E.m$^{-2}$.s$^{-1}$ for picoeukaryotes (Fig. 13b), 282 $\mu$E.m$^{-2}$.s$^{-1}$ for nanoeukaryotes (Fig. 13c) and 298 $\mu$E.m$^{-2}$.s$^{-1}$ for cryptophytes (Fig. 13d).

### NPP* vs Nutrients

The 30 approximations of group-specific daily productivity have been scaled to ammonium ions availability by maximum likelihood estimation (Table 4). The concentration of $NH_4^+$ measured in 2013 varied between 1 nM and 140 nM. Fits based on the 95 % confidence interval are shown in figure 14 for *Synechococcus*, picoeukaryotes, nanoeukaryotes and cryptophytes. $NO_3^-$, and $PO_4^{3-}$ did not significantly limit the productivity during DeWEX (data not shown). Their affinity of cells for $NH_4^+$ uptake, measured by the inverse half-saturation constant ($k_N$), diverged between the groups. Overall, the half-saturation constants covaried with the size. With a $k_N$ of 33.4 nM, *Synechococcus* cells were more adapted to assimilate ammonium under low concentration (Fig 14a). Cryptophytes showed the lowest affinity for $NH_4^+$ (Fig 14d), while picoeukaryotes (Fig 14b) and nanoeukaryotes (Fig 14c) assimilated ammonium at intermediate levels.

## 5.4 Discussion

Scales of Mediterranean productivity

Since the scale of variation of marine productivity is extremely high, phytoplankton production rates are generally scaled to Chl a concentration. Even scaled to the standing crop, the range of surface productivity lies between 0 and 1800 mg C.m$^{-3}$.d$^{-1}$ (Buithenius et al., 2013). Phytoplankton biomass, as revealed by spectral analysis, is controlled in space by the Kolmogorov turbulence and in time by the ultradian cycle (Platt and Denman, 1975). Since the coefficient of Chl a variation in the Sea is large, we must also enlarge our observation window. In the Mediterranean Sea, the frontier between the Eastern and Western basins marks a shift between productive regimes (D'ortenzio and Ribera d'Alcala, 2009). The later being on average 7 times more productive during specific periods of the year (Siokou-Frangou et al., 2010). Every year, the NW basin hosts a productive hot-spot in the period March-May (Mayot et al., 2016). The bloom alone represents 15% of the Mediterranean primary production (Marshall and Schott 1979). Its diversity, 170 taxa, is influenced by the ecological traits shaped by evolution (Percopo et al., 2011). NWM species are likely already threatened by climate change (Goffart et al., 2002).

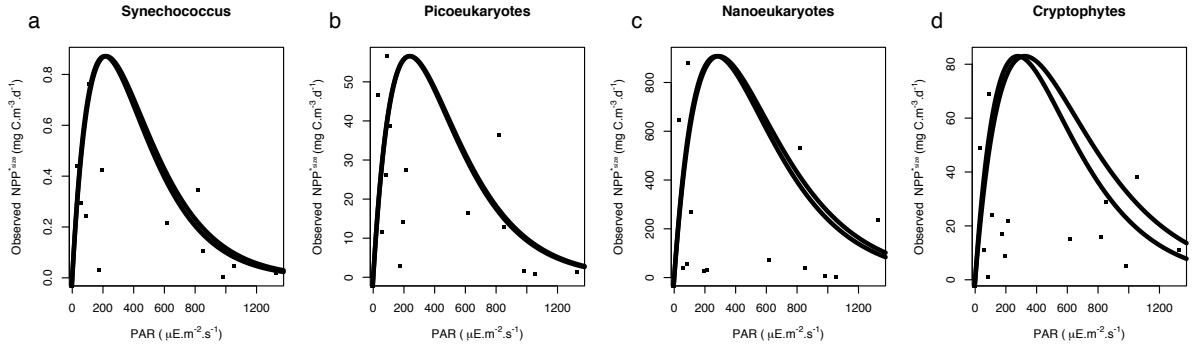


Figure 5.13: *Synechococcus* (a), picoeukaryotes (b), nanoeukaryotes (c) and cryptophytes (d) PE cruves. (Continuous line: 95 % confidence interval fit

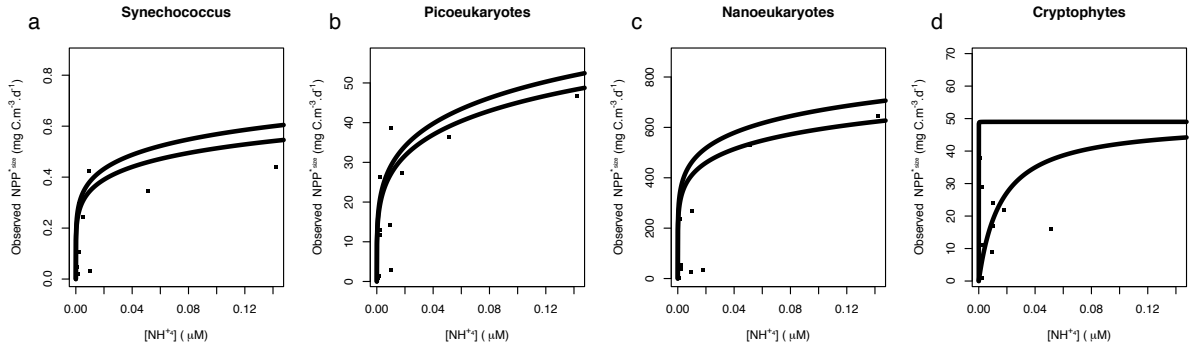


Figure 5.14: *Synechococcus* (a), picoeukaryotes (b), nanoeukaryotes (c) and cryptophytes (d) ammonium uptake. (Continuous line: 95 % confidence interval fit

***Populations***

During the Deep Water formation EXperiment, bulk $^{14}$C incubation varied between 0.9 and 200 mg C.$m^{-3}$.d$^{-1}$. Our maximum is superior. The sum of group-specific primary productivity reached 800 mg C.$m^{-3}$.d$^{-1}$ in spring, in correlation with nanoeukaryotes biomass (Fig. 10). Nanoeukaryotes were mainly represented by cells of *Minidiscus* (Leblanc et al, in prep). Cells of this group divided at least once a day in winter and spring time (Table 2). Cryptophytes growth rates were also equal to 0.63 d$^{-1}$ on average. Yet, its abundance limited the group's productivity between 1-100 mg C.$m^{-3}$.d$^{-1}$. Overall, the variation of cells productivity was large between the groups (Fig. 11a). With 100 pg C fixed per cell per day, cryptophytes displayed the highest capacity of C quota increase. The other individual productivity were low compared to cryptophytes. Nanoeukaryotes's uptake represented on average 35 ± 40 pg C.cell$^{-1}$.d$^{-1}$, while picoeukaryotes and *Synechococcus* cells fixed 2 ± 1.5 pg C.cell$^{-1}$.d$^{-1}$ and 0.06 ± 0.07 pg C.cell$^{-1}$.d$^{-1}$ respectively. The picoeukaryotes cells divided a lot with an average growth rates of 0.87 ± 0.38 d$^{-1}$. Despite their reproductive capacity, the C assimilation was inferior to 100 mg C.$m^{-3}$.d$^{-1}$.

The long-term time series available at DYFAMED station (43.4°N, 7.8°E) gives some insight about the productivity observed in the NW and its associated diversity. Between 1993 and 2000, the daily productivity at surface varied between 0.9 and 160 mg C.$m^{-3}$.d$^{-1}$. The standard deviation of primary production rates represents 1.5 times the average primary production, 20 mg C.m$^{-3}$.d$^{-1}$. HPLC analyses resolved the phytoplankton community, diagnosed by pigment concentration. Nanoeukaryotes, detected by fucoxanthin

derivatives, are dominant during the spring bloom (Vidussin et al., 2000). The proportion of cryptophytes cells, determined by Alloxanthin, is 12%, while cyanobacteria, containing Zeaxanthin, accounts for only 8% of the present community. $^{14}$C primary production hasn't been measured recently. In the Mediterranean Sea, the global picophytoplankton productivity ranges between 2 and 20 mg C.m$^{-3}$.d$^{-1}$ (Magazzu and Decembrini, 1995). Populations of cyanobacteria and small eukaryotes (< 3$\mu$m) are in steady-states. Nanophytoplankton dominates the production over the year but its productive peak is constrained between late January and May (Uitz et al., 2010).

***Chl a and standing crop***

The Chl a concentrations observed during DeWEX were unusually high, even for the spring bloom (Fig. 9). In April, a patch of high bulk biomass co-localised with the convective chimney formed in wintertime. For an average Chl a concentration of 1.5 ± 1.3 mg Chla.m$^{-3}$, the maximum biomass reached 4 mg Chla.m$^{-3}$ (Fig. 9). The Chl a concentrations measured at DYFAMED ranged between 0.03 and 1.57 mg Chla.m$^{-3}$. The gradient of Chl a concentration explained 74 % of the variability of productive regimes observed between February and April 2013. This result suggests that the algorithm of primary production based on bulk Chl a are indicated to foresee the spatial shifts of productive regimes at basin scales (Mayot et al, 2016). Although in absolute, the method is sensitive to the parameterisation of the light efficiency and Chla:C ratio ($\theta$) (Behrenfeld et al, 2002). They are both dependent on multifactorial limitations such as nutrient availability and temperature (Cullen et al., 1993).

The carbon-based estimations are less sensitive to the natural fluctuations of nutrients concentration and temperature since they integrate directly the cellular quotas in C (Cullen et al., 1988; Westberry et al., 2008). The changes of C biomass accounted for 82 % of the productivity variance during DeWEX. The predictability of size-based primary productivity were tested for the carbon biomass against the Chl a indicator. The likelihood ratio test returned a significant difference in predictability, in favour of the C indicator ($p$-value <0.001). Paradoxically, the total particulate organic carbon concentration measured by remote sensing (e.g. backscattering) is poorly correlated to phytoplankton biomass (Loisel et al., 2001). The concentration measured at DYFAMED between 1998 and 1999, varied between 80-150 mg C.m$^{-3}$. During DeWEX, the total carbon biomass (sum of the group) concentration varied between 2 and 1000 mg C.m$^{-3}$ (Fig. 10). The application of carbon-based productivity model in the Mediterranean Sea will likely require to account for detritus and heterotrophic bacteria depending on the period (Heimburger et al., 2013).

***Allometry***

In 2013, the average group-specific biovolume and corresponding equivalent spherical diameter (in parentheses) varied between 0.2 ± 0.04 $\mu$m$^3$ (0.8 ± 0.06 $\mu$m) for *Synechococcus* (Fig. 11b). Agawin et al. (1998) measured the mean course of *Synechococcus* size in the Bay of Blanes (NW Mediterranean), and found that cells dimensions varied between 0.2 and 1.1 $\mu$m$^3$ depending on the temperature. The relationship between average cells biovolume, growth rates and temperature clearly demonstrated the link between *Synechococcus* productivity and cells size in the Mediterranean Sea. We found that cells productivity were positively correlated to cells size during DeWEX (Table 6). The regression slope (3.72 ± 0.84) is largely superior to the classical 3/4 coefficient (Kleiber, 1947).

The average picoeukaryotes' biovolume and corresponding equivalent spherical diameter (in parentheses) varied between 3.4 ± 1.8 $\mu$m$^3$ (1.8 ± 0.2 $\mu$m) during DeWEX (Fig. 11b). The corresponding cellular pro-

ductivity averaged 1.8 ± 1.5 pg C.cell$^{-1}$.d$^{-1}$, with 1.7 ± 1.9 pg C.cell$^{-1}$.d$^{-1}$ in wintertime and 1.6 ± 1.5 pg C.cell$^{-1}$.d$^{-1}$ in springtime. Huete-Ortega et al. (2011) found that picoeukaryotes could fix 0.2 pg C.cell$^{-1}$.d$^{-1}$ with $^{14}$C uptake operated in the Atlantic Ocean (wintertime). Li (1993) measured a fixation of 0.1 pg C.cell$^{-1}$.d$^{-1}$ on sorted radiolabeled picoeukaryotes. For picoeukaryotes, the regression slope (0.005 ± 0.44) was not significant from 0 (Table 6). In the Mediterranean Sea, picoeukaryotes group a assemblages of prasinophyceae, stramenopiles, alveolates, which may be too diverse to distinguish a clear size to productivity relationship (Marie et al., 2006).

During DeWEX, the larger cells displayed high cellular productivity with a range of 0.6-200 pg C.cell$^{-1}$.d$^{-1}$ for nanoeukaryotes and a range of 15-2000 pg C.cell$^{-1}$.d$^{-1}$ for cryptophytes (Fig 11a). For Cermeno et al. (2005), large-sized phytoplankton present higher carbon-specific photosynthetic rates than small-sized cells due to the package effect. We found that cells productivity were negatively correlated to cells size for cryptophytes, with a slope of -1.12 ± 0.42, and positively correlated for nanoeukaryotes (slope: 0.87 ± 0.44) (Table 6). In culture, the large combination of chlorophytes, haptophytes and cryptophytes growth rates were scaled to cells biovolume with a slope of -0.06 (Finkel et al., 2010). With a compilation of $^{14}$C incubations in surface waters of the global ocean, Chen and Liu (2010) formulated a quadratic equation to fit growth rates to cellular quota. They demonstrated that cellular productivity peaks at 2.28 $10^{-5}$ $\mu$g C.cell$^{-1}$. The peak, equivalent to 22,800 fg C.cell$^{-1}$, appears between the cellular quotas measured for nanoeukaryotes (22,000 fg C.cell$^{-1}$) and cryptophytes (90,000 fg C.cell$^{-1}$) during DeWEX (Table 1).

Maranon et al. (2007) compiled data collected from natural assemblages to retrieve the slope of the interspecific allometry between cell size and individual C production. The assemblage was constituted of diatoms, dinoflagellates, cyanobacteria and coccolithophores, whose size accounted for 98 % of variability in carbon production (Maranon et l., 2008). They found that in natural populations, the slope (1.03) was larger than the coefficients derived from culture experiments. Laboratory analyses yielded to slopes between 0.53 and 0.74. Using the overall group-specific cellular productivity measured with the size-based estimations, we estimated the log-log regression coefficient and found a slope of 1.05 ± 0.04, coherent with Maranon et al study. This slope suggests that the isometric scale prevail in the Sea (Huete-Ortega et al., 2011).

### Growth niche model

Resource availability is the main descriptor of niche separation for phytoplankton (Hutchinson, 1957; Behrenfeld *et al.*, 2006). The quantity and quality of light is clearly predominant for photosynthetic utilisation in temperate climates (Sverdrup, 1953; Berhenfeld and Falkowski, 1997). Along with light energy, photosynthetic cells require inorganic sources of nitrogen (Caperon and Myer, 1972), phosphorus (Redfield, 1958), silicium (Azam a,d Chisholm, 1975), iron (Geider and LaRoche, 1994), zinc (Brand *et al.*, 1963), vitamins (Droop, 1968), etc., involved in their metabolic pathways (Odum, 9171; Dugdale, 1967; Downing *et al.*, 1999; Reynolds, 2006). Temperature is not strictly a resource, but thermic fluctuations have a direct influence on metabolic rates. Intensified by global warming, temperature variations play a major role in species adaptation and functional diversity. In predictive ecology, functional traits support scientists ambitions to predict the resilience of individuals faced to perturbations and their potential adaptation when they swamp there physiological plasticity (Mutschinda *et al.*, 2016). The mediation of temperature, light and nutrients,

on PFTs fitness is investigated by the relative scaling of DeWEX spatio-temporal hydrological context to measures of group-specific apparent primary production. Because PFTs respond to Roots' definition of guilds (i.e. group of species that have similar requirements and play a similar role within a community), their study is particularly suited to foresee the changes of atmospheric $CO_2$ fluxes in the Mediterranean Sea (Roots, 1967). Nutrients (Goering *et al.*, 1964), temperature (Davison, 1991) and light (Marra, 1978) all vary and impact phytoplankton growth on daily scales. We made sure that the response of PFTs productivity goes beyond the scope of the daily acclimation, that result from pulse perturbations (Glasby and Underwood, 1995), by integrating diel production rates and daily average of the resources.

***Traits of thermal adaptation***

*Synechococcus* is an eurytherm organism (0-30°C) reported at polar, equatorial and tropical latitudes (Neuer, 1992; Landry and Hirchman, 2002 and ref. within; Dubreuil et al., 2003; Flombaum et al., 2013). Amorim *et al.* (2016) highlighted the presence of two potential *Synechococcus* ecotypes in the Mediterranean Sea. One is adapted to wintertime conditions and the other more common in summertime. Picoeukaryotes and nanoeukaryotes encompass a large diversity of organisms. They are indexed in all seas within global studies (Worden and Not, 2008; Buithenius *et al.*, 2012; Rodriguez-Ramos *et al.*, 2015). A panel of $^{14}C$ incubations analysed during the North Atlantic spring bloom (49°N) showed that, under the range of 12-16°C, picoplankton productivity follows a gaussian curve with an optimum around 14°C (Agawin *et al.*, 2000). Cryptophytes have been inventoried in the Northern hemisphere, in the Norwegian, Japanese, Baltic, North and Meaditerranea Seas (Throndsen, 1969; Throndsen, 1983; Hill, 1992; Novarino et al., 1997; Bérard-Therriault et al., 1999; Casotti et al., 2000; Novarino, 2005) and in the Southern hemisphere along Brazilian coasts (Menezes and Novarino, 2003). In the Mediterranean Sea, cryptophytes seem to appear preferentially in spring-summer and fall (Cerino and Zigone, 2006). Between May-June 2013, Von de Poll *et al.* (2015) measured their high-specific productivity in correlation with low temperature.

In the context of global warming temperature anomalies are particularly studied in relation to regime shifts of phytoplankton communities (Huertas *et al.*, 2016) or bulk biogeochemistry (Sarmiento *et al.*, 2004). Climate changes enforce the variability of circulation regimes in the Mediterranean Sea (Mermex, 2011). By consequence, the hydrological characteristics of the typical water masses (Modified Atlantic Waters, Levantine Intermediate water and Western Mediterranean Deep Water) are invariably evolving (Shroeder *et al.*, 2016). Since 1943, Western Mediterranean Waters temperature increased by 0.002°C per year (Vargas-Yanez *et al.*, 2010). With no or limited dispersive capacities, planktonic organisms need to manage the change of their habitats via (i) their phenotypic plasticity which does not imply an uttermost regulation through natural selection and (ii) the adaptation of populations by selection of the standing genetic variability (Huertas *et al.*, 2016; Collins *et al.*, 2014). The interpretation of P vs T curve is not a simple transcription of activation/denaturation enzymatic kinetics for natural population due to the complexity of limiting regimes (Winder and Sommer, 2012). Thomas *et al.* (2016) noticed a close relationship between species temperature optimum and the average temperature at latitude they live in, as a consequence of genetic adaptation. Even before genetic adaptations, phytoplankton phenotypic plasticity are involved to buffer the influence of temperature on phytoplankton growth. Plasticity accounts for reactions that last less than one generation time and for adaptive acclimation. The later is

the process conducting to the selection of resistant individuals after vulnerable genotypes have progressively disappeared. The adjustment of the Chl:C ratio ($\theta$) (Geider, 1987; Thompson *et al.*, 1992), the activation of chemical bioreactions such as RUBISCO and other enzymes (Raven and Geider, 1988 and ref therein) and membrane transporters that might be involved in CCM or nutrients uptake (Li *et al.*, 1994), as well as respiration catabolism (LeFèvre *et al.*, 1994) act typically on photosynthetic rates by physiological acclimation.

The timeframe of this study goes beyond the scope of phytoplankton adaptation (~ 5-20 generation times) (Brand *et al.*,1981a; Rynearson and Armburst, 2004). This drawback likely involved adaptation in the pattern we observed since the variations of PTFs production in response to changes of temperature is strikingly singular among composites. The observed temperature encompassed the entire thermal tolerance of groups' productivity (12-17°C). In the Mediterranean Sea, the current western 14°C isotherm is slowly shifting northward, replacing the past century 13°C isotherm observed in winter (Coll *et al.*, 2010). Populations temperature optimum ranged from 13.5°C (*Synechococcus*) to 14.2°C (cryptophytes) (Table 3). The asymmetry of all thermal niche highlights that excess variation of temperature are slowly disturbing apparent production, with $\Delta T_{+}$(Synechococcus)=0.8°C, $\Delta T_{+}$(picoeukaryotes)=0.92°C, $\Delta T_{+}$(nanoeukaryotes)=1.03°C, $\Delta T_{+}$(cryptophytes)=1.9 °C. By comparison, cells productivity decreased quickly for temperature under the optimum: $\Delta T_{-}$(Synechococcus)=0.19°C, $\Delta T_{-}$(picoeukaryotes)=0.21°C, $\Delta T_{-}$(nanoeukaryotes)=0.40°C, $\Delta T_{-}$(cryptophytes)= 0.65°C. We suggest that organisms might have accustomed (via positive selection) to positive temperature anomalies at this period of the year. At DYFAMED observatory station (43.4°N, 7.8°E, http://www.emso-eu.org, http://www.fixo3.eu), the mean surface temperature between February and May is 13.4 ± 0.9°C (daily average standard deviation: 0.16°C) with an Interquartile Range (IQR) of 0.3°C between $Q_{25}/Q_{50}$ and of 1°C between $Q_{50}/Q_{75}$ (data collected between 2010-2013).

***Traits of light utilisation***

During DeWEX, *Synechococcus* productivity reached its maximum at 216 $\mu$E.m$^{-2}$.s$^{-1}$. Dupont et al (2008) grown marine cultures of *Synechococcus* strains under a continuous flux of 80 $\mu$E.m$^{-2}$.s$^{-1}$ and found an optimum at 70 $\mu$E.m$^{-2}$.s$^{-1}$. With *Prochlorococcus*, they form the *Deep Chlorophyll Maximum*, at light intensities attenuated to 99 % of the incident radiation (Algarra *et al.*, 1988). At the DCM, phototrophic cells grow on an optimised photosynthetic C uptake in order to occupy unfavourable niches (Ferris and Palenik, 1998). The DCM formed in numerous ecosystems, from subtropical gyres (Perez *et al., 2006*) to the Mediterranean Sea (Estrada, 1985; Raimbault *et al.*, 1993), translates the phenotypic adaptability of autotroph cells. By photoadaptation, *Synechococcus* cells acquired phycoerythrin pigments (Dubinsky, 1980; Perry *et al.*, 1981) to harvest the great part of blue-green light remaining in depth (Glover *et al.*, 1985). At surface, they manage to reduce the deleterious effect of subsaturating light through photo-protective mechanisms (Agusti and Llabres, 2007; Mella-Flores *et al.*, 2012). Under such light, the efficiency of photoinhibition is mediated by the presence of accessory pigments such as carotenoids present in *Cryptophyceae* (non-photochemical quenching) (Jeffrey, 1980). Cryptophytes cells were less subject to photoinhibition during DeWEX since their optimal light intensity was the highest, 298 $\mu$E.m$^{-2}$.s$^{-1}$. For picoeukaryotes, the high diversity of light-harvesting capabilities due to the variability of pigments (e.g. Chl a, Chl b, Chl c and dyvinil pheoporphirine)

cause subsequent changes in light harvesting capacities through the 'package' effect (Worden and Not, 2008 and ref. therein). They may be even more efficient than *Synechococcus* to capture light at the DCM at least under 450-470 wavelengths (Glover *et al.*, 1986). With an optimum productivity under 237 $\mu$E.m$^{-2}$.s$^{-1}$ and 282 $\mu$E.m$^{-2}$.s$^{-1}$ for nanoeukaryotes, surface populations were likely light-adapted. The lack of interspecific variability of the growth optimum is a global pattern evidenced in the review of Edwards *et al.* (2015).

Light is continuously constraining phytoplankton vertical distribution within the 200 first lightened meters, referred as the euphotic zone. Depending on the amount of absorbing material in this layer, including viable phytoplankton and detrital particles (CDOM), light exponentially vanishes under the surface. The availability of light is also dependent of incident insolation and mixing turbulence (Denman and Gargett, 1983), causing cells to pass a variable amount of time below the critical depth where integrated production equals respiration (Sverdrup, 1953). At low light intensities, carbon fixation increases linearly with light as a function of pigment content (Nielsen and Jorgensen, 1968). This theory predict that shade-adapted cells, derived from populations present near the critical depth for more or less than one generation (Cullen and MacIntyre, 1998), will reach their growth optimum $P_{max}$ at lower light intensity than light-adapted cells due to pigment photoacclimation (Falkowski, 1980; Geider, 1987; Cullen and Lewis, 1988; Raven and Geider, 2003). The adaptative ability of phytoplankton to optimise light harvesting in narrowed PAR spectrum is called chromatic adaptation (Dring, 1981; Bidigare *et al.*, 1990). In the field, both photoacclimation and chromatic adaptation may occur at the surface as both process act in synergy on photosynthetic rates (Dubinsky and Stambler, 2009), over ultradian (<24h) or infradian (>24h) cycles (Latasa *et al.*, 1992). The effect of cell size and Chl a:C ratio, both dependent on temperature and nutrients, may add up to these phenomenon by driving respiration and quantum efficiency (Langdon, 1988). Kirk (1994) proposed to use the light intensity at maximal production rates, $E_k$, to measure the adaptability of cells exposed to a gradient of irradiance. The optimal light intensity allows cells to grow optimally before photoinhibition cause the decrease of productivity (Long and Falkowski, 1994). The intensity of light at which the negative slope intercept the E axis is an indicator of cells sensitivity to non-photochemical (i.e. dispersion of absorbed energy in accessory pigments or heat as electron incomes exceed the capacity of PSII turnover) or photochemical (i.e. damage of photosystems) quenching (Gallegos and Platt, 1982).

To our knowledge, Gasol *et al.* (2016) are the first to report seasonal values of $E_k$ in the Mediterranean Sea between 2011 and 2014. Some distinctions must be clarified to compare their results with the present study but the main conclusion of their work is nevertheless transposable. From bulk incubations of $^{14}$C under an artificial PAR gradient (10-1500 $\mu$E.m$^{-2}$.s$^{-1}$), they provided the mathematical interpretation of the PE curve, with $E_k$~ 550 $\mu$E.m$^{-2}$.s$^{-1}$ in February and 1400 $\mu$E.m$^{-2}$.s$^{-1}$ in April. They showed that the saturating light intensities are close to the *in situ* irradiance intensity measured during the 2h incubations. Cultures progressively adapted to variable level of irradiance have the same comportment (Cullen, 1989). The intermittence of light regime can have a remarkable effects on C assimilation, depending on its frequency (Walsh and Legendre, 1982). Photoadaptation is the process by which cells will change their photosynthetic capacities in response to light variations when the mixing/intermittence rates is superior to adaptation scales (Kromkamp *et al.*, 1992). In Neale and Marra (1985), the timescales of direct deleterious photoinhibition (< 2h)

and longer acclimation (> 5h) are documented under natural irradiance. Between 1-10 Hz transitions, $CO_2$ uptake follows the rates observed under a steady-state average radiation. The mean daily incident Photosynthetic Available Radiation was used to investigate the role of light on diel specific-photosynthetic rates in this study. Arin *et al.* (2002) found a good correlation between diel phytoplankton growth rates integrated to the euphotic layer and the average irradiance. It is determinant to compare rates on the same dynamic scales because phytoplankton production is influenced by complex temporal adaptations. Under controlled conditions, the variation of instantaneous photosynthetic rates is clearly linked to the occurrence of the daily cell cycle (Claquin et al., 2004). The static PE curve parameterisation obtained from instantaneous studies is somehow unable to translate this capacity in natural populations (Pahl-Wostl, 1992).

***Traits of nutrients assimilation***

The dominance of picoplankton in oligotrophic regions is likely due to their small cell size associated to small diffusion boundary layers and large surface area per unit volume (Raven, 1986). The situation can be balanced in rich environment or transient upwelling systems since larger cells display higher absorption rates (Margalef, 1978). Using the analysis of nutrients uptake kinetics in 8 clones of 3 marine phytoplankton species, Carpenter and Guillard (1971) conclude that nutrients uptake is also likely driven by adaption to local concentrations. Monod (1950) explicitly parameterised the uptake rate of dissolved nutrients by planktonic cells using Michaëlis-Menten kinetics equation. Since the model relies on steady-state uptake, the time scale of production and nutrients turnover is important. Vincent (1992) recommend to account for the differential metabolism, irradiance, circadian rhythm and mixing by using the daily average concentration given the variability of nutrient uptake in relation with cells turnover. During DeWEX, the productivity varied preferentially in function of daily average $NH_4$ concentration ([$NH_4$](Leg 1)=4 ± 5 nM, [$NH_4$](Leg 2)=38 ± 54 nM). In the Mediterranean Sea, enrichment studies highlighted the role of lithogenic silicium (Leblanc *et al.*, 2003), iron (Fiala *et al.*, 1976), ammonium (Tsiola *et al.*, 2016) and phosphates (Jacques *et al.*, 1973) in promoting phytoplankton production. Following Liebig's law of minimum (1840), any element may potentially restrain plankton development under a basal requirement if present at lowest concentration. In the sea, phytoplankton internal quota of phosphorus usually account for 1/16 of the nitrogen quota, according to the Redfield ratio (Redfield, 1933). The affinity of cells for $NH_4$ varied as an inverse function of cells size: *Synechococcus* cells presented a $K_N$ of 33.4 nM, picoeukaryotes a $K_N$ of 56.7 nM, 83.1 nM for nanoeukaryotes and 94.1 for cryptophytes. Eppley *et al.* (1969) discovered relatively soon the role of cell size in nutrients kinetics. Lindemann *et al.* (2016) provided a theoretical framework to apprehend the allometric scaling of nutrient affinity to the square of cells radius by a global compilation of datasets. In ecological models, the ammonium half-saturation constant has been set to 2-10 nM to adjust model to DYFAMED data (Lévy *et al.*, 1998), 30-109 nM in <2 $\mu$m size fraction and 40-228 nM in >2 $\mu$m size fraction (L'Helguen *et al.*, 2008), or 1.03-2.64 $\mu$M in picoplankton cultures (Timmermans *et al.*, 2005).

Historically, phosphorus as been referred as the main limiting factor for marine productivity in the Mediterranean Sea (Berland *et al.*, 1980; Krom *et al.*, 2004). The exchanges at Gibraltar entertain the net loss of nutrients from the Mediterranean Sea towards the Atlantic ocean (Béthoux *et al.*, 1992), although several processes contribute to balance this disequilibrium. The entrance of richer Atlantic waters through the Strait of Gibraltar (Minas *et al.*, 1991),

river runoffs (Ludwig *et al.*, 2009; Strobl *et al.*, 2009), atmospheric deposit (Carbo *et al.*, 2005) and inputs of deep mineralised nutrients when upwelling promotes the water column mixing (Coste *et al.*, 1972) buffer the Mediterranean oligotrophy. Mesoscales vortices and convective plumes also reenforce the mixing of nutrients across basins (Taupier-Letage and Millot, 1988). In the NW Mediterranean Sea, the P:N elemental stoichiometry is close to 1:20 in deep layers and decrease to 1:15 at surface (Marty *et al.*, 2002). DeWEX N:P ratio reached 26 in wintertime and 14 in spring (Severin et al., submitted). Winter mixing consequently enriched surface water in nitrates ($[NO_3]$(Leg 1)=4.8 ± 2.7 $\mu$M, $[NO_3]$(Leg 2)=1.3 ± 1.5 $\mu$M) and phosphates ($[PO_4]$(Leg 1)=0.2 ± 0.14 $\mu$M, $[PO_4]$(Leg 2)=0.07 ± 0.06 $\mu$M) so that plankton were not limited by this source of nitrogen/phosphorus. The data collected by Agawin *et al.* (2000) during a mesocosm experiment deployed in the NW Mediterranean Sea also highlight the independence of picoplankton production rates to high N:P ratio (20:1). In marine ecosystems, allochthonous sources of nutrients are opposed to the continuous recycling of nutrients, by zooplankton excretion or microbial respiration, in the notion of new and regenerated production of Dugdale and Goering (1967). The main source of recycled nitrogen in the ocean consistes of ammonium ions, $NH_4^+$, derived from excreted compounds such as urea (Alcaraz *et al.*, 1994). At the DYFAMED observatory station (43.4°N, 7.8°E), the excretion of few individuals of ciliates per $cm^{-3}$ can fulfil growth requirements for natural consortium of pico- and nano- phytoplankton (Ferrier and Rassoulzadegan, 1991). With the consumption of nitrates, the distinct uptake of these two sources yield to the quantification of the *f-ratio*, defined as the ratio of $\rho NO_3$:$\rho NO_3 + \rho NH_4$ (Eppley *et al.*, 1979) or its inverse, the recycling index, denoted *I*. In the NW Mediterranean Sea, the *f-ratio* has been evaluated in several studies to 0.3 (Minas *et al.*, 1988; Diaz *et al.*, 2000). In the study of Diaz *et al.*, $NH_4$ uptake rates were at least equal to 45 $nM.d^{-1}$ compared to 10 $nM.d^{-1}$ for $NO_3$. Potential advantages of absorption of ammonia instead of nitrates are reviewed in Raven *et al.* (1992).

## 5.5 Conclusion

One of the main objective of predictive marine ecology is to foresee the potential impacts of various climatic scenario on biogeochemical cycles. PFTs dynamics are explicitly parameterised in most of the OBM systems. The accuracy of the prediction of PFTs response to global change depends strongly on the evaluation of $CO_2$ uptake rate in a wide diversity of environments. The assimilation of empirical data has so far been critical to reduce the uncertainties on phytoplankton $CO_2$ uptake, as a motor of the biological carbon pump. The Mediterranean Sea, perceived as a small-scale model of the ocean, is a favoured target to study the impact of global change. However the recurrent parameterisation of Mediterranean biogeochemical model has involved the collection of global datasets or under controlled conditions. Even in these conditions, our ability to grow planktonic strains is still limited and often represents biased observations that can only be used for natural populations extrapolation with caution. Only few studies integrate the intertwinement of several forcings on several ecological groups. It became the priority of the Ocean Observing and Prediction System (OOPS) to estimate such parameters in nature by supervising monitoring networks and promoting interdisciplinary scientific programs such as the Mermex French program for the Mediterranean Sea. The objective of the DeWEX cruise was to draw a global overview of the two main phenomenons driving the productive regime of the NW Mediterranean basin: the winter deep convection and the

sequel spring bloom. Continuous analyses of surface open waters by automated flow cytometry yielded to estimations of phytoplankton productive capacity directly interpretable in OBMs. In this paper, we propose a new utilisation of the size-structured population model to predict the group-specific production rates, and scale the predictions to the environment. The reliability of this method was tested. Some ecological traits were highlighted: the relative similarities of thermal niches for *Synechococcus*, picoeukaryotes, nanoeukaryotes and cryptophytes cells, the strong correlation between cell size and nutrients uptake affinity, and the contrast of light utilisation versus protection mechanisms.

## References


Agawin, N. S. R., Duarte, C. M. and Agusti, S. (1998). Growth and abundance of *Synechococcus sp.* in a Mediterranean bay: seasonality and relationship with temperature, *Mar. Ecol. Progr. Ser.*, *170*, 45-53.

Agawin, N. S. R., Duarte, C. M. and Agusti, S. (2000). Nutrient and temperature control of the contribution of picoplankton to phytoplankton biomass and production, *Limnol. Oceanogr.*, *45*(3), 591-600.

Agusti, S. and Llabres, M. (2007). Solar radiation-induced mortality of marine pico-phytoplankton in the oligotrophic ocean, *Photochemistry and Photobiology*, *83*, 793-801.

Alcaraz, M., Saiz, E. and Estrada, M. (1994). Excretion of ammonia by zooplankton and its potential contribution to nitrogen requirements for primary production in the Catalan Sea (NW Mediterranean), *Mar. Biol.*, *119*, 69-76.

Algarra, P., Estrada, M. and Niell, F. X. (1988). Phycobiliprotein distribution across the western Mediterranean divergence, *Deep Sea Res. II*, *35*(8), 1425-1430.

Amorim, A. L., Leon, P., Mercado, J. M., Cortes, D., Gomez, F., Putzeys, S., Salles, S. and Yebra, L. (2016). Controls of picophytoplankton abundance and composition in a highly dynamics marine system, the Northern Alboran Sea (Western Mediterranean), *J. of Sea Res.*, *112*, 13-22.

André, J.-M., Navarette, C., Blanchot, J. and Radenac, M.-H. (1999). Picophytoplankton dynamics in the equatorial Pacific: Growth and grazing rates from cytometric counts, *J. Geophys. Res.*, *104*(2), 3369-3380.

Arin, L., Anxelu G. Moran, X. and Estrada, M. (2002). Phytoplankton size distribution and growth rates in the Alboran Sea (SW Mediterranean): short term variability related to mesoscale hydrodynamics, *J. Plankton Res.*, *24*(10), 1019-1033.

Armbrust, E. V. and Chisholm, S. W. (1992). Patterns of cell size change in a marine centric diatom: variability evolving from clonal isolates, *J. of Phycol.*, *28*(2), 146-156.

Azam, F. and Chisholm, S. W. (1975). Silicic acid uptake and incorporation by natural marine phytoplankton populations, *Limnol. Oceanogr.*, *21*, 427-433.

Bender, M., Orchardo, J., Dickson, M.-L., Barber, R. and Lindley, S. (1999). In vitro $O_2$ fluxes compared with $^{14}C$ production and other rate terms during the JGOFS Equatorial Pacific experiment, *Deep Sea Res. I*, *46*, 637-654.

Bérard-Therriault, L., Poulin, M. and Bossé, L. (1999). Guide d'identification du phytoplancton marine de l'estuaire et du golfe du St Laurent incluant également certains protozoaires, *Publ. spec. can. sci. halieut. aquat*, *128*, 1-387.

Berdalet, E., Latasa, M. and Estrada, M. (1992). Variations in biochemical parameters of *Heterocapsa sp.* and *Olisthodiscus luteus* grown in 12:12 light:dark cycles, *Hydrobiologia*, *238*, 139-147.

Berhenfeld, M. J. and Falkowski, P. G. (1997). A consumer's guide to phytoplankton primary productivity models, *Limnol. Oceanogr.*, *42*(7), 1479-1491.

Berhenfeld, M. J., Maranon, E., Siegel, D. A. and Hooker, S. B. (2002). A photoacllimation and nutrient based model of light-saturated photosynthesis for quantifying oceanic primary production, *Mar. Ecol. Progr. Ser.*, *228*, 103-117.

Berhenfeld, M. J., Boss, E., Siegel, D. A. and Shea, D. M. (2005). Carbon-based ocean productivity and phytoplankton physiology from space, *Global biogeochemical cycles*, *19*, 1-14.

Berhenfeld, M. J., Hasley, K. H. and Milligan, A. J. (2008). Evolved physiological responses of phytoplankton to their integrated growth environment, *Phil. Trans. R. Soc. B*, *363*, 2687-2703.

Berland, B. R., Bonin, D. J. and Maestrini, S. Y. (1980). Azote ou phosphore? Considerations sur le paradoxe nutritionnel de la mer Méditerranée, *Oceanoligica Acta*, *3*(1), 135-142.

Béthoux, J.-P., Morin, P., Madec, C., Gentili, B. (1992). Phosphorus and nitrogen behaviour in the Mediterranean Sea, *Deep Sea res.*, *39*, 1641-1654.

Bidigare, R. R., Marra, J., Dickey, T. D., Iturriaga, R., Baker, K. S., Smith, R. C. and Pak, H. (1990). Evidence for phytoplankton succession and chromatic adaptation in the Sargasso Sea during spring 1985, *Mar. Ecol. Prog. Ser.*, *60*, 113-122.

Binder, B. J. and Chisholm, S. W. (1990). Relationship between DNA cycle and growth rate in *Synechococcus sp.* strain PCC 6301, *J. Bact.*, *172*(5), 2313-2319.

Bolnick, D. I., Amarasekare, P., Araujo, M. S., Burger, R., Levine, J. M., Novak, M., Rudolf, V. H. W., Schreiber, S. J., Urban, M. C. and Vasseur, D. (2011). Why intraspecific trait variation matters in community ecology, *Trends Ecol. Evol.*, *26*(4), 183-192.

Bode, A., Estevez, M. G., Varela, M. and Vilar, J. A. (2015). Annual trend patterns of phytoplankton species abundance belie homogeneous taxonomical group responses to climate in the NE Atlantic upwelling, *Mar. Env. Res.*, *110*, 81-91.

Brand, L. E. (1981).Genetic variability in reproduction rates in marine phytoplankton populations, *Evolution*, *35*(6), 1117-1127.

Brand, L. E., Sunda, W. G. and Guillard, R. R. L. (1983). Limitation of marine-phytoplankton reproductive rates by zinc, manganese, and iron, *Limnol. Oceanogr.*, *28*, 1182-1198.

Brewin, R. J. W., Lavender, S. J. and Hardman-Mountford N. J. (2010). Mapping size-specific phytoplankton primary production on a global scale, *J. of Maps*, 448-462.

Buithenius, E. T., Li, W. K. W., Vaulot, D., Lomas, M. W., Landry, M. R., Partensky, F., Karl, D. M.,

Ulloa, O., Campbell, L., Jacquet, S., Lantoine, F., Chavez, F., Macias, D., Gosselin, M. and G. B. McManus (2012). Picoplankton biomass distribution in the global ocean, *Earth Syst. Sci. Data*, *4*, 37-46.

Buithenius, E. T., Hashioka, T. and Le Quéré, C. (2013). Combined constraints on global ocean primary production using observations and models, *Global biogeochemical cycles*, *27*, 847-858.

Campbell, J. W. and Yentsch, C. M. (1989). Variance within homogeneous phytoplankton populations, I: Theoretical framework for interpreting histograms, *Cytometry*, *10*, 587-595.

Caperon, J. and Meyer, J. (1972). Nitrogen-limited growth of marine phytoplankton- Changes in population characteristics with steady-state growth rate, *Deep-Sea Res*, *19*, 601-618.

Carpenter, E. J. and Guillard, R. R. L. (1971). Intraspecific Differences in Nitrate Half-Saturation Constants for Three Species of Marine Phytoplankton, *Ecology*, *52*(1), 183-185.

Carbo, P., Kroom, M. D., Homoky, W. B., Benning, L. G., Herut, B. (2005).Impact of atmospheric deposition on N and P geochemistry in the southeastern Levantine basin, *Deep Sea Res. II*, *52*, 3041-3053.

Casotti, R., Brunet, C., Aronne, B. and Ribera D'Alacala, M.(2000). Mesoscale features of phytoplankton and planktonic bacteria in a coastal area as induced by external water masses, *Mar. Ecol. Prog. Ser.*, *195*, 15-27.

Cerino, F. and Zingone, A. (2006). A survey of cryptomonad diversity and seasonality at a coastal Mediterranean site, *European J. of Phycol.*, *41*(4), 363-378.

Cermeno, P., Maranon, E., Rodrigure, J. and Fernandez, E. (2005). Large-sized phytoplankton sustain higher carbon-specific photosynthesis than smaller cells in a coastal eutrophic ecosystem, *Mar. Ecol. Prog. Ser.*, *297*, 51-60.

Cermeno, P., Maranon, E., Perez, V., Serret, P., Fernandez, E. and Castro, C. G. (2006). Phytoplankton size structure and primary production in a highly dynamic coastal ecosystem (Ria de Vigo, NW-Span): Seasonal and short-time scale variability, *Estuarine, Coastal and Shelf Science*, *67*, 251-256.

Cermeno, P., Maranon, E., Harbour, D., Figueiras, F. G., Crespo, B. G., Huete-Ortega, M., Varela, M. and Harris, R. P. (2008). Resource levels, allometric scaling of population abundance, and marine phytoplankton diversity, *Limnol. Oceanogr.*, *53*(1), 312-318.

Cermeno, P., Choucino, P., Fernandez-Castro B., Figueiras, F. G., Maranon, E., Marrase, C., Mourino-Carballido, B., Perez-Lorenzo, M., Rodriguez-Ramos, T., Teixeira, I. G. and Vallina, S. M. (2016). Marine primary productivity is driven by a selection effect, *Frontiers*, *3*(173), 1-10.

Chang, F. H., Marquis, E. C., Chang, C. W., Gong, G. C. and Hsich, C. H. (2013). Scaling of growth rate and mortality with size and its consequence on size spectra of natural microphytoplankton assemblages in the East China Sea, *Biogeosciences*, *10*, 5267-5280.

Chisholm, S. W., Morel, F. M. M. and Slocum, W. S. (1980). The phasing

and distribution of cell division cycles in marine diatoms, *In P. G. Falkowski ed., Primary productivity in the Sea, Plenum Press, NY*, 281-300.

Chisholm, S. W. (1981). Temporal patterns of cell division of unicellular algae, *Can. Bull. Fish. Aquat. Sci.*, *210*, 150-181.

Chisholm, S. W. (1992). Phytoplankton size, *In Primary Productivity and Biogeochemical Cycles in the Sea, P. G. Falkowski and A. D. Woodhead, Plenum Press, NY*, 213-237.

Chen, B. and Liu, H. (2010). Relationships between phytoplankton growth and cell size in surface oceans: Interactive effects of temperature, nutrients, and grazing, *Limnol. Oceanogr.*, *55*, 965-972.

Claquin, P., Kromkamp, J. C. and Martin-Jezequel, V. (2004). Relationship between photosynthetic metabolism and cell cycle in a synchronized culture of the marine alga Cylindrotheca fusiformis (Bacillariophyceae), *Eur. J. Phycol.*, *39*(1), 33-41.

Claustre, H., Huot, Y., Obernosterer, I., Gentili, B., Tailliez, D. and Lewis, M. (2008). Gross community production and metabolic balance in the south Pacific Gyre, using a non intrusive bio-optical method, *Biogeosciences*, *5*, 463-474.

Collins, S., Rost, B., Rynearson, T. A. (2014). Evolutionary potential of marine phytoplankton under ocean acidification, *Evolutionary App., Willey and Sons ed.*, 140-155.

Connel, J. H. (1978). Diversity of tropical rainforests and coral reefs, *Science*, *199*, 1304-1310.

Coste, B., Gostan, J. and Minas, H. J. (1972). Influences des conditions hivernales sur les productions phyto- et zooplanctoniques en Méditerranée Nord-Occidentale. I. Structures hydrologiques et distribution des sels nutritifs, *Mar. Biol.*, *16*, 320-348.

Cullen, J. J. and Lewis, M. R. (1988). The kinetics of algal photoadaptation in the context of vertical mixing, *J. Plankton Res.*, *10*, 1039-1063.

Cullen, J. J. (1989). On models of growth and photosynthesis in phytoplankton, *Deep Sea Res.*, *37*(4), 667-683.

Cullen, J. J., Yang, X. and MacIntyre, H. L. (1993). Nutrient limitation of marine photosynthesis, *In Primary productivity and biogeochemical cycles in the Sea, P G. Falkowski and A. Woodhead, Plenum Press, NY.*

Cullen, J. J., Yang, X. and MacIntyre, H. L. (1998). Behavior, physiology and the niche of depth-regulating phytoplankton, *In NATO ASI Series, Vol. G 41 Physiological Ecology of Harmful Algal Blooms, D.M. Anderson, A.D. Cembella, and G. M. Hallegraeff eds., Springer-Verlag, Berlin, Heidelberg 1998*, 1-21.

Dapena, C., Bravo, I., Cuadrado, A. and Figueroa, R. I. (2015). Nuclear and cell morphological changes during the cell cycle and growth of the two toxic dinoflagellate *Alexandrium minutum*, *Protist*, *166*(1), 146-160.

Davison, I. R. (1991). Environmental effects on algal photosynthesis: temperature, *J. Phycol.*, *27*(1), 2-8.

Denman, K. L and Gargett, A. E. (1983). Time and space scales of vertical mixing and advection of phytoplankton in the upper ocean, *Limnol. Oceanogr.*, *28*(5), 801-815.

Diaz, F., Raimbault, P. and Conan, P. (200). Small-scale study of primary productivity during spring in a Mediterranean coastal area (Gulf of Lions), *Cont. Shelf Res.*, *20*, 975-996.

D'Ortenzio, F. and Ribera-D'Alcala, M. (2009). On the trophic regimes of the Mediterranean Sea: a satellite analysis, *Biogeosciences*, *6*, 139-148.

Downing, J. A., Osenberg, C. W. and Sarnelle, O. (1999). Meta-analysis of marine nutrient-enrichment experiments: variation in the magnitude of nutrient limitation, *Ecology*, *80*(4), 1157-1167.

Dring, M. J. (1981). Chromatic adaptation of photosynthesis in benthic marine algae: An examination of its ecological significance using a theoretical model, *Limnol. Oceanogr.*, *26*(2), 271-284.

Droop, M. R. (1966). Vitamin $B_{12}$ and marine ecology, *J. mar. biol. ass. UK*, *46*, 659-671.

Dubinsky, Z. (1980). Light utilization efficiency in natural phytoplankton communities, *In Falkowski PG ed. Primary productivity in the sea. Plenum, New York*, 83-97.

Dubinsky, Z. and Stambler, N. (2009). Photoacclimation processes in phytoplankton: mechanisms, consequences, and applications, *Aquat. Microb. Ecol.*, *56*, 163-176.

Dubreuil, C., Denis, M., Conan, P. and Roy, S. (2003). Spatial-temporal variability of ultraplankton vertical distribution on the Antarctic frontal zones within 60-66°E, 43-46°S, *Polar Biol.*, *26*, 734-745.

Dugdale, R. C. (1967). Nutrient limitation in the Sea: dynamics, identification, and significance, *Limnol. Oceanogr.*, (12), 685-695.

Dugdale, R. C. and Goering, J. J. (1967). Uptake of new and regenerated forms of nitrogen in primary production, *Limnol. Oceanogr.*, *12*, 196-206.

Dugenne, M., Thyssen, M., Nérini, D., Mante, C., Poggiale, J.-C., Garcia, N., Garcia, F. and Grégori, G. J. (2014). Consequence of a sudden wind event on the dynamics of a coastal phytoplankton community: an insight into specific population growth rates using a single cell high frequency approach, *Frontiers*, *5*(485), 1-14.

Dupont, C. L., Barbeau, K. and Palenik, B. (2008). Ni uptake and limitation in marine *Synechococcus* strains, *App. and Env. Microb.*, *74*(1), 23-31.

Edwards, K. F., Litchman, E. and Klausmeier, C. A. (2013). Functional traits explain phytoplankton community structure and seasonal dynamics in a marine ecosystem, *Ecology Letters*, *16*, 56-63.

Edwards, K. F., Thomas, M. K., Klausmerie, C. A. and Litchman, E. (2015). Light and growth in marine phytoplankton: allometric, taxonomic, and environmental variation, *Limnol. Oceanogr.*, *60*, 540-552.

Elledge, S. J. (1996). Cell cycle checkpoints: Preventing and identity crisis, *Science*, *274*, 1664-1672.

Eppley, R. W., Rogers, J.Ñ. and McCarthy, J. J. (1969). Half-saturation constants for uptake of nitrate and ammonium by marine phytoplankton, *Limnol. Oceanogr.*, *14*, 912-920.

Eppley, R. W. (1972). Temperature and phytoplankton growth in the Sea, *Fish. Bull.*, *70*(4), 1063-1085.

Eppley, R. W. and Sharp, J. (1975). Photosynthetic measurements in the central North Pacific: The dark loss

of carbon in 24-h incubations, *Limnol. Oceanogr.*, *20*(6), 981-987.

Estrada, M. (1985). Deep phytoplankton and chlorophyll maxima in the western Mediterranean, *In Mediterranean marine ecosystems, M. Moraitou-Apostolopoulou and Kiortsis, V. eds., NATO Conference Series, Ecology*, 247-278.

Falkowski, P. G. (1980). Primary productivity in the Sea, *P. G. Falkowski ed., Plenum Press, NY London*, 1-531.

Falkowski, P. G., Barber, R. T. and Smetacek, V. (1998). Biogeochemical controls and feedbacks on Ocean Primary Production, *Science*, *281*, 200-206.

Ferrier, C. and Rassoulzadegan, F. (1991). Density-dependent effects of protozoans on specific growth rates in pica- and nanoplanktonic assemblages, *Limnol. Oceanogr.*, *36*(4), 657-669.

Ferris, M. J. and Palenik, B. (1998). Niche adaptation in ocean cyanobacteria, *Nature*, *396*(19), 226-228.

Fiala,M., Cabet, G., Jacques, G., Neveux, J. and Panouse, J. (1976). Fertilisation de communautés phytoplanctoniques. I. Cas d'un milieu oligotrophe : Méditerranée nord-occidentale, *J. Exp. Mar. Biol. Ecol.*, *24*, 151-163.

Finkel, Z., Beardall, J., Flynn, K. J., Quigg, A., Alwyn V. Rees, T. and Raven, J. A. (2010). Phytoplankton in a changing world: cell size and elemental stoichiometry, *J. Plankton Res.*, *32*(1), 119-137.

Flombaum, P. et al. (2013). Present and future global distributions of the marine Cyanobacteria *Prochlorococcus* and *Synechococcus*, *PNAS*, *110*(24), 9824-9829.

Furnas, M. J. (1990). In situ growth rates of marine phytoplankton: approaches to measurement, community and species growth rates, *J. Plankton Res.*, *12*(6), 1117-1151.

Follows, M. J., Dutkiewicz, S., Grant, S. and Chisholm, S. W. (2007). Emergent biogeography of microbial communities in a model ocean, *Science*, *315*, 1843-1846.

Follows, M. J. and Dutkiewicz, S. (2011). Modeling diverse communities of marine microbes, *Annu. Rev. Mar. Sci.*, *3*, 427-451.

Gallegos, C. L. and Platt, T. (1982). Phytoplankton production and water motion in surface mixed layers, *Deep Sea Res.*, *29*, 65-76.

Gasol, J. M., Cardelus, C., Anxelu G. Moran, X., Balagué, V., Forn, I., Marrasé, C., Massana, R., Pedros-Alio, C., Montserrat Sala, M., Simo, R., Vaqué, D. and Estrada, M. (2016). Seasonal patterns in phytoplankton photosynthetic parameters and primary production at a coastal NW Mediterranean site, *Scientia Marina*, *80S1*, 63-77.

Geider, R. J., Platt, T. and Raven, J. A. (1980). Size dependence of growth and photosynthesis in diatoms: a synthesis, *Mar. Ecol. Prog. Ser.*, *30*, 93-104.

Geider, R. J. (1987). Light and temperature dependence of the carbon to chlorophyll a ratio in microalgae and cyanobacteria: Implications for physiology and growth of phytoplankton, *New Phytol.*, *106*, 1-34.

Geider, R. J. and LaRoche, J. (1994). The role of iron in phytoplankton photosynthesis, and the potential for iron-limitation of primary productivity in the Sea, *Photosynthesis Res.*, *39*(3), 275-301.

Glasby, T. M. and Underwood, A. J. (1995). Sampling to differentiate between pulse and press perturbations, *Env. Monitor. and Ass.*, *42*(3), 241-252.

Glover, H. E., Keller, M. D. and Guillrd, R. R. (1986). Light quality and oceanic ultraphytoplankters, *Nature*, *319*(9), 142-143.

Glover, H. E., Phinney, D. A. and Yentsch, C. S. (1995). Photosynthetic Characteristics of Picoplankton Compared with Those of Larger Phytoplankton Populations, in Various Water Masses in the Gulf of Maine, *Biological Oceanography*, *3*(3), 223-248.

Goffart, A., Hecq, J.-H. and Legendre, L. (2002). Changes in the development of winter-spring phytoplankton bloom in the Bat of Calvi (NW Mediterranean) over the last two decades: a response to changing climate, *Mar. Ecol. Prog. Ser.*, *236*, 45-60.

Goering, J. J., Dudgale, R. C. and Menzel, D. W. (1964). Cyclic diurnal variations in the uptake of ammonia and nitrate by photosynthetic organisms in the Sargasso Sea, *Limnol. Oceanogr.*, *9*(3), 448-451.

Goldman, J. (1980). Physiological processes, nutrient availability, and the concept of relative growth rate in marine phytoplankton ecology, *P. G. Falkowski ed., Primary productivity in the Sea, Plenum Press, NY London*, 179-194.

Hasley, K. H., Milligan, A. J. and Behrenfeld, M. J. (2010). Physiological optimization underlies growth rate-independent chlorophyll-specific gross and net primary production, *Photosynth. Res.*, *103*, 125-137.

Heimburger, L.-E., Lavigne, H., Mignon, C., D'Ortenzio, F., Estournel, C., Coppola, L. and Miquel, J.-C. (2013). Temporal variability of vertical export flux at the DYFAMED time-series station (Northwestern Mediterranean Sea), *Progr. in Oceanogr.*, *119*, 59-67.

Hill, D. R. A. (1992). *Plagioselmis prolonga* Butcher (Cryptophyceae). Baltic Sea Phytoplankton identification Sheet No. 8, *Ann. Bot. Fenn.*, *29*, 165-166.

Huertas, I. E., Rouco, M., Lopez-Rodas, V. and Costas, E. (2016). Warming will affect phytoplankton differently: evidence through a mechanistic approach, *Proc. R. Soc. B*, 1-10.

Huete-Ortega, M., Calvo-Diaz, A., Grana, R., Mourino-Carballido, B. and Maranon, E. (2011). Effect of environmental forcing on the biomass, production and growth rate of size-fractionated phytoplankton in the central Atlantic Ocean, *J. Mar. Syst.*, *88*, 203-213.

Hutchinson, G. E. (1957). Concluding remarks, *In Cold Spring Harbor Symposia on Quantitative Biology*, *22*, 415-427.

Jacques, G., Cahet, G., Fiala, M. and Panouse M. (1973). Enrichissement de communautés phytoplanctoniques néritiques de Méditerranée Nord Occidentale, *J. exp. mar. Biol. Ecol.*, *11*, 287-295.

Jeffrey, S. W. (1980). Algal pigment systems,*In Primary Productivity in the Sea, P. G. Falkowski ed., Plenum Press, NY*, 33-58.

Jeffrey, S. W. and Vesk, M. (1997). Introduction to maine phytoplankton and their pigment signatures, *In Jeffrey, S. W., Mantoura, F. C., Wright, S. W. eds., Phytoplankton pigments*

*in Oceanography. UNESCO Publishing, Paris*, 85-126.

Keller, A. A. (1989). Modeling the effects of temperature, light, and nutrients on primary productivity: An empirical and a mechanistic approach compared, *Limnol. Oceanogr.*, *34*(1), 82-95.

Kirchman, D. L. (2002). Processes in Microbial Ecology, *Oxford University Press*, 1-328.

Kirk, J. T. O. (1994), Light and Photosynthesis in aquatic ecosystems, *2nd ed. Cambridge University Press.*

Kleiber, M. (1947). Body size and metabolic rate, *Physiological Reviews*, *27*(4), 511-541.

Krom, M. D., Herut, B., Mantoura, R. F. C. (2004). Nutrient budget for the Eastern Mediterranean: Implications for phosphorus limitation, *Limnol. Oceanogr.*, *49*(5), 1582-1592.

Kromkamp, J., Van Spaendonk, A., Peene, J., Van Rijswijk, P., Goosen, N. (1992). Light, nutrient and phytoplankton primary production in the eutrophic, turbid Westerschelde estuary (The Netherlands), *In Jeep 92. Major biological processes in European Tiodal Estuaries, MAST Report, NIOO-Yerseke*, 115-126.

Kruk, C., Peeters, E. T. H. M., Van Nes, E. H., Huszar, V. L. M., Costa, L. S. and Scheffer, M. (2011). Phytoplankton community composition can be predicted best in terms of morphological groups, *Limnol. Oceanogr.*, *56*(1), 110-118.

Landry, M. R. and Kirchman, D. L. (2002). Microbial community structure and variability in the tropical Pacific, *Deep Sea Res. II*, *49*, 2669-2693.

Langdon, C. (1988). On the causes of interspecific differences in the growth-irradiance relationship for phytoplankton. II. A general review, *J. Plankton Res.*, *10*(6), 1291-1312.

Latasa, M., Estrada, M. and Delgado, M. (1992). Plankton pigment relationships in the Northwestern Mediterranean during stratification, *Mar. Ecol. Progr. Ser.*, *88*, 61-73.

Lazzari, P., Solidoro, C., Ibello, V., Salon, S., Teruzzi, A., Béranger, K., Colella, S. and Crise, A. (2012). Seasonal and inter-annual variability of plankton chlorophyll and primary production in the Mediterranean Sea: a modelling approach, *Biogeosciences*, *9*, 217-233.

Leblanc, K., Quéguiner, B., Garcia, N., Rimmelin, P. and Raimbault, P. (2003). Silicon cycle in the NW Mediterranean Sea: seasonal study of a coastal oligotrophic site, *Oceanologica Acta*, *26*, 339-355.

Le Bouteiller, A., Leynaert, A., Landry, M. R., Le Borgne, R., Neveux, J., Rodier, M., Blanchot, J. and Brown, S. L. (2003). Primary production, new production, and growth rate in the equatorial Pacific: Changes from mesotrophic to oligotrophic regime, *J. Geophysical Res.*, *108*(C12), 1-16.

LeFèvre, D., Bentley, T. L., Robinson, C., Blight, S. P. and Williams, P. J. LeB. (1994). The temperature response of gross and net community production and respiration in time-varying assemblages of temperature marine micro-plankton, *J. Exp. Mar. Biol. Ecol.*, *184*, 201-215.

Legendre, L., Demers, S., Yentsch, C. M., Yentsch, C. S. (1983). The $^{14}C$ method: patterns of dark $CO_2$, fixation and DCMU correction to replace

the dark bottle, *Limnol. Oceanogr.*, *28*(5), 996-1003.

Legendre, L. and Lefèvre (1989). Hydrodynamical singularities as controls of recycled versus export production in oceans, *In W. H. Berger et al. eds., Productivity of the ocean: Present and past*, 49-63.

Legendre, L. and Lefèvre (1995). Microbial food webs and the export of biogenic carbon in oceans, *Aquat. Microb. Ecol.*, *9*, 69-77.

Lévy, M, Mémery, L. and André, J.-M. (1998). Simulation of primary production and export fluxes in the Northwestern Mediterranean Sea, *J. Mar. Res.*, *56*, 197-238.

L'Helguen, S., Maguer, J.-F. and Caradec, J. (2008). Inhibition kinetics of nitrate uptake by ammonium in size-fractionated oceanic phytoplankton communities: implications for new production and f-ratio estimates, *J. Plankton Res.*, *30*(10), 1179-1188.

Li, K. W. and Goldman, J. C. (1981). Problems in estimating growth rates of marine phytoplankton from short-term $^{14}C$ assays, *Microbial Ecology*, *7*(2), 113-121.

Li, K. W. (1994). Primary production of prochlorophytes, cyanobacteria, and eucaryotic ultraphytoplankton: Measurements from flow cytometric sorting, *Limnol. Oceanogr.*, *39*(1), 169-175.

Liebig, J. (1840). Der Zustand der Chemie in Preussen, *Annalen der Chemie und der Pharmacie*, *34*, 102-104.

Lindeman, R. L (1942). The trophic-dynamic aspect of ecology, *Bull. of Math. Biol.*, *53*(1/2), 167-191.

Lindemann, C., Fiksen, O., Andersen, K. H. and Aksnes, D. L. (2016). Scaling Laws in Phytoplankton Nutrient Uptake Affinity, *Frontiers*, *3*(26), 1-6.

Litchman, E. and Klausmeier, C. A. (2008). Trait-based community ecology of phytoplankton, *Annu. Rev. Ecol. Evol. Syst.*, *39*, 615-639.

Loisel, H., Bosc, E., Stramski, D., Oubelkehir, K. and Deschamps, P.-Y. (2002). Seasonal variability of the backscattering coefficient in the Mediterranean Sea based on satellite SeaWIFS imagery, *Geophys. Res. Letters*, *28*(22), 4203-4206.

Long, S.nP. and Falkoswki, P. G. (1994). Photoinhibition of photosynthesis in nature, *Annu. Rev. Plant. Physiol. Plant Mol. Biol.*, *45*, 633-662.

Longhurst, A. R. and Harrison, W. G. (1989). The biological pump: Profiles of plankton production and consumption in the upper ocean, *J. Prog. Oceanogr*, *22*, 47-123.

Lopez-Sandoval, D. C., Rodriguez-Ramos, T., Cermeno, P., Sobrino, C. and Maranon, E. (2014). Photosynthesis and respiration in marine phytoplankton: Relationship with cell size, taxonomic affiliation, and growth phase, *J. Exp. Mar. Biol. Ecol.*, *457*, 151-159.

Lucik, (2003). Silicon cycle in the NW Mediterranean Sea: seasonal study of a coastal oligotrophic site, *Oceanologica Acta*, *26*, 339-355.

Ludwig, W., Dumont, E., Meybeck, M. and Heussnes, S. (2009). River discharges of water and nutrients to the Mediterranean and Black Sea: Major drivers for ecosystem changes during past and future decades, *Progr. Oceanogr.*, *80*, 199-217.

Magazzu, G. and Decembrini, F. (1995). Primary production, biomass and abundance of phototrophic picoplankton in the Mediterranean Sea: a review, *Aquat. microb. Ecol*, *9*, 97-104.

Malone, T. C. (1977). Environmental regulation of phytoplankton productivity in the lower Hudson Estuary, *Estuar. and Coast. Mar. Sci.*, *5*, 157-171.

Malone, T. C. (1980). Size-fractionated primary productivity of marine phytoplankton, *In Primary Productivity in the Sea, P. G. Falkowski ed., Plenum Press, NY*, 301-319.

Malone, T. C. and Ducklow, H. W. (1990). Microbial biomass in the coastal plume of Chesapeake Bay: Phytoplankton-bacterioplankton relationships, *Limnol. Oceanogr.*, *35*(2), 296-312.

Maranon, E., Cermeno, P., Rodriguez, J., Zubkov, M. V. and Harris, R. P., (2007). Scaling of phytoplankton photosynthesis and cell size in the ocean, *Limnol. Oceanogr.*, *52*(5), 2190-2198.

Maranon, E. (2008). Inter-specific scaling of phytoplankton production and cell size in the field, *J. Plankton Res.*, *30*(2), 157-163.

Maranon, E., Cermeno, P., Lopez-Sandoval, D. C., Rodriguez-Ramos, T., Sobrino, C., Huete-Ortega, Blanco, J. M., Rodrigure, J. (2013). Unimodal size scaling of phytoplankton growth and the size dependence of nutrient uptake and use, *Ecology Letters*, *16*, 371-379.

Maranon, E. (2015). Cell size as a key determinant of phytoplankton metabolism and community structure, *Annu. Rev. Mar. Sci.*, *7*, 241-264.

Marie, D., Zhu, F., Balagué, V., Ras, J. and Vaulot, D. (2006). Eukaryotic picoplankton communities of the Mediterranean Sea in summer assessed by molecular approaches (DGGE, TTGE, QPCR), *FEMS Microbiol. Ecol.*, *55*(3), 403-415.

Margalef, R. (1978). Life-forms of phytoplankton as survival alternatives in an unstable environment, *Oceanologica acta*, *1*(4), 493-509.

Marra, J. (1978). Effect of short-term variations in light intensity on photosynthesis of a marine phytoplankter: a laboratory simulation study, *Marine Biology*, *46*(3), 191-202.

Marra, J., Haas, L. W., Heinemann, R. (1988). Time course of C assimilation and microbial food web, *J. Exp. Mar. Biol. Ecol.*, *115*, 263-280.

Marra, J. (2002). Approaches to the measurement of plankton production, *Williams, P. B., Thomas, D. N., Reynolds, C. S. eds, Phytoplankton productivity, Balckwell, Science*, 1-386.

Marshall, J. and Schott, F. (1979). Open ocean convection: observations, theory, and models, *Rev. Geophys.*, *37*, 1-64.

Marty, J.-C., Chiavérini, J., Pizay, M.-D. and Avril, B. (2002). Seasonal and interannual dynamics of nutrients and phytoplankton pigments in the western Mediterranean Sea at the DYFAMED time-series station (1991-1999), *Deep Sea Res. II*, *49*, 1965-1985.

Mayot, N., D'Ortenzio, F., Ribera D'Alcala, M., Lavigne, H. and Claustre, H. (2015). Interannual variability of the Mediterranean trophic regimes from ocean color satellites, *Biogeosciences*, *13*, 1901-1917.

Mella-Flores, D., Six, C., Ratin, M., Partensky, F., Boutte, C., Le Corguillé, G., Marie, D., Blot, N., Gourvil, P., Kolowrat, C. and Garczarek, L. (2012). Prochlorococcus and Synechococcus have evolved different adaptive mechanisms to cope with light and UV stress, *Frontiers*, *3*(285), 1-20.

Menden-Deueur, S. and Lessard, E. J. (2000). Carbon to volume relationships for dinoflagellates, diatoms, and other protist plankton, *Limnol. Oceanogr.*, *45*(3), 569-579.

Menezes, M. and Novarino, G. (2003). How diverse are planktonic cryptomonads in Brazil? Advantages and difficulties of a taxonomic-biogeographical approach, *Hydrobiologia*, *502*(1), 297-306.

Mermex group (2011). Marine ecosystem's responses to climatic and anthropogenic forcings in the Mediterranean, *Progr. in Oceanogr.*, *91*, 97-168.

Minas, H. J., Minas, M., Coste, B., Gostan, J., Nival, P., Bonin, M. C. (1988). Production de base et de recyclage, une revue de la problématique en Méditerranée nord-occidentale, *Oceanologica Acta*, 155-162.

Minas, H. J. B., Coste, P., Le Corre, P., Minas, M. and Raimbault, P. (1991). Biological and geochemical signatures associated with the water circulation through the Strait of Gibraltar and in the western Alboran Sea, *J. Geophys. Res.*, *96*, 8755-8771.

Moisan, J. R., Moisan, T. A. and Abbott, M. R. (2002). Modelling the effect of temperature on the maximum growth rates of phytoplankton populations, *Ecological Modelling*, *153*,197-215.

Monod, J. (1950). La technique de culture continue théorie et applications, *Annls. Inst. Pasteur, Paris*, *79*,390-401.

Morris, I. (1980). Paths of carbon assimilation in marine phytoplankton, *In Primary Productivity in the Sea, P. G. Falkowski ed., Plenum Press, NY*, 139-160.

Moutin, T., Raimbault, P. and Poggiale, J.-C. (1999). Production primaire dans les eaux de surface de la Méditerranée occidentale. Calcul de la production journalière, *Life Sciences*, *322*, 651-659.

Nagata, T. (2000). Production mechanisms of dissolved organic matter, *In Kirchman, D.L. ed., Microbial Ecology of the Oceans, Wiley-Lissy*, 121-152.

Neale, P. J. and Marra, J. (1992). Short-term variation of Pmax under natural irradiance conditions: a model and its implications, *Mar. Ecol. Progr. Ser.*, *26*, 113-124.

Neuer, S. (1992). Growth dynamics of marine *Synechococcus spp.* in the Gulf of Alaska, *Mar. Ecol. Progr. Ser.*, *83*(2-3), 251-262.

Nielsen Steemann, E. and Jorgensen, E. G. (1968). The adaptation of plankton algae, *Physiologia Plantarum*, *21*(2), 401-413.

Nolle, M., Ellul, R., Ventura, F., Gusten, H. (2005). A study oh historical surface ozone measurements (1884-1900) on the island of Gozo in the central Mediterranean, *Atm. Envir.*, *39*, 5608-5618.

Nogueira, E., Woods, J. D., Harris, C., Field, A. J. and Talbot, S. (2006). Phytoplankton co-existence: Results from an individual-based simulation model, *Ecol. Mod.*, *198*, 1-22.

Novarino, G., Mills, D. K. and Hannah, F. (1997). Pelagic flagellate populations in the southern North Sea, 1988-89. Qualitative observations, *J. Plankton Res.*, *19*, 1081-1109.

Novarino, G. (2005). Nanoplankton protists from he western Mediterranean Sea. II Cryptomonads (Cryptophyceae= Cryptomonadea), *JSci. Mar*, *69*, 47-74.

Odum, E. P. (1971). Fundamentals of Ecology, *3rd Edition, W. B. Saunders, Philadelphia*, *198*, 1-22.

Pahl-Wostl, C. (1992). Dynamic versus static models for photosynthesis, *Hydrobiologia*, *238*(1), 189-196.

Percopo, I., Siano, R., Cerino, F., Sarno, D. and Zingone, A. (2011). Phytoplankton diversity during the spring bloom in the northwestern Mediterranean Sea, *Botanica Maina*, *54*, 243-267.

Perez,V., Fernandez, E., Maranon, E., Anxelu, X., Moran, G. and Zubkov, M. V. (2006). Vertical distribution of phytoplankton biomass, production and growth in the Atlantic subtropical gyres, *Deep Sea Res. I*, *53*, 1616-1634.

Perry, M. J., Talbot, M. C., Alberrte, R. S. (1981). Photoadaptation in marine phytoplankton: response of the photosynthetic unit, *Marine Biol.*, *62*, 91-101.

Platt, T. (1975). The mathematical representation and prediction of phytoplankton productivity, *Fish. Mar. Serv. Res. Dev. Tech. Rep.*, *523*, 1-110.

Platt, T. and Gallegos, W. G. (1980). Modelling primary production, *In Primary Productivity in the Sea, P. G. Falkowski ed., Plenum Press, NY*, 339-362.

Pedros-Allio, C. (2006). Marine microbial diversity: can it be determined, *Trends in Microbiology*, *14*(6), 257-263.

Raimbault, P., Coste, B., Boulhadid, M. and Boudjellal, B. (1993). Origin of high phytoplankton concentration in deep chlorophyll maximum (DCM) in a frontal region of the Southwestern Mediterranean Sea (algerian current), *Deep Sea Res. I*, *40*(4), 791-804.

Raven, J. A. (1986). Physiological consequences of extremely small size for autotrophic organisms in the sea, *Can. Bull. Fish. Aquat. Sci*, *214*, 1-70.

Raven, J. A. and Geider, R. J. (1988). Temperature and algal growth, *New Phytol.*, *110*, 441-461.

Raven, J. A., Wollenwebern B. and Handley, L. L. (1992). A comparison of ammonium and nitrate as nitrogen sources for photolithotrophs, *New Phytol.*, *121*, 19-32.

Raven, J. A. and Geider, R. J. (2003). Adaptation, acclimation and regulation in algal photosynthesis, *In : Larkum AWD, Douglas S, Raven JA, eds. Photosynthesis of algae. Dordrecht, the Netherlands: Kluwer Academic Publishers*, 385-412.

Redfield, A. C. (1933). On the proportions of organic derivatives in sea water and their relation to the composition of plankton, *in James Johnstone Memorial Volume ed. Daniel, R. J., Liverpool Univ. Press, Liverpool*, 176-192.

Redfield, A. C. (1958). The biological control of chemical factors in the environment, *Am. Scient.*, *46*(3), 205-221.

Reynolds, C. S. (2006). The ecology of phytoplankton, *Cambridge University Press, Cambridge*, 1-535.

Rodriguez-Ramos, T., Maranon, E. and Cermeno, P. (2015). Marine nano- and microphytoplankton diversity: redrawing global patterns from sampling-standardized data, *Global Ecol. Biogeogr.*, 1-12.

Root, R. B. (1967). The niche exploitation pattern if the blue-gray gnatcatcher, *Ecological Monographs*, *37*, 317-330.

Rynearson, T. A. and Armburust, E. V. (2004). Genetic differentiation among populations of the planktonic marine diatom *Dytilum brightwellii*, *Molecular Ecol.*, *14*, 1631-1640.

Sandgren, C. D. (1988). Growth and reproductive strategies of freshwater phytoplankton. *Cambirdge University Press ed.*, 1-8.

Shaltout, M. and Omstedt, A. (2014). Recent sea surface temperature trends and future scenarios for the Mediterranean Sea. *Oceanologia*, *56*(3), 411-443.

Siokou-Frangou, I., Christaki, U., Mazzochi, M. G., Montresor, M., Ribera D'Alcala, M., Vaqué, D. and Zingone, A. (2010). Plankton in the open Mediterranean Sea: a review. *Biogeosciences*, *7*, 1543-1586.

Smith, R. E. H. and Geider, R. J. (1985). Kinetics of intracellular carbon allocation in a marine diatom. *J. Exp. Mar. Biol. Ecol.*, *93*, 191-210.

Ryther, J. H. and Menzel, D. W. (1965). On the production, composition, and distribution of organic matter in the Western Arabian Sea. *Deep Sea Res.*, *12*, 100-200.

Sarmineto, J. L., Slater, R., Barber, R., Bopp, L., Doney, S. C., Hirst, A. C., Kleypas, J., Matear, R., Mikolajewicz, U., Monfray, P., Soldanov, V., Spall, S. A. and Stouffer, R. (2004). Response of ocean ecosystems to climate warming. *Global Biogeochemical cycles*, *18*, 1-23.

Shroeder, K., Chiggiato, J., Bryden, H. L., Borghini, M. and Ben Ismail, S. (2016). Abrupt climate shift in the Western Mediterranean Sea. *Scientific Report*, *6*, 1-7.

Siegel, D. A., Dickey, T. D., Washburn, L., Hamilton, M. K. and Mitchell, B. G. (1989). Optical determination of particulate abundance and production variations in the oligotrophic ocean. *Deep Sea Res.*, *36*(2), 211-222.

Soetaert, K. and Herman, P. M. (2009). ecolMod: A practical guide to ecological modelling using R as a simulation platform. *R package version 1.3.*

Sosik, H. M., Olson, R. J., Neubert, M. G. and Shalapyonok, A. (2003). Growth rates of coastal phytoplankton from time-series measurements with a submersible flow cytometer. *Limnol. Oceanogr.*, *48*(5), 1756-1765.

Steele, J. H. (1962). Environmental control of photosynthesis in the Sea. *Limnol. Oceanogr.*, *7*, 137-150.

Strobl, R. O., Somma F., Evans, B. M. and Zaldivar, J. M. (2009). Fluxes of water and nutrients from river runoff to the Mediterranean Sea using GIS and a watershed model. *J. Geophys. Res.*, *114*, 1-14.

Sverdrup, H. U. (1953). On condition ofr the vernal blooming of phytoplankton. *Journal du Conseil International pour l'Exploration de la Mer*, *18*, 287-295.

Tang, E. P. Y. (1995). The allometry of algal growth rates. *J. Plankton Res.*, *17*(6), 1325-1335.

Taupier-Letage, I. and Millot C. (1988). Surface circulation in the Algerian Basin during 1984. *Oceanologica Acta*, *9*, 119-131.

Taylor, K. E. (2001). Summarizing multiple aspects of model performance in a single diagram. *J. Geophys. Res.*, *106*, 7183-7192.

Thomas, M. K., Kremer, C. T. and Litchman, E. (2016). Environment and evolutionary history determine the global biogeography of phytoplankton temperature traits. *Global Ecol. Biogeogr.*, *25*, 75-96.

Thompson, P. A., Guo; M.-X. and Harrison, P. J. (1992). Effects of variation in temperature. On the biochemical composition of eight species of marine phytoplankton. *J. Phytol.*, *28*, 481-488.

Throndsen, J. (1969). Flagellates of Norwegian coastal waters. *Nytt. Mag. Bot.*, *16*, 252-268.

Throndsen, J. (1983). Ultra- and nannoplankton flagellates from Coastal waters of Southern Honshu and Kyushu, Japan. *In Working Party on Taxonomy in the Akashiwo Mondai Kenkyukai Fishing Ground Preservation Division, Research Dep., Fish. Agency, Japan M. Chihara and Haruhikol eds.*, 1-62.

Tian, R. C. (2006). Toward standard parameterizations in marine biological modeling. *Ecological Modelling*, *193*, 363-386.

Timmermans, K. R., Van der Wagt, B., Veldhuis, M. J. W., Maatman, A. and De Baar, H. J. W. (2005). Physiological responses of three species of marine pico-phytoplankton to ammonium, phosphate, iron and light limitation. *J. Sea Res.*, *53*, 109-120.

Tsiola, A., Pitta, P., Fodelianaskis, S., Pete, R., Magiopoulos, L., Mara, P., Psarra, S., Tanaka; T. and Mostajir , B. (2016). Nutrient Limitation in Surface Waters of the Oligotrophic Eastern Mediterranean Sea: an Enrichment Microcosm Experiment. *Microbiology of aquatic systems*, *71*, 575-588.

Uitz, J., Claustre, H., Gentili, B. and Stramski, D. (2010). Phytoplankton class-specific primary production in the world's oceans: Seasonal and interannual variability from satellite observations. *Global Biogoechemical cycles*, *24*, 1-19.

Vargas-Yanez, M., Zunino, P., Benali, A., Delpy, M., Pastre, F., Moya, F., Garcia-Martinez, M. and Tel, E. (2010). How much is the western Mediterranean really warming and salting?, *J. Geophys. Res Oceans*, *115*, 1-12.

Vaulot, D. (1995). The cell cycle of phytoplankton: coupling cell growth to population growth, *NATO ASI: Molecular ecology of aquatic microbes*, 1-18.

Vaulot, D., MArie, D., Olson, R. J. and Chisholm; S. W. (1995). Growth of *Prochlorococcus*, a photosynthetic prokaryote, in the Equatorial Pacific Ocean, *Science*, *268*, 1480-1482.

Vérity, P. G., Robertson, C. Y., Tronzo, C. R., Andrews, M. G., Nelson, J. R. and Sieracki, M. E. (1992). Relationships between cell volume and carbon and nitrogen content of marine photosynthetic nanoplankton, *Limnol. Oceanogr.*, *37*, 1434-1446.

Vichi, M., Pinardi, N. and Masina, S. (2007). A generalized model of pelagic biogeochemistry for the global ocean ecosystem. Part I: theroy, *J. Mar. Syst.*, *64*, 89-109.

Vidussi, F., Marty, J.-C. and Chiavérini, J. (2000). Phytoplankton pigment variations during the transition from spring bloom to oligotrophy in the northwestern Mediterranean Sea, *Deep-Sea Research I*, *47*, 423-445.

Vincent, W. F. (1992). The daily pattern of nitrogen uptake by phytoplankton in dynamic mixed layer environments, *Hydrobiologia*, *238*, 37-52.

Von de Poll, W. H., Boute, P. G., Rozema, P. D., Buma, A. G. J., Kulk, G. and Rijkenberg, M. J. A. (2015). Sea surface temperature control of taxon specific phytoplankton production along an oligotrophic gradient in the Mediterranean Sea, *Marine Chemistry*, *177*, 536-544.

Walsh, P. and Legendre, L. (1982). Effets des fluctuations rapides de la lumière sur la photosynthèse du phytoplancton, *J. Plankton Res.*, *4*(2), 313-327.

Westberry, T., Behrenfeld, M. J., Siegel, D. A. and Boss, E. (2008). Carbon-based ocean productivity modelling with vertically resolved photoacclimation, *Global biogeochemical cycles*, *22*, 1-18.

William, P. J. B. (1993). Chemical and tracer methods of measuring plankton production. *ICES marine science symposia*, *197*, 20-36.

Williams, P. J., Raine, R. C. T., Bryan, J. R. (1979). Agreement between the $^{14}C$ and oxygen methods of measuring phytoplankton production: reassessment of the photosynthetic quotient. *Oceanologica acta*, *2*(4), 411-416.

Winder, M. and Sommer, U. (2012). Phytoplankton response to a changing climate. *Hydrobiologia*, *698*, 5-16.

Woods, J. D. and Onken, R. (1982). Diurnal variation and primary production in the ocean- preliminary results of a Lagrangian ensemble model, *J. Plankton Res.*, *4*(3), 735-756.

Worden, A. Z. and Not, F. (2008). Ecology and diversity of picoeukaryotes. *In Microbial Ecology of the Oceans, Second Ed., D. L. Kirchman, John Wiley and Sons, Inc.*.

# 6.0 Empirical predictions of marine primary productivity: On the bayesian inference of the influence of environmental growth conditions - *Part A: Unravelling growth strategies*

**Abstract**

In the field of marine biogeochemistry, empirical models represent an alternative to mechanistic models to foresee the change of the main carbon uptake drivers, phytoplankton cells. To predict the main source of net primary production variations in climatic scenario, the relationships between the observations of phytoplankton daily productivity, representing the response variable, and its environment may be investigated by Generalized Linear regression Models (GLMs). In this paper, we detail the mechanistic limitations of phytoplankton growth by three main environmental descriptors: light and nutrients that influence resource acquisition, and the catalytic effect of temperature which constrains enzymatic activities. After a brief review of the mathematical modelling of marine production, we finally describe how to transform these descriptors, using the Poisson regression, to infer biologically interpretable parameters from a dataset grouping observations of temperature, light and/or nutrients. We fitted the Poisson regression to *in situ* data collected in the Mediterranean Sea by maximum likelihood in order to determine the growth strategies of several functional groups of phytoplankton. The set of functional parameters contributes to the global referencing of Mediterranean biological C pump.

M. Dugenne, D. Pommeret, M. Thyssen, J. Aristegui, N. Hernandez, M. Espino, G. Grégori

## 6.1 Introduction

***Marine primary productivity*** Primary production is a measure of the organic carbon produced by photosynthesis and made available to other trophic levels (Lindeman 1942). Photosynthesis requires light and $CO_2$ to produce carbohydrates in the Calvin cycle. In plants and algae, light is collected through specific structures containing photosynthetic pigments. Production rates thereby express a differential biomass produced by atmospheric C assimilation, reported to a given surface area or volume. Its resultant is measured by the instantaneous standing crop, wether expressed in absolute number of cells, density, or pigment and carbon concentrations. Since 70% of the Earth surface is covered by water, an important part of primary production takes place in the ocean. The global estimation of marine primary production dates back to the 90's with 45-50 Gt C.yr$^{-1}$ (Longhurst et al., 1995). Its part represents half of the atmospheric carbon fixation, and is mainly due to microscopic drifting algae, grouped by a common nomination , *phytoplankton* (Field et al., 1998). Although the result may compare, the spatio-temporal scales of marine and terrestrial productivities are significantly different (Steele 1991). Phytoplankton cells are fast growing (dou-

bling rates > 3 $d^{-1}$) and consequently numerous in the euphotic layer (i.e. layer where a sufficient amount of solar radiation persists to allow photosynthesis) (Furnas, 1991). They form patchy and dynamic spatial structures (D'Ovidio et al., 2010). Populations may be present from days to months and spread over less than one km to hundreds of kms (Denman et al., 1977). The difficulty to study phytoplankton lies in these scales. Cells drift in a unstable environment that control both their growth rates and their accumulation rates in the euphotic zone (Vernet and Smith, 2007).

***Current approaches to measure primary productivity*** In oceanography, mathematical models are used to explicitly represent the main descriptors that explain the variation of *in situ* observations or to understand how a particular biological system respond to a common mechanism. Both approaches are primordial to predict the functioning of marine ecosystems bound to evolve. Since the Joint Global Ocean Flux Study, a large panel of global observation programs are in charge of collecting data to improve the numerical resolution of the ocean carbon cycle (Doney et al., 2001). The first approach is mainly handled by empiric regression models, in which coefficients are tested against the null hypothesis to discriminate relevant descriptors. While the second is derived from mechanistic models in which parameters correspond to a interpretable propriety of the system. They represent the main source of prediction of net primary production at the global scale. Empirical models are more sparse in the literature. When not provided by measures of phytoplankton growth under controlled conditions, the datasets used to fit marine biogeochemical models are collected in the frame of various sampling strategies, either considered static or dynamic. The first type of experiment is Eulerian, in reference to Leonhard Euler. In this context, datasets result from the marginal or sustained observation of tracers at a fixed station and might be treated as time series. The second approach is Lagrangian, in reference to Joseph Louis Lagrange. It consists in following the dynamics of water masses displacement, directed by advection and/or convection, to measure tracer's temporal variations along streamlines (Davis, 1991). This approach is particularly indicated to study *plankton* since these organisms are floating in enclosed water masses. However this approach has been limited by so far due to technical requirements (e.g. near real time integration of the circulation). Although dynamic, oceanographic cruises are rarely adaptive and are consequently relying on sampling strategies laying between the Eulerian and Lagrangian approaches. Each strategy address a part of the time and/or spatial scales at which may vary primary production (Rossby, 2007).

The objective of the paper (part A and B) is to decline several empirical models in order to predict primary productivity and its resultant, the standing crop, according to the approach employed and the question being addressed. Part A focuses on the description of the global mechanistic model of primary productivity fitted by empirical multiple regression for simple datasets. Part B supports model variants in the case of nested and mixture of nested datasets.

## 6.2 Generalized Linear Models and daily primary production models: A review

GLMs

### Definition

As part of the Linear Models, Generalized Linear Models (GLMs) are used to predict a response variable, $Y$, of $n$ observations ($y_i$) by a set of $p$ explanatory descriptors according to the general formula:

$$\eta_i = x_i^T \vec{\beta} \tag{6.1}$$

i: iid observation, $\eta$: linear predictor, $x^T$: explanatory variables ($nxp$), $\beta$: linear coefficients

This class of model is an extension of simple linear regressions for non-normal residuals ($\epsilon_i$). In GLMs, predictions are derived from the linear descriptor ($\eta$) using a link function (g):

$$E(Y_i) = \mu_i = g^{-1}(\eta_i), \eta_i = g(\mu_i) \tag{6.2}$$

g: link function, $\mu$: expectation of $y$

GLMs are more specifically involved when the variance of $Y$ is not constant (i.e. heteroscedasticity). Heteroscedasticity means that we must consider that the variance ($\sigma^2$) is different for each observation, thus we may write $\mathrm{Var}(y_i)=\sigma_i^2:w_i$, with $w_i$ the weight attributed to observation $i$. The variable $Y$ follows a distribution of the exponential family (Nelder and Wedderburn, 1972), whose probability density functions are generalized by:

$$p(y|\Theta) = exp\left(\frac{y\Theta - b(\Theta)}{\phi} + c(y,\phi)\right)$$

p(y|Θ):pdf, $\phi$:scale parameter, {b,c}: arbitrary functions

For distributions part of this family, two important properties are:

$$E(Y) = \frac{db(\Theta)}{d\Theta}, Var(Y) = \phi\frac{d^2b(\Theta)}{d\Theta^2} = \phi E'(Y) \tag{6.3}$$

The main exponential family distributions used in GLMs are summarised in Table 1.

## Statistical inference: Maximum likelihood estimation, confidence intervals and Tests

To fit these models, the set of parameters ($\Theta$) corresponding to the linear coefficients $\vec{\beta}$ are statistically inferred using the maximum likelihood of the data y given $\Theta$, noted $\mathscr{L}(\Theta, y)$:

$$\begin{aligned}
&\mathscr{L}(\Theta, y) = p(y|\Theta) = \prod_{i=1}^{n} p(y_i|\Theta)\\
&p(\Theta|y) = \frac{p(y,\Theta)}{p(y)} \ \textit{(Bayes theorem)}\\
&p(\Theta|y) = \frac{p(y|\Theta)p(\Theta)}{p(y)}\\
&p(\Theta|y) \propto p(y|\Theta)p(\Theta)\\
&p(\Theta|y) \propto \mathscr{L}(\Theta, y)p(\Theta)
\end{aligned} \tag{6.4}$$

Θ: model parameters, $Y$: response variable, $\mathscr{L}$(y,Θ): likelihood, p(y,Θ): joint probability distribution, p(Θ): prior probability distribution, p(Θ|y): posterior probability distribution

According to equation (E 4), optimising the posterior density is equivalent to optimising the likelihood, or its linear form, the log-likelihood, noted $l(\Theta, y)$:

$$\begin{aligned}
&\hat{\Theta} = argmax(l(\Theta, y)), \hat{\Theta} = argmin(-l(\Theta, y))\\
&\frac{\partial l(\Theta, y)}{\partial \Theta}(\hat{\Theta}) = 0\\
&\frac{\partial \sum_{i=1}^{n} log_e(p(y_i|\Theta))}{\partial \Theta}(\hat{\Theta}) = 0\\
&\sum_{i=1}^{n} \frac{\partial log_e(p(y_i|\Theta))}{\partial \Theta}(\hat{\Theta}) = 0\\
&\sum_{i=1}^{n} U(\hat{\Theta}) = 0\\
&log_e(p(y|\Theta) = \frac{y\Theta - b(\Theta)}{\phi} + c(y,\phi)\\
&\textit{(exponential family distributions)}\\
&\frac{\partial \frac{y\Theta - b(\Theta)}{\phi} + c(y,\phi)}{\partial \Theta}(\hat{\Theta}) = 0\\
&\frac{\partial \frac{y\Theta - b(\Theta)}{\phi} + c(y,\phi)}{\partial \Theta}(\hat{\Theta}) = 0\\
&\frac{1}{\phi}\left(y - \frac{db(\Theta)}{d\Theta}(\hat{\Theta})\right) = 0\\
&\frac{1}{\phi}\left(y - \mu(\hat{\Theta})\right) = 0
\end{aligned} \tag{6.5}$$

$\hat{\Theta}$: maximum likelihood estimator (MLE), l(y,Θ): log-likelihood, U: score (derivative of the log-likelihood), $\mu$: expectation of observations

| Distribution | exponential family equivalence | Canonical link | Variance |
|---|---|---|---|
| Normal: $\mathscr{N}(\mu,\sigma^2)$ | $\Theta$: $\mu$, $\phi$: $\sigma^2$, b: $0.5\Theta^2$, c: $-0.5\left(\frac{y^2}{\phi}+log_e(2\pi\phi)\right)$ | identity: $\mu$ | cst=$\sigma^2$ |
| Poisson: $\mathscr{P}(\lambda)$ | $\Theta$: $\log_e(\mu)$, $\phi$: 1, b: $\exp(\Theta)$, c: $-\log_e(y)$ | log: $\log_e(\mu)$ | $\mu$ |
| Binomial: $\mathscr{B}(p)$ | n: 1, $\Theta$: $log_e\left(\frac{\mu}{1-\mu}\right)$, $\phi$: 1, b: $log_e(1+e^{\Theta})$, c: $log_e(1)$ | logit: $log_e\left(\frac{\mu}{1-\mu}\right)$ | $\mu(1-\mu)$ |
| Gamma: $\mathscr{G}(\alpha,\beta^{-1})$ | $\Theta$: $\frac{1}{\mu}$, $\phi$: $\beta$, b: $-\log_e(-\Theta)$, c: $(\phi^{-1}\text{-}1)\log_e(y)\text{-}\log_e(\Gamma(\phi^{-1}))$ | inverse: $\left(\frac{1}{\mu}\right)$ | $\mu^2$ |

Table 6.1: Family distributions in main Generalized Linear Models

An iterative weighted least square (IWLS) procedure is used to provide the MLE ($\hat{\Theta}$) (Nelder and Wedderbur, 1972). Assuming the residuals normality and taking into account their heteroscedasticity, the weighted least square (WLS) approach relies on the following equivalence:

$$
\begin{aligned}
& l(\Theta,y) \propto -\sum_{i=1}^{n}\frac{(y_i-\mu_i)^2}{2\sigma_i^2} \\
& -l(\Theta,y) \propto \sum_{i=1}^{n} w_i\frac{(y_i-\mu_i)^2}{2\sigma^2} \\
& \textit{with: } \sigma_i=\frac{\sigma}{w_i}, \mu_i = g^{-1}(x_i^T\vec{\beta}) = x_i^T\vec{\beta} \\
& \text{in matrix notation:} \\
& -l(\Theta,y) \propto (Y-X^T\vec{\beta})^T W (Y-X^T\vec{\beta})
\end{aligned}
\tag{6.6}
$$

w: weight, g: identity link

Hence, the MLE ($\hat{\beta}$) that minimise $(Y-X^T\vec{\beta})^T W(Y-X^T\vec{\beta})$ is given by:

$$
\begin{aligned}
& \frac{\partial (Y-X^T\vec{\beta})^T W (Y-X^T\vec{\beta})}{\partial\beta}(\hat{\beta}) = 0 \\
& X^T W(Y-X\hat{\beta}) = 0 \\
& X^T W X\hat{\beta} = X^T W Y \\
& \hat{\beta} = (X^T W X)^{-1} X^T W Y
\end{aligned}
\tag{6.7}
$$

$\hat{\beta}$: maximum likelihood estimator (MLE)

In GLMs, weights are unknown since the variance of the observations is a function of their expectations (equation E 3). The IWLS approach will first estimate $\mu$ from an initial guess of parameters $\Theta$ to predict the variance of the observations (see Table 1) and deduce the maximum likelihood estimator (equation E 7) with the known W matrix. $\hat{\Theta}$ are recursively fitted to observations in order to predict a new $\hat{\mu}$ until the series of optimal parameters converges. At convergence, the distribution, and confidence intervals, of the set of optimal parameters is approximated by the Normal distribution with mean equal to the true value of $\beta$ and variance :

$$
\hat{\beta} \sim \mathscr{N}(\beta, \phi(X^T W X)^{-1}) \tag{6.8}
$$

$\hat{\beta}$: maximum likelihood estimator (MLE)

This approximation is used to carry out a Wald test (Draper and Smith, 1998) in order to identify the significant descriptors in the optimal model:

$$
H_0 : \beta = 0 \; H_1 : \beta \neq 0
$$

Given the asymptotic variance, $\phi(X^T W X)^{-1}$, we can deduce the information matrix (Fisher information), $I(\hat{\beta}) = \frac{1}{Var(\hat{\beta})} = (X^T W X)\phi^{-1}$, whose inverse diagonal components are the MLE standard errors (E 9).

$$\sigma(\hat{\beta}) = \frac{1}{\sqrt{I(\hat{\beta})}}$$
$$\text{Wald test statistic: } \frac{\hat{\beta} - \beta_0}{\sigma(\hat{\beta})} \sim \mathscr{X}^2(p) \tag{6.9}$$

$\hat{\beta}$: maximum likelihood estimator (MLE), $\beta_0$: parameter of reference (0 to test for the implication of the corresponding variable in the model), I: Fisher information matrix

Another model testing procedure is the likelihood ratio test (LRT), which compare the likelihood of the fitted full model against the reduced model, using the deviance:

$$D = 2(l_{full} - l) \tag{6.10}$$

D: model deviance, l: log-likelihood, full: the full-model ($\hat{\mu_i} = y_i, \forall i$)

The full or saturated model fits the data perfectly ($\hat{\mu_i} = y_i$, $\forall$ i) by providing a distinct parameter for each observation and the reduced model corresponds to the MLE. The LRT statistic can be deduce from the deviance following:

$$\text{LRT statistic: } \frac{D}{\phi} \sim \mathscr{X}^2(n-p) \tag{6.11}$$

$\hat{\beta}$: maximum likelihood estimator (MLE), I: Fisher information matrix, $\phi$: Normalisation function, n: number of observations, p: number of parameters

Knowing the likelihood of the model given the data (see E 4) and replacing the prior distribution of the MLE by its asymptotic distribution (see E 8), the posterior distribution of the model parameters may be approximated by a Monte Carlo Markov Chain (MCMC) procedure (Neal, 1993):

$$\begin{aligned} p(\Theta|y) &\propto \mathscr{L}(\Theta, y)p(\Theta) \\ p(\Theta|y) &\propto \mathscr{L}(\Theta, y)\frac{1}{\sqrt{2\pi\Sigma^2}}exp\left(-\frac{(\vec{\beta} - \hat{\beta})^2}{2\Sigma^2}\right) \\ \text{with: } \Sigma^2 &= \phi(X^T W X)^{-1} \end{aligned} \tag{6.12}$$

$\Theta$: model parameters, y: response variable, $\mathscr{L}$(y,$\Theta$): likelihood, p($\Theta$): prior probability distribution, p($\Theta$|y): posterior probability distribution

This approach is based on the iterative simulation of a candidate set of parameters, whose distribution is specified by the prior, subjected to an acceptance/rejection decision that maximise the posterior probability until convergence (Metropolis et al., 1953). In the following section, we will use the Metropolis-Hastings MCMC approach to approximate the distribution of the biologically interpretable parameters derived from the Poisson regression coefficients from 5000 iterations and ignoring the first 1000 estimations ($burn-in$), to provide the 95 % confidence interval of the parameters fitted by maximum likelihood.

### Practical case: the $\mathscr{P}$oisson regression

If $Y$ corresponds to absolute or differential counts, which is the example treated in this article, then predictions should not be negative. In this case, we may specify the $Y$ distribution as a Poisson distribution:

$$\begin{aligned} Y &\sim \mathscr{P}(\lambda) \\ p(y|\lambda) &= \frac{exp(-\lambda)y^\lambda}{y!} \end{aligned} \tag{6.13}$$

$\lambda$: expectation of $y$

For a Poisson regression, the link function is the natural logarithm ($log_e$) and its inverse the exponential (exp) function (see Table 1). Therefore, in this paper, we will assume that the observations ($y_i$), as independent realisation of $Y$, with expectation E($y_i$)=$\mu_i$, follow the Poisson distribution with mean and variance equal to $\lambda$ and the natural logarithm canonical link of $\lambda$, is a linear combination of the explanatory variables $x_i^T$:

$$\begin{aligned} log_e(\mu_i) &= \eta_i \\ &= x_i^T \beta \\ &= \begin{bmatrix} x_i^1 & x_i^2 & \dots & x_i^p \end{bmatrix} . \begin{bmatrix} \beta^1 \\ \beta^2 \\ \vdots \\ \beta^p \end{bmatrix} \end{aligned} \tag{6.14}$$

For simulation, we used a random generator number according to:

$$\widetilde{Y} \sim \mathscr{P}(exp(\eta)) \tag{6.15}$$

Replacing the likelihood by the Poisson distribution function (E 13) in the deviance formula (E 10), the LRT statistics becomes:

$$\begin{aligned}(l_{full} - l) &= \frac{1}{2}D \\ &= log_e\left(\frac{p(y|\lambda = y)}{p(y|\lambda = exp(\eta))}\right) \\ &= log_e\left(\frac{y^y}{exp(\eta)^y}\frac{e^{-y}}{e^{-exp(\eta)}}\right) \\ &= y.log_e\left(\frac{y}{exp(\eta)}\right) - (y - exp(\eta))\end{aligned} \tag{6.16}$$

D: model deviance, l: log-likelihood, full: the full-model ($\hat{\mu_i} = y_i, \forall i$), p(y|λ): Poisson density function

The maximum likelihood estimator (MLE) of the linear coefficients, $\hat{\beta}$ is given by E 17:

$$\frac{\partial l(\beta, y)}{\partial \beta}(\hat{\beta}) = \frac{\partial \eta}{\partial \beta}\frac{d\mu}{d\eta}\frac{d\theta}{d\mu}\frac{\partial l(\theta, y)}{\partial \theta}(\hat{\beta}) = 0$$

with each derivative component:

$$\begin{cases} \dfrac{\partial \eta}{\partial \beta} = \dfrac{\partial X^T\beta}{\partial \beta} = X^T & \text{(see E 1)} \\ \dfrac{d\mu}{d\eta} = \dfrac{1}{\frac{d\eta}{d\mu}} = \dfrac{1}{\frac{dg(\mu)}{d\mu}} & \text{(see E 2)} \\ \dfrac{d\theta}{d\mu} = \dfrac{1}{\frac{d\mu}{d\theta}} = \dfrac{1}{\frac{d^2b(\theta)}{d\theta^2}} & \text{(see E 3)} \\ \dfrac{\partial l(\theta, y)}{\partial \theta} = \dfrac{1}{\phi}(y - \mu) & \text{(see E 5)} \end{cases}$$

Hence, for the Poisson regression:

$$\begin{aligned}&\frac{\partial l(\beta, y)}{\partial \beta}(\hat{\beta}) = \left(X^T\frac{1}{\mu}\mu(y - \mu)\right)(\hat{\beta}) \\ &= X^T(y - \mu(\hat{\beta})) \\ &X^T(y - \mu(\hat{\beta})) = 0 \\ &X^Ty = X^T\mu(\hat{\beta})\end{aligned} \tag{6.17}$$

The last property ensures that the asymptotic estimators are unbiased, the sum of the iid observations is equal to the sum of ML predictions if the model contains an intercept. Observations of interest in this paper consist in primary productivity or its derivative, absolute counts:

$$\begin{aligned}&P(t) = B(0)\delta(t) = N(0)C_{cell}\delta(t) = N(0)C_{cell}(exp(\mu(t)) - 1) \\ &log_e(P(t)) = log(N(0)C_{cell}(exp(\mu(t)) - 1)) = log_e(C_{cell}) + log_e(N(t) - N(0))\end{aligned} \tag{6.18}$$

P(t): Daily primary production rates $[C][L]^{-3}[T]^{-1}$, B(0): Initial biomass $[C][L]^{-3}$, N(0): Initial abundance $[cell][L]^{-3}$, N(t): Abundance at t $[cell][L]^{-3}$, $C_{cell}$: Carbon cellular quota $[C][cell]^{-1}$, $\delta(t)$: Daily mitotic index $[T]^{-1}$, $\mu(t)$: Daily growth rates $[T]^{-1}$

Phytoplankton primary production

In the ocean, observations of primary productivity and phytoplankton abundance span several orders of magnitude (Maranon et al., 2001). The system is non-linear, this is why we can't resort to classical regression. In main mathematical models, marine primary production is expressed with several non-linear functions of phytoplankton growth environment (Behrenfeld et al., 2008). They include direct or bottom-up controls, exercised by the limitation of re-

source in the environment phytoplankton live in. To grow, phytoplankton cells absorb a part of the light spectrum, the Photosynthetic Available Radiation (PAR), to transfer the electron energy required for photosynthesis. With light as their main energy source, photoautotrophs may build up their organic composites from the assimilation of nutrients. Nutrients group a few dissolved inorganic molecules ($CO_2$, $NH_4^+$, $PO_4^{3-}$) and several trace compounds (Reynolds, 2006). Even though some molecules might enter the cells by passive diffusion, the quantity required to fuel cells anabolism is globally fulfilled by active uptake and biochemical reactions (e.g. transmembrane protein and enzyme). The later is a process that may be indirectly limited by the *in situ* temperature. In all cells, the reaction rates are physically constrained by temperature to transform a substrate into a different product. In 1993, Cullen et al. took into account these factors, using multiplicative terms, to suggest a general mathematical formulation of marine primary productivity:

$$P(x,t) = P_{max}.P(T(x,t)).P(E(x,t)).P(N(x,t)) \tag{6.19}$$

x: geographic site, t: time, P: Daily primary production rates $[C][L]^{-3}[T]^{-1}$, $P_{max}$: Maximal production rates $[C][L]^{-3}[T]^{-1}$, T: *In situ* temperature [°C], E: Light intensity $[Quanta].[L]^{-2}.[T]^{-1}$, N: macronutrient concentration [MOLE]

Tian (2006) reviewed the functions currently used to predict marine primary production from observations of temperature, light and nutrients. The first control may be expressed by 10 functions, 6 supposing that growth rates increases monotonously with high temperature and 4 assuming the presence of an optimum above which, rates start to decrease. The same partition describe the action of light on marine production. Light-Photosynthesis (termed PI or PE) is the most basic and yet most equivocal relationship modelled by biological oceanographers. 13 functions are reported in Tian's review, with 4 formulations relying on the Michaelis-Menten equation to describe a hyperbolic functional response and 9 models that incorporate the inhibitory effect of high light intensities. 5 functions translate the repercussion of limiting nutrients on phytoplankton growth based on two basic model: (i) the Michaelis-Menten enzymatic control of nutrients uptake and (ii) the Droop cellular quotas (Q) with a critical value, $Q_{min}$, under which the present nutrients forms are no longer mobilisable for growth. The mechanistic/empiric terms of the equation (E 19) are detailed in the following sections in forms that allowed us to use a Poisson regression to define phytoplankton growth environment:

$$\begin{aligned} log_e(P(x,t)) &= log_e(P_{max}.P(T(x,t)).P(E(x,t)).P(N(x,t))) \\ log_e(P(x,t)) &= log_e(P_{max}) + log_e(P(T(x,t))) + log_e(P(E(x,t))) + log_e(P(N(x,t))) \end{aligned} \tag{6.20}$$

x: geographic site, t: time, P: Daily primary production rates $[C][L]^{-3}[T]^{-1}$, $P_{max}$: Maximal production rates $[C][L]^{-3}[T]^{-1}$, T: *In situ* temperature [°C], E: Light intensity $[Quanta].[L]^{-2}.[T]^{-1}$, N: macronutrient concentration [MOLE]

Some of the terms, such as nutrient-kinetic model, have already been specified by GLM (Nelder et al., 1991). Moreover, specific studies accounted for primary production variability by jointly or specifically using empiric measures of temperature, nutrients and PAR in log-transformed regression (Keller, 1989). In section (3), we will explicitly describe how to model each component of equation (E 20) and provide some goodness of fit statistics via simulations with Poisson errors ($\epsilon$) using GLMs. In section (4) we will present the joint predictions of a Poisson regression applied to the observations of group-specific (i) net primary production rates measured in the NW

Mediterranean Sea during the Deep Water EXperiment cruises and (ii) absolute abundance counted along a Mediterranean longitudinal gradient.

## 6.3 Utilisation of Generalized Linear Models to predict net primary production

Temperature: Mechanistic function, empirical transformation and parameters identifiability

### Mechanistic function

In 1972, Eppley compiled a collection of phytoplankton daily growth rates obtained under a 0-40 °C gradient of temperature in controlled conditions. The exponential increase of phytoplankton maximum growth capacity with temperature is now extensively described and explained by the universal dependence of kinematics on temperature (Raven and Geider, 1988 and ref within; Brown et al., 2004). Cells anabolism is subjected to the mechanistic Arrhenius law (1889) which translate the ability of temperature to produce the energy, denoted E, required for enzyme activation. This physical quantity may be empirically deduced in ratchet experiments from measure of $Q_{10}$, defined as the rate of kinetics (k) increase under a positive 10°C shift (for reaction-specific $Q_{10}$, see review of Raven and Geider, 1988).

$$\left.\begin{aligned} k(T=t) &= Ae^{-\frac{E}{R(t)}} \\ k(T=t+10) &= Ae^{-\frac{E}{R(t+10)}} \end{aligned}\right\} \quad (6.21)$$

$$Q_{10} = \frac{k(T=t+10)}{k(T=t)} = e^{-\frac{E}{R}.\left(\frac{1}{t+10}-\frac{1}{t}\right)}$$

$$\text{Hence } Q_{10} = e^{\frac{10.E}{RT.(T+10)}} \text{ and}$$

$$E = R.T^2.\frac{log_e(Q_{10})}{10} \text{ (Dixon and Webb, 1979)}$$

E: Enzymatic kinetics activation energy [kcal][MOLE]$^{-1}$, R=8.3: Gas constant [kcal][K]$^{-1}$[MOLE]$^{-1}$, k: reaction rates, T: Temperature [K]

For a given enzyme, temperature might be suboptimal when it exceeds the optimal condition, denoted $T_{opt}$, and leads to the decrease of enzymatic kinetics due to enzyme structural denaturation. $Q_{10}$ becomes inferior to 1. The Gauss equation transcribes this situation:

$$\begin{aligned} k(T) &= Ae^{\frac{E}{R}.\left(\frac{1}{T_{opt}}-\frac{1}{T}\right)}, E = \frac{R(T-T_{opt})^2.log_e(Q_{10})}{10} \\ k(T) &= Ae^{\frac{R.(T-T_{opt})^2.log_e(Q_{10})}{10.R}.\left(\frac{T-T_{opt}}{T.T_{opt}}\right)} \\ &= Ae^{\left(\frac{log_e(Q_{10}).(T-T_{opt})^2}{10.T_{opt}}-\frac{log_e(Q_{10}).(T-T_{opt})^2}{10T}\right)} \\ &= Ae^{\left(-\frac{log_e(Q_{10})}{10}.(T-2T_{opt}+T_{opt}^2T^{-1})\right)}.e^{-\left(\frac{-log_e(Q_{10}).(T-T_{opt})^2}{10.T_{opt}}\right)} \end{aligned} \quad (6.22)$$

$$\text{Hence } k \sim k_{max}(T)e^{-\left(\frac{(T-T_{opt})^2}{\Delta T_{\pm}^2}\right)}$$

Equation (E 22) applies for both the physiological temperature-dependence of phytoplankton organisms and the definition of Hutchinson' niche (1957). Fig 1a is an illustration of equation (E 22) under the average thermal gradient of global surface ocean

(Abraham et al., 2013). When T <$T_{opt}$ and $\log_e(Q_{10}^-)$> 0 ($Q_{10}^-$>1), $\mu$ increases with temperature up to $T_{opt}$. At $T = T_{opt}$, enzymatic kinematics is maximum, hence $P = P_{max}$. Above $T_{opt}$, $\log_e(Q_{10}^+)$< 0 ($Q_{10}^+$<1), the production rates progressively decrease to 0. The difference between the activation phase, with $Q_{10}^-$, and the denaturation phase, with $Q_{10}^+$, is modelled by distinct parameters $\Delta T_\pm$ that ensure the asymmetric response of growth under a large gradient of temperature (Moisan et al. ,2002).

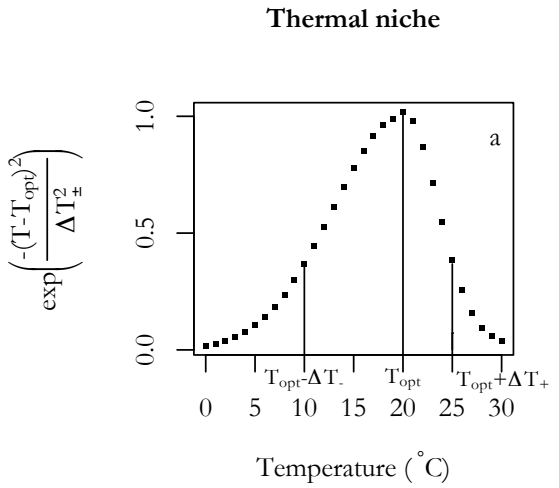


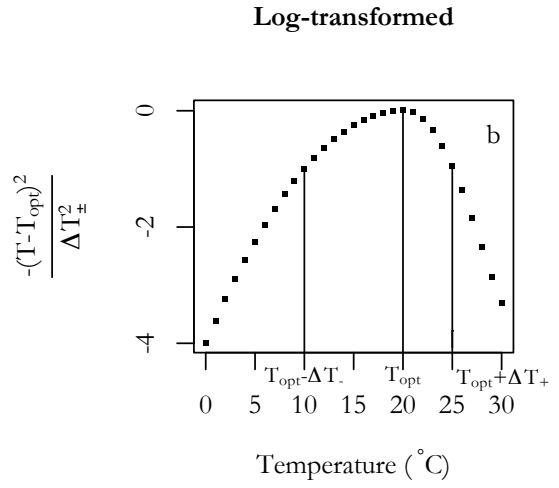


Figure 6.1: Untransformed (a) and $\log_e$ transformed (b) thermal niche expressed as a function of temperature. $T_{opt}$ is the optimal temperature for growth and $\Delta T_\pm$ ensures the asymmetry of the growth curve under suboptimal conditions.

**Empirical transformation**

After a $log_e$-transformation, equation (E 22) simplifies to the following equation:

$$
\begin{aligned}
P(T) &= exp\left(-\frac{(T-T_{opt})^2}{\Delta T_\pm^2}\right)\\
log_e(P(T)) &= -\left(\frac{(T-T_{opt})^2}{\Delta T_\pm^2}\right)\\
log_e(P(T)) &= -\frac{1}{\Delta T_\pm^2}(T-T_{opt})^2\\
log_e(P(T)) &= -\frac{1}{\Delta T_\pm^2}(T^2-2TT_{opt}+T_{opt}^2)\\
log_e(P(T)) &= \beta_0^T+\beta_1^T T'+\beta_2^T T\\
\text{with: } T' &= T^2
\end{aligned}
\tag{6.23}
$$

P: Daily primary production rates $[C][L]^{-3}[T]^{-1}$, $P_{max}$: Maximal production rates $[C][L]^{-3}[T]^{-1}$, T: *In situ* temperature [°C], $T_{opt}$: Optimal temperature [°C], $\Delta T_\pm$: Asymmetric deviations of the thermal niche curve [°C]

This formulation requires to use a piecewise regression, where $\Delta T_\pm$ is dependent wether temperature is inferior or superior to the optimal growth temperature. By definition, $T_{opt}$ is the temperature value at which we observe the maximum production rates ($T_{opt} = argmax(P(T))$). We may also consider the optimal temperature as a constant determined by the average *in situ* temperature (Thomas et al., 2012), to simplify equation (E 23) to a linear function of the unique transformed variable $(T-T_{opt})^2$ with a dummy variable that takes 0 and 1 when temperature observations are below and above the optimum or inversely (Fig 2). In the case where $T_{opt}$ is unknown, both coefficients of the Poisson regression and variables ($T^2$, $TT_{opt}$) become dependent.

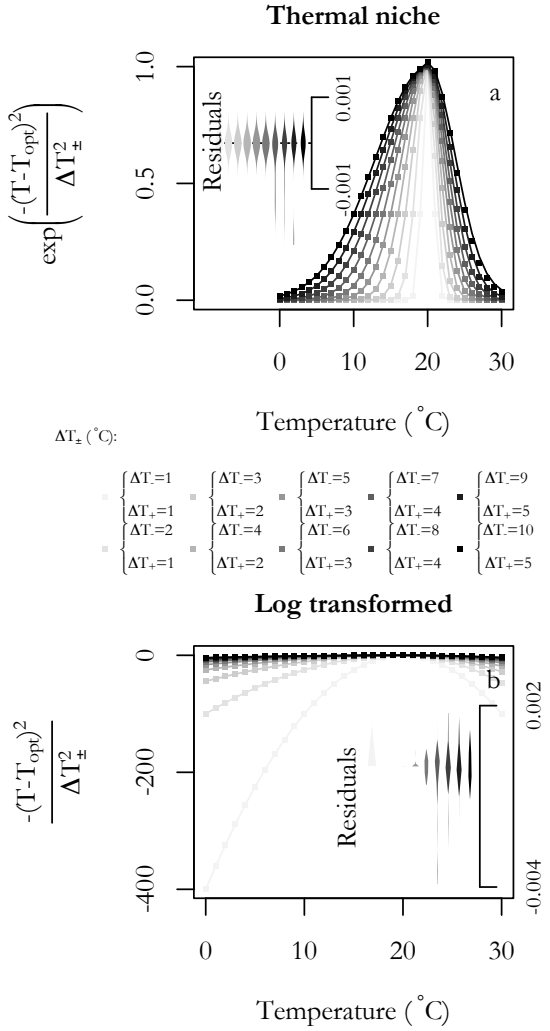


Figure 6.2: Simulation of untransformed (a) and $\log_e$ transformed (b) thermal niche (dots) expressed as a function of temperature ($n$=30). Data fitted by a piecewise Poisson regression (with a null intercept) are superimposed (lines). $T_{opt}$ is the optimal temperature for growth and $\Delta T_{\pm}$ ensures the asymmetry of the growth curve under suboptimal conditions.

Simulations were used to validate the specification of the GLM (E 23). Data were simulated by a RGN over a set of parameters $T_{opt}$, $\Delta T_{-}$, $\Delta T_{+}$ from a regular sequence of temperature bounded between 0 °C and 30 °C. MLE coefficients are shown in Table 2.

| n | SSE | $\Delta T_{-}$ | $\Delta T_{+}$ | $T_{opt}$ |
|---|---|---|---|---|
| 10 | $2.9 \times 10^{-10}$ | 5 | 2.78 | 20 |
| | | (4.24) | (3.97) | (909.58) |
| 50 | $1.2 \times 10^{-10}$ | 5 | 2.78 | 20 |
| | | (3.66) | (3.38) | (282.04) |
| 100 | $2 \times 10^{-10}$ | 5 | 2.78 | 20 |
| | | (3.39) | (3.18) | (190.67) |
| 150 | $3.6 \times 10^{-10}$ | 5 | 2.78 | 20 |
| | | (3.3) | (3.11) | (169.31) |
| 200 | $4.4 \times 10^{-10}$ | 5 | 2.78 | 20 |
| | | (3.17) | (3.03) | (142.25) |

Table 6.2: Sum of squared errors (SSE) and predicted thermal niche parameters ($\hat{\Theta} = \{T_{opt}; \Delta T_{-}; \Delta T_{+}\}$) derived from the fit of a piecewise Poisson regression (with a null intercept), with the response variable, y, simulated from n predictions with $\Theta = \{20; 5; 3\}$

For model comparison, MLE are compared to the least-squares estimations presented by Thomas et al. (2012) on the dataset they compiled (available at http://mridulkthomas.weebly.com/data–code.html). Results are shown in Table 3.

### Parameters identification

Given the GLM expressed in equation (E 23), the interpretable parameters of phytoplankton thermal growth curve are determined by:

$$\beta_0^T = -\frac{T_{opt}^2}{\Delta T_{\pm}^2},$$
$$\beta_1^T = -\frac{1}{\Delta T_{\pm}^2}, \beta_2^T = \frac{2T_{opt}}{\Delta T_{\pm}^2}$$
$$\Delta T_{\pm}^2 = -\frac{1}{\beta_1^T}, T_{opt} = -\frac{\beta_2^T}{2.\beta_1^T} = \sqrt{\frac{\beta_0^T}{\beta_1^T}}$$

Light: Mechanistic function, empirical transformation and parameters identifiability

### Mechanistic function

In 1974, Webb et al. introduced the P-E curve to describe the effect of a gradient of light on photosynthetic production. As the primary source of energetic excitation that transfer in algae photosystems, light is a limiting resource for photosynthesis at

| Species | $T_{opt}$ | $\widehat{T_{opt}}$ | IC ($T_{opt}$) | p-value | W/2 | $\widehat{W/2}$ | IC(W/2) | p-value | n |
|---|---|---|---|---|---|---|---|---|---|
| Calcidiscus leptoporus | 15.47 | 12.68 | 9.5-12.09 | 0.08 | 9.20 | 8.87 | 4.69-10.11 | 0.79 | 6 |
| Calcidiscus leptoporus | 18.50 | 18.96 | 17.84-19.7 | 0.61 | 9.10 | 9.60 | 5.6-10.97 | 0.70 | 6 |
| Calciodinellum albatrosianum | 33.00 | 32.81 | 6.35-112.3 | 0.99 | 28.10 | 21.61 | 15.45-34.77 | 0.13 | 11 |
| Chaetoceros deflandrei | 10.78 | 10.29 | 9.48-12.46 | 0.74 | 27.37 | 35.96 | 26.11-48.28 | 0.17 | 7 |
| Chaetoceros didymus | 21.20 | 22.74 | 22.53-31.72 | 0.26 | 12.20 | 13.79 | 6.34-21.38 | 0.71 | 9 |
| Chaetoceros sp. | 31.95 | 31.54 | 30.89-35.1 | 0.69 | 30.03 | 22.79 | 9.76-34.24 | 0.21 | 12 |
| Chlamydomonas | 8.11 | 7.84 | 5.33-9.35 | 0.83 | 49.53 | 50.17 | 26.47-83.77 | 0.97 | 6 |
| Coccolithus pelagicus | 16.45 | 16.28 | 11.32-25.31 | 0.97 | 12.18 | 10.31 | 4.49-19.76 | 0.60 | 4 |
| Corethron pennatum | 3.10 | 3.55 | 1.25-3.45 | 0.82 | 18.13 | 18.45 | 6.87-59.12 | 0.99 | 5 |
| Crocosphaera watsonii | 28.84 | 29.49 | 12.97-78.77 | 0.97 | 3.30 | 3.17 | 1.19-4.6 | 0.88 | 7 |
| Crocosphaera watsonii | 28.69 | 29.37 | 5.65-50.57 | 0.95 | 3.34 | 3.93 | 2.47-8.2 | 0.68 | 7 |
| Cryptomonas sp. | 26.80 | 26.49 | 16.17-26.04 | 0.91 | 7.37 | 7.52 | 4.97-10.59 | 0.91 | 4 |
| Emiliania huxleyi | 22.66 | 22.48 | 18.75-26.1 | 0.79 | 9.99 | 9.03 | 5.33-18.71 | 0.76 | 5 |
| Emiliania huxleyi | 23.58 | 23.49 | 21.61-22.55 | 0.97 | 11.39 | 11.91 | 4.63-27.71 | 0.95 | 8 |
| Fibrocapsa japonica | 22.65 | 22.74 | 19.33-22.01 | 0.95 | 14.54 | 13.45 | 8.24-17.05 | 0.57 | 10 |
| Fragilariopsis cylindrus | 4.54 | 6.24 | 4.81-21.15 | 0.71 | 30.39 | 27.46 | 14.77-53.16 | 0.78 | 6 |
| Fragilariopsis kerguelensis | 3.70 | 4.24 | 4.53-6.37 | 0.71 | 23.36 | 21.01 | 11.44-47.08 | 0.80 | 5 |
| Gephyrocapsa oceanica | 22.29 | 21.97 | 16.6-27.17 | 0.85 | 12.45 | 16.12 | 8.86-21.81 | 0.28 | 8 |
| Gymnodinium sp. | 25.99 | 24.23 | 7.6-36.12 | 0.82 | 8.48 | 9.78 | 7.95-12.94 | 0.45 | 12 |
| Isochrysis galbana | 28.46 | 28.43 | 15.55-32.03 | 0.99 | 17.49 | 16.78 | 5.57-52.74 | 0.97 | 6 |
| Koliella antarctica | 12.60 | 12.71 | 13.07-12.43 | 0.94 | 8.66 | 8.13 | 5.7-13.02 | 0.79 | 4 |
| Nannochloris sp. | 32.90 | 33.18 | 29.76-35.53 | 0.87 | 28.18 | 27.82 | 7.96-39.54 | 0.98 | 12 |
| Odontella mobiliensis | 26.85 | 26.41 | 22.31-29.09 | 0.78 | 11.18 | 11.16 | 5.63-37.3 | 1.00 | 8 |
| Pernambugia tuberosa | 23.84 | 24.45 | 13.59-25.3 | 0.84 | 10.51 | 11.64 | 3.06-41.16 | 0.91 | 9 |
| Phaeocystis antarctica | 3.46 | 3.37 | 3.68-4.86 | 0.89 | 4.94 | 3.08 | 2.19-4.87 | 0.01 | 6 |
| Rhizosolenia setigera | 24.03 | 23.60 | 20.41-26.1 | 0.74 | 11.83 | 12.53 | 6.66-21.98 | 0.89 | 9 |
| Skeletonema tropicum | 27.14 | 28.87 | 24.25-33.42 | 0.00 | 12.18 | 12.52 | 7.27-14 | 0.85 | 10 |
| Skeletonema tropicum | 29.57 | 29.08 | 29.08-29.08 |  | 14.28 | 13.18 | 8.48-24.77 | 0.81 | 7 |
| Skeletonema tropicum | 25.76 | 25.86 | 16.54-32.5 | 0.97 | 13.00 | 19.85 | 11.79-27.93 | 0.11 | 10 |
| Stellarima microtrias | 3.51 | 3.27 | 3.6-3.65 | 0.64 | 26.82 | 33.54 | 9.79-192.97 | 0.90 | 4 |
| Synedra sp. | 4.51 | 4.43 | 1.49-6.65 | 0.96 | 27.46 | 24.90 | 9.14-72.38 | 0.96 | 4 |
| Thalassionema nitzschioides | 27.01 | 25.95 | 23.54-28.23 | 0.17 | 12.98 | 11.11 | 5.06-38.08 | 0.86 | 8 |
| Trichodesmium erythraeum | 28.56 | 24.40 | 23.28-25.77 | 0.00 | 9.53 | 7.64 | 5.44-30.24 | 0.75 | 36 |

Table 6.3: Comparisons of specific thermal niche's optimum ($T_{opt}$) and width ($W/2$) obtained by least square estimations and maximum likelihood estimations for the dataset compiled by Thomas et al. (2012)

low intensities. Consequently, primary production increase linearly under an instantaneous flux of light emission, denoted E, with a slope $\alpha$, proportional to chlorophyll a concentration, as long as the electron transfer does not exceed the carrying capacity of the combined photosynthetic factories (Eilers and Petters, 1988). At high light intensity, the excess of electronic support results in ineffective excitation that inhibits the production, a process called *photoinhibition*. Steele (1962) formulated an empirical model to fit P-E data collected in the Sargasso Sea:

$$P(E) = P_{max}.\frac{E}{E_k}.exp(1-\frac{E}{E_k}) \qquad (6.24)$$

P: Primary production rates, $P_{max}$: Maximal productivity, $E_k$: Optimal light intensity [Quanta].$[L]^{-2}$.$[T]^{-1}$

By considering the derivative of equation (E 24) when E tends to 0 (Fig 4), and the carbon:chlorophyll a ratio ($\Theta$), Steele determined the relation between the initial slope ($\alpha$) of the P-E curve and the optimal light intensity ($E_k$):

$$\frac{\partial P}{\partial E} = P_{max}\left(\frac{1}{E_k}exp(1-\frac{E}{E_k}) - \frac{E}{E_k}\frac{1}{E_k}exp(1-\frac{E}{E_k})\right)$$

$$\frac{\partial P}{\partial E} = P_{max}\frac{1}{E_k}exp(1-\frac{E}{E_k})\left(1-\frac{E}{E_k}\right)$$

$$\left(\frac{\partial P}{\partial E}\right)_{|E\to 0} = P_{max}\frac{1}{E_k}e^1 = \frac{\alpha}{\Theta}$$

$$\Leftrightarrow E_k = \frac{e^1\Theta P_{max}}{\alpha} \qquad (6.25)$$

This expression is analogous to the probability of electrons hitting photosynthetic factories following the Poisson distribution

of parameter $\lambda$, $\mathscr{P}(\lambda)$. In this model, light quanta are defined as the discrete electron levels that may successfully excite a photosynthetic factory (Eilers et Peeters, 1988). Photosynthetic factories or photosystems (PS) are closed if they have been effectively hit by the photon flux, denoted $E$, otherwise they remain open and do not transfer electron for photosynthesis. Above a saturating photon flux, denoted $E_k$, photosynthesis decreases by *photoinhibition*. The states of phytoplankton photosynthetic factories are illustrated in Fig 4.

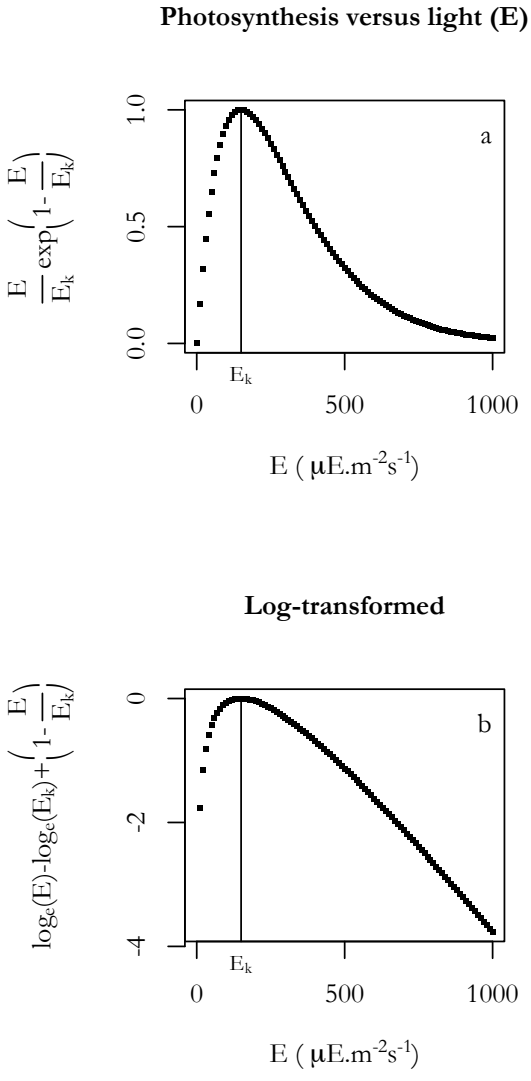


Figure 6.3: P vs E untransformed (a) and $\log_e$ transformed (b) curves expressed as a function of light irradiance (E). $E_k$ is the optimal light intensity

The maximum production, $P_{max}$, is reached if we consider that all factories were hit by a light quantum, with a probability Prob(X=1|$\lambda$)~ $\mathscr{P}(\lambda = E : E_k)$, given that it did not exceed a single quantum per PS, Prob(X≥1|$\lambda$).

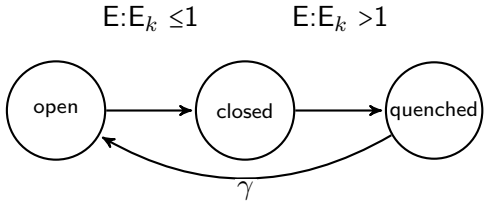


Figure 6.4: Sates and transition rates of a phytoplankton photosystem (PS) II (Eilers et Peeters, 1988). In the dark, PS are open or in a reduced state and photosynthesis is null. Under a constant photons flux, PS are activated and transfer electrons to the cells' reaction centres for photosynthesis, with a transition rate proportional to incident light ($E : E_k$). The proportions of closed PS II increase up to an optimal light intensity, $E_k$. Under a sursaturation photon flux, ($E : E_k$>1), PS are quenched or photoinhibited, as they are limited by the turnover of the electron chain transfer, until the photosynthetic electron transfer rates allows to reopen the PS at rate $\gamma$.

According to Bayes' theorem, this conditional probability is equal to $\frac{Prob(X = 1|\lambda = E : E_k)}{1 - (1 - Prob(X = 1|\lambda = 1)}$, under a continuous excitation light, denoted $E$:

$$
\begin{aligned}
&Prob(X = 1|\lambda) \sim \mathscr{P}(\lambda = E : E_k)\\
&\text{with } E_k = \frac{e^1 P_{max}\Theta}{\alpha}, \Theta = \frac{C_{cell}}{[Chla]}\\
&Prob(X = 1|\lambda = E : E_k) = \frac{exp^{-\lambda}.\lambda^x}{x!}\\
&Prob(X = 1|\lambda = E : E_k) = exp^{-\lambda}.\lambda\\
&Prob(X = 1|\lambda = E : E_k) = exp^{-\frac{E}{E_k}}.\frac{E}{E_k}\\
&Prob(X = 1|\lambda = E : E_k) =\\
&exp^{-\frac{\alpha E}{e^1 P_{max}\Theta}}.\frac{\alpha E}{e^1 P_{max}\Theta}
\end{aligned}
\tag{6.26}
$$

Transposed to primary productivity, E 26 becomes:

$$
\begin{aligned}
P &= P_{max}.\left(\frac{Prob(X=1|\lambda=E:E_k)}{Prob(X=1|\lambda=1)}\right)\\
P &= P_{max}.\left(exp(-\frac{E}{E_k}).\frac{E}{E_k}\right).\frac{1}{exp(-1)}\\
P &= P_{max}.\frac{\alpha.E}{e^1 P_{max}\Theta}.exp(-\frac{\alpha.E}{P_{max}\Theta e^1}).exp(1)\\
P &= P_{max}.\frac{E}{E_k}.exp(1-\frac{E}{E_k})
\end{aligned}
\tag{6.27}
$$

P: Primary production rates, $P_{max}$: Maximal productivity, $\alpha$: Initial slope of the P-E curve, E: Light intensity [Quanta].[L]$^{-2}$.[T]$^{-1}$, $E_k$: Optimal light intensity [Quanta].[L]$^{-2}$.[T]$^{-1}$, $\Theta$: carbon:chlorophyll a ratio

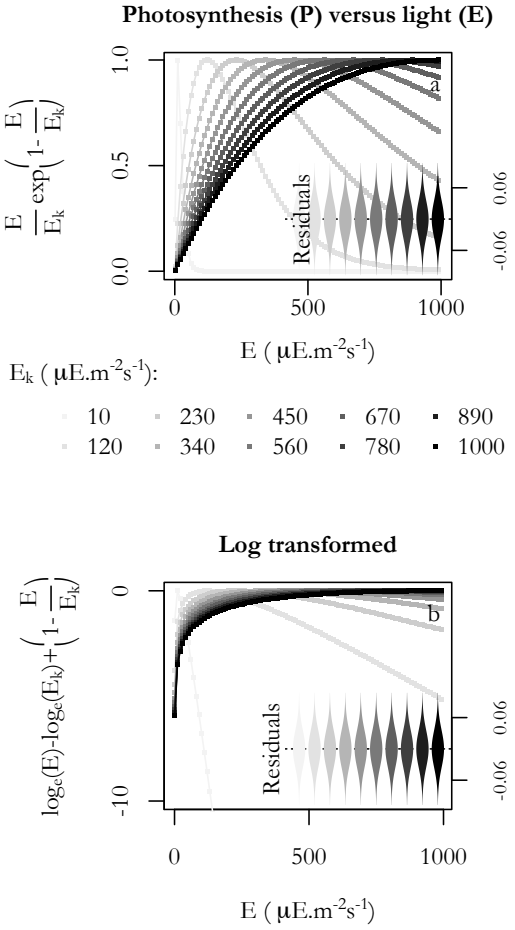


Figure 6.5: Simulation of P vs E untransformed (a) and $\log_e$ transformed (b) growth curves (dots) expressed as a function of light intensity ($n$=100). Data fitted by Poisson regression (with an intercept equals to 1-$\log_e(E_k)$) are superimposed (lines). $E_k$ is the optimal light intensity

Simulations were used to validate the specification of the GLM (E 27). Data were simulated by a RGN over several parameters $E_k$, from a regular sequence of light bounded between 0 $\mu$E.m$^{-2}$.s$^{-1}$ and 1000 $\mu$E.m$^{-2}$.s$^{-1}$. MLE coefficients are summarised in Table 4 and fitted curves are shown in Fig 5.

## Empirical transformation

The log-transformation of equation (E 27) corresponds to the following generalized linear regression:

$$
\begin{aligned}
log_e(P(E)) &= 1 - log_e(E_k) - \frac{E}{E_k} + \text{offset}(log_e(E))\\
log_e(P(E)) &= \beta_0^E + \beta_1^E E + \text{offset}(log_e(E))
\end{aligned}
\tag{6.28}
$$

A Wald test was applied to compare the optimal light intensity constant fitted by the Poisson regression and the reference of a global marine dataset compiled by Edwards at al. (2015). Species-specific optimal light intensities and p-values are reported in Table 5.

## Parameters identification

Given the GLM expressed in equation (E 27), the interpretable parameters of P vs E curve are determined by:

$$
\begin{aligned}
\beta_1^E = -\frac{1}{E_k}, \beta_0^E &= 1 - log_e(E_k)\\
E_k = -\frac{1}{\beta_1^E} &= exp(1-\beta_0^E)
\end{aligned}
$$

Nutrients: Mechanistic function, empirical transformation and parameters identifiability

## Mechanistic function

In response to nutrient enrichment, growth/production rates increase to saturation with the limiting nutrients availability, described in Monod's model (1949). The Michaelis-Menten model expresses the same process by assuming that nutrient uptake is

| $n$ | $E_k$ ($\mu$E.m$^{-2}$.s$^{-1}$) | | | | | | | | | |
|---|---|---|---|---|---|---|---|---|---|---|
| | 10 | 120 | 230 | 340 | 450 | 560 | 670 | 780 | 890 | 1000 |
| 200 | 10 | 120 | 230 | 340 | 450 | 560 | 670 | 780 | 890 | 1000 |
| | (4) | (12) | (23) | (43) | (73) | (117) | (178) | (258) | (365) | (504) |
| 150 | 10 | 120 | 230 | 340 | 450 | 560 | 670 | 780 | 890 | 1000 |
| | (5) | (14) | (27) | (50) | (87) | (140) | (214) | (314) | (449) | (630) |
| 100 | 10 | 120 | 230 | 340 | 450 | 560 | 670 | 780 | 890 | 1000 |
| | (8) | (18) | (34) | (64) | (111) | (181) | (281) | (422) | (619) | (897) |
| 50 | 10 | 120 | 230 | 340 | 450 | 560 | 670 | 780 | 890 | 1000 |
| . | (16) | (27) | (51) | (98) | (175) | (295) | (480) | (765) | (1221) | (1998) |
| 10 | 10 | 120 | 230 | 340 | 450 | 560 | 670 | 780 | 890 | 1000 |
| | (13) | (99) | (165) | (344) | (746) | (1821) | (7824) | (9428) | (4178) | (3167) |

Table 6.4: Optimal light intensity ($E_k$) derived from the parameterisation ($E_k$=-$\frac{1}{\beta_1^E}$) of a Poisson regression (with an intercept equals to 1-log$_e$($E_k$)) with data simulated from $E_k \in [10, 1000]$, following the formula $y = log_e(P(E)) = \beta_0^E + \beta_1^E E + offset(log_e(E))$ . (.) corresponds to $E_k + \frac{1}{\beta_1^E + \sigma(\beta_1^E)}$

| Species | $E_{opt}$ ($\mu$E.m$^{-2}$.s$^{-1}$) | $\hat{E}_{opt}$ ($\mu$E.m$^{-2}$.s$^{-1}$) | 95% CI ($\mu$E.m$^{-2}$.s$^{-1}$) | $n$ | p-value |
|---|---|---|---|---|---|
| Ceratium fusus | 493.00 | 491.00 | 361-830 | 6 | 0.98 |
| Chaetoceros calcitrans | 98.00 | 96.00 | 64-150 | 5 | 0.92 |
| Coscinodiscus granii | 192.00 | 191.00 | 176-214 | 13 | 0.94 |
| Cylindrotheca closterium | 95.00 | 101.00 | 60-185 | 5 | 0.87 |
| Dactyliosolen fragilissimus | 88.00 | 90.00 | 45-88 | 4 | 0.89 |
| Diacronema lutheri | 69.00 | 65.00 | 43-99 | 5 | 0.81 |
| Eucampia zodiacus | 229.00 | 224.00 | 157-378 | 13 | 0.93 |
| Leptocylindricus danicus | 61.00 | 79.00 | 56-116 | 13 | 0.22 |
| Nitzschia cylindrus | 141.00 | 262.00 | 219-564 | 4 | 0.02 |
| Nitzschia kerguelensis | 94.00 | 88.00 | 32-369 | 4 | 0.95 |
| Nitzschia turgiduloides | 113.00 | 105.00 | 76-178 | 4 | 0.75 |
| Phaeocystis pouchetii | 296.00 | 418.00 | 340-552 | 6 | 0.03 |
| Pseudochattonella farcimen | 91.00 | 89.00 | 48-165 | 10 | 0.95 |
| Rhizosolenia fragilissima | 88.00 | 90.00 | 53-134 | 4 | 0.94 |
| Rhodomonas salina | 76.00 | 62.00 | 41-99 | 4 | 0.35 |
| Skeletonema costatum | 257.00 | 263.00 | 146-447 | 5 | 0.93 |
| Tetraselmis sp. | 145.00 | 138.00 | 72-252 | 5 | 0.89 |
| Thalassiosira allenii | 100.00 | 99.00 | 68-148 | 6 | 0.96 |
| Thalassiosira curviseriata | 82.00 | 75.00 | 59-97 | 5 | 0.51 |

Table 6.5: Optimal light intensity ($\hat{E}_{opt}$) derived from the parameterisation (n) of a Poisson regression using the dataset compiled by Edwards et al. (2015). The agreement with the reference value is given by the p-value of the Wald test statistics under $\mathscr{X}^2(1)$. 95% confidence interval (CI) are approximated by MCMC

ruled by the law of mass action for a given couple enzyme-substrate (E-N).

If we consider the following enzymatic reaction $[N] + [E]_{free} \underset{k_{-1}}{\overset{k_1}{\rightleftharpoons}} [EN] \overset{k_2}{\rightleftharpoons} [N]_{intracellular} + [E]_{free}$, the law of mass action gives:

$$\frac{d[EN]}{dt} = k_1.[E]_{free}.[N] - k_2.[EN]$$

$$V = \frac{d[N]_{intracellular}}{dt} = k_2.[EN]$$

At equilibrium, we may write, given that $[E] = [E]_{free} + [EN]$:

$$\frac{d[EN]^*}{dt} = k_1.[E]^*_{free}.[N] - k_2.[EN]^* = 0$$

$$[EN]^* = \frac{k_1}{k_2}.([E]^* - [EN]^*).[N]$$

$$[EN]^* = \frac{k_1.[E]^*.[N]}{k_2 + k_1.[N]}$$

Hence,

$$\begin{aligned} V &= k_2.[EN]^* \\ V &= \frac{k_2.[E].[N]}{\frac{k_2}{k_1} + [N]} \\ V &= \frac{V_{max}.[N]}{K_N + [N]} \\ &\text{with } V_{max} = k_2.[E] \text{ and } K_N = \frac{k_2}{k_1} \\ P(N) &= V \\ P(N) &= P_{max}.\frac{N}{N + K_N} \end{aligned} \tag{6.29}$$

V: uptake rate, $V_{max}$: Maximal uptake rate, [N]: substrate concentration, P: Primary production rates, $P_{max}$: Maximal productivity, N: limiting nutrient concentration, $K_N$: half-saturation constant

An alternative to the steady-state assumption was given by Winter et al. (1975), who considered a constant lag time ($\delta t$). In this model, P(N,t) is equal to :

$$P(N,t) = P_{max}.\frac{N(t-\delta t)}{N(t-\delta t) + K_N} \tag{6.30}$$

P(N,t): nutrients-limited primary production rates, N (t): instantaneous limiting nutrient concentration, P: Primary production rates, $P_{max}$: Maximal productivity, $K_N$: half-saturation constant, $\delta$t: lag time of effective production derived from an instantaneous uptake

The half-saturation constant is an empiric parameter that correspond to the substrate concentration at which the production rates reaches half its maximum (Fig 6).

## Empirical transformation

Nelder et al. (1991) used a GLM to fit enzyme kinetics response to substrate enrichment according to the MM model. Equation (E 29) can be fitted to nutrients enrichment data alone using a logit transformation (see Table 1). If we consider the ratio $P : P_{max}$ bounded between 0 and 1 as a probability determined by the Binomial distribution, the natural logarithm of the odds (i.e. *logit* transformation) becomes:

$$\begin{aligned} \mu &= \frac{P}{P_{max}} = P(N) = \frac{N}{N + k_N} \\ \Theta &= log_e\left(\frac{\mu}{1-\mu}\right) \\ log_e\left(\frac{\mu}{1-\mu}\right) &= log_e\left(\frac{N}{k_N}\right) \\ log_e\left(\frac{\mu}{1-\mu}\right) &= log_e(N) - log_e(k_N) \end{aligned} \tag{6.31}$$

N: substrate concentration, P: Primary production rates, $P_{max}$: Maximal productivity, N: limiting nutrient concentration, $k_N$: half-saturation constant

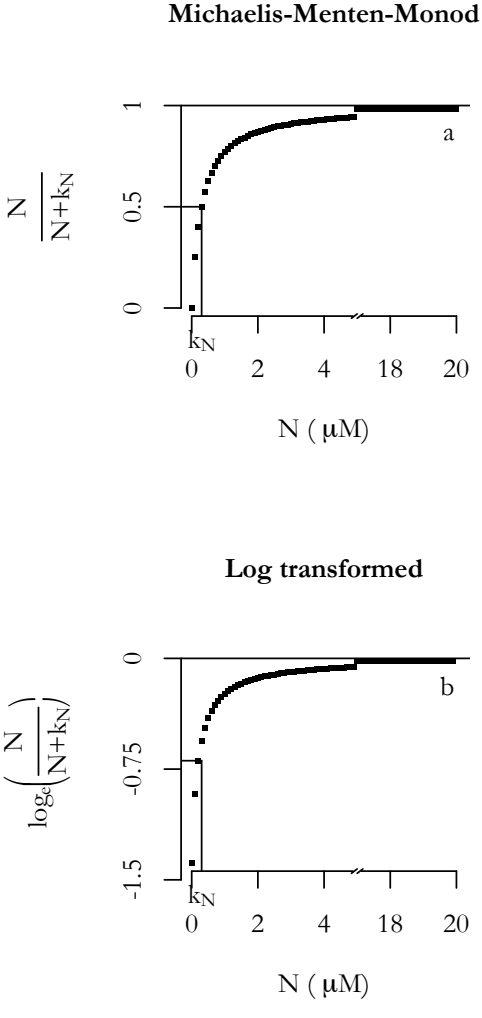


Figure 6.6: Monod's untransformed (a) and $\log_e$ transformed (b) growth curves expressed as a function of substrate concentration. $k_N$ is the concentration of the substrate at half saturation

Another equivalence is given by the hyperbolic tangent function (Jassby and Platt, 1976). Posing $x = log_e(\sqrt{2\frac{N}{k_N}+1})$, the hyperbolic tangent (tanh) is equivalent to the general form of sigmoid curve described in the Monod model:

$$\begin{aligned} tanh(x) &= \frac{exp(2.log_e(\sqrt{2\frac{N}{k_N}+1})) - 1}{exp(2.log_e(\sqrt{2\frac{N}{k_N}+1})) + 1} \\ tanh(x) &= \frac{2\frac{N}{k_N}}{2\frac{N}{k_N}+2} \\ tanh(x) &= \frac{N}{N+k_N} \end{aligned} \tag{6.32}$$

This model was used by Agawin et al. (2000) to fit the variation of *Synechococcus* primary production rates in the Mediterranean Sea to experimental DIN enrichments. Equation (E 32) satisfies the boundaries conditions:

$$\begin{gathered} \text{N=0, tanh(x)=0, tanh(x)}^n\text{=0} \\ \text{N} \to +\infty\text{, tanh(x)} \to \text{1,tanh(x)}^n \to 1 \end{gathered}$$

The natural logarithm of the hyperbolic tangent can be expressed with the inverse hyperbolic tangent, denoted atanh, following:

$$\begin{aligned} &log_e(tanh(x)) = 2.atanh(-exp(-2x)) \\ &\text{with } atanh(x') = \frac{1}{2}log_e\left(\frac{1+x'}{1-x'}\right) \end{aligned} \tag{6.33}$$

The adjustment of the hyperbolic tangent function to PE hyperbolic data is often both superior to alternative models, including the Monod model (Jassby and Platt, 1976; Agawin et al., 2000) and less subject to structural sensitivity (Adamson and Morozov, 2012). To fit the natural logarithm of an hyperbolic curve as a linear regression of the log-transformed hyperbolic tangent, we propose to transform the limiting nutrient concentration into $log_e(\sqrt{2N+1})$. This is based on the assumption that the catalytic rate ($k_2$) is close to that of the substrate-enzyme binding ($k_1$). This approximation yield to small residuals (Fig 7), ranging from -4.10$^{-2}$ to 1.2.10$^{-7}$ $\mu$M, dependent of the half-saturation constant. The formulation corresponds to the following generalized linear regression:

$$\begin{aligned} &log_e(P(N)) = \beta_1 N' \\ &\text{with: } N' = log_e(tanh(log_e(\sqrt{2N+1}))) \end{aligned} \tag{6.34}$$

This formulation will fit the function $\left(\frac{N}{N+1}\right)^{\beta_1}$, called the Hill equation, which is the generic form of the Monod model (Flynn et al., 1997). Fig 7 shows the fit of the Michaelis-Menten-Monod curves for distinct half-saturation constants using the Poisson regression model, with a null intercept ($log_e\left(\frac{N}{N+1}\right)^{\beta_1} = \beta_1.log_e\left(\frac{N}{N+1}\right)$). Considering the definition of the half-saturation constant (i.e.), the regression coefficient may be inferred following:

$$\begin{aligned} k_N &= arg\left(P = \frac{P_{max}}{2}\right) \\ \left(\frac{k_N}{k_N+1}\right)^{\beta_1} &= \frac{1}{2} \\ \frac{k_N}{k_N+1} &= \left(\frac{1}{2}\right)^{\beta_1^{-1}} \\ k_N &= \frac{1}{2^{\beta_1^{-1}}-1} \end{aligned} \tag{6.35}$$

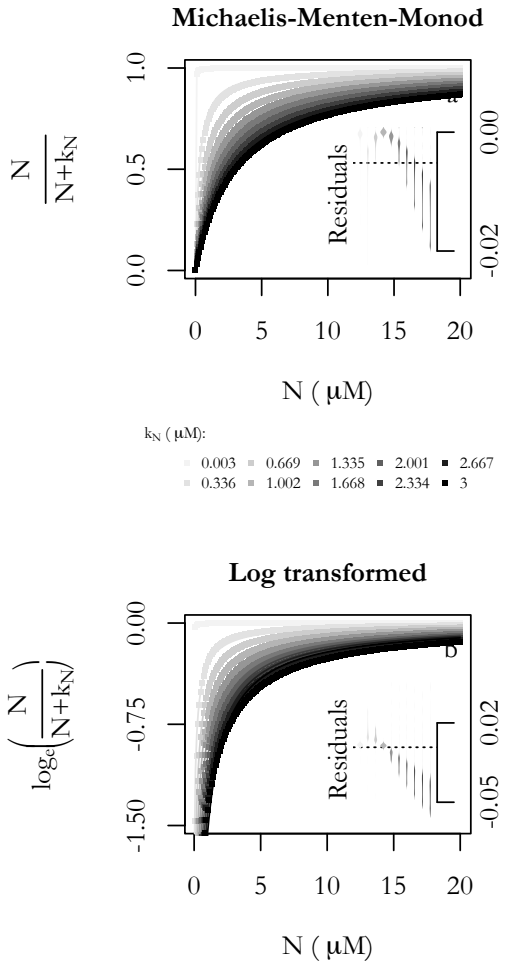


Figure 6.7: Simulation of Monod's untransformed (a) and $\log_e$ transformed (b) growth curves (dots) expressed as a function of substrate concentration ($n$=200). Data fitted by Poisson regression (with a null intercept) are superimposed (lines). $k_N$ is the concentration of the substrate at half saturation

A Wald test was applied to compare the half-saturation constant fitted by the Poisson regression using the hyperbolic tangent and the reference of a set of phosphates ($PO_4^{3-}$), nitrates ($NO_3^-$), ammonium ($NH_4^+$) and silicates ($Si(OH)_4$) constants from the global marine dataset compiled by Edwards at al. (2012). Species-specific half-saturation constants and p-values are reported in Table 6.

### Parameters identification

Given $\beta_1$=$n$ (*Hill coefficient*), the linear coefficient of the Poisson regression, the true value of the half-constant saturation may be deduced from the MLE following equation (E 35) with an mean error of 0.06 ± 0.07 $\mu$M (Table 7).

Primary production predictions

### The model

Recalling the general formulation expressed in equation (E 20) and the independent formulation for temperature (E 23), light (E 24) and nutrients (E 29), primary production can be predicted by the integrated growth model:

$$log_e(P) = log_e(P_{max}) + log_e(P(T)) + log_e(P(E)) + log_e(P(N))$$

$$log_e(P) = \beta_0 + \beta_0^T + \beta_1^T T' + \beta_2^T T + \beta_0^E + \beta_1^E E + \text{offset}(log_e(E)) + \beta_1^N N'$$

with linear coefficients:
$$\begin{cases} \beta_0 = log_e(P_{max}) \\ \beta_0^T = -\dfrac{T_{opt}^2}{\Delta T^2} \\ \beta_1^T = -\dfrac{1}{\Delta T^2} \\ \beta_2^T = \dfrac{2T_{opt}}{\Delta T^2} \\ \beta_0^E = 1 - log_e(E_k) \\ \beta_1^E = -\dfrac{1}{E_k} \\ \beta_1^N = n \end{cases}$$

and transformed variables:
$$\begin{cases} T' = T^2 \\ N' = tanh(log_e(\sqrt{2N+1})) \end{cases}$$

(6.36)

### Parameters identifiability

Each growth niche components (i.e. $T_{opt}$, $\Delta T_{\pm}$, $E_k$, $n$) were identified in sections 3.1.3, 3.2.3, 3.3.3 respectively. With the notation introduced in equation 36, they become:

$$T_{opt}=-\frac{\beta_2^T}{2.\beta_1^T},\ \Delta T_{\pm}=-\frac{1}{\beta_1^T},\ E_k=-\frac{1}{\beta_1^E},\ n=\beta_1^N$$

| Species | $k_{NH_4}$ ($\mu$M) | $k_{NO_3}$ ($\mu$M) | $k_{PO_4}$ ($\mu$M) | $k_{Si(OH)}$ ($\mu$M) | $\hat{k}$ ($\mu$M) | 95% CI ($\mu$M) | $n$ | p-value |
|---|---|---|---|---|---|---|---|---|
| Alexandrium catenella | | | 2.28 | | 2.48 | 2.43-4.63 | 12 | 0.85 |
| Alexandrium minutum | | 0.00 | | | 0.09 | 0-0.066 | 8 | 0.67 |
| Alexandrium minutum | 0.60 | | | | 0.71 | 0.21-1.14 | 10 | 0.83 |
| Alexandrium tamarense | | | 2.60 | | 2.34 | 2.63-5.11 | 10 | 0.83 |
| Asterionella glacialis | | 1.13 | | | 1.21 | 0.44-2.43 | 11 | 0.92 |
| Coscinodiscus wailesii | | 5.08 | | | 5.22 | 5.67-11.29 | 12 | 0.94 |
| Coscinodiscus wailesii | | | 5.62 | | 4.08 | 4.08-4.08 | 12 | |
| Cyclotella nana | | 1.19 | | | 1.60 | 0.52-1.53 | 13 | 0.58 |
| Dunaliella tertiolecta | | 1.60 | | | 1.36 | 0.7-2.34 | 6 | 0.73 |
| Eucampia zodiacus | | | 1.83 | | 1.76 | 1.4-3.35 | 12 | 0.94 |
| Eucampia zodiacus | | 2.59 | | | 2.56 | 1.4-7.82 | 10 | 0.99 |
| Fragilaria crotonensis | | | 4.64 | | 3.23 | 2.23-6.11 | 5 | 0.24 |
| Gymnodinium catenatum | | 7.60 | | | 6.49 | 8.86-8.86 | 8 | 0.31 |
| Gymnodinium catenatum | | | 3.40 | | 2.55 | 1.92-4.93 | 11 | 0.44 |
| Gymnodinium catenatum | 33.60 | | | | 31.09 | 31.09-31.09 | 14 | |
| Micromonas pusilla | | 0.47 | | | 0.36 | 0.2-1.16 | 6 | 0.86 |
| Micromonas pusilla | 0.40 | | | | 0.64 | 0.64-1.48 | 7 | 0.71 |
| Nitzschia closterium | | | 0.47 | | 0.60 | 0.49 - 1.38 | 8 | 0.84 |
| Nitzschia longissima | | 0.79 | | | 1.19 | 0.47-3.06 | 12 | 0.68 |
| Nitzschia sp. | | | 0.06 | | 0.07 | 0.09-0.14 | 16 | 0.96 |
| Pavlova lutheri | | | 0.44 | | 0.51 | 0.34-1.37 | 8 | 0.83 |
| Phaeocystis pouchetii | | | 0.31 | | 0.22 | 0.02-0.1 | 14 | 0.78 |
| Prochlorococcus | | | 0.75 | | 0.79 | 0.51-1.5 | 6 | 0.95 |
| Prorocentrum donghaiense | | | 1.73 | | 1.29 | 0.77-2.33 | 8 | 0.54 |
| Pyrocystis noctiluca | | | 6.66 | | 5.95 | 4.44-12.19 | 7 | 0.69 |
| Skeletonema costatum | | 1.93 | | | 2.06 | 2.06-2.06 | 7 | |
| Skeletonema costatum | | | 0.58 | | 0.97 | 0.79-1.89 | 11 | 0.57 |
| Skeletonema costatum | | 2.12 | | | 1.77 | 1.38-3.38 | 10 | 0.70 |
| Synechococcus sp. | | | 0.40 | | 0.37 | 0-0.73 | 7 | 0.94 |
| Synechococcus sp. | | | 0.67 | | 0.75 | 0.75-0.75 | 13 | |
| Tetraselmis subcordiformis | | | 0.68 | | 0.83 | 0.8-1.1 | 9 | 0.68 |
| Thalassiosira pseudonana | | | | 4.73 | 4.46 | 3.22-8.75 | 7 | 0.85 |
| Thalassiosira pseudonana | | | 0.60 | | 0.57 | 0.34-1.65 | 12 | 0.97 |
| Trichodesmium erythraeum | | | 0.42 | | 0.37 | 0.35-0.98 | 8 | 0.93 |
| Trichodesmium erythraeum | | | 0.64 | | 0.81 | 0.34-1.77 | 5 | 0.81 |

Table 6.6: Half-saturation constant ($\hat{k}$) derived from the parameterisation (n) of a Poisson regression (with a null intercept) using the dataset compiled by Edwards et al. (2012). The agreement with the reference value is given by the p-value of the Wald test statistics under $\mathscr{X}^2(1)$. 95% confidence interval (CI) are approximated by MCMC

**Model specification in JAGS**

model
{

for(i in 1:n){
y[i] ~ dpois(lambda[i])
log(lambda[i]) ← $\beta_0$ + 1 + log(E[i])
-log(-pow($\beta_1^E$,-1)) + $\beta_1^E$*E[i]
+ $\beta_1^N$*log(tanh(log(pow(1+2*N[i],0.5))))
+ $\beta_1^T$[1]*(pow(T[i]-$T_{opt}$,2))*step(T[i]-$T_{opt}$)
+ $\beta_1^T$[2]*(pow(T[i]-$T_{opt}$,2))*(1-step(T[i]-$T_{opt}$))
}
$\beta_0$ ~ dnorm(0,1E-06)
$\beta_1^E$ ~ dnorm(0,1E-06)
$\beta_1^N$ ~ dnorm(0,1E-06)
$T_{opt}$ ~ dnorm(mean(T),sd(T))
for(j in 1:2){
$\beta_1^T$[j]~ dnorm(0,1E-06)
}
}

## 6.4 *In situ* applications in the Mediterranean Sea

The Poisson regression was applied to distinct datasets acquired in the Mediterranean Sea (Figure 8) with automated flow cytometry. Flow cytometry was developed in oceanography to discriminate several groups of phytoplankton based on the autofluorescence emitted by their photosyn-

| $n$ | $k_N$ ($\mu$M) | | | | | | | | | |
|---|---|---|---|---|---|---|---|---|---|---|
| | 0.003 | 0.336 | 0.669 | 1.002 | 1.335 | 1.668 | 2.001 | 2.334 | 2.667 | 3 |
| 200 | 0 | 0.28 | 0.657 | 1.002 | 1.326 | 1.634 | 1.932 | 2.221 | 2.502 | 2.776 |
| | (0.042) | (0.348) | (0.431) | (0.49) | (0.539) | (0.584) | (0.625) | (0.663) | (0.699) | (0.733) |
| 150 | 0 | 0.274 | 0.654 | 1.002 | 1.327 | 1.637 | 1.935 | 2.223 | 2.505 | 2.779 |
| | (0.07) | (0.409) | (0.502) | (0.569) | (0.626) | (0.677) | (0.723) | (0.767) | (0.808) | (0.848) |
| 100 | 0 | 0.264 | 0.65 | 1.002 | 1.33 | 1.642 | 1.941 | 2.231 | 2.512 | 2.787 |
| | (0.137) | (0.519) | (0.628) | (0.707) | (0.774) | (0.835) | (0.891) | (0.944) | (0.994) | (1.042) |
| 50 | 0 | 0.239 | 0.636 | 1.002 | 1.341 | 1.66 | 1.965 | 2.258 | 2.542 | 2.819 |
| | (0.365) | (0.806) | (0.946) | (1.048) | (1.136) | (1.216) | (1.291) | (1.362) | (1.43) | (1.495) |
| 10 | 0 | 0.179 | 0.588 | 1.002 | 1.399 | 1.775 | 2.134 | 2.477 | 2.806 | 3.124 |
| | (2.529) | (3.026) | (3.235) | (3.395) | (3.537) | (3.669) | (3.795) | (3.916) | (4.033) | (4.147) |

Table 6.7: Half-saturation constant ($k_N$) derived from the parameterisation (n) of a Poisson regression (with a null intercept) with data simulated from $k_N \in [0.003, 3]$, following $k_N = 1 : (2^{n^{-1}} - 1)$. (.) corresponds to $k_N - (1 : (2^{(n+\sigma(n))^{-1}} - 1))$

thetic pigment. The automated cytometer used for the collection of datasets, the CytoSense, is especially designed to analyse a wide of planktonic particles, with dimensions inferior to 2 $\mu$m (i.e. picoplankton), between 2 and 20 $\mu$m (i.e. nanoplankton), and up to 800 $\mu$m (i.e. microplankton). Among the picoplankton, two genera of prokaryotes may be distinguished, *Prochlorococcus* and *Synechococcus*, while eukaryotes are grouped under the polyphyletic *picoeukaryotes* denomination. The nanophytoplankton analysed by flow cytometry designates an association of eukaryotes species. Microphytoplankton groups cells superior to 20 $\mu$m, wether single individuals or colonial forms. Flow cytometers were used to count and estimate group-specific primary production rates during extensive field deployment. During the Deep Water EXperiment, conducted in February (Leg 1) and April (Leg 2) 2013 in the Northwestern basin (Fig 8 top panel), an automated flow cytometer was plugged to a continuous inflow of surface water. The phytoplankton standing crop, represented by Chl a concentration, varied by 4 orders of magnitude between each period. Samples were analysed every hour during one month for each leg, allowing an actual estimation of production rates from the observations of populations high frequency dynamics (Dugenne et al., submitted) (Fig 9). During the biodiversity Hot-spots in Mixing zones (HotMix) cruise, conducted in April-May 2014 across the Mediterranean Sea, discrete bottle samples collected at 6 depths, located between the surface and 200 m, were analysed by a combination of automated and conventional flow cytometer (i.e. CytoSense and FACS Calibur) to determine phytoplankton abundance (Fig 8 bottom panel). As expected, abundance of phytoplankton groups varied by 3 orders of magnitude, from microphytoplankton (Fig 8H) and cryptophytes (Fig 8G) which counted only hundred of cells.cm$^{-3}$ mainly distributed between the surface and 100 m, to *Prochlorococcus* (Fig 8C) and *Synechococcus* (Fig 8D) showing densities close to $1.10^5$ cells.cm$^{-3}$.

We fitted direct abundances (see 4.2) and estimations of net primary productivity (see section 4.1) by a Poisson regression using observations of temperature, light and nutrients. A multiple generalized regression

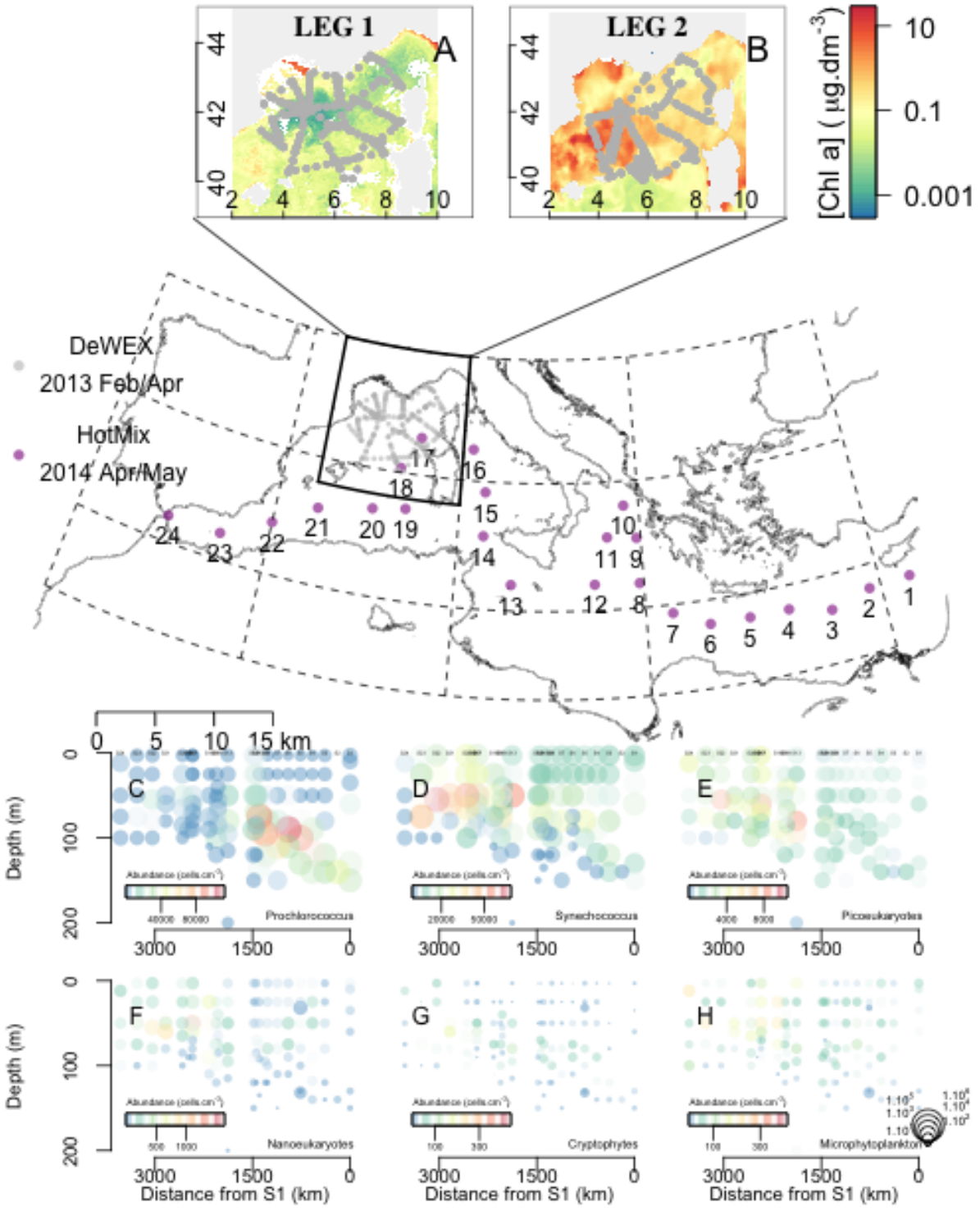


Figure 6.8: Location of the observation stations in the Mediterranean Sea during the DeWEX (gray dots) and HotMix (magenta dots) cruises. Top panel: DeWEX high resolutive surface stations (gray dots) during Leg 1 (a) and Leg 2 (b) superimposed on phytoplankton bulk biomass proxy, MODIS daily Chl a concentration. Bottom panel: Vertical distribution of *Prochlorococcus* (c), *Synechococcus* (d), picoeukaryotes (e), nanoeukaryotes (f), cryptophytes (g) and microphytoplankton (h) at HotMix stations.

was used to identify the parameters defining the growth niche in both situation. We tested the significance of each component of primary production predictions, P(T), P(E) and P(N), by running a likelihood ratio test of the full model ($P(T, E, N)$) against the corresponding reduced model: $P(E, N)$ for temperature, $P(T, N)$ for light and $P(T, E)$ for nutrients.

The Deep Water formation EXperiment dataset

Two legs were conducted in the NW basin in February and April 2013 on board of the R/V Suroit (Fig 9a). A dedicated inflow of surface water was pumped continuously to supply the CytoSense. High frequency analyses of population cell cycle proxies, derived from their optical properties, were used to estimate group-specific production rates from a total of 30 diel time series (Dugenne et al., submitted) (Fig 9b). The *in situ* temperature (Fig 9b) has been measured by a thermosalinometer plugged to the same water inflow. Photosynthetic Available Radiation (PAR) has been measured 6 times a day at fixed observation stations using a large band radiometer (Fig 9b). Dissolved ammonium ($NH_4^+$) concentration was analysed by a JASCO FP 2020 spectrofluorometer (detection limit : 0.002 $\mu$M) at the same dates. Surface samples were autonomously acquired along the R/V track and analysed by the CytoSense every hour in the NW basin. The size distribution of *Synechococcus* (Fig 9b), picoeukaryotes, nanoeukaryotes and cryptophytes was used to predict the cell cycle-driven diel productivity in a dynamic medium (Sosik et al., 2003) with concomitant hydrological measures. Net primary productivity (NPP) was estimated from the predicted size distribution, reflecting the increase of cellular size and carbon quota support by the photosynthetic fixation of atmospheric $CO_2$. The regression of NPP against temperature, light and ammonium concentration is shown in panels c, d, e of Figure 9.

The parameters defining *Synechococcus* growth niche identified by GLM are summarised in Table 8:

| | | | | | | | |
|---|---|---|---|---|---|---|---|
| GLM coefficients | $\beta_0$ | $\beta_0^T$ | $\beta_1^T$ | $\beta_2^T$ | $\beta_0^E$ | $\beta_1^E$ | $\beta_1^N$ |
| | -0.13 | -226.29 | -1.22 | 33.3 | -3.79 | -0.008 | 0.33 |
| Std | | | 0.21 | 6.3 | | 0.00013 | 0.009 |
| LRT p-value | | Temperature 2.2e-16 *** | | Light 2.2e-16 *** | | Nutrients 5.702e-09 *** | |
| Growth niche parameters | | $T_{opt}$ | $\Delta T^2$ | $\Delta T_+^2$ | $E_k$ | n | $k_N$ |
| | | 13.57 | 0.19 | 0.81 | 120.67 | 0.33 | 0.14 |
| IC 95% | | | 0.19-0.20 | 0.78-0.85 | 118.6-122.7 | 0.32-0.34 | 0.13-0.15 |

Table 6.8: The Poisson regression applied to *Synechococcus* net primary productivity (NPP) measured during the DeWEX cruise ($n$=30): $log_e(NPP) = \beta_0 + \beta_0^T + \beta_1^T T' + \beta_2^T T + \beta_0^E + \beta_1^E E + \text{offset}(log_e(E)) + \beta_1^N N'$

The HotMix dataset

A total of 24 Mediterranean stations were selected across the eastern and western basins to determine the abundance of several phytoplankton groups at discrete depth every day at 10:00 am on board of the R/V Sarmiento de Gamboa (Fig 10a). 6 depths were considered for analyses in order to have a good representation of the entire vertical distribution of phytoplankton (Fig 10b). These depths corresponded to samples at the surface, at the depths at which remain only 50% , 20% and 5% of the incident light, at the Deep Chlorophyll Maximum (DCM) and at the DCM + 20 m. The *in situ* temperature was determined for the same samples by a CTD SBE 911+. Photosynthetic Available Radiation (PAR) was measured on continuous profile using a large band radiometer. Dissolved nutrients ($NO_x$, $PO_4^{3-}$,$SiO_2$) were analysed through colorimetry by a Skalar SAN++. The vertical gradient of temperature, PAR and nutrients was used to fit a Poisson regression to *Prochlorococcus* abundance at station 6 (Fig 10c).

The parameters defining *Prochlorococcus* vertical distribution using a GLM are summarised in Table 9:

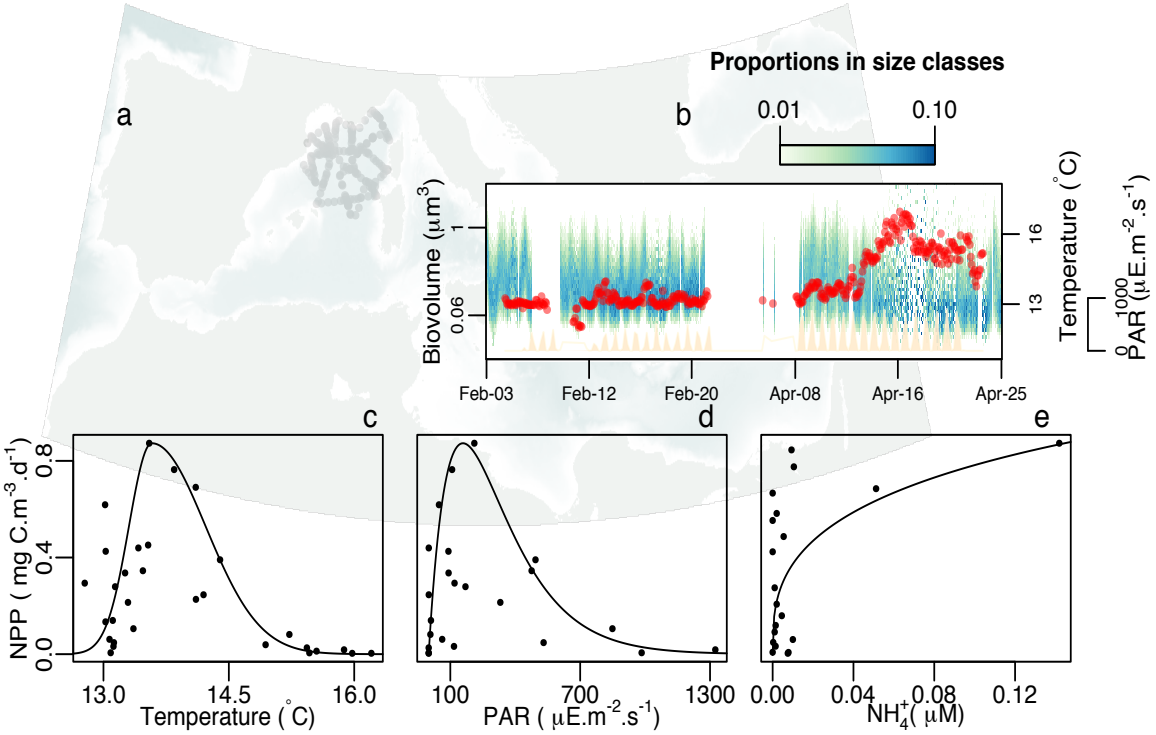


Figure 6.9: Map of the Deep Water Experiment (DeWEX) high resolutive surface stations (gray dots) (a). A multiple Poisson regression was applied on the estimations of primary productivity derived from populations' diel size distribution (b) against temperature (c), photosynthetic available radiation (d), and nutrients ($NH_4^+$) concentration (e). In panel b, the temperature (red dots) and PAR (yellow polygons) are superimposed on the *Synechococcus* size distribution (green colorbar) modelled to predict net primary productivity from the photosynthetic incrementation of cellular carbon after $CO_2$ fixation.

| | | | | | | | |
|---|---|---|---|---|---|---|---|
| GLM coefficients | $\beta_0$ | $\beta_0^T$ | $\beta_1^T$ | $\beta_2^T$ | $\beta_0^E$ | $\beta_1^E$ | $\beta_1^N$ |
| | 11.6 | -742.1 | -2.96 | 93.8 | 0.05 | -0.38 | 0.46 |
| Std | | | 0.17 | 5.7 | | 0.008 | 0.02 |
| LRT p-value | | Temperature | | Light | | Nutrients | |
| | | 2.2e-16 *** | | 2.2e-16 *** | | 2.2e-16 *** | |
| Growth niche parameters | $T_{opt}$ | $\Delta T^2$ | $\Delta T_+^2$ | $E_k$ | n | $k_N$ | |
| | 15.8 | 0.07 | 0.34 | 2.58 | 0.46 | 0.28 | |
| IC 95% | | 0.06-0.08 | 0.31-0.37 | 2.54-2.62 | 0.38-0.55 | 0.19-0.39 | |

Table 6.9: The Poisson regression applied to *Prochlorococcus* vertical distribution measured in station 6 (eastern basin) during the HotMix cruise ($n$=6): $log_e(NPP) = \beta_0 + \beta_0^T + \beta_1^T T' + \beta_2^T T + \beta_0^E + \beta_1^E E + \text{offset}(log_e(E)) + \beta_1^N N'$

## 6.5 Discussion

***Empirical regression to fit mechanistic models*** In the past, empiric and mechanistic models have been compared to predict marine primary productivity (Keller, 1989). Both models manage to provide a good fit of the dataset explained by variations in temperature, light and nutrients (70-80%). It is clearly linked to the nature of the predictions: mean productivity being equal to its variance for Poisson distributions (Lafontaine and Peters, 1986). However the empiric model failed to reach the same predictability achieved by the mechanistic approach. Predictions based on observations that fall outside the range of descriptors, originally included to construct the model, are unreliable. This difference is purely due to their nature, one being descriptive and the other explanatory. If latter models are indicated to foresee the variation of phytoplankton growth capacities, relying on theoretical assumptions that drive its functioning, the first approach is useful to apprehend the effects of the variability linked to strong non-linearities (Platt et al., 1975). Platt's study counts among the most significant work using non-linear regression to predict algae photosynthesis in response to light. The hyperbolic tangent

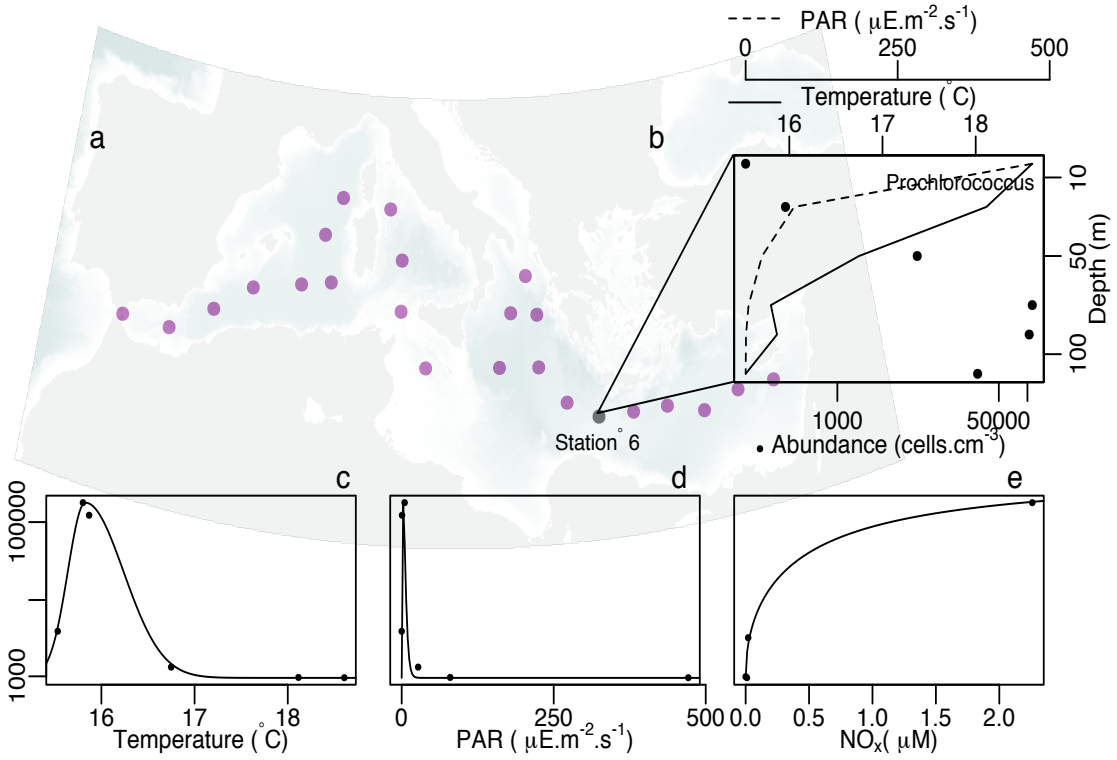


Figure 6.10: Map of the Biodiversity Hot-spots in Mixing zones (HotMix) fixed stations (a). A multiple Poisson regression was applied on the vertical profile of *Prochlorococcus* abundance (b) against temperature (c), photosynthetic available radiation (d), and nutrients concentrations (e). In panel b, the temperature (continuous line) and PAR (dashed line) are superimposed on the vertical distribution of *Prochlorococcus* abundance (dots) measured with the FACS Calibur.

(tanh) model is still commonly involved in PE curve analysis and model comparisons (Jones et al., 2014). In this paper we present a distinct model to predict photoactivation and photoinhibition (section 3.2). The introduction of Steele's model (1962) was motivated by the choice of the empiric approach and the possibility to integrate the effects of temperature, light and nutrients by linear combinations of log transformations (see section 2.2). This objective also motivated the selection of Jassby and Platt (1976) model to explain the limitation of dissolved nutrients (section 3.3). The decision to use Moisan's model to define phytoplankton thermal niche was made in regards to the clear presence of a growth optimal temperature and the asymmetric slopes around this optimum. To our knowledge, this paper is the first to attempt to reconcile both approaches by fitting PP mechanistic models by empiric regression. The combined model presented in this paper has been designed with a clear objective: being able to determine the parameters which describe temperature, light and nutrients effects on primary production from common observations of marine ecosystems. During their evolution, marine ecosystems have integrated these effects by selecting optimal growth strategies.

***Picophytoplankton growth strategies***

Picophytoplankton are the smallest and the most abundant unicellular algae present on Earth. Prokaryotes cells were the ancestor of all eukaryotes algal lineages and manage to persist since 2.4 billion years ago (Falkowski, 2004). The genera *Prochlorococcus* and *Synechococcus* are presently ubiquitous in the global ocean (40°S-40°N) with densities up to $1.10^5$ cells.cm$^{-3}$ in oligotrophic regions (Chisholm et al., 1988). In the subtropical Pacific gyre, *Prochlorococcus* can account for 20 to 40% of the photosynthetic biomass in oligotrophic oceans

and 10 to 50% of the net primary production (Campbell et al., 1997; Durand et al., 2001). Populations *in situ* growth rates were estimated by autonomous flow cytometry and ranged between 0.2-0.9 $d^{-1}$ (Ribalet et al., 2015). High division rates were linked to increasing temperature and efficient nutrient acquisition mechanisms which allow cells to multiply in poor waters. Johnson et al. (2006) found a positive correlation between the abundance of *Prochlorococcus* in the Pacific gyre and nitrates concentrations (0.0-0.4 $\mu$M). A similar nutritive status characterise the Mediterranean Sea. *Prochlorococcus* cells were discovered early in the NW basin with 5.10 $^4$ cells.$cm^{-3}$ (Vaulot et al., 1990). Compared to this study, we found a maximum of abundance of $1.10^5$ cells.$cm^{-3}$ at station 6 during the HotMix cruise (Fig 10b). Some mediterranean strains were grown in cultures to measure their PE curves. They displayed a low optimal irradiance (~ 10 $\mu E.m^{-2}.s^{-1}$) due to the presence of DV derivatives of Chl a, b, and c to support efficient light utilisation (Partensky et al., 1993). The value of $E_k$ estimated by Poisson regression (2.58 $\mu E.m^{-2}.s^{-1}$) is in agreement with Partensky's result (Figure 10d, Table 9). The author also proved, as suggested by figure 10e, that natural *Prochlorococcus* populations are limited by nitrates (Vaulot and Partensky, 1992). For phytoplankton, half-saturation constants are highly conserved across taxa of similar size (Chisholm, 1992). Small cells like *Prochlorococcus* and *Synechococcus* are favoured by their high surface:volume ratio for nutrients uptake. During the DeWEX cruise, ammonium half-saturation constant has been estimated to 0.14 $\mu$M for *Synechococcus* by fitting Poisson regression (Table 8), while Garcia et al. (2016) report 0.3 $\mu$M. According to Thomas et al. (2012), the optimal temperature is also conservatively determined by the average temperature across latitudes. Reported $T_{opt}$ supports this assumption as they correspond to 15.8°C during HotMix and 13.57°C during DeWEX for average *in situ* temperature of 15.82°C and 13.6°C respectively.

### 6.6 Conclusion

Poisson regressions are used to predict counts data for which variance scales to the mean. Measurements of phytoplankton abundance and production rates in presence of temperature, light and nutrients gradients were modelled by a Poisson multiple regression. We reviewed the panel of mechanistic models that can be fit by empiric regression. The specification of the combined model is detailed to provide efficient parameterisations of phytoplankton integrated growth niche. We managed to apply this model to distinct datasets collected in the Mediterranean Sea during two cruises. The vertical distribution of *Prochlorococcus* abundance at 6 depths was clearly marked by the abrupt attenuation of light in depth co-ocurring with nutrients enrichment. We showed that cells are not light limited due to an efficient capacity of light utilisation ($E_k$=2.58 $\mu E.m^{-2}.s^{-1}$) while the depletion of nitrates at the surface strongly reduce their potential to grow. Predictions based on these assumptions successfully reproduced the accumulation of *Prochlorococcus* below 100 m, near the nitracline. Group-specific primary production rates were measured during the DeWEX cruise. During two contrasted periods, the algal biomass spread over the NW basin as a result of enhanced productivity. The integrated growth niche has been defined in terms of temperature, light and nutrients requirements for *Synechococcus* cells. Favoured by their small size, cells are able to fulfil half of their maximal production at low N concentration ($k_N$=0.14 $\mu$M). Both *Prochlorococcus* and *Synechococcus* niches shared this similarity, along with the determinant role of average

temperature.

## References


Abraham, J. P. et al. (2013), A review of global ocean temperature observations: implications for ocean heat content estimates and climate change, *Reviews of Geophysics*, *51*, 450–483.

Adamson, M. W. and Morozov, A. Y. (2012), When can we trust our model predictions? Unearthing structural sensitivity in biological systems, *Proc. R. Soc. A*, *469*, 1–19.

Agawin, N. S. R., Duarte, C. M. and Agusti, S. (2000), Response of Mediterranean *Synechococcus* growth and loss rates to experimental nutrient inputs, *Mar. Ecol. Prog. Ser.*, *206*, 97–106.

Behrenfeld, M. J., Halsey, K. H. and Milligan, A. J. (2008), Evolved physiological responses of phytoplankton to their integrated growth environment, *Phil. Trans. R. Soc. B*, *363*, 2687–2703.

Brown, J. H., Gillooly, J. F., Allen, A. P., Savage, V. M. and West, G. B. (2004), Toward a metabolic theory of ecology, *Ecology*, *85*(7), 1771–1789.

Campbell, L., Liu, H., Nolla, H. A. and Vaulot, D. (1997), Annual variability of phytoplankton and bacteria in the subtropical North Pacific Ocean at Station ALOHA during the 1991-1994 ENSO event, *Deep Sea Research I*, *44*(2), 167–192.

Chisholm, S. W., Olson, R. J., Zettler, E. R., Goericke, R., Waterbury, J. B. and Welschmeyer, N. A (1988), A novel free-living prochlorophyte abundant in the oceanic euphotic zone, *Nature*, *334*(28), 340–343.

Chisholm, S. W. (1992), Phytoplankton size, *Primary Productivity and Biogeochemical Cycles in the Sea, eds P. G. Falkowski and A. D. Woodhead, Plenum Press, NY, 1992*, 213–237.

Cullen, J. J., Geider, R. J., Ishizaka, J., Kiefer, D. A., Marra, J., Sakshaug, E. and J. A.. Raven (1993), Toward a general description of phytoplankton growth for biogeochemical models, *NATO ASI Series, Vol I 10, G. T. Evans and M. J. R. Fasham eds., Springer-Verlag Verlin Heidelberg*, 153–176.

Davis, R. E. (1991), Lagrangian ocean studies, *Annual reviews*, *23*, 43–64.

Denman, K., Okubo, A. and Platt, T. (1977), The chlorophyll fluctuation spectrum in the sea, *Limnol. Oeanogr.*, *22*(6), 1033–1038.

Dixon, M. and Webb, E. C. (1979), Enzymes, *3rd ed., Academic press, London*, 1–234.

Doney, S. C., Lima, I., Lindsay, K. and Moore, J. K. (2001), Marine biogeochemical modeling: Recent advances and future challenges, *Oceanography, JGOFS special issue*, 14(4), 93–107.

D'Ovidio, F., De Monte, S., Alvain, S., Dandonneau, Y. and Lévy, M. (2010), Fluid dynamical niches of phytoplankton types, *PNAS*, 1–5.

Draper, N. R., and Smith, H. (1998), Applied regression analysis, *NY, John Wiley and Sons, Inc*, 1–706.

Durand, M. D., Olson, R. J. and Chisholm, S. W. (2001), Phytoplankton population dynamics at the Bermuda

Atlantic Time-series station in the Sargasso Sea, *Deep Sea Research II*, *48*, 1983–2003.

Edwards, K. F., Thomas, M. K., Klausmeier, C. A. and Litchman, E. (2012), Allometric scaling and taxonomic variation in nutrient utilization traits and maximum growth rate of phytoplankton, *Limnol. Oceanogr.*, *57*(2), 554–566.

Edwards, K. F., Thomas, M. K., Klausmeier, C. A. and Litchman, E. (2015), Light and growth in marine phytoplankton: allometric, taxonomic, and environmental variation, *Limnol. Oceanogr.*, *60*, 540–552.

Eilers, P. H. C. and Peeters, J. C. H. (1988), A model for the relationship between light intensity and the rate of photosynthesis in phytoplankton, *Ecological Modelling*, *42*, 199–215.

Eppley, R. W. (1972), Temperature and phytoplankton growth in the sea, *Fishery bulletin*, *70*(40), 1063–1085.

Falkowski, P. G., Katz, M. E., Knoll, A. H., Quigg, A., Raven, J. A., Schofield, O., Taylor and F. J. R. (2004), The evolution of modern eukaryotic phytoplankton, *Science*, *305*, 354–360.

Field, C. B., Behrenfeld, M. J., Randersin, J. T. and Falkowski, P. (1998), Primary production of the biosphere: Integrating terrestrial and oceanic components, *Ecology*, *23*, 399–418.

Flynn, K. J., Fasham, M. J. R. and Hipkin, C. R. (1997), Modelling the interactions between ammonium and nitrate uptake in marine phytoplankton, *Phil. Trans. R. Soc. Lond. B*, *352*, 1625–1645.

Furnas (1991), Net in situ growth rates of phytoplankton in an oligotrophic, tropical shelf ecosystem, *Limnol. Oceanogr.*, *36*(1), 13–29.

Garcia, N. S., Bonachela, J. A. and Martiny, A. C. (2016), Interactions between growth-dependent changes in cell size, nutrient supply and cellular elemental stoichiometry of marine *Synechococcus*, *ISME Journal*, *10*, 2715–2724.

Hutchinson, G. E. (1957), Concluding remarks, *Cold Spring Harbor Symposia on Quantitative biology*, *22*(2), 415–427.

Jassby, A. D. and Platt, T. (1976), Mathematical formulation of the relationship between photosynthesis and light for phytoplankton, *Limnol. Oceanogr.*, *21*(4), 540–547.

Johnson, Z. I., Zinser, E. R., Coe, A., McNulty, N. P., Malcolm, E., Woodward, S. and Chisholm, S. W. (2006), Niche partitioning among *Prochlorococcus* ecotypes along ocean-scale environmental gradients, *Science*, *311*, 1737–1739.

Jones, C. T., Craig, S. E., Barnette, A. B., MacIntyre, H. L and Cullen, J. J. (2014), Curvature in models of the photosynthesis-irradiance response, *J. Phycol.*, *50*, 341–355.

Keller, A. (1989), Modeling the effects of temperature, light, and nutrients on primary productivity: An empirical and a mechanistic approach compared, *Limnol. Oceanogr.*, *34*(1), 82–95.

Lafontaine, Y. and Peters, R. H. (1986), Empirical relationship for marine primary production: the effect of environmental variables, *Ooceanologica acta*, *9*, 65–72.

Lindeman, P. L. (1942), The trophic-dynamic aspect of ecology, *Ecology*, *23*, 399–418.

Longhurst, A., Sathyendranath, S., Platt, T. and Caverhill, C. (1995), An estimate of global primary production in the ocean from satellite radiometer data, *J. Plank. Res.*, *17*(6), 1245–1271.

Maranon, E., Holligan, P. M., Barciela, R., Gonzalez, N., Mourino, B., Pazo, M. J. and Varela, M. (2001), Patterns of phytoplankton size structure and productivity in contrasting open-ocean environments, *Mar. Ecol. Prog. Ser.*, *216*, 43–56.

Metropolis, N., Rosenbluth, A. W. , Rosenbluth, M. N. and teller, A. H. (1953), Equation of state calculations by fast computing machines, *J. of chemical physics*, *21*(6), 1087–1092.

Moisan, J. R., Moisan, T. A. and Abbott, M. (2002), Modelling the effect of temperature on the maximum growth rates of phytoplankton populations, *Ecological Modelling*, *153*, 197-215.

Monod, J. (1949), The growth of bacterial cultures, *Annual review of microbiology*, *3*, 371-394.

Neal, R. M. (1993), Probabilistic inference using Markov Chain Monte Carlo Methods, *Technical Report CRG-TR-93-1, Dept. of Computer Science, University of Toronto*, 1–144.

Nelder, J. A. and Wedderburn, R. W. M. (1972), Generalized Linear Models, *J. R. Statist. Soc. A*, *135*(3), 370–384.

Nelder, J. A., Rupper, D., Cressie, N. and Carroll, R.J. (1991), Generalized Linear Models for enzyme-kinetic data, *Biometrics*, *47*(4), 1605–1615.

Partensky, F., Hoepffner, N., Li, W. K. W., Uiloa, O. and Vaulot, D. (1993), Photoacclimation of *Prochlorococcus sp.* (Prochlorophyta) strains isolated from the North Atlantic and the Mediterranean Sea, *Plant Physiol.*, *101*, 285–296.

Platt, T., Denman, K. L. and Jassby, A. D. (1975), The mathematical representation and prediction of phytoplankton productivity, *Fisheries and marine service, Technical report 523*, 1–110.

Raven, J. A. and Geider, R. J. (1988), Temperature and algal growth, *New Phytol.*, *110*, 441–461.

Reynolds, C. S. (2006), The ecology of phytoplankton, *ed. C. S. Reynolds. Cambridge University Press, 2006.*

Ribalet, F., Swalwell, J., Clayton, S., Jimenez, V., Sudek, S., Lin, Y., Johnson, Z. I., Worden, A. Z. and Armbrust, E. V. (2015), Light-driven synchrony of *Prochlorococcus* growth and mortality in the subtropical Pacific gyre, *PNAS*, *112*(26), 8008–8012.

Rossby, T. (2007), Evolution of Lagrangian methods in oceanography, *ed. A. Griffa, D. Kirwan, A. Mariano, T. Ozgokmen, T. Rossby. Cambridge University Press, 2007.*

Steele, J. H. (1962), Environmental control of photosynthesis in the sea, *Limnol. Oceanogr.*, *7*, 137–150.

Steele, J. H. (1991), Marine functional diversity, *Bioscience*, *41*(7), 470–474.

Thomas, M. K., Kremer, C. T., Klausmeir, C. A., Litchman, E. (2012), A global pattern of thermal adaptation in marine phytoplankton, *Science*, *338*, 1085–1088.

Tian, R. C. (2006), Toward standard parameterizations in marine biological modeling, *Ecological modelling*, *193*, 363–386.

Vaulot, D., Partensky, F., Neveux, J., Mantoura, R. F. and Llewellyn, C. A. (1990), Winter presence of prochlorophytes in surface waters of the northwestern Mediterranean Sea, *Limnol. Oceanogr.*, *35*(5), 1156–1164.

Vaulot, D. and Partensky, F. (1992), Cell cycle distributions of prochlorophytes in the north western Mediterranean Sea, *Deep Sea Research*, *39*(5), 727–742.

Vernet, M. and Smith, R. C. (2007), Measuring and modelling primary production in marine pelagic ecosystems, *P. G. Falkowski eds., Primary Productivity in the Sea, Plenium press, NY.*

Webb, W. L., Newton, M. and Starr, D. (1974), Carbon dioxide exchange of *Alnus rubra*: A mathematical model, *Oceanologia*, *17*, 281–291.

Winter, D. F., Banse, K. and Anderson, G. C. (1975), The dynamics of phytoplankton blooms in Puget Sound, a Fjord in the Northwestern United States, *Marine Biology*, *29*, 139–176.

# 7.0 Empirical predictions of marine primary productivity: On the bayesian inference of the influence of environmental growth conditions- *Part B: Challenging the concept of Phytoplankton Functional Types*

**Abstract**

Generalized Linear regression Models (GLMs) may be used to predict the main source of net primary production variations from a set of growth environmental niche descriptors (e.g. temperature, nutrients, light) (see part A). In this paper, we apply mixed-effects GLMs (GLMMs) to the measurements of primary productivity on repeated structures (e.g. station and flow cytometry group). We also introduce the finite mixture of GLMMs to test wether cytometry groups are effective functional groups with distinct growth niches by statistical means. After a brief review of the definition of GLMMs and finite mixture models, we describe how to infer parameters describing phytoplankton growth environment and to identify distinct functional groups from group-specific primary production rates. The application of these models to *in situ* data collected in the Mediterranean Sea is presented for datasets detailed in part A. In this context, models will provide an answer to the questions: Is the distinction between the Eastern and Western basins productivity observed in the Mediterranean Sea caused by longitudinal gradients of nutrients concentrations? Are the growth niche of flow cytometry populations overlapping?

M. Dugenne, D. Pommeret, M. Thyssen, J. Aristegui, N. Hernandez, M. Espino, G. Grégori

## 7.1 Introduction

***The Mediterranean Productivity*** In the oligotrophic Mediterranean, colimitation is a perennial feature that constrains the annual rates of primary productivity to 68 g $C.m^{-2}.yr^{-1}$ (Uitz et al., 2012). By comparison with a similar approach (i.e. remote sensing), the global ocean productivity averages 130 g $C.m^{-2}.yr^{-1}$ with a maximum of 400 g $C.m^{-2}.yr^{-1}$ in eutrophic regions (Antoine et al., 1996). According to Uitz et al., the amplitude of production rates may vary a lot, depending on the season and the ecological regions. A first phenology (i.e. annual and seasonal climatology) based on remote sensing Chl a, derived from phytoplankton biomass, was addressed in the Mediterranean by D'Ortenzio and Ribera D'Alcala in 2009. In this phenology, some regions can be clearly differentiated by the strong and recurrent accumulation of Chl a concentration at the surface, a phenomenon called *bloom*. These regions are located in the Alboran, Liguro-Provencal and Thyrrenian basins. On the other hand, a large part of the Eastern basin remains stable all year long with concentration inferior to 0.1 mg Chl $a.m^{-3}$. This contrast is often attributed to the nutrients gradient linked to the balance of river turnoffs, wind-driven convection, at-

mospheric deposit, exchanges at the Gibraltar strait, and biological fixation (Béthoux et al., 1998). A N and P co-limitation has been demonstrated in a microcosm experiment conducted in the eastern basin (Tsiola et al., 2016). The N:P molar ratio is often larger (~ 20-25N:1P) than the standard elemental requirements of the surface plankton, the Redfield ratio of 16N:1P, at surface due to biological depletion and close to 17.7N:1P in the mineralization layer due to the presence of the nitracline and phosphacline (Pujo-Pay et al., 2011). This vertical gradient is constrained by the density barrier induced by the thermal stratification of the water column. Mimicking the thermohaline circulation of the global ocean, the Mediterranean wintertime convection is a miniaturised wind-driven process that influences the mixing of the water column (Mermex group, 2011). In general, the mixed layer depth (MLD) impacts both the availability of nutrients and the *in situ* temperature in the euphotic layer (De Boyer Montegut et al., 2004). The euphotic layer is the upper ocean zone delimited by the depth where the incident solar radiation is attenuated for up to 1%. In the Mediterranean Sea, the Chl a phenology is strongly linked to the climatology of the MLD (D'Ortenzio et al., 2005; Lavigne 2013). The main objective of the section 2.1 (GLMMs) is to test wether the east-to-west vertical gradients are driving the spatial distribution of phytoplankton groups across the Mediterranean Sea. For this purpose, we used the vertical distribution of flow cytometry groups and hydrological variables measured at 24 stations located across in the Mediterranean Sea during the biodiversity Hot-Spot in Mixing zones cruise (HotMix).

***The Concept of Functional Types***

Although phytoplankton holds a tremendous genetic diversity, the concept of species does not integrate a unique ecological trait (Wood and Leatham, 1992). The comparison of intra- and inter- specific differences under controlled growth conditions likely directed phytoplankton ecologists to study diversity at a coarser level of organisation than species. Among these levels, Litchman et al. (2012) proposed to use the concept of *ecological traits*, grouping elements of phytoplankton phenotype (e.g. pigments, size) that determines its fitness, to provide a mechanistic basis to predict the absence/presence of phytoplankton, absent in the more specific Species Distribution Models (SDM). *Phytoplankton Functional Types* may define the main biogeochemical cycles drivers (e.g. C, N, DMS, $CaCO_3$, $SI(OH)_4$) (Nair et al., 2008), size fractions (Uitz et al., 2010; Ward et al., 2012), trophic networks compartments (Baklouti et al., 2006), classes of survival strategists (Margalef, 1978), depending on the question being addressed. The approach used to detect them and discuss about their role and impact is also a question of studies objectives (IOCCG, 2014). They include large scale sensors such as ocean colour remote sensing to small scale methods like flow cytometry and microscopy. If PFTs are mainly integrated in Ocean Biogeochemical Models (OBM) in contemporaneous oceanography, *ecological guilds* have been defined early in Roots's publication (1967) while the concept of *niche* introduced by Hutchinson in 1957 goes further back in time. For Root, a guild is a group of species that exploits the same class of environmental resources in a similar way. Reynolds et al. (2002) reinterpreted Root's definition to constrain species in functional groups in order to distinguish peculiar adaptations and requirements for phytoplankton. Among the physiological requirements of phytoplankton, light is the first resource that might have triggered the diversification of harvesting strategies along phytoplankton evolution (Ting et al., 2002; Green, 2007). By controlling the turbulent mixing of water masses, climatic thermal gradient drove nutrients fluxes and taxa dis-

tribution over the fossil records (Falkowski and Oliver, 2007). The past primary productivity has mainly been limited by nitrogen fluxes leading to the apparition of diazotrophic organisms ($N_2$ fixers) (Falkowski, 1997). In the present, all these resource, grouped into Behrenfeld *integrated growth niche*, are still selecting phytoplankton taxa (Behrenfeld et al., 2008; Boyd et al., 2010). It is this growth-based functional types description that we want to challenge in this paper using the dataset collected by flow cytometry. The main objective of the section 2.2 (finite mixture models) is to test, by statistical means, wether flow cytometry groups may be interpreted as *Functional Types* or *guilds* in the sense of their resource requirements for productivity. For this purpose, we used diverse response of group-specific growth to light and nutrients availability, as well as surface temperature measured in the Mediterranean Sea during the Deep Water EXperiment cruises (DeWEX).

## 7.2 Generalized Linear Mixed-Models and finite mixture models: review and applications

GLMMs

### Definition

As part of the Generalized Linear Models, multivariate Generalized Linear Mixed-Models (GLMMs) are used to predict a response variable, $Y$, of $n$ observations ($y_i$) by a linear combination of a set of $p$ explanatory descriptors ($\eta$) using a link function (g):

$$\eta = g(\mu), \mu = g^{-1}(\eta) \tag{7.1}$$

g: link function, $\mu$: expectation of $y$

GLMs are more specifically involved when the variance of $Y$ is not constant (i.e. heteroscedasticity) and/or residuals are non-Normal. The errors heteroscedasticity means that we must consider that the variance ($\sigma^2$) is different for each observation, thus $\mathrm{Var}(y_i)=\sigma_i^2:w_i$, with $w_i$ the weight attributed to observation $i$. In mixed-models, we consider that observations are hierarchically structured by pseudo-replication, which means that the variance of observation depends on the categorisation of independent samples replicates, or repeated individuals, called the random effect(s) ($\xi_i$). The random effects categorical variable should in essence only influence the variance of the response variable $Y$, while the linear regressor, $X^T\beta$, influence its mean. Random effects are mainly normally distributed and summed up to the fixed-effects to predict observations $y_i$:

$$\begin{aligned} E(y_{ij}|\xi_i) &= g^{-1}(\eta_{ij}) = g^{-1}(x_{ij}^T\vec{\beta} + u_{ij}\xi_i) \\ \xi_i &\sim \mathcal{N}(0, \Sigma_i^2) \end{aligned} \tag{7.2}$$

i: repeated class $\in$ [1,q], j: dependent/repeated observations on class i $\in$ [1,$n_i$], $\eta_{ij}$: linear predictor of observation j on class i, $X_j$: fixed-effects design matrix ($n_j$x$p$), $\beta$: linear coefficients of the fixed effects (px1), $U_i$: mixed-effects design matrix ($n_i$x1), $\xi_i$: random effects (1xq), $\Sigma$: Variance-Covariance diagonal matrix, $\epsilon_i$: class residuals

The expectation and variance of $Y$ are expressed using the same properties of Generalized Linear Models, given the random effects. The observations in GLMMs are distributed among the exponential family distributions (Nelder and Wedderburn, 1972), whose probability density function may be generalised by:

$$p(y|\Theta) = exp\left(\frac{y\Theta - b(\Theta)}{\phi} + c(y,\phi)\right)$$

p(y|$\Theta$): pdf, $\phi$: scale parameter, {b,c}: arbitrary functions

For distributions part of this family, two important properties are:

$$E(Y) = \frac{db(\Theta)}{d\Theta}, Var(Y) = \phi\frac{d^2b(\Theta)}{d\Theta^2} = \phi E'(Y) \tag{7.3}$$

The main exponential family distributions used in GLMMs are summarised in Table 1.

| Distribution | exponential family equivalence | Canonical link | Variance |
|---|---|---|---|
| Normal: $\mathscr{N}(\mu,\sigma^2)$ | $\Theta$: $\mu$, $\phi$: $\sigma^2$, b: $0.5\Theta^2$, c: $-0.5\left(\frac{y^2}{\phi}+log_e(2\pi\phi)\right)$ | identity: $\mu$ | cst=$\sigma^2$ |
| Poisson: $\mathscr{P}(\lambda)$ | $\Theta$: $\log_e(\mu)$, $\phi$: 1, b: $\exp(\Theta)$, c: $-\log_e(y)$ | log: $\log_e(\mu)$ | $\mu$ |
| Binomial: $\mathscr{B}(p)$ | n: 1, $\Theta$: $log_e\left(\frac{\mu}{1-\mu}\right)$, $\phi$: 1, b: $log_e(1+e^{\Theta})$, c: $log_e(1)$ | logit: $log_e\left(\frac{\mu}{1-\mu}\right)$ | $\mu(1-\mu)$ |
| Gamma: $\mathscr{G}(\alpha,\beta^{-1})$ | $\Theta$: $\frac{1}{\mu}$, $\phi$: $\beta$, b: $-\log_e(-\Theta)$, c: $(\phi^{-1}\text{-}1)\log_e(y)-\log_e(\Gamma(\phi^{-1}))$ | inverse: $\left(\frac{1}{\mu}\right)$ | $\mu^2$ |

Table 7.1: Family distributions in main Generalized Linear Mixed-Models

### Statistical inference: Maximum likelihood estimation, model specification and validation

**MLE:** Mixed-Models are defined conditionally to random effects $\xi$. $\xi$ being unobserved, the structure of the data is incomplete. The full log-likelihood of the parameters $\vec{\Theta} = [\beta, \Sigma]$, is consequently defined by the integer:

$$l(\beta,\Sigma;Y) = \int_{\xi}\prod_{i=1}^{n} f(y_i|\xi)g(\xi)d\xi \qquad (7.4)$$

$f$: $Y$ density distribution, $g$: Normal density distribution

The numerical approximation of the integrate are computationally extensive if the dimension $q$ of the random effects is large. *Monte Carlo* methods such as the *Gibbs sampling* or Metropolis-Hastings has been proposed to perform the maximisation of the marginal likelihood (Zeger and Karim, 1991; McCulloch, 1997). The general algorithm is called the *Expectation Maximization* ($EM$) approach or *Monte Carlo Expectation Maximization* in McCulloch's variant. The approach is iterative (with $t$ iterations) and works in 2 steps until parameters' convergence:

1. The Expectation step: Approximate the complete likelihood by the expectation of the data distribution given the actual values of $\Theta^t$ and the random effects $\xi$: $E(log_e(f(Y,\xi|\Theta^t)|y,\Theta^t) = E(log_e(f(Y|\xi,\Theta^t).f(\xi|\Theta^t))|y,\Theta^t)$
2. The Maximization step: Maximize the expectation to estimate $\Theta^{t+1}$

**Specification of the algorithm in JAGS:** The MCEM algorithm for mixed Poisson models used in this paper is written in JAGS:

```
    model
{

for(i in 1:n){
y[i] ~ dpois(lambda[i])
log(lambda[i]) ← inprod(X[i,],β)+
inprod(U[i,],ξ)
}

for (q in 1:Q){
 ξ[q] ~ dnorm(0,σξ[q])
 σξ[q] ← 1 / pow(tau[q],0.5)
 tau[q] ~ dgamma(0.001,0.001)
}

 for (p in 1:P){
 β[p] ~ dnorm(0,1E-06)
}

}
```

**Model validation over simulations:** Simulations were performed to validate the model specification. Simulations were chosen to reproduce the effect of nutrient concentration on phytoplankton abundance according to equation:

$$
\begin{aligned}
&P([N]; i = 1, 2, ..., Q) = \\
&P_{max_{i=1,2,...,Q}} tanh(log_e(\sqrt{1 + 2 * [N]}))^{\beta_1^N} \\
&log_e(P([N]; i = 1, 2, ..., Q)) = \xi_{i=1,2,...,Q} + \\
&\beta_1^N log_e(tanh(log_e(\sqrt{1 + 2 * [N]})) \\
&\xi_{i=1,2,...,Q} = log_e(P_{max_{i=1,2,...,Q}})
\end{aligned}
\tag{7.5}
$$

Since we are interested in the effect of the Q random intercept in this model, we directly set the values of $\xi_{i=1,2,...,Q}$ in the simulations instead of generating them from the Normal distribution. The maximum likelihood estimators are tested for a range of Q random effects and several values of $\beta_1^N$. Observations $P([N]; i = 1, 2, ..., Q)$ were simulated using a Poisson random number generator (RNG) based on equation (E 5) with $[N]$, a regular sequence of length 200 bounded between 0.01 $\mu$M and 0.2 $\mu$M. Results of the simulations are summarised in Table 2.

| True values | $\widehat{\beta_1^N}$ | | $\widehat{\xi_{1,...,Q}}$ | |
|---|---|---|---|---|
| | Average | Std | Average | Std |
| $\beta_1^N$=0.2 | | | | |
| $\xi$=[2,11] | 0.2 | $8.10^{-4}$ | [2.013,10.999] | [0.04,0.001] |
| $\xi$=[2,5,11] | 0.2 | $1.10^{-3}$ | [2.04,4.99,11.0] | [0.05,0.01,0.001] |
| $\xi$=[2,5,8,11] | 0.199 | $1.10^{-3}$ | [2.05,4.99,8.00,10.99] | [0.06,0.01,0.003,0.001] |
| $\beta_1^N$=2 | | | | |
| $\xi$=[2,11] | 2.0 | $7.10^{-3}$ | [2.1,11.0] | [0.13,0.01] |
| $\xi$=[2,5,11] | 1.99 | $7.10^{-3}$ | [2.10,5.01,10.99] | [0.2,0.05,0.01] |
| $\xi$=[2,5,8,11] | 2.01 | $8.10^{-3}$ | [1.89,5.08,8.00,11.01] | [0.3,0.06,0.01,0.01] |

Table 7.2: Simulations of mixed-effects nutrients enrichments on phytoplankton abundance according to equation (E 5) over several random intercepts ($\xi_{1,...,Q}$) and fixed slopes ($\beta_1^N$). Nutrient concentrations are bounded between 0.01 $\mu$M and 0.2 $\mu$M ($n$=200).

## In situ application

The dataset consists in vertical profiles of *Prochlorococcus* abundance measured by a FACS Calibur flow cytometer, distributed across the Mediterranean Sea (see Part A). Abundance were determined along 6 depths, located between the surface and 200 m, at 24 stations during the HotMix oceanographic cruise. The objective of the application of GLMMs is to model by multiple Poisson regression phytoplankton vertical distribution, using the fixed-effects of limiting nutrients concentration while accounting for the random-effects intercepts due to spatial dependence. We used equation (E 6) to model each pooled data sets by a multiple Poisson regression:

$$
\begin{aligned}
&N(x) = N_{max}(x).tanh(log_e(\sqrt{1 + 2[NO_x]}))^{\beta_1^N} \\
&log_e(N(x)) = \xi_x + \beta_1^N log_e(tanh(log_e(\sqrt{1 + 2[NO_x]}))) \\
&\text{with } \xi_x = log_e(N_{max}(x))
\end{aligned}
\tag{7.6}
$$

x: station geographic position, P: Daily primary production rates $[C][L]^{-3}[T]^{-1}$, $N_{max}$(x): Station-specific abundance [cells.cm$^{-3}$], N: Abundance [cells.cm$^{-3}$], $[NO_x]$: concentration of dissolved nitrates ($NO_3^-$) + nitrites ($NO_2^-$) [$\mu$M]

The vertical profiles of *Prochlorococcus* abundance and $NO_x$ concentration along the east-to-west longitudinal transect are presented in Figure 1.

*Prochlorococcus* is more abundant in the eastern basin (stations 1 to 12) where it accumulates at depths between 75 and 150 m with concentrations of up to $1.10^5$ cells.cm$^{-3}$. At these stations, abundance are positively correlated to $NO_x$ concentrations, present on average at 0.78 ± 1.04 $\mu$M in the mineralised layer. In the surface layer, the concentration decreases to 0.04 ± 0.12 $\mu$M. In the western basin, the average concentrations of NOx reach 0.82 ± 1.45 $\mu$M at the surface and 2.61 ± 1.81 $\mu$M below 75 m. To test wether *Prochlorococcus* are limited by nitrates at the HotMix stations, we used the mixed model represented by equation (E 6). Fits are shown in Figure 2.

For this model, the estimation of the fixed slope is $\beta_1^N$=0.95 ± 0.002 and the equivalent half-saturation constant is $k_{NO_x}$=0.94 ± 0.002 $\mu$M. The random-effect

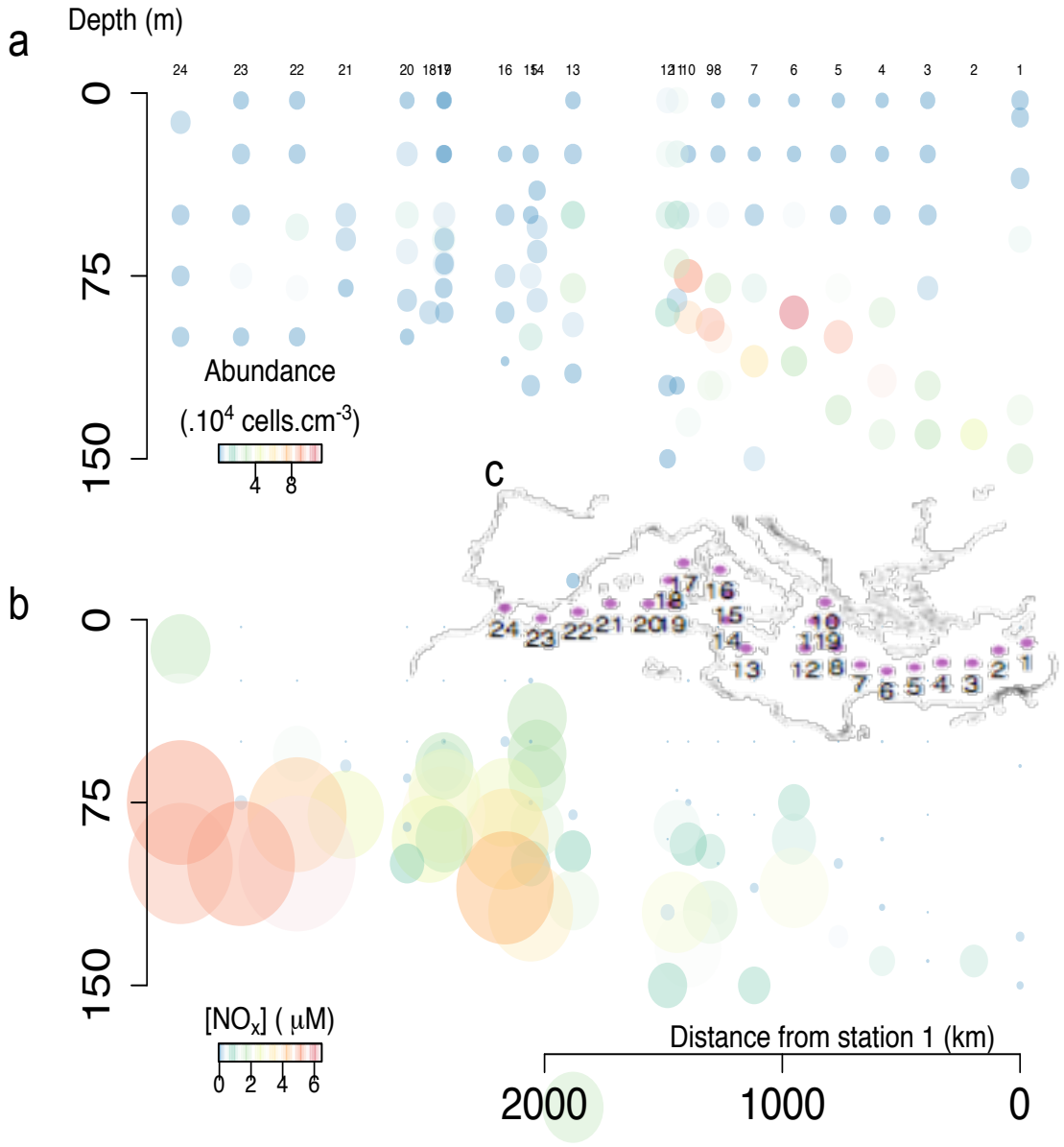


Figure 7.1: Vertical profiles of *Prochlorococcus* abundance (a) and $NO_x$ concentration (b) measured at the 24 HotMix stations (c)

maximal abundance vary between 1-7.$10^5$ cells.cm$^{-3}$ for stations 1-12 and fall below 1.$10^5$ cells.cm$^{-13}$ for stations of the western basin (average: 5.$10^4$ cells.cm$^{-3}$).

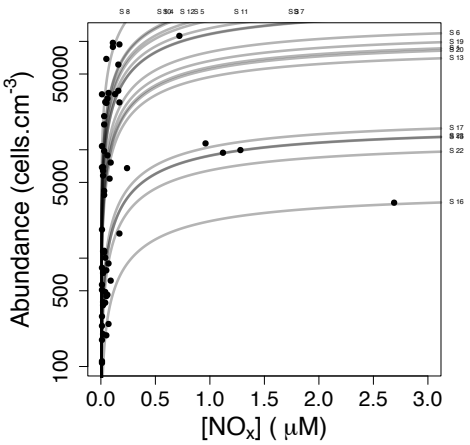


Figure 7.2: Scatter plot of *Prochlorococcus* abundance against $NO_x$ concentration measured at the 24 HotMix stations (points). Predictions using the mixed model in equation (E 6) are superimposed (continuous line).

Finite mixture models

**Definition**

Mixture models are convex combination of several density distributions (McLachlan and Peel, 2000). By consequence, they are able to efficiently reproduce local approximation of any multi-modal distribution. They are indicated when the dataset collected is complex and heterogenous. In a k-latent classes mixture model, the density function $f(y|x;\theta_1\theta_2,...,\theta_k;\pi_1,\pi_2,...,\pi_k)$ is equal to the weighted sum of the k latent classes density functions of the exponential family (see Table 1):

$$f(y|x;\theta_1\theta_2,...,\theta_k;\pi_1,\pi_2,...,\pi_k) = \sum_{c=1}^{k}\pi_c f(y|x;\theta_c)$$
$$\text{with}\begin{cases} 0<\pi_c<1 \\ \sum_{c=1}^{k}\pi_c = 1 \end{cases} \tag{7.7}$$

f: density distribution of the exponential family, $\theta_c$: canonic parameter of the $c$ latent class, k: number of latent classes, $\pi_c$: mixing proportion of the $c$ latent class

If models are multivariate and generalized, the canonic parameter of each latent class is expressed by :

$$\theta_c = g^{-1}(\eta_c) = g^{-1}(X\vec{\beta}_c) \tag{7.8}$$

c: latent class component, $\theta_c$: canonic parameter of the $c$ latent class, $g^{-1}$: inverse link function, $\eta_c$: linear predictor of the $c$ latent class, $\beta_c$: linear coefficients of the $c$ latent class (px1), X: fixed design matrix (nxp)

Mixture of mixed-effects models integrate the distinction between $n_i$ repeated measures on individual $i$ by introducing the random design matrix $U$ ($n_i$x1) and the random-effects linear coefficients $\xi_i$ (1x$q$):

$$\theta_{ijc} = g^{-1}(\eta_{ijc}) = g^{-1}(x_{ij}^T\vec{\beta}_c + u_{ij}\xi_i) \tag{7.9}$$

i: repeated class, j: dependent observation on class i, c: latent class component, $\theta_{ijc}$: canonic parameter of the $c$ latent class , $g^{-1}$: inverse link function, $\eta_{ijc}$: linear predictor of the $c$ latent class, $\beta_c$: linear coefficients of the $c$ latent class (px1), $X_i$: fixed design matrix ($n_i$xp), $U_i$: mixed-effects design matrix ($n_i$x1), $\xi_i$: random effects coefficients (1xq)

The clustering of observation $ij$ is given by the probability that observation $ij$ belong to the latent class c, $z_{ijc}$ such that:

$$P(z_{ijc} = c) = \pi_c \tag{7.10}$$

with $z_{ijc}$, the label component that equals 1 if observation $ij$ belongs to the latent class $c$ and 0 if not.

**Statistical inference: Maximum likelihood estimation, model selection and validation**

**MLE:** For a mixture of density distributions $f$, the likelihood, $\mathscr{L}$, and log-likelihood, $l$, are given by:

$$\mathscr{L}(\Theta,y) = \prod_{ij=1}^{n=n_i*q}\sum_{c=1}^{k}\pi_c f_c(y_{ij}|\Theta_{ijc})$$
$$l(\Theta,y) = \sum_{ij=1}^{n=n_i*q} log_e(\sum_{c=1}^{k}\pi_c f_c(y_{ij}|\Theta_{ijc})) \tag{7.11}$$

In finite mixture models, the structure of the data is incomplete: the mixing proportions $\pi_k$ and the vector of latent classes $z_{jk}$ are both unknown. Random-effects coefficients $\xi_i$ are also to be determined in mixed models. The estimation of the full likelihood is consequently not straightforward. Given the latent component, the log-likelihood is written as follow:

$$
\begin{aligned}
l(\Theta, y) &= \prod_{ij=1}^{n=n_i*q} \sum_{c=1}^{k} \pi_c f_c(y_{ij}|\Theta_{ijc})^{z_{ijc}} \\
\mathscr{L}(\Theta, y) &= \sum_{ij=1}^{n=n_i*q} \sum_{c=1}^{k} z_{ijc} log_e(\pi_c) + \\
&\sum_{ij=1}^{n=n_i*q} \sum_{c=1}^{k} z_{ijc} log_e(f_c(y_{ij}|\Theta_{ijc}))
\end{aligned}
\tag{7.12}
$$

The *Expectation Maximization* algorithm is used to estimate the posterior probabilities of the mixture parameters $\hat{\phi}=\{\pi_k, z_{jk}, \beta_k\}$ that maximise the conditional likelihood of the data, fixing the number of latent classes $k$ (see *Model selection* for a statistics decision on k). It is an iterative algorithm that ensure the progressive maximisation of conditional likelihood.
The $E$ step consists in estimating the expectation of the log likelihood given the parameters estimated at the previous iteration: $E(\mathscr{L}(\phi^{t-1}, y))$. Using the expectation of the log likelihood, we deduce the expectation of the vector of label component as follows:

$$
\begin{aligned}
t_c^t(y_j) &= E(z_{jc}|y, \phi^{t-1}) \\
&= \frac{\pi_c^{t-1} f(y_j; \phi_c^{t-1})}{\sum_{g=1}^{k} \pi_g^{t-1} f(y_j; \phi_g^{t-1})}
\end{aligned}
\tag{7.13}
$$

and the mixing proportions:

$$
\pi_c^t = \frac{1}{n} \sum_{j=1}^{n} t_c^t(y_j) \tag{7.14}
$$

The $M$ step take advantages of the fixed $t_c^t(y_j)$ to evaluate the maximum likelihood estimations of the k linear coefficients $\hat{\beta}_c^t$ considering the complete likelihood $\mathscr{L}(z|\phi^{t-1}, y)$:

$$
\sum_{j=1}^{n} t_c^t(y_j) \frac{\partial log_e f_c(y_j|\phi_c^t)}{\partial \beta_c}(\hat{\beta}_c^t) = 0 \ \ \forall c = 1, ..., k \tag{7.15}
$$

In mixed models the missing data also comport the random effects coefficients $\xi_i$. $\hat{\phi}=\{\pi_k, z_{ijk}, \beta_k, \xi_i\}$ is therefore iteratively approximated with the *EM* algorithm including a supplementary step. For this algorithm, The $E/M$ steps follow the introduction of a *Monte Carlo Markov Chain* to evaluate the expectation of the random-effects $E(\xi_i)$ at the given iteration by accepting candidates, $\xi_i^*$, sampled from the normal priors with a probability given by:

$$
\begin{aligned}
\alpha(\xi_i(t), \xi_i^*) &= min\left\{1, \frac{f(\xi_i^*|y_i; \phi^t) h(\xi_i^t)}{f(\xi_i^t|y_i; \phi^t) h(\xi_i^*)}\right\} \\
&= min\left\{1, \frac{f(y_i|\xi_i^*; \phi^t)}{f(y_i|\xi_i^t; \phi^t)}\right\}
\end{aligned}
\tag{7.16}
$$

*(Bayes theorem)*
$\alpha$:acceptance probability

The full algorithm is called *MCEM* which stands for *Monte Carlo Expectation Maximization* (Wei and Tanner, 1990):

1. Generate random effects candidates from the $\mathscr{N}$ormal distribution: $\xi_{ic} \sim \mathscr{N}(0, \sigma_c^2)$ and perform a Metropolis-Hastings MCMC. Estimate the expectation $E(\xi_i)$ from the chain

2. Perform the Expectation step to approximate $t_c^t(y_j)$ and $\pi_c^t$ according to equations E 13-14

3. Perform the Maximization step to approximate $\beta_c^t$ according to equation E 15

4. Reproduce the steps until convergence of $\phi$

**Specification of the algorithm in JAGS:**

The E step for a k-components mixture of mixed-effects Poisson models used in this paper is written in JAGS:

```
    model
{

for(i in 1:n){
for(c in 1:k){
t_c[i,c] ← π[c]*dpois(y[i,c],lambda[i,c])
y[i,c] ~ dpois(lambda[i,c])
log(lambda[i,c]) ← inprod(X[i,],β[c,])+
inprod(U[i,],ξ)
}
}

for (q in 1:Q){
 ξ[q] ~ dnorm(0,σ_ξ[q])
 σ_ξ[q] ← 1 / pow(tau[q],0.5)
 tau[q] ~ dgamma(0.001,0.001)
}


}
```

Note that $t_c$ are not yet normalised. At this step, provided data are the actual mixing proportions, $\pi^{t-1}$ and the fixed-effects $\beta^{t-1}$. The algorithm is used to estimate the expectation of the label component, $E(z|y,\phi^{t-1})$ according to equation (E 13) and the random-effects coefficients $\xi^{t-1}$. Fixed-effects coefficients are sequentially estimated by the M step:

```
    model
{

for(i in 1:n){

y[i] ~ dpois(lambda[i])
log(lambda[i]) ← inprod(X[i,],β[z[i],])+
inprod(U[i,],ξ)
 z[i] ~ dcat(π[]*t_c[i,]);
}

π[1:k] ~ ddirch(α[])
for (q in 1:Q){
 ξ[q] ~ dnorm(0,σ_ξ[q])
 σ_ξ[q] ← 1 / pow(tau[q],0.5)
 tau[q] ~ dgamma(0.001,0.001)
}

 for (p in 1:P){
 for (c in 1:k){
 β[c,p] ~ dnorm(0,1E-06)
 α[c] ← 1
}
}

}
```

**Model selection:** Information Criteria are used to determine the optimal number of latent class according to the principle of parsimony (see Gelman et al., 2013, for a general review of IC). The general formulation of IC follows:

$$\begin{aligned} IC &= -2l(\Theta, y) + \mathscr{P}(\phi) \\ &= D(\Theta) + \mathscr{P}(\phi) \end{aligned} \tag{7.17}$$

$\mathscr{P}$: penalisation depending on the number of free model parameters ($\phi$), $D(\Theta)$: Deviance

For a similar penalisation, the optimal model consequently minimise the IC. The penalisation term is introduced to prevent the selection of a saturated model that contains as many parameters as observations with a null deviance, while not accounting for any predictive purpose. For the *Akaike Information Criterion* (AIC), the penalisation is set to $2(\phi+1)$ with $\phi$ equals $k.(p+q)-1$ in mixture models due to the constraint on the mixing proportions (E 7). The *Bayesian Information Criterion* (BIC) uses a penalisation equals to $log_e(n)\phi$. The *Deviance Information Criterion* (DIC) is defined as $2\overline{D(\Theta)} - D(\overline{\Theta})$ (Spiegelhalter et al., 2002).

**Model validation over simulations:** Simulations were performed to validate the model specification and the ability of selecting the right number of component with the information criterion. Simulations were chosen to reproduce the effect of nutrient enrichment on primary productivity according to equation (E 5):

$$
\begin{aligned}
&P([N]; i = 1,2) = \\
&P_{max_{i=1,2}} tanh(log_e(\sqrt{1 + 2 * [N]}))^{\beta_1^N} \\
&log_e(P([N]; i = 1,2)) = \xi_{i=1,2} + \\
&\beta_1^N log_e(tanh(log_e(\sqrt{1 + 2 * [N]}))) \\
&\xi_{i=1,2} = log_e(P_{max_{i=1,2}})
\end{aligned}
\tag{7.18}
$$

Observations $P([N]; i = 1,2)$ were simulated using a Poisson random number generator based on equation (E 18) with $[N]$, a regular sequence of length 200 bounded between 0.01 $\mu$M and 0.2 $\mu$M and $\xi_{i=1,2}$ set to 8 and 11 respectively. Results from the simulations are summarised in Table 3.

### In situ application

The dataset consists in measures of phytoplankton photosynthetic production rates acquired by automated flow cytometry in the Mediterranean Sea during the DeWEX cruise (see Part A). *Synechococcus*, picoeukaryotes, nanoeukaryotes and cryptophytes group-specific production rates were estimated from inverse modelling applied to the size-structure. The objective of the application of finite mixture of GLMMs is to determine the parameters that confine their growth niche and to test wether groups defined by flow cytometry may be regarded as functional groups. We assume that functional groups will be correctly identified as individual components of a finite mixture by model selection. We used equation (E 19) to model each pooled data sets by a multiple Poisson regression, with an intercept random effects, corresponding to the maximal response reached under optimal environmental conditions and components specific fixed-effects defining each thermal, light and nutrients niche:

$$
\begin{aligned}
&log_e(P(x,k)) = log_e(P_{max}(k)) \\
&+ log_e(P_k(T(x))) + log_e(P_k(E(x))) \\
&+ log_e(P_k(N(x)))
\end{aligned}
\tag{7.19}
$$

x: station geographic position, k: finite mixture component P: Daily primary production rates $[C][L]^{-3}[T]^{-1}$, $P_{max}$: Maximal production rates $[C][L]^{-3}[T]^{-1}$, T: *In situ* temperature [°C], E: Light intensity $[Quanta].[L]^{-2}.[T]^{-1}$, N: macronutrient concentration [MOLE]

**Nutrients assimilation:** We are looking for statistically distinct affinity of nutrients uptake by fitting the class of finite mixture of GLMMs to measures of primary productivity in response to nutrients availability. The model for the Deep Water EXperiment production rates is the following:

$$
\begin{aligned}
&P([NH_4^+]; i = 1,2,3,4) = \\
&P_{max_{i=1,2,3,4}} tanh(log_e(\sqrt{1 + 2 * [NH_4^+]}))^{\beta_1^N}
\end{aligned}
$$

$$
\begin{aligned}
&log_e(P([NH_4^+]; i = 1,2,3,4)) = \xi_{i=1,2,3,4} \\
&+ \beta_1^N log_e(tanh(log_e(\sqrt{1 + 2 * [NH_4^+]})))
\end{aligned}
$$

$$
\xi_{i=1,2,3,4} = log_e(P_{max_{i=1,2,3,4}})
\tag{7.20}
$$

$P$: Primary productivity [mg $C.m^{-3}.d^{-1}$], $[NH_4^+]$: Ammonium concentration [$\mu$M], i: random-effect individuals with i=1 for *Synechococcus*, i=2 for picoeukaryotes, i=3 for nanoeukaryotes and i=4 for cryptophytes , $\xi_{i=1,2,3,4}$: natural logarithm of the maximal productivity for random-effect individuals

Equation (E 20) has been fitted to the dataset using finite mixture of GLMMs. Results are presented in Table 4.

According to the estimations of the random intercepts, the maximal productivity are 0.934 ± 0.023, 57 ± 0.2, 965 ± 0.8 and 88 ± 0.2 mg $C.m^{-3}.d^{-1}$ for *Synechococcus*, picoeukaryotes, nanoeukaryotes and cryptophytes respectively.

The Akaike information criterion (AIC) and Bayesian information criterion (BIC)

| True values | $\pi^*$ | | $\beta_1^{N^*}$ | | $\xi^*$ | | IC |
|---|---|---|---|---|---|---|---|
| | Average | Std | Average | Std | Average | Std | (k=1,2,3,4) |
| $\vec{\pi}$=[0.5,0.5] | | | | | | | AIC=[3111.82,2630.6*,2833.204,2782.325] |
| $\vec{\beta}$=[1.0,0.8] | [0.50,0.50] | [0.05,0.05] | [0.99,0.80] | [0.005,0.005] | [7.99,11.0] | [0.001,0.0002] | BIC=[3113.118,2638.495*,2847.695,2803.414] |
| $\vec{\xi}$=[8,11] | | | | | | | DIC=[3060.286,2346.4*,2346.9,2346.6] |
| $\vec{\pi}$=[0.1,0.9] | | | | | | | AIC=[2633.473,2511.303*,2715.102,2867.9] |
| $\vec{\beta}$=[1.0,0.8] | [0.06,0.94] | [0.008,0.008] | [0.93,0.86] | [0.09,0.09] | [7.99,10.99] | [0.001,0.0002] | BIC=[2634.771,2519.198*,2729.594,2888.989] |
| $\vec{\xi}$=[8,11] | | | | | | | DIC=[2473.278,2328.345*,2328.415,2328.511] |
| $\vec{\pi}$=[0.33,0.33 0.33] | | | | | | | AIC=[28319.31,3413.164,3106.258*, 3152.12] |
| $\vec{\beta}$=[2.0,1.0,0.8] | [0.33,0.33, 0.33] | [$1.10^{-16}$,$1.10^{-16}$,$1.10^{-16}$] | [2.06, 1.07, 0.87] | [0.004,0.006,0.007] | [7.97,10.99] | [0.001,0.0002] | BIC=[28320.61,3421.059,3120.75*,3173.208] |
| $\vec{\xi}$=[8,11] | | | | | | | DIC=[25849.29,3021.384,2472.294*,2475.248] |
| $\vec{\pi}$=[0.1,0.2 0.7] | | | | | | | AIC=[7118.165,3251.543,2812.54*,3043.953] |
| $\vec{\beta}$=[2.0,1.0,0.8] | [0.08,0.24,0.68] | [0.01,0.04,0.04] | [1.99,0.99,0.80] | [0.01, 0.005,0.004] | [7.99,10.99] | [0.001,0.0002] | BIC=[7119.463,3259.438,2827.032*,3065.041] |
| $\vec{\xi}$=[8,11] | | | | | | | DIC=[14056.56,2969.302,2390.158*,2391.796] |
| $\vec{\pi}$=[0.25,0.25,0.25,0.25] | | | | | | | AIC=[37020.08,13697.6,3416.096,3070.659*] |
| $\vec{\beta}$=[3.0,2.0,1.0,0.8] | [0.23,0.25,0.25,0.27] | [0.02,0.03,0.03,0.04] | [2.99,1.86,1.10,0.83] | [0.006,0.47,0.56, 0.09] | [8.003,11.006] | [0.001,0.0001] | BIC=[37021.37,13705.49,3430.587,3091.747*] |
| $\vec{\xi}$=[8,11] | | | | | | | DIC=[78251.71,13703.2, 6523.504,2350.136*] |
| $\vec{\pi}$=[0.1,0.2,0.5,0.2] | | | | | | | AIC=[25389.61,7479.08,7026.01,2974.331*] |
| $\vec{\beta}$=[3.0,2.0,1.0,0.8] | [0.09,0.17,0.50,0.24] | [0.00,0.02,0.002,0.01] | [2.96,1.99,1.16,0.86] | [1.03,0.006,0.94,0.09] | [8.00,11.00] | [0.001,0.0001] | BIC=[25390.91,7486.975,7040.502,2995.42*] |
| $\vec{\xi}$=[8,11] | | | | | | | DIC=[36120.71, 7062.468,6639.941,2345.18*] |

Table 7.3: Simulations of primary productivity response to nutrients enrichment specified by equation (E 18) with concentrations bounded between 0.01 $\mu$M and 0.2 $\mu$M and $\xi_{i=1,2}$=8,11 ($n$=200). * underlines the selection of the optimal number of component ($k$)

both appoint a unique linear coefficient to describe the affinity of *Synechococcus*, picoeukaryotes, nanoeukaryotes and cryptophytes for ammonium. The half-saturation constant derived from this model is 0.31 $\mu$M for ammonium uptake. The productivity corresponding to this parameterisation is shown in Figure 3.

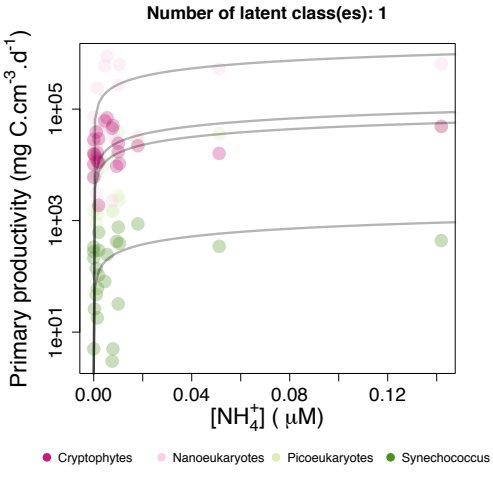


Figure 7.3: Fit (continuous lines) of finite mixture of GLMMs on measures of DeWEX primary productivity in response to nutrients availability with 1 latent class (Model selected by AIC/BIC)

The Deviance information criterion (DIC) indicates 4 components in the mixture with the linear coefficients, $\hat{\beta_1^N}$=[0.38;0.94;0.58;0.55] and respective half-saturations constant $\hat{k_N}(\mu M)$=[0.19;0.91;0.43;0.39]. Fits with this parameterisation are shown in Figure 4. The data point labelling indicates that the first component includes a majority of *Synechococcus* observations (56%) while the second component mainly group cryptophytes primary productivity (68%). The rest of the components are confounding picoeukaryotes and nanoeukaryotes.

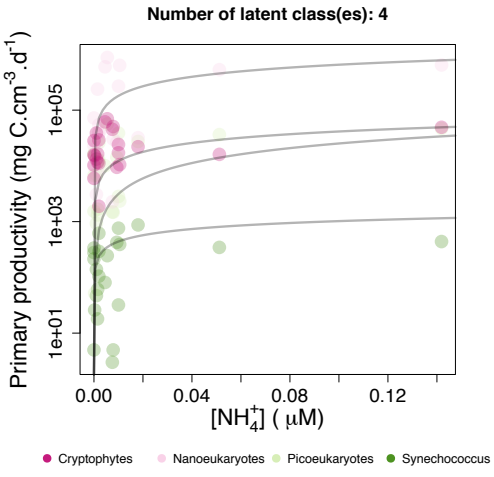


Figure 7.4: Fit (continuous lines) of finite mixture of GLMMs on measures of DeWEX primary productivity in response to nutrients availability with 4 latent classes (Model selected by DIC)

| $k$ | $\hat{\pi}$ | | $\hat{\beta_1^N}$ | | $\hat{\xi}$(i=1,2,3,4) | | [AIC,BIC,DIC] |
|---|---|---|---|---|---|---|---|
| | Average | Std | Average | Std | Average | Std | |
| 1 | [1] | [0] | [0.487] | [9.6 $10^{-5}$] | [6.84,10.95,13.78,11.39] | [0.01,0.001,0.0005,0.001] | [7259.767*,7260.085*,5230423] |
| 2 | [0.28,0.72] | [0.00,1.3 $10^{-16}$] | [0.49,0.38] | [0.15,0.15] | [6.84,10.95,13.78,11.39] | [0.01,0.001,0.0005,0.001] | [8713.722,8718.675,1511227] |
| 3 | [0.25,0.47,0.28] | [0.007,0.03,0.03] | [0.27,0.74,0.66] | [0.0001,0.16,0.19] | [6.84,10.95,13.78,11.39] | [0.01,0.001,0.0005,0.001] | [10765.5,10775.09,678020] |
| 4 | [ 0.24,0.23,0.21,0.32] | [0.09,0.02,0.05,0.07] | [0.38,0.94,0.58,0.55] | [0.12,0.34,0.29,0.29] | [6.84,10.95,13.78,11.39] | [0.01,0.001,0.0005,0.001] | [12978.77, 12993,455131.6*] |
| 5 | [0.24,0.08,0.63,0.04,0.03] | [ 0.05,0.06,0.07,0.007,0.19] | [0.44,0.63,0.64,0.32,0.31] | [0.15,0.28,0.26,0.12,0.13] | [6.84,10.95,13.78,11.39] | [0.01,0.001,0.0005,0.001] | [10578.32,10597.18, 485032] |

1: *Synechococcus*, 2: picoeukaryotes, 3: nanoeukaryotes, 4: cryptophytes

Table 7.4: Finite mixture models parameters estimated for DeWEX primary productivity in response to ammonium concentration ($n$=75, $n_1$=19, $n_2$=19, $n_3$=18, $n_4$=18). * underlines the selection of the optimal number of component ($k$)

**Light utilisation:** We are looking for statistically distinct ability to use light for growth by fitting the class of finite mixture of GLMMs to measures of primary productivity in response to light availability. The model for the Deep Water EXperiment production rates is the following:

$$P(E; i = 1,2,3,4) = P_{max_{i=1,2,3,4}} \frac{E}{E_k} exp\left(1 - \frac{E}{E_k}\right)$$

$$log_e(P(E; i = 1,2,3,4)) = \xi_{i=1,2,3,4} + \beta_1^E E - log_e\left(-\frac{1}{\beta_1^E}\right) + \text{offset}(1 + log_e(E))$$

$$\xi_{i=1,2,3,4} = log_e(P_{max_{i=1,2,3,4}}); \quad \beta_1^E = \frac{-1}{E_k} \tag{7.21}$$

$P$: Primary productivity [mg C.m$^{-3}$.d$^{-1}$], E: daily average of Photosynthetic available radiation [$\mu$E.m$^{-2}$.s$^{-1}$], i: random-effect individuals with i=1 for *Synechococcus*, i=2 for picoeukaryotes, i=3 for nanoeukaryotes and i=4 for cryptophytes , $\xi_{i=1,2,3,4}$: natural logarithm of the maximal productivity for random-effect individuals, $E_k$: Optimal light intensity [$\mu$E.m$^{-2}$.s$^{-1}$]

Equation (E 21) has been fitted to the dataset using finite mixture of GLMMs. Results are presented in Table 5.

According to the estimations of the random intercepts, the maximal productivity are 0.123 ± 9.10$^{-04}$, 21 ± 0.01, 750 ± 0.2 and 68 ± 0.04 mg C.m$^{-3}$.d$^{-1}$ for *Synechococcus*, picoeukaryotes, nanoeukaryotes and cryptophytes respectively (Table 5).

The Deviance information criterion (DIC) indicates the absence of mixture. All groups productivity is modelled by the optimal light utilisation at 62 $\mu$E.m$^{-2}$.s$^{-1}$ derived from the linear coefficient, $\hat{\beta_1^E}$=[-0.015]. Fit with this parameterisation is shown in Figure 5.

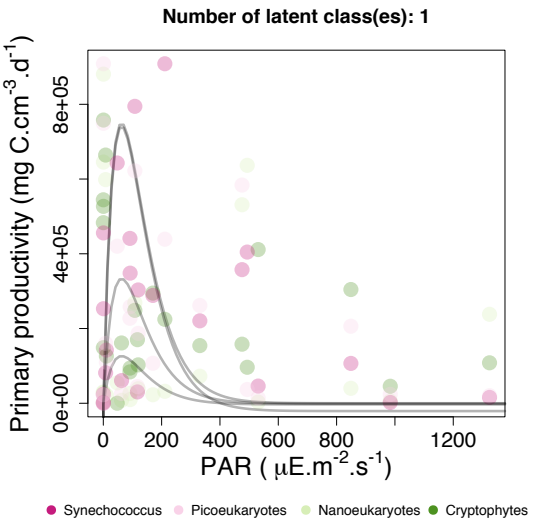


Figure 7.5: Fit (continuous lines) of finite mixture of GLMMs on measures of DeWEX primary productivity in response to light intensity with 1 latent class (Model selected by DIC)

The Akaike information criterion (AIC) and Bayesian information criterion (BIC) both appoint a two-component mixture model to describe the light utilisation by *Synechococcus*, picoeukaryotes, nanoeukaryotes and cryptophytes. The optimal light intensities derived from this model are 115 and 48 $\mu$E.m$^{-2}$.s$^{-1}$ respectively. The productivity corresponding to this parameterisation is shown in Figure 6. The data point labelling indicates that the second

| $k$ | $\hat{\pi}$ | | $\hat{\beta_1^E}$ | | $\hat{\xi}$(i=1,2,3,4) | | [AIC,BIC,DIC] |
|---|---|---|---|---|---|---|---|
| | Average | Std | Average | Std | Average | Std | |
| 1 | [1] | [0] | [-0.015] | [$3.10^{-06}$] | [4.8;9.94;13.52;11.13] | [ 0.01;0.001;0.0004;0.001] | [8425.779,8426.29,120 109 762*] |
| 2 | [0.05;0.95] | [0.006;0.006] | [-0.008;-0.02] | [1. $10^{-06}$;2. $10^{-06}$] | [4.8;9.94;13.52;11.13] | [ 0.01;0.001;0.0004;0.001] | [6467.424*,6472.957*,4 245 955 373] |
| 3 | [0.04;0.22;0.74] | [0.00;0.01;0.01] | [-0.008;-0.04; -0.029] | [$1.10^{-06}$;$1^{-02}$; $1^{-02}$] | [4.8;9.94;13.52;11.13] | [ 0.01;0.001;0.0004;0.001] | [6998.069,7008.623,791 271 094] |
| 4 | [0.05;0.67;0.16;0.12] | [0;0;0;0] | [-0.008;-0.05;-0.022;-0.04] | [$1.10^{-06}$; $2.10^{-02}$; $5.10^{-03}$; $2.10^{-02}$] | [4.8;9.94;13.52;11.13] | [ 0.01;0.001;0.0004;0.001] | [8583.484,8599.06,442 700 858] |
| 5 | [0.04;0.12;0.22;0.16;0.45] | [0;0;0;0;0] | [-0.008;-0.02;-0.03;-0.075;-0.11] | [$1.10^{-06}$; $6.10^{-06}$; $2.10^{-02}$; $4.10^{-02}$; $3.10^{-02}$] | [4.8;9.94;13.52;11.13] | [ 0.01;0.001;0.0004;0.001] | [12482.39,12502.98, 228 735 642] |

1: *Synechococcus*, 2: picoeukaryotes, 3: nanoeukaryotes, 4: cryptophytes

Table 7.5: Finite mixture models parameters estimated for DeWEX primary productivity in response to daily average light intensity ($n$=91, $n_1$=23, $n_2$=23, $n_3$=22, $n_4$=23). * underlines the selection of the optimal number of component ($k$)

component include all observations of cryptophytes and picoeukaryotes productivity. The first component groups few observations (< 5) belonging to nanoeukaryotes and *Synechococcus*.

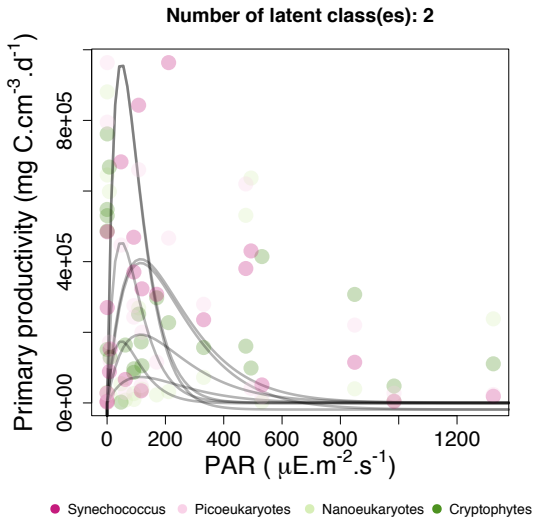


Figure 7.6: Fit (continuous lines) of finite mixture of GLMMs on measures of DeWEX primary productivity in response to light intensity with 2 latent classes (Model selected by AIC/BIC)

**Thermal niche:** We are looking for statistically distinct phytoplankton thermal niches by fitting classes of finite mixture of GLMMs to measures of primary productivity in response to daily average surface temperature. The model for the Deep Water EXperiment production rates is the following:

$$P(T; i = 1,2,3,4) = P_{max_{i=1,2,3,4}} exp\left(-\frac{(T - T_{opt})^2}{\Delta T_{\pm}^2}\right)$$

$$log_e(P(T; i = 1,2,3,4)) = \xi_{i=1,2,3,4} + \beta_2^T(T - \beta_1^T)^2$$

$$\xi_{i=1,2,3,4} = log_e(P_{max_{i=1,2,3,4}})$$
$$\beta_1^T = T_{opt};\ \beta_2^T = -\frac{1}{\Delta T_{\pm}^2} \quad (7.22)$$

$P$: Primary productivity [mg C.m$^{-3}$.d$^{-1}$], T: daily average surface temperature [°C], i: random-effect individuals with i=1 for *Synechococcus*, i=2 for picoeukaryotes, i=3 for nanoeukaryotes and i=4 for cryptophytes , $\xi_{i=1,2,3,4}$: natural logarithm of the maximal productivity for random-effect individuals, $T_{opt}$: Thermal niche optimum [°C], $\Delta T_{\pm}$: Thermal niche width for temperature less or greater than the optimum [°C]

Equation (E 22) has been fitted to the dataset using finite mixture of GLMMs. Results are presented in Table 6.

According to the estimations of the random intercepts, the maximal productivity are 1.4 ± $9.10^{-03}$, 75 ± 0.05, 930 ± 0.2 and 110 ± 0.05 mg C.m$^{-3}$.d$^{-1}$ for *Synechococcus*, picoeukaryotes, nanoeukaryotes and cryptophytes respectively.

The Akaike and Bayesian information criterion (AIC/BIC) indicate an homogeneous thermal niche for all groups. This model predict the growth optimal surface temperature at 14.94 ± $4.10^{-3}$°C with a gradient of productivity sharper above the optimum ($\Delta T_{-}$=0.7 ± $3.10^{-4}$°C; $\Delta T_{+}$=1.4 ± $5.10^{-4}$°C). Fit with this parameterisation is shown in Figure 7.

| $k$ | $\hat{\pi}$ | | $\beta_1^{T}$ | | $\beta_2^{T-}$ | | $\beta_2^{T+}$ | | $\xi$(i=1,2,3,4) | | [AIC,BIC,DIC] |
|---|---|---|---|---|---|---|---|---|---|---|---|
| | Average | Std | Average | Std | Average | Std | Average | Std | Average | Std | |
| 1 | [1] | [0] | [14.94] | [0.0004] | [-0.51] | [0.0003] | [-2.02] | [0.002] | [7.25;11.23;13.74;11.61] | [0.01;0.001;0.0004;0.001] | [10545.32*,10548.88*,8 656 420] |
| 2 | [0.52;0.48] | [0.07;0.07] | [14.87;13.84] | [0.20;0.03] | [-0.98;-2.63] | [0.44;0.22] | [-1.89;-1.13] | [0.29;0.33] | [7.25;11.23;13.74;11.61] | [0.01;0.001;0.0004;0.001] | [19568.94,19580.83,1 930 910] |
| 3 | [0.49;0.37;0.14] | [0.05;0.05;0.04] | [15.2;14.1;14.9] | [0.3;1.06;0.78] | [-1.1; -5.2;-0.9] | [1.4;5.3;1.1] | [-99.41;-0.70;-1.8] | [137.5;0.2;1.09] | [7.25;11.23;13.74;11.61] | [0.01;0.001;0.0004;0.001] | [15819.77,15840.01, 1 364 521] |
| 4 | [0.13;0.37;0.31;0.19] | [0.02;0.03;0.02;0.02] | [13.93;13.95;14.82;14.78] | [1.6;0.8; 0.9; 0.9] | [-0.3;-1.09;-808.67;-0.83] | [0.38;0.88;1143.3;0.40] | [-0.21;-389.8;-2.1;-295.6] | [0.37;551.2; 1.58;414.6] | [7.25;11.23;13.74;11.61] | [0.01;0.001;0.0004;0.001] | [23432.06,23460.63,774 204.9] |
| 5 | [0.28;0.18;0.29;0.12;0.13] | [0.03;0.02;0.01;0.02;0.01] | [14.4;15.3;15.08;14.19;15.06] | [0.47;0.65;1.58;0.28;0.95] | [-161.9;-0.7; -1.4;-0.9;-1.0] | [228.5;0.4; 0.7;1.1;0.5] | [-1.9;-2.2; -1.1;-0.3;-0.1] | [0.66;2.1;1.3;0.2;1.1] | [7.25;11.23;13.74;11.61] | [0.01;0.001;0.0004;0.001] | [18532.09,18569,329 699*] |

1: *Synechococcus*, 2: picoeukaryotes, 3: nanoeukaryotes, 4: cryptophytes

Table 7.6: Finite mixture models parameters estimated for DeWEX primary productivity in response to daily average surface temperature ($n$=119, $n_1$=30, $n_2$=30, $n_3$=29, $n_4$=30). * underlines the selection of the optimal number of component ($k$)

The Deviance information criterion (DIC) identified 5 distinct thermal niches among observations of *Synechococcus*, picoeukaryotes, nanoeukaryotes and cryptophytes productivity. The thermal niches corresponding to this parameterisation are shown in Figure 8. The mixing proportions ($\hat{\pi}$=[0.28;0.18;0.29;0.12;0.13]) confirm that the first and third models of thermal niche are the most representatives of the dataset, with respective optima at 14.4 ± 0.5 and 15.08 ± 1.6°C.

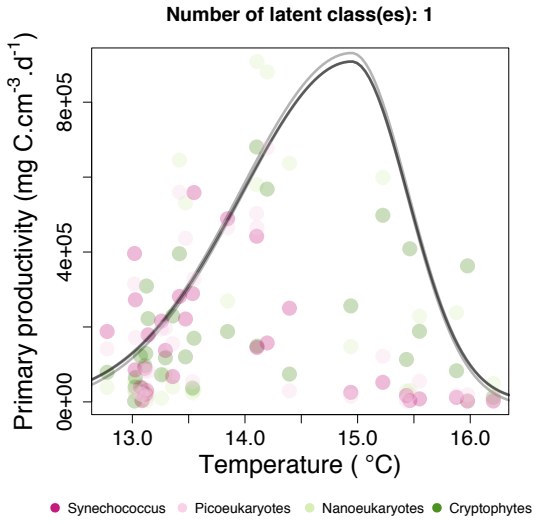


Figure 7.7: Fit (continuous lines) of finite mixture of GLMMs on measures of DeWEX primary productivity in response to surface temperature with 1 latent class (Model selected by AIC/BIC)

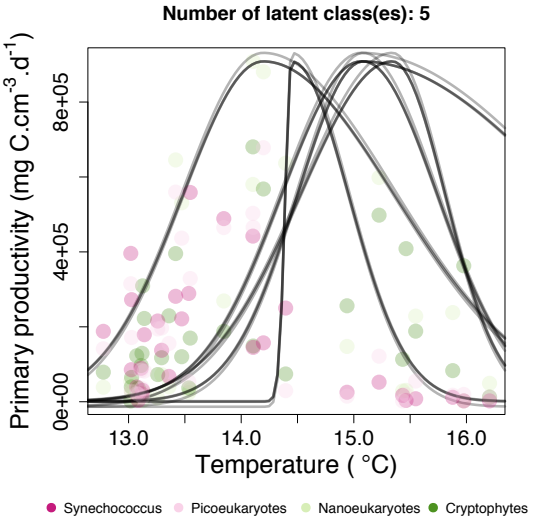


Figure 7.8: Fit (continuous lines) of finite mixture of GLMMs on measures of DeWEX primary productivity in response to surface temperature with 5 latent classes (Model selected by DIC)

**Integrated Growth environment:** We are looking for statistically distinct phytoplankton niche by fitting classes of finite mixture of GLMMs to measures of primary productivity along temperature, light and nutrient concentration gradients. The model for the Deep Water EXperiment production rates is the following:

$$
\begin{aligned}
&P(T,E,[NH_4^+];i) = P_{max_i} exp\left(-\frac{(T-T_{opt})^2}{\Delta T_{\pm}^2}\right).\left(\frac{[NH_4^+]}{[NH_4^+]+1}\right)^n.\frac{E}{E_k}exp\left(1-\frac{E}{E_k}\right)\\
&log_e(P(T,E,[NH_4^+];i)) = \xi_i + \beta_2^T(T-\beta_1^T)^2 + \beta_1^N log_e(tanh(log_e(\sqrt{1+2[NH_4^+]})))\\
&+ \beta_1^E E - log_e\left(-\frac{1}{\beta_1^E}\right) + \text{offset}(1+log_e(E))\\
&\xi_{i=1,2,3,4} = log_e(P_{max_{i=1,2,3,4}});\ \beta_1^T = T_{opt};\ \beta_2^T = -\frac{1}{\Delta T_{\pm}^2};\ \beta_1^N = n;\ \beta_1^E = -\frac{1}{E_k}
\end{aligned}
\tag{7.23}
$$

$P$: Primary productivity [mg C.m$^{-3}$.d$^{-1}$], T: daily average surface temperature [°C], i: random-effect individuals with i=1 for *Synechococcus*, i=2 for picoeukaryotes, i=3 for nanoeukaryotes and i=4 for cryptophytes , $\xi_{i=1,2,3,4}$: natural logarithm of the maximal productivity for random-effect individuals, $T_{opt}$: Thermal niche optimum [°C], $\Delta T_{\pm}$: Thermal niche width for temperature less or greater than the optimum [°C], [$NH_4^+$]: Ammonium concentration [$\mu$M], E: daily average of Photosynthetic available radiation [$\mu$E.m$^{-2}$.s$^{-1}$], $E_k$: optimal light intensity [$\mu$E.m$^{-2}$.s$^{-1}$]

Equation (E 23) has been fitted to the dataset using finite mixture of GLMMs. Information Criterion are presented in Table 7.

| $k$ | AIC | BIC | DIC |
|---|---|---|---|
| 1 | 7990.653* | 7997.472* | 12 486 194 |
| 2 | 9014.029 | 9031.871 | 3 388 609 |
| 3 | 12284.22 | 12313.08 | 3 678 323 |
| 4 | 19424 | 19463.88 | 2 197 536* |
| 5 | 9977.846 | 10028.76 | 2 589 861 |

Table 7.7: Finite mixture models selection estimated for DeWEX primary productivity in response to growth integrated environment ($n$=67, $n_1$=16, $n_2$=18, $n_3$=17, $n_4$=16). * underlines the selection of the optimal number of component ($k$)

The Akaike and Bayesian information criterion (AIC/BIC) both advocate a single functional trait to describe DeWEX primary productivity along temperature, light and ammonium gradients. On the other hand, the DIC supposes that the 3D growth niche may be modelled by 4 latent classes of parameters. In this model, *Synechococcus* productivity corresponds to the class presenting the lowest half-saturation constant ($k_N$=0.057 $\mu$M) and optimal light intensity ($E_k$=5 $\mu$E.m$^{-2}$.s$^{-1}$). The second latent class, with $k_N$=0.52 $\mu$M and $E_k$=7 $\mu$E.m$^{-2}$.s$^{-1}$, includes a majority of picoeukaryotes production rates (50%), while the third class, defined by $k_N$=1.04 $\mu$M and $E_k$=93 $\mu$E.m$^{-2}$.s$^{-1}$, represents 63% of nanoeukaryotes observations. The last component ($T_{opt}$=14.5 °C) is equally distributed between cryptophytes and picoeukaryotes. The 3 axis niches for the 4-component mixture model are shown in Figure 9.

## 7.3 Discussion

***Phytoplankton Integrated growth niches*** Section 2.1 illustrates the application of mixed models to predict phytoplankton abundance from correlated data collected at several depths of specific stations. Since station-dependent observations display a structural correlation, the variance of station-specific vertical distributions must be accounted in statistical analyses. The purpose of mixed model is to correctly predict a categorical dataset. The dataset used in this section corresponds to 24 vertical distribution of *Prochlorococcus* cells along a longitudinal gradient. All distributions were unimodal with the maximum present in depth located between 75 and 120 m in the eastern basin and shallower (75 m) in the western basin (Figure 1). They showed a strong correlation with $NO_x$ concentration, enriched in deep layers by heterotrophic mineralisation (Pujo-Pay et al., 2011). The local accumulation of

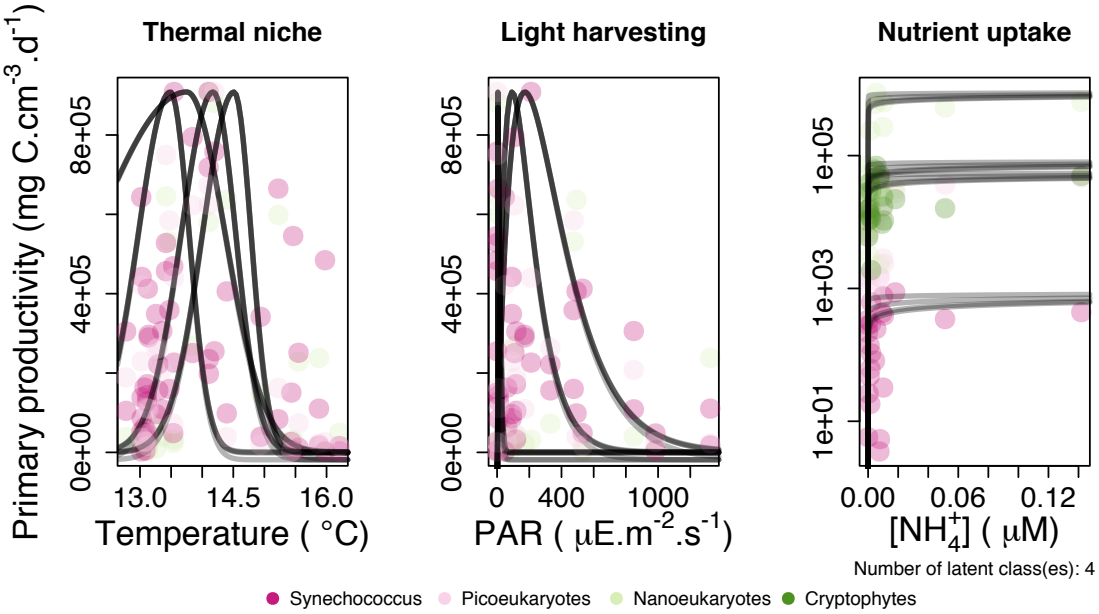


Figure 7.9: Fit (continuous lines) of finite mixture of GLMMs on measures of DeWEX primary productivity in response to the integrated growth environment with 4 latent classes
(Model selected by DIC)

biomass at the nutricline is a general feature called the *Deep Chlorophyll Maximum* (DCM) also observed in the global ocean (Lavigne et al., 2015). The positive correlation between *Prochlorococcus* and nitrates concentration supposes that nitrogen may support a non negligible part of its production (Casey et al., 2007). In this paper, the assimilation of nitrates is assumed to drive cellular growth and reproduction rates according to the Michaeilis-Menten-Monod model. The model predicts that *Prochlorococcus* growth curve will increase up to saturation. The concentration reached at saturation represents the random-effects and is consequently station-dependent. The concentration at which the abundance will be half of the maximum is the half-saturation constant, defining the affinity of cells for the nutrient of interest. The fixed-effect slope of the Poisson mixed-effects model was used to approximate the half-saturation constant, $k_{NO_x}$=0.94 ± 0.002 $\mu$M. To our knowledge this paper is the first to specifically provide an estimation of *Prochlorococcus* nitrates half-saturation constant. Due to their high affinity for nutrients uptake, picophytoplankton, including *Prochlorococcus*, *Synechococcus* and picoeukaryotes, are dominant in oligotrophic regions in both local and global scales (Chisholm, 1992). Since nutrients affinity may be predicted by the allometric law for phytoplankton, the size is the ecological trait used to fix half-saturation constant in several biogeochemical models. For instance Follows et al. (2007) use the reference 0.56 $\mu$M for small cells in microbial communities.

***Phytoplankton Functional Types*** In section 2.2, we attempted to predict estimations of primary productivity based on concurrent measurements of temperature, light intensity and nutrients concentration. These variables are regularly measured at observation stations and during oceanographic cruise. Estimations of primary productivity are more sparse and the collection of presence/absence data for phytoplankton is extensively limiting. Flow cytometry is a fast and reliable approach to count abundant phytoplankton cells specif-

ically discriminated by their optical properties linked to size and photosynthetic pigments. The same optical properties are used to estimate growth and production rates of phytoplankton (André et al., 1999; Sosik et al., 2003). Groups defined by flow cytometry are generally polyphyletic although some of them may contain cells belonging to a unique genus such as *Prochlorococcus* and *Synechococcus*. This is why groups are better defined by their size. The pico-, nano- and micro- size fractions referred to Sieburth's (1978) classification to delimit the dimensions of the cells under 2.0 and 20 $\mu$m respectively. Size is the principal ecological trait that determines nutrients assimilation according to the generic formula: $R = aW^b$, with R a metabolic rates and W, the organism dimension (Chisholm, 1992). For our dataset, the deviance information criterion was able to identify a 4-component mixture model to predict group-specific productivity in response to ammonium concentration. The respective half-saturation constant ranged between 0.19 and 0.91 $\mu$M, the two extrema being representative of the smallest cells (*Synechococcus*) and the largest cells (cryptophytes) respectively. According to the same criterion, the light utilisation was better predicted by an homogenous model determined by the optimal light intensity $E_k$=62 $\mu$E.m$^{-2}$.s$^{-1}$. The last axes involved to model phytoplankton growth niche, the surface temperature, did not support the statistical distinction of groups' thermal niche (AIC). However, this result is coherent with the local adaptation of cells to average *in situ* temperature highlighted by Thomas et al. (2012). Although phytoplankton compete for the same resource, the interaction of taxa leads rarely to the exclusion. *In situ* samples of phytoplankton count generally $10^4$ cells.cm$^{-3}$ spanning the two branches of the phylogenetic tree (i.e. prokaryotes and eukaryotes) (Maranon et al., 2007). This phenomenon has been called the *Paradox of the plankton* by Hutchinson (1961). In his definition, the niche is the multi-dimensional space that affect organisms fitness. The integrated growth sets of descriptors were combined to predict the interactive effects of the 3 individual models on the response of primary production. The full model predicts a clear distinction between small cells displaying a high affinity ammonium assimilation and the larger cells with low affinity.

## 7.4 Conclusion

Generalized mixed models account for the residuals dependence arising in models fitted to correlated or repeated observations. When conducting a longitudinal transect in the Mediterranean Sea, we measured the vertical distribution of phytoplankton abundance at 6 depths, dependent of the HotMix 24 stations. *Prochlorococcus* distribution was predicted by mixed models using the potential limitation of nutrient concentration. The random intercepts showed a clear distinction between the oligotrophic stations located in the eastern basin and the enriched stations located in the western basin. Using this model, we established an approximation of the half-saturation constant driving *Prochlorococcus* uptake in the Mediterranean sea, $k_{NO_x}$=0.94 ± 0.002 $\mu$M. Finite mixture of Generalized Linear Mixed Models are indicated to fit heterogenous observations with repeated measurements. They ensure an optimal approximation of the observations density function by means of the convex combination of known distributions. Moreover, statistical criterion can be used to validate the number of latent classes in the dataset. Since we measured several dependent observations of 4 group-specific primary production rates during the DeWEX cruises, we used this class of model to define the integrated growth niche of each group along temperature, light and nutrients gradients. The selection of the number of latent classes was performed by several information criterion: the AIC, BIC

and DIC. The full model, taking into account the interactive effects of temperature, light and nutrients on phytoplankton growth was better predicted by a one and four component(s) mixture according to the AIC/BIC criterions and the DIC criterion respectively. The 4 components mixture reflected the difference in resource requirements for *Synechococcus*, picoeukaryotes, nanoeukaryotes and cryptophytes cells. This result suggests that the groups defined by flow cytometry display separate ecological traits driving nutrients affinity and light utilisation.

## References


André, J.-M., Navarette, C., Blanchot, J. and Radenac, M.-H. (1999), Picophytoplankton dynamics in the equatorial Pacific: growth and grazing rates from cytometric counts, *J. of Geophys. Res.*, *104*(C2), 3369–3380.

Antoine, D., André, J.M. and Morel, A. (1996), Oceanic primary production: 2. Estimation at global scale from satellite (coastal zone color scanner) chlorophyll, *Global biogeochemical cycles*, *10*(1), 57–69.

Baklouti, M., Faure, V., Pawlowski, L. and Sciandra, A. (2006), Investigation and sensitivity analysis of a mechanistic phytoplankton model implemented in a new modular numerical tool (Eco3M) dedicated to biogeochemical modelling, *Progress in Oceanography*, *71*, 34–58.

Barlow, R. G.. (1984), Dynamics of the decline of a phytoplankton bloom after an upwelling event, *Mar. Ecol. Prog. Ser.*, *16*, 121–126.

Behrenfeld, M. J., Hasley, K. H. and Miligan, A. (2008), Evolved physiological responses of phytoplankton o their integrated growth environment, *Phil. Trans. R. Soc. B*, *363*, 2687–2703.

Boyd, P. W., Strzepek, R., Fu, F. and Hutchins, D. A. (2010), Environmental control of open-ocean phytoplankton groups: Now and in the future, *Limnol. Oceanogr.*, *55*(3), 1353–1376.

Bethoux, J. P., Morin, P., Chaumery, C., Connan, O., Gentili, B. and Ruiz-Pino D. (1998), Nutrients in the Mediterranean Sea, mass balance and statistical analysis of concentrations with respect to environmental change, *Marine Chemistry*, *63*, 155–169.

Casey, J. R., Lomas, M. W., Mandecki, J. and Walker, D. E. (2007), *Prochlorococcus* contributes to new production in the Sargasso Sea deep chlorophyll maximum, *Geophysical Res. letters*, *34*, 1–5.

Chisholm, S. W. (1992), Phytoplankton size, *Primary Productivity and Biogeochemical Cycles in the Sea, P. G. Falkowski and A. D. Woodhead eds., Plenum Press, NY*, 213–237.

De Boyer Montegut, C., Madec, G., Fischer, A. S., Lazar, A. and Iudicone, D. (2004), Mixed layer depth over the global ocean: An examination of profile data and a profile-based climatology, *J. Geophys. Res.*, *109*, 1–20.

D'Ortenzio, F., Iudicone, D., De Boyer Montegut, C., Testor, P., Antoine, D., Marullo, S., Santorel, R. and Madec, G. (2005), Seasonal variability of the mixed layer depth in the Mediterranean Sea as derived from in situ profiles, *Geophysical res. letters*, *32*, 1–4.

D'Ortenzio, F. and D'Alcala, M. R. (2009), On the trophic regimes of the Mediterranean Sea: a satellite analysis, *Biogeosciences*, *6*, 139–148.

Falkoswki, P. G. (1997), Evolution of the nitrogen cycle and its influence on the biological sequestration of $CO_2$ in the ocean, *Nature*, *387*, 272–275.

Falkoswki, P. G. and Oliver, M. J. (2007), Mix and match: how climate selects phytoplankton, *Nature Reviews Microbiology*, *5*, 813–819.

Gelman, A., Hwang, J. and Vehtari, A. (2013), Understanding predictive information criteria for Bayesian models, *Statistics and Computing*, 1–30.

Green, B. R. (2007), Evolution of light-harvesting antennas in an oxygen world, *Evolution of Primary Producers in the Sea, P. G. Falkowski and A. H. Knoll eds., Boston, Elsevier*, 37–53.

Hutchinson, G. E. (1957), Concluding remarks, *Cold Spring Harbor Symposia on Quantitative Biology*, *22*, 415–427.

Hutchinson, G. E. (1961), The paradox of the Plankton, *The American Naturalist*, *95*(882), 137–145.

IOCCG (2014), Phytoplankton Functional Types from space, *Sathyendranath, S. ed., Reports of the International Ocean-Colour Coordinating Group, IOCCG, Dartmouth, Canada*, *15*,1–156.

Lavigne, H. (2013), Impact de la variabilité saisonnière de la profondeur de la couche de melange sur le cycle saisonnier du phytoplancton en Méditerranée, *PhD Thesis, UPMC*, 1–145.

Lavigne, H., D'Ortenzio, F., D'Alcala, M. R., Claustre, H., Sauzede, R. and Gacic, M. (2015), On the vertical distribution of the chlorophyll a concentration in the Mediterranean Sea: a basin-scale and seasonal approach, *Biogeosciences*, *12*, 5021–5039.

Litchman, E., Edwards, K. F., Klausmeier, C. A. and Thomas, M. K. (2012), Phytoplankton niches, traits and eco-evolutionary responses to global environmental change, *Mar. Ecol. Prog. Ser.*, *470*, 235–248.

Maranon, E., Cermeno, P., Rodriguez, J., Zubkov, M. V. and Harris, R. P. (2007), Scaling of phytoplankton photosynthesis and cell size in the ocean, *Limnol Oceanogr.*, *52*(5), 2190–2198.

Margalef, R. (1978), Life-forms of phytoplankton as survival alternatives in an unstable environment, *Oceanol. Acta*, *1*(4), 493–509.

McCulloch, C. E. (1997), Maximum likelihood algorithms for generalized linear mixed models, *J. of the American statistical Association*, *92*, 162–170.

McLachlan, G. and Peel, D. (2000), Finite mixture models, *Wiley-Interscience, NY*, 1–407.

Mermex group (2011), Marine ecosystem's responses o climatic and anthropogenic forcings in the Mediterranean, *Progress in Oceanography*, *91*, 97–166.

Nair, A., Sathyendranath, S., Platt, T., Morales, J., Stuart, V., Forget, M.-H., Devred, E. and Bouman, H. (2008), Remote sensing of phytoplankton functional types, *Remote sensing of environment*, *112*, 3366–3375.

Nelder, J. A. and Wedderburn, R. W. M. (1972), Generalized Linear Models, *J. R. Statist. Soc. A*, *135*, 370–384.

Pujo-Pay, M., Conan, P., Oriol, L., Cornet-Barthaux, V., Falco, C., Ghiglione, J.-F., Goyet, C., Moutin, T. and Prieur, L. (2011), Integrated survey of elemental stoichiometry (C, N, P) from the western to eastern Mediterranean Sea, *Biogeosciences*, *8*, 883–899.

Reynolds, C. S., Huszar, V., Kruk, C., Naselie-Flores, L. and Melo, S. (2002), Towards a functional classification of the freshwater phytoplankton, *J. Plank. Res.*, *24*, 417–428.

Root , R. B. (1967), The niche exploitation pattern of the Blue-Gray Gnatcatcher, *Ecological Monographs*, *37*, 317–350.

Sieburth, J. (1978), Pelagic ecosystem structure: Heterotrophic compartments of the plankton and their relationship to plankton size fractions, *Limnol. Oceanogr.*, *23*(6), 1256–1263.

Sosik, H. M., Olson, R. J., Neubert, M. G. and Shalapyonok, A. (2003), Growth rates of coastal phytoplankton from time-series measurements with a submersible flow cytometer, *Limnol. Oceanogr.*, *48*(5), 1756–1765.

Spiegelhalter, D. J., Best, N. G., Carlin, B. P. and Van der Linde, A. (2002), Bayesian measures of model complexity and fit, *J. R. Statist. Soc. B*, *64*(4), 1085–1088.

Thomas, M. K., Kremer, C. T., Klausmerier, C. A. and Litchman, E. (2012), A global pattern of thermal adaptation in marine phytoplankton, *Science*, *338*, 583–639.

Ting, C. S., Rocap, G., King, J. and Chisholm, S. W. (2002), Cyanobacterial photosynthesis in the oceans: the origins and significance of divergent light-harvesting strategies, *Trends in Microbiology*, *10*(3), 134–142.

Tsiola, A., Pitta, P., Fodelianaskis, S., Pete, R., Magiopoulos, I., Mara, P., Psarra, S., Tanaka, T. and Mostajir, B. (2016), Nutrients limitation in surface waters of the oligotrophic eastern Mediterranean Sea: an enrichment microcosm experiment, *Microbiology of aquatic systems*, *71*, 575–588.

Uitz, J., Claustre, H., Gentili, B. and Stramski, D. (2010), Phytoplankton class-specific primary production in the world's oceans: Seasonal and interannual variability from satellite observations, *Global biogeochemical cycles*, *24*, 1–19.

Uitz, J., Stramski, D., Gentili, B., D'Ortenzio, F. and Claustre, H. (2012), Estimates of phytoplankton class-specific and total primary production in the Mediterranean Sea from satellite ocean color observations, *Global biogeochemical cycles*, *26*, 1–10.

Ward, B. A., Dutkiewicz, S., Jahn, O. and Follows, M. J. (2012), A size-structured food-web model for the global ocean, *Limnol. Oceanogr.*, *57*(6), 1877–1891.

Wei, G. C. G. and Tanner, M. A. (1990), A Monte Carlo implementation of the EM algorithm and the Poor Man's data augmentation algorithms, *J. of the American Statistical Association*, *85*, 699–704.

Wood, A. M. and Leatham, T. (1992), The species concept in phytoplankton ecology, *J. Phycol.*, *28*, 723–729.

Zeger, S. L. and Karim, M. R. (1991), Generalized Linear Models with random effects: A Gibbs sampling approach, *J. of the American Statistical Association*, *88*(413), 79–86.

# 8.0 Conclusion

Pour les organismes qui le consomment, pour le carbone dissous qu'il fixe par photosynthèse, et pour le carbone d'origine anthropique qu'il a contribué à exporter vers l'océan profond, la portée du phytoplancton est déterminante. Pourtant peu de moyens permettent d'en mesurer l'ampleur en considérant leur échelle de variation spatiale et temporelle.

## 8.1 Dynamique du phytoplancton en mer Méditerranée: Approche par modélisation

Un modèle biologique est une représentation simplifiée des organismes et de leurs interactions biotiques et abiotiques. En microbiologie, le modèle de dynamique cellulaire le plus simple est celui de la division par fission binaire. Les modèles de croissance présentés dans le chapitre 2 le décrivent. C'est le mode de reproduction le plus courant. La division asexuée n'est pourtant pas le seul mécanisme de croissance des populations phytoplanctoniques. D 'autres évènements majeurs, tels que la sortie de la phase de dormance et l'ensemencement des milieux par les banques de kystes jouent un rôle important pour la croissance du phytoplancton (Eilersten et wyatt, 2000). Malgré tout, la production primaire est continuellement façonnée par la division cellulaire. Les modèles qui définissent le phytoplancton pour étudier sa dynamique en milieu naturel s'appuient sur des processus physiques et mécaniques. Les modèles physiques intègrent les composantes du courant et de turbulence pour garder la position spatiale d'une population connue (Woods et Onken, 1982). Les modèles mécaniques permettent de suivre l'effet de ce déplacement physique sur la capacité de division du phytoplancton. La modification de la température, des ressources en sels nutritifs et en intensité lumineuse est prise en compte lors du déplacement vertical et/ou horizontal du phytoplancton. En écologie marine, le modèle de couplage physique-biologique le plus connu est certainement le modèle de Sverdrup (1953). Pour expliquer l'accumulation récurrente du phytoplancton au printemps, la restratification de la colonne d'eau après un mélange assez puissant pour entraîner la remontée des sels nutritifs vers la zone épipélagique est une raison suffisante pour favoriser sa production nette. Cette vision est basée sur l'équilibre entre les processus de pertes, liés à la respiration, à la dilution de la colonne d'eau et à la prédation, et la reproduction. La simple augmentation du taux de croissance due à la disponibilité des sels nutritifs et au réchauffement des masses d'eau de surface par la lumière accrue n'est donc pas nécessaire pour prédire les efflorescences si les pertes sont réduites. La dépendance des facteurs antagonistes de contrôle du phytoplancton a été mise en avant dans la théorie dite de *Dilution-Recoupling* proposée par Behrenfeld et al. en 2010. Dans le chapitre 4, l'étude couplée du phénomène de convection (i.e. plongée d'eau profonde) survenant dans le bassin méditerranéen nord occidental et de l'efflorescence qui s'en suit considère ces deux types de contrôle. Le contexte physique de déplacement horizontal et vertical du plancton a été intégré en parallèle des mesures de croissance intrinsèque

pour faire le lien entre leur perte physique et leur capacité de reproduction. Même si la croissance n'a été effective qu'au prix de la diminution de la dilution entraînée par la convection, les populations observées se sont multipliées rapidement aussi bien en hiver qu'au printemps 2013. Pour mettre ces deux processus en perspective, les fonctions mécaniques de production ont été déterminées et sont décrites en détail dans le chapitre 5. L'acclimatation des cellules à leur environnement est clair pour tous les groupes de phytoplancton présents pendant les campagnes de mesures DeWEX et HotMix (Chapitres 6-7). Il est donc évident que la complexité des variations et l'hétérogénéité de la dynamique du phytoplancton aux échelles spatio-temporelles observées en milieu marin viennent des phénomènes de perturbations. Bien avant de répondre à un cycle saisonnier, comme c'est le cas des efflorescences, le phytoplancton est soumis à des variations soudaines et discontinues de son environnement. Les perturbations liées au régime de vent ont été mises en évidence dans le chapitre 3. Contrairement aux milieux contrôlés, les cellules soumises constamment aux aléas des conditions qui peuvent limiter leur croissance, ne montrent certainement pas ou très peu de temps de latence pour s'acclimater (Chapitre 2). Elles sont tout de suite remplacées par des populations plus adaptées aux nouvelles conditions pour qu'un schéma de succession écologique se mette en place. Avec leur capacité de reproduction augmentée, la production nette du système est certainement influencée par la nouvelle population. Les cellules ne sont pas en équilibre à cause de l'interaction de leur cycle de vie et de la dynamique des milieux externes. L'interruption des perturbations induit la transition des populations vers un état plus ou moins stable jusqu'à l'arrivée d'une nouvelle perturbation, ce qui explique la persistence des blooms.

## 8.2 Dynamique du phytoplancton en mer Méditerranée: Approche par statistiques bayésiennes

Si la connaissance de la diversité du phytoplancton est primordiale pour comprendre l'évolution des écosystèmes marins, sa caractérisation est souvent plus sommaire pour prédire leur capacité d'assimilation du $CO_2$. Cette vision réduite est d'une part plus facile à appréhender quand les moyens d'observations sont encore limités; d'autre part elle peut s'appuyer sur des base de données à grande échelle. Les chapitres 6 et 7 présentent l'application de classes de modèles statistiques pour décrire les composantes de la production primaire par inférence bayésienne. En écologie, ces composantes groupent des traits phénotypiques, des stratégies d'adaptation, des domaines d'habitations, ou même des fonctions particulières (Reynolds et al., 2002). La réponse de populations polyphylétiques de *Synechococcus*, picoeukaryotes, nanoeukaryotes et cryptophytes a montré des différences notables, et identifiables d'un point de vue statistique, de leurs niches écologiques. L'effet des gradients de température, de l'intensité lumineuse, et de la teneur en sels nutritifs sur la croissance du phytoplancton peuvent être décrit de façon mécanique. Des lois physiques, qui ont un avantage prédictif, déterminent la forme non-linéaire de la réponse du phytoplancton. Le chapitre 6 montre comment ces modèles peuvent être généralisés sous forme de régressions linéaires exprimant des coefficients interprétables pour la définition des niches écologiques. L'inférence statistique permet de déterminer les paramètres qui régissent cette réponse selon l'adaptation des traits écologiques. L'application de modèles généralisés sur les populations décrites par cytométrie en flux a confirmé certains paradigmes observés en milieu marin. La niche thermale, par exemple, n'admet pas d'optimum spécifique. Elle est déterminée par la température moyenne à la surface de l'eau (Thomas et al., 2012). Au contraire, les traits

d'utilisation de la lumière pour la photosynthèse sont déterminés par les contenus pigmentaires, mesurés en partie par cytométrie en flux, pour permettre d'occuper des niches a priori peu favorables à la production en général. Des populations comme *Synechococcus* sont habituées à vivre en profondeur au niveau de la DCM et doivent optimiser la capture de l'énergie lumineuse. En surface, les populations telles que les cryptophytes, doivent se protéger d'intensités lumineuses inhibitrices. Dès le chapitre 2, l'extension des modèles de croissance a été introduite pour des populations au sens aspécifique du terme. Les populations décrites dans les chapitres suivants présentent des traits communs, en taille et en contenu pigmentaire. Il est clair que les populations au sens strict du phytoplancton contiennent des individus à la capacité de reproduction très différente. Pour cette raison, il est préférable de prendre en compte la variabilité de leur cycle de vie par la présence de multiples stades de développement. Le modèle de population structurée en taille permet de faire le lien entre un trait capable de moduler de façon très générale n'importe quel taux métabolique par allométrie et la fitness des organismes. Pour le phytoplancton, la taille est impliquée aussi bien pour marquer la différence des stades du cycle cellulaire que la capacité des cellules à utiliser les nutriments disponibles pour leur croissance (Edwards et al., 2012). Ce trait est clairement distinct chez les populations de *Synechococcus*, picoeukaryotes, nanoeukaryotes et cryptophytes observées par cytométrie en flux. Les petites cellules ayant une affinité accrue pour les sels nutritifs présents à l'état de trace dans le milieu. C'est d'ailleurs ce qui fait figure de paradoxe en milieu marin (Hutchinson, 1972). Si les populations sont contraintes à différents niveaux pour l'utilisation d'un nombre restreint de ressources, la mesure d'exclusion compétitive devrait prévenir la diversité des espèces. C'est pourquoi la définition des niches phytoplanctoniques en terme de nutriments, mais aussi d'utilisation lumineuse et d'adaptation thermique est importante. Ces trois facteurs mis en cause, les différentes stratégies de croissance peuvent être définies (chapitre 6) et séparées de manière statistique (chapitre 7). La différence effective des capacité d'assimilation entre populations de tailles distinctes a été statistiquement démontrée par l'inférence sur les modèles de mélange. Les compromis qui existent entre l'affinité des cellules pour les sels dissous, leur capacité d'assimilation du $CO_2$, et d'acclimatation à la lumière sont des traits distinctifs des cellules de *Synechococcus*, picoeukaryotes, nanoeukaryotes et cryptophytes. Ils expliquent la distribution spatiale et temporelle des populations phytoplanctoniques telles qu'elles sont définies par cytométrie en flux.

## Références


Agusti, S., Satta, M. P., Mura, M. P., Benavent, E. (1998), Dissolved esterase activity as a tracer of phytoplankton lysis: Evidence of high phytoplankton lysis rates in the northwestern Mediterranean, *Limnol. Oceanogr.*, *43*(8), 1836–1849.

Allen, J. I., Polimene, L. (2011), Linking physiology to ecology: towards a new generation of plankton models, *J. Plankton Res.*, *33*(7), 989–997.

Alvain, S., Moulin, C., Dandonneua, Y., Bréon, F.-M. (2005), Remote sensing of phytoplankton groups in case 1 waters from global SEAWIFS imagery, *Deep Sea Res. I*, *52*(11), 1989–2004.

Anderson, D. M., Kiefer, B. A. (1987), An endogenous annual clock in the toxic marine dinoflagellate Gonyaulax tamarensis. *Nature*, *325*, 616-617.

Antoine, D., Andre, J. M., and Morel, L. (1996), Oceanic primary production. Estimation at global scale from satellite (coastal zone color scanner) chlorophyll. *Global Biogeochem. Cycles*, *10*, 57-69.

Arrigo, K. R. (2005), Marine microorganisms and global nutrient cycles, *Nature*, *437*, 349–355.

Ayers, G. P., Gillett, R W.(2000), DMS and its oxidation products in the remote marine atmosphere: implications for climate and atmospheric chemistry. *J. Sea Res.*, *43*(3), 275-286.

Azam, F., Fenchel, T., Field, J. G., Gray, J. S., Meyer-Reil, L. A., Thingstad, F. (1983), The ecological role of water-column microbes in the Sea, *Mar. Ecol. Prog. Ser.*, *10*, 257-263.

Badger, M. R., Andrews, T. J., Whitney, S. M., Ludwig, M., Yellowiees, D. C., Leggat, W., Prince G. D. (1997), The diversity and coevolution of Rubisco, plastids, pyrenoids, and chloroplast-based $CO_2$-concentrating mechanisms in algae, *Can. J. Botany*, *76*, 1052–1071.

Barlow, (2009), Satellite-detected fluorescence reveals global physiology of ocean phytoplankton, *Biogeosciences*, *6*, 779–794.

Bec, B., Husseni-Ratrema, J., Collos, Y., Souchu, P. and Vaquer, A. (2005), Phytoplankton seasonal dynamics in a Mediterranean coastal lagoon: emphasis on the picoeukaryote community, *J. Plankt. Res.*, *27*(9), 881–894.

Behrenfeld, M. J., O'Malley, R. T., Siegel, D. A., McClain, C. R., Sarmiento, J. L., Feldman, G. C., Milligan, A. J., Falkowski, P. G., Letelier, R. M., Boss, E. (2006), Climate-driven trends in contemporary ocean productivity, *Nature*, *444*, 752–755.

Behrenfeld, M. J., Westberry, T. K., Boss, E. S., O'Malley, R. T., Siegel, D. A., Wiggert, J. D., Franz, B.A.., McClain, C. R., Feldman, G. C., Doney, S. C., Moore, J. K., Dall'Olmo, G., Milligan, A.J., Lima, I., Mahowald, N. (2009), Satellite-detected fluorescence reveals global physiology of ocean phytoplankton, *Biogeosciences*, *6*, 779–794.

Berges, J. A., Falkowski, P. G. (1998), Physiological stress and cell death in marine phytoplankton: Induction of proteases in response to nitrogen or light limitation, *Limnol. Oceanogr.*, *43*(1), 129–135.

Bernard, G., Boudouresque, C.-F., Picon, P. (2007), Long term changes in Zostera meadows in the Berre lagoon (Provence, Mediterranean Sea), *Estuarine, Coastal and Shelf Science*, *73*, 617–629.

Bertilsson, S., O. Berglund, D. M. Karl and S. W. Chisholm (2003), Elemental composition of marine *Prochlorococcus* and *Synechococcus*: Implications for the ecological stoichiometry of the sea, *Limnol. Oceanogr.*, *48*(5), 1721–1731.

Béthoux, J.-P., Morin, P., Ruiz-Pino, D. (2002), Temporal trends in nutrients ratios: chemical evidence of Mediterranean ecosystem changes driven by human activity, *Deep Sea Res.*, *49*, 2007–2016.

Bhattacharya, D., Medlin, L. (1995), The phylogeny of plastids: A review based on comparisons of small subunit ribosomal RNA coding regions, *J. Phycol.*, *31*, 489-498.

Bialik, S., Zalckvar, E., Ber, Y., Rubinstein, A. D., Kimchi, A. (2010), Systems biology analysis of programmed cell death, *Trends in Bioch. Sci.*, *35*(10), 1–9.

Bidle, K. D. (2015), The Molecular Ecophysiology of Programmed Cell Death in Marine Phytoplankton, *Annu. Rev. Mar. Sci.*, *7*, 341–375.

Binder, B. J., Anderson, D. M. (1990), Biochemical composition and metabolic activity of Scripsiella trochoidea (Dinophyceae) resting cysts, *J. Phycol.*, *26*, 289-298.

Binder, B. J. and S. W. Chisholm (1995), Cell cycle regulation in marine *Synechococcus* sp. Strains, *Applied and environmental microbiology*, *61*(2), 708–717.

Bjorkman, K. M., Chruch, M. J., Doggett, J. K., Karl, D. M. (2015), Differential Assimilation of Inorganic Carbon and Leucine by Prochlorococcus in the Oligotrophic North Pacific Subtropical Gyre, *Frontiers*, *6*(1401), 1-14.

Bjornsen, P. K. (1988). Phytoplankton exudation of organic matter: Why do healthy cells do it?, *Limnol. Oceanogr.*, *33*(1), 151-154.

Bloom, J., Cross, F. R. (2008), Multiple levels of cyclin specificity in cell-cycle control, *Nature Reviews*, *8*, 149-160.

Bonhomme, P. (2006), Database of diazotrophs in global ocean: abundance, biomass and nitrogen fixation rates, *Earth Syst. Sci. Data*, *4*, 47–73.

Bonachela, J. A., Raghib, M., Levin, S. A. (2011), Dynamic model of flexible phytoplankton nutrient uptake, *PNAS*, *108*(51), 20633-20638.

Bonin, D. J. (1982), Dynamique nutritionnelle du phytoplancton, *Oceanis*, *8*, 459-492.

Bopp, L., Le Quéré, C., Heimann, M., Manning, M. C. (2002), Climate-induced oceanic oxygen fluxes: Implications for the contemporary carbon budget, *Global Biogeochemical cycles*, *16*(2), 1-13.

Bopp, L., Aumont, O., Cadule, P., Alvain, S., Gehlen, M. (2005), Response of diatoms distribution to global warming and potential implications: A global model study, *Geophys. Res. Lett.*, *16*(2), 1-4.

Boyce, D. G., Lewis, M. R., Worm, B. (2010), Global phytoplankton decline over the past century, *Nature*, *32*(19), 591–596.

Bravo, I., Figueroa, R. I. (2014), Toward and ecological understanding of dinoflagellate cyst functions, *Microorganisms*, *2*, 11–32.

Bremer, H., Churchward, G. (1994), Control of cyclic chromosome replication in Escherichia coli, *Microbiol. Rev*, *55*, 459-475.

Brzezinski, M. A., Olson, R. J., Chisholm, S. W. (1990), Silicon availability and cell cycle progression in marine diatoms, *Mar. Ecol. Prog. Ser.*, *67*, 83-96.

Buma, A. G., De Boer, M. K., Boeden, P. (2001), Depth distributions of DNA damage in antarctic marine phyto- and bacterioplankton exposed to summertime UV radiation, *J. Phycol.*, *37*, 200-208.

Burton, J. D., Maher, W. A., Statham, P. J. (1983), Some recent measurements of trace metals in Atlantic Ocean waters, *In Trace metals in sea water. NATO Conf. Ser. 4: Mar. Sci. 9. Plenum*, 415–426.

Caceres, C., Taboada, F. G., Hofer, J., Anadon, R. (2013), Phytoplankton Growth and Microzooplankton Grazing in the Subtropical Northeast Atlantic, *Plos ONE*, *8*(7), 1-13.

Campbell, W. H. (1988), Nitrate reductase and its role in nitrate assimilation in plants, *Physiologia Plantarum*, *74*(1), 214-219.

Capone, D. G., Zehr, J., Paerl, H. W., Bergman, B., Carpenter, E. J. (1997), Trichodesmium, a globally significant marine cyanobacterium, *Science*, *276*, 1221-1129.

Casellas, C., Pena, G., Picot, B., Illes, S., Bontoux, J., (1990), Nutrients in Thau lagoon: 10 grouping of contiguous geographical zones, *Water Res*, *24*, 1479-1489

Cassis, D. (2005), The effect of harmful algae on the summer mortality of juvenile pacific oysters (Crassostrea gigas), *MSc Thesis, British Columbia University*, 1-73.

Chapman, D. V., Dodge, J. D., Heany, S. I. (1982), Cyst formation in the freshwater dinoflagellate Ceratium hirundinella (Dinophyceae), *J. Phycol.*, *18*, 121-129.

Chepurnov, V. A., Mann, D. G., Sabbe, K., Vyverman, W. (2004), Experimental studies on sexual reproduction in diatoms, *Int Rev Cytol*, *237*, 91-154.

Chisholm, S. W. (1992), Phytoplankton size, *In Primary Productivity and Biogeochemical Cycles in the Sea, P. G. Falkowski and A. D. Woodhead, Plenum Press, NY*, 213-237.

Collins, S., Rost, B. and Rynearson, T. A (2014), Evolutionary potential of marine phytoplankton under ocean acidification, *In Evolutionary Applications, J. Wiley and Sons 7*, 140–155.

Collos, Y., Vaquer, A., Bibent, B., Slawyk, G., Garcia, N., Souchu, P., (1997), Variability in nitrate uptake kinetics of phytoplankton communities in a Mediterranean coastal lagoon, *Estuar. Coastal Shelf Sci*, *44*, 369-375.

Collos, Y., Bec, B., Jauzein, C., Abade, E., Laugier, T., Lautier, J., Pastoureaud, A., Souchu, P., Vaquer, A. (2009), Oligotrophication and emergence of picocyanobacteria and a toxic dinoflagellate in Thau lagoon, southern France, *J. Sea Res.*, *66*, 68–75.

Costas, E., Huertas, E., Baselga-Cervera B., Garcia-Balboa, C., Lopez-Rodas, V. (2014), Phytoplankton Ability to Physiological Acclimatization and Genetic Adaptation to Global Warming, *Int. J. Biol.*, *6*(4), 24–36.

Courties, C., Vaquer, A., Trousselier, M., Lauutier, J., Chrétiennot-Dinet, M. J., Neveux, J., Machado, C., Claustre, H. (1994), Smallest eukaryotic organism, *Nature*, *370*, 255,

Cross, F. R., Umen, J. G. (2015), The Chlamydomonas cell cycle, *The Plant J.*, *82*, 370-392.

Cullen, J. J. (1982), The Deep Chlorophyll Maximum: Comparing vertical profiles of chlorophyll a, *Can. J. Fish. Aqaut. Sci.*, *39*, 791-803.

Dagenais-Bellefeuille, S., Bertomeu, T., Morse, D. (2008), S-Phase and M-Phase Timing Are under Independent Circadian Control in the Dinoflagellate Lingulodinium, *J. Biol. Rythms*, 23(5), 400–408.

Dale, B. (1983), Dinoflagellate resting cysts: 'benthic plankton', *In Survival Strategies of the Algae, ed. Fryxell, G.A., Cambridge University Press, Cambridge*, 69–136.

Dall'Olmo, G., Boss, E., Behrenfeld, M. J., Westberry, T. K., Courties, C., Prieur, L., Pujo-Pay, M., Hardman-Mountford, N., Moutin, T. (2011), Inferring phytoplankton carbon and eco-physiological rates from diel cycles of spectral particulate beam-attenuation coefficient, *Biogeosciences*, 8, 3423–3440.

Della Tommasa, L., Danovaro, R., Belmonte, G., Boero, F. (2004), Resting stage abundance in the biogenic fraction of surface sediments from the deep Mediterranean Sea, *Sci. Mar.*, *68*, 103–111.

Delpy, F., Pagano, M. Blanchot, J., Thibault-Botha, D. (2013), Impact des changements hydrologiques sur la communauté zooplanctonique de l'étang de Berre : le cas des proliférations d'organismes gélatineux, in Lagun'R, ed GIPREB (Étang de Berre).

Denman, K. L., Gargett, A. E. (1983), Time and space scales of vertical mixing and advection of phytoplankton in the upper ocean, *Limnol. Oceanogr.*, *28*(5), 801–815.

Deveraux, Q. L., Takahashi, R., Salvesen, G. S., Reed, J. C. (1997), X-linked IAP is a direct inhibitor of cell death proteases, *Nature*, *388*, 300–303.

Descolas-Gros, C., De Billy, G. (1987), Temperature adaptation of RuBP carboxylase: kinetic properties in marine Antarctic diatoms, *J. Exp. Mar. Biol. Ecol.*, *108*, 147–158.

Donald, K., Scalan, D. J., Carr, N. G., Mann, N. H., Joint, I. (1997), Comparative phosphorus nutrition of the marine cyanobacterium Synechococcus WH7803 and the marine diatom Thalassiosira weissflogii, *J. Plankton Res.*, *19*(12), 1793–1813.

D'Ortenzio, F. and M. Ribera D'Alcala (2009), On the trophic regimes of the Mediterranean Sea: a satellite analysis, *Biogeosciences*, *6*, 139–148.

D'Ovidio, F., Fernandez, V., Hernandez-Garcia, E., Lopez, C. (2004), Mixing structures in the Mediterranean Sea from Finite-Size Lyapunov Exponents, *Geophys. Res. Lett.*, *31*, 1-4.

D'Ovidio, F., De Monte, S., Alvain, S., Dandonneau, Y., Lévy, M. (2010), Fluid dynamical niches of phytoplankton types, *PNAS*, 1-5.

Downing, J. A., Osenberg, C. W., Sarnelle, O. (1999), Meta-Analysis of marine nutrient-enrichment experiments: Variation in the magnitude of nutrient limitation, *Ecology*, *80*(4), 1157-1167.

Dupouy, C., Benielli-Gary, D., Neveux, J., Dandonneau, Y., Westberry, T. K. (2013), An algorithm for detecting Trichodesmium surface blooms in the South Western Tropical Pacific, *Biogeosciences*, *8*, 3631-3647.

Durand, M D. (1995), Phytoplankton Growth and Diel Variations in Beam Attenuation through Individual Cell Analysis, *MIT Ph D*, 1–263.

Durand, M., Green, R. E., Sosik, H. M., Olson, R. J. (2000), Diel variations in optical properties of micromonas pusilla a prasinophytes, *Ocean Optics XV Conference*.

Edwards, K. F., Thomas, M. K., Klausmeire, A., Litchman, E. (2015), Light and growth in marine phytoplankton: allometric, taxonomic, and environmental variation, *Limnol. Oceanogr.*, *60*, 540–552.

Eilers, P. H. C. and Peeters, J. C. H. (1988), A model for the relationship between light intensity and the rate of photosynthesis in phytoplankton, *Ecological Modelling*, *42*, 199–215.

Engel, A., Szlosek, J., Abramson, L., Liu, Z., Lee, C. (2009), Investigating the effect of ballasting by CaCO3 in Emiliania huxleyi: I. Formation, settling velocities and physical properties of aggregates, *Deep Sea Res. II*, *56*, 1396–1407.

Eppley, R. W., Rogers, J. N. and McCarthy, J. J. (1969), Half-saturation constants for uptake of nitrate and ammonium by marine phytoplankton, *Limnol. Oceanogr.*, *14*, 912-920.

Eppley, R. W. (1972), Temperature and phytoplankton growth in the sea, *Fishery bulletin*, *70*(40),1063–1085.

Falkowski, P. G. (1975), Nitrate uptake in marine phytoplankton: Comparison of half-saturation constants from seven specie, *Limnol. Oceanogr.*, *20*(3), 412-417.

Falkowski, P. G., Kiefer, D. A. (1985), Chlorophyll a fluorescence in phytoplankton: relationship to photosynthesis and biomass, *J Plankton Res.*, *7*(5), 715-731.

Falkowski, P. G. (1994), The role of phytoplankton photosynthesis in global biogeochemical cycles, *Photosynth. Res.*, *39*, 235-258.

Falkowski, P. G., Raven, J. A. (1997), Aquatic Photosynthesis, *Princeton University Press*, 1–484.

Falkowski, P. G., Barber, R. T. and Smetacek, V. (1998), Biogeochemical controls and feedbacks on Ocean Primary Production, *Science*, *281*, 200-206.

Falkowski, P. G., Katz, M. E., Knoll, A. H., Quigg, A., Raven, J. A., Schofield, O., Taylor and F. J. R. (2004), The evolution of modern eukaryotic phytoplankton, *Science*, *305*, 354–360.

Falkowski, P. G., Raven, J. A. (2007), Aquatic Photosynthesis, *Princeton University Press*, 1–484.

Fasham, M. J. R. (1990), A nitrogen-based model of plankton dynamics in the oceanic mixed layer, *J. Mar. Res.*, *48*, 591–639.

Field, C. B., Behrenfield, M. J., Randerson, J. T., and Falkowski, P. G. (1998), Primary production of the biosphere: integrating terrestrial and oceanic components. *Science 281*, 237–240.

Figueroa, R. I., Dapena, C., Bravo, I., Cuadrado (2015), The Hidden Sexuality of Alexandrium minutum: An Example of Overlooked Sex in Dinoflagellates, *Plos ONE*, *10*(1), 1–21.

Fogg, G. E. (1983), Relationships between metabolism and growth in plankton algae, *J. gen. Microbiol.*, *16*, 294–297.

Foster, R. A., Kuypers, M. M. M., Vagner, T., Paerl, R. W., Musat, N., Zehr, J. P. (2011), Nitrogen fixation and transfer in open ocean diatom cyanobacterial symbioses, *The ISME Journal*, *5*, 1484–1493.

Franklin, D. J., Brussaard, P. D., Berges, J. A. (2007), What is the role and nature of programmed cell death in phytoplankton ecology?, *Eur. J. Phycol.*, *41*(1), 1–14.

Frenkel, J., Vyverman, W., Pohnert,G. (2014), Pheromone signalling during sexual reproduction in algae, *The Plant J.*, *79*, 632–644.

Furnas, M.-J. (1991), Net in situ growth rates of phytoplankton in an oligotrophic, tropical shelf ecosystem, *Limnol. Oceanogr.*, *36*(1), 13–29.

Gao, Y., Smith, G. J., Alberte, R. S. (2000), Temperature dependence of nitrate reductase activity in marine phytoplankton: biochemical analysis and ecological implications,. *J. of Phycol.*, *36*, 304-313.

Geider, R. (1987), Light and temperature dependence of the carbon to chlorophyll ratio in microalgae and cyanobacteria: Implications for physiology and growth of phytoplankton, *New Phytol.*, *106*, 1-34.

Geider, R. (1993), Quantitative phytoplankton physiology: implications for primary production and phytoplankton growth, *ICES mar Sci. Symp.*, *197*, 52-62.

Geider, R., La Roche, J. (2002), Redfield revisited: variability of C:N:P in marine microalgae and its biochemical basis. *Eur. J. of Phycol.*, *37*(1), 1-17.

Gentleman, W., Leising, A., Frost, B., Strom, S., Murray, J. (2003), Functional responses for zooplankton feeding on multiple resources: a review of assumptions and biological dynamics. *Deep Sea Res. II*, *50*, 2847-2875.

Genty, B., Briantais, J.-M., Baker, N. R. (1989), The relationship between the quantum yield of photosynthetic electron transport and quenching of chlorophyll fluorescence. *Biochimica Biophysica Acta*, *990*, 87-92.

Glibert, P. M., Wilkerson, F. P., Dugdale, R. C., Raven, J. A., Dupont, C. L., Leavitt, P. R., Parker, A. E., Burkholder, J. M., Kana, T. M. (2016), Pluses and minuses of ammonium and nitrate uptake and assimilation by phytoplankton and implications for productivity and community composition, with emphasis on nitrogen-enriched conditions. *Limnol. Oceanogr.*, *61*, 165-197.

Goldman, J. C., McCarthy, J. J., and Peavey, D. G. (1979), Growth rate influence on the chemical composition of phytoplankton in oceanic waters. *Nature*, *279*, 210-215.

Goussias, C., Boussac, A., Rutherford, A. W. (2002), Photosystem II and photosynthetic oxidation of water: an overview, *Phil. Trans. R. Soc. Lond. B*, *357*, 1369–1381.

Gouze, E., Raimbault, P., Garcia, N., Bernard, G., and Picon, P. (2008), Nutrient and suspended matter discharge by tributaries into the Berre Lagoon (France): the contribution of flood events to the matter budget. *C. R. Geosci., 340*, 233-244.

Gribble, K. E., Anderson, D. M., Coats, D. W. (2009), Sexual and Asexual Processes in Protoperidinium steidingerae Balech (Dinophyceae), with Observations on Life-History Stages of Protoperidinium depressum (Bailey) Balech (Dinophyceae), *J. Eukaryot. Mcirobiol*, *56*(1), 88–103.

Grover, J. P. (1997), Resource competition, *In Chapman and Hall, London.*

Grover, J. P. (2000), Resource competition and community structure in aquatic micro-organisms: experimental studies of algae and bacteria along a gradient of organic carbon to inorganic phosphorus supply, *J. Plankton Res.*, *22*(8), 1591–1610.

Grover, J. P., Hsu, S.-B., Wang, F.-B. (2011), Competition between microorganisms for a single limiting resource with cell quota structure and spatial variation, *J. Math. Biol.*, *64*, 713–743.

Gruber, N., Sarmiento, J. L. (1997), Global patterns of marine nitrogen fixation and denitrification, *Global Biogeochemical Cycles*, *11*(2), 235–266.

Hader, D.-P., Kumar, H. D., Smith, R. C., Worrest, R. C. (2007), Effects of solar UV radiation on aquatic ecosystems and interactions with climate change, *Photochem. Photobiol. Sci.*, *6*, 267-285.

Hallegraeff, G. M. (2010), Ocean climate change, phytoplankton community responses and harmful algal blooms: A formidable predictive challenge, *J. Phycol.*, *46*, 220-235.

Harris, G. P. (1978), Photosynthesis, productivity and growth, *In The physiological ecology of phytoplankton, Advances in Limnology, 10*, 1-171.

Healey, F. P., Hendzel, L. L. (1979), Fluorometric measurement of alkaline phosphatase activity in algae, *Freshwater Biol.*, *9*, 429-439.

Heaney, S. I., Chapman, D. V., Morison, H. R. (1983), The role of the cyst stage in the seasonal growth of the dinoflagellate Ceratium hirundinella within a small productive lake, *B. Phycol. J.*, *18*(1), 47-59.

Hellweger, F. L. (2008), The role of inter-generation memory in diel phytoplankton division patterns, *Ecol. Modelling*, *212*, 382-396.

Henson, S. A., Sanders, R., Madsen, E., Morris, P. J., Le Moigne F., Quartly, G. D. (2011), A reduced estimate of the strength of the ocean's biological carbon pump, *Geophys. Res. Letters*, *38*, 1-5.

Hernandez-Becerril, D. U., Bravo-Sierra, E. (2003), Planktonic Silicoflagellates (Dictyochophyceae) from the Mexican Pacific Ocean, *Botanica Marina*, *44*, 417-423.

Hirata, T., Hardman-Mountford, N., Brewin, R. J. W., Aiken, K., Barlow, R., Suzuki, K., Isada, T., Howell, E., Hashioka, T., Noguchi-Aita, M., Yamanaka, Y. (1985), Synoptic relationships between surface Chlorophyll-a and diagnostic pigments specific to phytoplankton functional types, *Biogeosciences*, *8*(2), 311-327.

Hildebrand, M. Dahlin, K. (2000), Nitrate transporter genes from the diatom Cyclindrotheca fusiformis (Bacillariophyceae): mRNA levels controlled by nitrogen source and by the cell cycle, *J. Phycol*, *36*, 702-713.

Ho, T.-Y., Quigg, A., Finkel, Z. V., Milligan, A. J., Wyman, K., Falkowski, P. G.,Morel, F. M. M. (2003), The elemental composition of some marine phytoplankton, *J. Phycol.*, *39*, 1145–1159.

Horowitz, J., Normand, M. D., Corradini, M. G. and Peleg, M. (2010), Probabilisitic model of microbial cell growth, division and mortality, *App. Env. Mirc.*, *76*(1), 230–242.

Huertas, I. E., Rouco, M., Lopez-Rodas, V., Costas, E. (2010), Estimating the capability of different phytoplankton groups to adapt to contamination: Herbicides will affect phytoplankton species differently, *New Phytol.*, *188*, 478-487.

Huisman, J., Weissing, F. J. (1999), Biodiversity of plankton by species oscillations and chaos, *Lett. Nature*, *402*, 407-410.

Huneke, H., Mulder, T. (2011), Deep-Sea sediments, *A.J. Van Loon ed., Elsevier, Developments in sedimentology, 63*, 215-351.

Hutchinson, G. E. (1957), Concluding remarks, *In Cold Spring Harbor Symposia on Quantitative Biology*, *22*, 415–427.

Hutson, V. (1984), Predator mediated coexistence with a switching predator, *Math. Biosci.*, *68*, 233–246.

Jacquet, S., Partensky, F., Marie, D., Casotti, R., Vaulot, D. (2001), Cell Cycle Regulation by Light in Prochlorococcus Strains, *App. Env. Microbiol.*, 782–790.

Jeffrey, S. W. and Vesk, M. (1997), Introduction to maine phytoplankton and their pigment signatures, *In Jeffrey, S. W., Mantoura, F. C., Wright, S. W. eds., Phytoplankton pigments in Oceanography. UNESCO Publishing, Paris*, 85–126.

Jiao, N., Herndl, G. J., Hansell, D. 1., Benner, R., Kattner, G., Wilhelm, S. W., Kirchman, D. L., Weinbauer, M. G., Luo, T., Chen, F., Azam, F. (2010), Microbial production of recalcitrant dissolved organic matter: long-term carbon storage in the global ocean, *Nature*, *8*, 593–599.

Jimenez, C., Capasso, J. M., Edelstein, C. L., Rivard, C. J., Lucia, S., Breusegem, S., Berl, T., Segovia, M. (2009), Different ways to die: cell death modes of the unicellular chlorophyte Dunaliella viridis exposed to various environmental stresses are mediated by the caspase-like activity DEVDase, *J. Exp. Bot.*, *60*(3), 815–828.

Jorgensen, C. B. (1966), Biology of Suspension Feeding, *Limnol. Oceanogr.*, *11*(4), 649–650.

Kantha, L., Clayton, C. A. (2003), Ocean mixed layer, *Boundary Layers*, 291–298.

Khatiwala, S., Tanhua, T., Fletcher, S. M., Gerber, M., Doney, S. C., Graven, H. D., McKinley, G. A., Murata, A., Rios, A. F., Sabine, L. (2013), Global ocean storage of anthropogenic carbon, *Biogeosciences*, *10*, 2169-2191.

Kim, K. T. (1983), Production primaire pélagique de l'Etang de Berre en 1977 et 1978. Comparaison avec le milieu marin (Méditerranée nord-occidentale). *Mar. Biol.*, *73*, 325-341.

Kirchman, D. L (1994), The uptake of inorganic nutrients by heterotrophic bacteria, *Mar. Ecol.*, *28*, 255–271.

Kirchman, D. L (2002), Calculating microbial growth rates from data on production and standing stocks, *Mar. Ecol. Prog. Ser.*, *233*, 303–306.

Kirk, J T. O. (1994), Light and photosynthesis in Aquatic ecosystems, *2nd ed., Cambridge University Press*, *22*(7), 1311–1327.

Klausmeier, C. A. (2002), Calculating microbial growth rates from data on production and standing stocks, *Mar. Ecol. Prog. Ser.*, *233*, 303–306.

Klausmeier, C. A., Litchman, E., Levin, S. A. (2004), Phytoplankton growth and stoichiometry under multiple nutrient limitation, *Limnol. Oceanogr.*, *49*, 1463–1470.

Kolber, Z., Falkowski, P. G. (1993), Use of active fluorescence to estimate phytoplankton photosynthesis in situ, *Limnol. Oceanogr.*, *38*(8), 1646–1665.

Kremp, A., Anderson, D. M. (2000), Factors regulating germination of resting cysts of the spring bloom dinoflagellate Scrippsiella hangoei from the northern Baltic Sea, *J. Plankton Res.*, *22*(7), 1311–1327.

Krom, M. D., Kress, N., Brenner, S., Gordon, S. I. (1991), Phosphorus limitation of primary productivity in the eastern Mediterranean Sea, *Limnol. Oceanogr.*, *36*(3), 424–432.

Lakeman, M. B., Von Dassow, P., Cattolico, R. A. (2009), The strain concept in phytoplankton ecology, *Harmful Algea*, *8*, 746–758.

Landry, M. R., Hassett, R. P. (1982), Estimating the Grazing Impact of Marine Micro-zooplankton, *Mar. Biology*, *67*, 282–288.

Landry, M. R. (1994), Methods and controls for measuring the grazing impact of planktonic protists, *Mar. Microb. Food Webs*, *8*, 37–57.

Lavigne, H. (2013), Impact de la variabilité saisonnière de la profondeur de la couche de mélange sur le cycle saisonnier du phytoplancton en Méditerranée, *PhD Thesis*, 1–145.

LeBlanc, K. et al. (2012), A global diatom database. Abundance, biovolume and biomass in the world ocean, *Earth Syst. Sci. Data*, *4*, 149–165.

LeDiréach, L., Bonhomme, P., Brosse, L., Girard, P., Bodilis, P. (2013), Inventaire ichtyologique de l'étang de Berre 2008-2009, in Lagun'R, ed GIPREB (Étang de Berre).

Legendre, L., and LeFèvre, L. (1989), Hydrodynamical singularities as controls of recycled versus export production in oceans, in Productivity of the Ocean: Present and Past, ed W. H. Berger (Chichester: John Wiley Sons), 44–63.

Le Quéré, C., et al. (2005), Ecosystem dynamics based on plankton functional types for global ocean biogeochemistry models, *Global Change Biology*, *11*, 2016–2040.

Li, H-T., Han, X.-G., Wu, J.-G. (1993), Lack of Evidence for 3/4 Scaling of Metabolism in Terrestrial Plants, *J. Integrative Plant Biol.*, *47*(10), 1173–1183.

Li, W. K. W. (1993), Primary production of prochlorophytes, cyanobacteria, and eucaryotic ultraphytoplankton: Measurements from flow cytometric sorting, *Limnol. Oceanogr.*, *39*(1), 169–175.

Liebig, J. Von (1955), Principles of Agricultural chemistry with special reference to the late researches made in England, *In Cycles of essential elements, Benchmark papers in Ecology Vol.1, L.R. Pomeroy, 1974, Dowden, Hutchinson, Ross Inc., Stroudsburg, Pennsylvania*, 11–28.

Lilly, E.L., Kulis, D.M., Gentien, P., Anderson, D.M. (2002), Paralytic shellfish poisoning toxins in France linked to a human-introduced strain of Alexandrium catenella from the western Pacific: evidence from DNA and toxin analysis, *J. Plankton Res*, *24*, 443-452.

Lindemann, C., St John, M. A. (2014), A seasonal diary of phytoplankton in the North Atlantic, *Frontiers*, *1*(37), 1–6.

Lindermann, C., Fiksen, O, Andersen, K. H., Aksnes, D. (2016), Scaling laws in phytoplankton nutrient uptake affinity, *Frontiers*, *3*(26), 1–6.

Litchman, E (2007), Resource Competition and the Ecological Success of Phytoplankton, *In Falkowski and Knoll*, 351–375.

Lochte, K., Ducklow, H. W., Fasham, M. J. R., Stienen, C. (1993), Plankton succession and carbon cycling at 47°N 20°W during the JGOFS North Atlantic Bloom Experiment,*Deep Sea Res. II*, *40*(2), 91–114.

Longhurst, A. (1998), Ecological Geography of the Sea *San Diego Academic Press*, 1–560.

Lopez-Sandoval, D., Rodriuez-Ramos, T., Cermeno, P., Sobrino, C., Maranon, E. (2014), Photosynthesis and respiration in marine phytoplankton: Relationship with cell size, taxonomic affiliation, and growth phase, *J. Ecp. Mar. Biol. Ecol.*, *457*, 151–159.

Lotka, A. J. (1924), Elements of Physical Biology, *Williams, Wilkins Company*, 1–460.

Luo, Y.-W. et al. (2012), Database of diazotrophs in global ocean: abundance, biomass and nitrogen fixation rates, *Earth Syst. Sci. Data*, *4*, 47–73.

Lyons, T. W., Reinhard, C. T., Planavsky, N. J. (2014), The rise of oxygen in Earth's early ocean and atmosphere, *Nature*, *506*, 307–315.

Malkassian, A. (2012), Méthodes d'analyse Fonctionnelle et Multivariée Appliquées à l'etude du Fonctionnement Ecologique des Assemblages Phytoplanctoniques de l'étang de Berre. These de doctorat, Université d'Aix-Marseille, France.

Mante, C., Bernard, G., Bonhomme, P., Nerini, D. (2013), Application of ordinal correspondence analysis for submerged aquatic vegetation monitoring, *Journal of Applied Statistics*, *40*(8), 1619–1638.

Maranon, E. (2008), Inter-specific scaling of phytoplankton production and cell size in the field, *J. Plankton Res.*, *30*(2), 157–163.

Marcus, N. H., Boero, F. (1998), Minireview: The importance of benthic-pelagic coupling and the forgotten role of life cycles in coastal aquatic systems, *Limnol. Oceanogr.*, *43*(5), 763–768.

Margalef, R. (1978), Life-forms of phytoplankton as survival alternatives in an unstable environment, *Oceanol. Acta*, *1*(4), 493–509.

Markager, S., Jesperen, A.-M., Madsen, T. V., Berdalet, E., Weisburd, R. (1992), Diel changes in dark respiration in a plankton community, *Hydrobiologia*, *238*, 119–130.

Martinez, L. F., Mahamud, M. M., Lavin, A. G., Bueno, J. L. (2012), Evolution of phytoplankton cultures after ultraviolet light treatment, *Mar. Poll. Bull.*, *64*(3), 556–562.

Martin-Jézéquel, V., Hildebrand, M., Brzezinski (2000), Silicon metabolism in diatoms: Implications for growth, *J. Phycol.*, *36*, 821–840.

Mayot, N., F. D'Ortenzio, M. R. D'Alacala, H. Lavigne and H. Claustre (2016), Interannual variability of the Mediterranean trophic regimes from ocean color satellites, *Biogeosciences*, *13*, 1901–1917.

McGill, B. J., Enquist, B. J., Weiher, E., Westoby, M. (2006), Rebuilding community ecology from functional traits, *Trends Ecol. Evol.*, *21*(4), 178-185.

McMinn, A., Martin, A. (2013), Dark survival in a warming world, *Proc. R. Soc. B.*, *280*, 1–7.

McQuoid, M. R., Hobson, L. A. (2001), A Holocene record of diatom and silicoflagellate microfossils sediments of Saanich Inlet, ODP Leg 169S, *Marine Geology*, *174*(1-4), 111-123.

Menden-Deueur, S. and Lessard, E. J. (2000), Carbon to volume relationships for dinoflagellates, diatoms, and other protist plankton, *Limnol. Oceanogr.*, *45*(3), 569-579.

Miklasz, K. A., Denny, M. W. (2010), Diatom sinking speeds: Improved predictions and insight from a modified Stokes law, *Limnol. Oceanogr.*, *55*(6), 2513-2525.

Millot, C., Taupier-Letage, I. (2005), Circulation in the Mediterranean Sea, *Hdb Env Chem*, *5*, 29–66.

Minas, M. (1974), Distribution, circulation and evolution of nutrients, inorganic phosphorus particularly, in Lake Etang de Berre. Influence of river Durance waters, *In Internationale Revue Der Gesamten Hydrobiologie*, *59*, 509–542.

Minas, M. (1976), Primary Organic Production in a Brackish Eutrophic Environment (Etang De Berre) - Effects of Strong Dilution (Diversion of Waters of Durance), *Mar. Biol.*, *35*, 13–29.

Minas, H. J., Minas, M. (1992), Net community production in 'High Nutrient-Low Chlorophyll' waters of the tropical and Antarctic Oceans: grazing vs iron hypothesis, *Oceanologica Acta*, *15*(2), 145–162.

Moberg, E. A. and Sosik, H. M. (2012), Distance maps to estimate cell volume from two-dimensional plankton images, *Limnol. Oceanogr.: Methods*, *10*, 278–288.

Mocquet, C., Bernard, O., Sciandra, A. (2010), Cell cycle modeling of microalgae grown under a light-dark signal, *11$^{th}$ International Symposium on Computer Applications in Biotechnology Leuven, Belgium*, *45*(3), 174–179.

Mocquet, C., Sciandra, A., Talec, A., Bernard, O. (2012), Cell cycle implication on nitrogen acquisition and synchronization in Thalassiosira weissflogii (Bacillariophyta), *J. of Phycol.*, *49*(2), 371–380.

Moller, E. F., Nielsen, T. G. (2000), Production of bacterial substrate by marine copepods: Effect of phytoplankton biomass and cell size, *J. Plankton Res.*, *23*(5), 527–536.

Monod, J. (1949), The growth of bacterial cultures, *Annual review of microbiology*, *3*, 371–394.

Montagnes, D. J. S., Berges, J. A (1994), Estimating carbon, nitrogen, protein, and chlorophyll a from volume in marine phytoplankton, *Limnol. Oceanogr.*, *39*(5), 1044-1060.

Mooney, P. A., Van Staden, J. (1985), Algae and Cytokinins, *J. Plant Physiol.*, *123*, 1–21.

Moore, C. M. et al (2013), Processes and patterns of oceanic nutrient limitation, *Nature geoscience*, *6*, 701–710.

Morel, A., Smith, R. C. (1974), Relation between total quanta and total energy for aquatic photosynthesis, *Limnol. Oceanogr.*, *19*, 591–600.

Morel, A., Prieur, L. (1977), Analysis of variations in ocean color, *Limnol. Oceanogr.*, *22*, 709–722.

Morel, A. (1988), Optical modeling of the upper ocean in relation to its biogenous matter content (case 1 water), *J. Geophys. Res.*, *93*(10), 749–768.

Morel, F. M. M., Ruester, J. G., Prince, N. M. (1991), Iron nutrition of phytoplankton and its possible importance in the ecology of ocean regions with high nutrient and low biomass, *Oceanography*, *1*(2), 56–61.

Morel, A., Ahn, Y.-H., Partensky, F., Vaulot, D., Claustre, H. (1993), Prochlorococcus and Synechococcus: A comparative study of their optical properties in relation to their size ad pigmentation, *J. Mar. Res.*, *51*, 617–649.

Morel, A. (2006), Meeting the challenge of monitoring chlorophyll in the ocean from outer space. Advance in Photosynthesis and respiration, *In Series Editor Godvindje, Springer, 25, Chlorophylls and Bacteriochlorophylls, B. Grimm, R.J. Porra, W. Rûdiger, and H. Scheer eds. Chap. 36*, 521–535.

Muller, E. B., Antia, A. N., LaRoche, J. (2008), Influence of cell cycle phase on calcification in the coccolithophore Emiliania huxleyi, *Limnol. Oceanogr.*, *53*(2), 506–512.

Muller, E. B., Ananthasubramaniam, B., Klanjseck, T., Nisbet, R. M. (2011), Entrainment of cell division in phytoplankton with dynamic energy budgets, *J. Sea Res.*, *66*, 447–455.

Murdoch, W. W. (1969), Switching in general predators: experiments on predator specificity and stability of populations, *Ecol. Monogr.*, *39*, 335–354.

Nair, A., Sathyendranath, S., Platt, T., Morales, J., Stuart, V., Forget, M.-H., Devred, E. and Bouman, H. (2008), Remote sensing of phytoplankton functional types, *Remote sensing of environment*, *112*, 3366–3375.

Nalewajko, C., Lean, D. R. S. (1980), Phosphorus, *In: Morris, I. (Ed.), The Physiological Ecology of Phytoplankton. University of California Press, Berkeley, CA*, 235–258.

Naselli-Flores, L., Padisak, J., Dokulil, M. T., Chorus, I. (2003), Equilibrium/steady-state concept in phytoplankton ecology, *Hydrobiologia*, *502*, 395–403.

Nehring, S. (1993), Mechanisms for recurrent nuisance algal blooms in coastal zones: resting cyst formation as life-strategy of dinoflagellates, *In Sterr, H., Hofstade, J., Plag, H.-P. eds., Interdisciplinary Discussion of Coastal Research and Coastal Management Issues and Problems*, 454–467.

Nerini, D., Mante, C., Durbec, J.-P., and Garcia, F. (2001), Une méthode statistique de détermination de séquences caractéristiques dans une série temporelle de plusieurs variables. Application à la physico-chimie des eaux de l'étang de Berre. *C.R.Acad.Sci.II. 332*, 457-464.

Ness, R. W., Morgan, A. D., Colegrave, N., Keightley, P. D. (2012), Estimate of the Spontaneous Mutation Rate in Chlamydomonas reinhardtii, *Genetics*, *192*(4), 1477–1454.

Neuer, S. (1992), Growth dynamics of marine Synechococcus spp. in the Gulf of Alaska,*Mar. Ecol. Prog. Ser.*, *83*, 251–262.

Olita, A., S. Sparnocchia, S. Cusi, L. Faziolo, R. Sorgente, J. Tinore and A. Ribotti (2014), Observations of a phytoplankton spring bloom onset triggered by a density front in NW Mediterranean, *Ocean Sci.*, *10*, 657–666.

Olson, R. J., Vaulot, D., Chisholm, S. W. (1986), Effects of environmental stresses on the cell cycle of two marine phytoplankton species, *Plant Physiol.*, *80*, 918–925.

O'Neil, J. M., Metzler, P. M., Glibert, P. M. (1996), Ingestion of $^{15}N_2$-labelled Trichodesmium spp. and ammonium regeneration by the harpacticoid copepod Macrosetella gracilis, *Marine biology*, *125*(1), 89–96.

Palmucci, M., Ratti, S., Giordano, M. (2011), Ecological and evolutionary implications of carbon allocation in marine phytoplankton as a function of nitrogen availability: A Fourier transform infrared spectroscopy approach, *J. Phycol.*, *47*, 313–323.

Parsons, T. R., LeBrasseur, R. J., Fulton, J. D. (1967), Some observations on the dependence of zooplankton grazing on the cell size and concentration of phytoplankton blooms, *J. Oceanogr. S. Jap.*, *23*(1), 10–17.

Partensky, F., Hess, W. R., Vaulot, D. (1999), Prochlorococcus, a Marine photosynthetic prokaryote of global significance, *Microb. Molecul. Biol. Rev.*, *63*(1), 106–127.

Perez-Ruzafa, A., Marcos, C., Perez-Rzafa, L. M. (2011), Mediterranean coastal lagoons in an ecosystem and aquatic resources management context, *Physics and Chemistry of the Earth*, *36*, 160–166.

Pfiester, L. A., Anderson, D. M. (1987), Dinoflagellate reproduction, *In Taylor, F.J.R. ed., The Biology of Dinoflagellates. Botanical Monographs, Volume 21. Oxford, Blackwell Scientific Publications*, 611–648.

Phinney, D. A., Cucci, T. L. (1989), Flow cytometry and phytoplankton, *Cytometry*, *10*, 511–521.

Pitcher, G. C., Probyn, T. A., Du Randt, A., Lucas, A. J., Bernard, S., Evers-King, H., Lamont, T., Hutchings, L. (2014), Dynamics of oxygen depletion in the nearshore of a coastal embayment of the southern Benguela upwelling system, *J. Geophys. Res.*, *119*, 2183–2200.

Plaetzer, K., Randall, T. S., Falkner, R., Falkner, G. (2005), The microbial experience of environmental phosphate fluctuations. An essay on the possibility of putting intentions into cell biochemistry, *J. of Theoretical Biol.*, *365*, 540–554.

Platt, T., Denman, K. L. and Jassby, A. D. (1975), The mathematical representation and prediction of phytoplankton productivity, *Fisheries and marine service, Technical report 523*, 1–110.

Prasil , O., Adir, N., Ohad, I. (1992), Dynamics of photosystem II: mechanism of photoinhibition and recovery processes, *In J Barber, ed, Topics in Photosynthesis, 11. Elsevier, Amsterdam*, 293–348.

Probyn, T. A. (1992), The inorganic nitrogen nutrition of phytoplankton in the southern Benguela: new production, phytoplankton size and implications for pelagic food webs, *S. Afr. J. mar. Sci.*, *12*, 411–420.

Probyn, T. A., Waldron, H. N., Searson, S., Owens, N. J. P. (1996), Diel variability in nitrogenous nutrient uptake at photic and subphotic depths, *J. Plankton Res.*, *18*(11), 2063–2079.

Pujo-Pay, M., Conan, P., Oriol, L., Cornet-Barthaux, V., Falco, C., Ghiglione, J.-F., Goyet, C., Moutin, T. and Prieur, L. (2011), Integrated survey of elemental stoichiometry (C, N, P) from the western to eastern Mediterranean Sea, *Biogeosciences*, *8*, 883–899.

Raimbault, P., Beker, B., Garcia, N., Fornier, M., and Gouze, E. (2013), L'étang de Berre, cycle de la matière, production primaire et communautés phytoplanctoniques, in Lagun'R, ed GIPREB (Étang de Berre).

Raven, J. A., Johnston, A. M. (1991), Mechanisms of inorganic-carbon acquisition in marine phytoplankton and their implications for the use of other resources, *Limnol. Oceanogr.*, *36*(8), 1701–1714.

Raven, J. A., Waite, A. M. (2004), The evolution of silicification in diatoms: inescapable sinking and sinking as escape?, *New Phycol.*, *162*, 45–61.

Raven, J. A., Giordano, M., Beardall, J., Maberly, S. C. (2012), Algal evolution in relation to atmospheric $CO_2$: carboxylases, carbon-concentrating mechanisms and carbon oxidation cycles, *Phil. Trans. R. Soc. B.*, *367*, 493–507.

Redfield, A. C. (1934), On the proportions of organic derivatives in sea water and their relation to the composition of plankton, *in James Johnstone Memorial Volume ed. Daniel, R. J., Liverpool Univ. Press, Liverpool*, 176-192.

Rengefors, K., Karlsson, I., Hansson, L.-A. (1998), Algal cyst dormancy: a temporal escape from herbivory, *Proc. R. Soc. Lond. B.*, *265*, 1353–1358.

Reynolds, C. S. (1980), Phytoplankton assemblages and their periodicity in stratifying lake systems, *Holarctic Ecol.*, *3*, 141–159.

Reynolds, C. S., Padisak, J., Sommer, U. (1993), Intermediate disturbance in the ecology of phytoplankton and the maintenance of species diversity: a synthesis, *Hydrobiologia*, *249*, 183–188.

Reynolds, C. S. (2006), The ecology of phytoplankton, *ed. C. S. Reynolds. Cambridge University Press, 2006.*

Reibeiro, S., Berge, T., Lundholm, N., Andersen, T. J., Abrantes, F., Ellegaard, M. (2014), Phytoplankton growth after a century of dormancy illuminates past resilience to catastrophic darkness, *Nature comm.*, *2:311*, 1-7.

Riding, R. (1992), The algal breath of life, *Nature*, *359*, 13–14.

Riemann, B., Simonsen, P., Stensgaard, L. (1989), The carbon and chlorophyll content of phytoplankton from various nutrient regimes, *J. Plankton Res.*, *11*(5), 1037–1045.

Rigual-Hernandez, A. S., Barcena, M. A., Sierro, F. J., Flores, J. A., Hernandez-Almeida, I., Sanchez-Vidal, A., Palanques, A., Heussener, S. (2010), Seasonal to interannual variability and geographic distribution of the silicoflagellate fluxes in the Western Mediterranean, *Marine Micropaleontology*, *77*, 46–57.

Riley, G. A., Stommel, H., Bumpus, D. F. (1949), Quantitative ecology of the plankton of the Western-North Atlantic, *Bull. Bingham Oceanogr. Coll.*, *12*, 1–169.

Robinson, A. R. and M. Golnaraghi (1994), The physical and dynamical oceanography of the Mediterranean Sea, *P. Malanotte-Rizzoli and A.R. Robinson (eds) Ocean Processes in Climate Dynamics: Global and Mediterranean Examples, NATO ASI Ser. C: Math and Phys. Sci. Springer*, 255-301.

Roelke, D. L., Spatharis, S. (2015), Phytoplankton Succession in Recurrently Fluctuating Environments, *PLOS ONE*, 1–17.

Roether, W. Jean-Baptiste, P., Fourré, E., Sultenfub, J. (2013), The transient distributions of nuclear weapon-generated tritium and its decay product $^3$He in the Mediterranean Sea, 1952-2011, and their oceanographic potential, *Ocean Sci*, *9*, 837-854.

Ross, O. N., Geider, R. J. (2009), New cell-based model of photosynthesis and photoacclimation: accumulation and mobilisation of energy reserves in phytoplankton, *Mar. Ecol. Prog. Ser.*, *383*, 53–71.

Rost, B., Riebesell, U., Burkhardt, S. (2003), Carbon acquisition of bloom-forming marine phytoplankton, *Limnol. Oceanogr.*, *48*(1), 55–67.

Ryther, J. H., Menzel, D. W. (1959), Light adaptation by marine phytoplankton, *Limnol. OCeanogr.*, *4*, 492–497.

Sabine, C. L. et al. (2004), The oceanic sink for anthropogenic $CO_2$, *Science*, *305*, 367–371.

Salter, I., Schiebel, R., Ziveri, P., Movellan, A., Lampitt, R., Wolff, G. A. (2014), Carbonate counter pump stimulated by natural iron fertilization in the Polar Frontal Zone, *Letters Nature*, *7*, 885–889.

Sarmiento, J. L., Gruber, N. (2006), Ocean Biogeochemical Dynamics, *Princeton University Press* , 1–526.

Sarthou, G., Timmermans, K. R., Blain, S., Tréguer, P. (2005), Growth physiology and fate of diatoms in the ocean: a review, *J. of Sea Research*, *53*, 25–42.

Schmidt, S., Harlay, J., Borgres, A. V., Groom, S., Delille, B., Roevros, N., Christodoulou, S., Chou, L. (2013), Particle export during a bloom of Emiliania huxleyi in the North-West European continental margin, *J. mar. Syst.*, *109-110*, 5182-5190.

Schneider, A., Tanhua, T., Kortzinger, A., Wallace, D. W. R. (2010), High anthropogenic carbon content in the eastern Mediterranean, *J. of Geophys. Research*, *115*, 1–11.

Schoemann, V., Becquevort, S., Stefels, J., Rousseau, V., Lancelot, C. (2004), Phaeocystis blooms in the global ocean and their controlling mechanisms: a review, *Limnol. Oceanogr.*, *37*, 1434-1446.

Segovia, M., Berges; J. A. (2009), Inhibition of caspase-like activities prevents the appearance of reactive oxygen species and dark-induced apoptosis in the unicellular chlorophyte Dunaliella tertiolecta, *J. of Phycol.*, *45*, 1116–1126.

Séverin, T., P. Conan, X. Durrieu de Madron, L. Houpert, M-J Oliver, L. Oriol, J. Caparros, J. F. Ghiglione and M. Pujo-Pay (2014), Impact of open-ocean convection on nutrients, phytoplankton biomass and activity, *Deep-Sea Research I*, *94*, 62–71.

Sieburth, J., V. Smetacek and J. Lenz (1978), Pelagic ecosystem structure: Heterotrophic compartments of the plankton and their relationship to plankton size fractions, *J. of Sea Research*, *53*, 43–66.

Siegenthaler, U., Sarmiento, J. L. (1993), The Guild Concept and the Structure of Ecological Communities, *Annu. Rev. Ecol. Syst.*, *22*, 115-143.

Sigee, D. C., Selwyn, A., Gallois, P., Dean, A. P. (2007), Patterns of cell death in freshwater colonial cyanobacteria during the late summer bloom, *Phycologia*, *46*(3), 284–292.

Simberloff, D., Dayan, T. (1991), Atmospheric carbon dioxide and the ocean, *Nature*, *365*, 119–125.

Sims, P. A., Mann, D. G., Medlin, L. K. (2006), Evolution of the diatoms: insights from fossil, biological and molecular data, *Phycologia*, *45*(4), 361–402.

Souchu, P., Vaquer, A., Collos, Y., Landrein, S., Deslous-Paoli, J.M., Bibent, B. (2001), Influence of shellfish farming activities on the biogeochemical composition of the water column in Thau lagoon, *Mar. Ecol. Prog. Ser.*, *218*, 141–152.

Sournia, A. (1973), La production primaire planctoniques en Méditerranée, Essai de mise à jour, *Bulletin de l'Etude en commun de la Méditerranée, numero spécial*, *5*, 1–128.

Steindinger, K. A. (1975). Basic factors influencing red tides, *In Proceedings of the first international conference on toxic dinoflagellate blooms. ed. V R. LoCicero. Mass. Sci. Technol. Found., Wakefield*, 153–162.

Stora, G., Arnous, A. (1983), Effects of Large Freshwater Diversions o n Benthos of a Mediterranean Lagoon, *Estuarines*, *6*(2), 115–125.

Strathmann, R. R. (1967), Estimating the organic carbon content of phytoplankton from cell volume or plasma volume, *Limnol. Oceanogr.*, *12*(3), 411-418.

Stross, R. G., Pemrick, S. M. (1974), Nutrient uptake kinetics in phytoplankton: A basis for niche separation. *J. Phycol.*, *10*, 164–169.

Swift, D. G. (1980), Vitamins and growth factors *In The physiological ecology of phytoplankton, ed. Morris I., Oxford, Blackwell*, 329–368.

Takahashi, J. S. (1992), Circadian clock genes are ticking, *Science*, *258*, 238–240.

Taniguchi, D.. A. A., Franks, P. J., Poulin, F. J. (2014), Planktonic biomass size spectra: an emergent property of size-dependent physiological rates, food web dynamics, and nutrient regimes, *Mar. Ecol. Prog. Ser.*, *514*, 13–33.

Tang, Y. Z., Gobler, C. J. (2015), Sexual resting cyst production by the dinoflagellate Akashiwo sanguinea: a potential mechanism contributing to the ubiquitous distribution of harmful algae, *J. Phycol.*,*51*, 298–309.

Thomas, M. K., Kremer, C. T., Klausmeier, C. A., Litchman, E. (2012), A global pattern of thermal adaptation in marine phytoplankton, *Science*, *338*, 1085–1088.

Thornton, D. C. O. (2014), Dissolved organic matter (DOM) release by phytoplankton in the contemporary and future ocean, *Env. J. Phycol.*, *49*(1), 20–46.

Thyssen, M., S. Alvain, A. Lefèbvre, D. Dessailly, M. Rijkeboer, N. Guiselin, V. Creach and L. F. Artigas (2015), High-resolution analysis of a North sea phytoplankton community structure based on in situ flow cytometry observations and potential implications for remote sensing, *Biogeosciences*, *12*, 4051–4066.

Tilman, D. (1982), Resource competition and community structure, *In Monogr. Pop. Biol. 17. Princeton University Press, Princeton*, 1–296.

Toselannd, A., Daines, S. J., Clark, J. R., Kirkham, A., Straussn J., Uhlig, C., Lenton, T. M., Valentin, K., Pearson, G. A., Moulton, V., Mock, T. (2013), The impact of temperature on marine phytoplankton resource allocation and metabolism, *Nature climate change*,*3*, 979–984.

Tsutsui, H., Tkahashi, K., Nishida, S., Nishiwaki, N. (2009), Intraspecific morphological variation with biometry of Distephanus speculum (Silicoflagellata), *Marine Micropaleotonlogy*, *72*, 239-250.

Tyrrell, T., Maranon, E., Poutlton, A. J., Bowie, A. R., Harbour, D. S., Malcolm, E., Woodward, S. (2003), Large-scale latitudinal distribution of Trichodesmium spp. in the Atlantic Ocean, *J. Plankton Res.*, *25*(4), 405–416.

Uitz, J., Huot, Y., Bruyant, F., Babin, M., Claustre, H. (2008), Relating phytoplankton photophysiological properties to community structure on large scales, *Limnol. Oceanogr.*, *53*(2), 614–630.

Uitz, J., Claustre, H., Gentili, B. and Stramski, D. (2010), Phytoplankton class-specific primary production in the world's oceans: Seasonal and interannual variability from satellite observations. *Global Biogoechemical cycles*, *24*, 1–19.

Uitz, J., D. Stramski, B. Gentili, F. D'Ortenzio and H. Claustre (2012), Estimates of phytoplankton class-specific and total primary production in the Mediterranean Sea from satellite ocean color observation, *Global biogeochemical cycles*, *26*, 1–10.

Vardi, A., Berman-Frank, I., Rozenberg, T., Hadas, O., Kaplan, A., Levine, A. (1999), Programmed cell death of the dinoflagellate Peridinium gatunense is mediated by $CO_2$ limitation and oxidative stress, *Cur. Biol.*, *23*(9), 1061–1064.

Vardi, A., Eisenstadt, D., Murik, O., Berman-Frank, I., Zohary, T., Levine, A., Kaplan, A. (2007), Synchronization of cell death in a dinoflagellate population is mediated by an excreted thiol protease, *Env.. Microbiol*, *9*, 360–369.

Vaulot, D., Frisoni, G.-F. (1986), Phytoplanktonic productivity and nutrients in five Mediterranean, *Oceanologica Acta*, *9*, 57–64.

Vaulot, D., Olson, R. J., Merkel, S. M., Chisohlm, S. W. (1987), Cell cycle response to nutrient starvation in two marine phytoplankton species, *Mar Biol*, *95*, 625–630.

Vaulot, D., Chisholm, S. (1987), A simple model of the growth of phytoplankton populations in light/dark cycles, *J. Plankton Res.*, *9*(2), 345–366.

Vaulot, D., Marie, D., Olson, R. J. and Chisholm; S. W. (1995), Growth of *Prochlorococcus*, a photosynthetic prokaryote, in the Equatorial Pacific Ocean, *Science*, *268*, 1480–1482.

Vérity, P. G., Robertson, C. Y., Tronzo, C. R., Andrews, M. G., Nelson, J. R. and Sieracki, M. E. (1992), Relationships between cell volume and carbon and nitrogen content of marine photosynthetic nanoplankton, *Limnol. Oceanogr.*, *37*, 1434–1446.

Volterra, V. (1926), Fluctuations in the abundance of a species considered mathematically, *Nature*, *118*, 558–560.

Von Dawson, P., Montresor, M. (2011), Unveiling the mysteries of phytoplankton life cycles: patterns and opportunities behind complexity, *J. Plankton Res.*, *33*(1), 3–12.

Williams, R. J., Martinez, N. D. (2000), Simple rules yield complex food webs, *Nature*, *404*(9), 180-1-83.

Webb, W. L., Newton, M., Starr, D.(1974), Carbon Dioxide Exchange of Alnus rubra: A Mathematical Model, *Ecologia*, *17*, 281–291.

White, W. B., Cayan,D. R. (1998), Quasi-periodicity and global symmetries in interdecadal upper ocean temperature variability, *J. Geophys. Res.*, *103*(C10), 335–354.

Yentsch, C. S. (1962), Measurement of visible light absorption by particulate matter in the ocean, *Limnol. Oceanogr.*, *7*(2), 207–217.

Yentsch, C. S., Menzel, D. W. (1963), A method for the determination of phytoplankton chlorophyll and phaeophytin by fluorescence, *Deep Sea Res.*, *10*, 221–231.

Young, J. R. (1994), Functions of coccoliths. *In: Winter, A. and Siesser, W.G., Eds., Coccolithophores, Cambridge University Press, New York*, 13–27.

Zehr, J. P., Waterbury, J. B., Turner, P. J., Montoya, J. P., Omoregie, E., Steward, G. F., Hansen, A., Karl, D. M. (2001), Unicellular cyanobacteria fix N2 in the subtropical North Pacific Ocean, *Nature*, *412*, 635–638.

Zigone, A., Sarno, D., Siano, R., Marino, D. (2011), The importance and distinctiveness of small-sized phytoplankton in the Magellan Straits, *Polar Biol*, *34*, 1269–1284.

## A.0 Automated flow cytometry

Flow cytometry has been transposed from the medical field to the oceanographic field to count cells suspended in a liquid medium at high speed (up to several thousands cells per second). To count particles, this techniques uses the natural (i.e. autofluorescence) or induced (i.e. fluorochromes) emission of fluorescence and the light scattered by the passage of the cells in a laser beam. Phytoplankton cells are particularly adapted to optical analyses since they contain molecules of chlorophyll a that fluoresce under an exciting light (Table 1.2). Automated devices have been developed to sustain the high frequency analyses of phytoplankton without a need to operate the instrument manually. The approach improved our understanding of phytoplankton dynamics considering its variability in the Sea.

The Cytosense (Cytobuoy, b.v.) uses a 488 nm laser beam to measure the autofluorescence of phytoplankton cells of size 0.8-800 $\mu$m. Phytoplankton cells are triggered by the emission of red fluorescence above a threshold level fixed for each instrument setting. This level may be defined by analysing 0.2 $\mu$m filtered water, free of phytoplankton, and decreasing progressively its value at an appropriate level of electronic noise. Fluorescences and light scattered at 90° are collected by photomultipliers (PMTs) that convert photons into electrons. The signal scattered at small angles is collected by photodiodes. The sample is pumped by a calibrated peristaltic pump and driven in the fluidic circuit by the sheath fluid running at speed 2 m.s$^{-1}$. Upon contact with the free-particle sheath fluid, the flow of cells is aligned to allow single-cell analysis of optical properties. The sheath fluid is continuously recycled during analyses by a set of filters (porosity of 0.1 and 0.45 $\mu$m).

Red (FLR), Orange (FLO), Yellow fluorescences (FLY), Forward (FWS) and Sideward (SWS) scatter light pulses are converted into electrons with a frequency of 4 MHz. The resolution of 0.5 $\mu$m of the 5 optical signals has been configured to identify peculiar cells, such as chains, by their pulse shape, and provide robust statistical descriptors, in addition to pictures taken by an integrated camera (image-in-flow). The usual descriptors of cells optical fingerprints used to discriminate groups in this manuscript are the individual integrated signal (Total), the timeframe of cells' passage in the laser beam converted to $\mu$m (Length) and the maximum of the signal (Max).

The Cytoclus software (updated versions, cytobuoy, b.v.) was used to define group of phytoplankton analysed by the Cytosense. Optical descriptors were projected on 2D plots (cytograms) to discriminate groups of cells sharing similar optical fingerprints. Examples of cytograms are given in Chapter 2, 3, 4 and 5. The main statistics of cells (Total, Length, Max for each optical signal) were exported in batch for further valorisations. Each export contained: the average, minimum and maximum values of each descriptor group in 'Avgs' files, their entire distribution per group in 'listmodes' files, the abundance per group in 'Counts' files and the pictures (up to 150 pictures per analysis). Listmodes were used as inputs for the population models detailed in appendix D.

The consolidation of the exported data (e.g. Avgs, Counts and pictures) has been

implemented on a R-dependent GUI application to support the development of a local database (http://www.mio.univ-amu.fr/cytobase/index.php). The application allows to:

1. consolidate the outputs of batch processes into a single table
2. merge the table with sampling coordinates based on the analysis date
3. complete with metadata
4. select pictures

The interface is shown in Figure A.1.

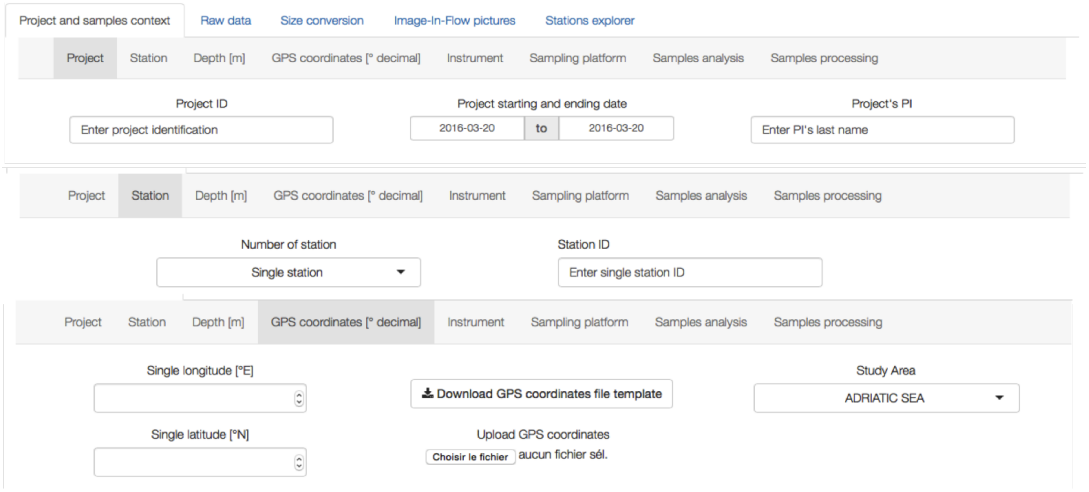


(a) Panel of metadata

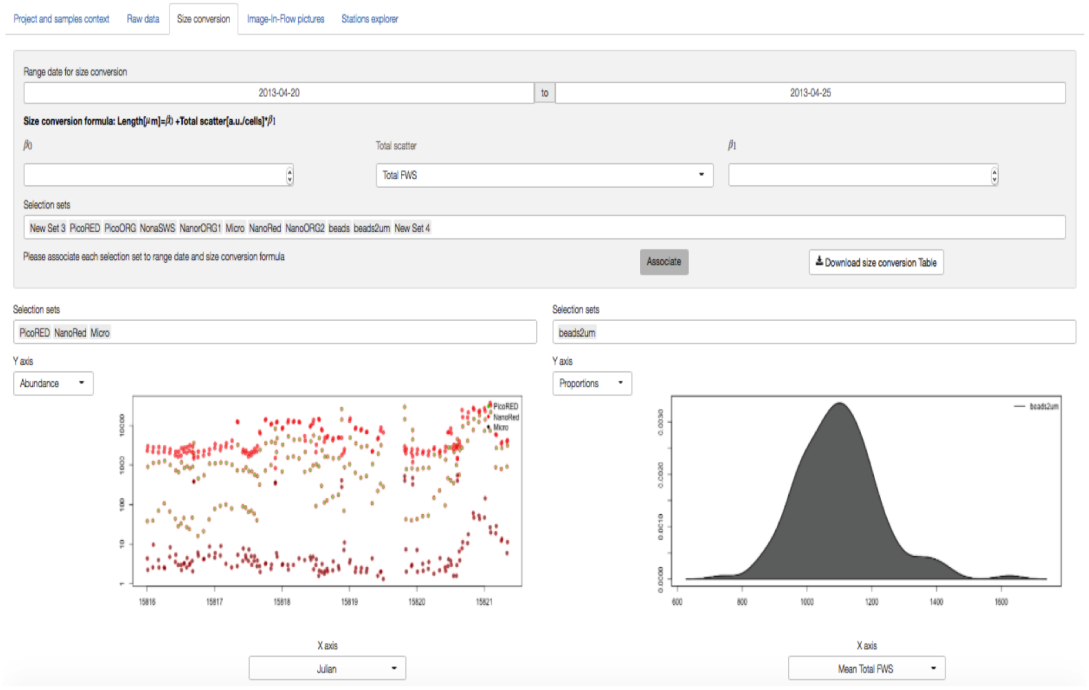


(b) Panel of size conversion

Figure A.1: Cytobase Pre-Processing tools

## B.0 Image Analyses and estimation of 3D volume

To convert cells' optical signal (e.g. light scatter) collected by flow cytometry into cell size, size calibration beads were primarily analysed with the Cytosense. A set of yellow fluorescing Polystyrene beads of diameter 2.0, 3.0, 6.0, 20.0 $\mu$m were analysed for the DeWEX cruises although their refractive index induce a scattering overestimation (Chapter 4). Silicate beads, with a refractive index close to phytoplankton cells, were used in controlled experiments (Chapter 2). For the high frequency survey conducted in the Berre lagoon, the regression was based on image analyses (Chapter 3).

In addition to standard beads, the image-in-flow pictures were used systematically to calibrate the scatter signal into biovolume for large cells (> 10 $\mu$m). The camera being not resolutive enough for cells smaller than 10 $\mu$m. Estimations of cells' biovolume from 2D pictures were made following the algorithm of Moberg and Sosik (2012). The algorithm is based on distance matrices (Fig. B.1).

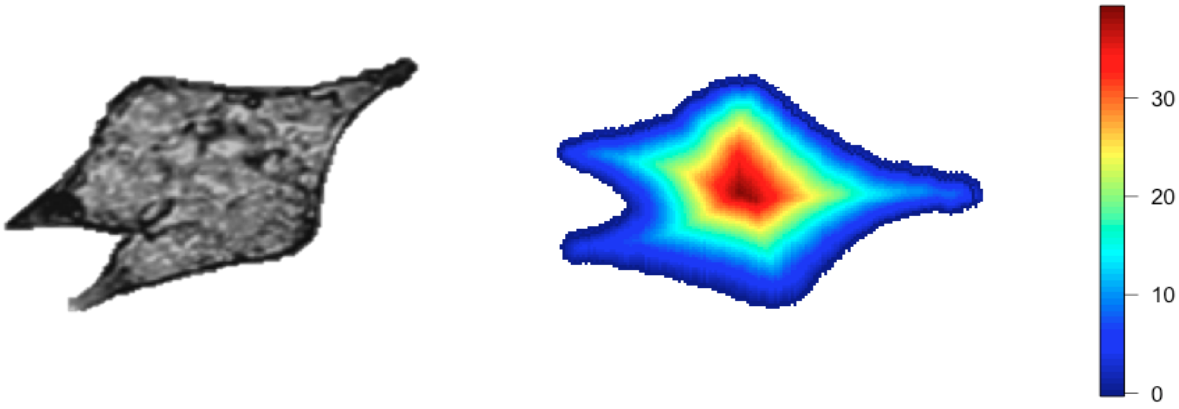


(a) Original 2D image

(b) Distance matrice. The colorbar represents the pixels' distance to the nearest contour pixel

Figure B.1: *Protoperidinium* 3D reconstruction

Distance matrices are squared matrices, whose dimensions are determined by the number of pixels in the picture, which summarise the distance of each pixel to its nearest contour pixel. The 2D distances are transposed on the $3^{rd}$ dimension to reconstruct the 2D images in 3D with voxels. The biovolume of the cells corresponds to the integral of the voxels. The algorithm is sensitive to the resolution of the pixel, determining the discretisation of the integral. 3D reconstructions of *Protoperidinium* and a zooplankton are shown in Figures B.2 and B.3 respectively.

(a) Original 2D image (b) 3D reconstruction

Figure B.2: *Protoperidinium* 3D reconstruction

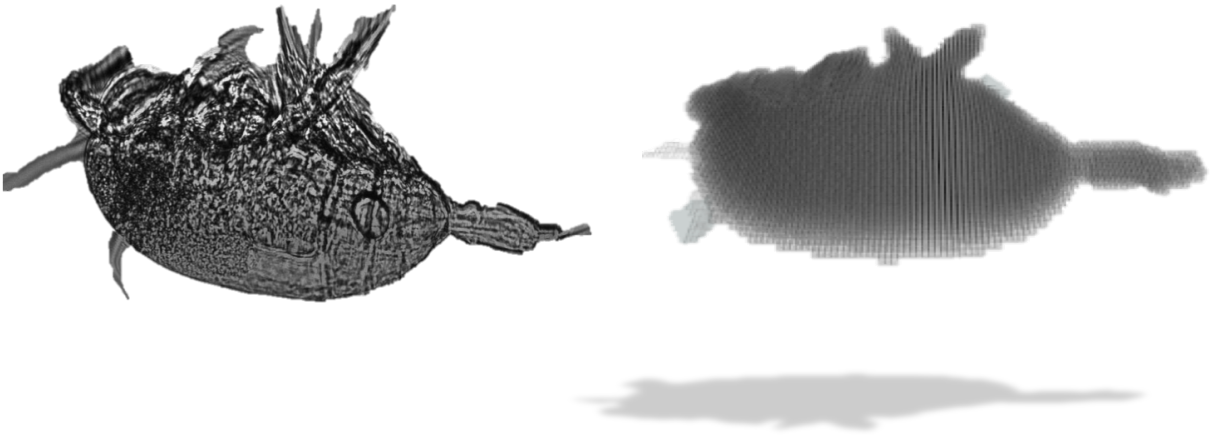

(a) Original 2D image (b) 3D reconstruction

Figure B.3: A zooplankton 3D reconstruction

## C.0 Bayesian statistics

Bayesian statistics are employed to infer models parameters values and their uncertainties. Determinist or stochastic models aim at either adjusting a known empiric or mechanistic relation to a dataset or run a model including some random effects. In the context of a new study, Bayesian statistics are used to confront the estimations of the parameters, $\hat{\theta}$, based on the dataset likelihood to prior estimations of the parameters ($\pi(\theta)$). A likelihood function ($\mathscr{L}$) is expressed to adjust a dataset to a model containing $x$ independent variables and $\theta$ parameters, in the light of *prior* distributions. The likelihood combines joints estimates to approximate the posterior probability of the parameters ($\theta$) given the observations ($y$): $p(\theta|y)$. $y$ denotes the vector ($n$ x $\mathbb{1}$) of $n$ observations and $\theta$, the set of $k$ parameters we want to estimate.

According to Bayes theorem:

$p(\theta|y) = \frac{p(y,\theta)}{p(y)}$, its conjugate $p(y|\theta) = \frac{p(y,\theta)}{\pi(\theta)} \Leftrightarrow p(y,\theta) = p(y|\theta).\pi(\theta)$

This theorem yields to $p(\theta|y) \propto p(y|\theta).\pi(\theta)$. The normalisation denominator factor $\frac{1}{p(y)}$ correspond to the integration constant with: $p(y) = \int_\theta p(y|\theta)p(\theta)d\theta$. The likelihood function is defined by $\mathscr{L}(\theta, y) = p(y|\theta) = \prod_{i=1}^{n} p(y_i|\theta)$. If both belong to an exponential family, the log-transformed likelihood ($l$) and prior are used to simplify algebraic expressions and the *posterior* becomes:

$$p(\theta|y) \propto l(y|\theta) + \mathscr{L}og(\pi(\theta))$$

For the normal density distribution $\mathscr{N}(\mu, \Sigma)$, maximizing the likelihood of the data, given a model $f(\theta, x)$, and the log-likelihood $l(y|\theta)$ is equivalent to maxizing:

$$\mathscr{L}og(\prod_{i=1}^{n} p(y_i|\theta)) \propto \sum_{i=1}^{n} log_e(exp(-0.5(y - \eta(\theta, x))\Sigma^{-1}(y - \eta(\theta, x)))) \propto -\sum_{i=1}^{n}(y - \eta(\theta, x))^2$$

The last expression corresponds to the negative sum of residuals between observations and model predictions, which is known as the least-square approach. In the simple case of a linear regression, the adequacy of the model, defined as $\eta(\theta, x) = \beta_0 + \beta_1 x$ with $\vec{\theta} = (\beta_0, \beta_1)$, to data will partially depend on the sum of $(y - (\beta_0 + \beta_1 x))^2$. In the best scenario, this might lead to an analytical solution of the posterior probability (with $p(y)$ still missing) or at least greatly facilitate its numerical approximation. Whereas exploring the entire states of possible parameters and their combinations ($\Theta^k$ possibilities) quickly represent an extensive computation. Although it would lead to the accurate numerical approximation of the integral $\int_\theta p(y|\theta).\pi(\theta)d\theta$.

The Markov Chain Monte Carlo (MCMC) approach (Gelfand and Smith, 1990) simulates the set of parameters, which are now considered as random variables from the conditional probability distribution to approximate the posteriors distributions. When

the *priors* are unknown, the distributions of the parameters can be estimated by non-parametric bootstraps.

The Monte Carlo Markov Chain approach

A Markov chain contains an ordered sequence of dependent random variables ($\theta$) $X^{(0)}, X^{(1)}, ..., X^{(t-1)}, X^{(t)}$ where the probability distribution of $X^{(t)}$ depends only on $X^{(t-1)}$. The conditional distribution of $X^{(t)}|X^{(t-1)}, X^{(t-2)}, ..., X^{(0)}$ is thus reduced to the transition kernel $P(X^{(t)}, X^{(t-1)}) \sim X^{(t)}|X^{(t-1)}$. In MCMC, a targeted density, $f$, is explored from a sequence of simulated candidates of parameters. The kernel is therefore defined by the ratio of posterior probabilities of a proposal set of parameters generated according to prior probabilities and the previous set of parameters:

$$P(X^{(t+1)}, X^{(t)}|y) \sim \frac{P(X^{(t+1)}|y)}{P(X^{(t)}|y)} \sim \frac{\mathscr{L}(X^{(t+1)}).\pi((X^{(t+1)}))}{\mathscr{L}(X^{(t)}).\pi((X^{(t)}))} \tag{C.1}$$

Monte Carlo refers to the stochastic decision process of acceptance/rejection of the new proposal given this ratio to avoid local convergence. The Metropolis-Hastings algorithm (Metropolis *et al.*, 1954; Hastings *et al.*, 1970) is one example of the MCMC method. With explicit formulation of parameters *priors* ($\pi$) and the *log-likelihood* ($l$), the MH algorithm will execute the following steps:

1. Set the initial set of values of the chain, $X^{(0)}$. If the Markov Chain is *recurrent*, its convergence becomes independent of the set of initial values.

2. Simulate a new candidate of parameters from *priors* distributions: $X^{(t)} \sim \pi(\theta)$

3. Calculate the log of the posterior probability $p(X^{(t)}|y) \propto l(y|X^{(t)}) + \mathscr{L}og(\pi(X^{(t)}))$

4. Compare with the previous estimate to estimate the transition kernel $p(X^{(t)}, X^{(t-1)}|y) = (l(y|X^{(t)}) + \mathscr{L}og(\pi(X^{(t)}))) - (l(y|X^{(t-1)}) + \mathscr{L}og(\pi(X^{(t-1)})))$

5. Proceed to the stochastic decision of acceptance/rejection:

   - If $p(X^{(t)}, X^{(t-1)}|y)>0 \Leftrightarrow \frac{\mathscr{L}(X^{(t)}).\pi((X^{(t)}))}{\mathscr{L}(X^{(t-1)}).\pi((X^{(t-1)}))}>1 \Leftrightarrow P(X^{(t)}|y)>P(X^{(t-1)}|y)$, accept the new candidate

   - If $p(X^{(t)}, X^{(t-1)}|y)<0$, accept the proposal with a probability equal to $P(X^{(t)}, X^{(t-1)}|y)$

6. Repeat steps 2-5 until convergence of the chain $X$

The MCMC is used to approximate the true posterior distribution, the mode of the set of parameters and their uncertainties.

Expectation Maximisation algorithm

For some classes of linear models, the structure of the data is not complete. The marginal likelihood may be estimated given some fixed values of parameters. The Maximum Likelihood Estimation may converge by an iterative algorithm which includes the expectation ($E$) and maximisation ($M$) steps. The $E$ step is used to evaluate the expectation of the log-likelihood based on the current estimate for the parameters. The $M$ step is used to find the set of parameters which maximise this log-likelihood. Mixed models and mixture models are two classes of model that may be inferred by EM algorithm. An example of MCEM algorithm, working with the software JAGS (Plummer, 2003), is given in Chapter 7.

Mixture of Models

The mixture model is defined for $n$ response observations, $y = (y_1, y_2, y_3, ..., y_n)$, realisations of random variables $Y = (Y_1, Y_2, Y_3, ..., Y_n)$ with exponential family distribution and latent classes $K$. With this class of model, we consider that the heterogeneity/complexity of the observed response variable $Y$ result from the presence of $K$ distinct subpopulations. The approach merges the bases of parametric and non-parametric inferences by considering that the distribution of interest is a linear combination of $k$ independent distributions. Considering that the true density of the observations is derived from a set of density distributions of the same family, exponential for numerical purpose, it follows:

$f(y) \backsimeq \sum_{k=1}^{K} p_k f(y|\theta_k)$ with $\sum_{k=1}^{K} p_k = 1$

This approximation is a weighted sum of distributions components, of $p_k$ mixture proportions and $\theta_k$ parameters. Mixture components, $f(y|\theta_k)$, are locally representative of the true observations distribution. A mixture add complexity to single linear models that favour the adequacy between the model and the observations. The structure of the data is not complete since the full distribution of observations requires to know *a priori* the probability of observing $y_i$ given that observation $i$ belong to the class k ($z_{ik}$):

$f(y|z)$ become $\sum_{i=1}^{k} p_{k|z} f(y|\theta_{k,z})$ with $z_{ik}$=1 if $y_i$ belong to the class $k$ and 0 if not.

Or we do not know the class the observation belong to before the inference. The marginal likelihood is known given that $z_{ik} = 1$:

$f(y_i|z_{ik} = 1) = f_k(y_i)$ with f, a density distribution from the exponential family.

and the full likelihood of the mixture:

$$\begin{aligned}
\mathscr{L}(y) &= \prod_{i=1}^{n} f(y_i|z_i = \prod_{i=1}^{n}\prod_{k=1}^{K} f_k(y_i|z_{ik}) = \prod_{i=1}^{n}\prod_{k=1}^{K} f_k(y_i|z_{ik} = Z_{ik}) \\
&= \prod_{i=1}^{n}\prod_{k=1}^{K} (f_k(y_i|z_{ik} = 1)P(Z_{ik} = 1))^{z_{ik}} = \prod_{i=1}^{n}\prod_{k=1}^{K} (f_k(y_i|z_{ik} = 1)p_k)^{z_{ik}} \qquad \text{(C.2)} \\
l(y) &= \sum_{i=1}^{n}\sum_{k=1}^{K} z_{ik} log_e(p_k) + \sum_{i=1}^{n}\sum_{k=1}^{K} z_{ik} log_e(f_k(y_i|z_{ik} = 1))
\end{aligned}$$

## D.0 Growth rates estimations

When individuals of a planktonic population display distinct physiological states, driven by the asynchronous entertainment of the cell cycle, growth models need to explicitly describe all possible states, their probability of observations and transitions. In a population, the net growth rates results from the sum of various individuals reproduction rates (Brand *et al.*,1981b; Rynearson and Armburst, 2000). The more the population is asynchronous, the more important is the good representation of multiple stages to predict its growth. Intraspecific genetic diversity is a major actor of individual fitness and might directly influence population growth rates by about 70% (Brand, 1980; Brand *et al.*,1981b; Koester *et al.*, 2003; Boyd *et al.*, 2013; Thomas, 2013; Collins *et al.*, 2014 and ref within). The following paragraph presents population models build to predict phytoplankton *in situ* growth rates. Models are based on the direct observations of abundance (Lagrangian model), on the variation of individual size (size-structured population) or on the variation of the number of DNA copies (cell cycle) (Fig. D.1).

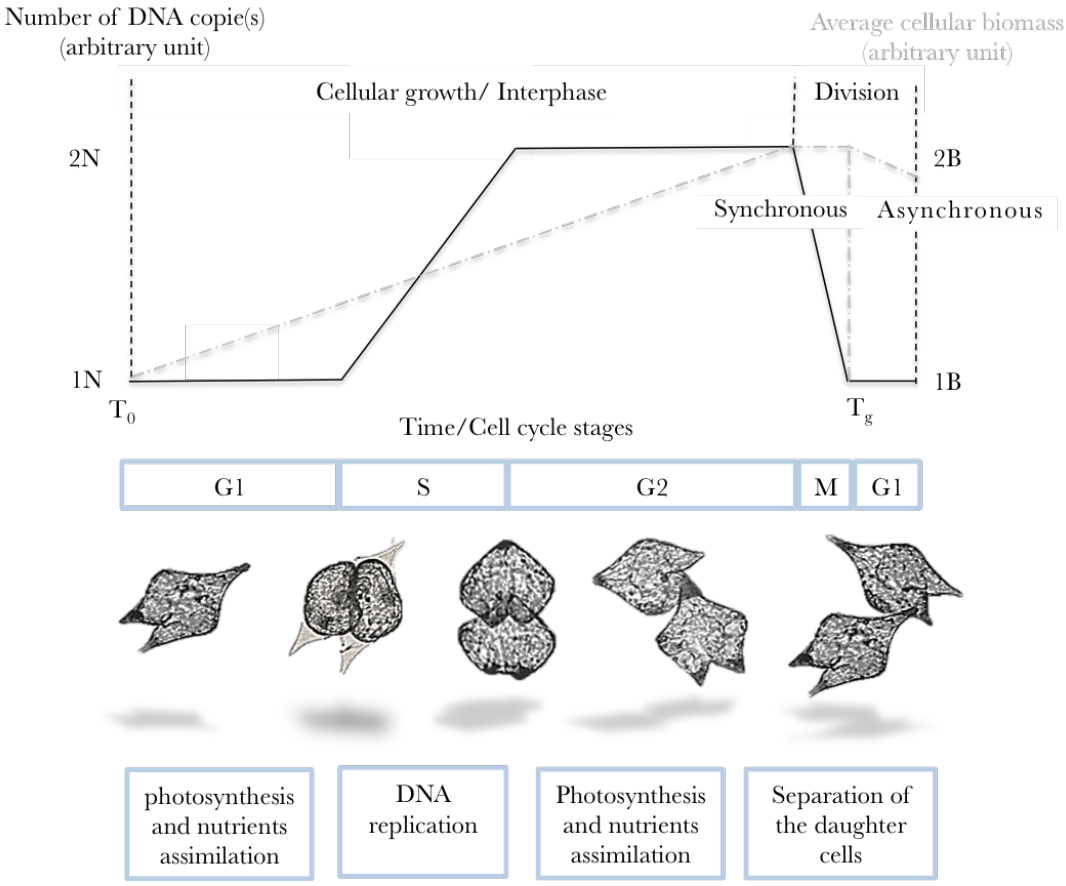


Figure D.1: Influence of the cell cycle on the individual size and number of DNA copies

Cell cycle method

The cell cycle method is currently derived from the mitotic index model introduced in 1982 (McDuff and Chisholm, 1982). The approach relies on the evaluation of the changes of fractions of cells in each stage of the cell cycle. The stages are differentiated by the individual amount of DNA. For a normalised number of DNA copies (c), the $1^{st}$ *Gap* ($G1$) contains new daughter cells with $c$ DNA copies. In the following stage, cells' DNA is duplicated to $2c$. Cells keep $2c$ DNA up to the final stage of $Mitosis$, the cytokinesis ($G2 + M$). The diagram of DNA copies across the cell cycle is illustrated in Figure D.1.

The mitotic index indicates the fraction of cells in the terminal stage of the cell cycle $M$:

$$f_M = \frac{N_M(t)}{\sum_g N_g(t)} \tag{D.1}$$

Cells that accomplished the $G2 + M$ stage are bound to divide into two daughter cells. The fraction of cells in the terminal event expresses a population growth rates:

$$\mu = \sum_t \frac{1}{n.t_d} log_e(1 + f_M(t)) \tag{D.2}$$

$\mu$: Daily growth rates, n: number of terminal events in 1 day, $t_d$: duration of the terminal event, $f_M$: mitotic index

Since $G2$ and $M$ are not clearly distinct by c, Carpenter and Chang (1988) substituted the terminal event by the sum of $G2$ and $M$. The general mitotic index is extended to $f_{G2+M}$. They used the time lag between the observation of the maximum fraction in $S$ and in $G2 + M$ to determine the duration of the terminal event, with the following assumptions:

1. At initiation, cells spend a undetermined duration, subject to environmental stress, in the stage $G_0$
2. Upon the circadian clock, a proportion $\phi(t)$ of cells is released in $G_1$ which is modelled by discrete compartments $1, 2, ..., g_1$
3. In $G_1$, cells are bound to travel up to the $G_2 + M$ stage at constant rate $\nu$, passing by small discrete compartments of the stage $S$ $(g_1 + 1, ..., g_1 + s)$ and the stage $G_2$ $(g_1 + s + 1, ..., g_1 + s + g_2)$
4. In compartment $k$, the effective cytokinesis occurs and the two daughter cells are back to $G_0$

The temporal variations of cells in each compartment is predicted by the derivatives:

$$\begin{aligned} \frac{dn_0}{dt} &= 2\nu n_k - \phi n_0 \\ \frac{dn_1}{dt} &= \phi n_0 - \nu n_1 \\ \frac{dn_i}{dt} &= \nu(n_{i-1} - n_i) \end{aligned} \tag{D.3}$$

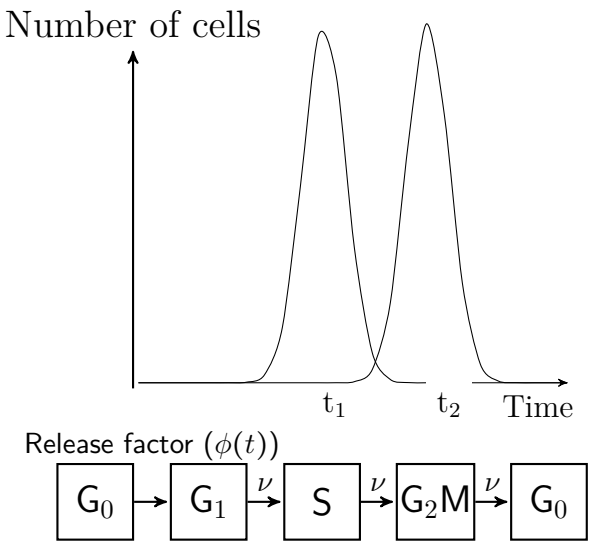


Figure D.2: Multiple stages compartments in the cell cycle model. At $G_0$, a cohort of cells is released with a factor $\phi(t)$ to the stages $G_1$, $G_2$ and $G_{2+M}$ of the cell cycle. Cells pass the different stages at the same rate ($\nu$). The mode of the cells cohort in stage $S$ is observed at $t_1$. The model of the cells cohort in stage $G2+M$ is observed at $t_2$

The model predicts the position of a cohort of cells released from $G_0$. An illustration is given in Figure D.2. Since the cohort is represented by a Normal distribution of cells with the mean corresponding to the comportment at time $t$, $n_{j-a}(t) = n_{j+a}(t)$.

For cells in stage $S$, the total number of cells is equal to $\sum_{i=g_1+1}^{g_1+s} n_i(t)$. The same goes for cells in $G_2 + M$: $n_{g_2+m} = \sum_{i=g_1+s+1}^{g_1+s+g_2+m}$. If their respective derivatives at mode are observed at time $t_1$ and $t_2$, we deduce:

$$\begin{aligned} &\left[\frac{dn_s}{dt}\right]_{t=t_1} = 0 \\ &\sum_{i=g_1+1}^{g_1+s} \frac{dn_i(t_1)}{dt} = 0 \\ &\nu[n_{g_1}(t_1) - n_{g_1+s}(t_1)] = 0 \\ &n_{g_1}(t_1) = n_{g_1+s}(t_1) \end{aligned} \tag{D.4}$$

Recalling the equivalence due to the distribution symmetry ($n_{j-a}(t) = n_{j+a}(t)$), equation (D.4) is used to determine the compartment at which the mode is observed:

$$\begin{aligned} &g_1 = j - a \text{ and } g_1 + s = j + a \\ &j = g_1 + 0.5s \end{aligned} \tag{D.5}$$

The compartment at which the mode $G_2 + M$ is observed is $h = g_1 + s + 0.5(g_2 + m)$. Since cells travel at a constant rate $\nu$, we deduce:

$$\begin{aligned} t_2 - t_1 &= \frac{h - j}{\nu} \\ t_2 - t_1 &= \frac{s}{2\nu} + \frac{g_2 + m}{2\nu} \end{aligned} \tag{D.6}$$

Since the duration of $S$ is $t_S = \frac{s}{\nu}$ and the duration of the $G_2 + M$ is $t_{G_2+M} = \frac{g_2 + m}{\nu}$, The terminal event grouping $S$ and $G_2 + M$ has a duration of :

$$t_d = 2(t_2 - t_1) \tag{D.7}$$

The modes observed for the absolute number of cells in $S$ $(t_1)$ and $G_2 + M$ $(t_2)$ respectively are preserved for the observation of fractions ($f_S$ and $f_{G_2+M}$):

$$\begin{aligned}
&f(t) = \frac{n(t)}{N(t)} \\
&\frac{df(t)}{dt} = \frac{d\left(\frac{n(t)}{N(t)}\right)}{dt} \\
&\frac{\frac{dn(t)}{dt}N(t) - n(t)\frac{dN(t)}{dt}}{N(t)^2} \\
&\frac{1}{N(t)}\left[\frac{dn(t)}{dt} - \frac{n(t)}{N(t)}\frac{dN(t)}{dt}\right] \\
&\frac{1}{N(t)}\left[\frac{dn(t)}{dt} - f(t)\mu(t)\right]
\end{aligned} \tag{D.8}$$

At t=$t_1$, $\frac{dn(t)}{dt}$=0 and $\frac{dN(t)}{dt}$=0 since the cohort has not passed compartment $k$

Hence, $\left[\frac{df_s}{dt}\right]_{t=t_1} = 0$

For a terminal event $S + G_2 + M$, the daily growth rates is measured by:

$$\mu = \sum_t \frac{1}{n.2(t_2 - t_1)} log_e(1 + f_{S+G_2+M}(t)) \tag{D.9}$$

$\mu$: Daily growth rates, n: number of terminal events in 1 day, $t_1$: timing of the observation of mode in $S$, $t_2$: timing of the observation of mode in $G_2 + M$, $f_{S+G_2+M}$: fraction of cells in $S + G_2 + M$

Size-structured population model

The asexual division, i.e. mitosis, is the stage that marks the production of two daughter cell whose size is divided by a factor 2. Unless zygotes are formed through sexual reproduction by the fusion of gametes, the multiplication of population is dependent of asexual division only and follows an exponential growth over the time course, in the absence of trophic constraints and/or physical transport. Using the fraction of cells undergoing mitosis, $f$, the daily growth rates is expressed as:

$$\begin{aligned}
f(t) &= \frac{N(t + t_d) - N(t)}{N(t)} \\
\mu(t) &= \frac{1}{t + t_d} log_e\left(\frac{N(t + t_d)}{N(t)}\right) = \frac{1}{t + t_d} log_e(1 + f(t))
\end{aligned} \tag{D.10}$$

$f(t)$: fraction of cells undergoing mitosis, N(t): abundance at time $t$, $t_d$: duration of cytokinesis

During the cell cycle, the increase of abundance co-occurs with the decrease of cellular size after mitosis. Cells transit in the different size classes upon a circadian clock regulating the cell cycle. Based on this indicator, the diel size pattern is used to estimate *in situ* growth rates independently of cell abundance. Explicitly formulated, the model unravels and quantify the relationship between a cell cycle happening in controlled conditions and the high frequency observations of size variation.

The publication of Sosik et al. (2003) described the fundamental mechanisms used in this approach. The diel variations of size histograms are measured by flow cytometry with the size classes ($\vec{v}$):

For i in 1, 2, ..., m $\vec{v} = v_1 2^{(i-1)\Delta v}$

The absolute number of cells ($\vec{N}$) and proportions of cells ($\vec{w}$) are counted during 24 hours to follow the transitions of cells in each size class. Following Sosik et al. (2003), the transitions account for mitotic division, with a probability $\delta$ and cellular growth, with a probability $\gamma$. An illustration of the transitions between size classes is given in Figure D.3.

The cellular growth is progressive. It is a process that allows cells to go in the superior size class when they receive sufficient light irradiance. Its probability is a bounded (0-1) function of light intensity (E):

$$\gamma(t) = \gamma_{max}\left[1 - exp\left(-\frac{E}{E^*}\right)\right] \tag{D.11}$$

$\gamma$: proportions of cells growing, $\gamma_{max}$: maximum proportion of cells, E: irradiance, E*: normalising constant

Since cells of size $v_m$ cannot reach a size superior, the odds of cellular growth at $v_m$ is null.

The mitotis marks the sudden division of cell size by a factor 2. It is a process that engender two daughter cells, hence the doubling of the absolute number of cells. Its probability is a bounded (0-1) function of time ($t$) and cell size ($v$):

$$\delta(t, v) = \delta_{max}\mathcal{N}(\mu_v, \sigma_v)\mathcal{N}(\mu_t, \sigma_t) \tag{D.12}$$

$\delta$: proportions of cells entering cytokinesis, $\delta_{max}$: maximum proportion of cells entering cytokinesis, $\mu_v$: mean of the size Normal distribution, $\sigma_v$: standard deviation of the size Normal distribution, $\mu_t$: mean of the time Normal distribution, $\sigma_t$: standard deviation of the time Normal distribution

Since cells size must be above $2v_1$ to be able to effectively divide, the odds of division for cells of size $v_1, v_2, ..., v_{j-1}$ are null, with :

For i in j, ..., m, j=1+1:Δ v $\frac{v_{i+1:\Delta v}}{v_i} = \frac{v_1 2^{(i+1:\Delta v-1)\Delta v}}{v_1 2^{(i-1)\Delta v}} = 2^{i\Delta v+1-\Delta v-i\Delta v+\Delta v} = 2$

The model considers populations to be asynchronous. If at each time step, a given proportion of cells are dividing while another may be growing, the model should also take into account the process of size stasis. This process is for cells that stay in their size class between time step projection. Its probability is retrieved from $\gamma$ and $\delta$, by counting the proportions of cells which did not divide nor grow.

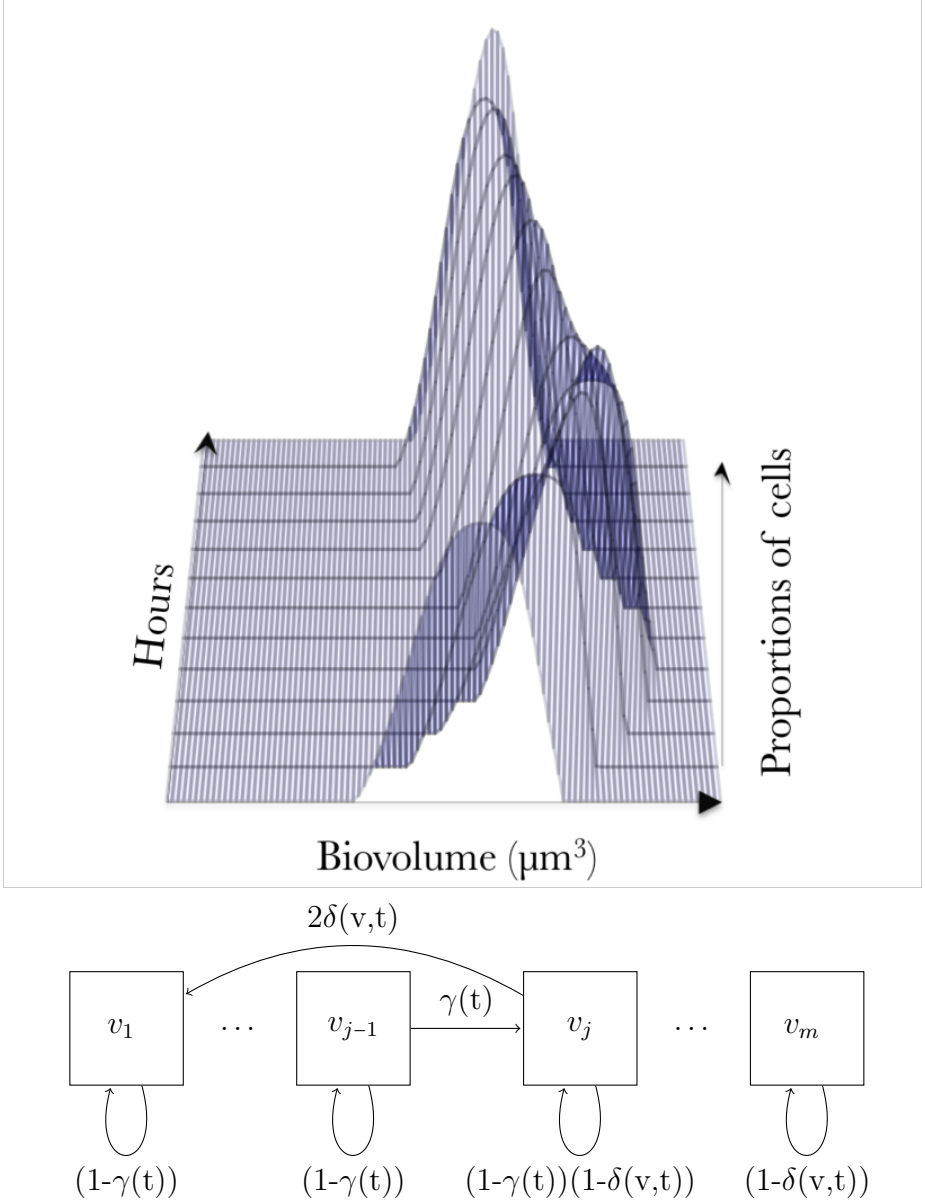


Figure D.3: Top panel: Diel variation of size distribution. Bottom panel: Transitions between size classes. $\delta$ is the probability of cell division. $\gamma$ is the probability of cellular growth. j=1+1:$\Delta$ v .

Individual transitions are summarised by the following set of equations:

$$N_{|v=v_1}(t+dt) = (1-\gamma(t)).N_{|v=v_1}(t) + 2\delta(v_j,t).N_{|v=v_j}(t)$$

$$N_{|v=v_j}(t+dt) = (1-\gamma(t))(1-\delta(v_j,t)).N_{|v=v_j}(t) + \gamma(t).N_{|v=v_{j-1}}(t) + 2\delta(v_{j+1:\Delta v},t).N_{|v=v_{j+1:\Delta v}}(t)$$

$$N_{|v=v_m}(t+dt) = (1-\delta(t)).N_{|v=v_m}(t) + \gamma(t).N_{|v=v_{m-1}}(t)$$

The initial size distribution is projected across the day by the set of parameters, $\hat{\theta}$ which maximise the likelihood of the Gaussian error function:

$$\hat{\theta} = argmin([\vec{w} - \vec{w}(\hat{\theta})]^2) \tag{D.13}$$

While the variation of absolute concentration of cells is penalised by the losses processes in the Sea, the size-structured population model uses the predictions of absolute cells abundance by temporal projection:

$$\mu(t) = \frac{1}{t + t_d} log_e \left( \frac{\hat{N}(t + t_d)}{N(t)} \right) \tag{D.14}$$

Lagrangian trajectories

Phytoplankton cells are drifting in the Sea. They are impacted by the dynamics and the physical scales that structure the flow of water. The vertical parcels of water are constrained by density gradients. Within these parcels, several processes contribute to the spatial heterogeneity observed in populations.

The oceanic circulation is influenced by gradients of density, the coriolis force, the tides, the wind etc.. These forces drive the flow along simple trajectories, according to the currents speed components: U=$u, v, w$. In the Sea, any trajectory is eventually deviated from its axis under the action of turbulence. Without a small level of turbulence, phytoplankton would not persist in the euphotic layer. Cells would sink with a speed proportional to the squared size (Stokes law).

Turbulence may have been the main forcing that drove the evolution of phytoplankton phenotypes towards the optimisation of their residence in the euphotic layer (Margalef, 1978). It also plays a major role in shaping the patchy distribution of phytoplankton at small spatial scales. Brownian motions might represent the turbulence in 3D scales and plankton displacements. Since they are very complex, turbulent trajectories are predicted by stochastic models (Siegel et al., 2003).

Lagrangian models are a class of stochastic models attached to predict the probability distributions of planktonic organisms. In practice, models predict the path of plankton to determine the dispersal kernel. *In situ*, Lagrangian models are used to predict plankton growth rates by following the parcel of water they inhabit. Since these models integrate directly the physical processes that redistribute organisms in space, populations growth rates are simply corresponding to the rate of changes of any biomass indicator (e.g. cells abundance, chlorophyll a concentration), $\partial C(x,t) : \partial t$.

The approach was combined to automated flow cytometry in the context of DeWEX (Chapter 4). To satisfy our a priori on the influence of hydrological gradients on phytoplankton growth, we used a Lagrangian approach to constrain our predictions of group-specific growth rates based on the size-structured population model. Plankton trajectories were propagated from each station of the cruise under the local current circulation derived from satellite altimetry (http://www.aviso.altimetry.fr/). The position of the trajectory along the stream were estimated by:

$$Stream^{x_0}(t) = x_0 + \int_0^t U(x,y,t).dt \tag{D.15}$$

The first objective of the Lagrangian model was to constrain the bayesian clustering of the stations based on temperature, salinity, mixed layer depth and integrated PAR. The illustration of the method is reported in Figure D.4.

The second objective was to compare the growth rates estimations made within the clustered water typology predicted from the size-structured population model and the Lagrangian model. The illustration of the method is reported in Figure D.5.

$$
\begin{array}{c}
 \\
S^{\circ 1}_{t=T_0} \\
S^{\circ 2}_{t=T_0+1\,hour} \\
\vdots \\
S^{\circ 200}_{t=T_0+20\,days}
\end{array}
\begin{array}{c}
\begin{array}{cccc}
S^{\circ 1}_{t=T_0} & S^{\circ 2}_{t=T_0+1\,hour} & \cdots & S^{\circ 200}_{t=T_0+20\,days}
\end{array} \\
\begin{pmatrix}
0 & d(S^{\circ 2}_{t=T_0+1h}, Stream^{T_0 -> T_0+20d}_{t=T_0+1h}) & \ddots & d(S^{\circ 200}_{t=T_0+20d}, Stream^{T_0 -> T_0+20d}_{t=T_0+20d}) \\
\ddots & 0 & \ddots & d(S^{\circ 200}_{t=T_0+20d}, Stream^{T_0+1h -> T_0+20d}_{t=T_0+20d}) \\
\ddots & \ddots & 0 & d(S^{\circ 200}_{t=T_0+20d}, Stream^{T_0+\ldots -> T_0+20d}_{t=T_0+20d}) \\
\ddots & \ddots & \ddots & 0
\end{pmatrix}
\end{array}
$$

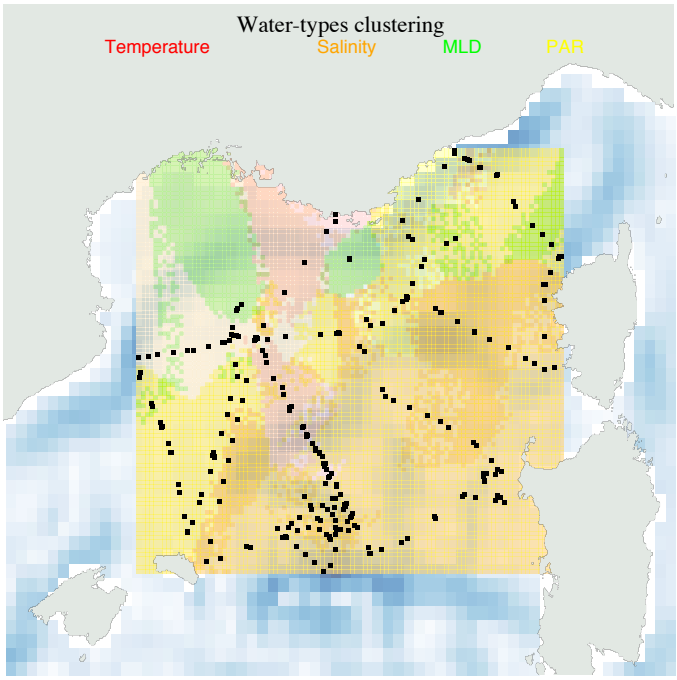


Figure D.4: A Lagrangian-constrained typology of the North Western Mediterranean Waters observed during DeWEX cruises. Top panel: Lagrangian trajectories were used to compute pairwise oceanographic distances between observation stations. Bottom panel: Clustering of water types by Normal mixture model of temperature, salinity, mixed layer depth (MLD) and photosynthetic available radiation (PAR)

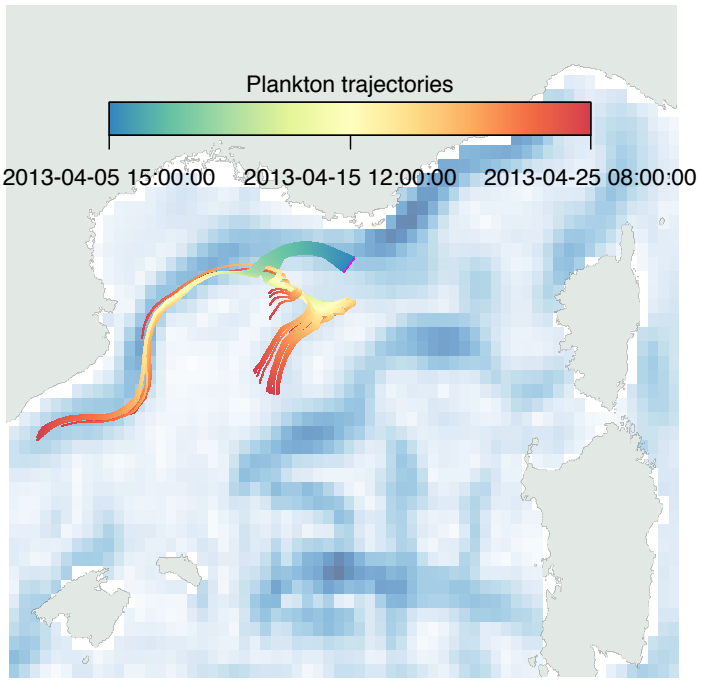


(a) Lagrangian plankton trajectories

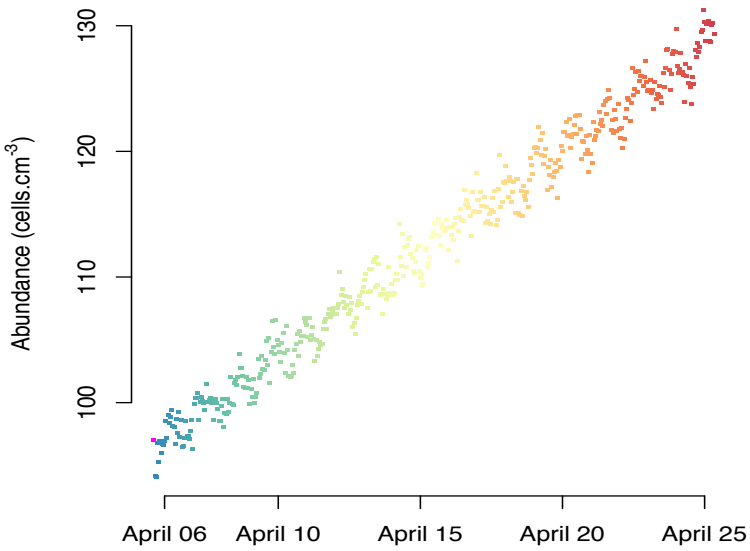


(b) Growth curve of an idealised phytoplankton population along plankton trajectories

Figure D.5: Lagrangian growth rates estimation